Layered Double Hydroxides for Packaging Applications

by

Kanittika Ruengkajorn



This thesis is submitted in partial fulfilment of the requirement for the degree of Doctor of Philosophy at the University of Oxford

Balliol College

October 2017

The work described in this thesis was carried out in the Chemistry Research Laboratory, Mansfield Road, Oxford between October 2014 and October 2017 under the supervision of Professor Dermot O'Hare. All the work is my own unless stated to the contrary, and has not been previously submitted for any degree at this or any other university.

Kanittika Ruengkajorn
Balliol College
October 2017

Abstract

Layered Double Hydroxides for Packaging Applications

Kanittika Ruengkajorn **D.Phil Thesis**
Balliol College **Michaelmas Term 2017**

The primary aim of this thesis is to synthesise and modify layered double hydroxides (LDHs) for using in packaging applications.

Chapter One provides an introduction of the basic manufacturing process of paper-based and flexible packaging and the relevant aspects of using inorganic materials in packaging materials. The principles of gas permeation and the role of two-dimensional platelets on the concept of a tortuous pathway are reviewed. In addition, the structure, synthesis methods and applications of LDHs are presented.

Chapter Two details the synthesis of LDH/cellulose fibre composites and their use as fillers in the papermaking process. The strength and optical properties of the obtained LDH/cellulose fibre based paper sheets are examined. Superhydrophobic organo-LDHs are synthesised and applied as a pigment in a water resistant coating for paper.

Chapter Three describes the novel post treatment for LDHs using aqueous immiscible solvents (AIM solvents). The effect of solvent functional groups and structure, along with some post treatment parameters such as rising volume, dispersion time, Mg/Al ratios, and solvent recycling on physicochemical properties of AIM-LDHs are explored. The interactions between solvents and LDHs *via* hydrogen bonding are investigated using solid state nuclear magnetic resonance spectroscopy (SSNMR).

Chapter Four presents the preparation of LDH nanoplatelets using a reconstruction of layered double oxides (LDOs) in a concentrated aqueous solution of amino acids. The effect of amino acid structure and other highly water-soluble compounds on the textural and chemical properties of the reconstructed LDHs are examined. The LDH nanoplatelets produced are used to formulate water-based dispersions for coating on polyethylene terephthalate films (PET). The effect of LDHs morphology, number of coating layers and loading amount of LDHs in the coating dispersion on an oxygen barrier performance and optical properties of the coated PET films are discussed.

Chapter Five provides an alternative method for preparation of LDH nanoplatelets using direct reconstruction of LDOs in water, water-soluble polymer (polyvinyl alcohol or PVA), and non-aqueous solvents. The effects of calcination temperature, reconstruction time, LDHs morphology, and PVA selection on the structural and physical properties of the reconstructed LDHs were investigated. Finally, the directly reconstructed LDHs are formulated into the coating dispersions and applied on PET films. The oxygen barrier and optical properties of the coated PET films are evaluated.

Details of the experimental procedures performed are included in **Chapter Six**. Supplementary information and data referred to in the main thesis are found in the **Appendices**.

Acknowledgements

Firstly, I would like to thank Professor Dermot O'Hare, who is a great super-duper good supervisor, for allowing me to join his group. I am deeply grateful for his guidance and advice, for supporting in several aspects of my life throughout my study and proof-reading all my chapters.

I must also thank SCG Packaging Thailand for sponsorship. Thanks to my bosses; Mr. Roongrote Rangsiyopash, Mr. Tanawong Areeratchakul, Dr. Pongsuda Pongtanya, and my mentors; Dr. Adisak Vorakunpinij and Mr Taweewat Tripattharanan (P'Wee) for their supports. I am very grateful for the opportunities that have given me. Especially to P'Wee, he is like my big brother who has always helped guiding me professionally and personally.

Huge thanks to Dr. Jean-Charles Buffet (JC) and Dr. Chunping Chen (Chunping), who have help me and bring me back to the academic research again. To JC, who I respect as a boss and a big brother, he has always supported me either in research and life, provided brilliant discussion on my work every month and proof-read all my chapters. To Chunping, who is my first friend in Oxford and my mentor, who introduced me to the world of LDHs and taught me everything about LDHs, who is always happy to answer questions.

I must thank Dr. Nick Rees for running SSNMR samples and providing me with tons of ska music; Chris for NMR titration for surface hydroxyl concentration Dana for spending her time at least a day helping me to calculate the LDH formula in the Chapter Four and Five; Jingfang for discussions on barrier project. Sincere thanks to all who have helped with many instruments: Dr. Robert Jacob for TGA and contact angle measurement training; Chunping for BET and FTIR training; Jingfang for cross-section TEM and AFM; Dr. Katie Cunnea and Dr. James Gilchrist with TEM and SEM at Harwell campus; Dr Kerstin Jurkschat for help with the zetasizer; all my colleagues at Product and Technology Development Center (PTDC), SCG Packaging PLC, Ratchaburi, Thailand for always helps and supports.

In particular, huge thanks to these people who have spent their time to proof-read this thesis (Dermot, JC, Chunping, Sandy, Haohong, Jingfang, Dana, Jess, Katarina, Valentine), their suggestions have made this a great art piece. I must thank SCG Chemicals team for kind supports, which I am deeply appreciated this. I have been fortunate to work with such inspiring people in the O'Hare group, past and present, who have made this place such a colourful and happy working environment. Chunping for inviting me to her house for Chinese hot pot and for her little boy, Jinyang, the 1st birthday party; Dana, Jingfang, and Haohong for helpful discussions and for having lunch (and beer) daily; Chris for always baking amazing cakes; Sandy for inviting me to the high table at Wadham; Golf for being a nice brother; Katarina for being an amazing Part II student and The Loopy Whisk; Duncan for beer at the uniclub; Tom R for my birthday caterpillar cake; Jess, Tom W, Joyce, Justin for entertaining in S4; To all my Oxford friends who have spent hard and fun time together: Valentaine, Dia, Nun, Guun, Insun, Helen, Korbua, Golf, Kwang (Nat), Pek, Kukkik, Pui, and Peace.

Finally, I am hugely grateful to my beloved family for their unconditional love and inspiration. To my husband, Al, thanks for his sacrificing to take care our little girl, Kant, who is simply an amazing daughter, who is an entertainer for our family. To my parents and my brother, for their love and encouragement. I love you all so much.

Abbreviations list

°C	degrees Celcius
Å	Ångström, 10^{-10} m
AFM	atomic force microscopy
Ala	alanine
AIM-LDH	aqueous immiscible organic solvent treated layered double hydroxide
AIOST	aqueous immiscible organic solvent treatment
AMO-LDH	aqueous miscible organic solvent treated layered double hydroxide
AMOST	aqueous miscible organic solvent treatment
ASTM	American Society for Testing and Materials
α_{OH}	hydroxyl number
atm	atmosphere, 101,325 Pa
BABA	beta-aminobutyric acid
BET	Brunauer-Emmett-Teller
BJH	Barrett-Joyner-Halenda
bp	boiling point
CA	contact angle values
CDL	crystallite domain length
CMC	critical micelle concentration
Cop	co-precipitation
CP/MAS	cross polarisation magic angle spinning
δ_{OH}	hydroxyl density
DP/MAS	direct polarisation magic-angle spinning
DRC	direct reconstruction
DS	dodecylsulfate
DTG	derivative thermogravimetric
EA	elemental analysis
EDS	energy dispersive X-ray spectroscopy
FTIR	fourier transform infrared
FWHM	full width half maximum
GABA	gamma-aminobutyric acid
Gly	glycine
h	hour

HEC	hectorite
HT	hydrothermal
ICP-MS	inductively coupled plasma mass spectrometer
ISO	International Organization for Standardization
IUPAC	International Union of Pure and Applied Chemistry
LbL	layer-by-layer
Leu	leucine
LDH	layered double hydroxide
LDO	layered double oxide
LR	laurate
MMT	montmorillonite
M_w	weight-average molecular weight
NMR	nuclear magnetic resonance
organo-LDH	organophilic layered double hydroxide
OTR	oxygen transmission rate
PET	polyethylene terephthalate
Phe	phenylalanine
ppm	parts per million
PVA	polyvinyl alcohol
PXRD	powder X-ray diffraction
RH	relative humidity
rpm	revolutions per minute
SEM	scanning electron microscopy
SR	stearate
TAPPI	Technical Association of the Pulp and Paper Industry
TEM	transmission electron microscopy
U	urea or urea method
UHT	urea hydrothermal
WVTR	water vapour transmission rate

Table of contents

Chapter One – Introduction 1

1.1. Packaging materials and fillers used 1

1.1.1. Use of fillers in paper and paper-based packaging 1

1.1.2. Use of fillers in flexible packaging 4

1.1.3. Gas permeation 6

1.1.4. The use of platelet materials in barrier coating for packaging applications 9

1.2. Layered double hydroxides (LDHs) 9

1.2.1. Structure of layered double hydroxides 10

1.2.2. Synthesis methods of LDHs 12

1.2.3. Applications of LDHs 20

1.2.4. LDHs used in packaging applications: 21

1.3. Aim of the thesis 22

Chapter Two – Synthesis and application of LDHs in papermaking and coating 24

2.1. Introduction 24

2.2. *In situ* synthesis of LDH/cellulose fibre composites 25

2.2.1. Effect of fibre pretreatment solution 25

2.2.2. Effect of fibre pretreatment time 31

2.2.3. Synthetic methods 32

2.3. LDH/cellulose fibre composites as a filler in papermaking 43

2.3.1. Preparation of paper 43

2.3.2. Effect of LDH/cellulose fibre composites on paper properties 44

2.4. Synthesis of functional LDHs for use in paper coating 50

2.4.1. Synthesis of organo-LDHs by co-precipitation method 50

2.4.2. Preparation of organo-LDHs by urea hydrolysis method 55

2.4.3. Application of LDHs to paper coatings 60

2.5. Conclusions 64

Chapter Three – Aqueous Immiscible Organic Solvent Treatment of Layered Double Hydroxides 66

3.1. Introduction 66

3.2. Effect of solvent washing on flower shape like $Mg_4Al\text{-}CO_3$ LDHs 69

3.2.1. Structural characteristics 70

3.2.2. Surface properties 71

3.2.3. Densityc74

3.3. Effect of solvent structure (ether and ketone solvents) 78

3.4. Effect of dispersion time 80

3.5. The weak hydrogen bonding solvents: effect of their structure and dispersion time 81

3.6. Effect of process parameters 84

3.6.1. Effect of rinsing volume 84

3.6.2. Effect of high speed mixing 85

3.7. The effect of recycled solvent 85

3.8. Effect of Mg/Al ratio at 2, 3, and 4 86

3.9. Effect of solvent washing on platelet like LDHs 87

3.10. Solid state NMR studies 88

3.11. Conclusions 93

Chapter Four – Preparation and application of LDH nanoplatelets 94

4.1. Introduction 94

4.2. Effect of amino acid types and LDHs morphology on reconstruction of LDHs 96

4.2.1. Reconstruction using amino acids with nonpolar side chains 97

4.2.2. Effect of LDH morphology on reconstruction of LDHs 107

4.2.3. Effect of other types of amino acid on reconstruction of LDHs 111

4.3. Effect of highly water soluble compounds 115

4.4. Barrier performance of amino acid reconstructed LDHs 118

4.4.1. Effect of amino acid, LDHs morphology and number of coating layer on barrier performance 119

4.4.2. Effect of the types of amino acids 129

4.5. Conclusion 130

Chapter Five – Direct reconstruction of layered double hydroxides and their use in barrier coatings 132

5.1. Introduction 132

5.2. Reconstruction behaviour of LDHs in water and non-aqueous solvents 133

5.2.1. Effect of calcination temperature on reconstruction behaviour in water 133

5.2.2. LDO reconstruction in non-aqueous solvents 150

5.2.3. Effect of the LDHs morphology on the reconstruction behaviour in water 152

5.2.4. Effect of the reconstruction conditions on reconstruction behaviour in water 157

5.3. Reconstruction behaviour of LDHs in PVA 161

5.3.1. Effect of calcination temperature on reconstruction behaviour in PVA 162

5.3.2. Effect of the LDHs morphology on reconstruction behaviour in PVA 164

5.3.3. Effect of PVA properties on reconstruction behaviour 165

5.4. Barrier performance of coatings with direct reconstructed LDHs 168

5.4.1. Effect of LDH morphology 169

5.4.2. Effect of calcination temperature on reconstruction behaviour in PVA 170

5.4.3. Effect of adding sequence 172

5.5. Conclusions 175

Chapter Six – Experimental details 176

6.1. Analytical techniques for LDH characterisation 176

6.1.1. X-ray powder diffraction (XRD) 176

6.1.2. Fourier transform infrared spectroscopy (FTIR) 176

6.1.3. Transmission electron microscopy (TEM) 176

6.1.4. Scanning electron microscopy (SEM) 176

6.1.5. Zeta potential and Dynamic light scattering (DLS) measurements 177

6.1.6. Water contact angle measurement 177

6.1.7. Surface area and pore size analysis 177

6.1.8. Thermogravimetric analysis 178

6.1.9. Surface hydroxyl titrations 178

6.1.10. Elemental analysis (EA) 178

6.1.11. Inductively coupled plasma mass spectrometer (ICP-MS) 179

6.1.12. Density 179

6.1.13. Solid state NMR spectroscopy 179
6.2. Analytical techniques for papermaking and paper characterisation 179
6.2.1. Wet-end process parameters measurement 180
6.2.2. SEM (surface and cross-section) for paper 180
6.2.3. Contact angle measurement for coated paper 180
6.2.4. Water vapour transmission rate measurement 181
6.2.5. Paper testing and characterisation 181
6.3. Analytical techniques for coated films characterisation 183
6.3.1. Oxygen transmission rate measurement 183
6.3.2. Optical properties of coated films 183
6.4. Starting materials and chemicals 184
6.5. Experimental details for Chapter Two 184
6.5.1. Mg_3Al-CO_3 LDHs synthesis 184
6.5.2. Fibre pretreatment 185
6.5.3. Preparation of Mg_3Al-CO_3 LDH /Cellulose Fibre composites 185
6.5.4. Preparation of paper sheets and wet-end process parameters measurement 186
6.5.5. Mg_3Al-NO_3-LDH by co-precipitation method 186
6.5.6. Synthesis of organo-LDHs by co-precipitation method 187
6.5.7. Synthesis of organo-LDHs by urea method 187
6.5.8. Water resistant coating for paper 187
6.5.9. Barrier coating for paper 188
6.6. Experimental details for Chapter Three 188
6.6.1. Synthesis of Conventional, AMO and AIM LDHs 188
6.7. Experimental details for Chapter Four 190
6.7.1. Synthesis of LDHs 190
6.7.2. Calcination and reconstruction of LDHs 191
6.7.3. Barrier coating performance of LDHs with different size and commercial clays 191
6.7.4. Barrier coating performance of LDHs with nanoplatelets from amino acid reconstruction 192
6.7.5. Coated films preparation 192

6.8. Experimental details for Chapter Five 192
6.8.1. LDHs used in this study 192
6.8.2. Calcination/reconstruction in water 192
6.8.3. Calcination/reconstruction in non-aqueous solvents 193
6.8.4. Calcination/reconstruction in PVA aqueous solution 193
6.8.5. Coated films preparation 193
References 194
Appendix A – Appendices to Chapter Two A1
A.1 Powder X-ray diffraction data and Crystallinity index of cellulose fibre A1
A.2 Transmission electron microscopy and scanning electron microscopy A2
A.3 Paper properties A3
A.4 Elemental analysis data A4
Appendix B – Appendices to Chapter Three A5
B.1. Characterising data for different solvent-treated LDHs A5
B.1.1. Powder X-ray diffraction A5
B.1.2. N_2 adsorption desorption isotherms A6
B.1.3. BJH desorption pore size distributions A7
B.1.4. Surface properties data A8
B.1.5. Thermogravimetric analysis A9
B.2. Characterising data for different ether and ketone solvents treated LDHs A10
B.2.1. Surface properties data A10
B.2.2. N_2 adsorption desorption isotherms A11
B.2.3. BJH desorption pore size distributions A12
B.2.4. N_2 adsorption desorption isotherms A13
B.2.5. BJH desorption pore size distributions A14
B.2.6. LDHs Formula A15
B.2.7. Transmission electron microscopy A15
B.3. Characterising data for ether solvents treated at different dispersion times A16
B.3.1. Surface properties data A16
B.3.2. LDHs Formula A16

B.3.3. N_2 adsorption desorption isotherms and BJH desorption pore size Adistributions A17
B.3.4. Transmission electron microscopy A18
B.4. Characterising data for weak hydrogen bonding solvents treated LDHs A18
B.4.1. Surface properties data A18
B.4.2. N_2 adsorption desorption isotherms A19
B.4.3. BJH desorption pore size distributions A20
B.4.4. LDHs Formula A21
B.4.5. Transmission electron microscopy A22
B.4.6. Solvation parameters A22
B.5. Characterising data for solvent-treated LDHs with different process parameters A23
B.5.1. Powder X-ray diffraction A23
B.5.2. LDHs Formula A24
B.5.3. Transmission electron microscopy A24
B.6. Characterising data for solvents treated LDHs at after solvent recycling A25
B.6.1. Surface properties data A25
B.6.2. LDHs Formula A25
B.7. Characterising data for solvent-treated on different Mg/Al ratios LDHs A26
B.7.1. LDHs Formula A26
B.7.2. Transmission electron microscopy A26
B.8. Characterising data for solvent-treated platelet like LDHs A27
B.8.1. N_2 adsorption desorption isotherms A27
B.8.2. BJH desorption pore size distributions A27
B.8.3. Surface properties data A28
B.8.4. Powder X-ray diffraction A28
B.9. Solid state NMR spectroscopy studies A29
B.9.1. ^{1}H MAS solid state NMR spectroscopy A29
B.9.2. ^{13}C CP MAS solid state NMR spectroscopy A30
B.9.3. ^{27}Al MAS solid state NMR spectroscopy A31
Appendix C – Appendices to Chapter Four A32

C.1. Solubility data of compounds A32
C.2. Appearance of reconstructed products using nonpolar amino acids A33
C.3. Characteristic data for reconstructed LDHs originated from Cop-AMO LDHs A34
C.3.1. Fourier transform infrared spectroscopy A34
C.3.2. Thermogravimetric analysis A35
C.3.3. LDHs composition data A36
C.4. Characteristic data for reconstructed LDHs originated from UHT-AMO LDHs A37
C.4.1. Powder X-ray diffraction A37
C.4.2. Fourier transform infrared spectroscopy A38
C.5. Appearance of reconstructed products using other compounds A39
C.6. Barrier performance of amino acid reconstructed LDHs A39
C.6.1. Oxygen transmission rate data A39
C.6.2. Scanning electron microscopy A40
C.6.3. Coated film properties A40
Appendix D – Appendices to Chapter Five A42
D.1. Appearance of reconstructed products in water A42
D.2. Characteristic data for reconstructed LDHs in water: Effect of calcination temperature A43
D.2.1. Powder X-ray diffraction data A43
D.2.2. Fourier transform infrared spectroscopy A44
D.2.3. N_2 adsorption desorption isotherms A45
D.2.4. BJH desorption pore size distributions A46
D.2.5. Dynamic light scattering measurement A47
D.2.6. Thermogravimetric analysis A48
D.3. Characteristic data for reconstructed LDHs in water: Effect of the LDHs morphology A49
D.3.1. Powder X-ray diffraction A49
D.3.2. Fourier transform infrared spectroscopy A50
D.3.3. Surface properties data A51
D.3.4. LDHs composition data A52
D.3.5. N_2 adsorption desorption isotherms A53

D.3.6. BJH desorption pore size distributions A54
D.3.7. Thermogravimetric analysis A55
D.3.8. Zeta potential measurement A55
D.4. Characteristic data for reconstructed LDHs in water: Effect of reconstruction conditions A56
D.4.1. Dynamic light scattering measurement A56
D.4.2. Transmission electron microscopy A56
D.4.3. Zeta potential measurement A56
D.5. Characteristic data for reconstructed LDHs in PVA: Effect of calcination temperature A57
D.5.1. Powder X-ray diffraction A57
D.5.2. Fourier transform infrared spectroscopy A59
D.6. Characteristic data for reconstructed LDHs in PVA: Effect of the LDHs morphology A60
D.6.1. Powder X-ray diffraction A60
D.6.2. Transmission electron microscopy A61
D.6.3. Powder X-ray diffraction A62
D.7. Characteristic data for reconstructed LDHs in PVA: Effect of PVA properties A63
D.7.1. Powder X-ray diffraction A63
D.8. Coated film properties A65
D.8.1. Oxygen transmission rate data A65
D.8.2. Coated film optical properties A66

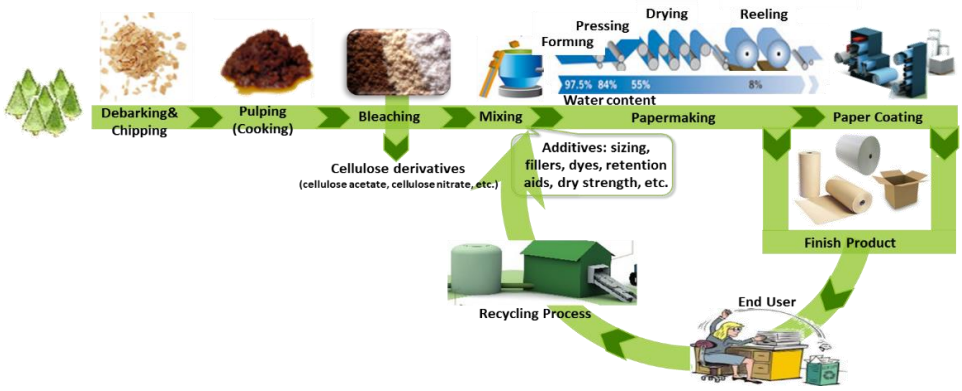
Chapter One – Introduction

1.1. Packaging materials and fillers used

The primary function of packaging is to protect the product during storage and distribution.[1] Generally, the packaging materials can be divided into five main categories: plastic, paper and board, glass, metal and wood.[2] Paper and plastic remain the leader thanks to their light weight and low-cost, the demand for these has greatly increased in the last decade.[3, 4] The expansion of on-line purchase and retail sales is favourable to paper and board packaging, including corrugated containers, paper bags and sacks, folding containers, and others.[5, 6] A trend in the paper business is to use recycled fibre with maintain strength properties. Coating is required to improve surface properties, functionality, and printability. On the other hand, the demand for flexible packaging (paper, plastic, complex/multi-layer materials) is increasing from various industries (e.g. food and beverage, cosmetic, and healthcare). This is primarily because of their high quality, low cost, and high barrier properties making them the most economical method to package, protect and preserve product that need extended shelf life. The future of this type of packaging is promising. Research in this area aims to replace aluminium foil and metallised films due to recycling problems. The trend in high-performance film structures with high barrier properties will dominate the market.[7]

1.1.1. Use of fillers in paper and paper-based packaging

Pulp and paper are manufactured from raw materials containing cellulose fibres, generally wood and recycled paper. The main production processes in pulp and paper are raw material preparation, the pulping process, and the papermaking process (Scheme 1.1).[8]



Scheme 1.1. Schematic representation of the pulp and paper making process.

In the conventional papermaking process, mineral fillers are widely used and directly added into the fibre suspension, surface filling, and surface coating steps to improve the opacity, brightness, dimensional stability, printability, and reduce cost.[9-13] At least 31 million dry metric tons of mineral fillers were used worldwide in 2010 for filling and coating in paper manufacturing industries, as presented in Figure 1.1.[10, 13, 14] It was reported that 13.6 and 16.2 million dry metric tons were used for filling and coating purposes, respectively. The remaining portion was used for other purposes such as pitch (organic contaminants from wood) and stickies (organic contaminants from recycled fibre) removal agent. The main types of mineral fillers for papermaking are calcium carbonate, clay, talc and titanium dioxide, depending on the grade of paper being made and their main functions as summarised in Table 1.1.[10-12, 15] Precipitated calcium carbonate (PCC) has become the mostly used filler whereas ground calcium carbonate (GCC) is the leading material in coating applications of paper.[13] The filler content in paper depends markedly by grades of paper; some contain little or no filler (tissue and milk carton board), in contrast, printing/writing papers usually contain 5-30 percent by mass.[10] Fillers have played a prominent role in manufacture of printing paper, they provide smoothness, opacity, brightness, and gloss which are the requirements for high-end printing papers.[10]

Table 1.1. Summary of fillers used in papermaking process.[10-13, 15, 16]

Filler	Functions
Ground calcium carbonate (GCC)	Improve porosity, water drainage, brightness
Precipitated calcium carbonate (PCC)	Improve gloss and opacity
Kaolin	Provide high density paper and lessen coating Improve ink penetration and high gloss
Talc	Control pitch and sticky in papermaking
Titanium dioxide	High opacity but high price and abrasiveness
Silica	Retention aid in papermaking (colloidal silica) Better ink fixing (inkjet coating)

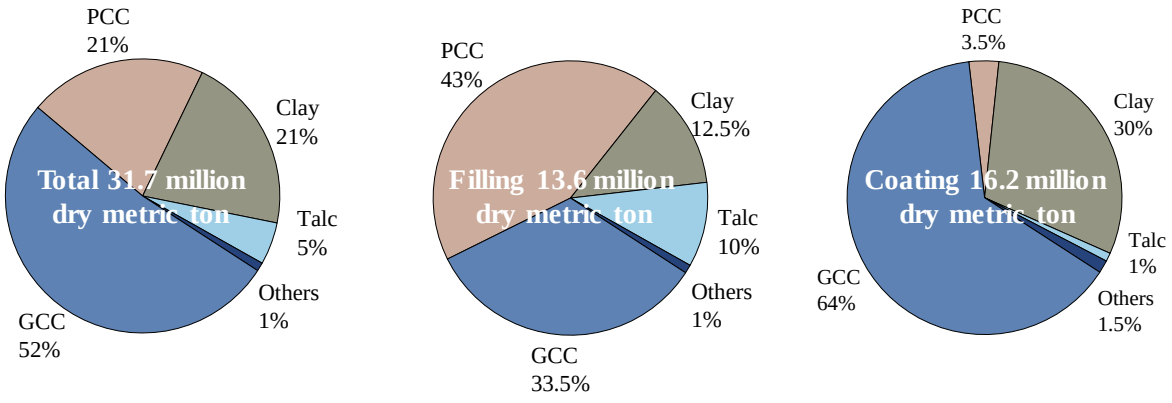


Figure 1.1. Global consumption of mineral pigments in paper and board in 2010.[13]

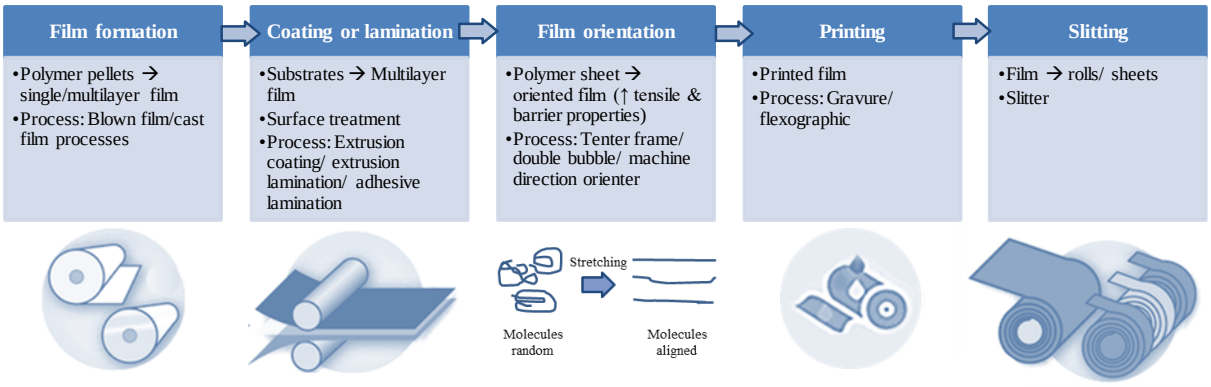
The trend in papermaking today is to increase the filler content and to replace the expensive fibre component, mainly for cost saving. However, strength properties are inevitably decreased by adding fillers due to the reduction of interfiber bonding.[9, 10] Conventional methods are normally performed to increase filler content such as furnish optimisation (fibre composition and refining), filler selection (size and morphology), and chemical utilisation (dry strength additives such as polyacrylamide, quaternary ammonium type cationic starch and tertiary amino type cationic starch). Alternatively, filler preflocculation technology has been introduced to pretreate fillers and to reduce the interference to fibre-fibre bonding.[17] This technique, using pre-flocculation of calcium carbonate, is now widely used in the paper industry.[18, 19]

The surface treatments of paper had been thoroughly explored to control surface properties and functionalise paper, which can be performed by two approaches: surface sizing and surface coating.[20] Surface sizing is mainly employed to improve surface strength and printability of paper. Such process uses aqueous dispersion of starch, carboxy methyl cellulose, polyvinyl alcohol, styrene acrylic acid, and others, or the combination of these materials.[20, 21] Fillers/pigments may be added into the surface sizing dispersion, so called pigmented surface sizing, to improve printability of paper.[20] The coating process differs from the surface sizing due to different formulation and composition, which includes fillers (calcium carbonate, kaolin, titanium dioxide, silica), binders (polyvinyl alcohol, styrene butadiene latex), co-binder (carboxy methyl cellulose), and other additives (dispersant, dyes, lubricant, insolubiliser).[20, 22]

Extensive study had been carried out to enhance surface functionality of paper for specific applications, especially food packaging.[23] Poor barrier properties and sensitivity towards moisture are some of the main challenges facing cellulose-based materials, therefore high-performance packaging utilising cellulose based materials has been developed with strong barrier characteristics. While giving good barrier properties, wax impregnation and extrusion coating using plastic polymer (polyethylene) creates problems with recycling. Alternatively, biopolymers (such as starch, cellulose derivatives, poly(lactic acid)) as well as nanomaterials (such as montmorillonite) have been incorporated to improve barrier properties of paper.[23, 24] Therefore, upgrading to water-based coatings with inorganic materials has become necessary to functionalise paper, which has the potential to add value to the final product.

1.1.2. Use of fillers in flexible packaging

Over the last decades, flexible packaging has grown faster than other packaging materials.[1, 25] Multilayer structure, whereby two or more components are combined to create a single packing structure, drives the growth by allowing better performance with specialised layers. Due to the lightweight nature and more cost-effective production, flexible packaging is replacing some traditional rigid packaging such as metal retort cans, glass bottles and paperboard cartons.[1, 25] Several manufacturing processes can be used to form these structures for a variety of applications.[1, 25, 26] The definition of flexible packaging coined by PCI Films Consulting, '*it embraces the manufacture, supply and conversion of plastic, aluminium foils and papers that are used separately or in combination*',[1] flexible packaging production is part of the converting industry, which is the process of taking thin or flat materials (known as webs) through processing machines (such as laminating, coating, printing and slitting machines) to create an intermediate or finished product. The manufacturing process involves more than one step which may include film formation, orientation, metallisation, lamination or coating, printing, winding and slittling (to cut film or paper into narrow strips or sheets).[1, 27] The basic process steps are outlined in Scheme 1.2.



Scheme 1.2. Summary of the major converting processes for flexible packaging.[1]

Traditionally, fillers were added to polymer as additives to improve stiffness and lower the expensive materials component fraction.[28] Addition of mineral fillers creates small air voids during film orientation and reduces flexibility of the films at high loading.[1] Hence, uniform particle size and good dispersion are essential for utilising these fillers in flexible packaging.[1] Although, the use of fillers in flexible packaging is typically low on a percent weight basis,[29] the total filler consumption that undergoes surface treatment is estimated to reach 1.5 million tonnes.[30]

There are two main approaches to add fillers into a flexible film; mixing filler with the polymer (compounding process)[31] and coating on the surface of film (extrusion coating or lamination process). By blending mineral filler in the polymer, the filler needs to be predispersed then mixed with the polymer and pelletised.[31] Then the obtained pellets are fabricated to form a film. Inorganic fillers are usually added to polymer to improve light barrier or aesthetics.[1] Typically, fillers used in flexible film are calcium carbonate, titanium dioxide, clay, talc and mica, their functions are summarised in Table 1.2.[1] Titanium dioxide and calcium carbonate are conventionally used to improve opacity of the polymer.[29] Hydrated fillers (such as $Al(OH)_3$, $Mg(OH)_2$ and hydrotalcite) are typically used as flame retardant additive and plate-like fillers are employed to improve barrier properties of polymers.[28]

Table 1.2. Example of fillers used and their functions.[28]

Function	Example of fillers
Modification of mechanical properties	High aspect ratio: glass fibres, mica, nanoclays, carbon nanotubes Low aspect ratio: talc, calcium carbonate, kaolin
Control of permeability	Reduce permeability: mical, talc, nanoclays, glass flakes Enhance permeability: calcium carbonate
Fire retardant	$Al(OH)_3$, $Mg(OH)_2$, hydrotalcite
Modification of optical properties	Titanium dioxide, calcium carbonate
Enhancement of processability	Colloidal silica, bentonite, hydrotalcite

However, the compounding of those fillers into the polymer requires surface treatment to improve surface compatibility to the polymer matrix and ensure homogeneous dispersion within the polymers.[32] The studies of filler/polymer nanocomposites have been reported over few decades.[30, 32] Delamination and dispersion of organoclays in polymer matrices provided significant improvements in gas barrier and mechanical properties of the film although,[32] the nanocomposites are still considered expensive.[30]

Alternatively, fillers can be applied in the coating or laminating process to allow multifunctional addition to packaging structure and cost reduction.[27] The extrusion coating or laminating process provides several creative, innovative film structures and more cost-effective.[27] Optical and barrier properties of films can be improved, for example, titanium dioxide was applied as a white pigment in an extrusion coating.[27] Coating contained inorganic fillers can reduce the permeability of the film.[33-36] Metallised film and metal-oxide coatings are widely used as gas barrier but they are neither flexible nor stretchable, as a result, crack and pinholes are formed upon flexing and diminish their barrier performance.[35, 36]

Therefore, the development of flexible and transparent films with high-barrier performance is considered to be a highly attractive target.[7, 37-39]

1.1.3. Gas permeation

Permeability is the rate at which a gas or vapour passes through a barrier layer consisting of three processes; absorption, diffusion and desorption.[40] Two main factors having impact on permeability (*P*) of polymer are diffusion coefficient (*D*), and solubility coefficient (*S*).[40, 41] Moreover, the permeability can also be affected by several parameters such as chain packing and side group complexity, polarity, crystallinity, orientation, fillers, humidity, plasticisation, cracks or pinholes.[40] In order to be simplified, the permeability of film can be expressed as a product of the diffusivity and solubility as follows in Equation 1 based on the assumption that the value of *D* is independent of the concentration and the value of *S*:[40, 41]

$$P = D \cdot S \quad (1)$$

The diffusion coefficient (*D*) describes the kinetic aspects of the transport based on Fick's law diffusion theory,[40] which indicates the mobility of permeating molecules (depends on type of molecule, polymer, temperature and concentration). The solubility coefficient (*S*) describes the interaction between polymer and diffused molecule based on the 'like dissolves like' concept, which relates to a combination of dispersion, polar and hydrogen-bonding interactions described by the Hansen solubility parameter, (*HSP* or δ).[40]

Over the past two decades, plastic polymers have replaced conventional packaging materials (glass, tin) mainly because plastic polymers offer lightweight, ease of process and low cost. Many polymers have been widely used in packaging applications such as polyethylene, polypropylene, polystyrene, and polyethylene terephthalate.[1, 27] Despite the versatility of polymeric materials, their inherent permeability to gases and vapour has a critical effect on their performance.[42] A concerted effort has been made to improve their gas barrier performance.[43-48] In general, permeability of polymer is affected by many parameters such as manufacturing process (to control molecular orientation), modifiers, copolymerisation, the degree of crystallisation and density.[49, 50] For example, polymer orientation can be controlled during polymer processing by stretching the film at a controlled speed and temperature, to make the molecules changes in crystalline morphology and are more aligned, resulting in a decrease in gas permeation.[1] A semi-crystalline nylon has excellent gas barrier properties and is not as sensitive to humidity as crystalline nylon.[50] Pure polyvinyl alcohol has poor moisture resistance, however, by modifying with ethylene can

improve the resistance to moisture. Alternatively, it was reported that the water vapour transmission rate of polyvinyl alcohol can be reduced by chemical grafting of fatty acid chlorides on the surface of the polymer.[49] The incorporation of two-dimensional (2D) platelets has been employed either as fillers to form polymer-filler nanocomposites[51-54] or as a barrier coating layer.[55-57] Such approaches can improve the gas-barrier properties of the polymers by increasing the diffusion path way of the permeating molecules through the polymeric film, generally referred to as a tortuous pathway, so-called brick-mortar or nacre-like structure.[39, 47, 55, 56, 58-60] The permeants navigate around impenetrable platelets through interfacial zones which have different permeability characteristics than those of the pure polymer, thus increasing pathway and suppressing the gas permeability.

In the case of polymer/filler composites, the gas solubility in the binary system can be simplified as in Equation 2 based on the assumption that the polymer local characteristics are not affected by the presence of particles and the polymer/filler interactions are strong enough to avoid void creation at the interface. Moreover, the diffusion rate is slowed down due to the obstacle of diffusing molecules through the composites and can be expressed by Equation 3. Hence, the relative permeability can be obtained by dividing the permeability coefficient in the nanocomposites (P) by the permeability coefficient in the pure polymer (P_0), as shown in Equation 4.

$$S = (1 - \emptyset)S_0 \quad (2)$$

$$D = \frac{D_0}{\tau} \quad (3)$$

$$\frac{P}{P_0} = \frac{1-\emptyset}{\tau} \quad (4)$$

S = the solubility coefficient in the nanocomposites

S_0 = the solubility coefficient in the neat polymer

$\emptyset$ = the filler volume fraction

D = the diffusion coefficient in the nanocomposites

D_0 = the diffusion coefficient in the pure polymer

τ = the tortuosity factor

Different models have been proposed in the literature to describe the tortuosity induced by the dispersion of impermeable lamellar fillers in a polymer matrix and as a consequence the decrease of permeability.[58, 61-64] Each model considered the geometry of the dispersed fillers and type of dispersion to express the tortuosity factor (τ). The most common one is Nielsen's model with an assumption of a perfect alignment of particles having a finite length (L) and

thickness (t).[58] Therefore, the tortuosity factor can be defined as shown in Equation 5 and as a consequence the relative permeability can be expressed in Equation 6. Scheme 1.3 illustrates the "tortuous pathway" suggested by Nielsen in 1967.[58]

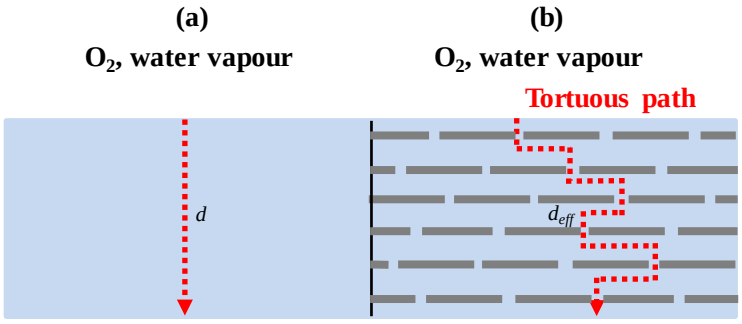
$$\tau = \frac{d_{eff}}{d} = 1 + \frac{L\emptyset}{2t} \quad (5)$$

$$\frac{P}{P_0} = \frac{1-\emptyset}{\tau} = \frac{1-\emptyset}{1+\frac{L\emptyset}{2t}} = \frac{1-\emptyset}{1+\frac{\propto\emptyset}{2}} \quad (6)$$

d_{eff} = the ratio of the actual distance travelled by a diffusing molecule to the shortest distance, d

$\propto$ = the aspect ratio= L/t

$\emptyset$ = the volume fraction of the flake



Scheme 1.3. Schematic diagram showing the tortuous pathway, according to Nielsen's model,[58] created by incorporation of platelets into a polymer matrix film (a) polymer and (b) polymer containing platelets (adapted from Duncan, 2011[65]).

The key to achieve such enhancements is to form a well-aligned layered arrangement. Non uniform particle size, random alignment, aggregation, and phase separation of such those platelets drastically decrease barrier performance.[60, 66] The gas permeation behaviour in the polymer filled platelets is generally governed by three main factors: the volume fraction of the platelets; the orientation of the platelets relative to the diffusion direction and their aspect ratio. Morphology of platelets also plays an important role in a reduction of permeability, since it increases the tortuosity of a permeant. In general, the higher aspect ratio particles (larger diameter with thinner particle) provide better reduction in permeability, which makes them effective at low loading levels and offers cost reduction and less impact on other properties.[67] For example, At only 3% loading of the nanofillers, the one with an aspect ratio of 200 reduced permeability by about 50% while the one with an aspect ratio of 80 reduced the relative permeability only 25%.

1.1.4. The use of platelet materials in barrier coating for packaging applications

Layered or flake-like materials including cationic clays, such as montmorillonite,[68] alumina flakes,[69] and graphene[41] have been employed to improve barrier properties of polymers. Polymer/filler composites have been developed over the few decades with enhanced mechanical, thermal and barrier properties.[42, 51-54] Despite their high versatility, the preparation process is complex. For example, surface modification of the filler may be required to improve compatibility with polymers.[42, 70] High shear and sonication techniques are crucial to deaggregate/exfoliate the filler during pretreatment and ensure a good dispersion of the filler in a polymer,[42, 71] which limits their practical implementation. Alternatively, barrier coatings are noted as the most frequently used and more efficient approaches to enhance the barrier performance of polymers, either for flexible[55-57, 72] or rigid packaging.[73]

A rich intercalation chemistry of layered materials and the possibility of ion exchange within their structures allow them to be chemically modified and fine-tuned their surface with various guest species to become compatible with the polymer matrix.[74, 75] Moreover, intercalation of ionic species can increase the layer spacing and weakening the interlayer adhesion of the layered materials.[76] Many layer silicate materials such as smectite (e.g. montmorillonite, hectorite)[34, 45, 46, 66] and vermiculite[63] clays and graphene and graphene-like materials[41] are materials of choice for the design of polymer nanocomposites design. Layer-by-layer (LbL) assembly[39, 45, 55, 77-81] has been substantially reported to reach such performance; however, the elaborate and complex nature of such method restricts their implementation on an industrial scale. Only few studies deal with preparation of barrier coating using a simple approach by a coater or applicator,[34, 72] therefore, the development in this area is of great essential.

1.2. Layered double hydroxides (LDHs)

Layered double hydroxides (LDHs) are a type of anionic clays. These layered materials can be turned to have different compositions, structures, and morphologies,[82-84] and can be of both natural and synthetic origins. LDHs are usually discussed alongside other layered silicate materials such as smectite clays (montmorillonite, saponite, hectorite)[85] since they have ion-exchangeable layered structure.[86] Extensive study of clay modification and hybridisation have been widely reported.[86] These layered silicate materials can only be exchanged with a limited range of cations, mostly alkyl-ammonium based, on the other hand, LDHs can be exchanged with wide varieties of anionic species. Moreover, the anion exchange capacity value (AEC) of

LDHs range from 200 to 400 meq/100 g (= cmol/kg), which is much higher than those clay minerals.[87] The cation exchange capacity (CEC) of montmorillonite (belongs to smectite family) varies from 70 to 100 meq/100 g.[88] This allows LDH a suitable candidate for various applications as well as polymer nanocomposite preparation.[89]

1.2.1. Structure of layered double hydroxides

The naturally-occurring mineral LDH, hydrotalcite, was firstly discovered in Sweden in 1842 and the composition was defined as $[Mg_6Al_2(OH)_{16}](CO_3)\cdot 4H_2O$ in 1915 by Mamasse.[90] Subsequently, hydrotalcite materials were synthesised in the 1940s[91, 92] and their structural features were well-characterised in the 1960s.[93, 94] The structure of an LDH is closely related to that of brucite, $Mg(OH)_2$, consisting of neutral layers of edge-sharing $Mg(OH)_6$ octahedral based on the hexagonal CdI_2 structure and linking by hydrogen bonding.[95] The general chemical formula for LDHs is written as $[M^{z+}_{1-x}M'^{y+}_{x}(OH)_2]^{a+}(X^{n-})_{a/n}.bH_2O$, where M and M′ are metal cations (z = 1 or 2; y = 3 or 4) and x is the molar ratio of $M^{z+}/(M^{z+} + M'^{y+})$, $0 < x < 1$.[96] Partial replacement of M^{z+} ions by M'^{y+} gives a net positive charge to the mixed metal hydroxide layers ($a = z(1 - x) + xy - 2$), which is balanced by the anions accumulated in the interlayer region (X^{n-}, n is 1 to 3). This layer gallery also contains water molecules which have an electrostatic interaction and can form hydrogen bonds with hydroxyl groups in the metal hydroxide layer and the interlayer anions to stabilize the layered structure.[97-99] The amount of water molecules (b = 0–10), including both structural and physically adsorbed water, depends on the synthesis parameters (anion and reaction temperature).[96, 100]

The typical composition for LDH family is based on a combination of divalent and trivalent metal cations: common divalent cations include Ca^{2+}, Mg^{2+}, Mn^{2+}, Fe^{2+}, Co^{2+}, Ni^{2+}, Cu^{2+} or Zn^{2+} whilst known trivalent cations can be Al^{3+}, Cr^{3+}, Mn^{3+}, Fe^{3+}, Co^{3+}, Ni^{3+}, or Ga^{3+}. Li^+ is the only monovalent cation reported to prepare LDH, such as $[LiAl_2(OH)_7]\cdot 2H_2O$,with extra positive charge compensated by an increase of Al^{3+}.[101] It is also possible to synthesis LDHs with tetravalent cations such as Zr^{4+} and Sn^{4+}.[102, 103]

LDHs have the advantage over the analogous layered materials of having more extensive intercalation chemistry with various inorganic and organic anions. These range from common inorganic anions such as halides, carbonate, sulfate, and nitrate to organic anions such as carboxylates, dicarboxylates, alkylsulfates, and alkylsulfonates.[97, 104] Moreover, larger biologically molecules such as amino acids, polysaccharides, nucleosides, and also DNA have

been introduced to the LDH structure.[105-108] A schematic representation of the archetypal carbonate LDHs is shown in Figure 1.2.

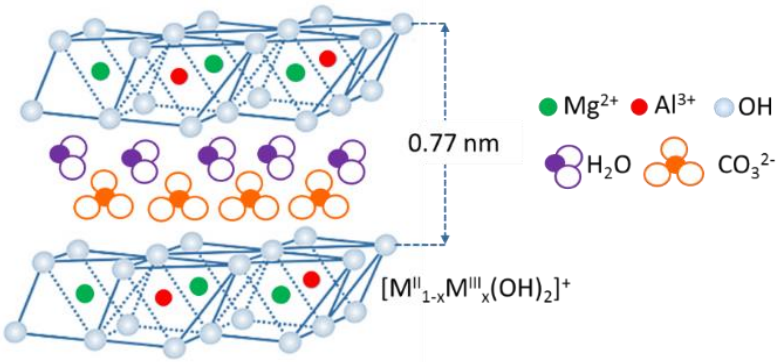


Figure 1.2. Schematic representation of a typical MgAl-CO_3-LDH structure (source: Edited from Salomão *et al*., 2011[84]).

LDHs possess polymorphism with two different stacking sequences observed, hexagonal (2H) and rhombohedral (denoted as 3R).[109, 110] Considering to the position of the hydroxide ions in the layers, A, B, and C, *m* and *x* representing the metal and anion positions, the hexagonal stacking sequence can be defined as A*m*B *x* B*m*A *x* A*m*B *x*… whilst the rhombohedral sequence is A*m*B *x* B*m*C *x* C*m*A *x*…. as presented in Figure 1.3 (a) and (b), respectively. The lattice parameters, *c*, in the hexagonal and rhombohedral forms are equal to twice and three times the interlayer distance, respectively.[100] Although, most naturally-occurring LDHs are of rhombohedral symmetry, some LDHs contain both symmetry types such as naturally occurring pyroaurite $[Mg_6Fe_2(OH)_6](CO_3)\cdot 4H_2O$.[93] A wide range of LDHs can be now synthesised as a single pure phase.[100]

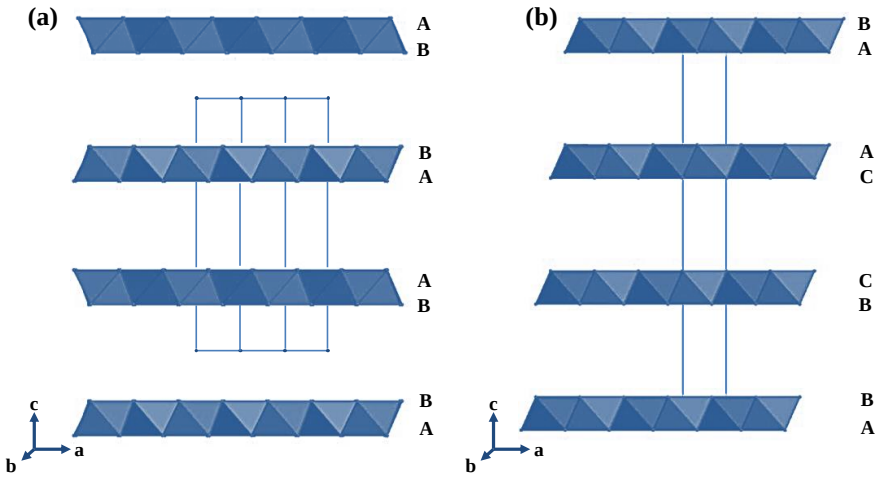


Figure 1.3. Schematic structure of LDHs with (a) hexagonal (2H)[110] and (b) rhombohedral (3R)[109] packing sequences. Blue lines indicate the unit cell; A, B, and C present the hydroxide packing sequence relative to the *c*-axis, anions and water molecules are omitted for clarity.

1.2.2. Synthesis methods of LDHs

LDHs can be synthesised with a wide range of compositions (different combinations of metal cations and interlayer anions) in order that the desired physicochemical properties can be obtained.[82, 83, 111-113] A main advantage of LDHs over other analogous layered silicates is their anionic exchange capacity making them being unique and attractive. A number of synthetic techniques have been developed to prepared LDH and to intercalate guest species into the interlayer regions of host lattices. Commonly used approaches relevant to the work in this thesis are explained in the following sections.

1.2.2.1. Co-precipitation method

The most commonly used preparative method for LDHs is coprecipitation, also called salt-base method.[82, 83, 114] A solution of mixed metal salts is added to a basic solution of the target anion at a controlled temperature under stirring for a given time. The brucite-like layers having a uniform distribution of both metal cations and solvated intercalated species are formed at the early stage of the condensation of hexa-aquo complexes in the solution leading the precipitate of LDH particles.[82, 83, 114] Two coprecipitation methods have been typically used: high supersaturation (so called variable-pH) and low supersaturation (so called constant-pH).

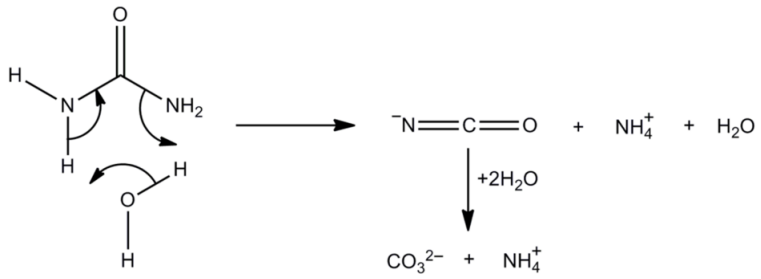
The high supersaturation precipitation method requires the rapid addition of a mixed metal salt solution to the basic solution of the desired target species. Consequently, nucleation rate is fast and a large number of particles are formed with low crystallinity.[82, 102, 115, 116] The low supersaturation method is recommended to prepare LDH with high chemical homogeneity by slow addition of mixed metal salts solution into a solution containing the target intercalated species at a controlled pH value, which depends on the nature of metal cations forming LDHs (typically from 7 to 10).[82, 117] Other synthetic parameters also play very important role such as solution concentration, ageing time, temperature, mixing and ratio of cations, which have been extensively reported.[113, 118, 119] Metal nitrates and chlorides are commonly used as precursor materials. Ageing methods have been explored such as hydrothermal treatment, sonication and microwave irradiation, which will be discussed in section 1.2.2.3.[120-122]

The advantage of this method is that a wide variety of anionic species can be directly intercalated between the layered host lattices by controlling the synthesis parameters. It is usually employed for preparation of inorganic- and organic-containing LDHs.[82] In spite of its many benefits, this method can be limited to the intercalation some anions; such as oxoanions

with high metal ion affinities (*i.e.* phosphate and oxometallates) due to the competitive metal salt-precipitation. For neutral or larger molecules, which the anion exchange approach using an LDH precursor is more applicable.[102] Furthermore, the preparation of LDHs with an accurate stoichiometric composition is not always straightforward; for example, an initial ratio Mg/Al of 3 prepare MgAl-NO_3 LDH, may result in final product with a Mg/Al with the ratio of 2.69.[123]

1.2.2.2. Urea hydrolysis method

Urea has been used in gravimetric analysis to precipitate metal cations as hydroxides or insoluble salts.[124] Urea is a very weak Brønsted base with pK_b of 13.8, it can be hydrolysed at high temperature yielding the formation of ammonium cyanate (NH_4CNO), which subsequent produces ammonium carbonate, and finally ammonia and carbonate ions that raise the pH of about 7-9, as shown in Scheme 1.4.[82, 125] As pH increases with increasing temperature, an aluminium hydroxide-like substance precipitates initially, followed by conversion to an LDH by deposition of magnesium hydroxide on the surface of the aluminium hydroxide-like species. The impurity phase hydromagnesite may be observed if the rate of magnesium hydroxide deposition is faster than that of diffusion of Mg^{2+} and Al^{3+} ions in the solid lattice, is suggested by Hibino and Ohya.[126]



Scheme 1.4. The decomposition of urea in aqueous solution.[82]

The urea method (so called homogeneous precipitation) is used to synthesis LDHs with uniform size, high crystallinity, and well-defined hexagonal shape.[125, 127-129] The composition, crystallinity and particle size of LDHs can be controlled by temperature, ageing time, concentration and ratio of the reactants.[125, 127, 129] The rate of urea hydrolysis (also pH of the system) depends on the temperature; the rate constant increases about 200 times upon increasing the temperature from 60 to 100 °C.[102]

Effect of synthetic parameters on particle size of LDHs can be explained on the basis of crystal growth mechanism in term of the primary nucleation process.[130-132] Generally, the

crystal size is related to the concentration and the number of crystal as follows: $L \propto (c\upsilon/N)^{1/3}$, where L = crystal size, c = concentration, υ = molecular volume and N = number crystals.[125, 130] Therefore, at higher reaction temperatures, the rate of urea decomposition is faster, leading to a fast nucleation rate, increasing of number of aluminium hydroxide seeds, which disturb the crystal growth of LDHs, to produce smaller particle size LDHs. Furthermore, a low concentration of the reactants results in the decrease in nucleation rate (number of crystal) and leads to a larger crystal size.[125, 130] This result could also be explained by in terms of the primary nucleation process. A higher concentration leads to a boost of the number of nuclei exceeding the critical nucleus radius, r_c,[133] they then can take part in crystal growth and result in a decrease in free energy. In addition, in a highly supersaturated solution, r_c becomes smaller.[132] Hence, the increase of concentration will result in the reduction of crystal size.[125] Okamoto *et al.* suggested that at lower urea concentration, less nucleation sites were produced, resulting in a slow crystal growth and larger particles.[134]

In general, this method is used to prepare only carbonate containing LDHs, which originates from the urea decomposition, hence, it is not suitable for preparation of low charge density MgAl LDHs.[135] This may limit a wide applicability of this method since carbonate containing LDHs cannot be generally deintercalated due to high charge density of the carbonate anions unless thermal treatment or acid treatment is performed.[129] The new guest molecules can now then introduced into the interlayer space of LDHs, the remaining carbonate anion still can be observed.[136-138]

1.2.2.3. Hydrothermal, microwave and ultrasound treatment

In order to control structure and textural properties of LDHs, different *in situ* or post-synthesis treatments have been employed.[82, 102] Microwave treatment was performed to improve the efficiency of the synthetic method and properties of LDHs such as fasten the growing and ageing processes during synthesis of LDHs,[139, 140] improve crystallinity[139] or the surface area[141] of the products. Moreover, the presence of structural water molecules and charge distribution within the hydrotalcite framework lead to effective absorption of microwaves facilitating long-range ordering of the LDHs during treatment.[102] An ultrasound treatment can improve crystallinity of the LDHs with enhancing the adsorption capacities.[142] Post-treatment using hydrothermal methods, involves treating LDHs in autoclaves under autogenous vapour pressure at elevated temperatures, it provides a route to better crystallinity products that improves with higher temperatures and longer times.[143] It was also reported that

increased autogenous pressure during hydrothermal treatment leads to larger crystal size and higher crystallinity.[144] In addition, hydrothermal conditions facilitate the solubility of solids and so particle grow *via* the Ostwald ripening phenomenon, where the small particles dissolute and recrystallise around the large ones until the small ones disappear, and result in improved morphology with well-defined thin hexagonal particles.[143-147] Such treatment has a strong effect on the composition of the synthetic MgAl-LDHs.[147]

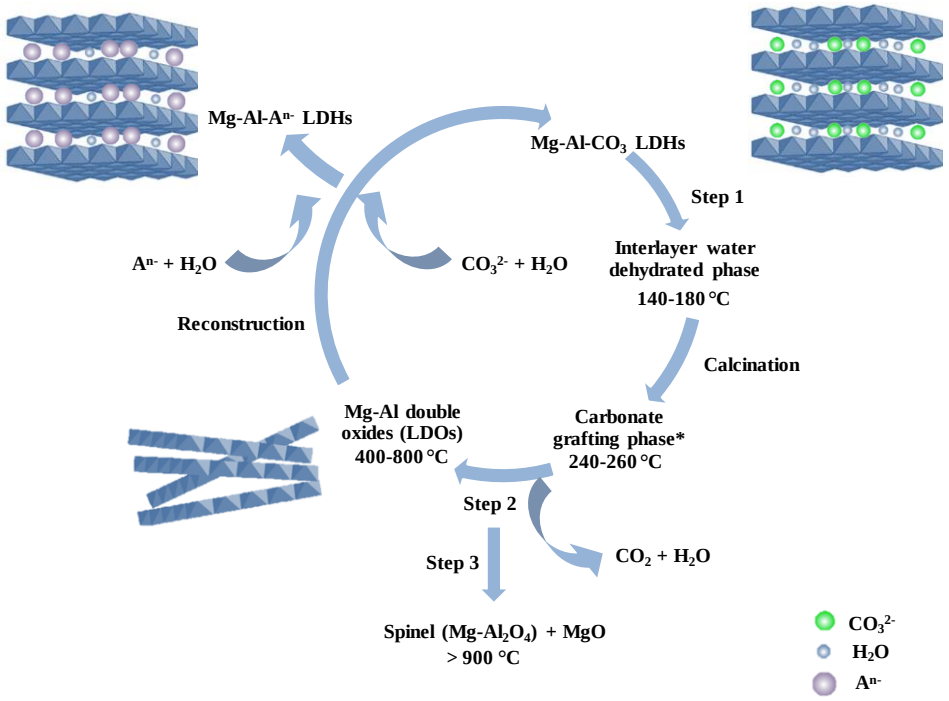
1.2.2.4. Ion exchange method

The ion exchange method is an important method to functionalise LDHs when the coprecipitation method is inapplicable by exchanging the intercalated anions by the new guests on the basis of the electrostatic interactions between positively charged layers and the guests.[82, 148-151] An increase of layer charge density leads to a high content of intercalated species, anions and water molecules, and a tight stacking of the sheets, as a result.[128] In addition, ion exchange is favoured with an increase of charge density and decreasing ionic radius; $CO_3^{2-} > SO_4^{2-} > OH^- > F^- > Cl^- > Br^- > NO_3^- > ClO_4^-$.[135] According to this ordering of anion affinity, nitrate- and chloride-containing LDHs are commonly used as precursors for intercalation of desired species.[102] This preparative method allows the intercalation of a wide variety of organic anions [113, 152] yielding organophilic LDHs, also called organo-LDHs, which will be detailed in 1.2.2.6.

1.2.2.5. Reconstruction method

A unique property of LDHs is a structural memory effect; the reconstruction of the original LDH structure by hydration of the calcined LDH, first discovered by Miyata in 1980.[145] This method is normally used to avoid the competitive intercalation of inorganic anions originating from the metal salts. The LDH is firstly calcined to remove water molecule (140-180 °C), intercalated anions and surface hydroxyl frameworks (400-800 °C) leading to the collapse of the ordered layered structure and formation of atomic mixed-metal oxide (so called layered double oxide, LDO).[153, 154] Stanimirova *et al.*[155] suggested that the metahydrotalcite phase was formed at 240-260 °C due to dehydroxylation of a part of hydroxyl frameworks and carbonate anions in the layer to produce water (hydroxyl frameworks with an inclusion of an oxygen atom from the carbonate anions) and carbon dioxide molecules, they then were removed from the structure during calcination.[155] At this stage, the positive charge of layers vanished and the symmetry of carbonate ion changed from D_{3h} to C_{2v}.[155] After progressive dehydroxylation, the LDOs are formed and the quasi-

amorphous mixed oxides, such as spinel-like phase and the divalent metal oxide, are obtained at higher temperatures.[102, 156] To reform the LDH structure, the LDO is then rehydrated in water or an aqueous solution containing the desired guest molecule, as shown in Scheme 1.5.[82, 102, 153] This method is also referred to reconstruction, rehydration, regeneration, or the calcination-rehydration process.



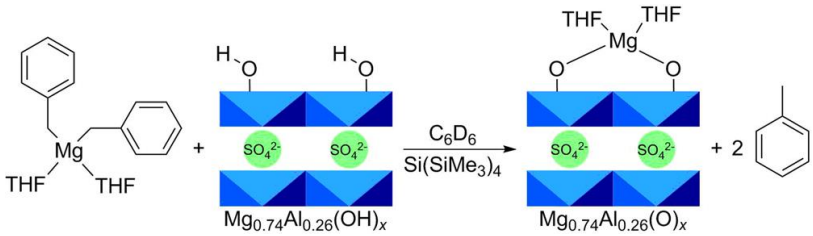
Scheme 1.5. Calcination and reconstruction of MgAl–CO_3 LDHs. Adapted from Forano *et al.*.[102] *: Suggested in Stanimirova *et al.*[155]

There are several factors influencing the reconstruction process such as calcination conditions (*i.e.* time, temperature, inert, vacuum), chemical composition of the LDHs, and rehydration conditions (*i.e.* time, temperature, concentration of media).[102, 145, 155, 157-159]

In the case of MgAl-CO_3 LDHs, a layered structure is retained up to 360 °C suggested by the *in situ* time resolved energy dispersive X-ray diffraction (EDXRD) studied.[154] With vacuum treatment, LDOs can be obtained at 300 °C.[160] An increase of calcination temperature leads to the migration of Al^{3+} ion from octahedral to tetrahedral sites, through three oxygen atoms from the hydroxyl framework and one apical oxygen from the interlayer, destroying crystallinity and giving rise to cation vacancies in the layer.[156] Numerous studies have reported monitoring of the structural changes during calcination of LDHs.[117, 154, 161]

A number of techniques have been widely reported to measure the number and type of surface hydroxyl groups on SiO_2 and TiO_2, such as infrared spectroscopy (IR),[162, 163] thermogravimetric analysis (TGA),[164] solid state nuclear magnetic resonance

(solid state NMR)[165] and deuterium exchange.[163] In the case of LDHs, the degree of dehydroxylation or the surface hydroxyl concentration as function of calcination temperature has been recently reported by O'Hare *et al.* using NMR titration technique.[160] The organometallic reagent, $Mg(CH_2Ph)_2(THF)_2$,[166] was employed to titrate with the surface hydroxyl groups, the amount of toluene produced can be measured and converted to the molar equivalents of hydroxyls per gram of solid (Scheme 1.6). Finally, the hydroxyl number is calculated by utilising of the BET surface area analysis and the data from titration measurements.[160] It was found that the hydroxyl number decreased as increasing calcination temperature. The LDOs have relatively high surface areas compared to the pristine LDHs.[160, 167]



Scheme 1.6. The determination of surface hydroxyl concentration by NMR titration method.[160]

The "memory effect" is reduced with increasing calcination temperature of the parent LDH;[102, 156, 157] high temperature induces the solid-state diffusion of cations into tetrahedral sites resulting in the formation of spinel and MgO phases while the crystalline structure is progressively destroyed according to the powder XRD and solid state ^{27}Al MAS NMR spectroscopy studies.[156, 157] The layered LDH structure is recovered to varying extents, depending on the calcination temperature and rehydration time; for example, the structure can be recovered within a day if the calcination temperature remains below 550 °C, while equilibration for three days is required if it is calcined at 750 °C and the reconstruction is partial obtained after calcining at 1000 °C.[156, 157]

The change of the aluminium content in hydrotalcite influences the temperature of structural transformations of LDHs and also the rehydration process,[155, 159] which can be explained by the chemical structure.[159] In LDHs, water adsorption occurs *via* hydrogen bonding between the water protons and activated surface oxygen atoms of LDHs, the oxygen concentration of different Mg/Al ratios is typically similar. However, in the Al rich LDH (Mg/Al at 2), the distribution of the cations are in a honeycomb-like structure (each Mg centre is surrounded by 3 Al and 3 Mg while each Al octahedral surrounded by six Mg). The layered

structure collapses upon calcination leading to changes in the arrangement of the cations, which is expected to differ for different Mg/Al ratios. This influences on the reconstruction behaviour but it is not in a linear relation[159, 168]

This method can be utilised for intercalating particularly wide range of neutral and ionic guest species such as surfactants,[169] amino acids and peptides,[106] large guests[170-172] (*i.e.* organometallic complexes and extended dye molecules) and neutral moieties[173, 174] (*i.e.* pentose and hexose sugars) into the LDH interlayer space.[175, 176]

1.2.2.6. Organophilic LDHs

Hydrophilic surface character makes LDH weak affinity to most of non-ionic compounds and poor compatible with hydrophobic polymers, hence, hydrophobic modification of LDH surface is required.[177, 178] The replacement of the inorganic ions by organic anions has been shown to change the surface property from hydrophilic to hydrophobic, to form organophilic LDHs, so-called organo-LDHs.[179] The organo-LDHs were firstly reported in ZnAl-LDH by Miyata and Kumura in 1973. Several approaches have been reported to prepare the organo-LDHs such as conventional co-precipitation,[179] reconstruction of calcined LDHs,[180] ion-exchange,[181, 182] urea hydrolysis[183] and thermal or melt intercalation methods.[184, 185] A number of studies in other long chain anions, such as mono- and dicarboxylates, alkyl sulfate dodecyl glycol ether sulfate, and alkyl sulfonate anions, have been extensively reported.[179, 181, 182, 186, 187]

It was reported that the interlayer space linearly increased as increasing number of the carbon chain length.[186, 188] Iyi *et al.* reported that the basal spacings (d_{003}) increased from 2.175 nm to 3.055 nm for MgAl-LDHs containing long-chain carboxylates with alkyl-chain length of C10 and C18, respectively.[186] However, unintercalated host LDH may co-exist with the intercalated products which depends on reaction condition.[185] The expansion of the interlayer region also depends on the arrangement or orientation of the organic guest molecules, which depends upon the functionality of molecules, synthetic conditions, and loading levels; these aspects were reviewed by Carlino.[185]

The introduction of large organic molecules into the LDH leads to an increase of interlayer distance inducing hydrophobic surface properties,[179, 188] allowing these materials as candidates for adsorption of other organic molecules[152, 169, 189, 190] or even exfoliation of LDHs.[191] Moreover, the organic molecules have an influence on the LDH morphology due to

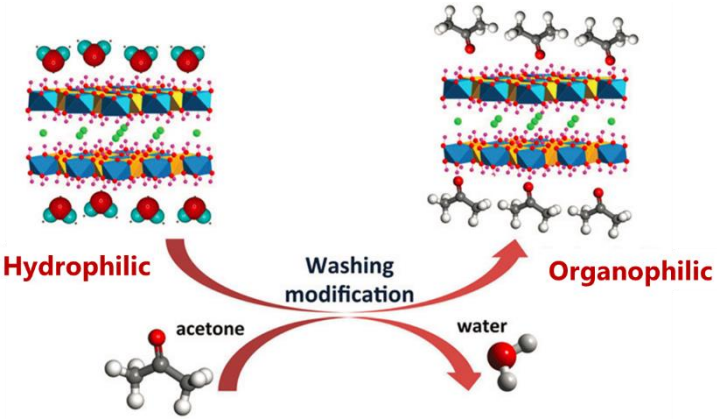
the template effect of the surfactant molecules.[192, 193] Post-synthesis hydrothermal treatment can be used to improve the crystallinity of the obtained organo-LDHs.[194]

1.2.2.7. Aqueous miscible organic solvent treatment

Due to the high charge density, strong electrostatic interaction in the structure and the hydrophilic nature of inorganic LDH particles, conventionally synthesised LDHs are usually heavily aggregated with tight *ab*-face stacking resulting in non-porous "stone-like" particles.[195, 196] These conventional LDHs normally poorly disperse in non-polar solvents, thereby limiting their practical application.[197] Current approaches involve surfactant modification, intercalation of organic surfactant anions, as well as preparation of nanoplatelets *via* delamination of LDHs, which was reviewed by O'Hare and Wang.[197, 198] For example, Naik *et al.* reported that dodecyl sulfate intercalated LDHs was delaminated and formed a clear transparent dispersion in toluene.[199] Hibino and Jones prepared MgAl-glycine LDHs (by co-precipitation), which was clearly dispersed in formamide.[200] However, such approaches are expensive and impractical for large-scale application.

O'Hare *et al.* recently reported the post treatment of LDHs by employing an aqueous miscible organic solvent treatment (AMOST), obtained LDHs noted AMO-LDHs,[195, 197] the general formula is defined as $[M^{z+}_{1-x}M'^{y+}_{x}(OH)_2]^{a+}(X^{n-})_{a/n}\cdot bH_2O\cdot c$(AMO-solvent).[197, 201] The AMOST method involves treating the as-prepared LDHs by a simple washing procedure using 100% aqueous miscible organic solvents, so-called AMO solvents. The AMO-LDHs are highly dispersed in certain non-polar hydrocarbon solvents and exhibit significantly higher surface area, porosity and low powder density.[96, 195, 196] It has been suggested that the solvent needs to be 100% miscible with water (e.g. acetone, ethanol) and introduced into the final washing process before isolation and drying the LDHs.[195] It has also been suggested that the treatment of the LDH slurry with an excess of an AMO solvent leads to the partial replacement of the interlayer and surface-bound water molecules by solvent molecules,[195, 197] yielding a dramatic reduction in the hydrogen bonding capacity of the LDH particles and layers, thereby decreasing the tendency for particle-particle aggregation and layer stacking, respectively, as shown in Scheme 1.7.[96, 196] Such treatment can lead to dispersion into thin nanosheets, exfoliation or even form single layers as monitored by XRD. In case of Zn_2Al-borate and Mg_3Al-borate LDHs, the (00*l*) Bragg reflections disappear but the (012) and (110)/(113) planes still remained indicating insufficient coherence stacking along *c*-axis and completely exfoliation of the platelet after AMO treatment even after drying.[195] These

exfoliated LDHs can be restacked to their original form when contacted with water and even more rapidly and pronounced if exposed to sodium carbonate solution to provide highly crystalline CO_3-LDHs.[195] The complete exfoliation of LDHs using this method is not applicable for high charge density LDHs such as carbonate containing LDHs; due to low charge density of the borate ions it makes exfoliating LDHs more facile. It is noted that the metal cation ratios remain unchanged, therefore, this method does not change the structure and composition of LDHs, and also the swelling or intercalation of LDHs cannot be detected after AMO treatment.[96, 197, 201] In general, surface area and pore volume of AMO-LDHs increase drastically compared to the water washed samples, typically from 13.4 to ~460 m^2/g and 0.08 to 2.15 cm^3/g in the case of Zn_2Al-borate LDH.



Scheme 1.7. The proposed mechanism of AMO-LDHs formation.[196]

A series of AMO-solvents were investigated to treat the LDHs[201] as well as process parameters (solvent dispersion volume, dispersion times, and number of re-dispersion cycle, and drying process).[96, 196] Such post treatment offers a new class of LDHs having immediate and substantial impact for many applications such as sorbents, catalyst precursors, catalyst supports or nanoadditives.[96, 195, 196, 201]

1.2.3. Applications of LDHs

Apart from mixed metal hydroxide layer, the intercalated molecules influence the chemical and physical properties of LDHs. A wide range of anions have been intercalated into the LDH interlayer spaces, which is a remarkable characteristic of LDHs. Due to their tuneable structure and flexible composition, various applications of unmodified and modified LDHs and their LDOs have been reported; for example, catalysts and supports,[102, 117, 202, 203] adsorbents,[102, 202, 204, 205] biomolecules and drugs carrier agents,[102, 206, 207] electrochemical applications,[208-211] flame retardant materials, and polymer additives.[102, 212, 213]

1.2.4. LDHs used in packaging applications:

A few studies have been reported using LDHs in paper applications; LDHs have been added in the wet-end process of papermaking as a pitch (organic contaminants from wood) and stickies (organic contaminants from recycled fibre) removal agent,[214] retention aid for optical brightening agent (OBA),[215] and filler for flame-retardant paper.[216] Moreover, LDHs have been used as a pigment in coating mixture for ink jet paper.[217, 218] To date, only one report has explored barrier properties of LDHs coated paperboard. By adding in combination with the condensation of tetraethoxysilane (TEOS) and 3-aminopropyltriethoxysilane (APTES), and applied on the substrate, water permeation value was lowered by ~80% compared to the uncoated paper.[219]

Despite LDHs have been commercially used in a lesser extent than montmorillonite and other cationic clays as fillers in polymer and nanocomposites, they have exhibited massive more potentially advantages than natural clay minerals.[220, 221] Especially their high purity and morphology and crystallinity control, easily functionalised of the layer environment with different chemicals in different ways, allow LDHs to be simply optimised their compatibility with the polymer thus using LDHs in coatings therefore allows a high degree of control over the gas barrier properties of a packaging material.[221]

Oxygen transmission rate (OTR) is a measurement of the rate of oxygen transmission through a film under defined conditions of temperature and relative humidity. The rate of oxygen exchange through the film from an oxygen flow in a chamber to a nitrogen filled chamber in another side was monitored. Once the transmission is no longer fluctuating, the rate is reported.[1] Value are normally expressed in $cc \cdot m^{-2} \cdot day^{-1}$ in metric (or SI) unit and in $cc \cdot 100\ in^{2} \cdot day^{-1}$ in US standard units. It is widely accepted that a material can be considered a 'high oxygen barrier' if the OTR value is less than 1 $cc \cdot m^{-2} \cdot day^{-1}$ (at 23 °C, 0% RH).[222]

Recent research has focussed on coatings *via* layer-by-layer (LbL) assembly of LDH nanoplatelets and polymer, usually by alternate spin or dip coating of the LDH dispersion and polymer solution thus reducing the OTR value, to as low as $<0.005\ cc \cdot m^{-2} \cdot day^{-1}$.[39, 55-57] However, such approaches are complicated and impractical on an industrial scale.

1.3. Aim of the thesis

The aim of the thesis is to explore several approaches for synthesising and modifying layered double hydroxides (LDHs), and their uses in packaging applications. The follow aspects can be carried out within the framework of the thesis:

- **The synthesis of LDH/cellulose fibre composites and their used in papermaking process**

Method for pre-treatment of cellulose fibre and preparing LDH/cellulose fibre composites are presented in Chapter Two. The obtained composites are then used as an additive in papermaking process and formed into paper sheets. The obtained composites are expected to decrease the fibre collapsibility, leading to an overall decrease density and increase stiffness of the paper.

- **The synthesis and application of organo-LDHs in paper coating**

The development of organo-LDHs with introduction of organic molecules is described in Chapter Two in order to improve hydrophobicity of LDHs. The performance of the organo-LDHs is investigated by applying them as a pigment in water-based coatings for paper in order to replace fluorocarbon and extruded polymer coatings, which are toxic and difficult to recycle.

- **The novel post treatment of LDHs by aqueous immiscible solvents (AIM solvents)**

Although the using aqueous miscible organic solvent treatment (AMO solvent) have been reported to increase surface area of LDHs and improve organophilicity of LDHs, such treatment requires a high energy distillation process for solvent recovery and the interaction between AMO solvent and the LDHs is still underexplored. The use of non-AMO solvents, so called AIM solvents, in the post-synthesis step of LDHs are examined in Chapter Three. The role of the solvent and its interaction with the LDH surface are examined by comparing organic solvents having different functional groups and structures, along with some post treatment parameters. This novel process is believed to allow flexibility of solvent selection for various applications and enhance the efficiency of the production process.

- **The preparation of LDH nanoplatelets and their application in barrier coating**

Two approaches for preparation of LDH nanoplatelets and their application in barrier coating are explored in Chapter Four and Five. Even though a number or studies have been reported to prepare nanoplatelets by using exfoliation/delamination methods, such approaches require toxic chemicals (*i.e.* formamide), mechanical treatment, and/or inert atmosphere, which are impractical in large scale production. Moreover, the application of LDHs in gas barrier coatings has focused on coating *via* layer-by-layer (LbL) assembly, which is complicated and believed not economical for large-scale industrial application.

The preparation of LDH nanoplatelets are explored into two approaches; Chapter Four describes the preparation of LDH nanoplatelets *via* a reconstruction method with amino acids and related compounds, while Chapter Five describes the alternative method for preparation of nanoplatelets *via* direct reconstruction process either in water or an aqueous solution of polymer (polyvinyl alcohol). Their uses in the water-based coating on the polymeric substrates using a single step coating process (a simple automatic rod coater), along with a series of tests on optical and barrier properties of these coated films are evaluated. Both novel methods are believed to provide a facile and cost-effective strategy for preparation of LDH-based barrier coated films, which could be useful in packaging applications and other areas.

Chapter Two – Synthesis and application of LDHs in papermaking and coating

2.1. Introduction

Folding boxboard and cartonboard are used in many packaging applications. High stiffness paper is required to ensure product protection and keep its shape when boxes are stacked upon each other.[223] In general, calcium carbonate and clays are used to improve opacity of paper, but paper stiffness and strength are decreased.[10, 11, 223, 224] Moreover, the fibres are collapsed during drying in the papermaking process and even more densified during recycling.[225] New developments such as precipitated fillers within fibre walls may increase fibres stiffness, with some impact also on light scattering and paper stiffness.[226-229] Although many fillers have been incorporated inside the fibre lumen, *e.g.* calcium carbonate, silica and titanium dioxide,[227-230] only a few articles can be found regarding precipitation of LDH particles onto the fibre surfaces.[231-234] The mineralisation of MgAl-LDHs into cellulose fibres was reported revealing the decrease in polymerisation degree of cellulose, exothermic heat, and fibre flexibility but increase an adsorption capacity towards anionic species.[232, 234] The obtained fibres were suggested to apply in flame retardant and adsorbent applications and they could be functionalised with surfactants to introduce hydrophobic character.[231-233] Indeed, a few studies reported the use of LDHs in paper applications such as an adsorbent for pitch and stickies (organic contaminants from wood and from recycled fibre, respectively),[214] a retention aid for an optical brightening agent (OBA) [215] in the papermaking process, and as a filler for flame-retardant paper.[216] Nevertheless, the use of LDH-mineralised fibres in papermaking and their effect on papermaking parameters and paper properties is still underexplored.

Poor barrier properties and sensitivity towards moisture are some of the main challenges facing cellulose-based materials.[235, 236] While giving good barrier properties, wax impregnation and extrusion coating create problems with recycling.[236, 237] Upgrading to water-based coatings with inorganic materials therefore has become necessary. Various inorganic materials have been used as pigments in coating applications such as kaolin, calcium carbonate and titanium dioxide.[238-240] There is a dearth in LDHs in paper coating applications, mostly used as a pigment for ink-absorptive coating layer for ink jet paper.[217, 218] Only one report explored the barrier properties of coated paperboard by adding LDHs (prepared by co-precipitation method) after the condensation of tetraethoxysilane

(TEOS, 95% v/v) and a secondary silica precursor (5% v/v) such as 3-aminopropyltriethoxysilane (APTES), applied on the substrate and lowered water permeation value by ~80% compared to the uncoated paper.[219] Hence, further exploration of LDHs in paper-based coating applications is required.

The aim of this work is to investigate the utilisation of LDHs in two main aspects in paper applications including papermaking and paper coating processes, respectively. Firstly, the preparation of LDH/cellulose fibre composites and their uses as an additive in papermaking process were investigated. The cellulose fibres used were cotton linter fibre (Whatman filter paper number 3) or wood fibres (bleached eucalyptus fibres which were provided by SCG Packaging PLC, Thailand). Two synthetic methods of preparing $Mg_3Al\text{-}CO_3$ LDHs (co-precipitation and urea hydrolysis) followed by hydrothermal treatment were carried out in this study. Structural aspects and characterisation of the LDH/cellulose fibre composites were studied. The obtained composites were then formed into paper sheet and paper properties (such as strength, physical and optical properties) will be tested. Next, the synthesis and application of organo-LDHs in water-based paper coating applications were explored. Tailor-made LDHs with improving hydrophobicity by *in situ* synthesis of organo-LDHs with the introduction of organic molecules will be investigated. The obtained LDHs will be applied in coating formulations as functional pigments (and compared with the commercial coating pigments) and coated on paper packaging. Paper properties (such as strength, physical and optical properties) and barrier properties (such as water resistance and water vapour transmission rate or WVTR) of the coated paper will also be tested.

2.2. *In situ* synthesis of LDH/cellulose fibre composites

2.2.1. Effect of fibre pretreatment solution

In general, natural cellulosic fibres have poor wettability and interfacial bonding which limit their chemical modification and mechanical performance.[241-244] Alkaline treatment (known as mercerisation) is one of the most common chemical treatments for natural fibres in the pulp industry with solutions of sodium hydroxide or sodium carbonate used as alkali pulping agents.[244-249] This process can help to remove some cementing materials from the native fibres (lignin, hemicellulose, waxy substances *etc*.), depending on the type of fibre, type and concentration of the selected alkali agent, temperature and time.[241, 243, 250] This treatment causes changes in both structural and morphological properties of the fibres, which increase the surface roughness, reduces aggregation, and leads to fibrillation, resulting in

increased accessibility to chemicals and better mechanical interlocking.[241, 251] Therefore, alkali pre-treatment has been used to improve the physicochemical interactions between the fibres and the matrix.[252]

In this study, 0.5 g of Whatman filter paper number 3 (noted as W-cellulose fibre) and 0.5 M sodium carbonate solution were used as the pristine cellulose fibre and dispersing solution, respectively. Sodium carbonate was used to pretreate fibres in this study. The obtained sample was named as W-cellulose fibre-nc. Alternatively, the fibre was dispersed in deionised water, noted as W-cellulose fibre-w. The slurry was stirred for three days at room temperature to ensure full dispersion. Then treated fibres were filtered, dried in vacuum, and analysed by powder X-ray diffraction (PXRD or XRD), scanning electron microscopy (SEM) and transmission electron microscopy (TEM) imaging.

The Whatman filter paper (W-cellulose fibres) is manufactured from cotton linters.[253] This type of fibre is ribbon-like or twisted fibres as shown in the SEM and TEM images (Figure 2.1).[254] The prolonged soaking time of three days with mechanical stirring leads to fibrillation of the fibres. It is more pronounced in sodium carbonate solution resulting in slow pulping of fibre.[255, 256] Sodium carbonate dissociates into carbonic acid and sodium hydroxide when dissolved in water and forms a moderately basic solution (pH of sodium carbonate solution used in this study was ~12).

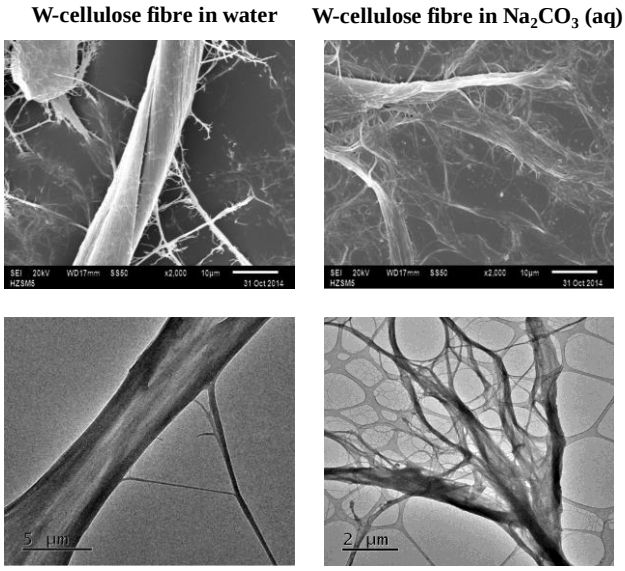


Figure 2.1. SEM and TEM images of W-cellulose fibre in water and in sodium carbonate solution.

The W-cellulose fibres are produced from high quality cotton linters and treated to guarantee quality > 98% α-cellulose content.[253] The XRD patterns of the virgin W-cellulose fibres are shown in Figure 2.2. The characteristic reflection planes at 2θ = ~15°, ~17°, ~22°,

and ~34° corresponding to the (1$\bar{1}$0), (110), (002) and (004) diffraction planes of cellulose type I, as no doublet in the main peak around ~22°.[253, 257, 258] The Bragg reflections at 2θ in the range between 15 and 18° and ~22° are the characteristic peaks of cellulose which are assigned to amorphous and crystalline regions, respectively.[259]

The crystallinity of cellulose has an important effects on cellulose fibre accessibility.[260] The crystallinity reveals that the cellulose molecules are closely packed and parallel to one another. The crystallinity index (*C.I.*) of cellulose can be calculated by using an equation described by Segal *et al.*,[259] (Equation1) which is:

$$C.I. = \left(1 - \frac{I_{am}}{I_{002}}\right) \times 100 \quad (1)$$

where I_{002} is the maximum peak intensity of the (002) crystalline peak at 2θ ~ 22° and I_{am} is the minimum peak intensity of the amorphous band at 2θ ~ 18−19°. The estimated crystalline index of the virgin W-cellulose fibre is 88%, indicating a typical semi-crystalline cellulose structure. The degree of crystallinity was virtually unchanged at 86% in both water and sodium carbonate solution. This minor change indicates the preservation of fibre crystallinity. Hence, such treatment did not affect the crystalline structure of cellulose but impacted on the texture of the fibre.

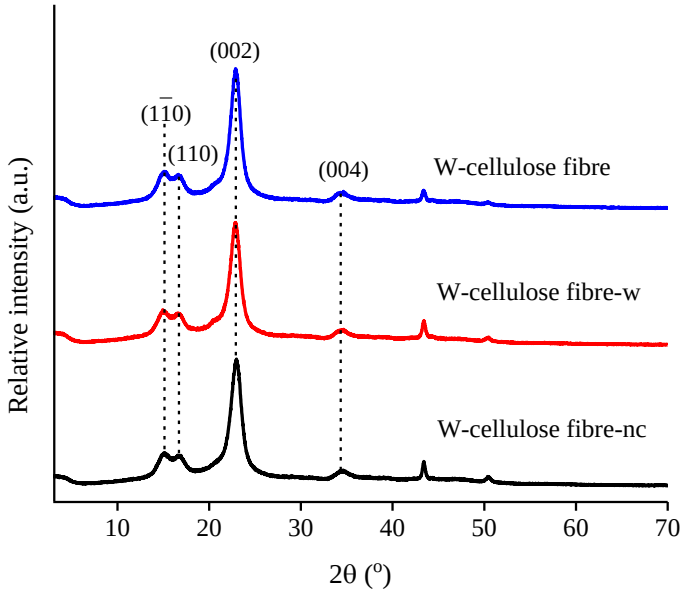
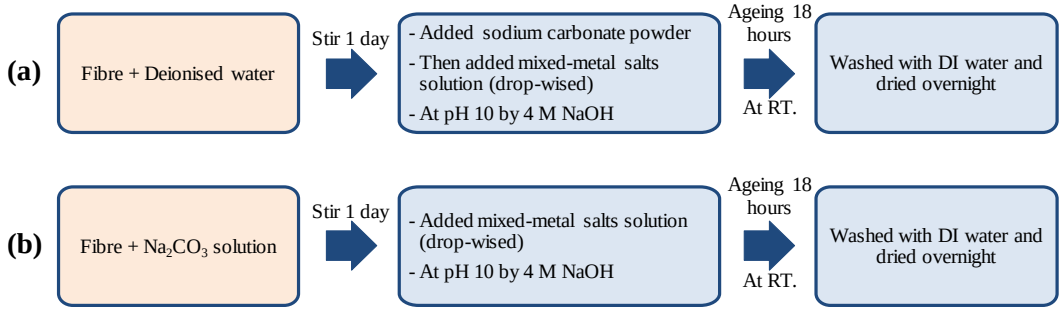


Figure 2.2. XRD patterns of W-cellulose fibres before and after dispersed in water and sodium carbonate solution.

LDH/cellulose fibre composites were prepared by *in situ* co-precipitation of MgAl-CO_3 LDHs on the obtained cellulose fibres by dropping the mixed metal salts solution into the fibre slurry with controlling the pH at 10 and aged for 18 hours at room temperature

while stirring, as shown in Scheme 2.1. Then samples were filtered, washed with deionised water, dried in vacuum, and finally analysed by PXRD, SEM and TEM imaging.



Scheme 2.1. Synthesis conditions for preparing LDH/fibre composites: (a) LDH/W-cellulose fibre-w composites and (b) LDH/W-cellulose fibre-nc composites.

The XRD patterns in Figure 2.3 show that LDHs can be introduced into the cellulose fibres. The main XRD peaks of the composites correspond to the characteristic LDH peak (003) at 2θ ~11°. In general, XRD diffractograms for LDHs show sharp, intense and symmetric peaks at low 2θ values and broaden in the mid 2θ region (30−55°).[261, 262] LDHs prepared by co-precipitation method are formed large aggregates of sheet-like LDHs with broad particle size distribution and small crystallite size, resulting in broadening of the peaks in the XRD pattern.[262] Although the (002) reflection of cellulose fibre at 2θ ~22° overlapped with the (006) reflection plane of the LDHs, low intensity peaks of the (1$\bar{1}$0) and (110) planes of cellulose were observed. Free LDH particles were observed in SEM images making it the dominant phase in the XRD pattern.

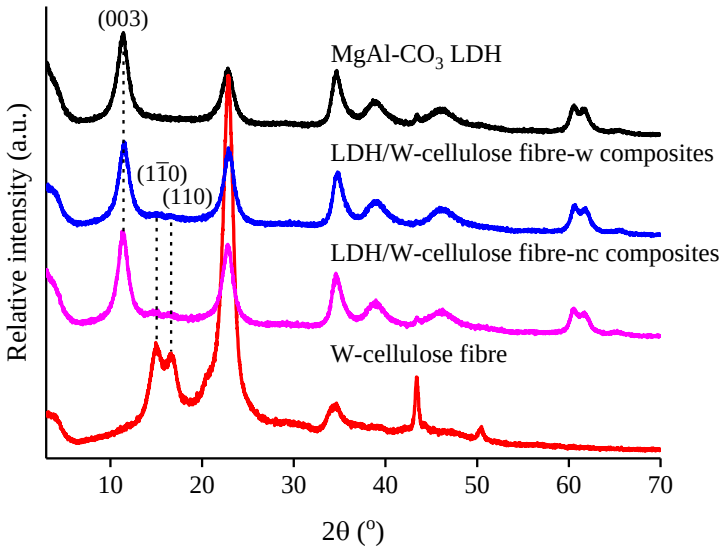


Figure 2.3. XRD pattern of LDH/W-cellulose fibre composites.

Figure 2.4 presents SEM and TEM images of obtained composites. LDH/W-cellulose fibre-nc composites reveals a denser surface than the LDH/W-cellulose fibre-w composites, indicating better deposition of LDH particles. Such weak-base pretreatment of fibre in sodium carbonate solution promotes a separation between the fibre bundles, as indicated by increased fibrillation of the pretreated fibres, which facilitates penetration and improves accessibility of the reagents during synthesis.[245]

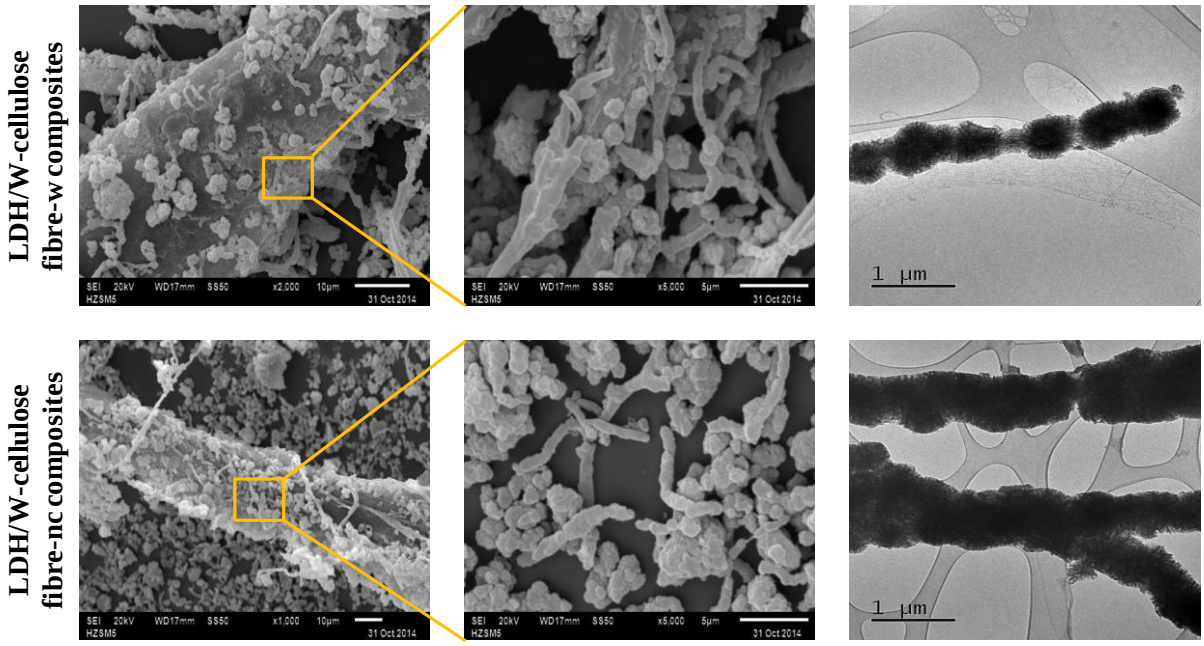


Figure 2.4. SEM and TEM and images of LDH/W-cellulose fibre composites.

The thermogravimetric analysis (TGA) and derivative thermogravimetric (DTG) curves were performed to determine the thermal properties and residual material level. The TGA and DTG curves of the pristine and composites materials are shown in Figure 2.5, and some of their thermal parameters are listed in Table 2.1. Pristine MgAl-CO_3 LDH prepared from co-precipitation method (termed as Cop-MgAl-CO_3 LDH) exhibits three main mass loss events which are highlighted in the first derivative curves (DTG). The first one is attributed to evaporation of adsorbed and interlayer water, ranging from 100 to 200 °C. The dehydroxylation of metal hydroxide layers and decomposition of carbonate anions with maximum decomposition temperature at 396 °C.[263] Finally, a residual material level of about 54% was obtained. The thermal degradation of the W-cellulose fibre reveals three main mass loss steps, where the first region at a temperature up to 200 °C is based on the removal of the adsorbed water. A drastic mass loss at 200 to 400 °C is assigned to the decomposition of polymer chains of the cellulose and the remained char undergoes above this temperature with final residue of 7.43%.[232, 264-266] Unlike the DTG plots of cellulose fibres, the

LDH/W-cellulose fibre composites show similar thermal decomposition steps as pure LDHs. The final residual mass is higher than the pristine fibre but slightly lower than the pure LDHs. This may due to excessive amount of LDHs remained in the composites due to poor washing process using filtration with filter paper and Buchner funnel. Hence, the free LDH was retained in the final products. An estimated content of LDHs and fibres in the composites can be calculated by subtracting the residue (at 700 °C) of the composites from their pristine LDHs (Table 2.1), indicating a very high amount of LDHs in the samples.

Table 2.1. Thermal propertied data of samples.

Sample	$T_{peak\ DTG}$[a]			Residue 700 °C[b]	%LDH:%Fibre[c]
	35-150 °C	150-350 °C	350-700 °C		
Cop-MgAl-CO_3 LDH	79	190	396	54.2	-
W-cellulose fibre	68	345	-	7.43	-
LDH/W-cellulose fibre-nc	107	181, 345	394	48.5	94:6
LDH/W-cellulose fibre-w	93	237, 341	397	50	96:4

[a] Temperature at the peak of DTG curve.
[b] Percentage mass of material left after TGA analysis at 700 °C.
[c] The contents of LDH and fibre in the composites were calculated from the difference residue mass between the composites and their neat LDHs at 700 °C.

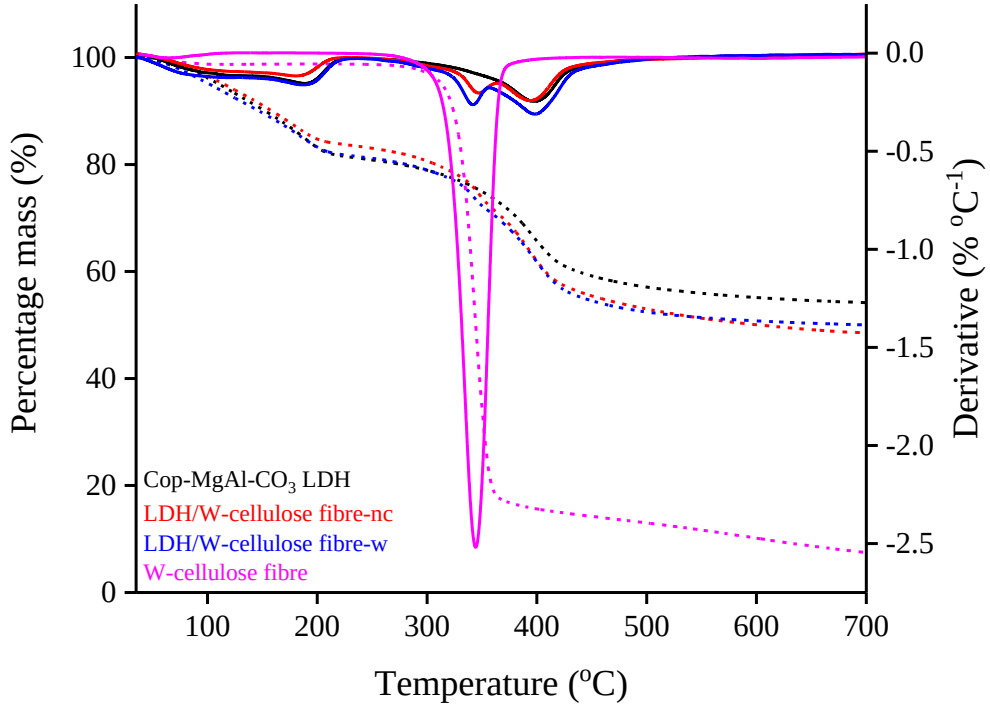
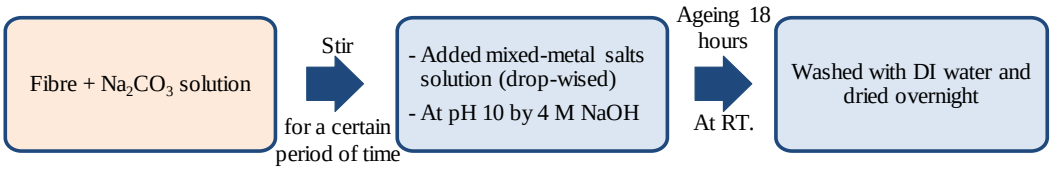


Figure 2.5. TGA (dashed line) and DTG (full line) curves of pristine LDHs, fibre and their composites under air flow.

2.2.2. Effect of fibre pretreatment time

It was reported that the soaking time of the fibre in the sodium hydroxide solution has a significant role in improving surface roughness, mechanical properties of fibres and adhesion to the matrix.[267] However, the pH of sodium hydroxide solution is relatively high (pH ~14), which may cause severe fibrillation of the fibres with prolonged soaking time. In this study, the dispersion time of the fibre in sodium carbonate solution (pH ~12) was varied from two hours to three days. Then, the mixed metal salts precursor solution was added dropwise into the slurry to prepare the composites, as shown in Scheme 2.2. Finally, the sample was filtered, washed and dried in the vacuum oven and characterised by XRD, TEM and SEM imaging.



Scheme 2.2. Synthesis conditions for preparing LDH/fibre composites.

In Figure 2.6 (a), the XRD results indicate that there is no significant impact of dispersion time on phase and crystallinity index of cellulose fibres (Appendix, Table A.1).[268] However, the longer the fibre dispersion time, the more fibrillation and surface roughness of the cellulose fibres were obtained, as shown in the SEM images (Figure 2.7 (a)-(e)).[251] As a result, denser deposition and full coverage of LDH particles on the fibre surface was observed in the composites using the dispersion time of at least a day in the sodium carbonate solution (TEM images in Figure 2.7 (f)-(j)). The XRD patterns of the obtained composites confirmed that LDHs can be introduced to the cellulose fibre. However, the amorphous region peaks of cellulose can be seen with low intensity peaks. They show similar interlayer spacing values of about 7.8 Å which represents the dominant phase of LDHs in the composites. This may be due to excess amount of loosely bound LDHs in the samples, which agrees with previous study in 2.2.1. It is possibly due to poor washing process using filtration, the removal of unbound LDH particles from the composites is difficult. The *d*-spacing of cellulose fibre and LDHs in the composites are summarised in the Appendix (Table A.1).

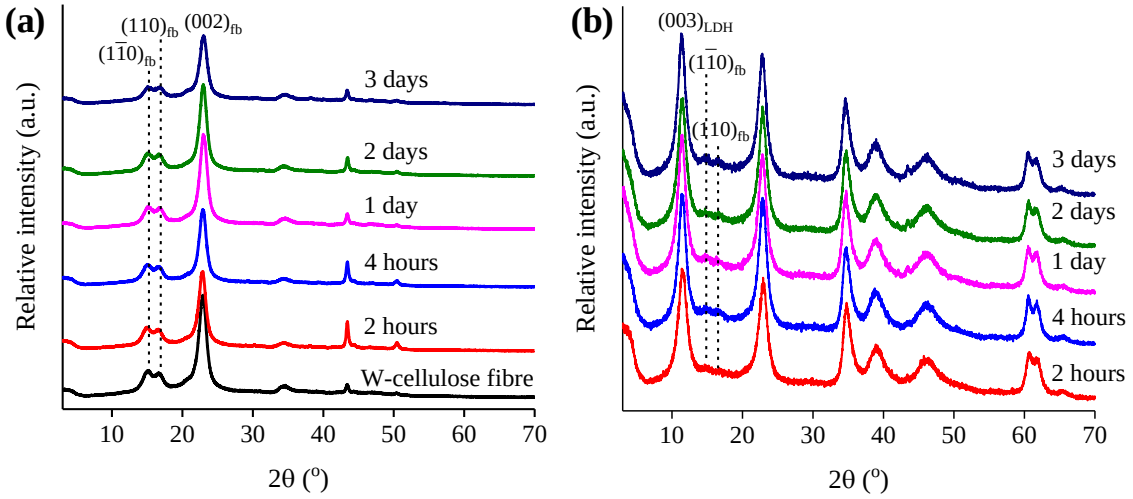


Figure 2.6. XRD patterns showing the effect of fibre dispersion time (a) cellulose fibre (b) LDH/Cellulose fibre composites at different fibre dispersion time.

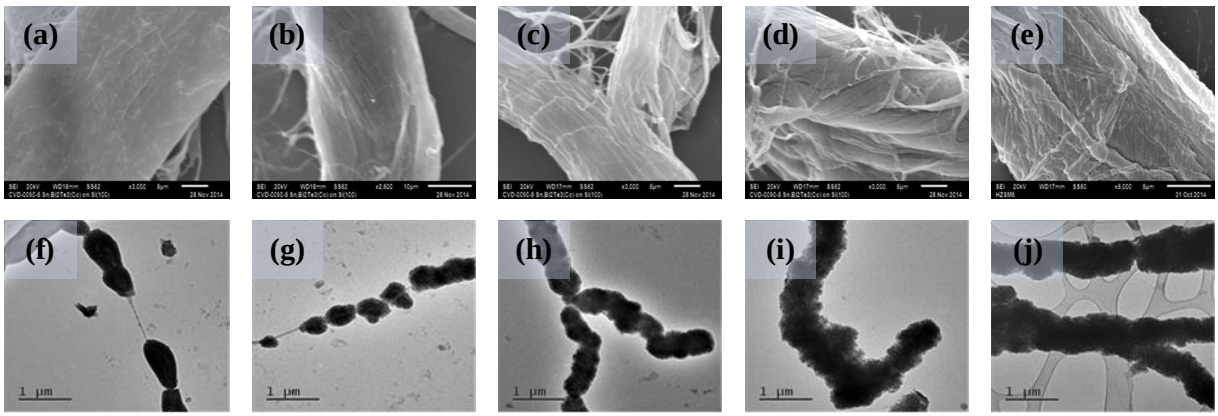
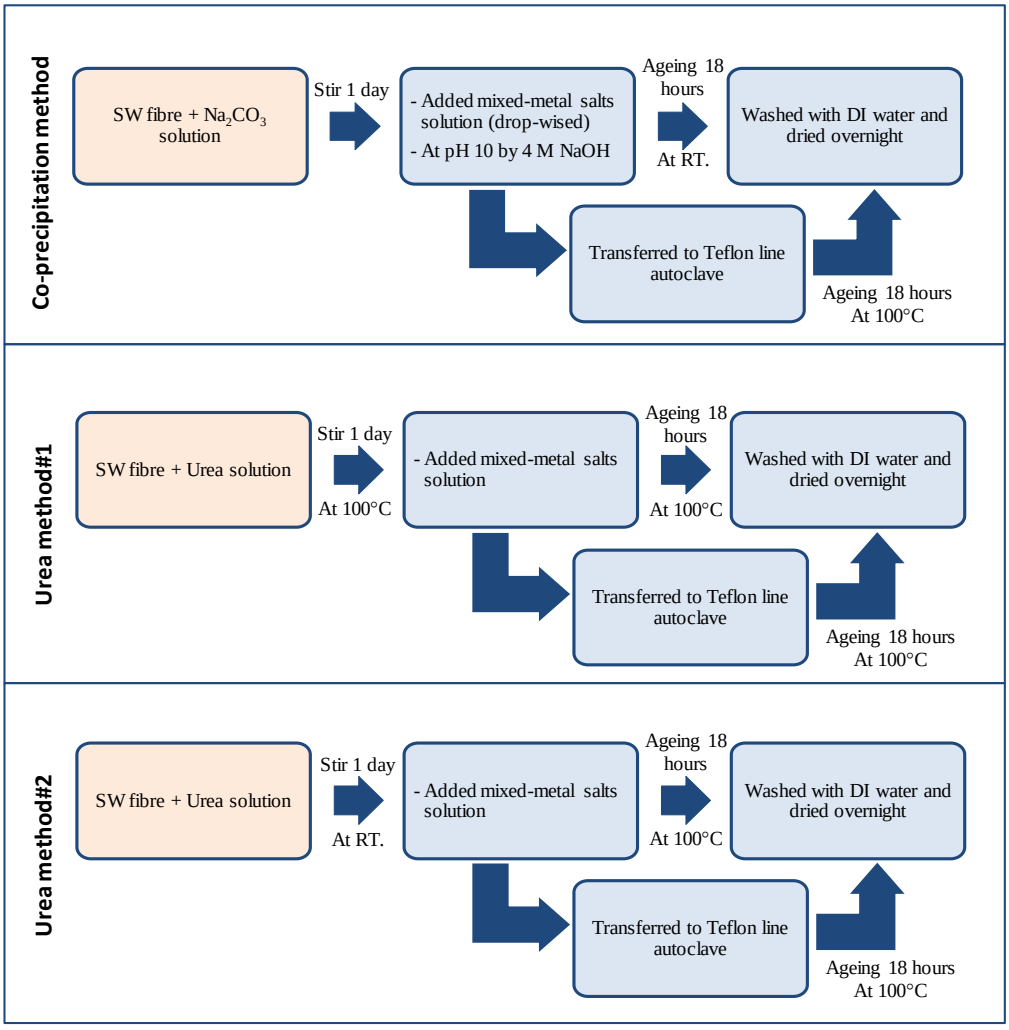


Figure 2.7. (a)-(e) SEM images of W-cellulose fibre at various dispersion time in sodium carbonate solution and (f)-(j) TEM images of their LDH/W-cellulose fibre composites: (a), (f) 2 hours; (b), (g) 4 hours; (c), (h) 1 day; (d), (i) 2 days, and (e), (j) 3 days.

2.2.3. Synthetic methods

As mentioned above, Whatman filter paper is a cellulose of very high purity,[254] leading to high degree of polymerisation and crystallinity compared with wood fibres.[253] However, wood fibre is the dominant raw material in pulp and paper manufacturing industries.[269] In order to study the effect of wood fibre types on the composites characteristics, a commercial bleached eucalyptus fibre (short fibre), denoted as SW-fibre, was provided by SCG Packaging PLC, Thailand. The effect of the synthetic method on the LDH/cellulose fibre composite properties was also studied. Two synthetic methods (co-precipitation and urea) followed by hydrothermal treatment were carried out in this study. The concentration of the mixed metals salt solution was controlled the same for all conditions. The preparation procedure for each method is summarised in Scheme 2.3. In this study, the fibre pretreatment in all studies were

fixed at 24 hours (a day) but different in the pretreatment solutions depending on synthetic methods used. For co-precipitation method, the SW fibre was immersed in sodium carbonate solution for a day prior to the synthesis. In case of the urea hydrolysis method, since this method requires high temperature (100 °C) to hydrolyse urea and release ammonia,[126] the fibre was pretreated in the urea solution at 100 °C for 24 hours before adding the mixed metals salt solution, denoted as Urea#1. Another fibre sample was dispersed in the urea solution for 24 hours at room temperature before the synthesis, and denoted Urea#2. After pretreatment, the fibres were mixed with the mixed-metal salt solution following each synthesis process (Scheme 2.3). After ageing for 18 hours, the products were washed with deionised water. Finally, another washing step was performed by thoroughly rinsing the product with deionised water over a 200 μm mesh. Samples were collected on the mesh, dried in vacuum overnight and characterised by XRD, SEM, TEM and TGA.



Scheme 2.3. Synthesis conditions for preparing LDH/fibre composites from different synthetic methods.

The appearance of fibre before and after pretreatment is shown in the SEM images (Figure 2.8). Fibrillation of the SW-fibre was observed after pretreatment in all medias. In the case of the pretreatment in the sodium carbonate solution, the fibrillation of the SW−fibre is less pronounced than in the Whatman fibre (W-fibre), originated from cotton linters (fibres that adhere to the seeds of the cotton plant). In general, the cotton fibres are more highly swollen, thinner cell wall than this eucalyptus fibre leading to better access of chemical and more fibrillated of the fibre.[244, 270] However, more fibrillation was observed in fibre that pretreated in the urea solution at 100 °C than in other conditions (Urea#1). High temperature can promote penetration of urea molecules, which can be hydrolysed at high temperature producing ammonium ions and slowly raising the pH of the mixture.[126]

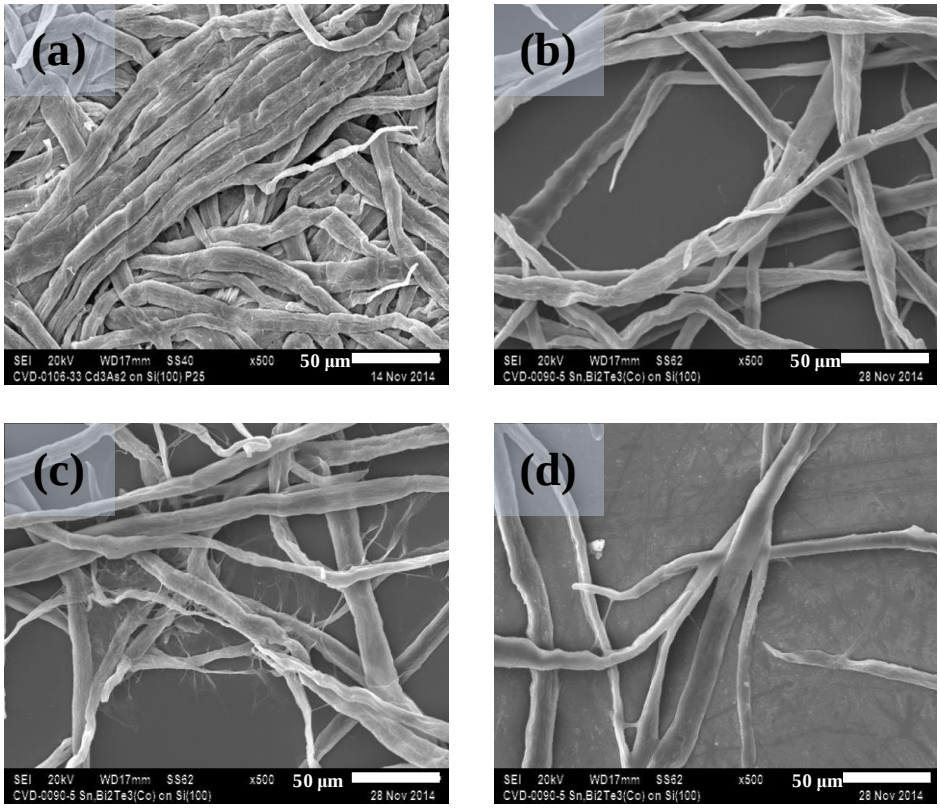


Figure 2.8. SEM images of SW-fibre before (a) and after pretreatment in (b) Na_2CO_3 solution, (c) urea solution at 100 °C and (d) urea solution for 24 hours.

From the XRD results of the untreated SW-fibre (Figure 2.9 (a)), all samples exhibit diffraction planes of cellulose type I similarly to the W-fibre.[253, 257] A broad feature in the range of $2\theta = 13-18°$, indicating that the fibre contains large amount of amorphous material resulting in a lower crystallinity index than the W-fibre at the value of 83.[271, 272] All composites present characteristic peaks of both LDHs and fibres (Figure 2.9 (b)). In addition, the phase of the cellulose fibre in the obtained composites was more pronounced than

previously observed. An amorphous region of cellulose can be seen in all samples regardless of the synthesis method. This broad feature is even more pronounced in samples prepared under hydrothermal conditions. LDHs in this study were assumed a 3R layer stacking (hexagonal unit cell, space group $R\bar{3}m$).[154, 273] The sharp (003) and (006) Bragg reflections at low 2θ region (2θ = 11−23°) with broad asymmetric peaks at the higher angle (2θ = 34−65°) are present.

These products show XRD patterns having intense and narrow Bragg reflections of the LDH phase indicating a high crystallinity product after hydrothermal treatment. On the other hand, the (002) Bragg reflection was not observed in samples obtained from co-precipitation method even under hydrothermal treatment, the (006) Bragg reflection of the LDHs overlaps with the (002) Bragg reflection of the cellulose fibre. This may be due to less crystallinity in the nature of the LDHs prepared *via* co-precipitation process than urea and urea hydrothermal processes, respectively. The XRD patterns of neat LDHs prepared by each method are shown in Figure 2.9 (a).

Table 2.2. 2θ position of the SW fibre, MgAl-CO_3 LDHs and LDH/SW fibre composites from different synthetic methods.

Sample	**2θ (°)**		
	$(003)_{LDH}$	**$(006)_{LDH}$**	**$(002)_{Fibre}$**
SW-fibre	-	-	22.78
Co-precipitation LDH (Cop LDH)	11.35	22.83	-
Co-precipitation-Hydrothermal LDH (Cop-HT LDH)	11.35	22.83	-
Urea LDH	11.78	23.68	-
Urea-Hydrothermal LDH (UHT LDH)	11.78	23.61	-
Cop LDH/SW-fibre composites	11.56	22.93	
Cop-HT LDH/SW-fibre composites	11.74	23.19	
Urea#1 LDH/SW-fibre composites	12.04	24.09	22.90
UHT#1 LDH/SW-fibre composites	12.01	23.85	22.72
Urea#2 LDH/SW-fibre composites	11.83	23.69	22.60
UHT#2 LDH/SW-fibre composites	11.88	23.76	22.78

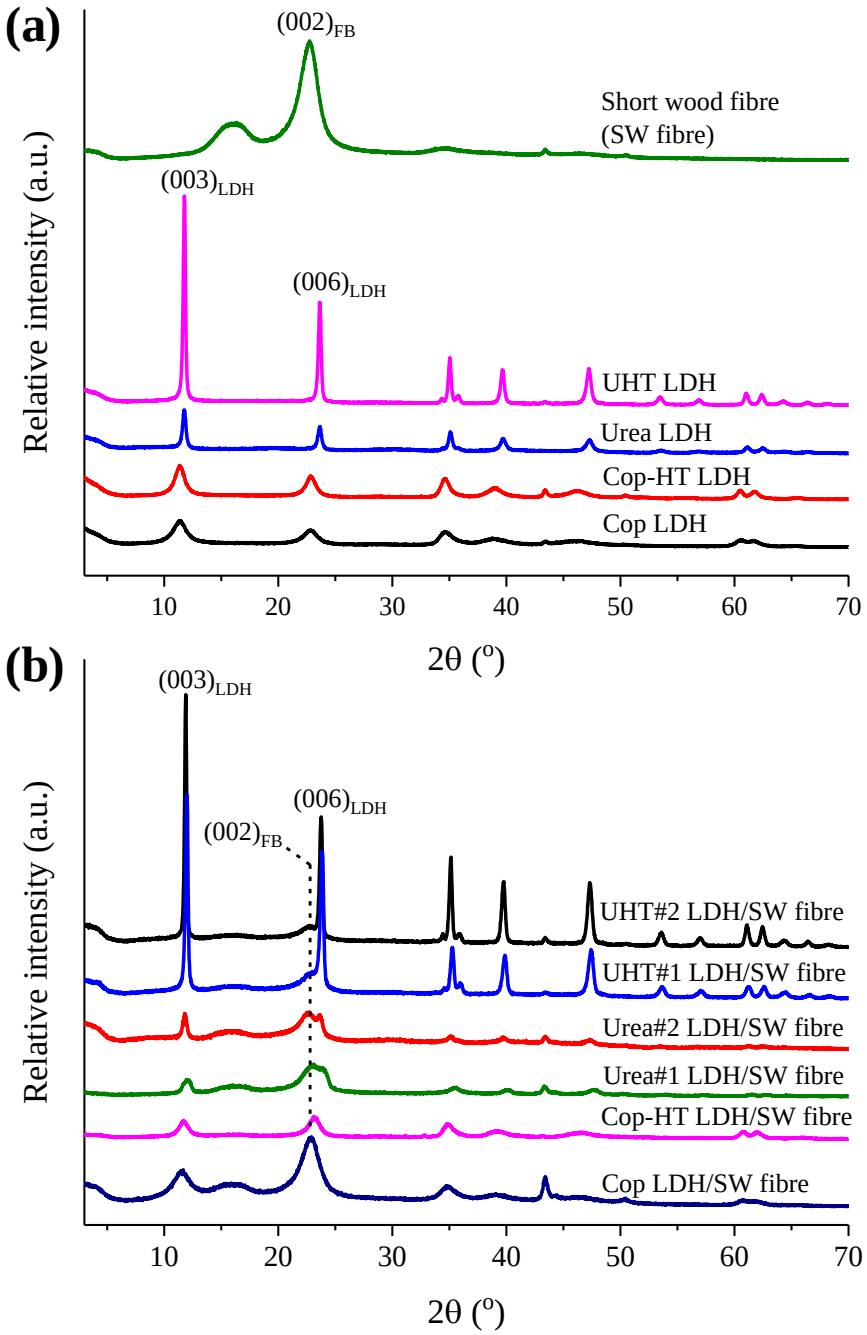


Figure 2.9. XRD patterns of (a) SW fibre and MgAl-CO_3 LDHs from different synthetic methods and (b) LDH/SW fibre composites from different synthetic methods.

The effect of the synthetic method is revealed by TEM images in Figure 2.10. Appearance of the obtained composites depends on preparation method. Generally, the co-precipitation method provides a rosette morphology whereas the urea hydrolysis yields platelets and even larger platelets with hydrothermal treatment as presented in the Appendix (Figure A1). All products present the deposition of LDH particles on the surface of the fibres which confirms successful incorporation of the LDHs onto the fibres as shown in Figure 2.10 and A2.

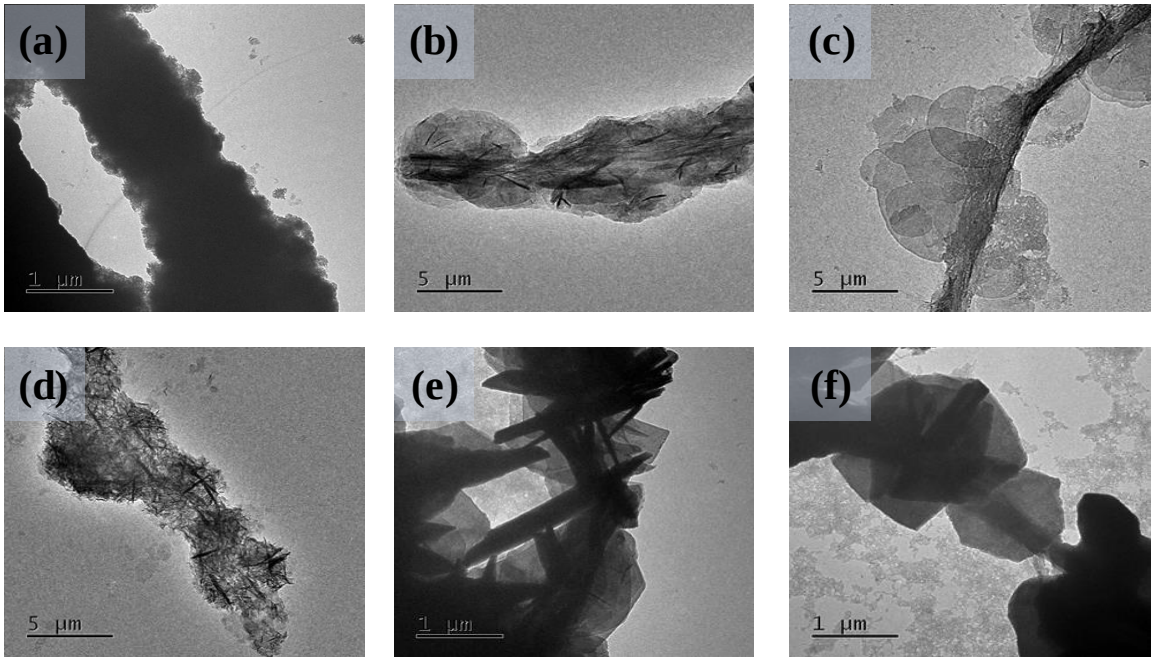


Figure 2.10. TEM images of obtained LDH/SW fibre composites from different methods: (a) Cop LDH/SW-fibre (b) Urea#1 LDH/SW-fibre, (c) Urea#2 LDH/SW-fibre, (d) Cop-HT LDH/SW-fibre, (e) UHT#1 LDH/SW-fibre, and (f) UHT#2 LDH/SW-fibre.

The fibre cell wall is composed of several layers, including the middle lamella, primary cell wall, secondary cell wall, and lumen (Figure 2.11).[274] The secondary cell wall is divided into different layers, S_1, S_2 and S_3. The S_2 cell wall is thickest, 75-85% of total cell wall thickness, and most important for mechanical properties.[275] Lange *et al.* reported the effect of LDH synthesis method on nucleation site of particles in the fully bleached Kraft fibres from pine (softwood or long fibre).[232] They found that particle nucleation was discovered in the S_2 fibre cell wall after urea hydrothermal synthesis while particles were found on the external surface of fibres in high saturation and co-precipitation methods.

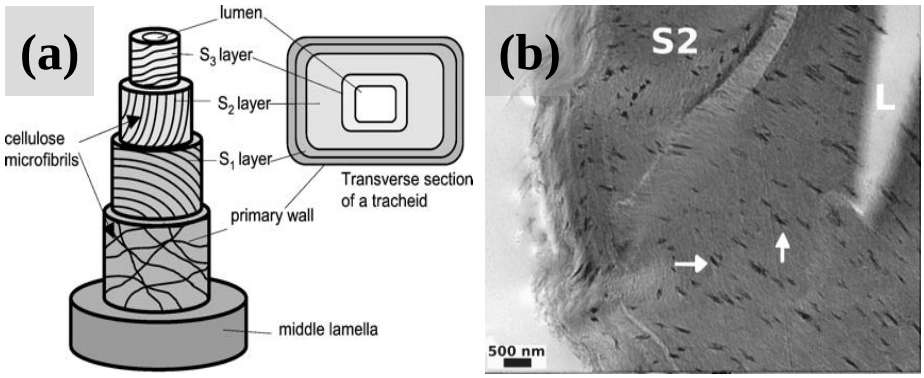


Figure 2.11. Images of (a) structure of the fibre cell wall (received from Plomion *et al.*[274]) and (b) transverse cut TEM image of *in situ* nucleation of LDH with pine fibres *via* urea hydrolysis method reported by Lange *et al.*. Fibre lumen and S_2 cell wall are marked as L and S2, respectively. LDH is marked with arrows. showing LDH/cellulose fibre product from.[232]

Unlike our process, the fibres were soaked in the mixed metal salts solution (pH ~3.7) before hydrothermal treatment. Water molecules in the S_2 cell may partially exchange urea, after increasing temperature, ammonia and carbonate (generated from urea) induce a system pH increase within the fibre wall favouring the diffusion of metal cations into the cell wall and ultimately leading to nucleation of LDH particles, which is slow and can be controlled by the rate of urea hydrolysis.[232] On the other hand, fibres were saturated and swollen in alkaline solution for co-precipitation method or rapid change of pH in high saturation method thus prevented nucleation within the fibre cell wall.[232]

In this study, the fibres were soaked in sodium carbonate and urea solutions for co-precipitation and urea hydrolysis methods, respectively. Diffusion of metal cations into the fibres cell wall may be difficult, thus, it was assumed that most nucleation of LDH particles were expected only at the external surface of the fibres. The composites prepared by co-precipitation method in Figure 2.10 (a) shows similar morphology as observed in W-fibre (Figure 2.7). On the other hand, large platelets were observed on the surface of the composites using both urea methods. The product from Urea#1 (Figure 2.10 (b)) exhibits denser deposition of platelets than in Urea#2 (Figure 2.10 (c)). As mentioned above, the Urea#1 procedure promotes penetration of urea as well as its hydrolysed products such as carbonate and ammonium ions facilitating the growth of LDHs on the surface of fibre. In the case of the Urea#2, the fibre was soaked in the urea solution for a day at room temperature. Although the urea molecules can also penetrate through the fibre, the facilitator for growing LDHs such as carbonate and ammonium ions are generated more slowly than in the Urea#1. This may lead to less covering of the LDH particles on the surface of the fibre than using the Urea#1 approach. The coverage of fibre can be slightly improved by using hydrothermal conditions. In addition, larger particles were found after hydrothermal treatment, especially for products from urea method. On the other hand, the fibre bundle was not observed in the sample prepared *via* the co-precipitation with hydrothermal treatment. Majority of this product presents small fraction of fibrils fully covered with LDH platelets. This may due to high pH at 10 (with presence of sodium carbonate and sodium hydroxide) with high temperature leads to harsh fibrillation of the fibre and only fibrils can be observed in this product. Consequently, the removal of free LDHs from the composites was difficult, confirming by the low intensity of cellulose phase than the LDHs in the XRD pattern of this product in Figure 2.9 (b). Hence, this approach may be not suitable for preparing the LDH/fibre composites.

From this observation, it can be suggested that the cellulose fibre should be soaked in the solution of the target anion with slight caustic conditions to promote the growth and the deposition of the LDH particles on the surface of the fibre. This concept may be useful for growing LDHs on other substrates.

The thermograms and derivative curves of the neat fibre, LDHs and the composites prepared from different methods and their thermal parameters are shown in Figure 2.12 and Table 2.3, respectively. From the thermograms, it can be seen that the pure SW-fibre show the initial mass loss below 100 °C which is attributed to elimination of moisture. The major mass loss took place at 327 °C due to decomposition of the cellulose yielding a residual mass of 0.25% at 700 °C.[232, 264-266] The residue level in the SW-fibre (0.25%) is much lower than in the W-fibre (7.43%). This might be due to some additives in the Whatman filter paper during papermaking process whereas the SW-fibre was provided as pulp sheet form (no additive was added during pulp sheet forming process). In case of pure LDHs prepared from different synthesis method, all of them exhibit three main mass loss steps; removal of water at low temperature range, dehydroxylation, and decomposition of carbonate anions with maximum decomposition temperature at 350-450 ^{o}C.[263] They produced the same amount of residue material level of about 54-57% regardless of synthesis method. The LDH/SW-cellulose fibre composites show similar thermal decomposition steps as the neat LDHs. The estimated content of LDHs and fibres in the composites are shown in Table 2.3. They exhibit less LDHs content than previously (Table 2.1). The percentage of LDH to Fibre (%LDH:%Fibre) of the composites prepared from co-precipitation in the previous study was 94:6 (Table 2.1) whereas in this study was 66:34 (Table 2.3) due to the unbounded LDHs (free LDHs) were better removed out from the composites by thoroughly rinsing the product with deionised water over a 200 μm mesh.

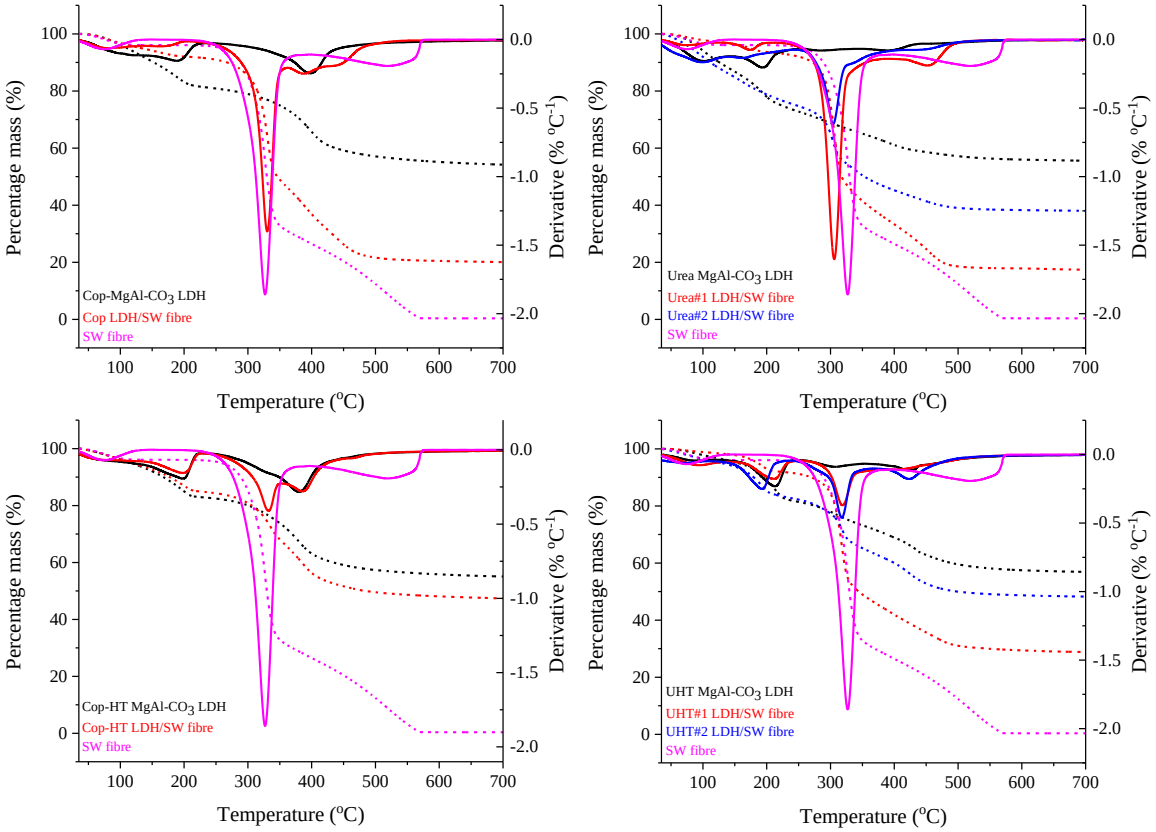


Figure 2.12. TGA (dashed line) and DTG (full line) curves of pristine LDHs, fibre and their composites under air flow.

Table 2.3. Thermal propertied data of LDHs from different methods and SW-fibre under air flow.

Sample	$T_{peak\ DTG}$[a]			Residue 700 °C[b]	%LDH:%Fibre[c]
	35-150 °C	150-350 °C	350-700 °C		
Cop-MgAl-CO_3 LDH	79	190	396	54.2	-
Cop-HT-MgAl-CO_3 LDH	75	199	382	55.1	-
Urea-MgAl-CO_3 LDH	101	194, 289	396, 480, 520	55.5	-
UHT-MgAl-CO_3 LDH	87	214, 309	427	56.9	-
SW-fibre	78	327	523	0.25	-
Cop-LDH/SW-fibre composites	79	171, 331	388, 447	20.2	66:34
Cop-HT LDH/SW-fibre composites	76	202, 332	388	47.5	92:8
Urea#1 LDH/SW-fibre composites	77	175, 305	457	17.6	62:38
UHT#1 LDH/SW-fibre composites	94	211, 320	423	28.9	72:28
Urea#2 LDH/SW-fibre composites	97	165, 304	453	37.9	82:18
UHT#2 LDH/SW-fibre composites	73	192, 318	423	48.3	91:9

[a] Temperature at the peak of DTG curve.
[b] Percentage mass of material left after TGA analysis at 700 °C.
[c] The contents of LDH and fibre in the composites were calculated from the difference residue mass between the composites and their neat LDHs at 700 °C.

High LDH content was observed in sample prepared *via* the co-precipitation with hydrothermal treatment with the %LDH:%Fibre of 92:8. This is in agreement with the XRD pattern (Figure 2.9 (b)) and TEM image (Figure 2.10 (d)) of this sample that contained only small fraction of fibre in the sample due to severed synthetic condition (high pH under hydrothermal treatment). This caused harsh fibrillation of fibres and free LDHs was difficult to be separated, resulting in high LDH content in this sample. The product prepared from UHT#2 method also contained large amount of LDH portion with the %LDH:%Fibre of 91:9. This could be due to very large particle size of the free LDH particles, which is larger than the diameter of the mesh (200 μm), making the removal of unbounded LDHs is not effective.

The FTIR spectrum of the SW-fibre, MgAl-CO_3 LDH and LDH/SW-fibre composites is displayed in Figure 2.13. The typical cellulose peaks are presented in the SW-fibre including the stretching of -OH and C-H at 3350 and ~2900 cm^{-1}, respectively.[276] The band of the carbonyl group (C=O, 1736 cm^{-1}), aromatic ring (1509 cm^{-1}), and acetyl group (-COO, 1251 cm^{-1}) are not detected because of the removal of lignin and hemicellulose during the chemical treatment in the pulping process.[277, 278] The bands at 1426, 1325, 1163, and 893 cm^{-1} are assigned to -CH_2 scissoring, -OH bending, C-O antisymmetric bridge stretching, and C-H rocking vibrations of cellulose, respectively.[276-278] Two sharp bands at 1055 and 1110 cm^{-1} reflect the C-O-C vibration of the pyranose ring of the cellulose.[279] On the other hand, the MgAl-CO_3 LDH exhibits a broadband at 3400-3600 cm^{-1} corresponding to the OH stretching vibration. The presence of a shoulder at 1640 cm^{-1} can be ascribed to the bending motion of interlayer water. The characteristic bands for carbonate anion are observed at 850 and 1370 cm^{-1} for υ_2 and υ_3 stretching vibration modes, respectively.[83, 280] The peaks at 660 cm^{-1} is associated with the M-O-M stretching modes in the LDH sheets.[281] In the case of the composites, main characteristic peaks of both cellulose and LDH can be distinguished. The strong broad OH stretching, υ_3 carbonate vibration and C-O-C vibration are presented in the composites indicating the presence of both cellulose fibre and LDH in the sample.

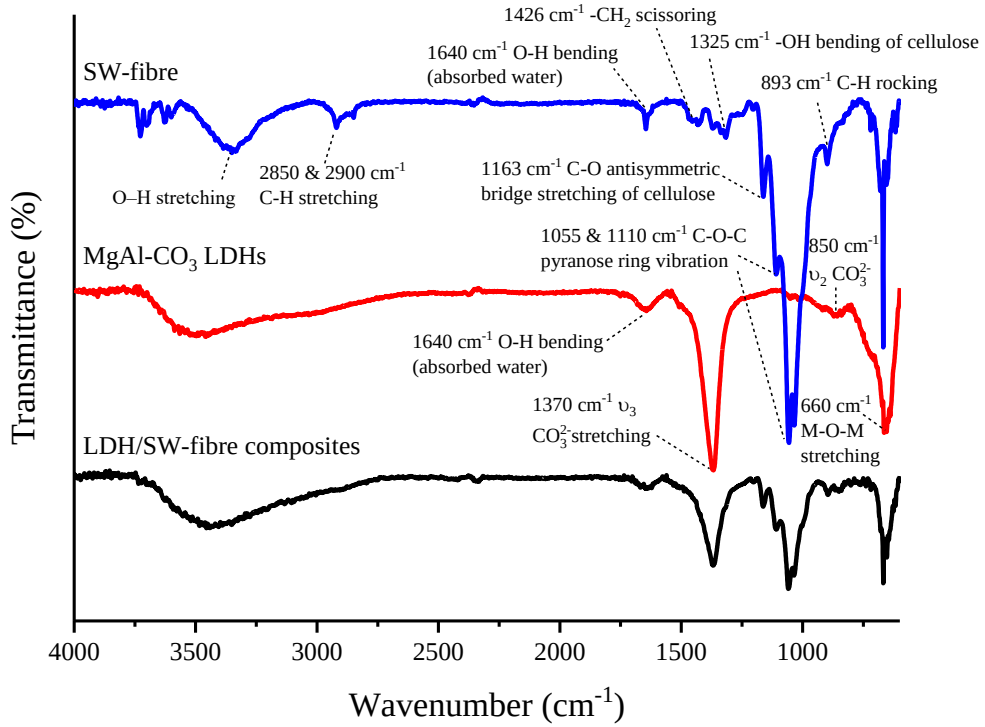


Figure 2.13. FTIR spectra of SW-fibre, MgAl-CO_3 LDH and LDH/SW-fibre composites.

^{13}C Cross Polarisation Magic Angle Spinning (CP/MAS) and ^{27}Al Direct-Polarisation Magic-Angle Spinning (DP/MAS) NMR spectroscopy were carried out to study the interaction between the LDHs and the fibres in the LDH/fibre composites.

Figure 2.14 (a) shows the chemical shift range of 60-170 ppm of the SW-fibre comparing with the composites prepared *via* co-precipitation method. Both spectra show characteristic resonances of the cellulose fibres, belonging to the six carbon atoms of the cellulose molecules. In the case of the composites, low intensity peaks at 165 to 170 ppm were detected and assigned to the resonance of carbonate anions from the LDH. The ^{27}Al (DP/MAS) NMR spectroscopy was used to identify the aluminium environment in the samples as presented in Figure 2.14 (b). Both the LDH and LDH/cellulose fibre composites exhibit a broad asymmetric signal centred at 8.7 ppm which indicates the presence of only octahedrally coordinated aluminium in the samples. These results confirm that the interaction between the LDHs and the fibres is not a chemical bonding interaction. A possible explanation may be the physisorption *via* hydrogen bonds between the LDH and the cellulose fibres.

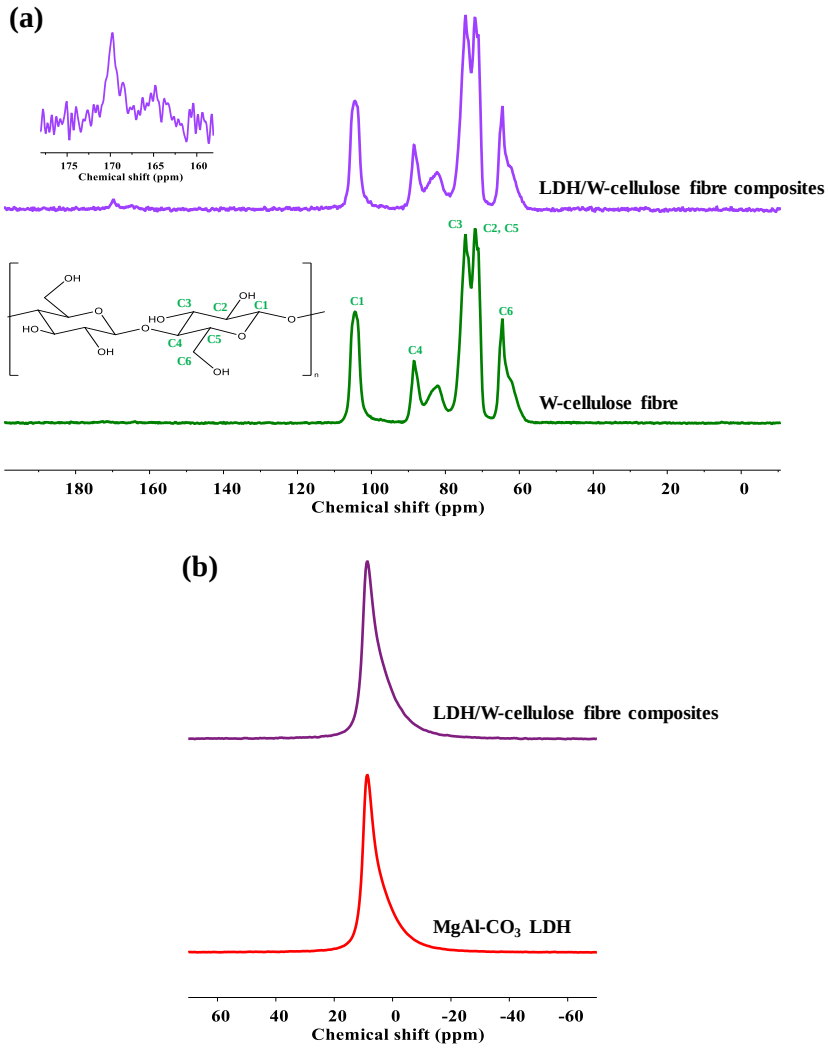


Figure 2.14. (a) ^{13}C (CP/MAS) and (b) ^{27}Al (DP/MAS) solid state NMR spectroscopy of LDH/SW-fibre composites and MgAl-CO_3 LDH.

2.3. LDH/cellulose fibre composites as a filler in papermaking

The present study deals with the effects of different synthetic methods of preparing LDH/cellulose fibre composites on the properties of paper sheets.

2.3.1. Preparation of paper

Paper handsheets having a basis weight of 60 g/m^2 were prepared for all experiments. Regarding to morphology of the obtained composites, three composites from three synthetic methods; Cop LDH/SW fibre, Urea#1 LDH/SW fibre, and UHT#1 LDH/SW fibre, were chosen in this study. They were mixed with the pure SW fibre (bleached eucalyptus fibres) in water at 0, 10, and 20% by mass to the pure fibres and disintegrated to ensure full dispersion of the fibre suspension. Then paper sheets were formed, pressed and dried to remove water

(Figure 2.15). Parameters such as the drainage time (dewatering time during paper forming process) and Zeta potential (charge monitoring) were measured. SEM-EDS analysis was performed to observe the distribution of the composites in the obtained paper sheet. The amount of the inorganic filler was determined by ashing the paper at 525 ^{o}C (ASTM D 586-97). Paper properties including paper density, porosity, strength (tensile index and stiffness index) and opacity were also tested.



Figure 2.15. Paper sheet preparation procedure.

2.3.2. Effect of LDH/cellulose fibre composites on paper properties

The first stage in papermaking is the formation of paper sheet (wet web/forming section) from the fibre suspension. The dewatering rate or drainage time is defined as the time used to remove water from the wet web during paper formation, which is one of the factors to predict the profitability for the paper machine.[282] The shorter drainage time can increase the production rate of the paper machine. As shown in Figure 2.16 (a), the drainage times were decreased after loading the composites and at higher loading. This means that water can be drained off from the paper web easier than with the blank sample, which can offer benefits including fasten machine speed and energy saving for papermaking manufacturers.[283]

In order to exploit the electrical interaction in the papermaking process, it is important to measure and control the charge. Surface charge plays a vital role in controlling performance of additives and chemicals (e.g. filler, retention aid, wet and dry strength agents) in papermaking.[284] In addition, surface charge density of fibres contributes in tensile strength development of paper structure.[284] However, these charges cannot be directly measured since the particle charges are screened by a diffuse layer of counter-ions, which is defined as the zeta potential.[282, 285] The zeta potential measurement was used to monitor the charge of the mixed fibre slurry in terms of colloidal chemistry and control the amount of chemicals and additives used during papermaking process.

Zeta potential measurement of fibre suspensions were performed using Mütek SZP-06 at SCG Packaging PLC, Thailand. The zeta potential is calculated on the basis of the measured

streaming potential, the conductivity and the pressure differential after several measurement cycles with the unit of mV while Drainage time was performed following the TAPPI T221 by measuring the time required to form a standard sheet weighing 60 g/m^2, detailed experiment are explained in Chapter 6 (session 6.2).

As shown in Figure 2.16 (b), the pure fibre slurry was negatively charge with the zeta potential values of −20.2 mV and became more negatively charged (~−21 mV) after addition of the composites. It was suggested that an increase in surface charge gave negative effect on filler retention, hence, higher dosage of retention aids (such as acrylamide copolymers are used to improve retention of fillers and additives during paper formation) and other additives is required to balance the charge of the system, and maintain adequate performance and cleanliness of paper machine.[284]

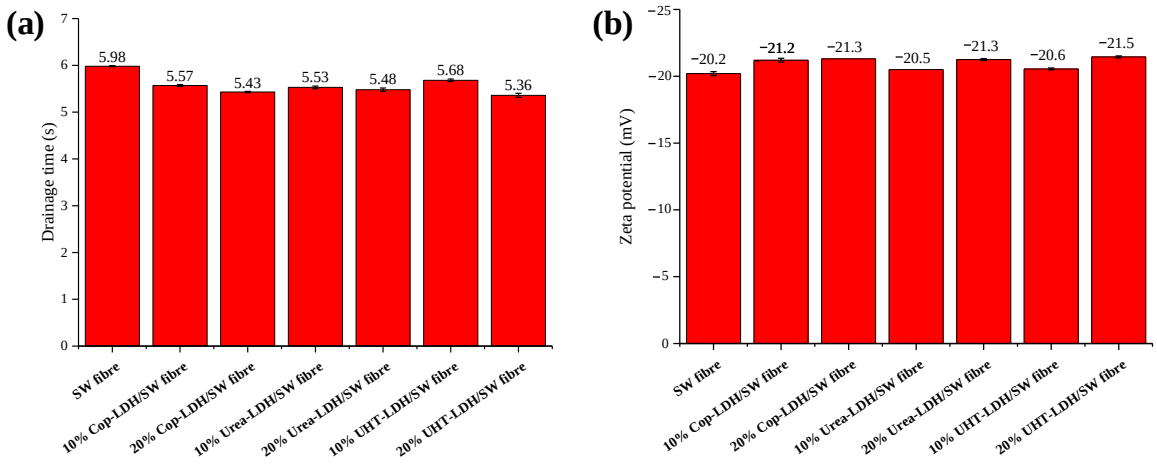


Figure 2.16. (a) Drainage time and (b) zeta potential of fibre slurry. All measurements were test at least five times, the average and standard deviation (shown as error bars) values were reported.

SEM and SEM-EDS images of obtained paper sheets are shown in Figure 2.17, demonstrating that the composites are well distributed in the paper sheets. Only in paper containing the cop LDH/SW fibre, flocculation of the composites was observed in the cross-sectioned SEM−EDS image in this sample. In order to determine the filler content in paper, the ash content determination was performed by combustion of the obtained paper at 525 °C. The residue was recorded as a percentage ash content. Figure 2.18 shows the percent ash content in prepared samples. At the same loading level, the composites prepared from the urea hydrothermal method has higher ash content than the others. This correlates with the TGA results in Table 2.3 showing that the LDH content in UHT#1 LDH/SW fibre is higher than Cop LDH/SW fibre and Urea#1 LDH/SW fibre.

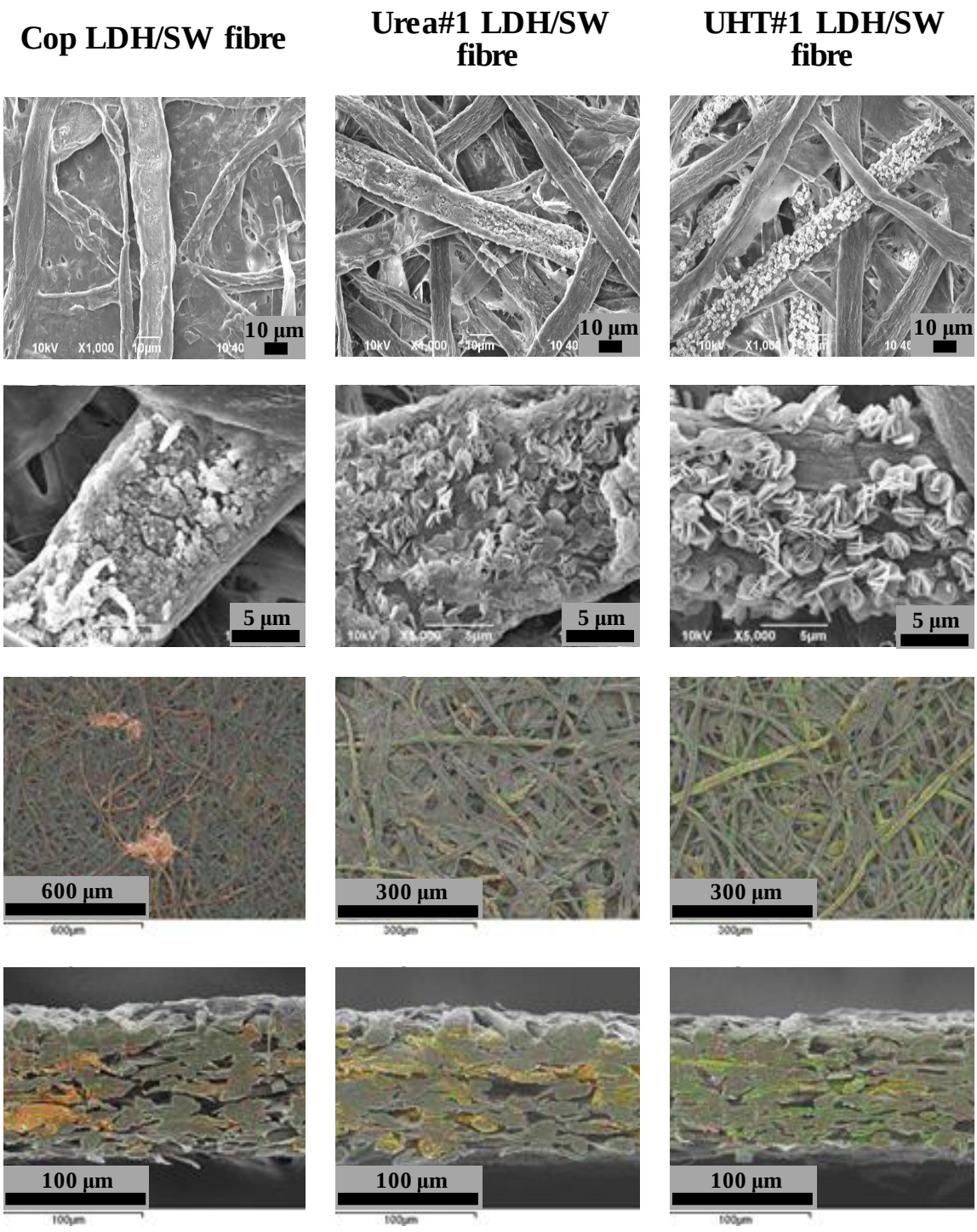


Figure 2.17. SEM and SEM-EDS images of the obtained paper sheets containing composites at 20% loading, (Red = Mg, Green = Al).

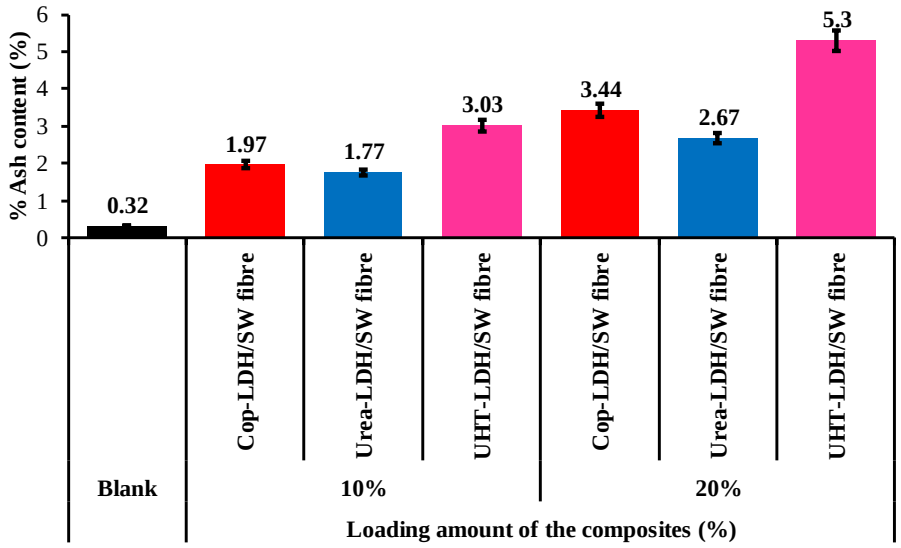


Figure 2.18. Ash content testing results, samples were test at least three times, the average and standard deviation values were reported. Blank (black), Cop-LDH/SW fibre (red), Urea-LDH/SW fibre (blue) and UHT-LDH/SW fibre (pink).

Fibres are generally collapsed during pressing and drying,[225] resulting in high density paper as shown in Figure 2.19 (a). In addition, paper density increases with increasing amount of conventional filler and it also depends on the type of filler used.[224] It was found that the paper density decreased after adding the composites. This is probably due to the precipitation of LDHs on the fibre surface, which decreases the fibre collapsibility, leading to an overall decrease in the density of the paper.[226, 228]

Stiffness is one of the most important and most challenging aspects among the different strength properties.[10] High stiffness is required for boxboard to ensure product protection.[223] The paper stiffness depends upon the elastic modulus and thickness of the paper.[10, 224] In general, fillers tends to interfere with the interfibre bonding, lowering the elastic modulus and stiffness.[286] It can be seen from Figure 2.19 (b) that the stiffness index of paper handsheets was higher in the case of composites loaded sheets as compared to the blank. This is probably due to less collapsibility of the composites leading to an increase of the elastic modulus of the fibre.[224] Lange *et al.* suggested that fibre flexibility decreased about 50% after mineralisation by LDHs.[232] Furthermore, the fibre thickness is expected to increase due to gluing effect of the LDH precipitate. Thus, the stiffness index increased as increasing the loading amount of the composites up to 30% as compare to the pure fibre. However, in the case of UHT#1 LDH/SW fibre, the stiffness decreased slightly afterwards with increasing the loading amount of the composites due to higher ash content in this sample than others as shown in Figure 2.18.

Moreover, the flexibility of the fibres will affect the porosity of paper. Uncollapsed fibres normally create a network with higher porosity and leads to easier dewatering (faster drainage time).[287] This agrees with the results in Figure 2.16 (a) and Figure 2.19 (c), as the paper porosity increased and drainage time decreased on increasing the amount of the composites fraction.

The tensile strength strongly depends on the hydrogen bonding between fibre. The better the inter-fibre bonding, the higher tensile strength is obtained. However, the tensile strength decreased after adding the composites and afterwards decreased at higher amount of the composites, as shown in Figure 2.19 (d). Since the LDHs precipitate outside of the fibre which tend to reduce the inter-fibre bonding area yielding in low tensile strength value.[224] It can be compensated by adding a dry strength agent such as cationic starch to increase the bonding interaction and strengthen the strength properties of paper.[288]

Generally, fillers are used to improve optical properties of paper.[11] The internal voids of particles offer high light scattering ability, which contributes to opacity.[11] As expected, the optical properties were improved with increasing the loading level of the composites (Figure 2.19 (e) and (f)). Due to an increase of the scattering coefficient value by LDH particles of the composites there is an increase in opacity of paper. The other properties are shown in the Appendix (Figure A3).

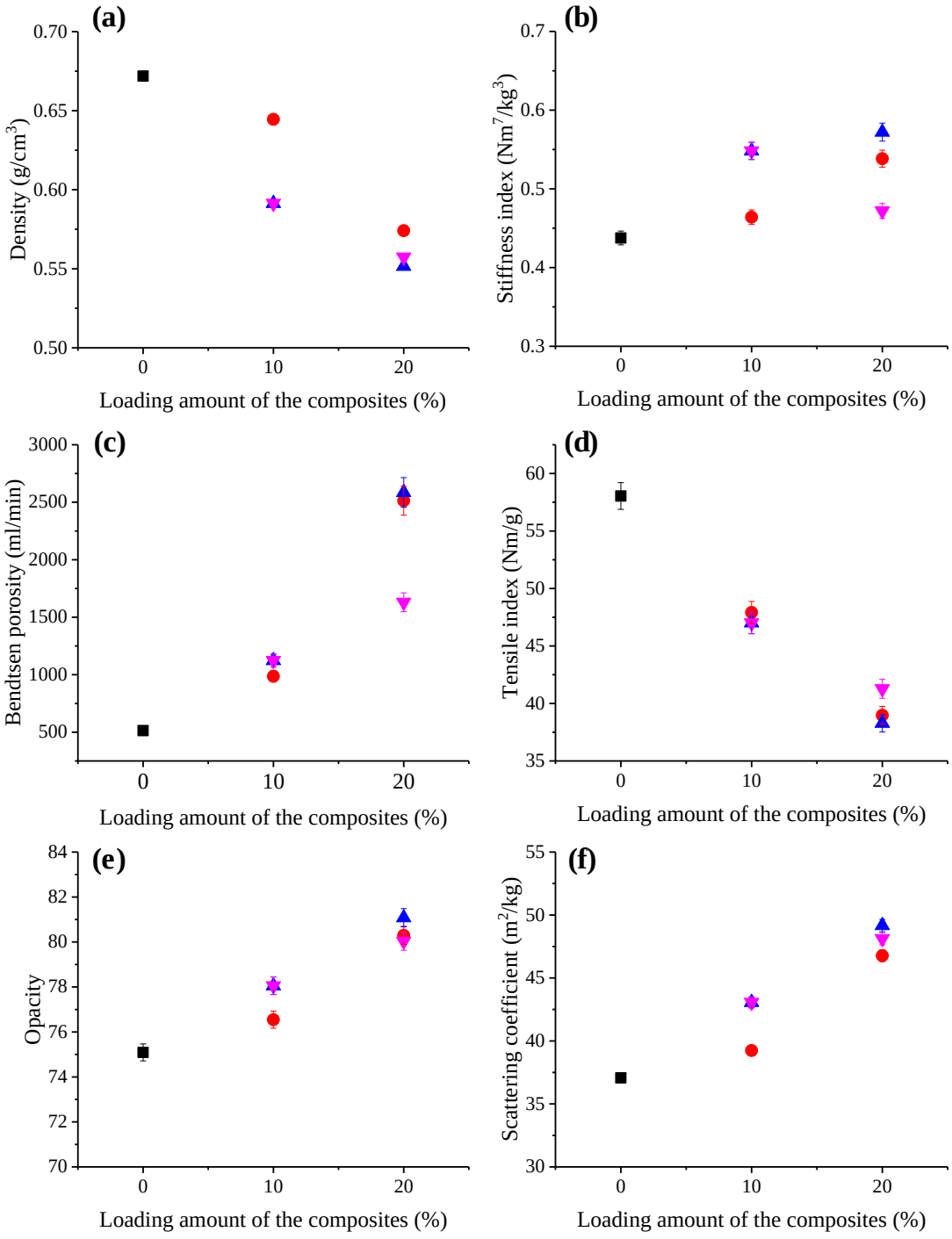


Figure 2.19. Physical properties of paper samples: (a) density, (b) stiffness index, (c) Bendtsen porosity, (d) tensile index (e) opacity, and (f) scattering coefficient.
■ Blank, ● Cop LDH/SW fibre, ▲ Urea#1 LDH/SW fibre and ▼ UHT#1 LDH/SW fibre.

2.4. Synthesis of functional LDHs for use in paper coating

In previous session, it has been found that the LDH/cellulose fibre composites can be used as an additive to provide low density, high stiffness and opacity paper, which seems promising for utilising in paper-based packaging application. However, paper easily absorbs water due to the hydrophilic nature of cellulose. As a result, it loses physical and mechanical strength.[289] Therefore, an improvement of moisture barrier properties of paper is crucial.

Wax coatings have been traditionally used as a moisture barrier to preserve the strength of paper-based containers. [237] In addition, paper is usually combined with other materials such as plastic and aluminium foil for providing better barrier properties.[290] However, such approaches are not readily recyclable and leads to extra cost for disposal.[237] Alternatives have become attractive including aqueous polymer containing fillers coatings on paper substrate. This study will explore the synthesis and application of hydrophobic organo-LDHs in paper coating. Three organic molecules (dodecylsulfate (DS), laurate (LR), and stearate (SR)) were introduced into MgAl-LDHs with a Mg/Al ratio of 3. The first two molecules have same alkyl chain lengths (C12) with different functional groups of sulfate and carboxylate, respectively, and the last one is C18 with carboxylate group. Two synthesis methods; co-precipitation and urea hydrolysis methods were performed. The water contact angle measurement is generally used to evaluate the hydrophobicity of the materials. Then the most promising organo-LDHs having highest water contact angle value have been chosen to prepare coating mixture and coat on paper.

2.4.1. Synthesis of organo-LDHs by co-precipitation method

In this study, the effect of loading level of dodecylsulfate (DS) and laurate (LR) was varied from 3, 6, 12, and 24 mmol (equal to Al/surfactant molar ratio of 4.2, 2.1, 1.0 and 0.5, respectively) using the co-precipitation method with metal nitrate precursors (under N_2 flow to eliminate dissolved carbonate). The resulting organo-LDHs were named as DS-LDHs and LR-LDHs for dodecylsulfate and laurate modified, respectively.

Figure 2.20 compares the FTIR spectra of NO_3-LDH, DS-LDHs and LR-LDHs, which confirms that both dodecyl sulfate anion (DS) and laurate anion (LR) were introduced to the LDHs by using the co-precipitation method. Moreover, the characteristic peak of nitrate anion at 1360 cm^{-1} decreased with higher loading of DS molecules. This peak was no longer present at a DS loading level of 24 mmol, indicating the incorporation of nitrate ion in the sample, which is confirmed by the elemental analysis results as shown in Appendix (Table A.2). The

percentage of carbon and hydrogen contents increased and nitrogen decreased as increasing the loading level of organic molecules.

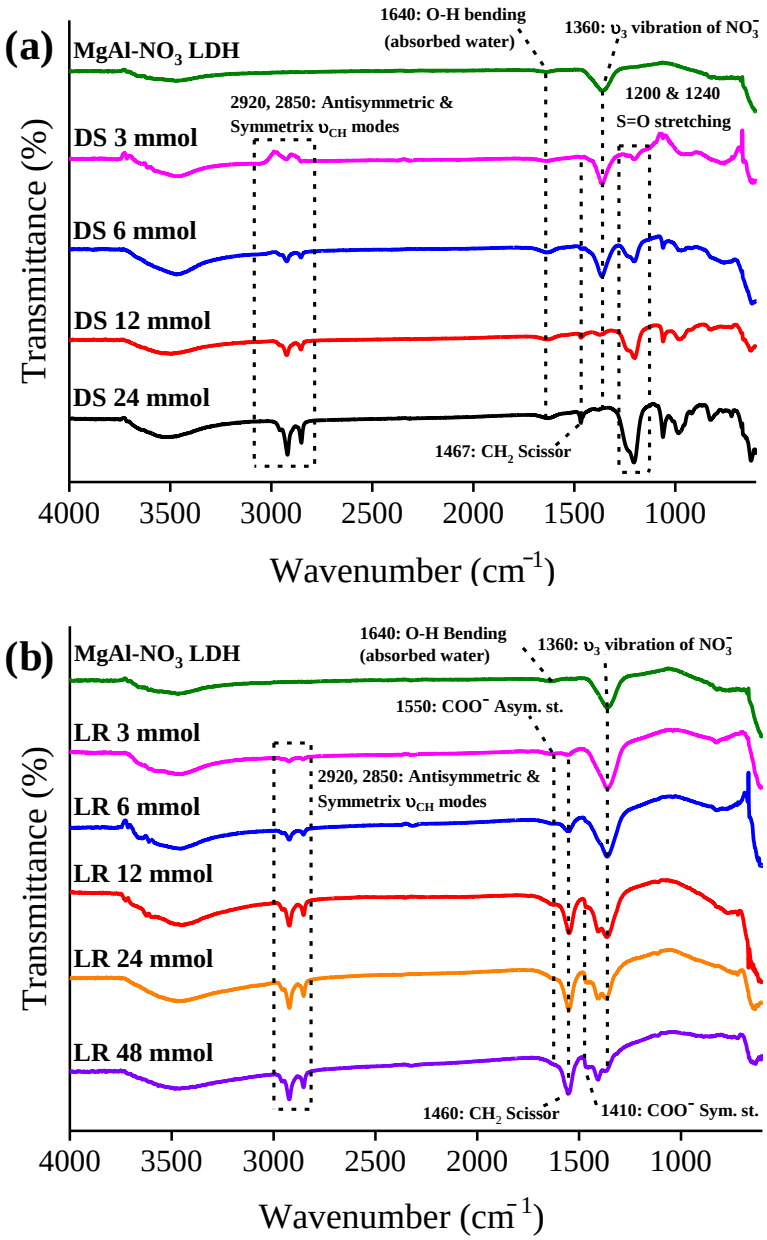


Figure 2.20. FTIR spectra of the NO_3-LDH and organo-LDHs (a) DS-LDHs and (b) LR-LDHs at different loading levels prepared *via* the co-precipitation method.

The XRD patterns (Figure 2.21) of the DS-LDHs and LR-LDHs exhibited the characteristic diffraction pattern of NO_3-LDH. The first Bragg peak belongs to the (003) basal plane, which can be used to calculate *d*-spacing (d_{003}) by using Bragg's equation.[192] The obtained NO_3-LDH has a *d*-spacing value of 8.0 Å. At low loading level of organic anions, DS-LDH and LR-LDHs have d_{003} values of 7.8 and 8.2 Å respectively, similar to the NO_3-LDH. It can be inferred that both anionic molecules might be just attached to the outside

surface or the edges of LDH.[291] In addition, the peak in the 2θ region between 19.5-21.5° was broader for both DS-LDHs and LR-LDHs than in the pure NO_3-LDH. This is attributed to the lateral stacking of alkyl chains in the LDH interlayer.[292] The DS molecules can be partially intercalated into the LDH galleries at loading levels above 6 mmol since new reflections were found at low angle regions with *d*-spacing of 26.8 Å (2θ = 3.29°), whereas LR-LDHs requires a higher loading, above 12 mmol, with a *d*-spacing of 25.8 Å. This may be attributed to the higher charge affinity of the sulfate versus the carboxylate group,[293] which is supported by the zeta potential values in Figure 2.22.

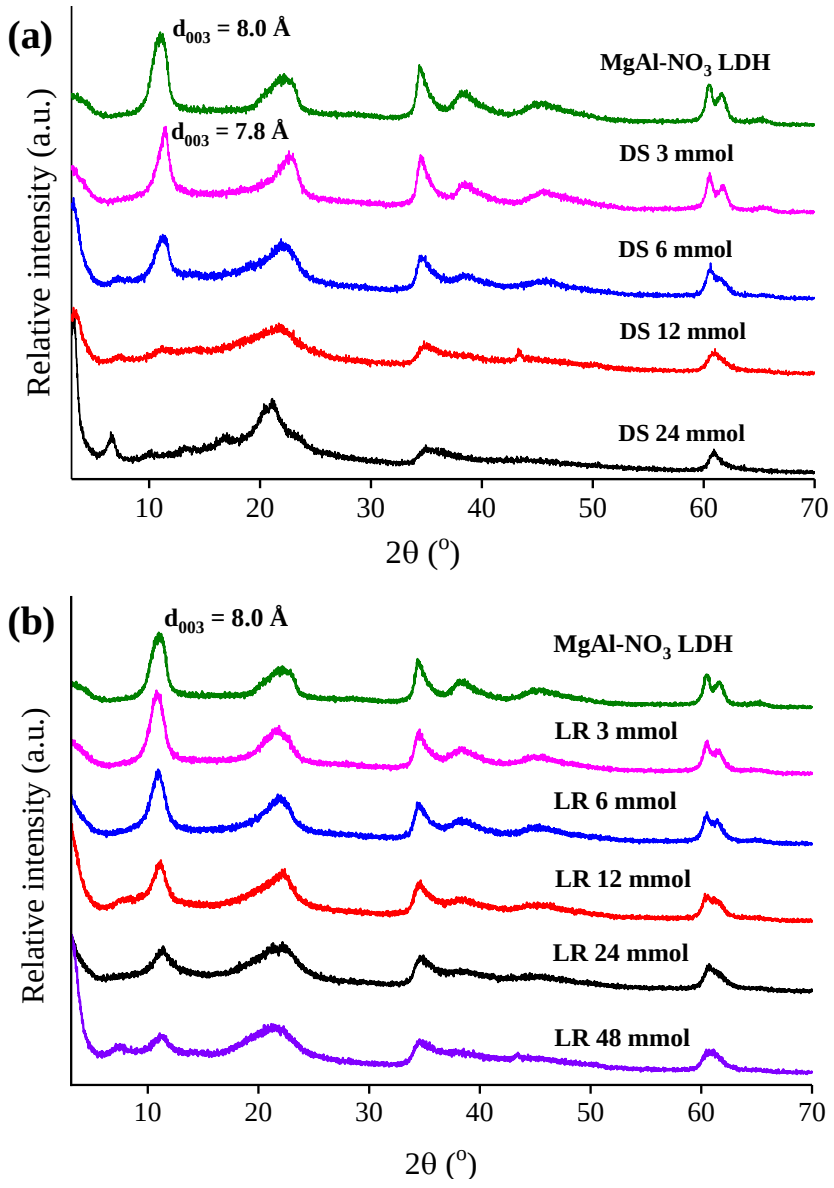


Figure 2.21. XRD pattern of the NO_3-LDH and organo-LDHs (a) DS-LDHs and (b) LR-LDHs at different loading levels prepared *via* the co-precipitation method.

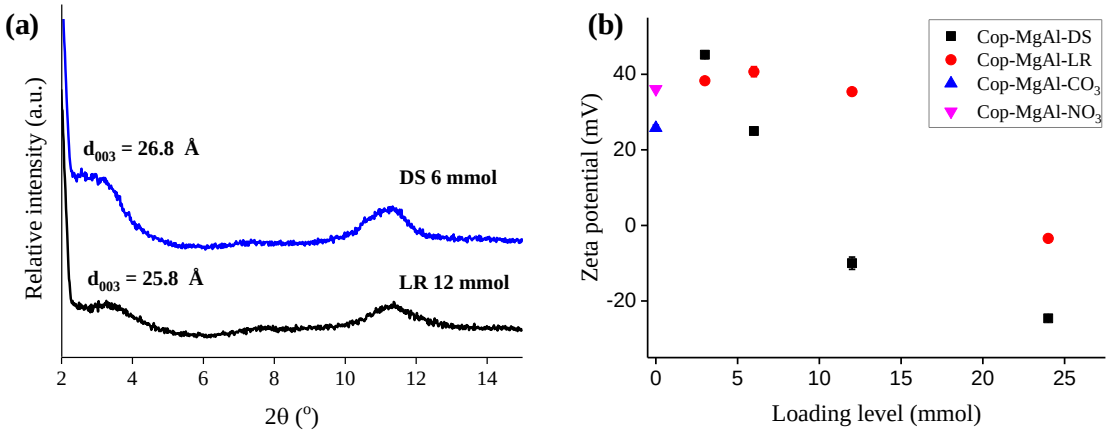


Figure 2.22. (a) XRD patterns at low angle region and (b) zeta potential of LDHs of DS-LDHs and LR-LDHs prepared *via* the co-precipitation method.

At the same loading level, DS-LDH gives a lower zeta potential value than LR-LDH. The aforementioned basal spacings are greater than the length of the DS (17.8 Å)[291] and LR (14.9 Å)[294] anions which imply that DS and LR anions form a paraffin-type bilayer arrangement in the interlayer space, organic anions orient double layer between the layers with the molecular axis slightly slanted from the normal of the basal plane.[291, 292] Both sulfate and carboxylate groups attach to the hydroxyl on LDH layers through electrostatic attraction and hydrogen bonding.[192]

Water contact angle measurements are generally used to evaluate the hydrophobicity of materials. Inorganic LDHs, such as CO_3-LDH, NO_3-LDH, are hydrophilic due to formation of hydrogen bonds between the intercalated species, surface hydroxyl and water in the solvation shell.[295, 296] As a result, the water contact angle of the pristine LDHs cannot be measured directly. In general, hydrophobic properties are improved by increasing surface roughness (micro-submicron range) and reducing surface energy of the materials.[297, 298] The introduction of organic moieties into LDHs results in the formation of a hydrophobic phase in the interlayer region as well as on the surface, hence, low surface energy of the surface.[179, 295, 296, 299, 300] As expected, in Figure 2.23, the water contact angle values (CA) of both organo-LDHs (the DS- and LR-LDHs) increases with increasing loading of anionic surfactants indicating the hydrophobicity of the products. The CA values are up to ~130° for DS-LDHs (DS 12 mmol) and 141° for LR-LDHs (LR 48 mmol). At high loading the DS-LDHs become hydrophilic, which meant that CA can no longer be measured, whereas LR-LDHs remain hydrophobic. Since the affinity of sulfate group is higher than the carboxylate group, the sulfate group can readily replace the surface nitrate anion in the LDH layers, starting from the edge and then throughout the basal plane. At high loading levels of surfactant (DS), DS is

forced to form the micelle-like structure, bilayer or micellisation, resulting in a negatively charged and hydrophilic surface.

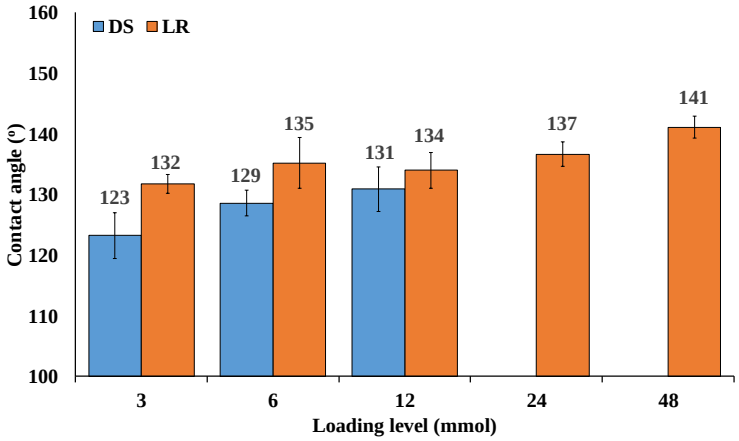


Figure 2.23. The effect of organic anion loading level on water contact angle value for DS-LDHs and LR-LDHs prepared *via* the co-precipitation method.

It was reported that organic molecules or supramolecules influence the LDH morphology by acting as a soft template.[192, 301] Due to strong interactions between the soft-template agents and inorganic species, the morphology of the obtained LDHs can be controlled.[192] The morphology of MgAl-NO_3 LDH, DS-LDHs and LR-LDHs were investigated by TEM (Figure 2.24). The morphology of LDHs changed from rose-like to aggregated morphology after incorporation of organic molecules. The DS-LDH sample presented severe aggregate structures with poorly-defined morphology compared to the LR-LDH. It was suggested by Zhang *et al.* that the LDH morphology are ascribed to the shape and number of micelles of the surfactant in solution.[192] The minimum concentration of a surfactant required to form micelles is defined as the Critical Micelle Concentration (CMC); for sodium dodecyl sulfate and sodium laurate, they are 8.2 and 24.4 mM, respectively.[302] The effect of DS concentration on LDH morphology was reported on the LDHs prepared *via* hydrothermal treatment at 160 °C.[192] At the concentration lower than the CMC value, the rose-like structure was obtained. Once the concentration exceeds the CMC, the micelles act as soft-templates inducing the nucleation and growth of LDH particles along the spherical micelle interface through electrostatic interactions between the head group of DS and metal cations, forming 3D flower-like microstructures.[192] However, at high DS concentration, the micelles aggregate together leading to aggregate morphology LDH products.[192] From TEM observation in this study (Figure 2.24), the concentration of DS used are much higher than its CMC, resulting in a large amount of micelles and aggregation of the final products. On the other hand, the

LR-LDHs show less severe aggregation of LDH particles than the DS-LDHs. This is probably due to the CMC of LR being about three times that of DS, the lower number of micelles in the mixture yields less aggregated LDH particles.

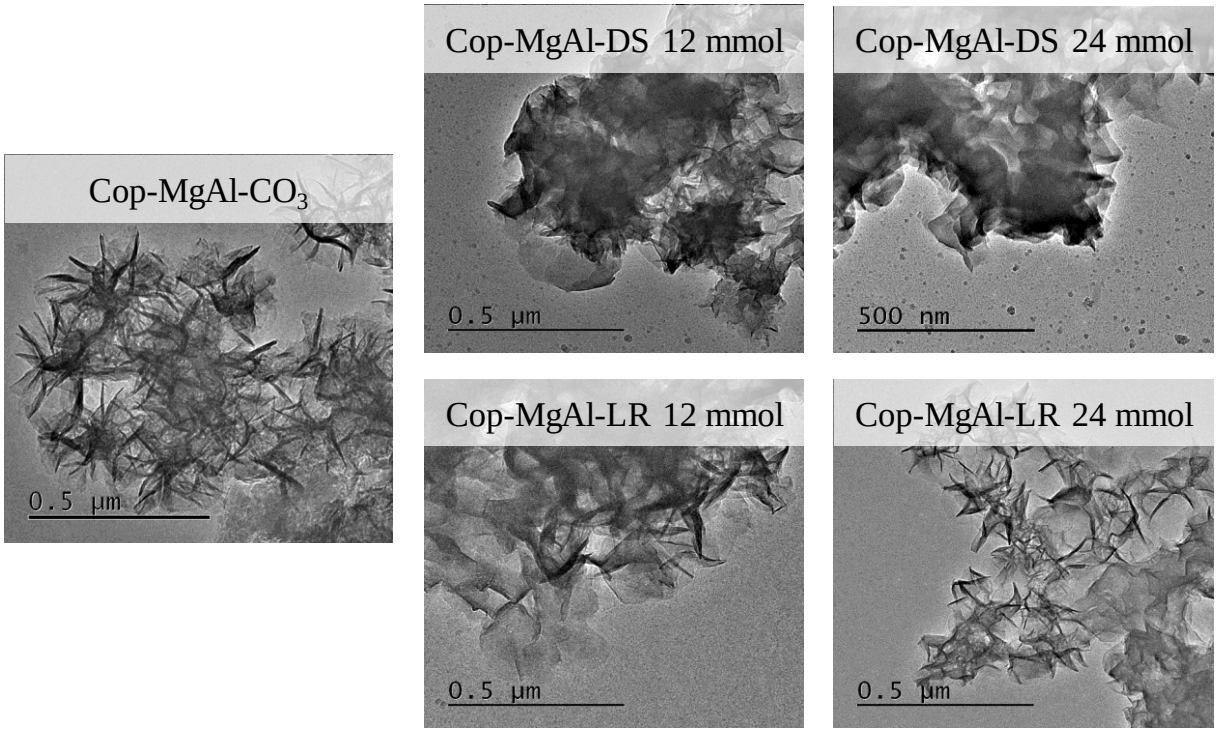


Figure 2.24. TEM images of organo-LDHs prepared by co-precipitation method.

2.4.2. Preparation of organo-LDHs by urea hydrolysis method

In general, it is relatively difficult to intercalate organic molecules into LDH using the urea hydrothermal method without co-intercalation of the carbonate anions.[303] As urea (an ammonia-releasing agent) generates carbon dioxide and ammonia under high temperature (>100 °C),[126] the generated gases cannot be released from the reaction in the autoclave reactor. Also, due to strong charge density of the carbonate anion, incorporation is unavoidable.[127]

In order to compare the effect of synthesis method on the properties of the obtained organo-LDHs, the urea hydrolysis method was employed. Three organic molecules; dodecylsulfate (DS), laurate (LR), and stearate (SR) at the loading level of 12 mmol were incorporated into the MgAl-LDHs with a Mg/Al ratio of 3. The obtained products were termed as U-DS LDH, U-LR LDH, and U-SR LDH, respectively. U-CO_3 LDH was noted as the conventional carbonate LDHs by urea method.

Figure 2.25 shows the FTIR spectra of organo-LDHs as compared to U-CO_3 LDH. All organo-LDHs presents the characteristic bands of the organic molecules used confirming the presence of these molecules in the LDH products. Generally, the presence of carbonate anions in the organo-LDHs is unavoidable unless inert atmosphere is used.[304] However, the incorporation of carbonate anion was not observed in all organo-LDHs in this study.[305] This may be because of forming of urea-carboxylate complexes *via* hydrogen bonds,[306] which could prevent the incorporation of atmospheric carbon dioxide. Alternatively, pH of the reaction mixture was about 3−4, which was acidic environment, and urea was slowly decomposed. After heating, pH of the mixture increased due to formation of ammonium cyanate from urea decomposition, which subsequent produced ammonium and carbonate anions.[82, 125] According to Bjerrum plot in Figure 2.26, when the carbonate anions was generated at the early stage of reaction, which was acidic, the carbonic acid was predominant and subsequently regenerated water and carbon dioxide.[307] Due to the reactions not being performed in an autoclave reactor, the generated carbon dioxide from the hydrolysis of urea molecules can escape from the reaction (more the open system). These may explain why no carbonate ions or nitrate ions (originated from metal salts) are incorporated, which is confirmed by the elemental analysis results as shown in Appendix (Table A.2). With heating the reaction at 100 °C for 18 hours, ammonium anion (along with carbon dioxide) was continuously produced from the hydrolysis of urea and yield the final pH of the reaction mixture was about 7.6−7.9.

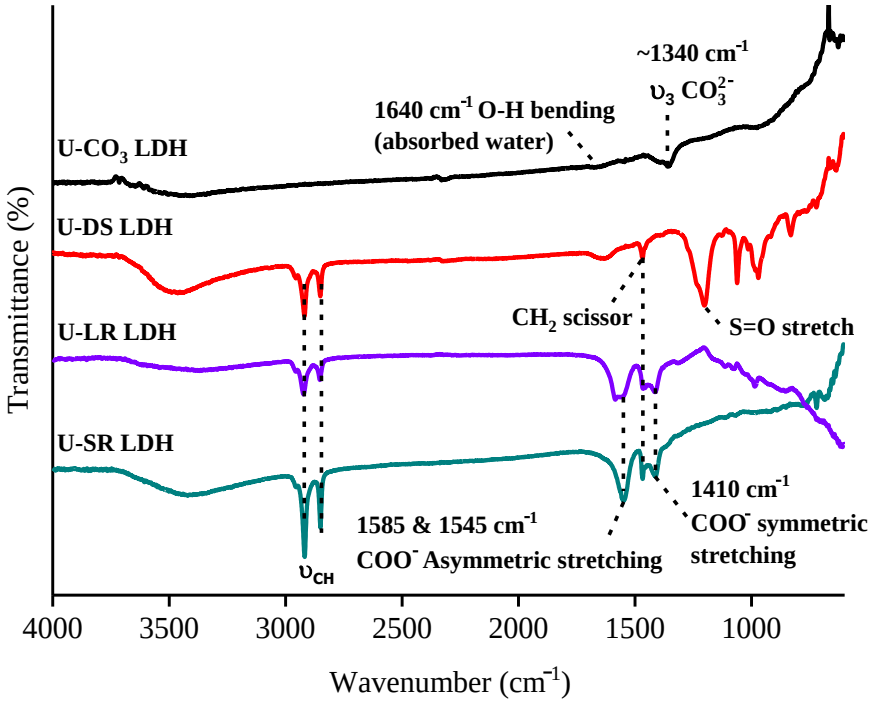


Figure 2.25. FTIR spectra of LDHs prepared from the urea method: U-CO_3 LDH, U-DS LDH, U-LR LDH and U-SR LDH at loading level of 12 mmol.

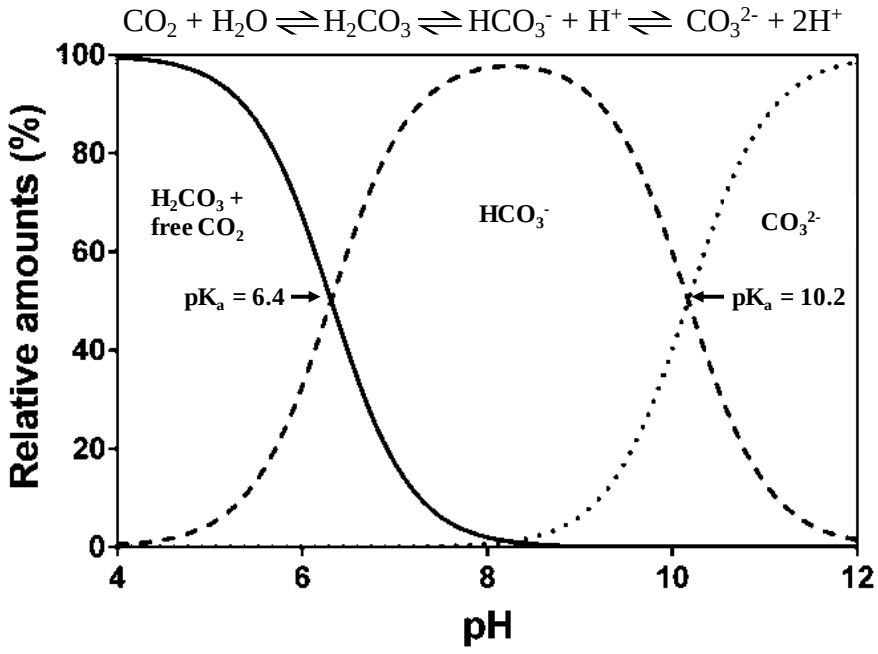


Figure 2.26. Bjerrum plot showing the activities of inorganic carbon species in water, carbon dioxide (CO_2), bicarbonate (HCO_3^-), and carbonate (CO_3^{2-}) as a function of pH. (Modified from Pedersen *et al.*.[307])

The presence of organic molecules in the LDH interlayer galleries was confirmed by XRD. Figure 2.27 shows that the d_{003} reflection of all organo-LDHs shift to lower 2θ angles from that of U-CO_3 LDH (2θ = 11.71°) indicating an increase in the interlayer space by intercalation of long chain organic molecules. This suggests that DS, LR and SR anions were intercalated into LDH layer galleries using the urea method. At low angle region at 2θ ~2-3° shows Bragg reflections corresponding to *d*-spacing values of 27.59 Å (1.6 x DS length), 33.29 Å (~2 x LR length), and 41.80 Å (1.7 x SR length) for U-DS LDHs, U-LR LDHs and U-SR LDHs respectively. Hence, the basal spacing increases with longer alkyl-chain length. In the co-precipitation method, the intercalation of LR molecules into the LDH interlayer at the same loading level (12 mmol) is not obviously seen.

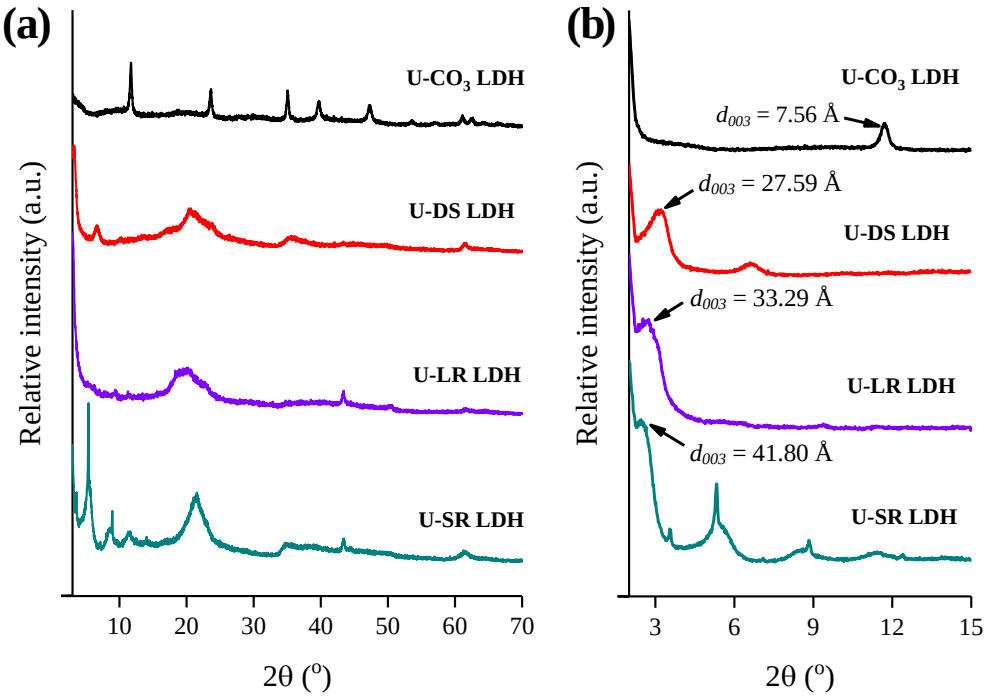


Figure 2.27. XRD pattern of LDHs prepared from the urea method: U-CO_3 LDH, U-DS LDH, U-LR LDH and U-SR LDH at loading level of 12 mmol (a) high angle (3-70°) (b) low angle region (2-15°).

The TEM images (Figure 2.28) show the difference in morphology of the organo-LDHs prepared from the urea method. It can be found that the morphology of LDHs became irregular after intercalation with organic anions, which possibly disturb the growth of LDH particles.

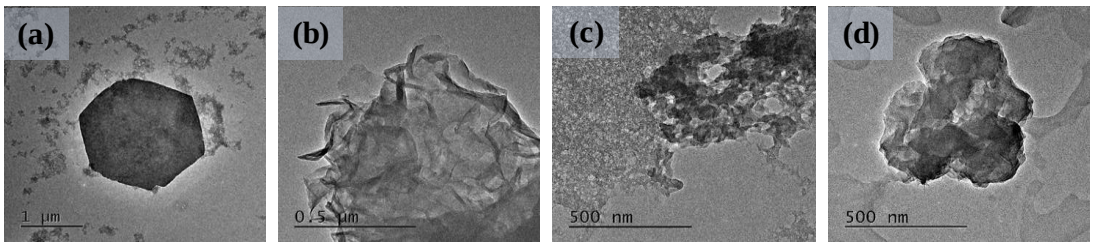


Figure 2.28. TEM images of LDHs obtained from the urea method (a) U-CO_3 LDH, (b) U-DS LDH, (c) U-LR LDH and (d) U-SR LDH.

In Figure 2.29, by using the urea method, the obtained organo-LDHs exhibit higher hydrophobicity than those obtained using the co-precipitation method. Figure 2.23 shows that the LR-LDH obtained from the co-precipitation method has a CA value of 134° while the urea method produces a superhydrophobic (CA > 150°)[308] organo-LDH with a CA value of 152° (but the U-DS LDH become hydrophilic). As predicted, the hydrophobic properties increase with increasing alkyl-chain length. The CA value of organo-LDHs can reach to 164° from U-SR LDH using the urea method. Therefore, organo-LDHs with superhydrophobic properties can be prepared from a one-pot synthesis by using the urea method.

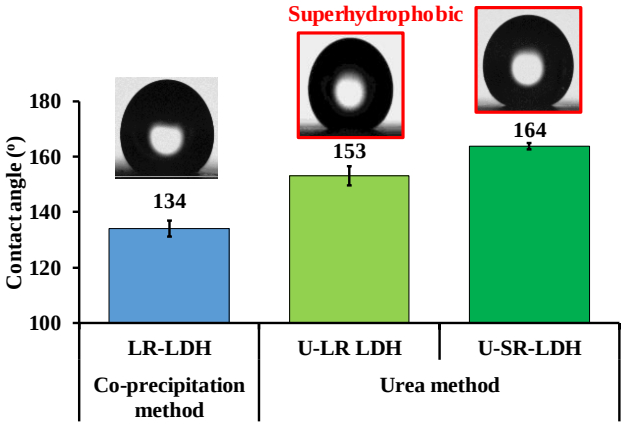


Figure 2.29. Comparison of the water contact angle values of organo-LDHs prepared by coprecipitation and urea methods. The image of the water drop on the surface was captured by IT Concept Tracker. The contact angle values were determined by the DropeSnake plugin in the ImageJ software. At lease three separate measurements carried out at the different locations on the surface and the average and standard deviation (error bar) values were reported.

Figure 2.30 shows the ^{13}C Cross Polarization Magic Angle Spinning (CP/MAS) NMR spectroscopy in the chemical shift range of −50-300 ppm. High intensity peaks at 10 to 50 ppm in both organo-LDHs were assigned to the ^{13}C resonances of long chain hydrocarbon from laurate and stearate molecules. Their functional groups were detected with low intensity peaks at 175 to 185 ppm, which belong to the ^{13}C resonance of carbonyl group (C=O) in the carboxylate ion. The ^{13}C resonance due to the carbonate anions from the LDHs at 165 to 170 ppm were found only in the U-CO_3 LDHs but no such signals in both

organo-LDHs. This confirms that the carbonate free organo-LDHs has been successful prepared by simple one-pot synthesis *via* urea method.

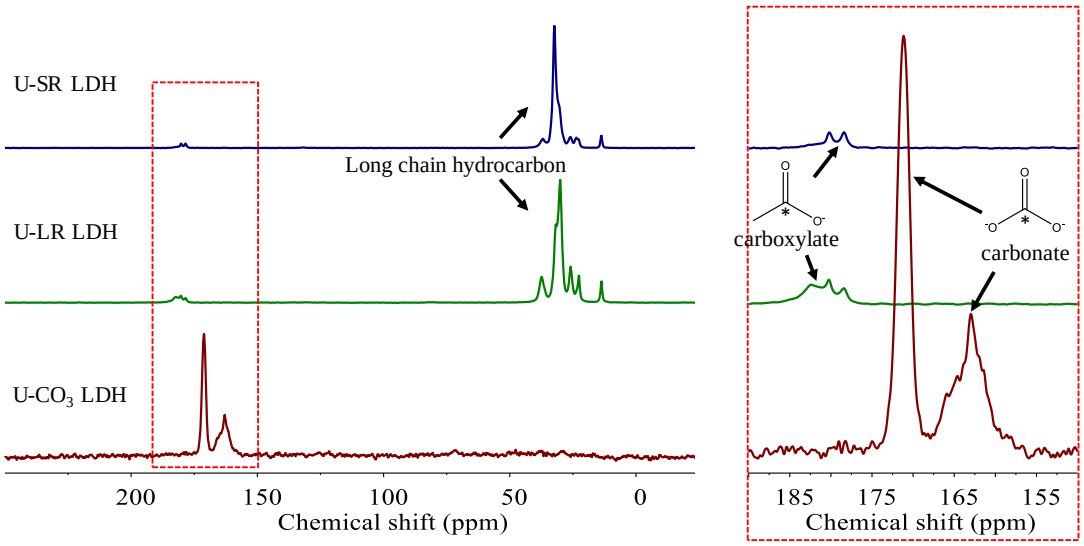


Figure 2.30. ^{13}C (CP/MAS) NMR spectroscopy of U-SR LDH, U-LR LDH and U-CO_3 LDH.

2.4.3. Application of LDHs to paper coatings

Recyclability and sustainability are the key driving trends for water-based barrier coatings to replace fluorocarbon and extruded polymer barrier coatings.[55] Clay platelets incorporated with appropriate polymers can provide effective barrier performance against water and gases.[309] Thus, this study aims to introduce organo-LDHs with high hydrophobicity and high shape factor in the water-based coating formulation for paper packaging. The effect of organo-LDH content, polymer types, and coat weight will be investigated. The barrier performance of the organo-LDHs will be monitored and compared with conventional coating pigments such as kaolin. The water vapour and oxygen permeability will be measured to determine the barrier performance of the coated paper.

2.4.3.1. Water resistance coating for paper application

It was found that by using the urea method the obtained organo-LDHs exhibit better hydrophobicity than those obtained using the co-precipitation method. Also, the hydrophobic properties increase with increasing alkyl-chain length with the water contact angle value up to 164° with the U-SR LDH. Therefore, in this study, the U-SR LDH was chosen to verify its hydrophobic performance by using it as a pigment in paper coating. The conventional kaolin clay was used as a comparison. The water resistance performance was evaluated by using the water contact angle measurement.

Figure 2.31 presents the water contact angle values of the coated papers. Hydrophobic characters can be increased by improving surface roughness (micro-submicron range) and reducing surface energy of the materials.[297, 298] The obtained U-SR LDHs coated paper shows superhydrophobic properties by being extremely repellent to water with a water contact angle value of 164° whereas kaolin coated paper produces a value of only 80°. This result seems promising for self-cleaning, water-proof paper applications.

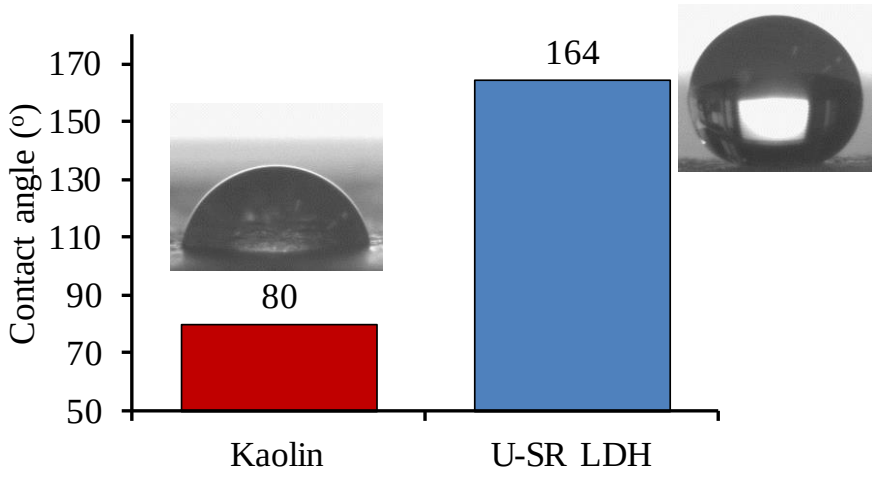


Figure 2.31. Water contact angle values of coated papers.

2.4.3.2. Water vapour barrier coating

Different pigments were employed including kaolin as a main pigment and U-CO_3 LDH and U-SR LDH as co-pigments at the loading level of 10 wt%. The conventional high barrier performance clay, nanoclay, was also compared and set as a benchmark in this study. Styrene butadiene latex (SB latex) was employed as a binder. Due to hydrophobicity of the U-SR LDH, it was firstly dispersed in ethanol then directly added to the SB latex. The pigment/latex ratio and the total solid content were controlled at 4/5 and 50 wt%, respectively. The coating mixture was applied on the commercial machine glaze paper (35 g/m^2) at a coat weight of 10 g/m^2.

All coated paper samples present similar grammage and thickness of paper (Figure 2.32), indicating a good control of coating amount on the paper. Figure 2.33 show that all coatings can improve smoothness with reduction of porosity of paper surface except only in U-SR LDH containing formulations due to coarse morphology of the U-SR LDH. At 10% loading, the U-CO_3 LDH loaded formulation show better surface coverage indicated by higher surface smoothness and lower porosity than the coating contained U-SR LDH. Platelet morphology of U-CO_3 LDH produces good coverage on paper surface. Coarse

morphology of U-SR LDH creates pores in coating structure leading to high surface roughness and porosity of coated paper, which may contribute to better hydrophobicity of the coated paper Figure 2.31.

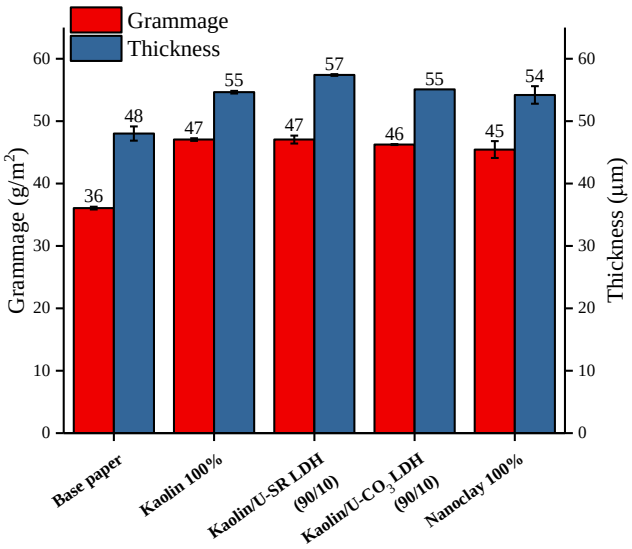


Figure 2.32. Grammage and thickness of coated paper.

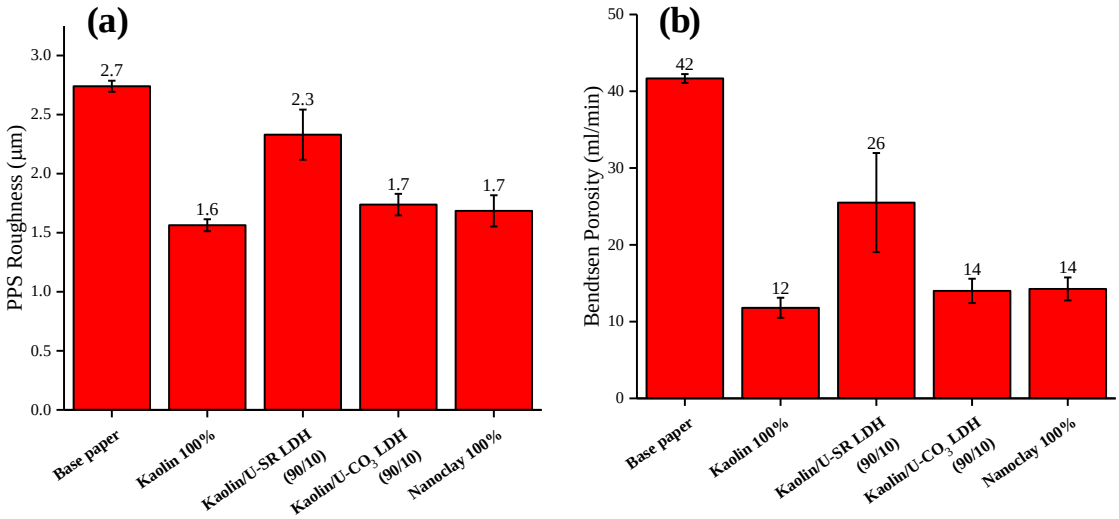


Figure 2.33. (a) Parker Print Surf (PPS) roughness and (b) Bendtsen porosity of coated paper.

Understanding the impact of coating structure, morphology (size and shape) and degree of packing of pigments are important in developing a coating design with excellent barrier properties. The complete film formation will form a stronger coating layer with reduction of permeability. The water vapour transmission rate (WVTR) increases with incomplete film formation of the coating layer and also a more porous coating, which indicates poor barrier properties.

The WVTR values of the coated paper are shown in Figure 2.34. An increase of WVTR value was observed after adding spherical pigments like U-SR LDH due to poor coverage of coating (uncoated areas were observed) as can be seen from SEM images (Figure 2.35 (b) and (f)) resulting in high surface roughness and porosity with poor barrier property. On the other hand, other coated paper showed uniformity of the coating layer. Especially in the coated paper samples with nanoclay (Figure 2.35 (d) and (h)) and the platelet LDHs like U-CO_3 LDH (Figure 2.35 (c) and (g)) provided better smooth surface due to well aligned parallel to each other and perpendicular to the direction of diffused molecules can reduce permeability. Only 10% loading of U-CO_3 LDH can achieve superior water vapour barrier with WVTR value at 49.4 g/m^2/day which is comparable with 100% loading of commercial nanoclay (44.9 g/m^2/day). Overall, it was found that morphology and coating coverage of LDHs play important role in barrier coating performance rather than the hydrophobicity of the LDHs. Hence, the U-CO_3 LDH seems to be a promising material for water vapour barrier coating application while the U-SR LDH is promising for water resistance coating.

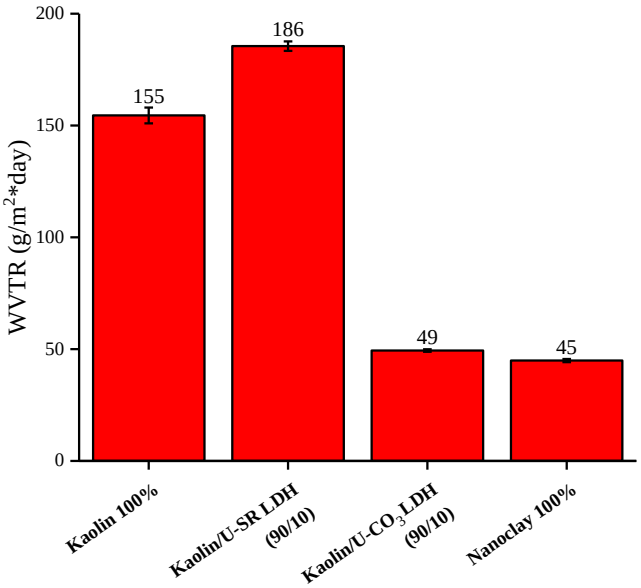


Figure 2.34. Water vapour transmission rate (WVTR) of coated papers.

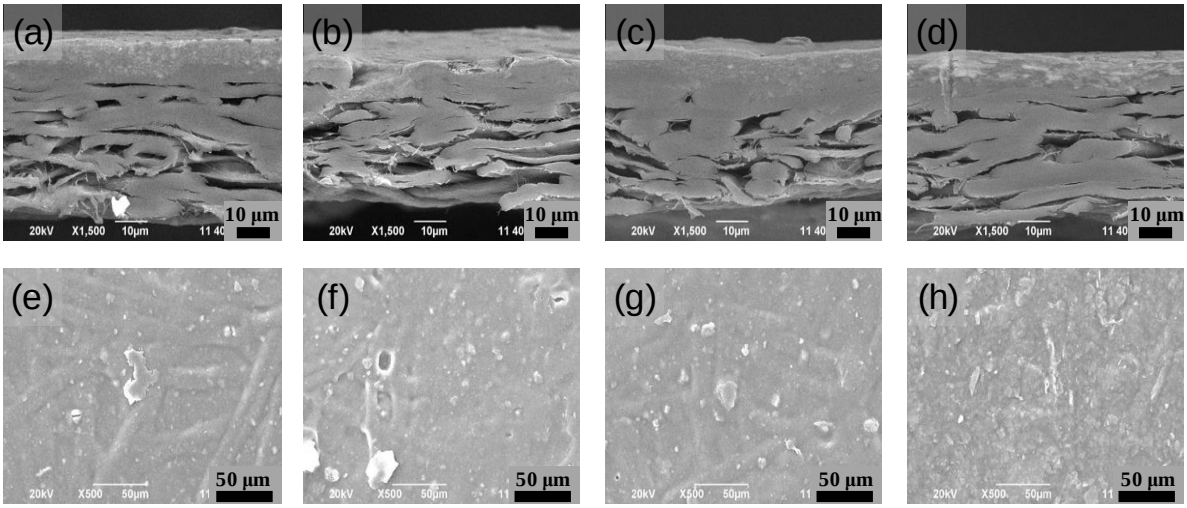


Figure 2.35. SEM (a)-(d) cross-sectional and (e)-(h) surface of coated paper with different coating composition: (a), (e) Kaolin, (b), (f) Kaolin/U-SR LDH 90/10, (c), (g) Kaolin/U-CO_3 LDH 90/10, and (d), (h) Nanoclay.

2.5. Conclusions

LDH/cellulose fibre composites have been synthesised by different methods and subsequently characterised. The fibre pretreatment condition seems important for precipitating the LDHs onto the fibres; fibres should be soaked in an alkali solution containing the target anions to get full coverage. Solid state NMR spectroscopy studies suggested that the interaction between LDHs and fibres could be the chemisorption *via* hydrogen bonding. It was shown that the synthesis method has an important effect on morphology of the composites. These composites can increase paper stiffness up to 30% as well improving the optical properties. These composites may be useful for packaging paper that requires high stiffness such as box or carton box.

The precipitation of LDH particles on the surface of cellulose fibre can provide a simple platform for functionalisation of natural based fibres since no toxic chemical is required. The pretreatment of fibres promoted good affinity between LDH particles and fibres, which is useful for growing LDHs on other substrate. Considering the results, we propose that the LDH/cellulose fibre composites can be used as specialty filler for producing high stiffness paper and widen the utilisation of fibre in other applications besides papermaking.

Hydrophobic and super hydrophobic organo-LDHs have been prepared by co-precipitation and urea hydrolysis methods. Increasing the concentration of the organic molecules leads to increase in the hydrophobicity of the LDHs products. Urea hydrolysis method provides organo-LDHs with higher hydrophobicity than using co-precipitation method. The organo-LDHs are suitable for water resistant coating application providing a

superhydrophobic surface to the coated paper with a water contact angle value up to 164°. Platelets CO_3-LDHs formed by the urea hydrolysis method are more preferred for application in a water vapour barrier coating application, providing WVTR values at the same levels as a specialty commercial clay.

These results suggest that type and concentration of anionic surfactant, and synthetic condition play a very important role on surface modification, and controlling the hydrophobicity properties of LDHs. The presence of organic molecules in the structure of LDHs results in a low surface energy and an increase in surface roughness (but give negative impact on water vapour barrier) of the particle, subsequently improves hydrophobicity of LDHs. It is our belief that such organo-LDHs will open new platform for utilising them in water-proof coating in many applications besides paper coating.

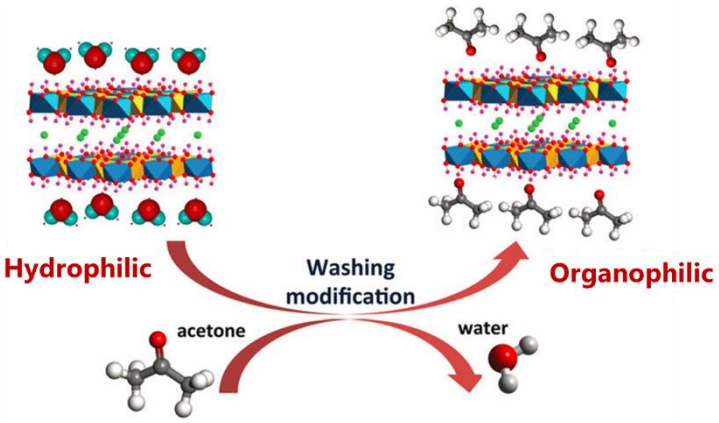
Chapter Three – Aqueous Immiscible Organic Solvent Treatment of Layered Double Hydroxides

3.1. Introduction

In recent years, LDHs have gained a lot of attention for use as catalysts and supports,[117, 202, 203] adsorbents,[202, 204, 205] flame retardant materials and polymer additives[212, 213] owing to their highly flexible composition, morphology and properties.[82, 83] The synthesis of high surface area and highly dispersed LDHs is of great interest for such applications. However, it is well known that the interlamellar hydrogen bonding networks and interlayer electrostatic interactions play a very important role in the structure of the LDHs, leading to a tight stacking and heavily aggregated layers.[310] As a result, primary LDH particles intercalated with inorganic anions (nitrate, chloride, carbonate, and sulfate) usually yield low surface areas (5−15 m^2/g).[311] It was reported that LDHs can be delaminated in formamide, butanol, and acrylate.[191, 198, 200, 312, 313] These molecules can disrupt the hydrogen bonding networks and the electrostatic interactions between layers, hence facilitating the exfoliation and delamination of LDHs. However, to isolate and recover the delaminated LDHs from such media without their aggregation is still a big challenge and not yet practical on a commercial scale application.

Recently, O'Hare and co-workers discovered a novel post-synthesis step[96, 195, 201] that dramatically increases their dispersion and organophilicity by using aqueous miscible organic solvent treatment, entitled as Aqueous Miscible Organic Layered Double Hydroxide (AMO-LDH).[195, 196] The composition of AMO-LDHs is defined as $[M^{z+}_{1-x}M'^{y+}_{x}(OH)_2]^{a+}(X^{n-})_{a/n} \cdot bH_2O \cdot c$(AMO-solvent), which instantly distinguishes them from the normal general formula of LDH, $[M^{z+}_{1-x}M'^{y+}_{x}(OH)_2]^{a+}(X^{n-})_{a/n} \cdot bH_2O$, wherein M and M′ are metal cations, z = 1 or 2; y = 3 or 4, $0 < x < 1$, b = 0–10, c = 0–10, X is an anion, n is 1 to 3 and $a = z(1 - x) + xy - 2$.[96] It has been observed that the AMO-LDHs are highly dispersed in certain non-polar hydrocarbon solvents and exhibit significantly higher surface areas.[96, 196] Such treatment can lead to dispersion into thin nanosheets, exfoliation or even form single layers.[195] Treatment parameters such as solvent dispersion volume, dispersion times, and number of re-dispersion cycle, and drying process have been investigated.[96, 196, 201] Their surface areas and total pore volumes have reached up to ~460 m^2/g and 2.15 cc/g.[195]

It was postulated that the organic solvent should be 100% miscible with water in order to replace the surface bound water from the surface of primary LDH particles as shown in Scheme 3.1.[196] Hence, the hydrophilic nature of the LDHs was suppressed and particle aggregation diminished.



Scheme 3.1. The proposed mechanism of AMO-LDHs formation.[196]

Despite the fact that the AMO process is simpler and more cost effective than other delamination processes, a high energy distillation process is required for solvent recovery. Moreover, the interaction between the AMO solvent and the LDHs is still underexplored. Herein, the use of non-AMO solvents will be examined in the post-production process of LDHs and the resulting LDH properties compared with AMO solvents. These solvents are identified as an aqueous immiscible organic solvent treatment (AIOST, so called AIM). Such solvents are easily separated from any displaced water and thus readily recycled. This would greatly enhance the efficiency of the manufacturing process and allow wider solvent selections. In this study, thirty organic solvents bearing different functional groups, structures, and properties will be compared. Furthermore, some post treatment parameters such as rinsing volume, dispersion time, Mg/Al ratios (2, 3 and 4), and recycling of solvents will be investigated. The solvents used in this chapter and their properties are summarised in Table 3.1.

Table 3.1. Solvent properties.[314]

Solvent		Molecular Formula	bp (°C)	Solubility in water (g/L)
Aqueous miscible solvent*	Acetone	C_3H_6O	56	Miscible
	Ethanol	C_2H_6O	78	Miscible
	Isopropyl alcohol	C_3H_8O	82	Miscible
	1-Methyl-2-pyrrolidinone	C_5H_9NO	202	Miscible
Aqueous immiscible solvent	Ethyl acetate	$C_4H_8O_2$	77	80
	Triethylamine	$C_6H_{15}N$	89	55
	Nitromethane	CH_3NO_2	101	111
	1-Butanol	$C_4H_{10}O$	117	68
	1-Hexanol	$C_6H_{14}O$	155	5.9
	Diethyl ether	$C_4H_{10}O$	35	60
	Diisopropyl ether	$C_6H_{14}O$	69	8.8
	Di-n-butyl ether	$C_8H_{18}O$	141	0.3
	Tert-butyl methyl ether	$C_5H_{12}O$	55	48
	Cyclopentyl methyl ether	$C_6H_{12}O$	106	11
	Tert-amyl methyl ether	$C_6H_{14}O$	86	10.7
	Anisole	C_7H_8O	155	1.52
	Methyl ethyl ketone	C_4H_8O	80	223
	2-Pentanone	$C_5H_{10}O$	102	0.43
	3-Methyl-2-butanone	$C_5H_{10}O$	94	0.52
	Methyl isobutyl ketone	$C_6H_{12}O$	117	19
	3-Pentanone	$C_5H_{12}O$	102	0.47
	Diisopropylketone	$C_7H_{14}O$	128	5.7
	4-Heptanone	$C_7H_{14}O$	144	3.19
	5-Nonanone	$C_9H_{18}O$	188	0.36
	Toluene	C_7H_8	111	0.00052
	Hexane	C_6H_{14}	69	0.0095
	Chloroform	$CHCl_3$	61	8
	Dichloromethane	CH_2Cl_2	40	13.2
	Cyclohexane	C_6H_{12}	81	0.06

*Organic solvent that 100% miscible with water.

3.2. Effect of solvent washing on flower shape like $Mg_4Al\text{-}CO_3$ LDHs

Both AMO and AIM solvents were compared in this study. The AMO solvents were acetone, ethanol, isopropyl alcohol, and 1-methyl-2-pyrrolidinone. Several AIM solvents with different functional groups and structures were employed; alcohol (1-butanol and 1-hexanol), ester (ethyl acetate), ether (diethyl ether and tert-butyl methyl ether (MTBE)), amine (triethylamine), nitro (nitromethane), ketone (2-butanone or methyl ethyl ketone (MEK)), hydrocarbon (hexane, toluene), and halogenated (chloroform).

After washing the LDHs with DI water several times to reach neutral pH, they were rinsed and re-dispersed in a certain solvent for 4 hours. The LDHs were easily dispersed in all AMO and most AIM solvents except in hydrocarbon and halogenated solvents (Figure 3.1). The shorthand term AMO-LDHs and AIM-LDHs are given for AMO and AIM solvents treated LDHs, respectively.

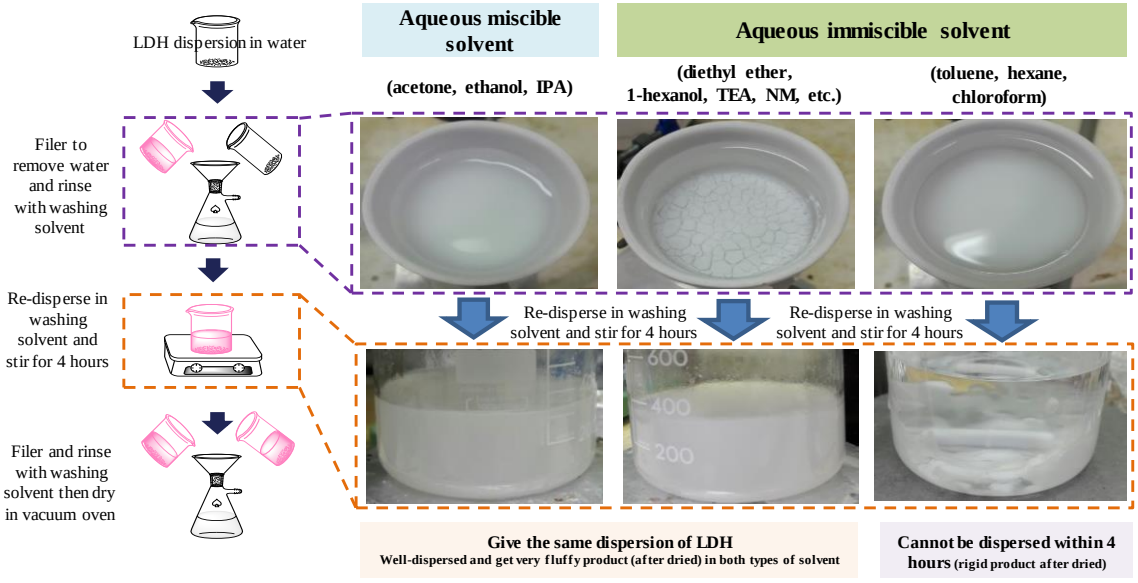


Figure 3.1. Process of post-treatment of LDHs by solvent washing and the appearance of LDH dispersion in different solvents.

3.2.1. Structural characteristics

The XRD patterns of water washed LDH, AMO-LDHs and AIM-LDHs with various washing solvents are shown in Figure 3.2 and Figure B1. They show the same XRD patterns, indicating that both AMO and AIM treatments do not affect the structure of the LDHs, assuming a 3R stacking of the layers and space group $R\bar{3}m$.[154, 273] The *d*-spacing of (110) Bragg reflection remained unchanged, suggesting that no detectable change the structure of the layer. In most cases, the shift of (003) Bragg reflection was not significant only peak broadening was observed, indicating the removal of the physisorbed water with no impact on the layer structure.[154]

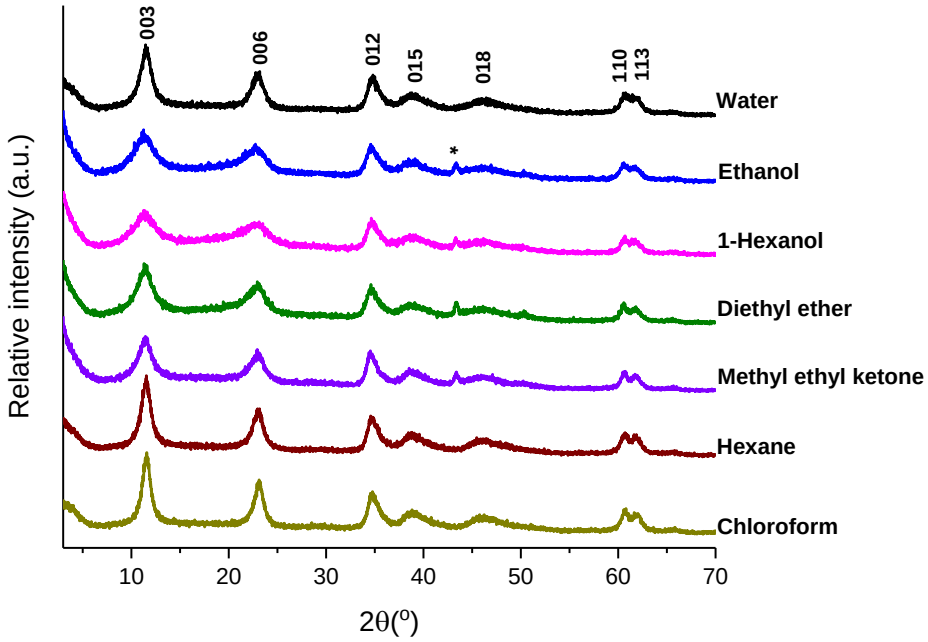


Figure 3.2. Powder X-ray diffraction patterns of some solvent-treated $Mg_4Al–CO_3$ LDHs. * is a Bragg reflection from the Al sample holder.

The Scherrer's equation is used to estimate the mean crystallite domain length (CDL) of the LDHs; $CDL = K\lambda(\beta cos\theta)^{-1}$, where *CDL* = the mean crystallite domain length, *K* = Scherrer constant, λ = the wavelength of the radiation = 1.5406 Å, and β = the full-width at half-maximum height (FWHM) values of a reflection located at 2θ.[315] The Scherrer constant (*K*) depends on the crystallite shape and assume the value 0.89 in this study, assuming a spherical shape for the crysallites.[316] Thus, the *CDL* along *c*-axis (CDL_{003}) can be calculated from the full-width at half-maximum height values of the (003) Bragg reflection, which is assumed to be the total crystal thickness along the *c*-axis. Moreover, a layer thickness of LDHs from the d_{003} spacing using the Bragg's law; $n\lambda = 2d(sin\theta)$, n is assumed to be one.[196] Therefore,

by application of the Bragg's law and the Scherrer equation, the number of LDH layers can be estimated dividing CDL_{003} value with d_{003} spacing value as shown in Table 3.2.[196] The results illustrate a massive reduction in the stacking length of LDHs from about 107 to 35 Å. Moreover, the number of LDH layers decreases from 14 to 4 layers after treatment, indicating the vital role of solvent in the formation of thinner primary platelets. Although the (003) Bragg reflection of hexane and chloroform treated LDHs are as intense as the water washed one, their (003) reflection slightly shift to higher 2θ (d_{003} spacing values decrease) then results in less number of LDH layers than the water washed product.

Table 3.2. Mean crystallite domain lengths of water washed, AMO, and AIM-LDHs

Washing solvent		(003)				No. of layers**	(110)	
		2θ (°)	d_{003} (Å)	FWHM (°)	CDL_{003} (Å)*		2θ (°)	d_{110} (Å)
Water		11.49	7.70	0.74	107.3	14	60.78	1.52
Aqueous miscible solvent	Acetone	11.33	7.80	2.01	39.4	5	60.67	1.53
	Ethanol	11.36	7.78	2.18	36.2	5	60.67	1.53
	Isopropyl alcohol	11.41	7.75	2.17	36.4	5	60.66	1.53
Aqueous immiscible solvent	Ethyl acetate	11.38	7.77	2.10	37.5	5	60.66	1.53
	Diethyl ether	11.43	7.74	1.76	44.9	6	60.64	1.53
	1-Hexanol	11.42	7.74	2.14	36.9	5	60.70	1.52
	Triethylamine	11.44	7.73	2.27	34.7	4	60.71	1.52
	Nitromethane	11.42	7.74	1.31	60.2	8	60.56	1.53
	Toluene	11.59	7.63	1.21	65.1	9	60.73	1.52
	Hexane	11.54	7.66	1.23	64.1	8	60.70	1.52
	Chloroform	11.54	7.66	1.16	68.1	9	60.74	1.52

* Mean crystallite domain lengths along *c*-axis (CDL_{003}) obtained from the Scherrer equation. $CDL = K\lambda(\beta cos\theta)^{-1}$, K = 0.89, λ = 1.5406 Å, β = $FWHM_{003}$.[315] **Number of layer = CDL_{003}/ d_{003}.

3.2.2. Surface properties

The Brunauer-Emmet-Teller (BET) method is the most widely used for evaluating the surface area of materials based on some assumptions; no interaction between each adsorption layer and the Langmuir theory can be applied to each layer, detailed equation was in Chapter Six.[317] The specific surface area of LDHs was determined by the BET method using the nitrogen adsorption, as shown in Figure 3.3. The specific surface area increases dramatically from 9 to almost 380 m^2/g after solvent treatment. The nitrogen adsorption-desorption isotherms of LDHs treated with six solvents were compared with the water washed LDH for clarification (Figure 3.4). The isotherms for all solvents were placed in the Appendix (Figure B2). All LDHs exhibit type IV isotherm and H3 type hysteresis loop which represents the plate-like particles with slit-shape pores of LDHs, according to the IUPAC classification.[317-319]

Characteristic features of type IV isotherm are formation of monolayer followed by multilayer adsorption at low relative pressure regions. Capillary condensation takes place in mesopores, and the limits uptake over a range of high relative pressure, which presents in its hysteresis loop. This behaviour reveals the mesoporous character of the samples. The H3 hysteresis loop suggests non-rigid aggregates of plate-like particles with lots of non-uniform slit pore sizes and/or shapes present in samples.[317, 320] Pore size distribution was determined by the Barrett-Joyner-Halenda (BJH) desorption, based on the application of the Kelvin equation (as shown in Chapter Six) with a correction for the multilayer thickness on the pore walls. Pore size distribution curves (Figure 3.5 and B3) point out the importance of the solvent washing process in the pore size range of LDH samples. According to IUPAC technical report, pores are classified into three types: macropores (>50 nm), mesopores (2-50 nm), and micropores (<2 nm).[321-323] For the water washed sample a sharp peak at a maximum around 40 Å appears, indicating presence of micropores and very small mesopores in this material. Clearly defined multi-pore ranges are generated either in AMO and AIM treatment. Large mesopores and some macropores are developed after solvent treatment. The micropores contribute to the near edge zone of the interlayer region and the meso-/macropores are attributed to the external surface area of the LDH platelets.[319] In some solvents, the pore size distribution curves became broad and shifted to a larger size with disappearance of the peak around 40 Å indicating the characteristics of mesoporosity. Some pores are larger than 50 nm, confirming macropores formation. Therefore, both isotherm and pore size distribution curves reveal that the nonuniformity of the porous structure is accentuated after solvent treatment. The surface properties of LDHs are summarised in Table B1.

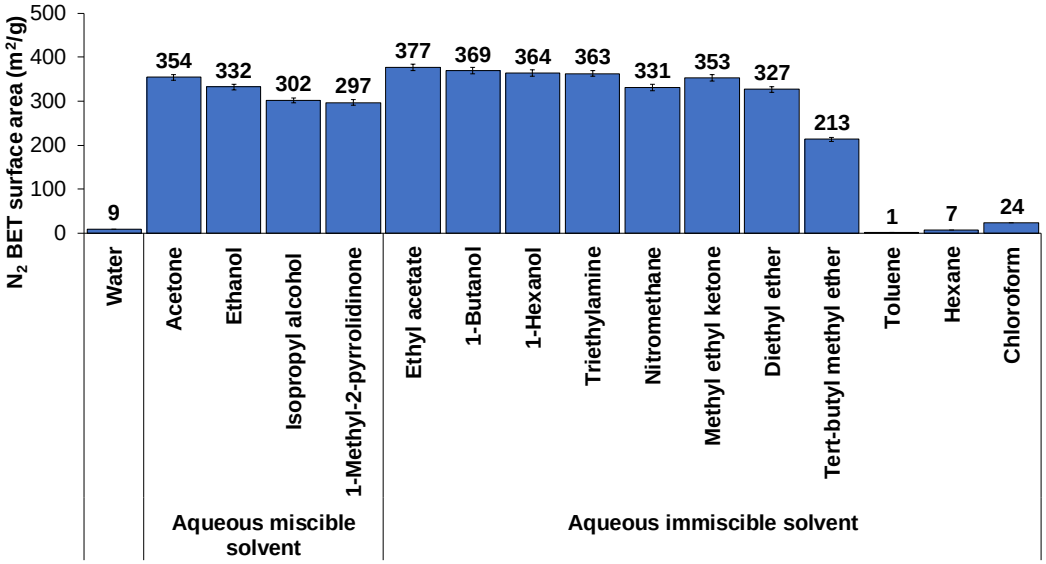


Figure 3.3. N_2 BET surface area of different solvent-treated $Mg_4Al–CO_3$ LDHs. 2% error bars are given.[201]

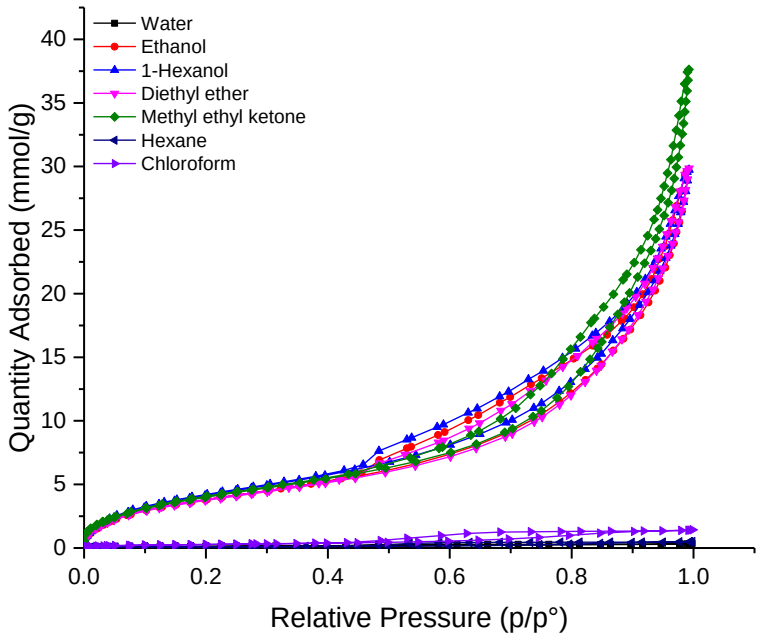


Figure 3.4. The N_2 adsorption-desorption isotherms of selected solvent-treated $Mg_4Al–CO_3$ LDHs.

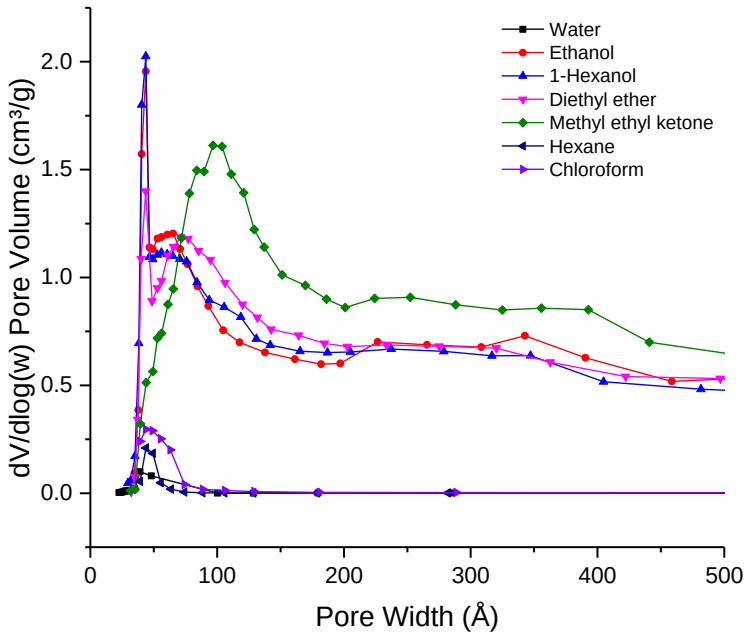


Figure 3.5. The Barrett-Joyner-Halenda (BJH) desorption pore size distributions (0-500 Å) of selected different solvent-treated $Mg_4Al–CO_3$ LDHs.

3.2.3. Density

Tap densities are calculated following a standard testing method (ASTM D7481-09).[96] The LDH powder was filled into a cylinder and a precise weight of sample (m) was measured. The volume was measured before (V_0) and after 1000 taps (V_t). The loose bulk and tap densities were calculated by: Loose bulk density = m/V_0; Tap density = m/V_t .

Figure 3.6 presents tap density value of LDHs. Most solvent treated LDHs are much more loose and show 80-90% reduction in powder density compared to water washed LDHs (from 1.21 to 0.20 g/ml). This indicates the replacement of the surface bound water and delamination of LDHs, resulting in thin nanosheets and high surface areas.

However, rigid solids were obtained after stirring LDHs in chloroform, toluene and hexane for 4 hours, resulting in high density and low surface area products. A slight increase in surface area and pore volume was observed in chloroform, indicating partial interaction between the solvent and the LDHs surface. The densities of LDHs are summarised in Table B1.

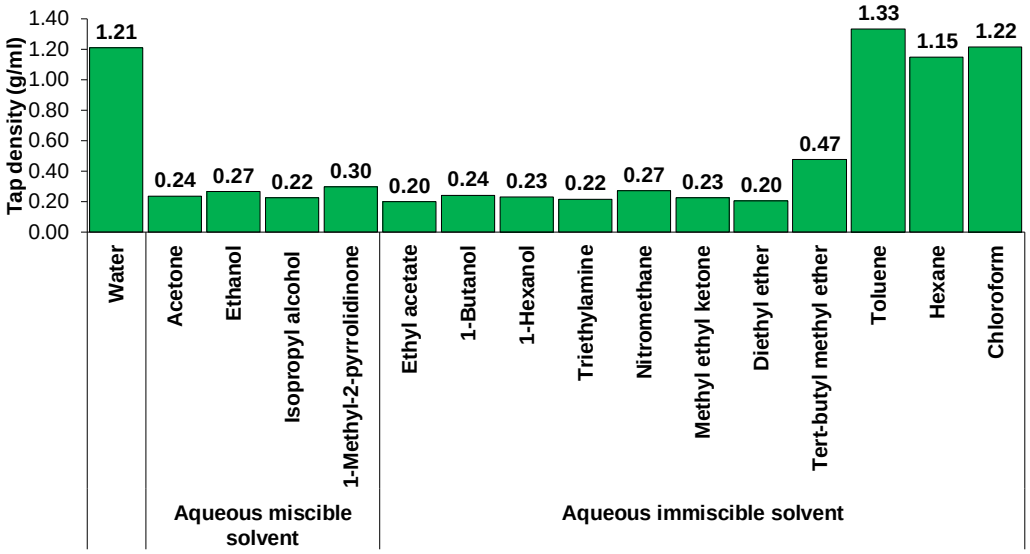


Figure 3.6. Tap densities of different solvent-treated $Mg_4Al–CO_3$ LDHs.

The formula for the solvent treated LDHs is defined as $[M^{z+}_{1-x}M'^{y+}_{x}(OH)_2]^{a+}(X^{n-})_{a/n}\cdot bH_2O\cdot c$(solvent). The solvent content (*c*) in the LDH structure was determined by using the thermogravimetric analysis (TGA) in the low temperature region.[96, 196] However, this approach is limited to solvents having boiling point close to water, or a high boiling point. As presented in the Appendix, Figure B4 shows the TGA and the first derivative curves (DTG) of water washed and different solvent-treated LDHs. It can be seen from the mass loss below 250 °C that the acetone treated LDHs produces two mass loss peaks of which the first is believed to be due to loss of acetone. High boiling point solvents (such as hexanol, bp. 155 °C) and hydrocarbon solvents (such as hexane and toluene) exhibit a broad peak in this region making solvent content determination difficult. Therefore, the amount of solvent in LDHs (*c*) can be determined by the elemental analysis (the Mg/Al ratio of 4 is assumed), which is summarised in Table 3.3. The solvent is probably bound to the surface of the LDH *via* hydrogen bonding and/or intercalated in the galleries of the LDH, indicated by the reduction of water content (*b*) from 0.634 to 0.033 with presence of solvent molecules (*c*) in the LDH formula in most solvents. In toluene, hexane and chloroform, a slight decrease of water content is observed (in the range of 0.402-0.593) with a low content of solvent in the structure. Among them, chloroform had a higher solvent content of 0.042, whereas hexane and toluene possessed solvent content of 0.002 and 0.001, respectively. This may indicate a better interaction of chloroform with LDHs than the toluene and hexane, which is in agreement with the surface area results.

Table 3.3. Summary of water (*b*) and solvent content (*c*) in the AMO-LDHs and AIM-LDHs compared to conventional water washed LDH as determined by the elemental analysis.

Washing solvent		*b*	*c*	Formula of LDHs*
Water		0.634	0.000	$[Mg_{0.80}Al_{0.20}(OH)_2(CO_3)_{0.10}]\cdot 0.634H_2O$
AMO solvents	**Acetone**	0.225	0.113	$[Mg_{0.80}Al_{0.20}(OH)_2(CO_3)_{0.10}]\cdot 0.225H_2O\cdot 0.113$(Acetone)
	1-Methyl-2-pyrrolidinone	0.512	0.092	$[Mg_{0.80}Al_{0.20}(OH)_2(CO_3)_{0.10}]\cdot 0.512H_2O\cdot 0.092$(1-Methyl-2-pyrrolidinone)
	Ethanol	0.245	0.215	$[Mg_{0.80}Al_{0.20}(OH)_2(CO_3)_{0.10}]\cdot 0.245H_2O\cdot 0.215$(Ethanol)
	Isopropyl alcohol	0.033	0.109	$[Mg_{0.80}Al_{0.20}(OH)_2(CO_3)_{0.10}]\cdot 0.033H_2O\cdot 0.109$(Isopropylalcohol)
AIM solvents	**1-Butanol**	0.041	0.099	$[Mg_{0.80}Al_{0.20}(OH)_2(CO_3)_{0.10}]\cdot 0.041H_2O\cdot 0.099$(1-Butanol)
	1-Hexanol	0.110	0.087	$[Mg_{0.80}Al_{0.20}(OH)_2(CO_3)_{0.10}]\cdot 0.110H_2O\cdot 0.087$(1-Hexanol)
	Diethyl ether	0.370	0.021	$[Mg_{0.80}Al_{0.20}(OH)_2(CO_3)_{0.10}]\cdot 0.370H_2O\cdot 0.021$(Diethyl ether)
	Methyl ethyl ketone	0.051	0.082	$[Mg_{0.80}Al_{0.20}(OH)_2(CO_3)_{0.10}]\cdot 0.051H_2O\cdot 0.082$(Methyl ethyl ketone)
	Methyl tert-butyl ether	0.247	0.040	$[Mg_{0.80}Al_{0.20}(OH)_2(CO_3)_{0.10}]\cdot 0.247H_2O\cdot 0.040$(Methyl tert-butyl ether)
	Nitromethane	0.214	0.049	$[Mg_{0.80}Al_{0.20}(OH)_2(CO_3)_{0.10}]\cdot 0.214H_2O\cdot 0.049$(Nitromethane)
	Triethylamine	0.124	0.036	$[Mg_{0.80}Al_{0.20}(OH)_2(CO_3)_{0.10}]\cdot 0.124H_2O\cdot 0.036$(Triethylamine)
	Toluene	0.402	0.001	$[Mg_{0.80}Al_{0.20}(OH)_2(CO_3)_{0.10}]\cdot 0.402H_2O\cdot 0.001$(Toluene)
	Hexane	0.548	0.002	$[Mg_{0.80}Al_{0.20}(OH)_2(CO_3)_{0.10}]\cdot 0.548H_2O\cdot 0.002$(Hexane)
	Chloroform	0.593	0.042	$[Mg_{0.80}Al_{0.20}(OH)_2(CO_3)_{0.10}]\cdot 0.593H_2O\cdot 0.042$(Chloroform)

* The solvent treated LDHs is defined as $[M^{z+}_{1-x}M'^{y+}_{x}(OH)_2]^{a+}(X^{n-})_{a/n}\cdot bH_2O\cdot c$(solvent), wherein M and M′ are metal cations, $z = 1$ or 2; $y = 3$ or 4, $0 < x < 1$, $b = 0$–10, $c = 0$–10, X is an anion, n is 1 to 3 and $a = z(1 - x) + xy - 2$.

The change in morphology of AMO and AIM treated LDHs was observed by TEM (Figure 3.7). Both AMO- and AIM-LDHs exhibit thin platelets and are less aggregated which suggests delamination of LDHs after solvent treatment. Therefore, the concept of solvent and LDHs interaction needs to be changed and further explored.

Considering the structure and functional group of each solvent, the similarity for all of them is hydrogen bonding. We have hypothesised that the residual water present between the layers of the LDHs or on its surface can be efficiently removed by an organic solvent having hydrogen bonding characteristics (hydrogen bond donor or acceptor). The solvent can interact with the surface hydroxyl group of the LDHs layer *via* hydrogen bonding and replace the surface bound water of the LDH, thereby resulting in a fluffy and high surface area LDH product.

By considering the definition of conventional hydrogen bonding 'The force of attraction between a hydrogen atom bonded to an electronegative species such as a N, O or F atom and another electronegative species such as a N, O or F atom.',[324, 325] all AMO and most AIM can be identified as conventional hydrogen bonding solvents.

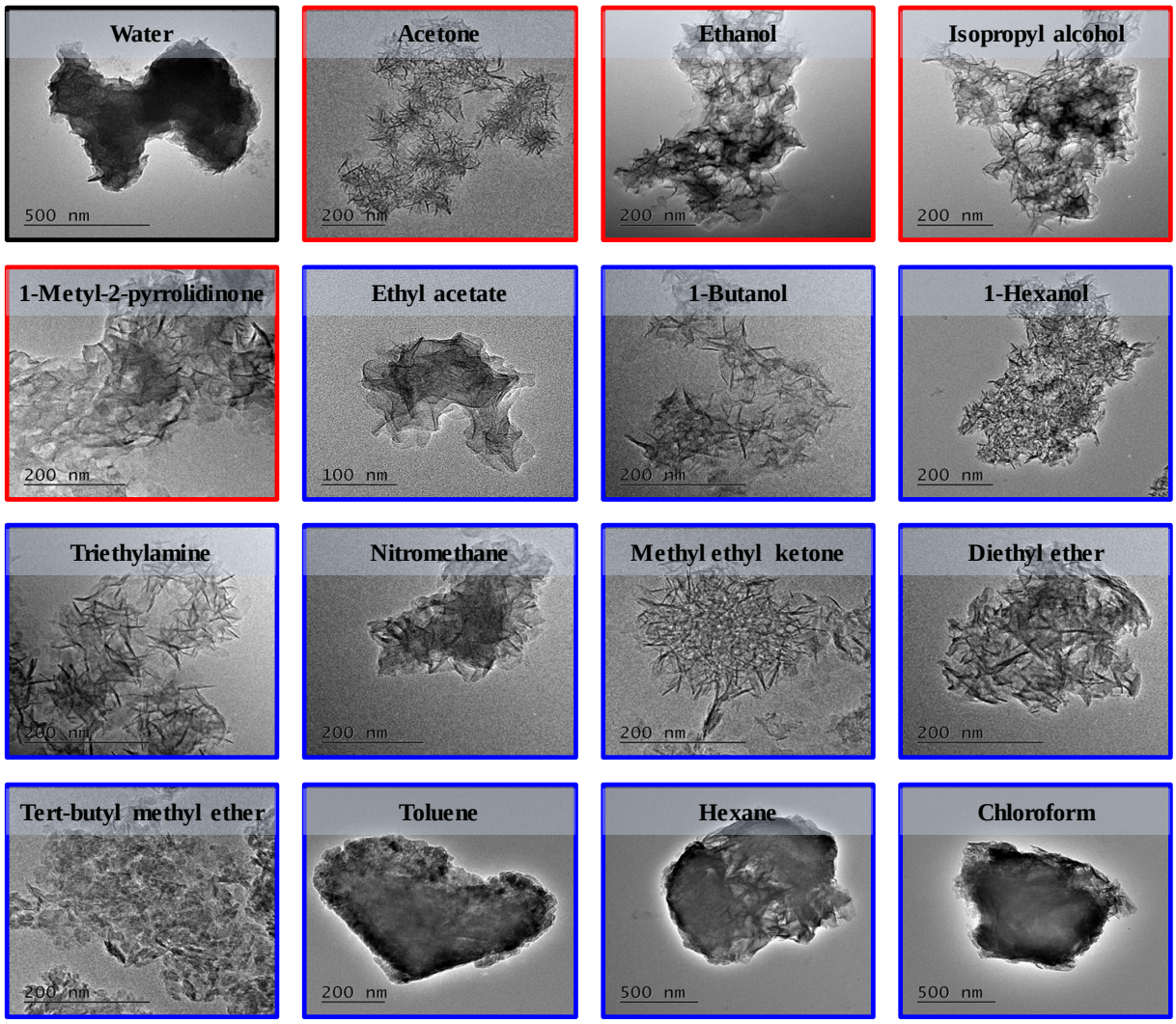
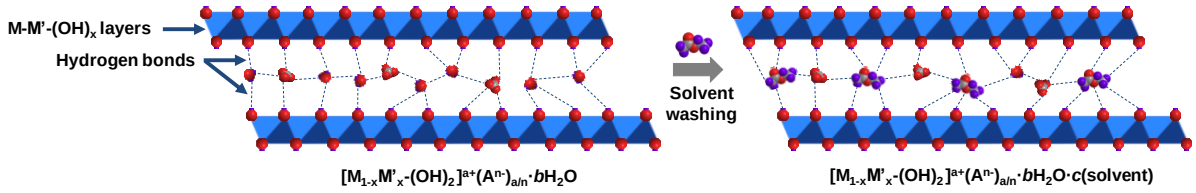


Figure 3.7. TEM images of different solvent-treated $Mg_4Al–CO_3$ LDHs.

However, hydrogen bonding can also exist with other atoms.[325, 326] In 1999, Desiraju-Steiner gave a definition for a new type of hydrogen bonding, so called 'weak hydrogen bonding', as an interaction X–H···A wherein a hydrogen atom forms a bond between two structural moieties X and A, of which one or even both are of moderate to low electronegativity.[327] It is now clearly recognised that X can be any element having higher electronegativity than H, and A could be any of these elements and also π-electrons.[328, 329] Hence, hydrocarbon and halogenated solvents can be recognised as weak hydrogen bonding solvents.

The conventional hydrogen bonding solvents have a much stronger bond than the Van der Waals force, so they may have strong interaction to the LDHs surface. On the other hand, the weak hydrogen bonding solvents are much weaker than a Van der Waals force and have a weak

interaction with the LDHs surface, requiring much longer dispersion time to interact with the surface hydroxyl groups of LDHs and replace surface bound water to generate high surface area LDHs.[327, 330] The proposed interaction between solvents and LDHs is shown in Scheme 3.2.



Scheme 3.2. The proposed interaction between solvent molecules and LDHs.

3.3. Effect of solvent structure (ether and ketone solvents)

As shown in Figure 3.3, diethyl ether washed LDHs has a surface area of 327 m^2/g while tert-butyl methyl ether gives 213 m^2/g. AMO or AIM treatment efficiency might also depend on the steric hindrance or structure of the solvent. Ether has a general formula R_1–O–R_2 and ketone $R_1C(=O)R_2$, where R_1 and R_2 can be a variety of carbon-containing substituents (alkyl or aryl groups). The alkyl groups can be the same on both sides (symmetrical) or different (unsymmetrical). Hence, the effect of solvent structure or steric effect of solvent on their treatment efficiency was examined. A series of ether and ketone solvents were introduced in this study; their structures are shown in Figure 3.8.

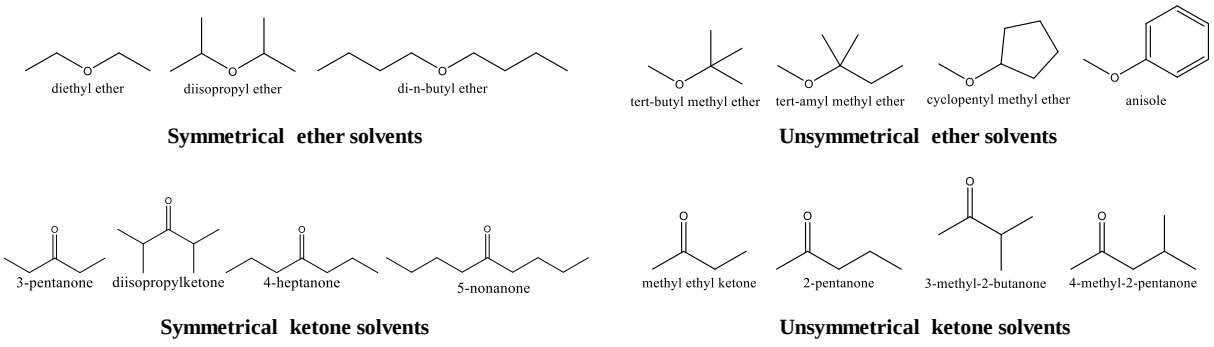


Figure 3.8. Structures of ether and ketone solvents.

In the ether solvent series, it was found that LDHs can be completely dispersed in most solvents, except in the case of long chain hydrocarbon or aryl group. As expected, LDHs treated with these solvents exhibit lower surface area and higher density than others (Figure 3.9). The N_2 adsorption-desorption isotherms and BJH desorption pore size distributions are in the Appendix (Figures B5 and B6).

In the case of symmetrical ether ($R_1 = R_2$), LDHs can be totally dispersed in diethyl ether (327 m^2/g) whereas when ether and di-n-butyl ether were used, partial dispersion occurred with

a surface area only about 200 m^2/g. In addition, the water content increased (with lower amount of solvent in the formula) with increasing chain length; 0.370 (diethyl ether), 0.525 (diisopropyl ether), and 0.630 (di-n-butyl ether). It was suggested from simulation studies of AMO solvents that the small solvent molecule is able to adsorb closely onto the LDH surface and disrupt the hydrogen bonding network between water and LDHs.[331] This is possibly due to the steric effect of the hydrocarbon chain length which interferes with the accessibility of the solvent to the LDHs surface, resulting in a lower surface area and pore volume and higher density of LDHs. Surface properties and formula of ether solvents treated LDHs are shown in the Appendix (Table B.2 and Table B.3).

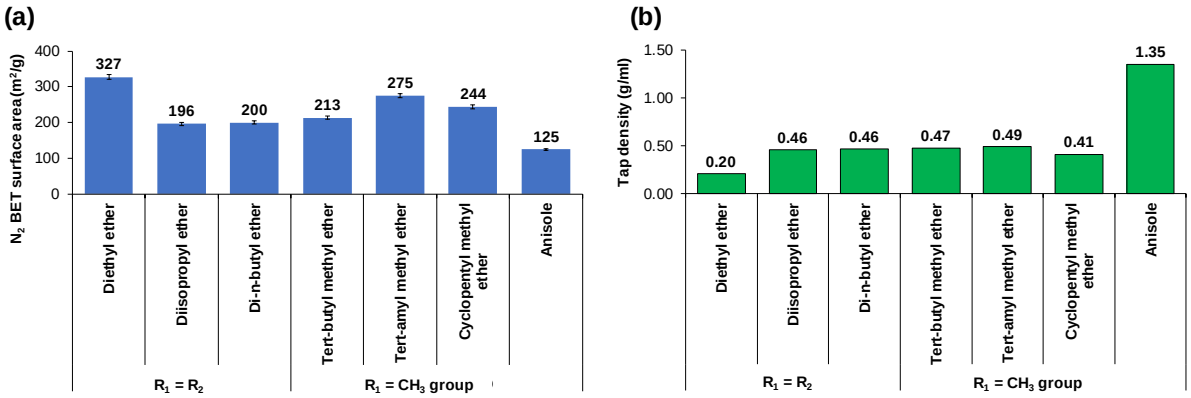


Figure 3.9. (a) N_2 BET surface areas and (b) tap densities of $Mg_4Al–CO_3$ LDHs treated with different ether solvents.

For unsymmetrical ether solvents (R_1 = CH_3 group), surface area remained slightly higher than for symmetrical ones (one exception is diethyl ether) with values above 200 m^2/g (up to 275 m^2/g) even when long chain hydrocarbon ether was used. This was confirmed by a lower water content (0.247 in methyl tert-butyl ether) and a slightly higher amount of solvent (0.040 in methyl tert-butyl ether) in the structure. However, there is a limitation in the R_2 substitution group; the effect of steric hinderance was clearly observed when aryl substitution group was used (anisole) and a dramatic reduction of surface area was observed (125 m^2/g). This might be due to steric or hydrophobic effects of the aryl group which limit the accessibility of anisole to LDHs surface matched by the very low anisole content of 0.007 in the formula. The effect of chain length or steric hinderance of unsymmetrical ethers could be clearly observed if the R group was changed from methyl to ethyl or to a longer hydrocarbon chain group. The composition of these LDHs is shown in the Appendix (Table B.5). Product appearance obtained from different ether solvents is shown in TEM in Figure B9.

Ketone solvents show similar trends to ether solvents, except that the LDHs can be fully dispersed (by appearance) in all the ketones used (Figure 3.10). The effect of hydrocarbon chain length on surface area of the resulting LDH was observed in unsymmetrical ketone solvents when using methyl ethyl ketone as a solvent the surface area of LDHs reached 353 m^2/g, while the surface area decreased and remained similar in the range of 224-250 m^2/g when longer chain length ketones were used. Their morphology was observed by TEM (Figure B10) and exhibits thin platelets in all ketone solvents. Their isotherm and pore size distribution curves are in the Appendix (Figures B7 and B8). Surface properties and formula of ketone solvents treated LDHs are shown in the Appendix (Table B.2 and Table B.4).

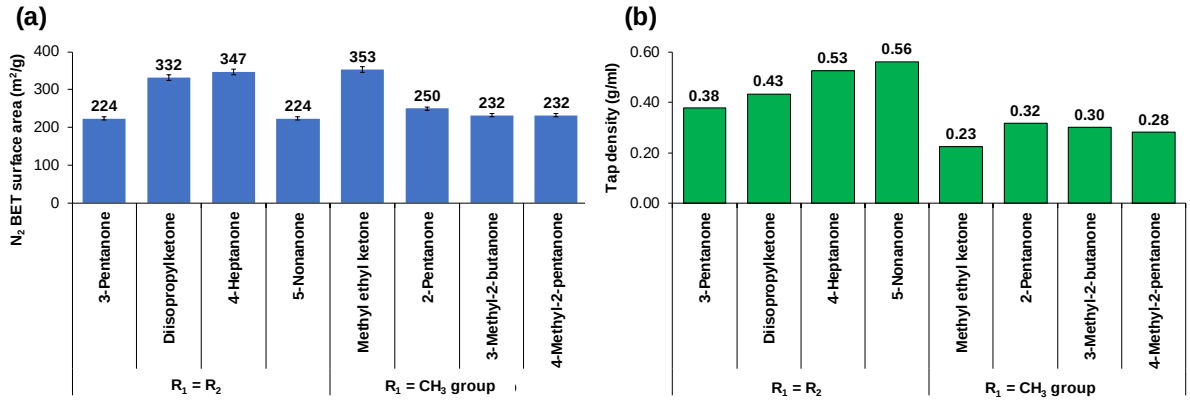


Figure 3.10. (a) N_2 BET surface areas and (b) tap densities of $Mg_4Al–CO_3$ LDHs treated with different ketone solvents.

The water content increased with increasing chain length; similarly to unsymmetrical ethers. On the other hand, in symmetrical ketones, the effect of steric hinderance is still unclear. 4-heptanone, which has 4 carbon chain length both sides, provides higher surface area product (347 m^2/g) than 3-pentanone (224 m^2/g), which has only 2 carbon chain length both sides. There is also no trend in terms of water and solvent content in the formula. This may be due to different behaviour of the solvent orientation on the surface. Once the longer chain hydrocarbon was used, 5-nonanone, the obtained LDH has surface area 224 m^2/g. The tap density of LDHs increased with increasing hydrocarbon chain length.

3.4. Effect of dispersion time

It was reported that 1 hour dispersion time is enough to reach high surface area LDHs with AMO treatment with acetone.[196] However, the observation from ether solvent study reveals that at 4 hours dispersion time is not enough to get full dispersion (by appearance) in the steric ether

solvents resulting in low surface area LDHs (Figure 3.9). These solvents are di-isopropyl ether, di-n-butyl ether and anisole.

In this study, the dispersion time of LDHs was varied until full dispersion of LDHs in each solvent was achieved. Figure 3.11 shows nitrogen BET surface area values of LDHs treated with ether solvents at different dispersion time. Isotherm and pore size distribution curves are shown in the Appendix (Figure B11). Both symmetrical ethers, di-isopropyl ether and di-n-butyl ether, required about 8 hours to reach full dispersion of the LDH. Even though only a modest increase in surface area (from 200 to 230 m^2/g) and decrease in powder density were observed the amount of water was reduced drastically. For example, the value was about halved after 8 hours for diisopropyl ether treated LDH. Surface properties and composition of these LDHs is shown in the Appendix (Table B.5 and Table B.6).

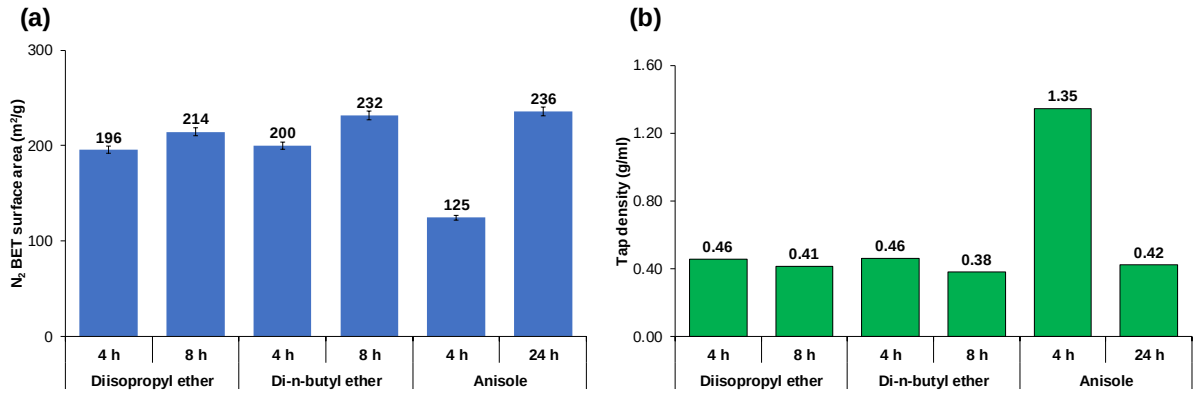


Figure 3.11. (a) N_2 BET surface areas and (b) tap densities of ether washed LDHs with varied dispersion time.

On the other hand, in the case of anisole, an aryl ether solvent, 24 hours is needed to get full dispersion of the LDH. This results in a higher surface area from 125 to 236 m^2/g and dramatic decrease in density from 1.35 to 0.42 g/mL. Water content was also minimised from 0.506 to 0.022. Morphology of obtained LDHs is shown in Figure B12.

3.5. The weak hydrogen bonding solvents: effect of their structure and dispersion time

To further understand the relationship between the solvent structure and required dispersion time, weak hydrogen bonding solvents like hydrocarbon and halogenated solvents were studied.

The dispersion times were varied until full dispersion, in each solvent, was reached; including hexane, cyclohexane, toluene, dichloromethane and chloroform. It was observed that LDHs can also be dispersed in weak hydrogen bonding solvents with prolonged dispersion time. With longer dispersion times, higher surface areas and lower densities were obtained

(Figure 3.12). All weak hydrogen bonding treated LDHs show type IV isotherm with H3 hysteresis loop. Pore volume and size were enlarged with prolonged dispersion in these solvent types, as shown in the Appendix (Figures B13 and B14). Their surface properties were summarised in the Appendix (Table B7).

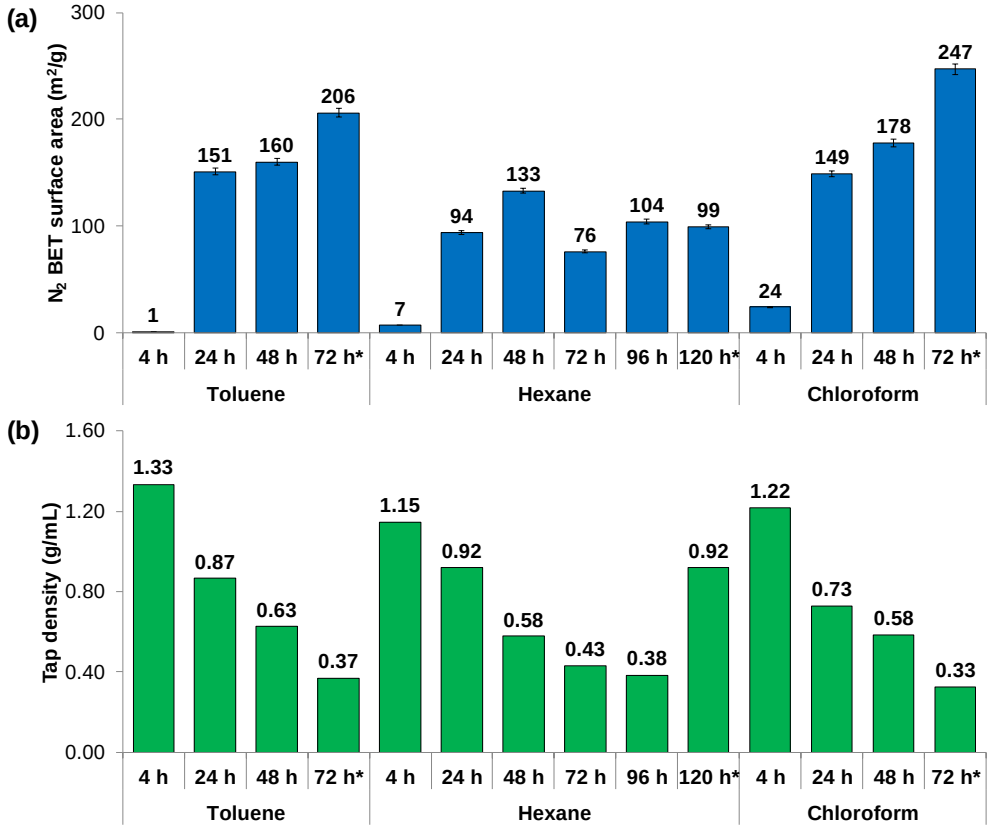


Figure 3.12. (a) N_2 BET surface areas and (b) tap densities of $Mg_4Al–CO_3$ LDHs washed different weak H-bond solvents with varies dispersion time. * Time to reach full dispersion.

Water content decreased with longer dispersion time from 0.548 to 0.211 in hexane for 4 and 120 hours respectively, indicating successful replacement of surface bound water (Appendix, Table B.8). In comparison with Figure 3.7, the morphology of these LDHs reveals thin platelets Figure 3.13, (Figures B15 and B16). Long chain hydrocarbons required longer times to achieve full dispersion. After full dispersion, chloroform produced the highest surface area LDHs (247 m^2/g) in comparison with other weak hydrogen bonding molecules.

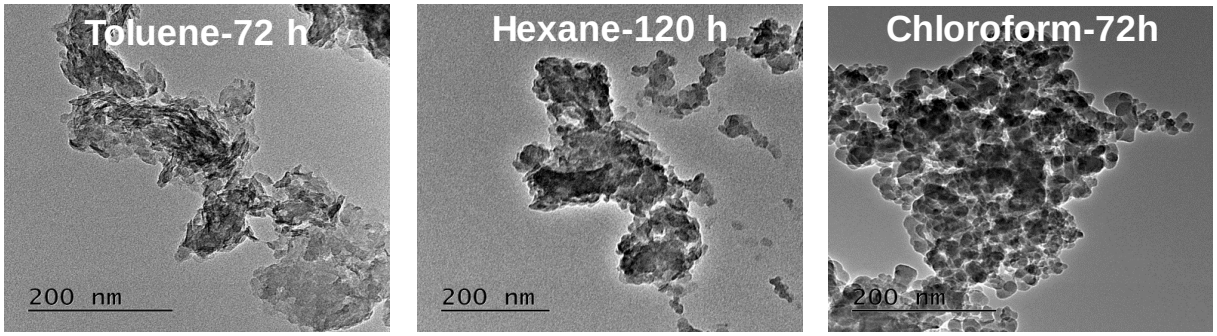


Figure 3.13. TEM images of different weak hydrogen-bond solvent-treated $Mg_4Al–CO_3$ LDHs at varied dispersion time.

At similar dispersion time of 72 hours, chloroform treated LDHs possessed the lowest water content and moderate amount of solvent molecules in the LDH formula (0.430 and 0.0450, respectively). While with hexane, LDHs contained 0.550 and 0.007 for water and solvent, respectively. This may be explained by the hydrogen bonding capability of the solvent. Hydrogen bonding is actually composed of physical (i.e. orientation preference) and chemical (Van der Waals, dipole, dispersion, electrostatic, covalent, etc.) interactions. In the case of chloroform, three chlorine atoms are able to form weak hydrogen bonds with free hydroxyl groups (either in water or LDHs). These chlorine atoms induce the C-H bond to act as a weak acid (proton donor group) and interact with a free electron pair on the hydroxyl frameworks (i.e. a free proton acceptor centre).[332] This could be a possible explanation for the higher surface area of LDHs in chloroform than in other weak hydrogen bonding solvents. The hydrocarbon solvents (hexane and cyclohexane) have low cohesion and minimal capacity for polar interactions (dipole-type and hydrogen-bond). Although hexane and cyclohexane have similar characteristics, cyclohexane is more effective than hexane. A unifying explanation is still unclear. One possibility is that the lack of functionality and low electric polarisation of hexane results in a very weak interaction through dispersive force as well as the steric of the long alkyl chain.[333] Another option is that cyclohexane is preferentially adsorbed onto the LDH surface over linear alkanes,[334] hence it is more effective in the disruption of the hydrogen bonding network which may result in a higher surface area of LDHs than in hexane.[314, 331] In comparison, dichloromethane is less efficient than chloroform. Due to the lower amount of chlorine atoms, dichloromethane yields a weaker proton donor capacity, less acidity of the C-H group, and a lower surface area product than in chloroform. However, dichloromethane is quite dipolar making it more efficient than alkyl hydrocarbon solvents (Table B.9).[335] Even though toluene has moderate polarity, the C-H group of toluene can act as a proton acceptor atom due to π-

bonds in the aromatic ring. The existence of mobile π electron clouds of the aryl alkane creates a very strong electrostatic field available for interaction.[333]

For the weak hydrogen bonding solvents, the surface area values of LDHs decrease in the following hierarchy: chloroform (247 m^2/g) > toluene (206 m^2/g) > dichloromethane (141 m^2/g) > cyclohexane (138 m^2/g) > hexane (99 m^2/g). The strong hydrogen-bond solvents, like alcohols, are highly cohesive, have strong hydrogen bond capacities and are relatively dipolar, this makes them interact with the surface bound water and hydroxyl frameworks of LDHs more efficiently than the weak hydrogen-bond solvents.

3.6. Effect of process parameters

3.6.1. Effect of rinsing volume

The volume of two AIM solvents (diethyl ether and ethyl acetate) was varied from 100, 300, 500 and 1000 mL.

It was reported that surface area increased with increasing rinsing volume of solvent,[196] however, there is no significant impact of the rinsing volume on the number of layers of LDHs (Figure B17 and Table B.10). Correspondingly, there is only a slight change in the surface area (Figure 3.14) increased from 262 to 290 m^2/g for diethyl ether). This might be due to the prolonged dispersion time of 4 hours, which may be enough to reach high surface area with a lower amount of rinsing solvent.[196] However, the amount of water decreased with increasing rinsing volume from 0.537 to 0.370 with diethyl ether at 100 and 500 mL, respectively. The composition of these LDHs is shown in the Appendix (Table B11).

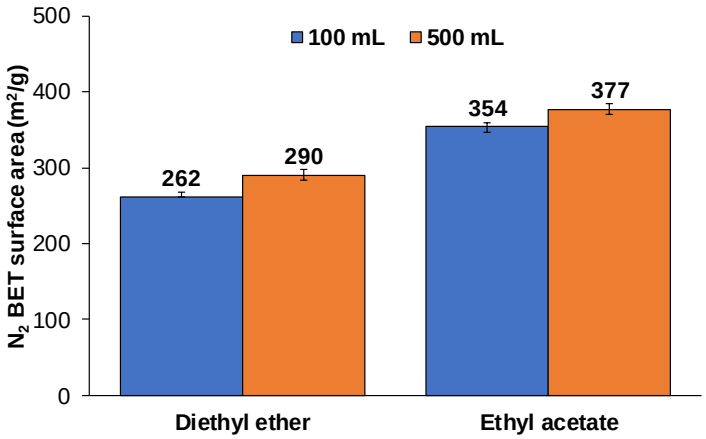


Figure 3.14. N_2 BET surface areas of $Mg_4Al–CO_3$ LDHs treated with 100 and 500 mL of diethyl ether and ethyl acetate.

3.6.2. Effect of high speed mixing

In this study, we compared the mixing speeds (750 and 10,000 rpm) using a stirrer plate and homogeniser, respectively. The dispersion was mixed for 30 minutes. Hexane was used as a solvent for comparison with water. Results show that high speed mixing seems to improve surface area and decrease the density in both water and solvent washed LDHs, as shown in Figure 3.15. High shear might break the agglomerates of LDHs yielding a more open structure exposing them to solvent. Their TEM images are shown in Figure B18.

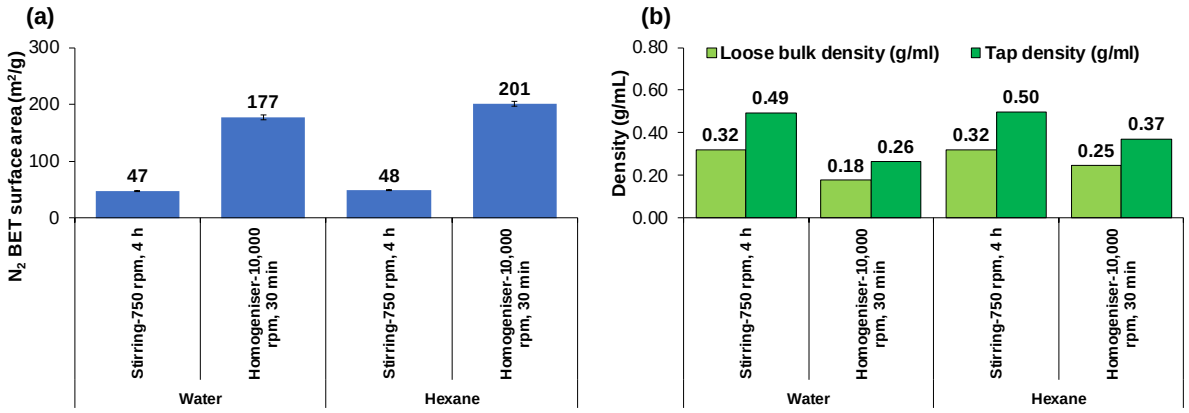


Figure 3.15. (a) N_2 BET surface areas and (b) densities of $Mg_4Al–CO_3$ LDHs treated with water and hexane washed at different mixing speed.

3.7. The effect of recycled solvent

To confirm the benefit of using AIM solvent rather than AMO solvent, the effect of recycling both AMO and AIM solvents was compared using ethanol and 1-hexanol (representative of AMO and AIM solvents, respectively).

Considering the amount of solvent used in each step during solvent treatment, the rinsing step consumes the largest volume. Therefore, we recycled solvent collected from this step to rinse LDHs in the new batch. As expected, AIM solvent is more efficient than AMO solvent. The surface area of hexanol washed LDHs remained constant even after the 4th solvent recycle, whereas the surface area of ethanol washed LDHs decreased after the 1st recycled solvent was used (Figure 3.16). Correspondingly, the tap density of hexanol treated LDHs remained the same, while the tap density of ethanol treated LDHs dramatically increased with increasing number of solvent recycling steps. AIM solvent washing demonstrated to be more efficient than using AMO solvent. The surface properties and composition of these LDHs are summarised in the Appendix (Table B12 and Table B13).

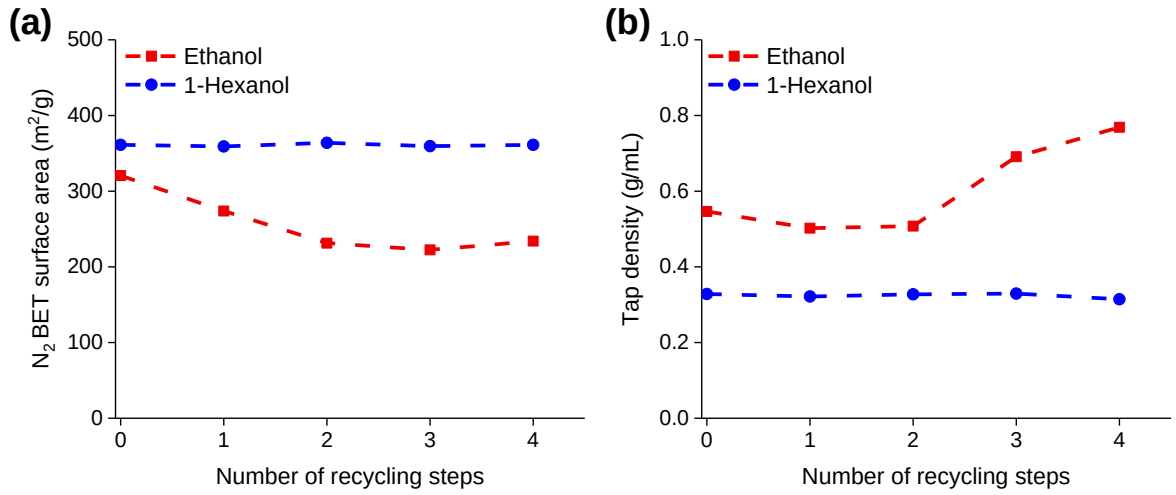


Figure 3.16. (a) N_2 BET surface areas and (b) tap densities of LDHs after solvent recycling.

3.8. Effect of Mg/Al ratio at 2, 3, and 4

To further explore the efficiency of AIM treatment in comparison with AMO treatment, both processes were performed in MgAl-CO_3 LDHs with different Mg/Al ratio. The number of LDH layers decreases, after solvent treatment, for all Mg/Al ratios (Figure 3.17 (a) and Table 3.4). In accordance, the nitrogen BET surface area of LDHs dramatically increases from 8−15 m^2/g to 300-330 m^2/g in diethyl ether and 370-420 m^2/g in ethyl acetate, indicating the formation of thinner platelet LDHs, Figure 3.17 (b). This agrees with the reduction in the number of layers (Table 3.4) and the TEM images in Figure B19. The composition of these LDHs is shown in Table B.14.

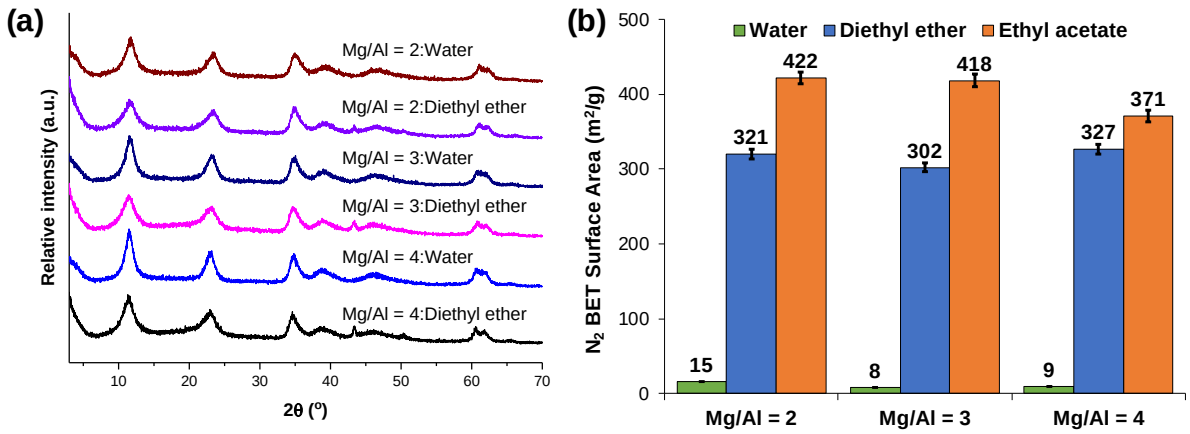


Figure 3.17. (a) XRD patterns and (b) N_2 BET surface areas of water washed and AIM-LDHs with different ratios of Mg/Al.

Table 3.4. Mean crystallite domain lengths and unit cell parameters (*a* and *c*) of AIM-LDHs with different ratios of Mg/Al.

Mg/Al ratio	Washing solvent	d_{003} (Å)	CDL_{003} (Å)*	No. of layers	d_{110} (Å)	*a*	*c*
2	Water	7.52	147.5	20	1.48	2.96	22.56
	Ethyl acetate	7.67	29.6	4	1.52	3.03	23.00
	Diethyl ether	7.63	33.7	4	1.52	3.03	22.89
3	Water	7.62	107.3	14	1.53	3.05	22.87
	Ethyl acetate	7.70	40.8	5	1.52	3.04	23.11
	Diethyl ether	7.73	36.6	5	1.52	3.04	23.20
4	Water	7.70	107.3	14	1.52	3.05	23.09
	Ethyl acetate	7.77	37.5	5	1.53	3.05	23.31
	Diethyl ether	7.74	44.9	6	1.53	3.05	23.21

* Mean crystallite domain lengths along *c*-axis (CDL_{003}) obtained from the Scherrer equation. $CDL = K\lambda(\beta\cos\theta)^{-1}$, K = 0.89, λ = 1.5406 Å, $\beta = FWHM_{003}$.[315]

3.9. Effect of solvent washing on platelet like LDHs

The effect of solvent washing was explored on plate-like LDHs, prepared from the urea hydrothermal method with an average particle size of about 3 μm. The nitrogen BET surface area of the LDHs slightly increased for treatment using AIM solvents from 24 to 64 m^2/g for water washed and 1-hexanol treated LDHs, respectively (Figure 3.18 (a)). The surface area remained constant or slightly decreased with AMO treatment. The surface properties of these LDHs are summarised in the Appendix (Table B15). All solvent washed LDHs show similar morphology as shown in Figure 3.19. Slightly thinner platelets can be distinguished after solvent treatment. All AMO-LDHs and AIM-LDHs exhibit the same XRD patterns as the water washed LDHs (Figure B22), indicating that both AMO and AIM treatments do not affect the structure of the LDHs. All LDHs exhibit type IV isotherm and H3 type hysteresis loop which represents the plate-like particles with slit-shape pores of LDHs (Figure B20). A pore size of 44 Å increased significantly with 1-hexanol washing and slightly increased in diethyl ether and ethyl acetate washing (Figure B21). Ethanol and ethyl acetate washing show a similar increase in pore size of 27 Å. Loose bulk and tap densities of LDH products were also measured; the results are shown in Figure 3.18 (b). A decrease in LDHs powder density for both AMO and AIM washing solvents were observed. Although the change in surface area of LDHs after solvent treatment was slightly increased, the obtained products still have a lower density than the water washed LDHs. This might indicate the removal of the residual water present on the LDHs surfaces, thereby resulting in a lower density and higher surface area of the LDH products.

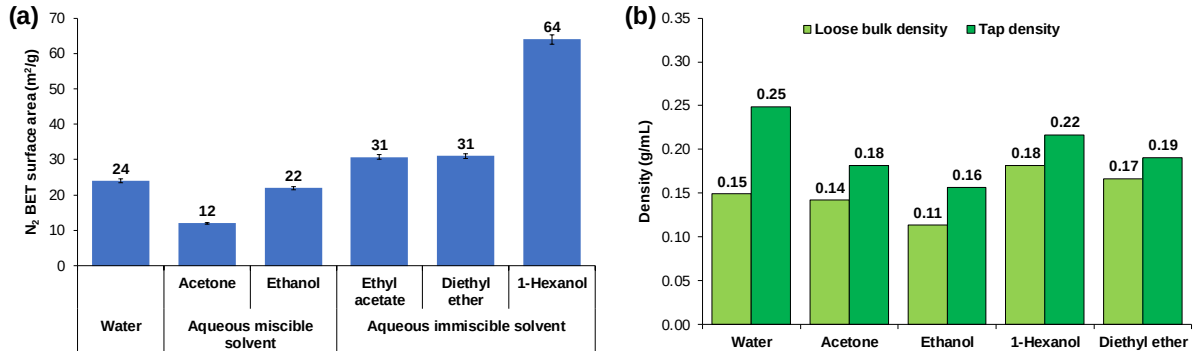


Figure 3.18. (a) N_2 BET surface areas and (b) densities of different solvent-treated platelet Mg_4Al-CO_3 LDHs.

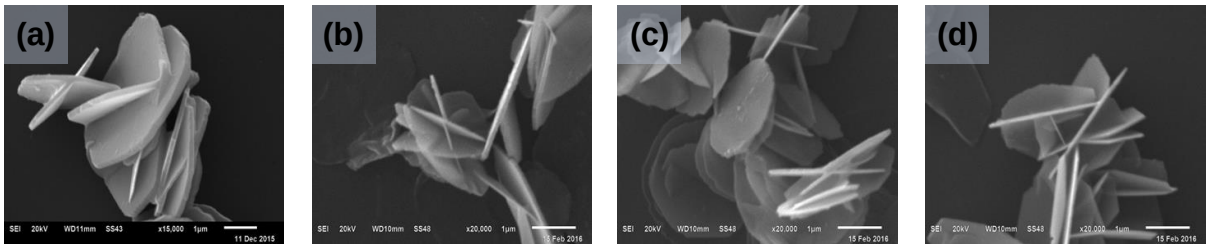


Figure 3.19. SEM images of LDHs (a) water, (b) acetone, (c) ethanol, and (d) ethyl acetate washed LDHs.

3.10. Solid state NMR studies

Magic angle spinning nuclear magnetic resonance (MAS-NMR) studies are attractive to probe site-specific structural information of LDHs, such as cation ordering and intercalated water, carbonate and nitrate anions.[98, 148, 336-338] However, an NMR spectroscopy study into the interaction among those species and solvents is underexplored. Hence, ^{1}H MAS, ^{13}C CP MAS, and ^{27}Al MAS NMR spectroscopy study was carried out on water washed and selected AMO- and AIM-LDHs.

For ^{1}H MAS NMR, there are four possible distinct ^{1}H environments in the case of MgAl LDHs due to different hydroxyl coordination modes (each either Mg or Al): Mg_3-OH, Mg_2Al-OH, $MgAl_2$-OH, and Al_3-OH[338] while brucite (Mg_3OH) contains one proton environment at ~0 ppm.[148, 339] The ^{1}H chemical shifts and relative intensities are dominated by presence of Al nuclei. From the previous reports, only three resonances were observed in the ^{1}H MAS NMR studies as summarised in Table 3.5.[339]

Table 3.5. Summary of observed hydroxyl environments in the LDH structure from the literature.[339]

Ratio of MgAl	^{1}H Chemical shifts and percentage amounts of OH framework in LDHs			Chemical shift of structural water
	Mg_3−O*H***	**Mg_2Al−O*H***	**$MgAl_2$−O*H***	
2	1.3 ppm (6±2 %)	3.4, 3.8 ppm (85±6 %)	5.3 ppm (10±4 %)	4.6 ppm
2.5	0.2, 1.3 ppm (16±5 %)	3.3, 3.8 ppm (84±5 %)	-	4.7 ppm
3	0.4, 1.2 ppm (27±5 %)	3.1 ppm (73±5 %)	-	4.8 ppm
3.5	0.6, 1.1 ppm (36±3 %)	2.6, 3.6 ppm (64±3 %)	-	4.9 ppm

In Mg rich LDHs (high Mg/Al ratios), only two hydroxyl environments corresponding to Mg_3−O*H* and Mg_2Al−O*H* should predominate.[148, 337, 339] With increasing Al content the acidity of the hydroxyl group is increased resulting in a downfield shift,[148, 340] suggesting stronger hydrogen bonding to the interlayer anions and water with increasing charge on the hydroxide layers.[339] Hence, in the Al rich LDHs (low Mg/Al ratio LDHs), three major hydroxyl local environments are present: Mg_3−O*H*, Mg_2Al−O*H* and $MgAl_2$−O*H*.[339] For the Al rich LDHs, the Mg_2Al–O*H* was assigned to the dominant resonance and accompanied by a decrease in the intensity of the Mg_3−O*H* environments. Both resonances also gradually shifted to the downfield region with increasing Al content.[148, 339-341] In general, the chemical shift of the 4.1 to 4.7 ppm resonance can be ascribed to structural OH groups in the LDH and to the intercalated and/or adsorbed water.[148, 338, 339, 342] The $MgAl_2$−O*H* moieties generally overlap with the water resonance and their amount is as low as that of the Mg_3−O*H* species, making them difficult to indentify.[148, 339]

High concentration of interlayer water and hydroxyl groups contribute to strong ^{1}H homonuclear coupling or dipolar coupling, which broadens the resonances and prevents both ready identification and quantification of chemically distinct ^{1}H environments, particularly at spinning speeds below 25 kHz.[336, 338, 342, 343] However, the strong dipole-dipole interactions are almost completely resolved, and the individual H sites resolved, by using MAS frequencies above 40 kHz.[148]

In Figure 3.20, a broad resonance was observed in water washed LDH, Cop-water LDH, by ^{1}H MAS at 15 kHz. The fine structures can be resolved under MAS frequencies at 60 kHz, demonstrating three distinct ^{1}H resonances at 0.85, ~3.4 and ~5.0 ppm. The broad resonance at ~5.0 ppm observed in Cop-water LDH indicates exchanges between labile proton in

$MgAl_2$−O*H* and structural water molecules and anions *via* hydrogen bonding.[337, 339] However, it overlaps with the water peak at ~4.9 ppm.[337, 339] Hence, perturbation of this resonance will be employed to indicate the interaction between the $MgAl_2$−O*H* environments and the interlayer species. A small shoulder at ~7 ppm was also observed, which can be contributed to background signal, water or strongly hydrogen-bonded intercalated water or carbonate anion.[337] The other two broad resonances whose centres are at ~3.4 and 0.85 ppm, are consistent with the assignment of Mg_2Al−O*H* and Mg_3−O*H* environments, respectively.

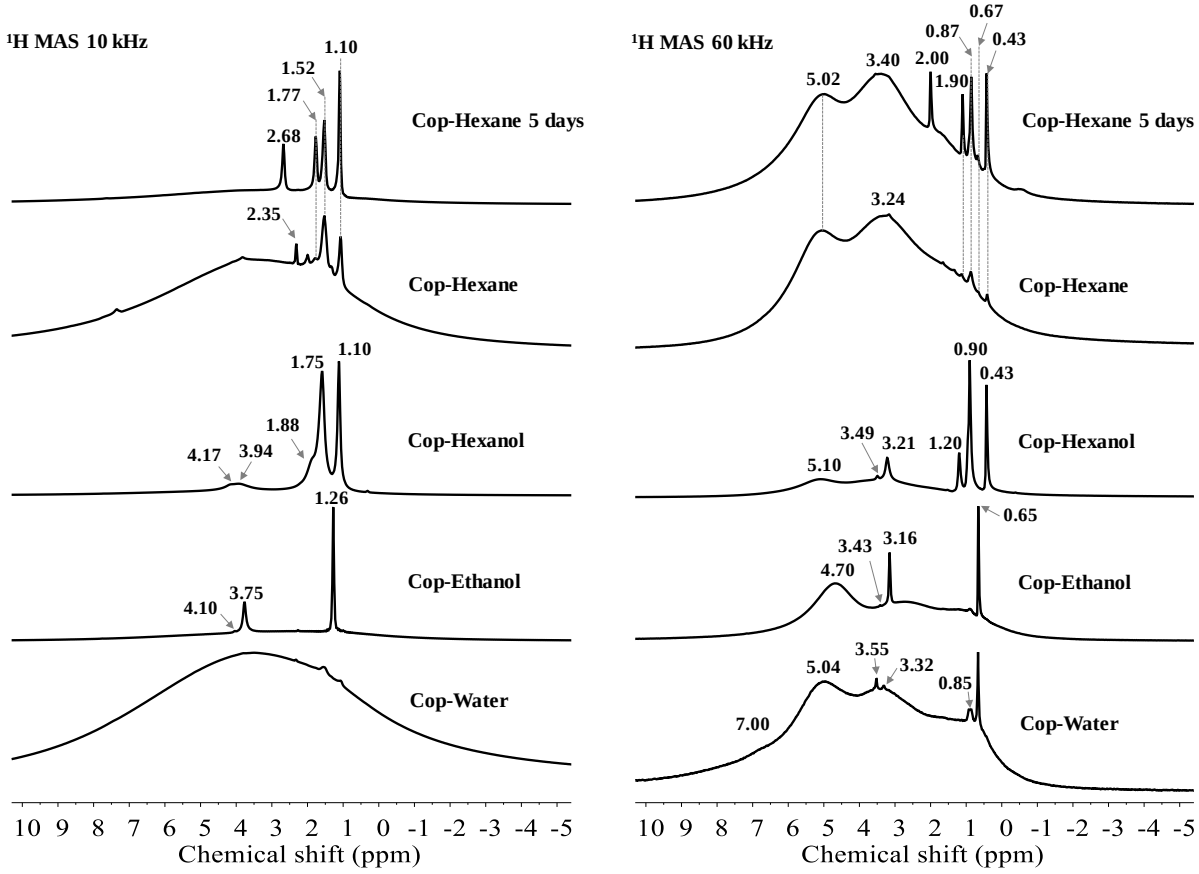


Figure 3.20. ¹H MAS NMR spectra of Cop-W LDH recorded at spinning speed of 15 and 60 kHz. (Sharp resonances between 0-1 ppm are consistent with solvents which may be the contaminants from cleaning solvent during changing sample.).

A number of studies have been reported to investigate the local metal ordering, OH−water environments, as well as the orientation of anions.[148, 336, 337, 339] The interaction among such species and solvents is underexplored; only a report from O'Hare and co-workers reporting that no change in the octahedral Al sites of LDHs after AMO treatment (^{27}Al MAS NMR study).[196] Hence, the interaction between solvents and LDHs could not be completely explained.

Solvent could interact with LDHs *via* hydrogen bonding; the hydroxyl group of solvent can act as hydrogen bond acceptor (electron donor) and the surface hydroxyl groups of LDHs act

as hydrogen bond donor group (electron acceptor). Hence, ^{1}H MAS NMR was performed in this study. Ethanol, hexanol and hexane were chosen as representatives for AMO, AIM and weak hydrogen bonding solvents for post treatment of LDHs. ^{1}H MAS NMR spectra of post treatment materials at two spinning rates of 15 and 60 kHz are shown in Figure 3.20. The other solvents were only recorded at 15 kHz and their spectra are placed in the Appendix (Figure B23). At spinning rate of 15 kHz, spectra broadening disappeared after treatement with most solvents, except in hexane washed LDHs. The conventional hydrogen bonding solvents, Cop−Ethanol and Cop−Hexanol (AMO and AIM), show a significant solvent residue of ^{1}H resonances from the alkyl chain. This is an indication of the dramatic removal of water molecules from the LDHs structure since the broad resonance due to dipolar coupling between hydroxyl frameworks and water molecules was suppressed by the replacement of solvent in the LDHs. However, the hydroxyl protons of solvent were not detected in both samples, which can be explained by proton exchange between alcohol solvent, water molecules and hydroxyl frameworks. In Cop−Ethanol, the dominant resonance at 1.26 ppm is assigned to protons from the methyl group and the peak at 3.75 ppm is assigned to the methylene protons. A very tiny resonance at 4.10 ppm may be due to the presence of water in the sample, however, no peak shift was observed.

Five resonances were revealed in the Cop-Hexanol sample. Two dominant peaks are at 1.10 and 1.75 ppm, which are assigned to protons from the methyl group and methylene species, respectively. A broad resonance in the region between 3.94 and 4.17 ppm could be assigned to the methylene group adjacent to the alcohol group and water. Also, a shoulder at 1.88 ppm may indicate the present of the Mg_3−O*H* species in this region that could overlap with the resonances from hexanol, suggesting an interaction between hexanol and the local hydroxyl groups of LDHs. The methylene group of hexanol was deshielded and therefore shifts to the down field region. However, as the dipole coupling present due to the proton exchange is still faster than the NMR time scale, peak broadening is observed.

According to the elemental analysis results in section 3.5 and Table B.8, in the case of hexane (a weak hydrogen bonding solvent), a short dispersion time is not enough to remove water from the LDH structure, however; proton resonances from hexane were still observed from ^{1}H MAS NMR spectra (Figure 3.20). Two major resonances at 1.10 ppm (methyl group) and 1.52 ppm (methylene protons) due to the protons in the alkyl chain were also shown, and the broad peak was observed. This is characteristic of the water and hydroxyl groups of LDHs at the spinning rate of 15 kHz and suggests that hexane just only adsorbs on the surface of the

LDHs with short dispersion time. However, after prolonged dispersion time to 5 days (120 hours), resonances derived from the hexane residue became intense, indicating a successful partial water removal from the LDH structure which may suppress the broad resonance of LDH substrate due to dipole coupling. An additional two resonances are also present at 1.77 and 2.68 ppm which is a representative of Mg_3−O*H* and Mg_2Al−O*H* species, respectively.[148, 339-341] Since hexane is categorised as the weak hydrogen bonding solvent,[327] it requires much longer time to interact with the hydroxyl framework of the LDHs and replace water; as confirmed by the elemental analysis results (Table B.8). This can be an evidence of the interaction between the solvent and surface hydroxyl groups of LDHs.

In 60 kHz ^{1}H MAS NMR spectra, the LDH structures are much more resolved, although a similar trend was presented as discussed in the results using 15 kHz; and the predominant resonance of water was observed in the region of ~5.0 ppm. Slight shifts were observed in Cop-Ethanol (4.70 ppm) and Cop-Hexanol (5.10 ppm) samples. This could indicate the interaction between the solvent structure and the hydroxyl frameworks of the LDHs *via* hydrogen bonding. The intensities of the resonances become lower in Cop-Ethanol and even more pronounced in Cop-Hexanol. As the water and solvent content in Cop−Ethanol are higher than Cop-Hexanol, as observed from the elemental analysis data (Table 3.3), proton exchange between alcohol solvent, water molecules and hydroxyl frameworks still occurs and results in a broad resonance in the Cop−Ethanol sample. In the other words, hexanol is immiscible with water, which makes it remove water from the LDH structure easily. However, it is a large molecule and steric effects may limit the amount of this solvent into the LDH structure, resulting in low solvent content in the LDH after treatment. Consequently, the dipole coupling effect is much less than in the Cop-Ethanol sample.

However, this shift was not revealed in both Cop−Hexane LDHs (5.0 ppm). Although prolonged dispersion time can reduce water content, according to the elemental analysis data in Table B8, the water content decreased to 0.211 after treatment for 5 days, which was just slightly lower than the Cop-Ethanol (0.225). As a result, peak broadening due to proton exchange is still present. On the other hand, the amount of hexane in the LDHs increased by about ten times after prolonged dispersion time. Subsequently, the strong resonances of protons from the alkyl chain are dominant in the Cop-Hexane 5 days sample, suggesting that hexane is loosely bound to the LDHs as a mobile solvent. Moreover, a shift of Mg_2Al−OH moieties was observed from 3.24 to 3.40 ppm in Cop-Hexane and Cop-Hexane 5 days, respectively. These could be some indication of solvent-hydroxyl frameworks interaction.

The ^{13}C CP MAS NMR spectra of water washed and different solvent-treated LDHs are shown in the Appendix (Figure B24). The isotropic chemical shift at 170 ppm, which is assigned to the intercalated carbonate anion was observed in all samples.[83] For all solvent-treated LDHs, the resonances from different carbon environments were present, which indicates the presence of solvent in the structure of LDHs. All samples show the same ^{27}Al MAS NMR result with resonances at 8.90 ppm, confirming that solvent treatment does not affect the distribution of octahedral Al environments of LDHs, as shown in the Appendix (Figure B25). This observation agrees with the previous report.[196]

3.11. Conclusions

A novel post-production organic solvent treatment step for LDHs using an aqueous immiscible organic solvent treatment (AIM solvent) has been investigated. We proposed that the hydrogen bonding characteristics of the solvent play an important role for removing residual water present between the layers or on the surface of the LDHs, which can be confirmed by the elemental analysis and solid state MAS NMR studies.

The solvent treatment results in a finer, free-flowing LDH powder with a very high surface area and low powder density compared to conventional LDHs. The LDH properties depend on the types of solvent used; conventional solvents such as AMO and AIM solvents generally provide high surface area LDHs after short dispersion time. Solvents with steric hindrance require a long dispersion time to achieve high surface area LDHs, and the weak hydrogen bonding solvents require much longer dispersion time due to weak interaction of the solvent. However, the dispersion time can be shortened by using a high speed mixing process.

This study allows flexibility of solvent selection for future applications along with post treatment parameters (such as rising volume of solvent, mixing speed, dispersion time and solvent recycling) for controlling textural properties of LDHs. Considering the results, we propose that the solvent molecules interact with the hydroxyl framework, structural water molecules and intercalated species *via* hydrogen bonding, as suggested by the ^{1}H MAS NMR studies. Furthermore, the use of AIM treatment could greatly enhance the efficiency of the manufacturing process, allowing the solvent to be easily separated from the displaced residual water and readily recycled for use. This study provides better understanding of solvent-LDH interaction and widens the utilisation and modification of LDHs in many applications.

Chapter Four – Preparation and application of LDH nanoplatelets

4.1. Introduction

Demand for flexible and transparent packaging materials have increased in various fields such as food and beverage, cosmetic, healthcare, and electronics.[7, 37, 38] The trend is that high-barrier performance film structures will dominate the market.[7] Due to high gas permeability of polymers, the development of ultra-high barrier polymeric materials is an active research field.[38, 59] Incorporation of platelet fillers can improve the gas-barrier properties of polymers by increasing the diffusion pathlength of the permeating molecules, generally referred to as a tortuous pathway (brick-mortar structure).[39, 59, 344] Non uniform particle size, random alignment, aggregation, and phase separation of such platelets drastically decreases barrier performance.[60, 345] Although nanostructured artificial nacre-like clay-based materials have been reported, they were not highly transparent due to the high loading of the fillers and thick coating layers.[60, 346, 347] Therefore, the development of high gas barrier films with high transparency is essential.

In order to overcome the above mentioned problems, exfoliation/delamination methods have been explored. The exfoliation/delamination of layered materials (graphite and graphite-like,[41, 348-352] metal oxides,[353, 354] zirconium phosphate[355, 356] and clays[357, 358]) has attracted the most attention since it yields nanosheets and facilitates novel physical and chemical properties of nanostructured materials.[359-364] A wide variety of exfoliation methods have been developed; such as sonication/high shear mixing in surfactants,[41, 348, 350] solvents,[349, 351, 355] polymers.[41, 353, 358] Pre-modification by ion exchange to first enlarge the interlayer separation and to weaken the interlayer interactions followed by exfoliation have been explored.[352, 354, 356, 358]

Although the use of layered silicate materials has been widely reported, they can only be exchanged with a limited ranged of cations, mostly alkyl-ammonium based, which restricts their modifications and potential applications.[359] Hence, positively charge nanosheets such as LDHs have become more attractive.[359, 365] However, the exfoliation/delamination of LDHs is more difficult than clay minerals due to the inter-lamellar hydrogen bonding networks and interlayer electrostatic interactions leading to a tight stacking of layers which prevents the facile exfoliation of the sheets in water or other solvents, as a result the direct exfoliation of LDHs in water is very difficult.[191, 198, 365-368] Until now, many researchers have been exploring

alternative methods for exfoliation/delamination of LDHs. The first successfully exfoliation of LDHs was reported by Adachi-Pagano *et al.* using an intercalation/exfoliation process.[191] By replacing interlayer inorganic anions with organophilic anions such as dodecyl sulfate, LDHs can be delaminated in organic solvents, such as alcohol. It is postulated that the van der Waals interactions introduced from the organic species weakens the electrostatic interactions between the layers, which favours interaction of LDHs with non-aqueous solvents. A year later, Hibino and Jones reported another approach in which amino-carboxylate ions were intercalated in the interlayer region of the LDH to achieve delamination in formamide (a polar aprotic solvent).[200] They also investigated a range of amino acids (glycine, serine and L-aspartic acid) and polar solvents (water, ethanol, acetone, formamide, ethylene glycol and diethyl ether). Formamide has been widely employed to exfoliate LDHs since its carbonyl groups and amino groups have strong interactions with the LDHs layers, the interlayer water molecules and anions.[310] This solvent can disrupt the hydrogen bonding networks and electrostatic interactions of layers, hence facilitates the exfoliation and delamination of LDHs. Although direct synthesis is challenging to obtain nanosheets LDHs, reports of a one-step direct synthesis for preparing LDHs with single-layer nanosheets do exist.[365, 369-372] However, these processes have several limitations as they require high temperatures, inert atmosphere to avoid the competition of the carbon dioxide, ultrasonic or mechanical treatment, or the use of solvents (butanol and formamide), which is difficult to remove and recover solvent after treatment. Recently, a greener process was reported by exfoliation of ZnAl-LDHs in NaOH/urea aqueous solution,[373] however, this is not suitable for practical use since a relatively low temperature at -10 ^{o}C is required to achieve exfoliation.

A special feature of LDHs compared to many other materials is the "memory effect". As a result these materials can be rehydrated in water to re-form LDHs after calcination or reconstructed in the solution of the new guest, which is called the "reconstruction process".[374] This is the method often used to intercalate large molecules into the LDHs galleries and to avoid the competitive intercalation of smaller inorganic anions. To date, many reports have been published concerning the synthesis of nanosheets by exfoliation/delamination of LDHs. In very early research, the LDHs delamination was only performed in highly polar organic solvents.[200, 375, 376] Amino acids having similar structure to formamide (containing carbonyl and amino groups) are expected to facilitate the exfoliation of LDHs. Indeed, several approaches have been reported to intercalate amino acids into the LDH structure such direct coprecipitation,[200] reconstruction method,[106, 377, 378] the obtained product can be delaminated

in formamide.[200] The effects of the synthesis conditions and the physicochemical properties of amino acids on the intercalation behaviour were reported, their effect on the textural properties of the LDHs is still underexplored.[106, 377, 378]

Recently, O'Hare and co-workers discovered a new approach for preparing nanoplatelets *via* calcination/reconstruction of LDHs using glycine.[379] A gel was formed after reconstruction in a concentrated aqueous solution of glycine resulting in very thin LDH nanosheets. It was found that the LDH platelet thickness decreased and diameter increased on increasing the reconstruction time, furthermore the higher calcination temperature seems to shorten reconstruction time.[379] Although calcination process is necessary for this approach, it is safer and more practical than many of the other reported studies[200, 369, 373, 375, 380] since no toxic chemicals (e.g. formamide), nor mechanical treatment, and nor an inert atmosphere is required for this approach.

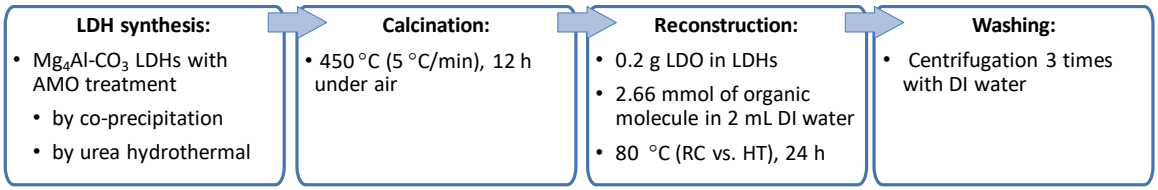
In order to further widen the applicability and flexibility of this process, different types of amino acid (including glycine) and other compounds were employed in this study. The effect of original morphology; rosette shape and platelet-like LDHs were compared. Then, the obtained nanoplatelets were selected to prepare coating mixtures and applied onto a polymer film substrate. Barrier and optical properties of the coated films were consequently examined.

4.2. Effect of amino acid types and LDHs morphology on reconstruction of LDHs

As mentioned above, reconstruction of LDHs in an aqueous solution containing excess amount of glycine can provide nanosheets.[379] However, the effect of amino acid type and morphology of LDHs used on reconstruction behaviour and morphology of final products have not been fully explored. Glycine is identified as an amino acid with a nonpolar side chain; therefore, other nonpolar side chain amino acids and possibly other types are also potentially used in this process.

In this study, a series of nonpolar and polar side chain amino acids were examined for reconstruction of rosette-like LDHs (prepared from co-precipitation method). To probe the effect of original morphology, platelet 3−4 μm LDHs (prepared from urea hydrothermal method) were also studied with the series of nonpolar side chain amino acids. All LDHs used in this study were synthesised as $Mg_4Al{-}CO_3$ LDHs and washed by ethanol using AMOST process[96] before drying. All LDHs were calcined in a conventional furnace at 450 °C for 12 hours. After cooling down, 0.2 g of calcined product (so called LDO) added into a selected solution of organic molecule. The concentration of all organic molecule was fixed at 2.66

mmol in 2 mL of deionised water for all experiment. The reconstruction was conducted at 80 °C for 24 hours and finally washed with deionised water by centrifugation, as summarised in Scheme 4.1. The organic molecules used in this study are listed in the Appendix (Table C1).



Scheme 4.1. Procedure for reconstruction of LDHs in organic molecule aqueous solution.

4.2.1. Reconstruction using amino acids with nonpolar side chains

In this study, different nonpolar side chain amino acids; glycine (Gly), β-alanine (Ala), β-leucine (Leu), and β-phenylalanine (Phe) were examined for reconstruction of calcined LDHs. Also, β-aminobutyric acid (BABA) and γ-aminobutyric acid (GABA) were employed to observe the effect of amine group position on reconstruction process of LDHs. All studies were performed with the rosette-shape prepared from co-precipitation method with AMOST treatment (Cop-AMO LDHs). The morphology of Cop-AMO LDHs and structure of non-polar amino acids used are shown in Figure 4.1. The reconstruction procedure was conducted at 80 °C for 24 hours, using different systems: in a round bottom flask using oil bath heating (denoted RC) and an autoclave hydrothermal reactor (denote HT). For simplification, products were defined as Cop-RC-amino acid and Cop-HT-amino acid.

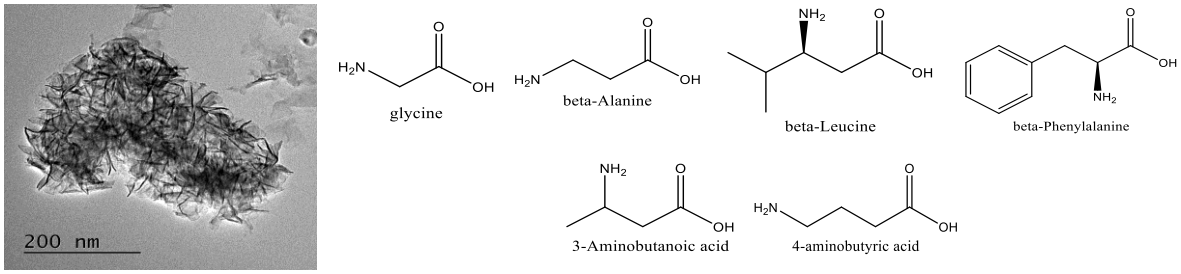


Figure 4.1. TEM image of Cop-AMO LDHs before reconstruction and structure of nonpolar amino acids used in this study.

Figure 4.2 displays the appearance of the obtained product after reconstruction. The products obtained have a gelatinous appearance in most cases (except in β-phenylalanine). Similar observations were reported for exfoliated LDH-glycine[381] and LDH-NO_3[382] in formamide, and delaminated cationic clays.[383, 384] Although Iyi *et al.*[385] reported semitransparent gel formation for ClO_4-LDHs in concentrated aqueous solutions

with amino acid-like zwitterionic compounds. In this study, transparent gels were observed. Appearance of all products is shown in the Appendix (Figure C1). The gel formation can be explained by swelling behaviour of these LDHs.[385] There were few reports using LDHs containing short chain molecules such as carboxylates, sulfonates, and also amino acids, which are classified as zwitterionic compounds, causing gel formation of LDH products.[106, 385-392] Hence, LDHs containing these molecules can be swelled and exfoliated in water, which is quite similar to our gel like products.

It has been suggested that hydrogen bonding interaction within the sheets, interlayer water molecules and zwitterionic species such as amino acids are necessary for hydration and swelling of LDHs.[385] Hydrogen atoms and lone pairs from nitrogen atom of amino acid act as hydrogen bond donors (bond to water molecules) and hydrogen bond acceptors (accept hydrogen from water molecules), respectively.[385, 393] This research also reported that the swelling efficiency is decreased if the amine and carboxylate groups are in closer proximity due to decreasing in relative permittivity value of the zwitterion solution.[385, 393] However, the position of amine group seems to have no effect on gel formation, as observed in the case of β- and γ-aminobutyric acid. The hydrophobic effect was obviously seen in β-phenylalanine reconstructed LDHs, white solid product was obtained. This may be due to steric hindrance of the phenyl group (hydrophobic effect) which suppresses hydrogen bond formation and prevent gelation process.

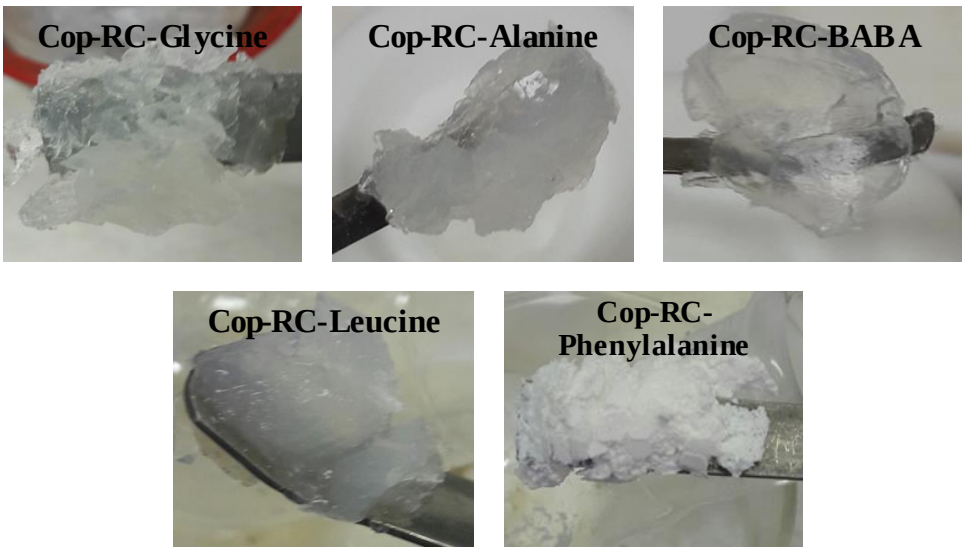


Figure 4.2. Appearance of products obtained after reconstruction of the calcined Cop-AMO LDHs in different amino acids in an open oil bath heated reactor (Cop-RC-amino acid).

Powder X-ray diffraction (XRD) data of the LDH products obtained from LDH reconstruction are shown in Figure 4.3. All LDHs appear to be phase pure by XRD, except for the ones that are reconstructed with β-leucine and β-phenylalanine due to low water solubility of these amino acids making them difficult to remove by washing process. No expansion of the interlayer spacing was observed in most amino acids reconstructed LDHs, it was suggested that intercalation had occurred.[106] Due to small size of amino acids such as glycine (3.9 and 3.5 Å in length and width) and alanine (5.5 and 3.3 Å in length and width),[394] which is smaller than the basal spacing of typical carbonate or nitrate containing LDHs (7.9 Å).[96] Those molecules may horizontally align parallel to the LDH layers, resulting in no expansion of the interlayer. On the other hand, enlargement of the interlayer spacing was observed in products reconstructed with β-leucine (8.5 and 5.0 Å in length and width)[394] and β-phenylanine (9.7 and 4.7 Å in length and width).[394] Since molecular size of both molecules is larger than those former molecules, accompanying with the hydrophobic interaction which induced the bilayer arrangement, can enlargement of the interlayer spacing.[106, 377, 378, 386, 395] *d*-spacing values of obtained products are summarised in Table 4.1. The basal spacing of all leucine reconstructed LDHs is in the range 12−13 Å. It is postulated that those molecules prefer bilayer arrangement in the LDH interlayers through the oxygen atoms of the carboxylate group, giving a net positive charge on the layer[395] (see zeta potential results in Figure 4.6). Furthermore, the phenyl rings form hydrophobic regions in near centre of the interlayer.[395] At the surface hydroxide layers region, the carboxylate groups interact with water molecules forming hydrogen bonding network.

Effective intercalation of phenylalanine only occurs under closed hydrothermal reaction at 80 °C with the basal spacing expanding to 15.43 Å. At the same reaction temperature, the reaction in an open oil bath heated reactor was not effective to intercalate phenylalanine into the LDH, possibly because of a competition between the atmospheric carbon dioxide and strong π−π interaction of phenyl rings, which may prevent the intercalation of the phenylalanine molecule. In addition, considering the electrical neutrality of the intercalation compound, the competition of carbonate and hydroxyl anions from the environment, therefore, the co-intercalation of these molecules can occur. On the other hand, reaction under hydrothermal conditions may favour the introduction of this hydrophobic amino acid into the LDH interlayer regions.

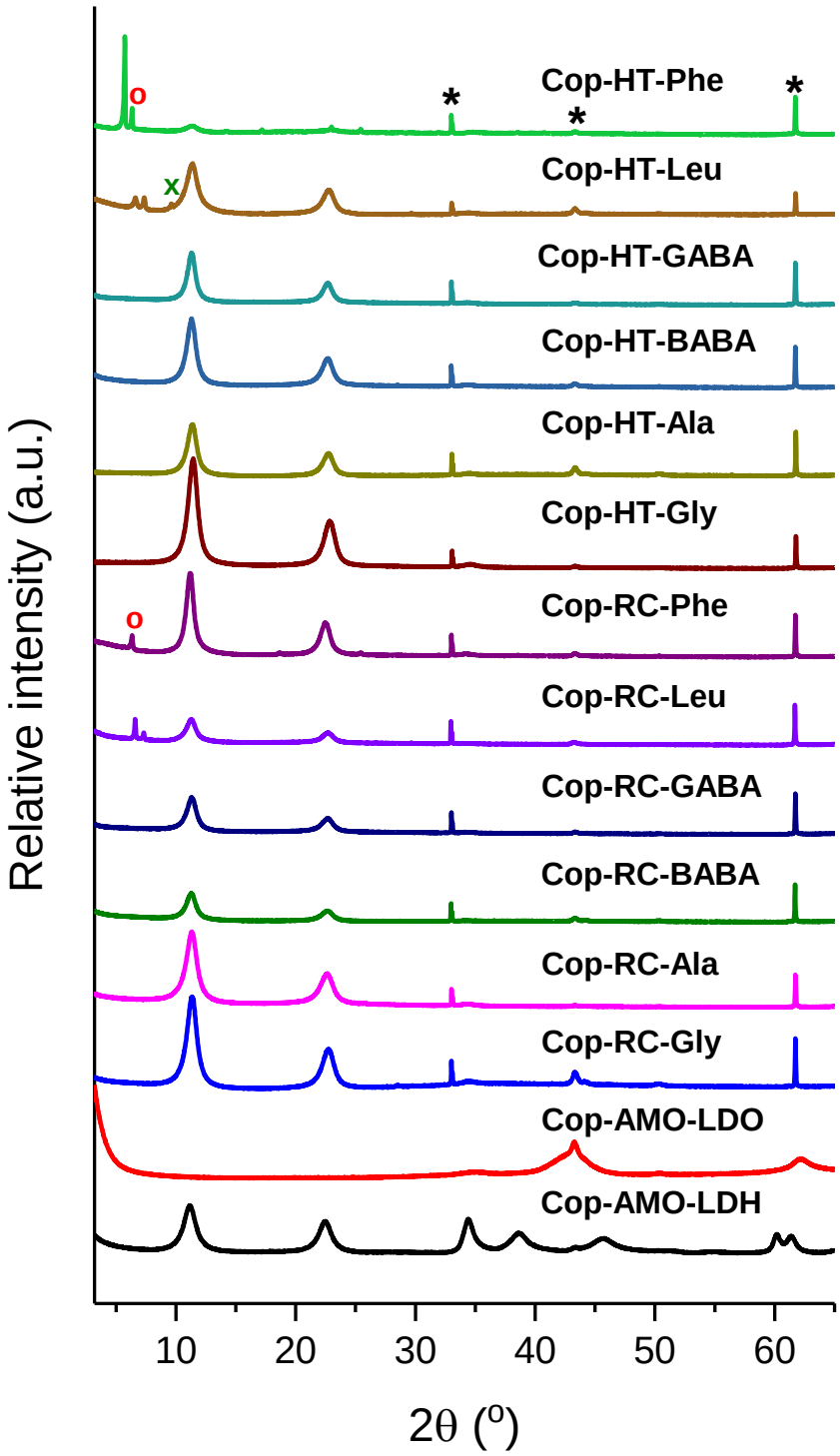


Figure 4.3. XRD pattern of reconstructed LDHs (Cop-RC-amino acid and Cop-HT-amino acid) using nonpolar amino acids. **o** and **x** denote the Bragg reflections of impurities from phenylalanine (**o**) and leucine (**x**). (*Bragg reflections due to the sample holder were observed at 2θ = 43-44° and 50° and reflections from the silicon wafer were located at 2θ = 33° and 62°.) Cop-AMO-LDO and Cop-AMO-LDH were prepared from the powder sample, not on the silicon wafer.

Table 4.1. Summary of *d*-spacing of reconstructed LDHs using different nonpolar amino acids. 'RC' and 'HT' were denoted as product from an oil bath heated and hydrothermal conditions, respectively.

Sample		*d*-spacing (Å)
Cop-AMO LDHs		7.93
RC	Glycine	7.78
	β-Alanine	7.8
	β-Aminobutyric acid	7.83
	γ-Aminobutyric acid	7.8
	β-Leucine	7.83, 12.05, 13.41
	β-Phenylalanine	7.9
HT	Glycine	7.71
	β-Alanine	7.76
	β-Aminobutyric acid	7.82
	γ-Aminobutyric acid	7.83
	β-Leucine	7.76, 12.02
	β-Phenylalanine	7.79, 13.91, 15.43

Fourier transform infrared (FTIR) spectra were recorded for all amino acid reconstructed LDHs between 600 and 4000 cm^{-1}. FTIR spectra of obtained products after reconstruction of calcined Cop-AMO LDHs in different nonpolar amino acids in an oil bath heated reactor are shown in Figure 4.4. The FTIR of products obtained from the closed hydrothermal reaction are presented in the Appendix (Figure C2).

A broad band in the region 3000-3600 cm^{-1} is assigned to O–H stretching vibrations due to the hydroxide groups from the basal plane of LDH and solvated interlayer water. Two bands at 1400 and around 1540 cm^{-1} in all amino acid reconstructed LDHs can be assigned to symmetric and asymmetric stretching vibrations of carboxylate ($–COO^–$) groups in amino acids, respectively. However, C-H and N-H stretching vibrations of the amino acid generally found at 3030-2900 cm^{-1} are very weak compared with other peaks. The band at approximately 1500 cm^{-1} can be assigned to the C−H bending vibration. The weak absorptions due to the mono-substituted benzene are recorded in the 770 cm^{-1} in products reconstructed with phenylalanine.[396] A peak around 1640 cm^{-1} is ascribed to the bending mode of water molecules. The carbonate peak at 1370 cm^{-1} (the υ_3 carbonate stretching mode in D_{3h} symmetry) is very intense in the original LDHs.[397] This peak is observed in all reconstruction LDHs indicating the presence of co-intercalated carbonate ions. It is suggested that amino acid is a zwitterion within the layer space of the LDHs and other anions such as carbonate (CO_3^{2-}), hydrogencarbonate (HCO_3^-), or hydroxide (OH^-) must be co-intercalated in order to balance the electrical neutrality of LDH/amino acid.[395]

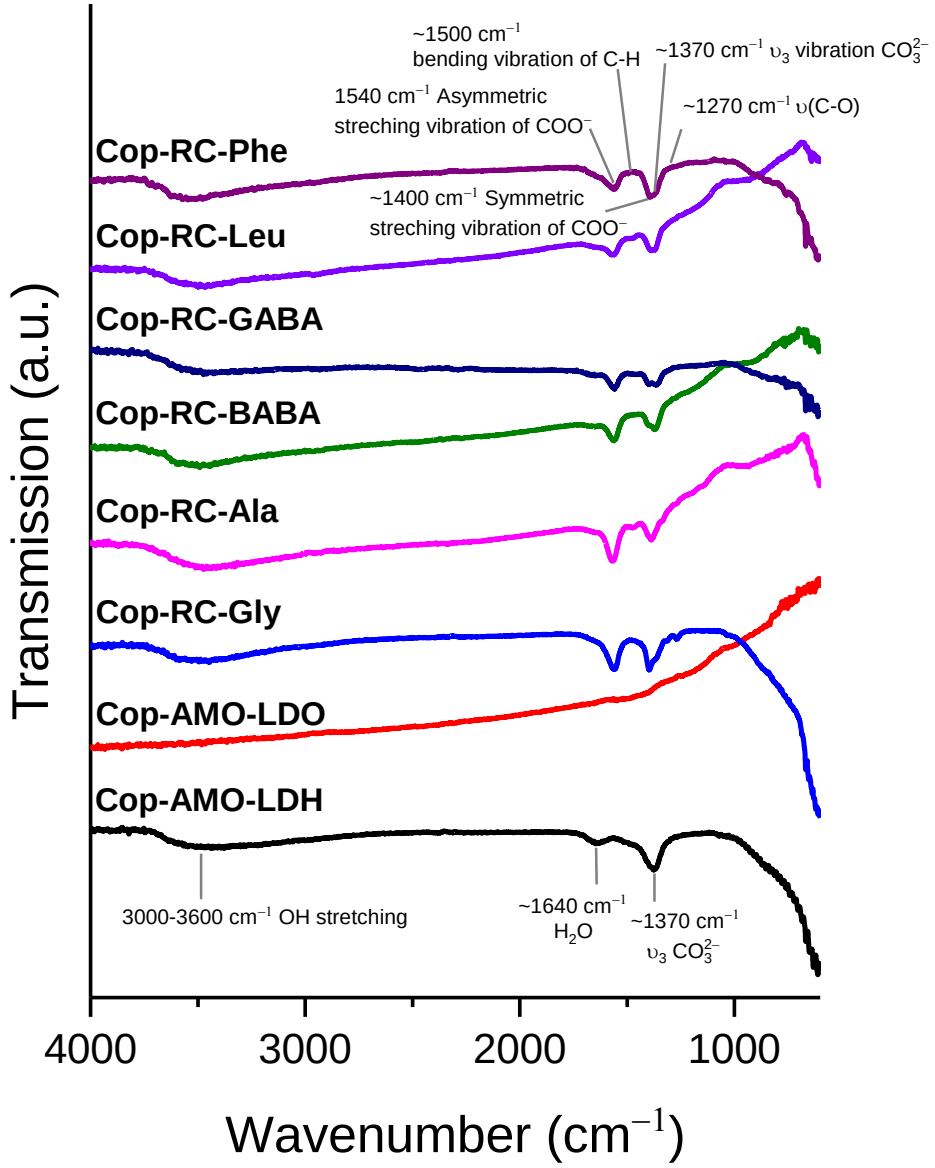


Figure 4.4. FTIR spectra of reconstructed LDHs (Cop-RC-amino acid) using nonpolar amino acids.

TEM was used to determine the particle sizes and size distribution. TEM images and particle size distribution curves of LDHs are shown in Figure 4.5 and summarised in Table 4.2. In general, the key point of the reconstruction process (memory effect) is to recover the original structure as well as original morphology.[82, 102, 153] In this study, the average particle sizes decreased drastically to 40-60 nm after reconstruction and formed uniform LDH platelets, indicating original structure was not retained. However, it is difficult to find a direct relationship between the chain length of the amino acids and the particle size of the final reconstructed LDHs. It is believed that hydrogen bonding should play a role in directing morphology transformation of the LDHs.

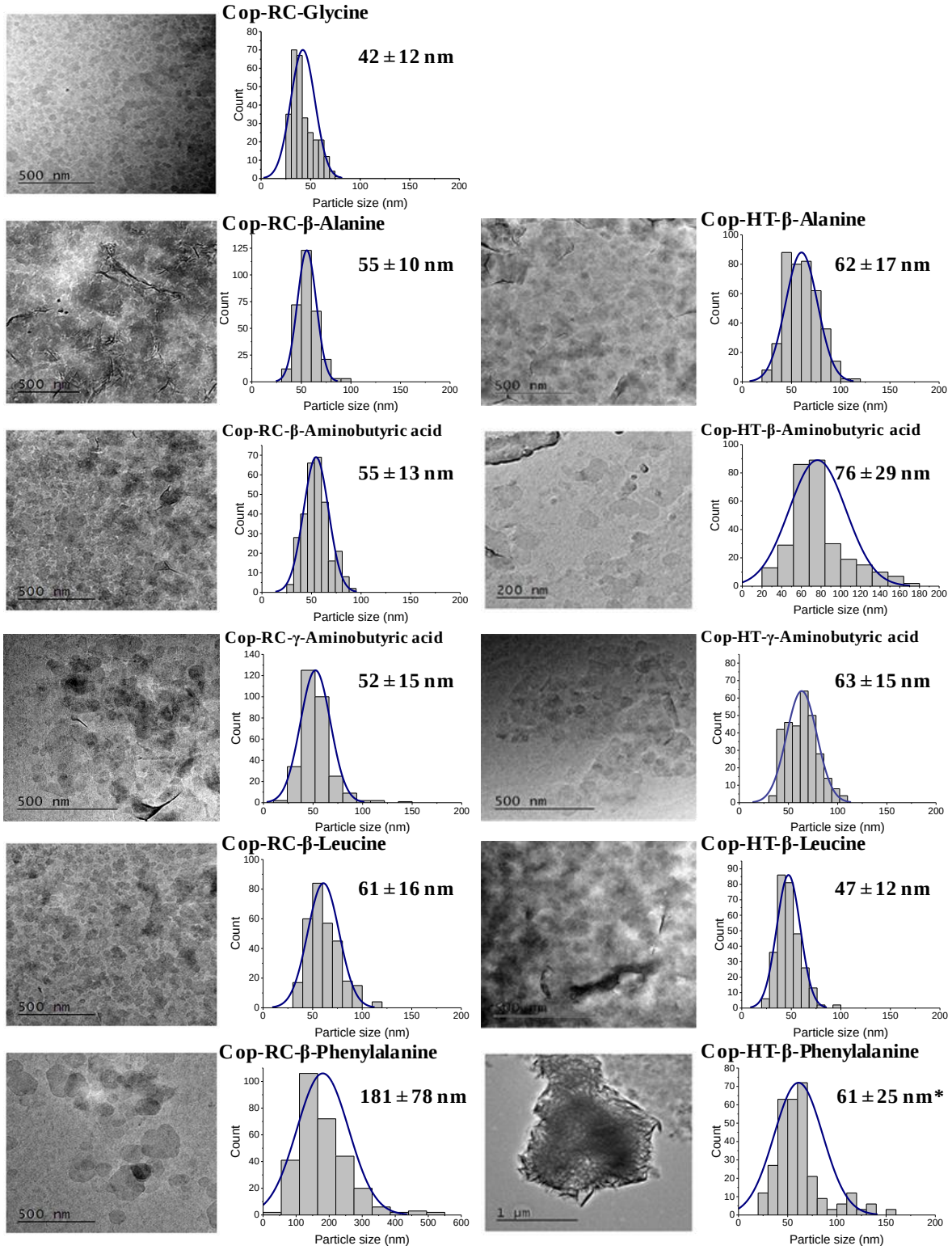


Figure 4.5. TEM images with particle size distributions of reconstructed products from co-precipitation LDHs (Cop) with different nonpolar amino acids. 'RC' and 'HT' were denoted as product from round bottom flask using oil bath heating and hydrothermal reactors, respectively. Navy lines indicate the best fit of a Gaussian distribution, showing approximately a normal distribution. Mean values and standard deviation were obtained from measurement of 300 particles. '*' indicates that only small size particles were plotted the size distribution curves.

Table 4.2. Summary of average particle size of reconstructed LDHs using different nonpolar amino acids. 'RC' and 'HT' were denoted as product from an oil bath heated and hydrothermal conditions, respectively. The TEM images were used to determine the mean values and standard deviation by measurement of 300 particles.

Sample		Particle size
Cop−AMO LDHs		1131±504 nm*
RC	Glycine	42±12 nm
	β-Alanine	55±10 nm
	β-Aminobutyric acid	55±13 nm
	γ-Aminobutyric acid	52±15 nm
	β-Leucine	61±16 nm
	β-Phenylalanine	181±78 nm
HT	β-Alanine	62±17 nm
	β-Aminobutyric acid	76±29 nm
	γ-Aminobutyric acid	63±15 nm
	β-Leucine	47±12 nm
	β-Phenylalanine	61±25 nm, 0.5-1 μm

*measured from the secondary particles of LDHs.

In general, the zeta potential of a suspension must be below −30 mV or above +30 mV in order to be stable with respect to flocculation.[398] Typical LDHs have positive zeta potential values in deionised water, which is attributed to the positive charge of the metal hydroxide layers and the electrical double layer on the LDH surface.[296, 399, 400] Although the metal hydroxide layer charge is balanced by the interlayer anions, it cannot be fully neutral at the surface of the layer. The existence of the electric double layer, i.e. Stern layer and diffusion layer make LDHs positively charged.[401] However, zeta potential also depends on the pH and ionic strength of the suspension medium, since they may have a profound effect on the size of the electrical double layer and the charges at the surface of the particles.[402]

As shown in Figure 4.6, the zeta potential of the Cop-AMO LDH is 12.8 mV indicating low zeta potential value of the particles. There is not enough force to prevent the particle flocculation, which can be observed during the measurement.[398] Zeta potential is significantly increased to 32−40 mV after reconstruction with amino acids, suggesting a stable colloid dispersion in water.[398] This might be attributed to the replacement of carbonate anions by the amino acids, which have positively and negatively charged groups from carboxylic and amino group, respectively.[403] It was postulated that most intercalated amino acids are zwitterions which may be neutral in the interlayer region of the LDHs but can be bound at the outer positive surface of the LDHs. Newman *et al.*[395] suggested that the oxygen atoms of the carboxylate group of the amino acid can form hydrogen bonds with the hydroxide layers of

LDHs, the unbound amino group giving the positive charge of the layers.[395] The surface hydroxyl groups of the LDHs behave as hydrogen-bond donors and the oxygen atoms from water and carboxylate groups acts as the acceptors.[395] These contribute to the increase in the zeta potential value of the LDHs after the reconstruction process. However, the amine group does not directly interact with the surface hydroxyl layers and prefers to be orientated away from the surface of the LDHs. It forms hydrogen bonds with surrounding water molecules.[395, 404] In addition, the reduction of particle size of LDHs from micron size to nano size and formation of stable dispersion in water could explain the change in the zeta potential after reconstruction.

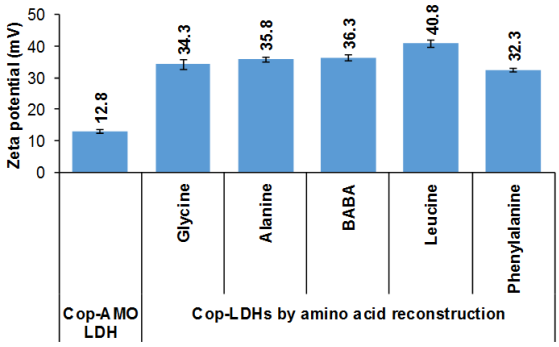


Figure 4.6. Zeta potential of reconstructed LDHs by different amino acids.

Thermal properties of Cop-AMO LDH, LDOs and reconstructed LDHs by different amino acids were determined by thermogravimetric analysis (TGA), as shown in Figure 4.7. Typical water washed LDH (Cop-W LDH) was compared in this study to avoid mass loss from solvent in Cop-AMO LDH. Also, a controlled sample was performed by mixing the calcined product in deionised water and stirring at room temperature, labelled Cop-LDO in water. The controlled sample exhibits 4.5 wt% lower total weight loss than the original LDHs indicating a reduction of intercalated carbonate anion, solvent and water molecules. This is confirmed by the elemental analysis results (EA) listed in Table 4.3. The carbon content in the control sample is much less than in the original sample, which suggests a reduction of the carbonate anion in the LDH structure during the calcination process. However, the carbonate anion still exists in the sample since the reconstruction process was not performed under inert atmosphere. Although trace amounts of carbonate could possibly originate from deionised water and the environment, its relative amount is significantly less than the original LDHs. The charge of the LDH layers need to be balanced, the hydroxide anion should be co-intercalated with the carbonate anion in the reconstructed LDHs.

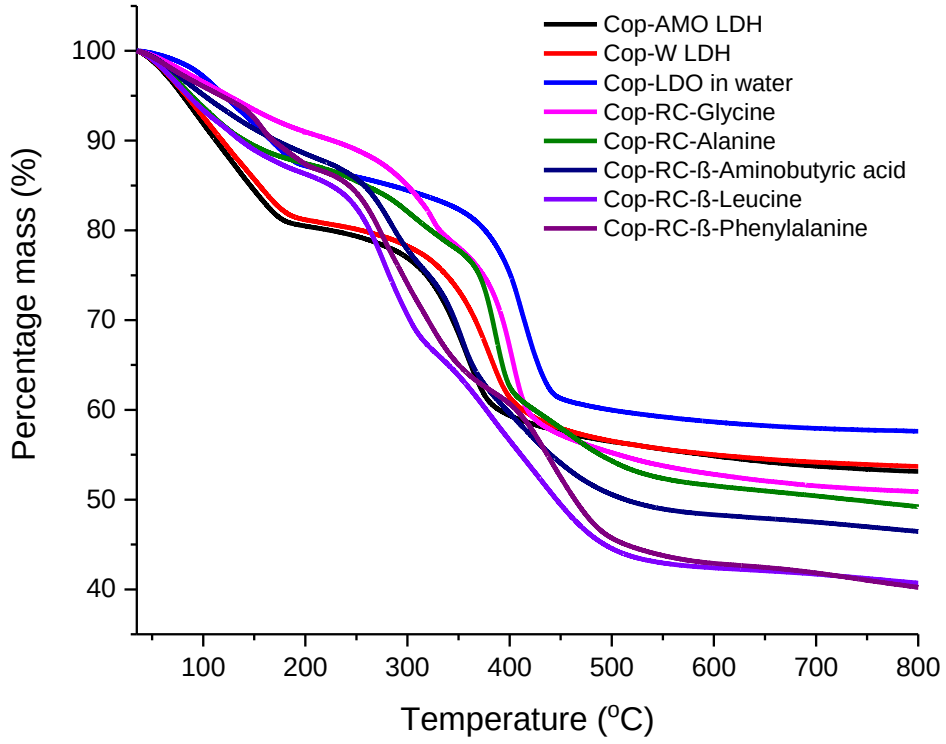


Figure 4.7. TGA curves of reconstructed LDHs (Cop-RC-amino acid) using nonpolar amino acids.

For amino acid reconstructed LDHs, the total mass loss increased with increasing molecular weight of the amino acid, 50 to 60 wt% for glycine and phenylalanine, respectively. In other words, a reduction of total mass from the original LDHs and controlled sample is in the range of 2.2−13.1 wt% and 6.7−17.60 wt%, respectively (Table 4.3). In general, the decomposition temperature of the amino acids is in the range of 200-300 °C and for some cases higher than 400 °C.[375, 386, 405] Three steps of a major weigh losses were observed for all amino acid reconstructed LDHs as shown in the differential thermogravimetric curves (DTG) in the Appendix (Figure C3). The first step occurs below 200 °C due to the removal of adsorbed water and interlayer water. The second step, corresponding to the dehydroxylation of LDH layers and the decomposition of the intercalated amino acids, occurs between 250−400 °C. The last step corresponds to the combustion of the intercalated amino acids and formation of a carbonaceous residue produced from the decomposition of the amino acid.[406]

The amino acid content in all reconstructed products was determined by elemental analysis (EA), the results are summarised in Table 4.3. Amino acid content in the LDH was assumed to be the sole source of nitrogen in the samples. In addition, it was also used to determine the carbon and hydrogen content which do not originate from the amino acid. These carbon and hydrogen contents indicate the amount of carbonate and hydroxide

intercalated anions and structural water molecules in the reconstructed LDHs. A massive reduction of carbon content of all amino acid reconstructed LDHs was found, suggesting a low amount of co-intercalated carbonate anions in the structure. On the other hand, the hydrogen content is slightly lower than the original one and the controlled sample. For all the computations, it is assumed that all amino acids present in samples are in the zwitterionic form for simplicity. It was suggested by Carteret *et al.* that when the CO_3-MgAl LDH contacted with air, an exchange with atmospheric carbon dioxide occurred *via* a mechanism that involved both carbonate (CO_3^{2-}) and hydrogencarbonate (HCO_3^-), and the amount of the later specie increased with the Mg/Al ratio.[407] Hence, the layer charge of the amino acid reconstructed samples should be balanced by both species rather than the hydroxide anion, which was not detected by FTIR. The raw data for EA and ICP results and formula of LDHs before and after reconstruction are in the Appendix (Table C.2, C.3 and C.4).

Table 4.3. Elemental analysis (EA) and TGA studies.

Sample	%Amino acid*	%C apart from amino acid*	%H apart from amino acid*	%Mass different from 'original LDH'**	%Mass different from 'controlled sample'**
Cop-AMO LDH	-	3.50	4.35	-	−4.50
Cop-W LDH	-	2.01	3.54	0.61	−3.89
Cop-LDO in water	-	1.46	4.29	4.50	-
Cop-RC-Glycine	16.67	0.06	2.33	−2.24	−6.74
Cop-RC-β-Alanine	27.56	0.53	4.43	−3.97	−8.47
Cop-RC-β-Aminobutyric acid	22.46	0.00	2.81	−6.73	−11.23
Cop-RC-β-Leucine	32.43	0.01	2.99	−12.54	−17.04
Cop-RC-β-Phenylalanine	38.82	3.98	2.28	-13.10	−17.60

*Calculated on the basis of EA results and ** from TGA results.

4.2.2. Effect of LDH morphology on reconstruction of LDHs

To investigate the effect of original morphology, 3−4 μm platelet AMO LDHs (prepared from urea hydrothermal method, UHT-AMO LDHs) as shown in Figure 4.8 were examined with the series of nonpolar side chain amino acids. Two reconstruction conditions were also compared, in a round bottom flask using oil bath heating (RC) and in a hydrothermal reactor (HT) at 80 °C for 24 hours. Products were defined as UHT-RC-amino acid and UHT-HT-amino acid for the ones initiated from UHT-AMO LDHs. The appearances of the as obtained products are shown in the Appendix (Figure C1).

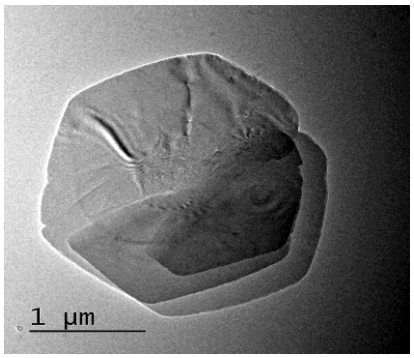


Figure 4.8. TEM image of UHT-AMO LDHs used in this study.

Similar to 4.2.1, gel-like products were obtained after reconstruction under most conditions. Solid products were formed using both leucine and phenylalanine even with hydrothermal condition while gel products were obtained in co-precipitation LDH with leucine. Therefore, the swelling and gel formation behaviour of LDHs depends on the type of amino acid and morphology of the original LDHs. XRD patterns of reconstruction products are presented in Appendix (Figure C4) and *d*-spacing values are summarised in Table 4.4. Similar trends were observed in products originated from co-precipitation LDHs (Figure 4.3 and Table 4.1). No layer spacing expansion was obtained using small size amino acids. An increase of the basal spacing was observed in products produced from leucine (12 Å) but it was not found in the case of phenylalanine. This is probably due to several factors such as: the large particle size of the original LDHs, the contact area and accessibility of the amino acid. In addition, the hydrophobicity of the phenylalanine could suppress the interaction with the LDH surface.

The characteristic bands for phenylalanine (as well as the other amino acids) are present in FTIR spectra shown in Figure C5 (Appendix). The spectra suggest the presence of amino acid molecules in the product. The carbonate band at 1370 cm^{-1} was observed in all reconstruction LDHs indicating the co-intercalated carbonate ion in the samples.[397]

TEM images and particle size distributions are shown in Figure 4.9 and Table 4.4 for all samples. The obtained products from the UHT-AMO LDH produce a mixture of small and large particles particularly in air, the large platelets were almost all transformed into small particles under hydrothermal conditions. Normally hydrothermal conditions favour larger particle size formation of LDHs.

Table 4.4. Summary of *d*-spacing and average particle size of reconstructed LDHs using different nonpolar amino acids. 'RC' and 'HT' were denoted as product from an open oil bath heated reactor and hydrothermal conditions, respectively. The TEM images were used to determine the mean values and standard deviation by measurement of 300 particles. Bragg reflections of excess amino acids in samples were excluded in this table.

Sample		***d*-spacing (Å)**	**Particle size**
UHT-AMO LDHs		7.62	3-4 μm
RC	Glycine	7.58	87±22 nm, 3±1 μm
	β-Alanine	7.36	132±40 nm, 3±1 μm
	β-Aminobutyric acid	7.61	105±32 nm, 3±1 μm
	γ-Aminobutyric acid	7.51	101±41 nm
	β-Leucine	7.65, 12.08	131±42 nm, 3±1 μm
	β-Phenylalanine	8.12	352±176 nm, 3±1 μm
HT	Glycine	7.52	109 ± 25 nm, 3±1 μm
	β-Alanine	7.6	135±41 nm
	β-Aminobutyric acid	7.63	89±28 nm
	γ-Aminobutyric acid	7.56	100±37 nm
	β-Leucine	7.55, 11.99	135±31 nm, 3±1 μm
	β-Phenylalanine	8.08	125±88 nm

From the results obtained in this study, it was found that gel and nanoplatelet formation of LDHs depends on the amino acid, reconstruction conditions and morphology of the original LDHs. Amino acid having steric hinderance (or low water solubility) prevent nanoplatelet formation, especially those that originated from the large particle LDH precursors.

The inter-lamellar hydrogen bonding networks and interlayer electrostatic interactions in LDHs lead to a tight stacking of layers and prevent the exfoliation of the sheets in water or in solvents.[191, 198, 365-368] These interactions could be weakened by the removal of water during calcination. The reformation of the layer structure depends on, hydration and swelling processes. Amino acids contain oxygen functional groups capable of forming hydrogen bonds, while lone pairs from primary amine groups can be H-bond acceptors. It is believed that when the LDOs are put into contact with amino acid solution, H-bond formation occurs rapidly. At the same time, amino acid molecules may disrupt the hydrogen bonding networks and electrostatic interaction from water and other anions (hydroxide and carbonate), which prevent stacking of the layer and avoid aggregation of the primary particles.

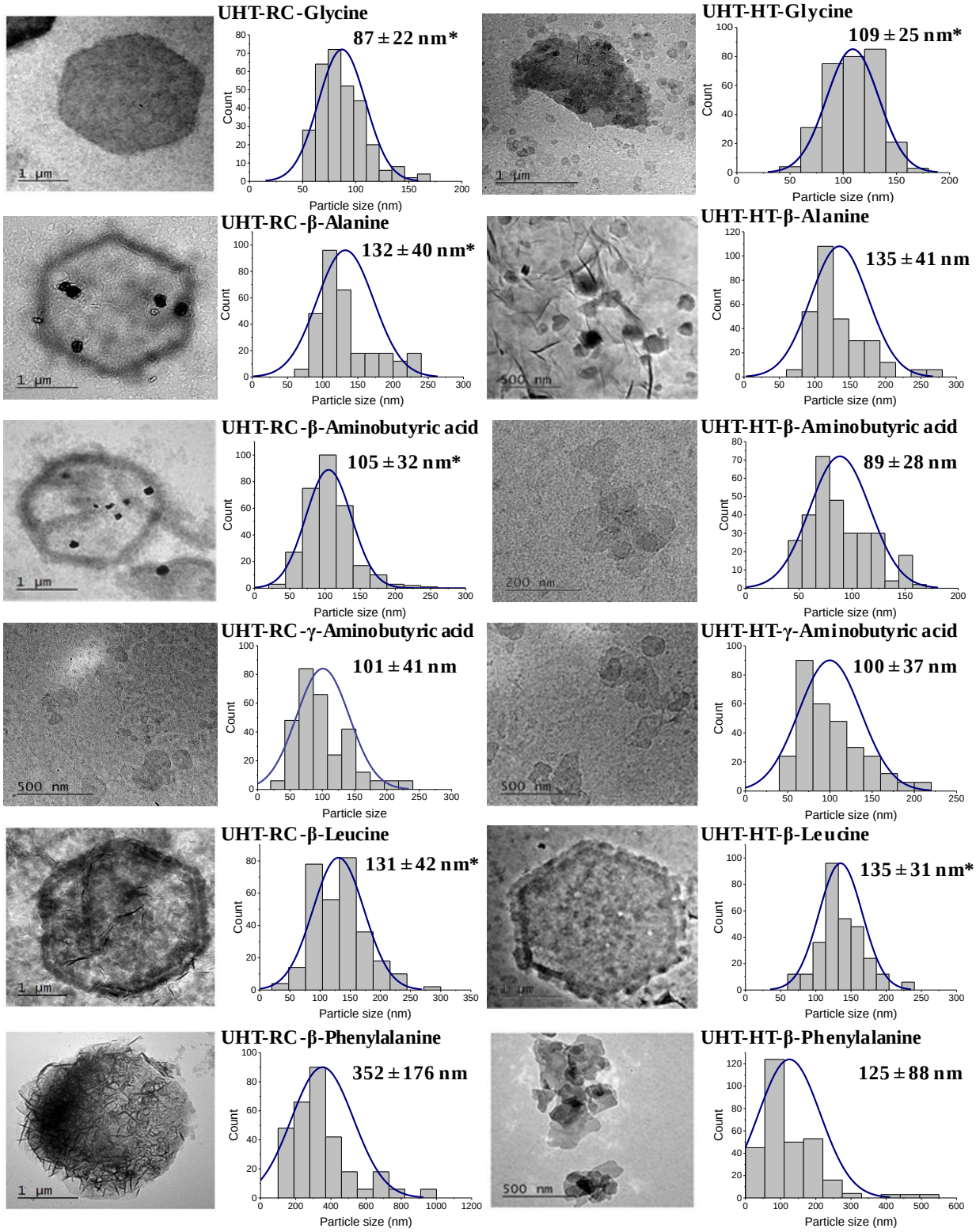


Figure 4.9. TEM images with particle size distributions of reconstructed products from urea-hydrothermal LDHs (UHT) with different nonpolar amino acids. 'RC' and 'HT' were denoted as product from round bottom flask using oil bath heating and hydrothermal reactors, respectively. Navy lines indicate the best fit of a Gaussian distribution, showing approximately a normal distribution. Mean values and standard deviation were obtained from measurement of 300 particles. '*' indicates that only small size particles were plotted the size distribution curves.

Another possible explanation is the dissolution-recrystallisation process, which was initially proposed by Stanimirova *et al.*.[408] These researches reported the change of the composition of the octahedral layer after regeneration.[409] However, in terms of the morphology change, they found that the particles were thinner than the original sample. Compared to the present study, no significant change in size and morphology was observed by Stanimirova *et al.*.[410] In the case of LDHs from urea hydrothermal method, the particle sizes of the reconstruction products are in two ranges, 3−4 μm and about 100 nm. The large particles are the same size as the parent materials but they show thicker edges (the dark area in the TEM image, Figure 4.9) with thinner particles (the light area). At the same time, many small particles were formed, supporting the concept of dissolution and recrystallisation of the LDHs. On the other hand, the LDHs from co-precipitation are flower-like shaped with strong aggregation of the individual platelets. This morphology disappeared and was totally transformed into uniform nanoplatelets after reconstruction but the performance of the amino acids on this behaviour is suppressed by an increase in the hydrophobicity of the amino acid substituents. Hence, combining these two concepts, rapid H-bonding formation from amino acids *via* dissolution-recrystallisation of LDHs could explain the size reduction of LDHs after the reconstruction process.

4.2.3. Effect of other types of amino acid on reconstruction of LDHs

As discussed in section 4.2.1, the effect of nonpolar amino acids on gelation and nanoplatelet formation have been studied. In this section, amino acids containing different polar side chains; serine (additional OH group), asparagine (additional amide group), aspartic and glutamic acids (additional carboxylate group) were examined, their structures are presented in Figure 4.10. All studies were performed with the rosette-shape LDH prepared using the co-precipitation method with AMOST treatment (Cop−AMO LDHs). Reconstruction condition was conducted in round bottom flask in air at 80 °C for 24 hours.

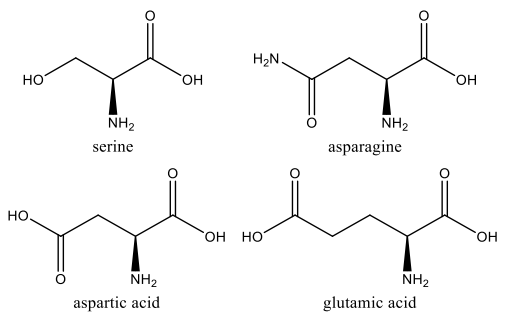


Figure 4.10. Structures of the polar amino acids used in this study.

As expected, gel-like products were obtained in the case of asparagine and serine (Figure 4.11), while aspartic acid and glutamic acid produced white dispersions as shown in the Appendix (Figure C6). Serine and asparagine have a high propensity for hydrogen bonding due to their extra hydroxyl and amide groups, respectively, which enhance the efficiency of gel formation. The extra amide group can accept two and donate two hydrogen bonds, as well as the extra hydroxyl group of serine can facilitate the hydrogen bonding network. Since the swelling behaviour represents the incorporation of water in the interlayer space though hydrogen bonding network.[385] Thus, the additional functional groups in the amino acids would strongly participate in the incorporation of water, formation of hydrogen bonds and improved water permittivity by zwitterions resulting in swelling and gel formation of LDHs after reconstruction. The reconstructed product from serine shows brown colour, suggesting the Maillard browning and caramelisation occurred.[411] It was reported that by heating sugars and some amino acids, especially under alkaline condition, for a long time, both reactions are greatly accerlerated and browning and loss of the reactants are observed.[411]

The investigation of the interaction of aspartic and glutamic acids; negatively charged or acidic side chain amino acids, with the LDHs has been widely studied by molecular dynamic simulations.[392, 404] It was suggested that those amino acid as well as water molecules arrange in the LDH structure *via* hydrogen-bond interaction and adsorb on the LDH surface by their C-termini.[392, 395, 404] In this study, the gel formation was not observed in case of aspartic and glutamic acids. Although the extra carboxylate group also has hydrogen bonding capacity, it may prefer to form a hydrogen bonding network with the surface hydroxyl of the LDH layers rather than with the water molecules. Hibino suggested that the divalent anions of those acidic amino acids likely vertical oriented in the interlayers by connecting to the LDH layers above and below them.[375] This may induce the LDH sheets to come closer and form a tight connection rather than swell in water, resulting in strong attractions between LDHs layers. In addition, these amino acids are much less soluble in water than serine and asparagine which may limit the swelling of LDH particles and yield white solid products and not gel-like LDHs.

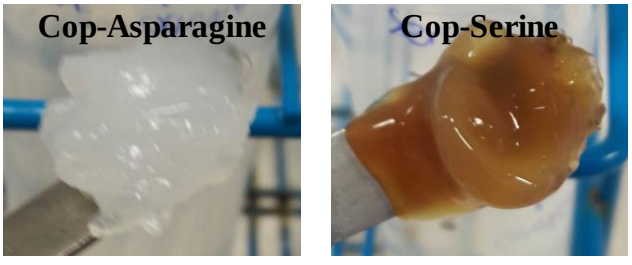


Figure 4.11. Appearance of products obtained after reconstruction in asparagine and serine.

Figure 4.12 displays the TEM images of the reconstruction products, their size distribution is summarised in Table 4.5. Well-dispersed LDH hexagonal platelets (with lateral size <100 nm) were formed after reconstruction with asparagine (63 nm), serine (25 nm) and partially in glutamic acid (59 nm) and slightly in aspartic acid (46 nm). In the case of aspartic acid, a flower like shape was observed. The formation of this morphology is still unclear. However, the appearance of final products after reconstruction by serine is brownish, which may be due to Maillard browning and caramelisation occurred *via* a chemical reaction between this amino acid and LDHs with heating (80 °C).[411]

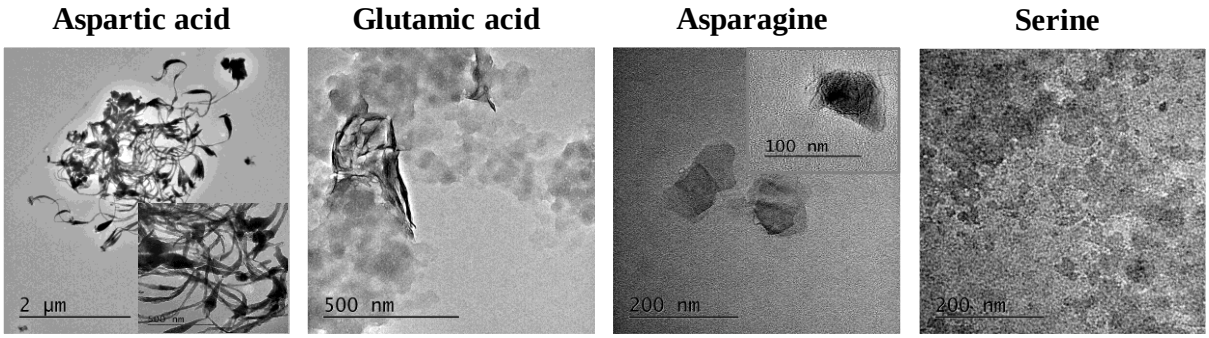


Figure 4.12. TEM images of reconstructed LDHs using different polar amino acids.

Figure 4.13 shows XRD data and FTIR spectra of the reconstructed LDHs using polar side-chain amino acids. Their interlayer distances are summarised in Table 4.5, which agree with the reported from literature (Nakayama *et al.*) that the intercalation occurred with no expansion of the interlayer spacing, peak shift from the original parent LDH was observed in all cases.[106]

It could be concluded that to obtain a gel product with uniform platelets, a highly water soluble amino acid is essential.

Table 4.5. Summary of *d*-spacing and average particle size of reconstructed LDHs using polar amino acids. The TEM images were used to determine the mean values and standard deviations by measurement of 300 particles.

Sample	*d*-spacing (Å)	Particle size (nm)
Aspartic acid	7.60	46±13
Glutamic acid	7.60	59±25
Asparagine	7.74	63±27
Serine	7.74	25±5

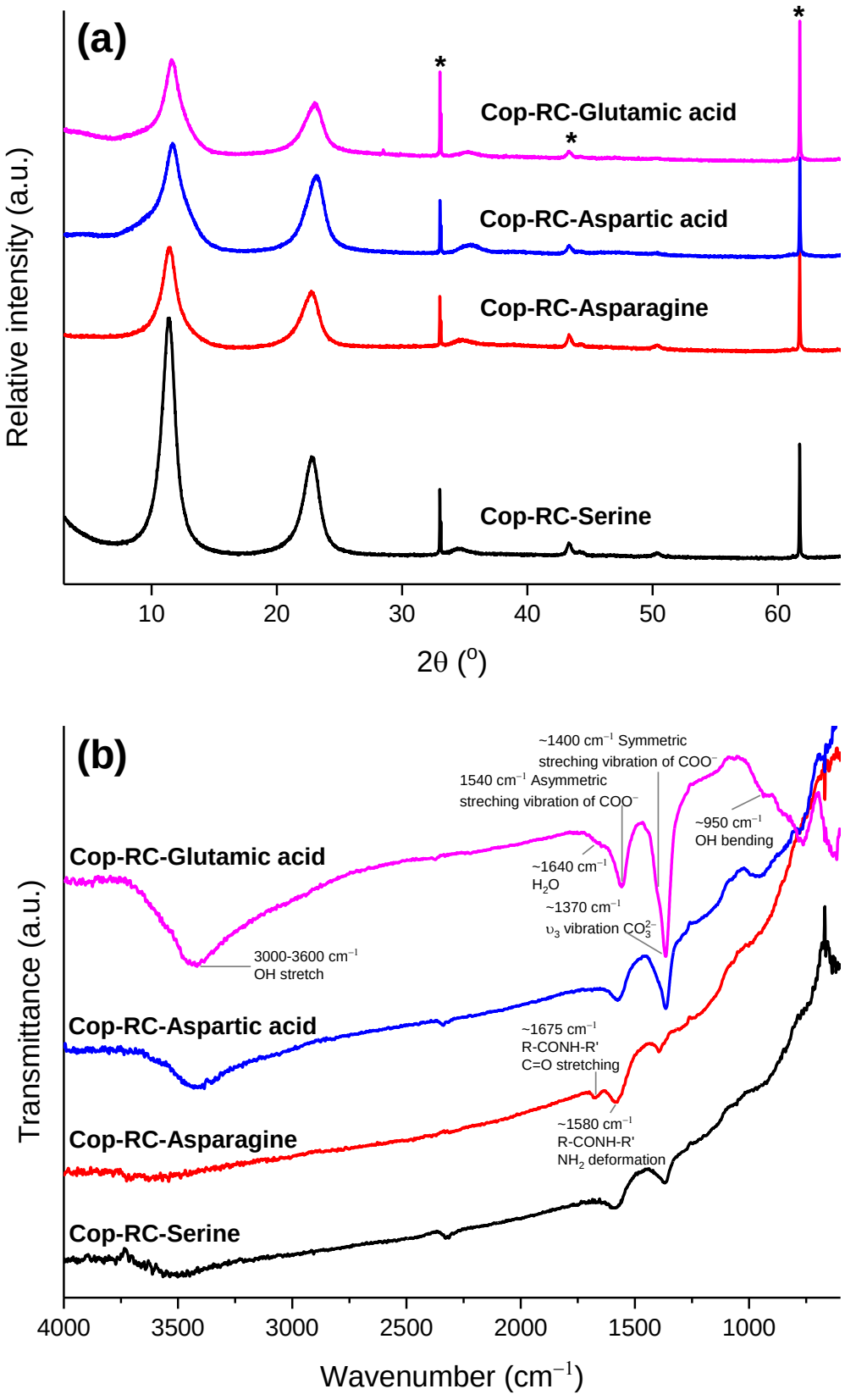


Figure 4.13. (a) XRD patterns and (b) FTIR of reconstructed LDHs using polar side chain amino acids. (*Bragg reflections due to the sample holder were observed at 2θ = 43-44° and 50° and reflections from the silicon wafer were located at 2θ = 33° and 62°.)

4.3. Effect of highly water soluble compounds

It was found that highly water soluble amino acid can be used to prepare gel-like LDH nanoplatelets. Hence, the reconstruction behaviour of LDHs in different highly water soluble compounds; alpha-hydroxy acid salt (sodium lactate), diamine (ethylene diamine), dicarboxylic (carboxylate) and polyhydroxy (sugar/glucose), were studied to reconstruct rosette-shape LDHs (Cop-AMO LDHs). In the case of reconstruction in lactate solution, both Cop-AMO and UHT-AMO LDHs were employed. Reconstruction was conducted in an oil bath heated reactor at 80 °C for 24 hours.

The obtained products are shown in the Appendix (Figure C7). An opaque gel was only found in the reconstructed samples with lactate while others yielded white solid products (ethylene diamine and oxalic acid) and brown solid (may be due to Maillard browning and caramelisation reactions of glucose with LDHs under prolonged heating[411]). None of them provided transparent gel products similar to those obtained using amino acids. This may indicate that both amine and carboxylic groups play an important role in hydrogen bonding, swelling and nanoplatelet formation during reconstruction process.

Figure 4.14 (a) shows the XRD data of the products, *d*-spacing values are summarised in Table 4.6. The Bragg reflections of glucose reconstructed LDHs are very broad with a basal spacing of 8.67 Å. The sample reconstructed by oxalic acid, exhibit a Bragg (003) reflection that is also very broad and less intense compared to the original LDHs, indicating a loss of crystallinity of product. This basal plane also shifts to the lower 2θ value with a *d*-spacing of 8.83 Å which is in agreement with the data presented in the literature.[412] Other intense Bragg reflections in this sample come from excessive oxalic acid present.[413] Very sharp and highly intense Bragg reflections were observed in ethylene diamine reconstructed samples, since the pH of this solution is about 13, which favours the reconstruction process of the LDHs. In the case of lactate reconstructed LDHs a similar basal spacing value as the parent material was observed. The interlayer distances of all samples is summarised in Table 4.6.

The FTIR spectra, Figure 4.14 (b), indicate the presence of the organic guests in the products. The FTIR spectrum shows the stretching vibration of the carboxylate groups at 1640−1660 and 1320−1370 cm^{-1} and O-C-O stretching at 820 cm^{-1}. An IR band at 1370 cm^{-1} was observed indicating the presence of carbonate anions in all samples.

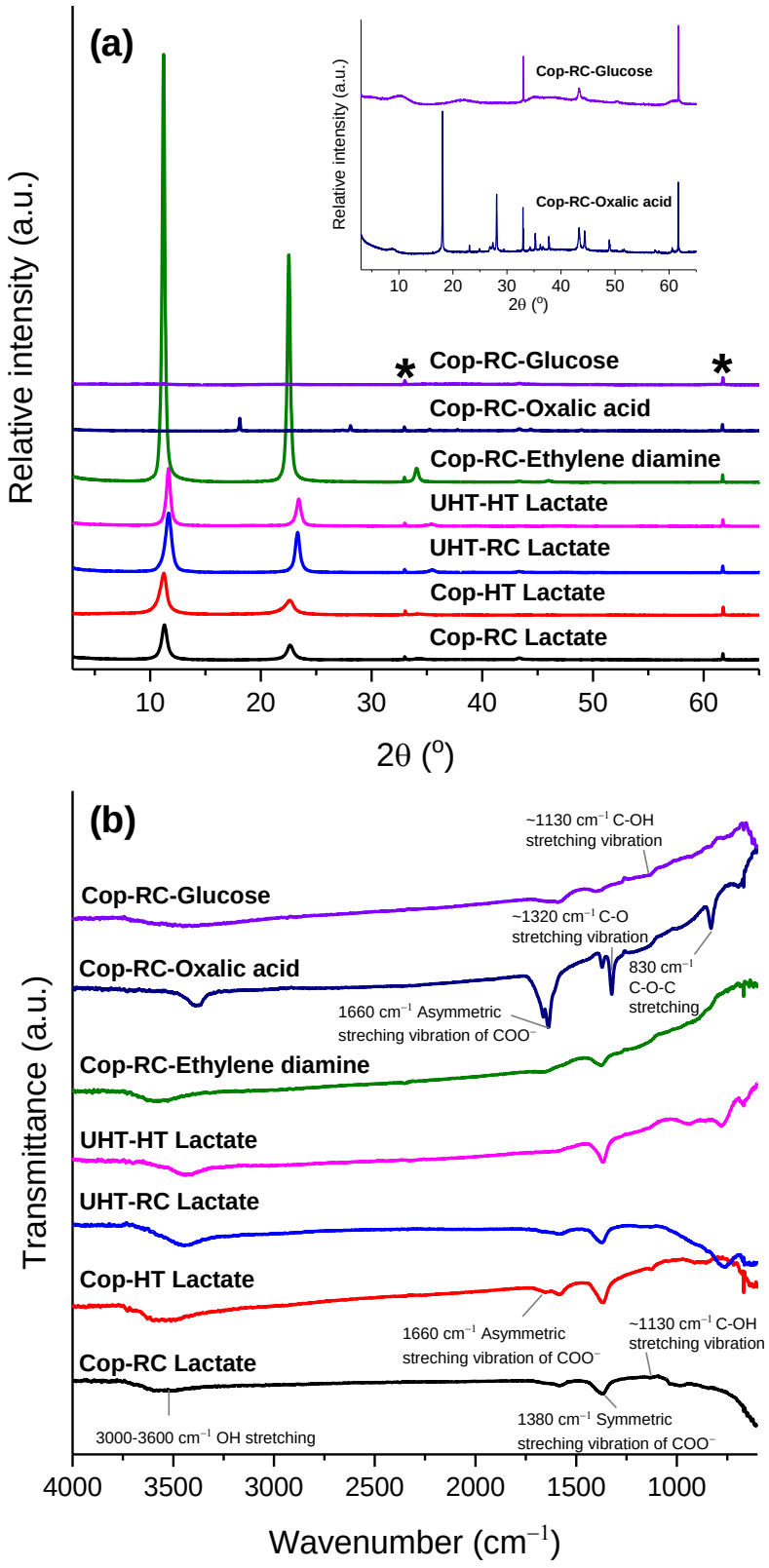


Figure 4.14. (a) XRD data and (b) FTIR spectra of reconstructed LDHs using a selection of highly water soluble compounds. (*Bragg reflections due to the sample holder were observed at 2θ = 43-44° and 50° and reflections from the silicon wafer were located at 2θ = 33° and 62°.)

Table 4.6. Summary of *d*-spacing and average particle size of reconstructed LDHs using a selection of highly water soluble compounds. The TEM images were used to determine the mean values and standard deviations by measurement of 300 particles.

Sample	*d*-spacing (Å)	Particle size (nm)
Cop−AMO LDHs	7.93	1131±504 nm*
UHT-AMO LDHs	7.62	3-4 μm
Cop-RC-Lactate	7.83	132±86
Cop-HT-Lactate	7.88	194±232
UHT-RC-Lactate	7.56	379±221
UHT-HT-Lactate	7.59	287±127
Cop-RC-Ethylene diamine	7.92	399±79
Cop-RC-Oxalic acid	10.00	258±91
Cop-RC-Glucose	8.67	231±109

*measured from the secondary particles of LDHs.

The TEM images (Figure 4.15) show platelet morphology in samples reconstructed with lactate, however, the particle size is not uniform. In comparison with amino acid reconstructed LDHs under the same conditions, the lactate reconstructed LDHs exhibit a larger size and wider size distribution (Table 4.6). Irregular shaped LDHs were obtained after reconstruction in other compounds. Very strong aggregation of platelet particles was found in ethylene diamine reconstructed samples and irregular platelets in oxalic acid and glucose reconstructed products, respectively. Sodium lactate was reported to reconstruct LDHs, resulting in delamination of LDHs.[414] It was stated that the size of the reconstructed LDHs increased from 10−20 to 50−150 nm with a thickness value of 4−8 nm after reconstruction, which is the opposite trend compared to the results presented in this study since they used very small size of starting LDH (10-20 nm). This may be due to different synthesis conditions and the LDHs used. This also suggests that the reconstruction/delamination behaviour of LDHs depends on both the synthetic conditions and the type of LDH.

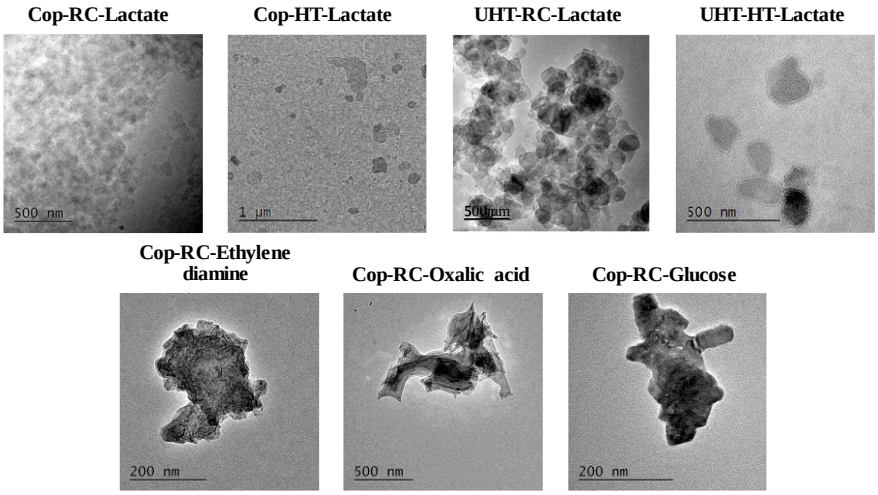


Figure 4.15. TEM images of reconstructed LDHs from different compounds.

4.4. Barrier performance of amino acid reconstructed LDHs

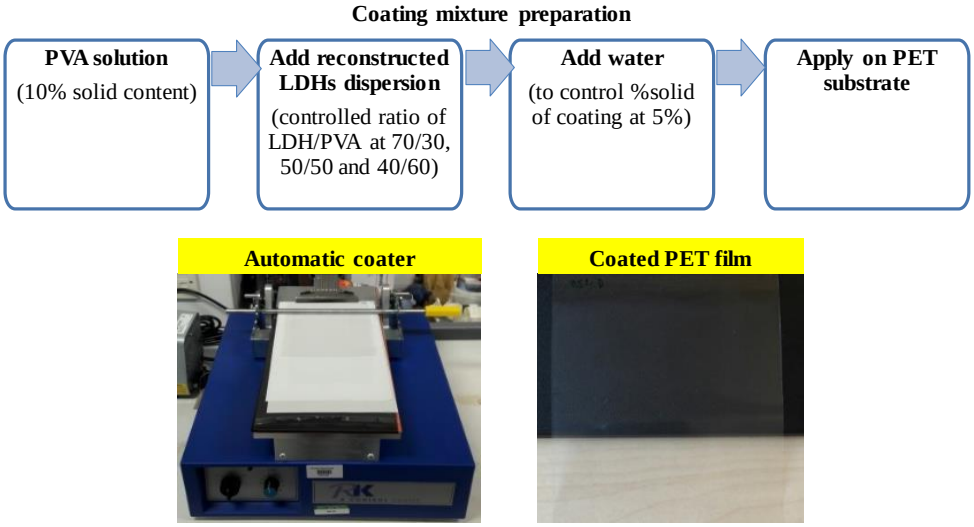
The demand for flexible packaging (paper, plastic, complex/multi-layer materials) is increasing in many industries (e.g. food and beverage, cosmetic, and healthcare). High-performance film structures with high barrier properties will soon dominate the market.[415]

In recent years, a concerted effort has been made to improve the gas barriers performance of polymeric materials.[43-45, 47, 48, 416] Organic/inorganic nanocomposites have been widely examined to obtain high barrier and mechanical properties of polymeric materials.[52-54] Inorganic nanoplatelets can suppress permeation of small molecules through a polymeric film. The key to achieve such enhancements is to form a well-aligned layered arrangement, which is similar to a brick-mortar structure, to create the so-called tortuous path.[39, 47, 60, 78, 344, 417-421] The rich intercalation and ion-exchange chemistry has meant that many layered silicate materials such as smectite clays (e.g. montmorillonite (MMT), hectorite (HEC)) are materials of choice for polymer nanocomposites design. Such performance has been achieved by using many approaches such as layer-by-layer (LbL) assembly and [39, 45, 55, 78-81] self-standing film.[47, 48, 60] However, the elaborate and complex nature of such methods severely restricts their implementation on an industrial scale.

Herein, the application of LDH nanoplatelets obtained from amino acid reconstruction was explored for barrier coating. One of the criteria to select the polymer used to prepare a coating mixture is its film formation property, which requires that the polymer molecules are mobile and stable during the early stages of solvent evaporation and/or solvent absorption into the substrate.[422] The polymer needs to be solvated to resist precipitation. If precipitation

occurs before the film formation, a powdery solid will obtain after drying.[422] Polyvinyl alcohol (PVA) is a water soluble polymer, has good film formation character (ability to form homogeneous films after solvent evaporation), non-toxic, and has moderate gas barrier properties.[423] Hence, PVA was employed as polymeric binder in this study.

Aqueous barrier coating mixtures were prepared by mixing LDH nanosheets with PVA (Kuraray; Mowiol 4-88, M_w 31,000, 88% hydrolysis) and subsequently applied on the corona-treated polyethylene terephthalate (PET) substrate (SARAFIL Transparent TF101, Polyplex Thailand supplied by SCG Packaging PLC), using an automatic coater (K101, RK Print Coat Instruments Ltd.) and dried naturally at room temperature. The coating mixture preparation is summaried and shown in Scheme 4.2. All coatings were prepared at the final total solid content of 5 wt%. The PET substrate and the coated film with 5 wt%. PVA were prepared and tested as control samples.



Scheme 4.2. Procedure for preparing coating mixture.

4.4.1. Effect of amino acid, LDHs morphology and number of coating layer on barrier performance

In order to study the effect of LDH morphology, two LDH nanoplatelets prepared using the reconstruction process with β-aminobutyric acid were selected to prepare the coating mixtures. From TEM image in Figure 4.5 and Figure 4.9, Cop-RC-β-aminobutyric acid LDH shows product uniformity with the average particle size of 55±13 nm, while UHT-RC-β-aminobutyric acid LDH produces larger particles (105±32 nm) with a combination of the original particles (3-4 μm), their TEM images are shown in Figure 4.16.

The coating mixture preparation is summaried and shown in Scheme 4.2. All coatings were prepared at the final total solid content of 5 wt%. The solid weight ratios (in a hundred

part) of reconstructed LDH to PVA (LDH/PVA) were varied from 70/30, 50/50 and 40/60, which are summarised in Table 4.7. The PET substrate and the coated film with 5 wt%. PVA were prepared and tested as control samples.

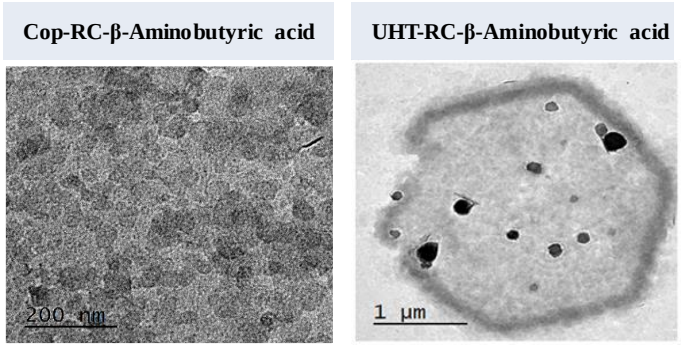


Figure 4.16. TEM images of Cop-RC-β-aminobutyric acid and UHT-RC-β-aminobutyric acid LDHs.

Table 4.7. Summary of coating formulation containing amino acid reconstructed LDHs.

Coating formulation at 5 wt% solid content	LDH (part, %)	PVA (part, %)
PVA	-	100
Cop-RC-β-Aminobutyric acid (unwashed)/PVA	70	30
	50	50
	40	60
UHT-RC-β-Aminobutyric acid (unwashed)/PVA	70	30
	50	50
	40	60

Oxygen transmission rate (OTR) is a measurement of the rate of oxygen transmission through a film under defined conditions of temperature and relative humidity. The rate of oxygen exchange through the film from an oxygen flow in a chamber to a nitrogen filled chamber in another side was monitored. Once the transmission is no longer fluctuating, the rate is reported.[1] Value are normally expressed in $cc \cdot m^{-2} \cdot day^{-1}$ in metric (or SI) unit and in $cc \cdot 100\ in^{2} \cdot day^{-1}$ in US standard units. It is widely accepted that a material can be considered a 'high oxygen barrier' if the OTR value is less than 1 $cc \cdot m^{-2} \cdot day^{-1}$ (at 23 °C, 0% RH).[222]

Figure 4.17 shows the results for the oxygen transmission rate of PET substrate, PVA coated film and LDH nanoplatelets/PVA coated films. PVA can enhance barrier performance of the substrate with a reduction of OTR value from 61.30 to 16.30 $cc \cdot m^{-2} \cdot day^{-1}$. Moreover, it was found that a coating mixture containing only amino acid (β-aminobutyric acid) and PVA (at total solid content at 2 wt%) can also reduce the oxygen transmission value of the coated

film from 61.30 to 16.70 cc·m^{-2}·day^{-1} (PVA coated film 25.80 cc·m^{-2}·day^{-1}), as shown in the Appendix (Figure C8).

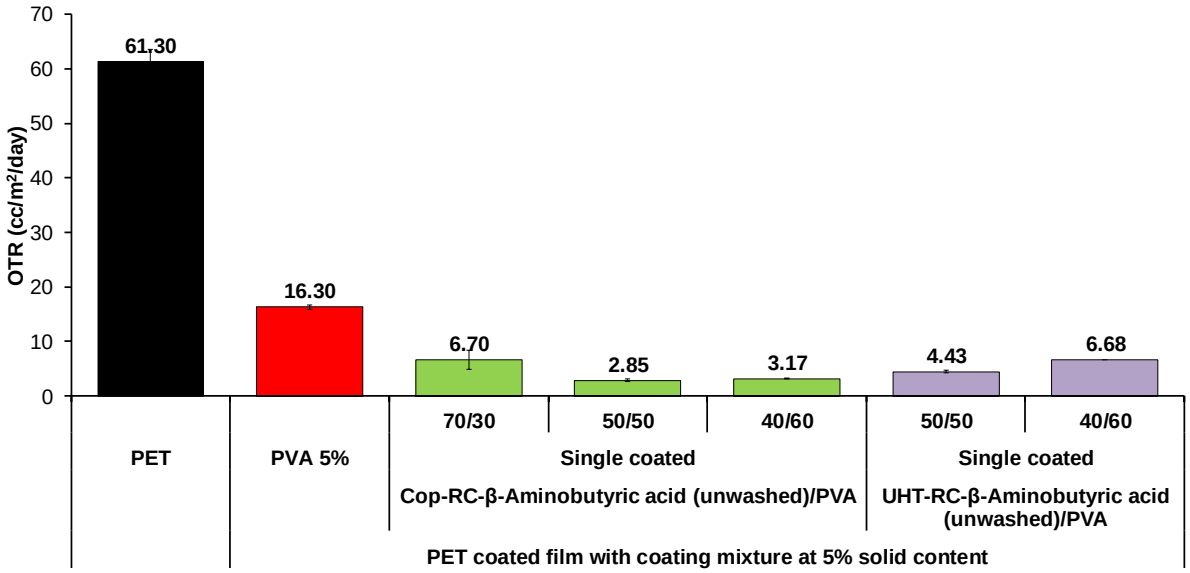


Figure 4.17. Oxygen transmission rate values of PET substrate (black), coated films with PVA (red) and coated films with various coating mixtures at different ratios of reconstructed LDH/PVA, Cop-RC-β-Aminobutyric acid (light green) and UHT-RC-β-Aminobutyric acid (light purple).

The OTR values of coated films decreased significantly in all cases in comparison to the pure PVA coated film. With single layer coating, the OTR values decreased to 2.85–6.70 cc·m^{-2}·day^{-1}. In general, the permeation of the polymer filled flake-like particle system depends on the loading level, orientation and morphology of the platelets.[60, 344, 345] The coated films with the reconstructed LDHs of calcined Cop-AMO LDH in β-aminobutyric acid (Cop-RC-β-aminobutyric acid) give lower OTR values than using the one that reconstructed from the calcined UHT-AMO LDH (UHT-RC-β-aminobutyric acid) due to better particle uniformity. This indicates the incorporation of those nanoplatelets in the coating layer increases the diffusion pathway of the oxygen molecules through the substrate, suggesting that a tortuous pathway has been created.[55, 309, 344, 345, 424] The ratio of nanoplatelets/PVA also affects the barrier performance of the coated films. The OTR value decreased with increasing LDHs loading. For example, the lowest OTR value (2.85 cc·m^{-2}·day^{-1}) was achieved at LDH/PVA ratio of 50/50. However, if the loading is too high it may cause aggregation of particles leading to an open structure in the coating layer, thus the barrier performance is decreased, OTR value increased to 6.70 cc·m^{-2}·day^{-1} when increased the LDH/PVA ratio to 70/30.[425-427]

Double coating layers leads to a better surface coverage, thicker coating layer, and longer diffusing pathway, resulting in a dramatically improved barrier performance even with high LDH/PVA ratio coatings with OTR value down to 0.43 $cc \cdot m^{-2} \cdot day^{-1}$ (Figure 4.18).

Amino acids can reduce OTR value of the coated film; however, the excess amount of amino acid in the reconstructed LDHs has a reverse effect on barrier performance. Coated film with a washed LDH sample significant improved barrier property of the coated film, the OTR decreased from 2.85 to 0.35 $cc \cdot m^{-2} \cdot day^{-1}$. This may be due to as excess of amino acids interfering with the alignment of the platelets resulting in high oxygen permeation of the coated films.

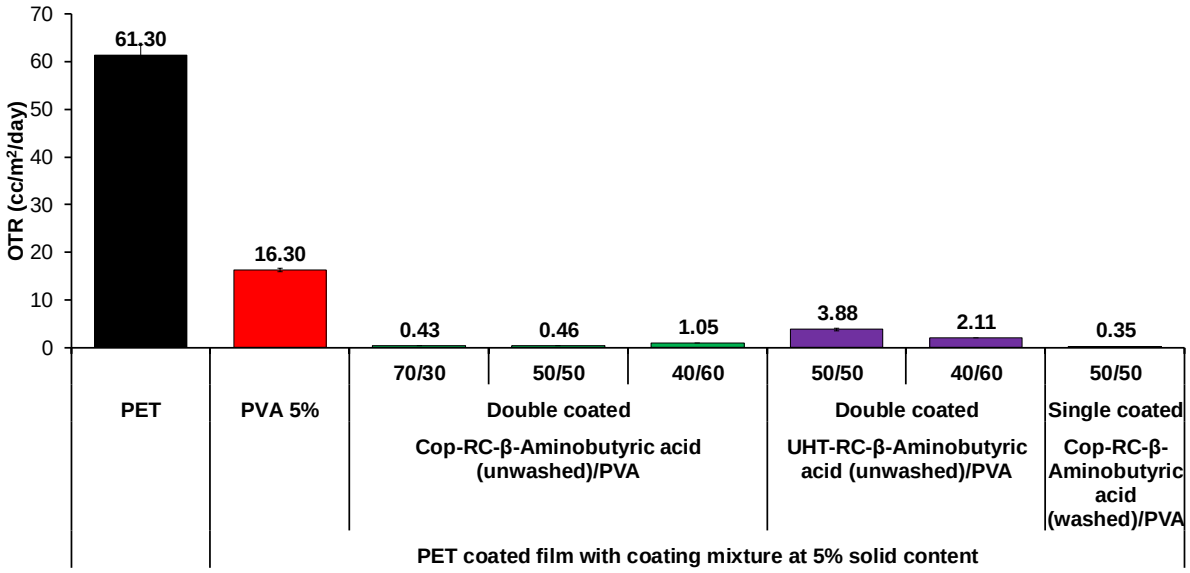


Figure 4.18. Oxygen transmission rate values of the double layers coated film with various coating mixtures at different ratios of reconstructed LDH/PVA, Cop-RC-β Aminobutyric acid (green) and UHT-RC-β-Aminobutyric acid (purple). Single layer coated film with coating mixture containing washed Cop-RC-β-Aminobutyric acid/PVA at the ratio of 50/50 (blue) and PVA coated film (red) were compared to the PET substrate (black).

Alternatively, unmodified LDHs with different sizes and commercial clays were compared in this study, their SEM images were placed in the Appendix, Figure C9. The coated films were prepared using unmodified LDHs with different particle sizes (0.5, 3 and 7 μm) and coating grade commercial kaolin clays (Barrisurf, Imerys Minerals Ltd., and Nuclay, Engelhard Corporation) using the same PVA and substrate. These coating mixtures were formulated at 10% solid with the weight ratios of LDH/PVA or clay/PVA at 20/80 and 50/50 (summarised in Table 4.8). The PET substrate and the coated film with 10 wt%. PVA were prepared and tested as control samples.

Table 4.8. Summary of coating formulation containing different clays and LDHs.

Coating formulation at 10 wt% solid content	**LDH (part, %)**	**PVA (part, %)**
PVA	-	100
Barrisurf	20	80
	50	50
Nuclay	20	80
	50	50
0.5 μm LDH	20	80
	50	50
3 μm LDH	20	80
	50	50
7 μm LDH	20	80
	50	50

In the case of unmodified LDHs in Figure 4.19, a decrease of OTR value for all coated samples was observed as compared to the PET substrate. The OTR values of coated films were decreased after coated with PVA (10% solid content) having the OTR value of 9.68 $cc \cdot m^{-2} \cdot day^{-1}$ which is lower than in previous study that used PVA 5%. The OTR values further decreased respectively with larger size of LDHs in both PVA/LDH ratios. A minimum OTR value was obtained in the coated film with a 7 μm size LDH with a ratio of PVA/LDH of 50/50. While in other LDHs and clays, a significant increase in OTR value was obtained. Figure C9 (in the Appendix) shows the morphology of LDHs and clays used in this study. Clay particles are strongly aggregated; in general, they require a dispersing agent to fully disperse in water. The obtained OTR results, from these clays, without any dispersing agent added, are about 11 $cc \cdot m^{-2} \cdot day^{-1}$. This indicates that commercial clays dispersed in PVA give low barrier performance due to poor dispersion of the clay in the PVA solution.

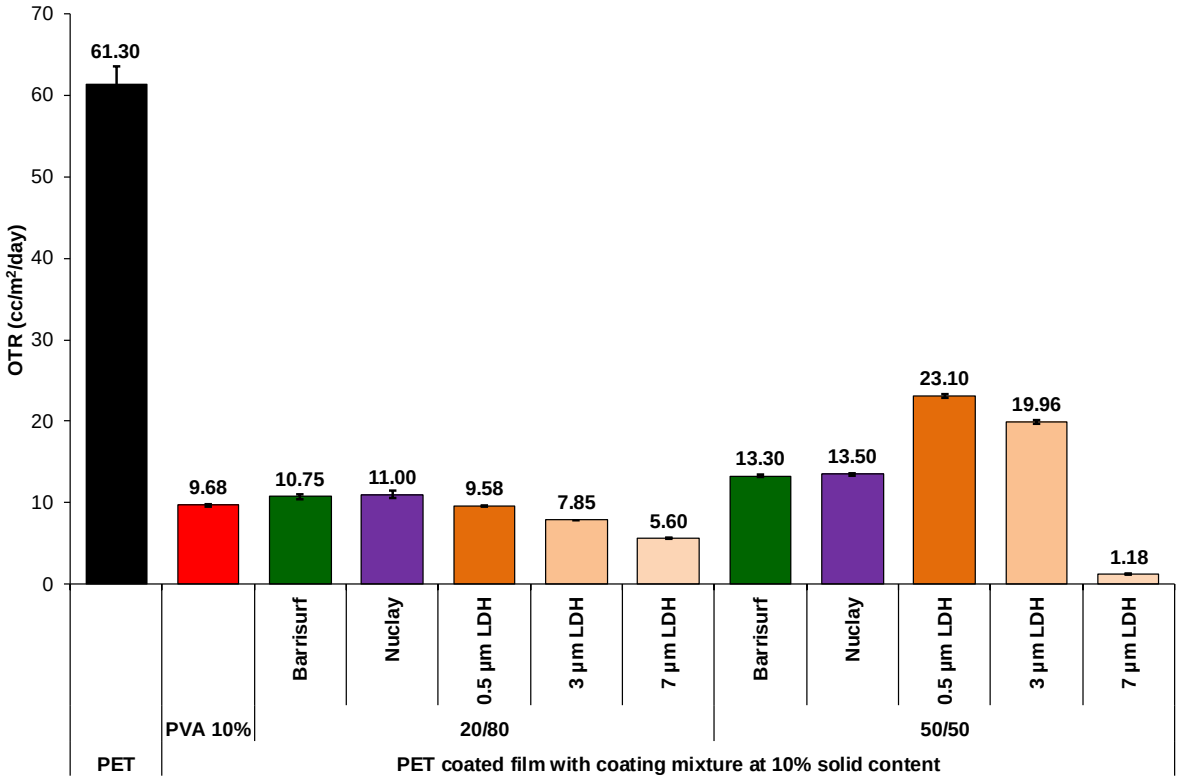


Figure 4.19. Oxygen transmission rate value (OTR) of uncoated and coated films with different clays and LDHs at the ratio clay/PVA and LDH/PVA of 20/80 and 50/50 at 10% solid content.

An increase in the OTR values of the coated films on decreasing size of LDH particles can be explained by the Critical Pigment Volume Concentration (CPVC), which is the point that the pigments are sufficiently covered by the polymers. [425-427] Above CPVC, voids will appear in the coating structure, negatively affecting packing and permeability of the coated film. If the particles are not well covered with the polymer, there will be void around particles, which leads to an increase in the free volume.[425-427] The explanation of poor OTR performance using small size LDHs may be due to the small particles are insufficiently covered by PVA, giving an open coating structure and resulting poor OTR values.

Figure 4.20 shows the cross-section SEM images of the coated films with different size LDHs, all of them show poor dispersion and aggregation of the LDHs on the coated films showing the thickness of the coating layer in the range of 0.5 – 1.5 µm, which correlates to the thickness values of the coated film as shown in the Appendix (Figure C10 (a)). High barrier coating will be obtained if the LDHs surface is modified to improve the LDHs dispersion and its coverage on the substrate. In the case of reconstructed LDHs with amino acid, the coated layer was not clearly resolved by SEM (Figure 4.21), which may be due to the very thin thickness of the coating layer. No difference in the film thickness was observed between the coated and uncoated films measurement (Figure C10 (b)). The cross sectional

TEM would be a better option to determine the alignment of LDHs and thickness of the coating.

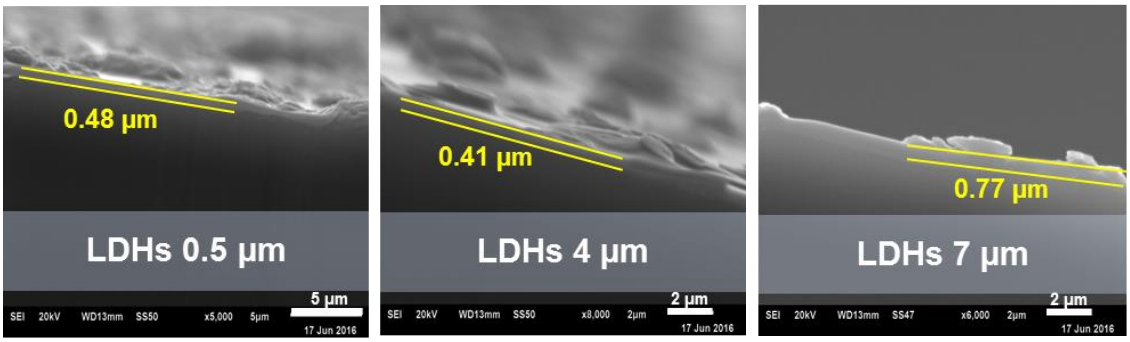


Figure 4.20. Cross sectional SEM of coated films with the coatings with PVA/LDHs at 50/50 at 10% solid content.

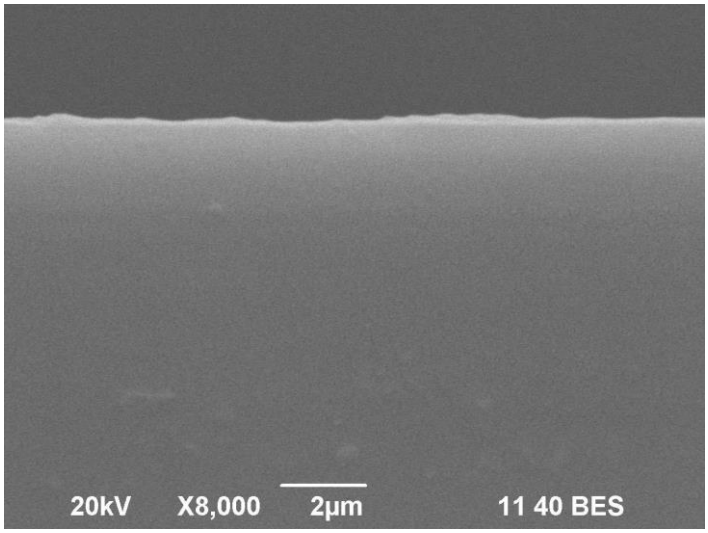


Figure 4.21. Cross sectional SEM of coated films with the coatings with PVA/Cop-RC-β-amino butyric acid LDHs at 50/50 at 5% solid content.

Normally three measurements; total transmittance, haze and clarity are tested to evaluate the optical properties of flexible films.[1] Total transmittance is the ratio of transmitted light to the incident light. The haze measurement is the ratio of transmitted light which in passing through that deviates from the incident beam greater than 2.5 degrees on average. On the other hand, the see-through quality or clarity is determined in an angle range smaller than 2.5 degrees, which describes how well very fine details can be seen through the specimen.

Figure 4.22 shows the optical properties of the coated films containing unmodified LDHs and commercial clays. All coated films show similar transparency compared to the blank sample. However, haze increase and clarity values decrease as increasing LDHs loading, while the commercial clay give slightly better in haze and clarity values. On the other hand, the optical properties of coated films obtaining from β-aminobutyric acid reconstructed LDHs

were shown in Figure 4.23. It has found that the coating does not significantly affect optical properties of the coated film unless the double coating is applied, which is the advantage of using these nanoplatelets over unmodified LDHs and commercial clays.

In general, the light scattering of inorganic nanoparticles is responsible for the opacity of the obtained material.[428-430] In order to obtain highly transparent film, the size of nanoparticles in the matrix should be less than 1/10 of the wavelength of the visible light (400−790 nm) to avoid Rayleigh scattering, the higher the transparency of the sample, the lower the Rayleigh scattering.[428-430] Therefore, the coated films with unmodified LDHs and commercial clays, which have micron size particles, the scattering can occur and results in a decrease in optical properties of the coated films. On the other hand, the Cop-RC-β-aminobutyric acid LDHs have the average size of 55±13 nm (Table 4.2), which is smaller than the visible light wavelength, furthermore there is no agglomeration of the particles by using a low solid content coating mixture that produces high film transparency (Figure 4.23 (a)).[428-430] However, significant differences in the optical properties of the coated films using different LDHs morphology was observed in this study. Although UHT-RC-β-aminobutyric acid LDHs contains two types of particles (Table 4.4), 105±32 nm and 3±1 μm, the majority of particles are in small size range, hence, the effect of Rayleigh scattering is not obvious. If the second layer of coating is applied or very high loading LDHs is used, the light scattering is increased which reduces film transparency. Itoh *et al*.[429] also suggested that the transmittance (visible light) and haze values of the coated film depend on the thickness of the films and the average diameter of the particles used in the film or in the coated layer; the thicker films or the larger size particles lead to low transmission and high haze values of the coated film. Hence, the transmission and haze values of the coated films decreased in the double coated layer samples (Figure 4.23 (a) and (c)). The clarity depends on the size distribution of the particles; a narrow particle size distribution yields the high film clarity of the coated film.[431] However, the effect of LDHs morphology and double coating did not impact on the clarity of the coated films unless a high amount LDHs used in the coating.

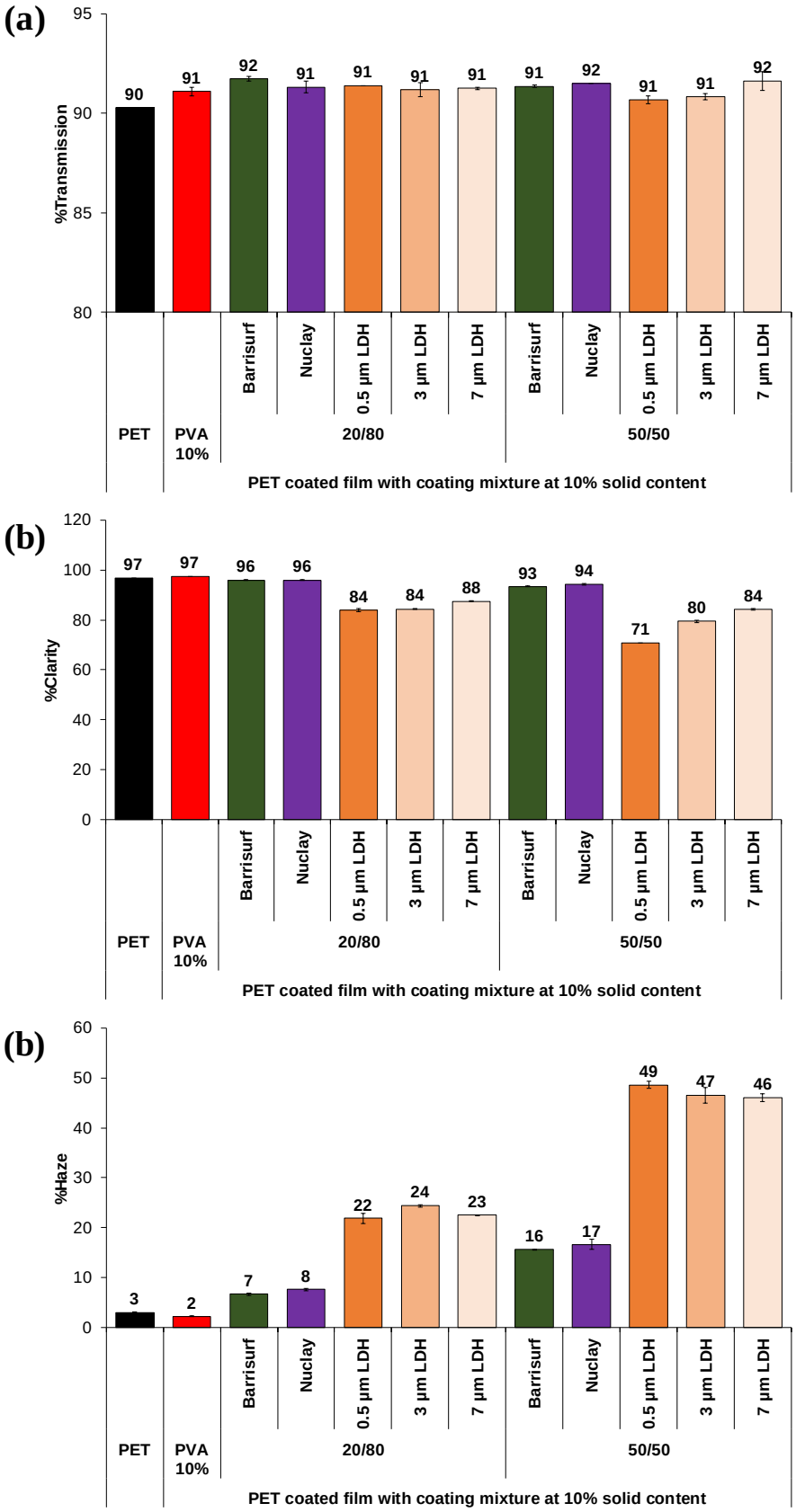


Figure 4.22. Optical properties of the coated films with unmodified LDHs and commercial clays with PVA at different ratios with 10% solid content: (a) % transmission, (b) % clarity and (c) % haze.

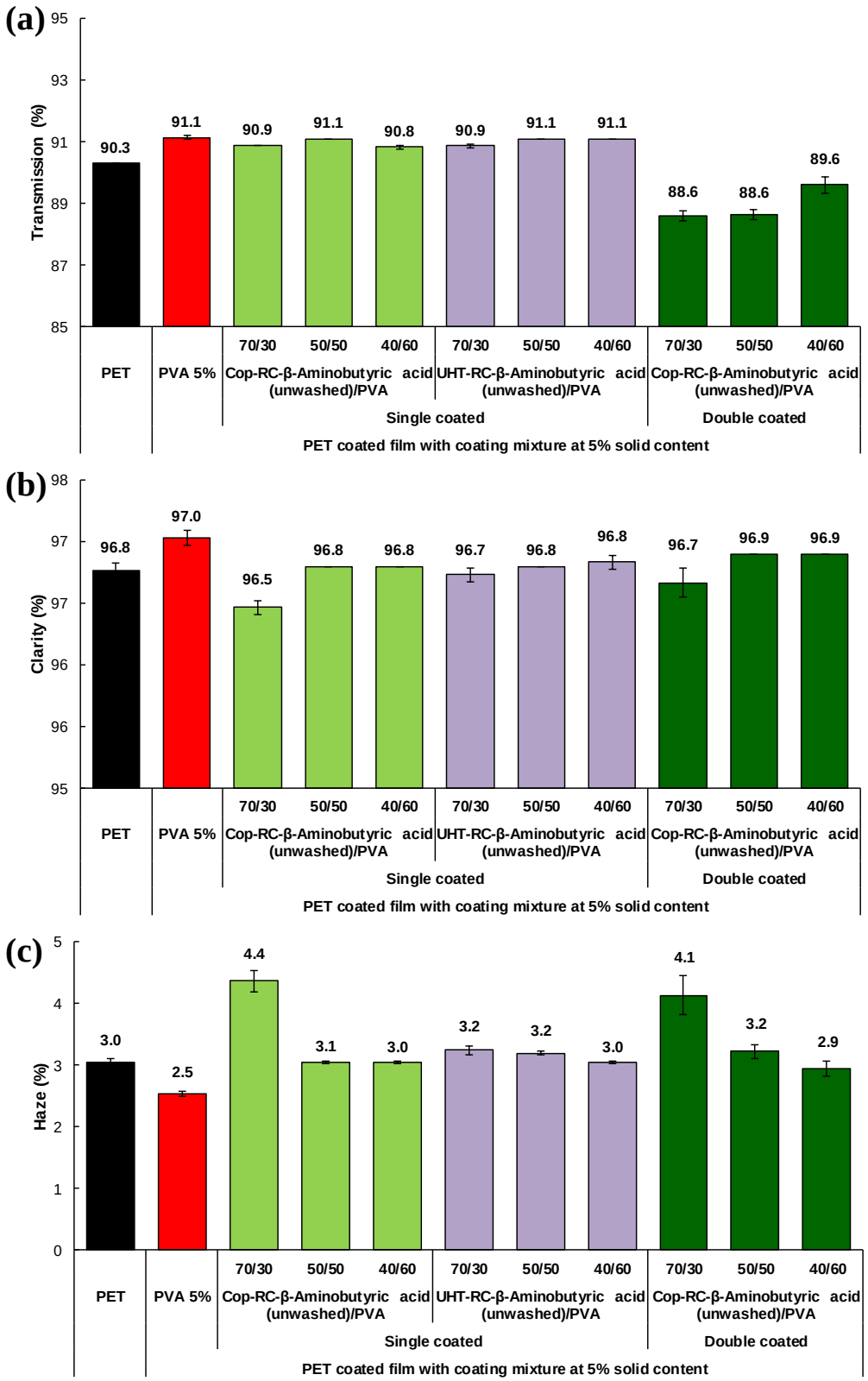


Figure 4.23. Optical properties of the coated films with β-aminobutyric acid reconstructed LDHs with PVA at different LDH/PVA ratios with 5% solid content: (a) % transmission, (b) % clarity and (c) % haze.

4.4.2. Effect of the types of amino acids

In order to examine the effect of amino acid used in reconstruction of LDHs on their barrier coating performance, the reconstructed LDH (co-precipitation LDH) from different amino acids were compared in this study. The coating mixture preparation was prepared at the LDH/PVA ratio of 50/50 with a final total solid content of 5 wt%. (summarised in Table 4.9). The PET substrate and the coated film with 5 wt%. PVA were prepared and tested as control samples.

Table 4.9. Summary of coating formulation containing amino acid reconstructed LDHs.

Coating formulation at 5 wt% solid content	LDH (part, %)	PVA (part, %)	Average particle size of LDH (nm)
PVA	-	100	-
Cop-RC-Glycine/PVA	50	50	42±12
Cop-RC-β-Alanine/ PVA	50	50	55±10
Cop-RC-β-Aminobutyric acid/PVA	50	50	55±13
Cop-RC-β-Leucine/PVA	50	50	61±16
Cop-RC-β-Phenylalanine/PVA	50	50	181±78

The effect of the amino acid used in reconstruction of co-precipitation LDHs was examined as shown in Figure 4.24. No significant difference was observed in OTR values among coated films containing glycine, alanine and aminobutyric acid reconstructed LDHs were found. This might be due to the similarity of the particle size after reconstruction as well as uniformity of the particles (assuming similar alignment on the substrate), enhancing their performance as barrier layers. On the other hand, leucine and phenylalanine gave poor barrier properties. It is believed that since they have a low solubility in water, it is difficult to wash them from the reconstructed LDH products (impurities were shown in XRD) and they may then interfere with the alignment of LDH particles. Furthermore, the non-uniformity of the size, especially in phenylalanine reconstructed LDHs, may be a contributory factor for the poor barrier performance of the coated films.

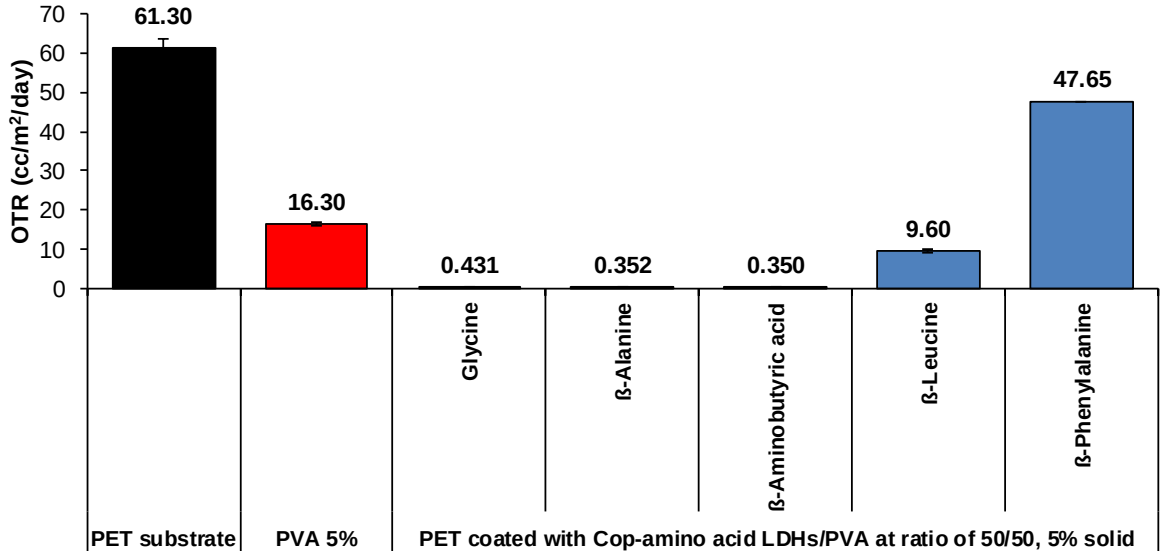


Figure 4.24. Oxygen transmission rate results of the coated film: comparison of the LDHs reconstructed from different amino acids on barrier property at reconstructed LDH/PVA ratio of 50/50 at 5% solid content.

The optical properties and film thickness of coated films are shown in the Appendix (Figure C11). All samples show similar film transparency, clarity and haze values as the PET substrate, except in the coated film containing phenylalanine reconstructed LDHs. From TEM images in Figure 4.5, the present of large particles (181±78 nm, Table 4.2 and Table 4.9) of this sample leads to increases of light scattering and a broad particle size distribution, reduces film transparency and clarity values and considerably increase haze value of the coated film. No difference in the thickness of the coated and uncoated films could be measured using a micrometer.

4.5. Conclusion

A novel strategy for preparing LDH nanoplatelets has been developed by employing a reconstruction method in a concentrated aqueous solution of amino acids. The original LDH particles are broken down and transformed into small uniform particles and formed gel-like product after the reconstruction process. Large platelet LDH samples seem to have more difficulty in forming gels and a uniform particle size after reconstruction by amino acids. Highly water soluble amino acids seem to be the most suitable for producing uniform nanoplatelets dispersions. Other compounds such as sodium lactate can also be used. Hence, it is believed that the compound that is most suitable to prepare LDH nanoplatelets should be small molecule, have two functional groups that have high propensity for hydrogen bonding and be highly water soluble.

The new LDH nanoplatelets were dispersed in PVA and investigated as an oxygen barrier coating film on PET substrate. Transparent and high oxygen barrier PET coated films have been prepared with the OTR value of 0.35 $cc \cdot m^{-2} \cdot day^{-1}$ with a single coating, which is advantageous over unmodified LDHs and commercial clays. The barrier coating mixtures are simultaneously applied onto the substrate in a single step (e.g. roller-and-bath apparatus) and could be potentially applied to the film in an industrial scale. This process possesses several advantages over the reported conventional LbL assembly techniques. Therefore, this work provides a facile and cost-effective strategy for preparation of an LDH-based oxygen barrier coated films and could be particularly useful in packaging applications. The non-toxic nature of LDH will also potentially allow this system to be applied to food packaging applications.

This work presents a green process for preparation of LDH nanosheets *via* a calcination-reconstruction in amino acid aqueous solution. We propose that the hydrogen bonding in the LDH structure was weaken after calcination, along with the penetration of amino acid molecules during the reconstruction process of LDH would lead to a transformation of particles into nanoplatelets due to rapid disruption of the hydrogen bonding network. This result suggests that the nanosheets are potentially applied in barrier coating applications and may be applicable in other applications. The insight of the mechanism of this phenomenon should be further studied.

Chapter Five – Direct reconstruction of layered double hydroxides and their use in barrier coatings

5.1. Introduction

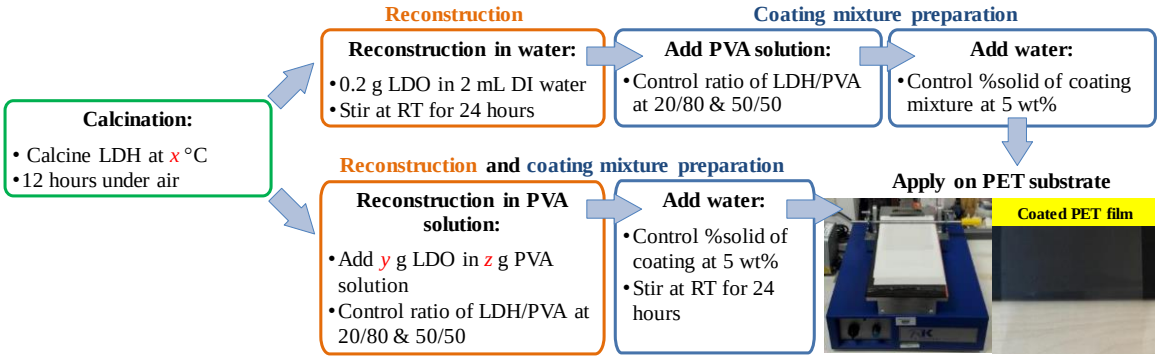
The application of LDH nanoplatelets prepared by the amino acid reconstruction process was previously studied in Chapter 4. It was revealed that the hydrogen bond donor and acceptor groups in the amino acids could be an important factor in the formation of hydrogen bonding with the LDH structure during the reconstruction process in aqueous solution. To compare with the previous studies, the reconstruction of LDHs in water, so-called rehydration or calcination-rehydration process, was performed.

An interesting feature of LDHs is a structural "memory effect", which is the reconstruction of a calcined LDH (a mixed-metal oxide, so-called layered double oxide (LDO)) back to the original LDH structure *via* a rehydration process, as discussed in Chapter 1 (section 1.2.2.5).[153, 154] It is known that the reconstruction process depends on the calcination temperature, chemical composition of the LDH, and reconstruction condition (such as relative humidity, amount of water, pH, target anion, temperature and etc.).[156-159, 374, 432] Although numerous studies have reported the monitoring of structural changes during the calcination of LDHs and the preparation of LDHs by reconstruction method;[117, 154, 161] to the best of our knowledge, no detailed explanation of the morphology changes during the reconstruction process has been published to date. Although the applications of LDO and LDHs prepared by the reconstruction method have been exploited in several aspects especially in adsorption and catalysis applications,[156-159, 374, 432] the application of them in barrier coatings has not been extensively studied.

In this Chapter, different factors such as calcination temperature and the morphology of the original LDHs have been explored to examine the reconstruction behaviour of the LDHs in water. LDH powder was calcined in at a certain temperature under air for 12 hours, then added into deionised water and stirred at room temperature for 24 hours under open atmosphere (without nitrogen flow). The ratio of the calcined product (layered double oxide, LDO) to water was fixed at 0.2 g and 2 mL, respectively. The reconstructed LDHs were mixed with polyvinyl alcohol to prepare coating mixtures with controlling LDH/PVA dry weight ratio at 20/80 and 50/50. The final solid content of the coating mixture was adjusted to

5 wt% by adding deionised water. Finally, the coating mixtures were then applied on a 23 µm polyethylene terephthalate (PET) substrate (SARAFIL Transparent TF101, Polyplex Thailand supplied by SCG Packaging PLC), using an automatic coater (K101, RK Print Coat Instruments Ltd.) and dried naturally at room temperature. The PET substrate and the coated film with 5 wt% PVA were prepared and tested as control samples.

Alternatively, the reconstruction processes were done directly in the PVA aqueous solution (LDH/PVA dry weight ratio at 20/80 and 50/50 was controlled) and the obtained mixtures were subsequently coated on the PET substrate. Finally, the barrier and optical properties of the PET coated films were examined. All preparation processes are summarised in Scheme 5.1 and details of experiment are explained in Chapter Six (section 6.8).

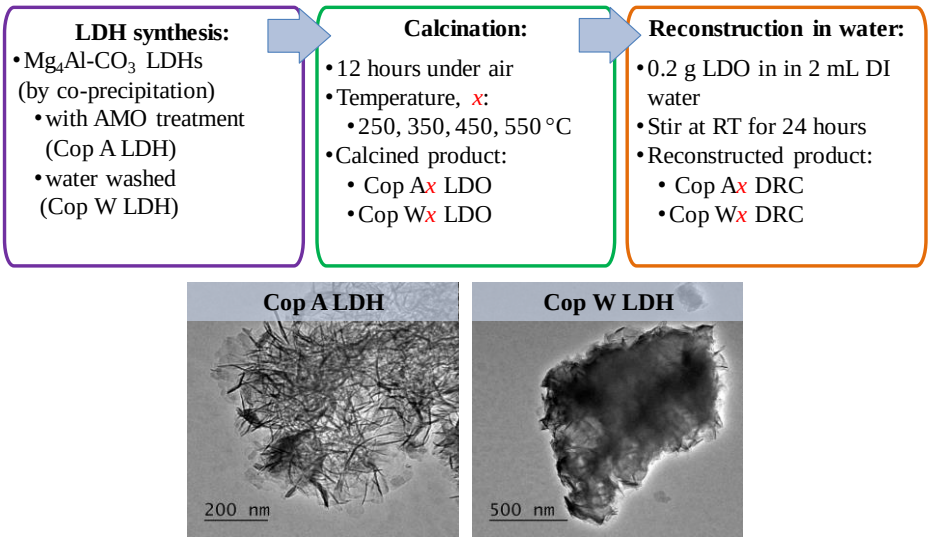


Scheme 5.1. Preparation procedures for reconstruction process and coating mixture preparation in this study.

5.2. Reconstruction behaviour of LDHs in water and non-aqueous solvents

5.2.1. Effect of calcination temperature on reconstruction behaviour in water

The calcination temperature is an important factor on the reconstruction process. It was reported that the LDH structure can be reformed in a day if the calcination temperature is below 550 °C.[156, 157] This study, the calcination temperature was varied from 250, 350, 450 and 550 °C for Mg_4Al-CO_3 LDHs prepared by co-precipitation method. Moreover, the effect of AMO treatment by ethanol dispersion (Cop A LDH) was compared with a conventional water washed LDH (Cop W LDH). The reconstruction process was carried out by adding the pre-calcined LDH samples into deionised water and stirred for 24 hours under open atmosphere (without nitrogen flow), as summarised in Scheme 5.2. For simplification, the calcined and direct reconstructed samples were defined as Cop Ax-LDO and Cop Ax-DRC, for Cop A series, x is the calcination temperature, for Cop W series, they were noted as Cop Wx-LDO and Cop Wx-DRC.



Scheme 5.2. Overall process of reconstruction process in this study.

Figure 5.1 (a) displays the appearance of the obtained product after reconstruction in water, Cop A450 DRC. After reconstruction, the Cop A450 DRC products had a translucent gelatinous appearance and glass-like product obtained after drying (Figure 5.1 (c)), other DRC products from Cop A series also show similar appearance except for Cop A250 DRC. Translucent gel demonstrated Tyndall light scattering effect in Figure 5.1 (b) indicating the colloid nature of the dispersion and the presence of nanoplatelets in the suspension.[433-436] The Tyndall effect is more obvious if the dispersion is diluted as shown in the Appendix (Figure D1). On the other hand, product obtained from Cop W series show more opaque gel with no Tyndall effect even after dilution.

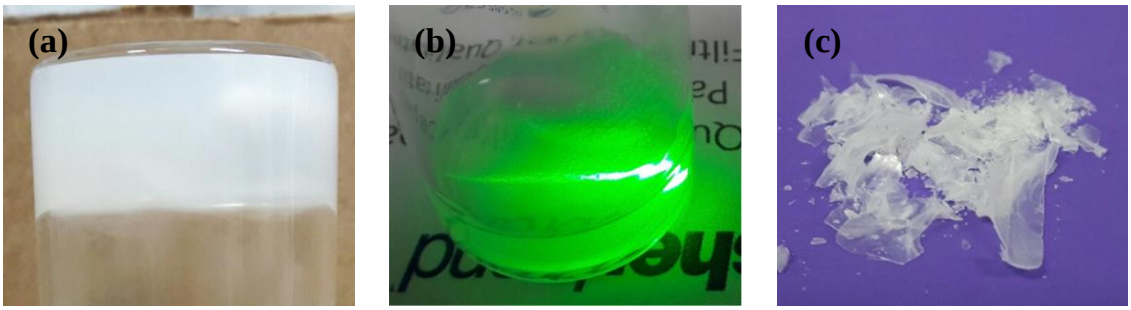


Figure 5.1. (a) Appearance of Cop A450DRC product, (b) Green laser beam confirms the colloid nature of the dispersion in deionised water. Tyndall effect is observed for this sample (100 g/L), and (c) the appearance of the product after drying.

Figure 5.2 (a) and (b) show XRD patterns of LDOs calcined at different temperature compared to their original Cop A and Cop W LDHs, respectively. LDHs structures started collapsing at calcination temperature above 250 °C in Cop A series. While no appreciable change was observed in Cop W250 LDO sample, which is almost identical to the original

Cop W LDH, indicating the removal of the physisorbed water with no impact on the layer structure.[154] It is of note that the intensity of the (006) Bragg reflection decreases much more than that of the (003) Bragg reflection. The broadening of (00*l*) indicates the interstratification disorder of the structure due to the removal of interlamellar water and loss of periodicity in the stacking direction. These results are in agreement with previous reported by O'Hare *et al.*[2] and Rocha *et al.* [156] that the layered structure of this sample is partially retained. On the other hand, Cop A250 LDO exhibits slightly weaker and broader peaks with the decrease of intensity of the (006) Bragg reflection being much more prominent than that of the (003) Bragg reflection. In addition, the new phase nearby the (003) reflection was observed at 2θ~13° in this sample. This result is in accord with those previously reported by Kanezaki,[437] who suggested that the new phase was formed at 200° due to removal of interlayer species and formation of a hydroxyl-containing layered material. It was also reported that this phase is not stable and disappeared at the calcination above 380 °C as observed by high temperature PXRD analysis. However, the new phase was not observed in the sample that was calcined at 350 °C in our studies, which may be due to longer calcination time (12 hours). The non-basal reflections ((*h*0*l*), 2θ = 30-50°) became broaden and their intensities decreased, along with the overlapping of (113) reflection with (110) reflection, indicating the turbostratic disorder in the structure and formation of Mg-Al dehydrated phase. However, no peak shift was observed suggesting that the samples retain a layer structure with similar metal-metal distances.

On increasing calcination temperature further, the layer structure was destroyed and a mixed-metal oxide was formed as evident from the absence of diffraction peaks corresponding to the LDHs due to dehydroxylation of the LDH layers and decomposition of the intercalated anions.[154] For example, only three broad peaks are found after calcination at 350 °C, which is coincide with a mixed oxide phase with MgO-like structure (periclase), as reported by O'Hare *et al*..[154] It was claimed that MgO is the sole crystalline phase, while the Al ions are dissolved in the lattice at these calcination temperature. The migration of Al^{3+} ion from octahedral to tetrahedral sites, through three oxygen atoms from the hydroxyl framework and one apical oxygen from the interlayer, destroys crystallinity and gives rise to cation vacancies in the layer.[154, 156] An increase in sharpness of the peaks, with increasing calcination temperature due to sintering of the materials, results in increasing crystallinity of the mateirals.[154]

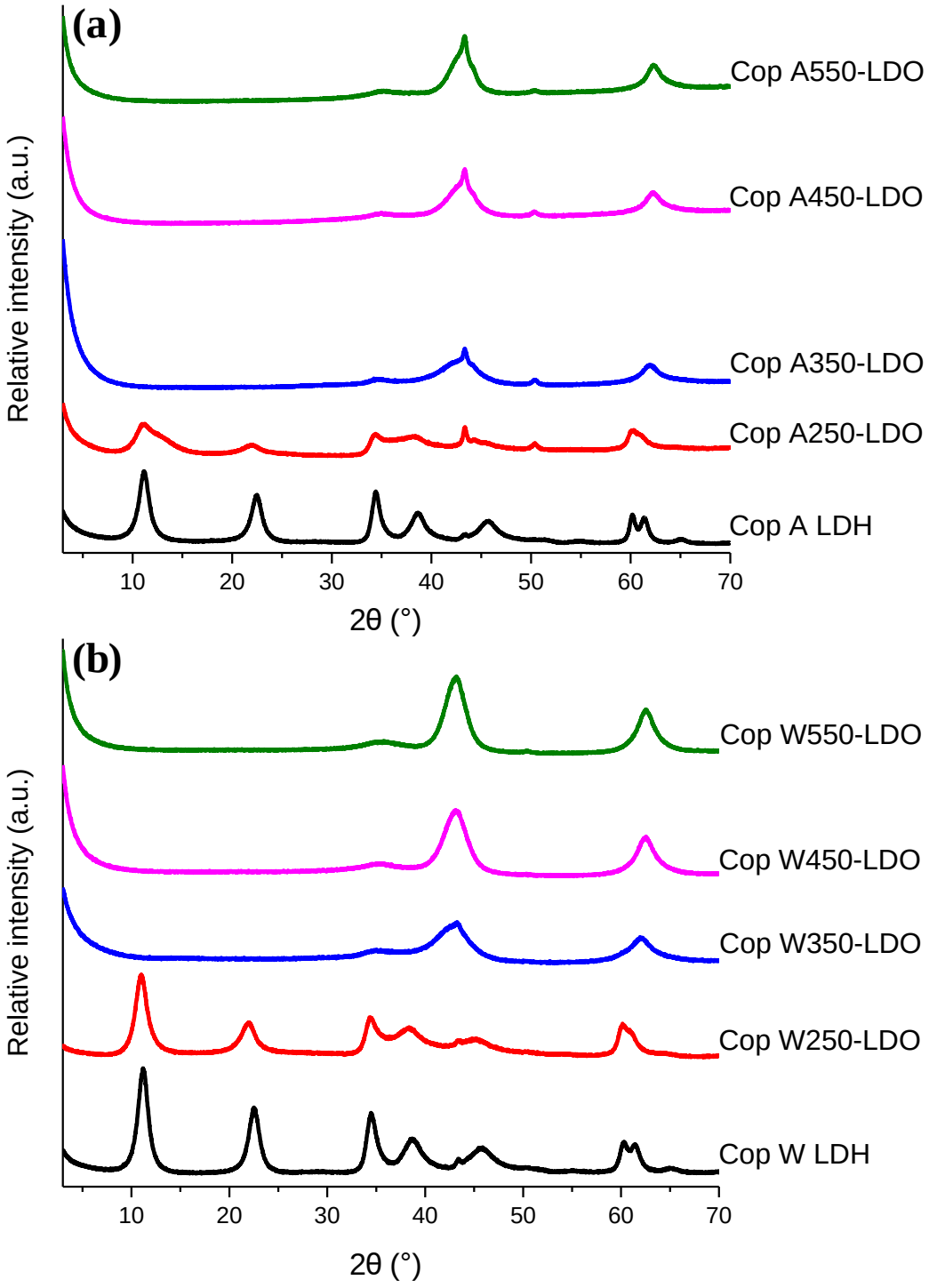


Figure 5.2. XRD patterns of co-precipitation Mg_4Al-CO_3 LDHs and LDOs at different calcination temperature: (a) Cop A series and (b) Cop W series (Bragg reflections due to sample holder were observed at 2θ = 43-44º and 50º).

XRD analysis of reconstructed samples (DRC) are shown in Figure 5.3 (a) and (b), for Cop A and Cop W series. The DRC samples revealed a high degree of crystallinity and the interlayer distance with similar XRD patterns as their parent materials as summarised in the Appendix (Table D1). The sharp (003) and (006) Bragg reflections at low 2θ region (2θ = 11-23°) with broad asymmetric peaks at the higher angle (2θ = 34-66°) are present. The reconstructed products in Cop A series, calcined at 350-550 °C, show sharp peaks and peak intensities increase with increasing calcination temperature, indicating high crystallinity of products after reconstruction whereas sharp reflections were observed once calcination temperature above 350 °C in Cop W series.

The unit cell parameters *a* and *c* have been determined based on the positions of the (003) and (110) planes and are shown in the Appendix (Table D1), assuming a 3R layer stacking (hexagonal unit cell, space group $R\bar{3}m$).[154, 273] Only a slight change in the *a* parameter ($a = 2d_{110}$) was observed in the reconstructed samples. The slight decrease of the *a* parameter was observed in the reconstructed LDHs, which may indicate the change in the metal-metal distance in the layer and suggests the changes in metals ordering in the layer of LDHs after reconstruction.

FTIR spectra of LDOs from Cop A series are shown in Figure 5.4 (a), for Cop W series are shown in the Appendix (Figure D2). The broad band around 3,000–3,600 cm^{-1} in Cop A LDH is attributed to the O-H stretching vibration of the metal hydroxide basal layer and the interlayer water molecules. A small shoulder present around 3,000–3,100 cm^{-1} is caused by the interaction between the carbonate anions and water molecules present in the interlayer region.[438]

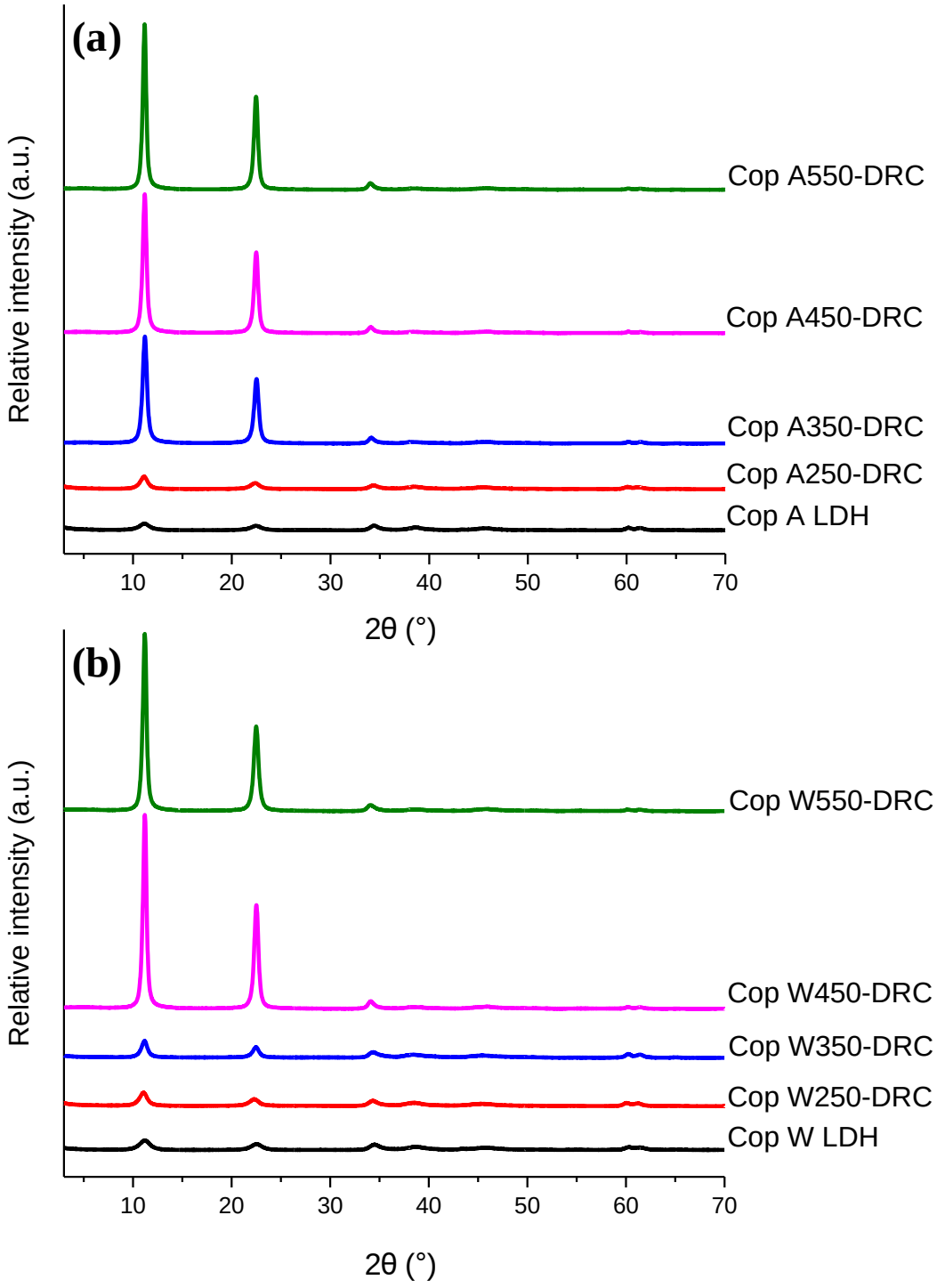


Figure 5.3. XRD patterns of co-precipitation Mg_4Al-CO_3 LDHs after reconstruction (DRC): (a) Cop A series and (b) Cop W series (Bragg reflections due to sample holder were observed at 2θ = 43-44º and 50º).

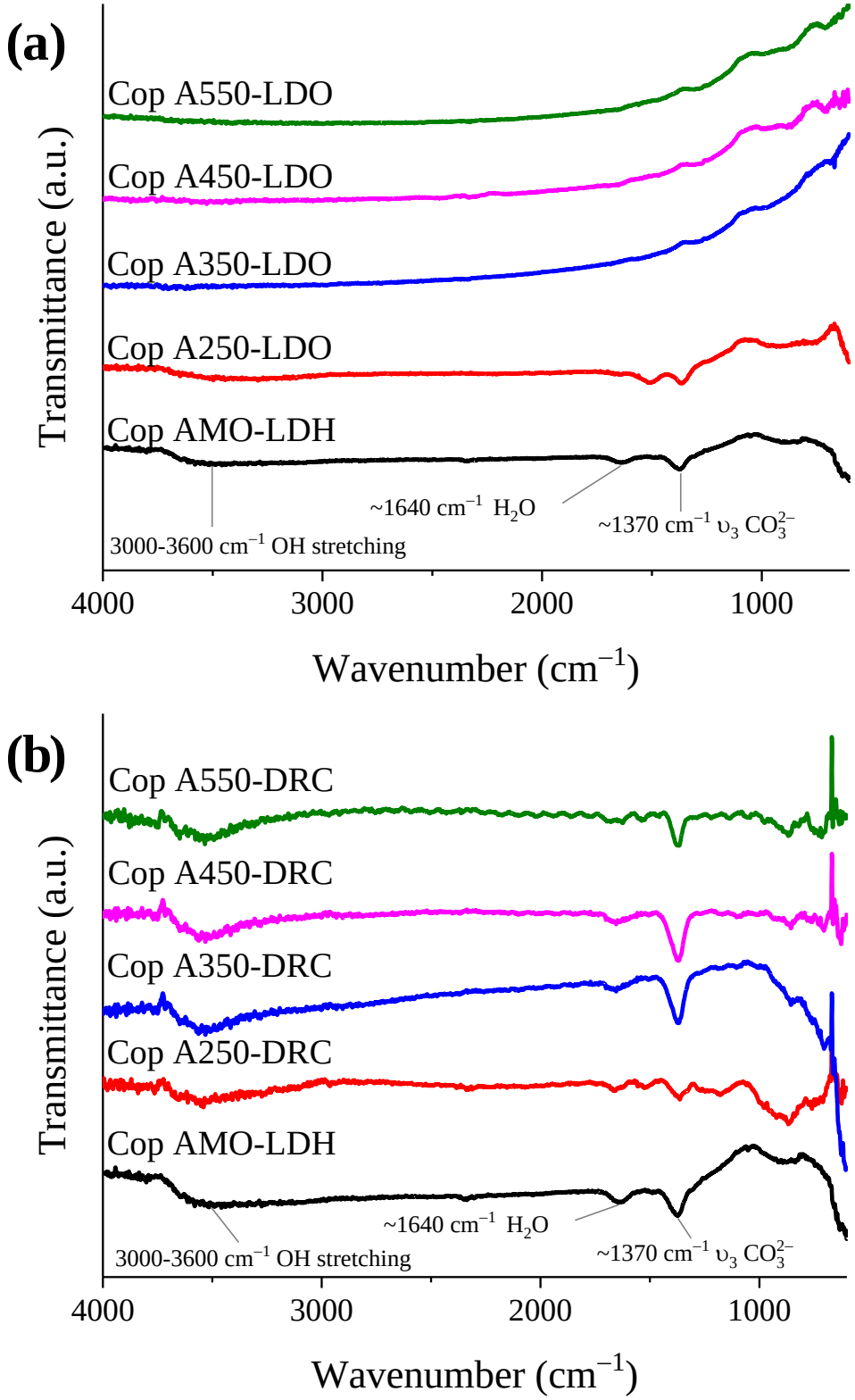


Figure 5.4. FTIR spectra of Cop AMO LDHs compared to (a) LDOs and (b) their reconstruction products (DRC).

Most LDOs show a decrease in band intensities corresponding to the vibrations of the intercalated carbonate anions, structural water molecules, and hydroxyl framework at 1370, 1640, and 3000-3600 cm^{-1}, respectively, suggesting a decreased amount of those species in the LDH structure after calcination. At 250 °C, characteristic absorption bands of both carbonate and water were observed, indicating that the layered structure was maintained, in agreement with the XRD data in Figure 5.2. It was found that 350 °C is sufficient to remove the intercalated species and water in the Cop A series, whereas the Cop W series requires a higher calcination temperature ≥ 450 °C. This may be due to the fact that Cop W LDHs have a higher water content as compared to Cop A LDHs, and therefore require higher temperatures to remove the structural water and also the intercalated carbonated anions. In the case of DRC samples (Figure 5.4 (b)), characteristic peak of carbonate anion at 1370 cm^{-1} was revealed in all DRC, confirming the presence of carbonated anions in these samples. Due to the reaction was performed in an open vessel (an oil bath heated reactor); the incorporation of carbonate anions arising from atmospheric carbon dioxide is unavoidable.

Table 5.1 shows the composition of Cop A and Cop W LDHs and their reconstruction products in water (DRC), which were calculated from inductively coupled plasma mass spectrometer (ICP-MS) and elemental analysis (EA) results (Table D3 and D4). The water content in Cop A LDH is lower than in the Cop W LDH due to the replacement of water by ethanol during the AMO treatment process. After reconstruction in water, DRC products contain a smaller amount of the carbonate anion than their parent LDHs. To balance out the positive charge of the LDH metal hydroxide layers, other anions must be co-intercalated in the layered structure. It was suggested by Carteret *et al.* that when the CO_3-MgAl LDH contacted with air, an exchange with atmospheric carbon dioxide occurred *via* a mechanism that involved both carbonate (CO_3^{2-}) and hydrogencarbonate (HCO_3^-), and the amount of the later specie increased with the Mg/Al ratio.[407] Hence, the layer charge of the reconstructed samples should be balanced by both species rather than the hydroxide anion, which was not detected by FTIR.

The reconstruction process does not significantly affect the Mg/Al ratio of the LDHs, as determined by inductively coupled plasma mass spectrometer (ICP-MS) analysis (Table D3). A small decrease in the Mg/Al ratio from 4.06 (Cop A LDH) to ~3.80 (Cop A450 DRC/Cop A550 DRC) was observed. This is an indication a slight change in the cation composition, suggesting a process of dissolution of the mixed-metal oxide and subsequent crystallisation of the LDHs.[154, 273, 408, 409, 439]

Table 5.1. Formula of LDHs before and after reconstruction in water, calculated by elemental analysis and ICP technique.

Sample	Formula of LDHs
Original Cop A LDH	$[Mg_{0.80}Al_{0.20}(OH)_2](CO_3)_{0.10}\cdot 0.245H_2O\cdot 0.215(Ethanol)$
Cop A350 DRC	$[Mg_{0.79}Al_{0.21}(OH)_2](HCO_3)_{0.05}(CO_3)_{0.08}\cdot 0.630H_2O$
Cop A450 DRC	$[Mg_{0.79}Al_{0.21}(OH)_2](HCO_3)_{0.11}(CO_3)_{0.05}\cdot 0.678H_2O$
Cop A550 DRC	$[Mg_{0.79}Al_{0.21}(OH)_2](HCO_3)_{0.09}(CO_3)_{0.06}\cdot 0.765H_2O$
Original Cop W LDH	$[Mg_{0.80}Al_{0.20}(OH)_2](CO_3)_{0.10}\cdot 0.634H_2O$
Cop W350 DRC	$[Mg_{0.79}Al_{0.21}(OH)_2](HCO_3)_{0.05}(CO_3)_{0.08}\cdot 0.603H_2O$
Cop W450 DRC	$[Mg_{0.79}Al_{0.21}(OH)_2](HCO_3)_{0.09}(CO_3)_{0.06}\cdot 0.772H_2O$
Cop W550 DRC	$[Mg_{0.79}Al_{0.21}(OH)_2](HCO_3)_{0.07}(CO_3)_{0.07}\cdot 0.716H_2O$

The N_2 adsorption and desorption isotherms of LDOs and DRCs of Cop A and Cop W series compared to their original LDHs are shown in the Appendix (Figure D3). Both pristine LDHs exhibit a type IV adsorption isotherm according to the IUPAC classification with a H3-type hysteresis loop in the desorption isotherms.[317] This is characteristic of mesoporous materials as a result of capillary condensation of slit-shaped pores created by the packing of plate-like particles. The multilayered physisorption of nitrogen takes place between the aggregates of platelet-shaped particles and confirms the lamellar structure of the materials. The calcined samples (LDOs) also exhibit type IV isotherms and H3 type hysteresis loops which correspond to the plate-like particles with slit-shape pores, similar to their parent precursors.

The surface areas were calculated by the Brunauer–Emmett–Teller (BET) method while the pore size distribution and pore volume were determined by the Brunauer-Joyner-Hallenda (BJH) method, as described in Chapter Four and Chapter Six, the results are summarised in Table 5.2. The Cop A LDH and Cop A LDOs exhibit a higher surface area and a larger pore volume than the Cop W series. In most cases, the surface areas and pore volumes of LDOs have increased with increasing calcination temperature up to a maximum of 550 °C. Auxilio *et al.* suggested that the slit-shaped pores of LDHs increased after calcination process.[440] The porous surface of the mixed oxides was previously attributed to CO_2 gas and water escaping at the surface, thus creating uniform spaced holes.[161, 441, 442] Consequently, the surface area and pore volume increase during the calcination process. This is confirmed by the pore size distribution curves in Figure 5.5 (a), (c) and D4 for LDOs of Cop A and Cop W series, which clearly indicate that at higher calcination temperatures produces wider and larger pores.

In Cop A series, significant shift of the pore size distribution to larger values occurs when the calcination temperature is increased. For initial pore size of 40 Å, pore sizes in the range 40-100 Å were obtained after calcination at 350 °C, whereas calcination at 450-550 °C resulted in pore sizes in the range 50-200 Å. In the Cop W series, an increase of pore volume of pore size 40 Å was observed at calcination temperatures between 250 and 350 °C with no peak shift. A peak shift only appeared at 450 °C, higher than the Cop A series and suggests that Cop W LDH require a higher calcination temperature to generate pores. This is due to the fact that Cop W LDH contains higher amounts of water than the Cop A LDH,[96] and therefore requires more energy to remove water and generate pores.

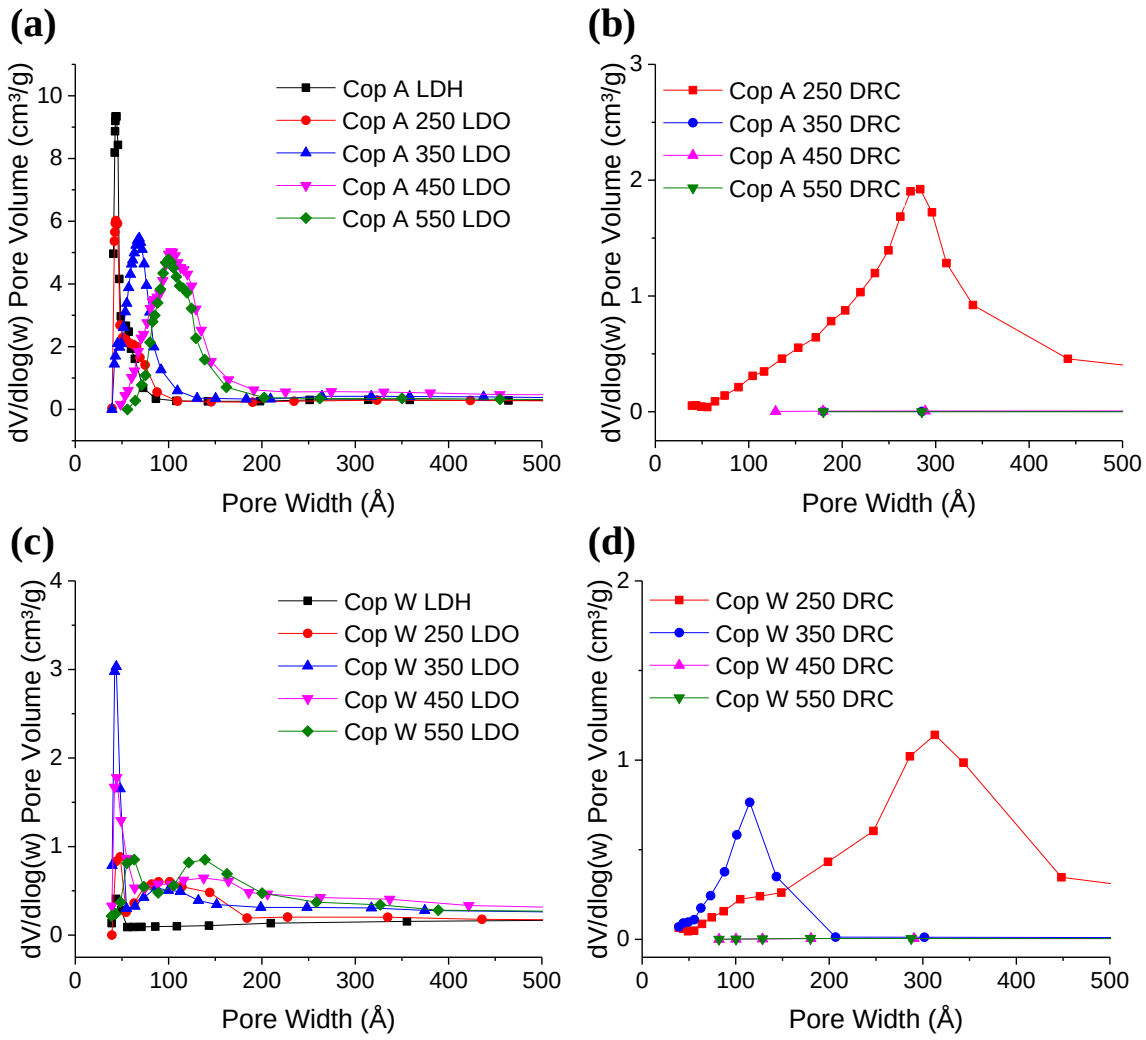


Figure 5.5. The Barrett-Joyner-Halenda (BJH) desorption pore size distributions of (a) Cop A LDOs, (b) Cop A DRC products, (c) Cop W LDOs, and (d) Cop W DRC products.

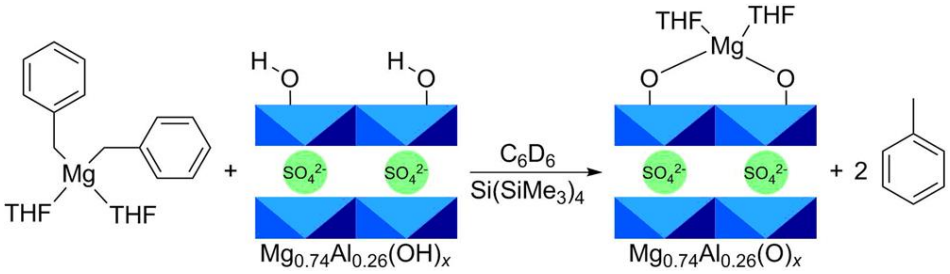
For most cases, the surface area decreases significantly after the reconstruction process, which is in good agreement with previous report.[439, 443-445] The nitrogen isotherm of type II (Figure D3), characteristic of non-porous or macroporous materials are observed in most DRC samples, which can be seen in the pore size distribution curves in Figure 5.5 (b), (d) and D4.[317, 446] The very low surface areas indicate that no micropores or mesopores are present after reconstruction in water in most cases,[439] suggesting that the original flower-like LDH morphology has been destroyed during reconstruction. In some cases like Cop A250, Cop W250 and Cop W350 DRC samples, the type IV isotherm was preserved even after reconstruction, indicating that the mesoporous structures were retained in these samples. This may be due to the formation of aggregates of the platelet-shaped particles and the lamellar morphology of LDHs, suggesting that the original morphology of LDHs was partial destroyed in those samples.

Table 5.2. The N_2 BET surface areas and total pore volumes of LDHs, LDOs, and DRC products of Cop A and Cop W series. 'n.a.' notes as the surface area is below the measurable limit.

Sample			**N_2 BET surface area (m^2/g)**	**Total pore volume (cm^3/g)***
Cop A series	LDH		267±5	0.86±0.02
	250 °C	LDO	60±1	0.77±0.02
		DRC	89±2	0.56±0.01
	350 °C	LDO	332±7	1.22±0.02
		DRC	0.1±0.0	n.a.
	450 °C	LDO	370±7	1.54±0.03
		DRC	0.4±0.0	0.01±0.00
	550 °C	LDO	244±5	1.10±0.02
		DRC	n.a.	n.a.
Cop W series	LDH		47±1	0.21±0.00
	250 °C	LDO	221±4	0.36±0.01
		DRC	63±1	0.39±0.01
	350 °C	LDO	166±3	0.54±0.01
		DRC	42±1	0.16±0.00
	450 °C	LDO	214±4	0.67±0.01
		DRC	0.5±0.0	n.a.
	550 °C	LDO	153±3	0.58±0.01
		DRC	0.5±0.0	n.a.

*Single point adsorption total pore volume of pores less than 2,283.340 Å width at p/p° = 0.991694568.

Although the effects of thermal treatment on the structural properties of LDHs are well-understood, there has been little research into the degree of dehydroxylation as a function of calcination temperature.[117, 154, 447, 448] The amount of hydroxyl groups is likely to correlate to the reconstruction or hydration process of LDHs. Recently, O'Hare *et al.* has reported a method for determining the surface hydroxyl concentration as a function of the calcination temperature by using NMR spectroscopy titration with the organometallic reagent, $Mg(CH_2Ph)_2(THF)_2$.[160, 166] In their studies, LDH powder sample was calcined over a range of temperature (100−450 °C) under a vacuum with nitrogen flow and subsequently characterised sample after taking out from the furnace. The calcined sample was titrated with the reagent, the amount of toluene produced can be measured, converted to the molar equivalents of hydroxyls per gram of solid, and finally converted to the hydroxyl number by utilising of the BET surface area analysis data (Scheme 5.3).[160]



Scheme 5.3. The determination of surface hydroxyl concentration by NMR titration method.[160]

In our studies, LDH powder sample was calcined in conventional furnace (not in an inert atmosphere). After naturally cooling down, sample was taken out and collected in a sealed container and put in the vacuum oven to prevent from the moisture and air before for further analysis. Then calcined sample was taken out for NMR titration and detail of experiment was explained in Chapter Six (section 6.1.9). It was found that the hydroxyl number decreased with increasing calcination temperature, the results are shown in in Table 5.3.[160, 162]

Table 5.3. Surface hydroxyl numbers of LDOs calcined at different temperatures.

Calcination temperature (°C)	**Hydroxyl number, α_{OH} (OH/nm^2)**	
	Cop A LDO	**Cop W LDO**
250	15.35±0.49	17.70±0.42
350	8.62±1.08	6.17±0.46
450	6.50±0.66	9.55±1.03
550	9.63±1.61	10.75±0.56

Although the surface areas and pore volumes of Cop A LDOs are larger than Cop W LDOs, the surface hydroxyl titration studies show similar results, as it is independent of the surface area.[160, 162] The hydroxyl numbers were determined from the molar equivalents of hydroxyl per gram of solid and the nitrogen BET surface area. A significant drop in the surface hydroxyl number was observed for calcination temperatures above 350 °C. This is an indication of the successful removal of water molecules, intercalated species and surface hydroxyl groups after calcination over the range of 350−550 ^{o}C, which is in good agreement with the XRD patterns of these LDOs as shown in Figure 5.2. These results also agree with previous studies in this area.[160] However, the hydroxyl number of LDOs calcined over the range of 350−550 ^{o}C varied from 6 to 10 OH/nm^2. This is likely a consequence of the samples being thermally treated in conventional furnace with no vacuum treatment. Therefore, they may have adsorbed moisture during the cooling process and storage, resulting in seemingly higher hydroxyl numbers.

Typically LDHs using the co-precipitation method followed by ageing at room temperature exhibit flower-like/rosette morphologies (due to large aggregates of LDH sheet with secondary particle size about >1 μm) and this morphology contributes to the surface area of the LDHs, which accounts for the multi layered N_2 physisorption between the aggregates of the platelets. In order to observe how the morphology of LDHs changes during the reconstruction process, LDOs from Cop A and Cop W LDHs were sonicated in water for five minutes and then casted on the TEM grid. Alternatively, toluene was used instead of water to disperse samples as a control experiment to avoid the rehydration and compare with the ones in water. The morphologies of the samples are shown in the TEM images in Figure 5.6. All samples, both in water and in toluene retained their original morphology. As previous shown in Table 5.2, pore volumes increased after calcination, which was generated by the escaping CO_2 resulting in regularly spaced craters perpendicular to the basal plane,[161, 449] these pores would favour the access of small molecules through the inner part of the particles.[161, 441] Hence, once the LDOs are put into contact with water, the rehydration process occurs simultaneously; the porous surface cannot be observed in TEM. On the other hand, the ones dispersed in toluene with a short dispersion time of 5 minutes, the rehydration process has not occurred; hence the porous surface is still retained.

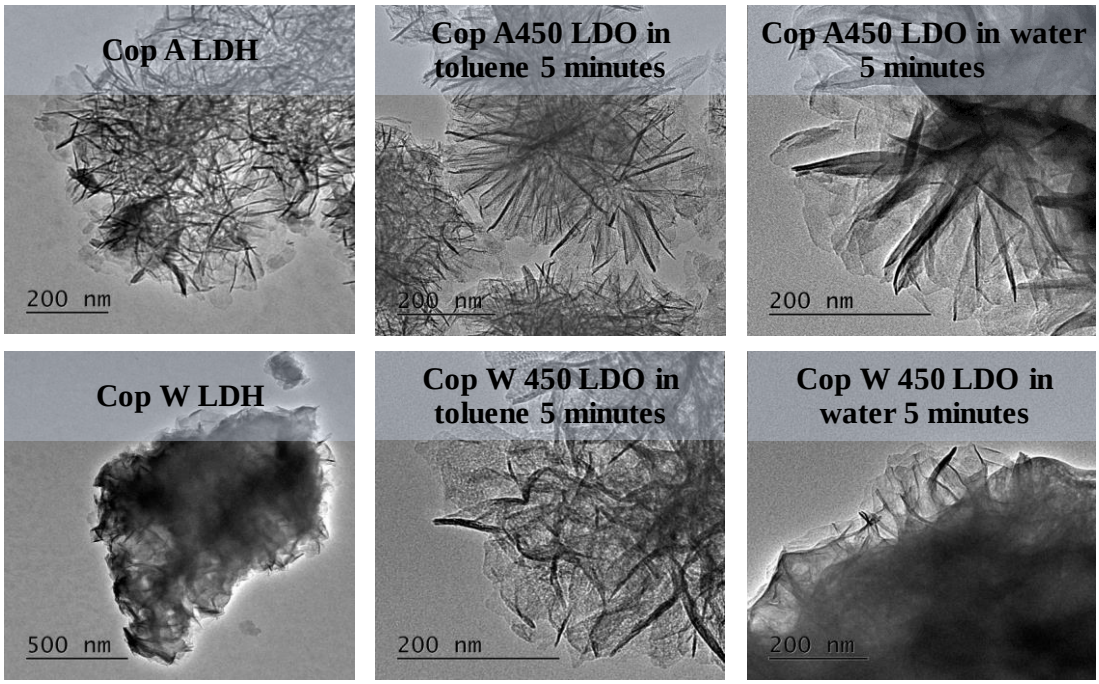


Figure 5.6. TEM images of Cop A and Cop W LDHs, their 450 LDOs after dispersed in toluene and deionised water for 5 minutes.

After prolonged reconstruction time in water for 24 hours, most products have the morphology of uniform platelets in the nanosize range, as shown in TEM images in Figure 5.7, similar to products prepared by the amino acid reconstruction described in Chapter 4. Therefore, there is a morphology change occurring during the reconstruction process, with the flower-like pristine materials transforming into nanoplatelets. The latter tend to be more aggregated after drying, resulting in a decreased total pore volume and surface area, as previously shown in Table 5.2.[442, 450, 451]

TEM was used to determine the particle sizes and size distribution of LDHs are shown in Figure 5.7 and Table 5.4. Dynamic light scattering measurement (DLS) was also performed to determine the average sizes, showing similar trend as observed from TEM but the results obtained from DLS show larger particle size due to agglomeration of particles during measurement (Table 5.4 and Figure D5). Particle size of both Cop A LDH and Cop W LDH cannot be measured by DLS due to samples settled down in the cuvette during the measurement. The platelets diameter increases with increasing calcination temperature of the LDOs used, which is in agreement with the higher peak intensities in XRD patterns, as formerly shown in Figure 5.3. Only in some cases, the rosette morphology as presented in the parent LDHs was observed. The Cop A250 and Cop W250 DRC samples present similar morphology as their original LDHs, indicating that the original structure was still retained, which may be the reason for the observed high surface area as compared to other

reconstruction products. Moreover, formation of small platelets was observed in both samples but it is more pronounced in Cop A250 DRC than Cop W250 DRC. This can be explained by the XRD data of the LDOs (Figure 5.2), at the calcination temperature of 250 °C, the layer structure of Cop A250 LDO is slightly collapsed (while the Cop W250 LDO is retained), which may favour transformation of the Cop A250 morphology during the reconstruction process.

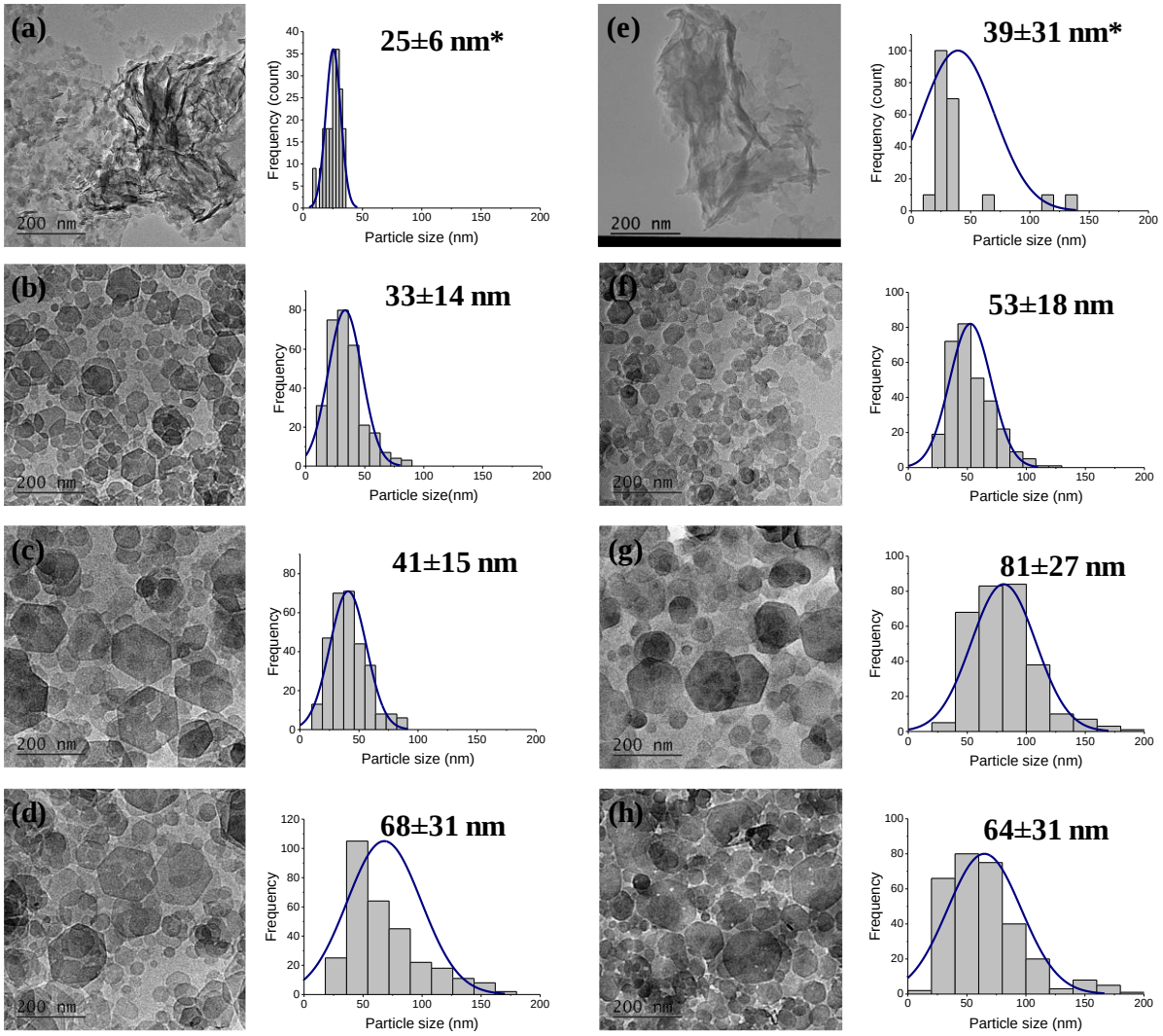


Figure 5.7. TEM images and particle size distribution curves of DRC products (the rehydrated LDH in deionised water from LDO calcined at different calcination temperature): Cop A series (a) Cop A250 DRC, (b) Cop A350 DRC, (c) Cop A450 DRC, and (d) Cop A250 DRC and Cop W series (e) Cop W250 DRC, (f) Cop W350 DRC, (g) Cop W450 DRC, and (h) Cop W550 DRC. Navy lines indicate the best fit of a Gaussian distribution, showing approximately a normal distribution. Mean values and standard deviation were obtained from measurement of 300 particles. '*' indicates that only small size particles were plotted the size distribution curves.

Table 5.4. Average particle size of LDHs after direct reconstruction (DRC) obtained from DLS data and TEM imaging. Data for the most intense peak from DLS studies was reported. The TEM images were used to determine the mean values and standard deviation by measurement of 300 particles.

Sample	Average particle size			
	from DLS		from TEM	
	Cop A series	Cop W series	Cop A series	Cop W series
Original LDH	n.a.*	n.a.*	1131±504 nm **	1230±363 nm **
250 DRC	790 nm	900 nm	25±6 nm and 1±0.5 μm	39±31 nm and 1±0.5 μm
350 DRC	110 nm	103 nm	33±14 nm	53±18 nm
450 DRC	146 nm	139 nm	41±15 nm	81±27 nm
550 DRC	129 nm	148 nm	68±31 nm	64±31 nm

*not possible to measure by DLS. **measured from the secondary particles of LDHs.

To the best of the author's knowledge, such a dramatic transformation of the LDH morphology *via* rehydration or reconstruction process has not been reported to date. Previous observations of morphology changes after the reconstruction process include irregular morphology, aggregates, rounded particles and less well-defined platelets.[273, 439, 441, 442, 449, 450] The observed textural and morphological changes can be explained with a dissolution-recrystallisation mechanism occurring during the reconstruction process.[273, 408-410, 439, 441, 451]

Based on the above findings, it can be hypothesised that the platelet-shaped LDHs can be prepared by first transforming the LDHs into LDOs, followed by the rehydration of the calcined products in water or in other aqueous solution. The removal of water from the LDH structures is likely to a crucial step in this process. As discussed in Chapter 4, water molecules play an important role in the LDH structure, by forming very strong hydrogen bonding to the hydroxyl groups and intercalated anions, leading to tightly stacked layers. Water bonds layers together, limiting the accessibility of the interlayer space to other molecules and swelling of LDHs in water or other media. The removal of water molecules from the structure weakens the hydrogen bonding network. Placing the LDOs in contact with water leads to the rapid formation of the hydrogen bonds between water molecules and surface oxides groups of the LDOs, resulting in the formation of hydroxide layers and consequently the LDHs structure.

Thermal properties of LDHs, LDOs and DRC products of Cop A and Cop W series was determined by thermogravimetric analysis (TGA), the TG and the first derivative (DTG) curves are shown in the Appendix (Figure D6). All LDHs and DRCs products exhibit the typical thermal decomposition behaviour of LDHs with three weight losses in the ranges from

30 to 800 °C, the temperature at the maximum weight loss in each step are noted as T1, T2 and T3, and present in Table 5.5.

The DTG curves show two regions, 100-200 °C and 300-400 °C, corresponding to the loss of coordinated surface and interlayer water and solvent molecules and dehydroxylation of metal hydroxide layers and decomposition of carbonate anions, respectively.[263] The Cop A LDH shows lower decomposition temperatures compared to Cop W LDH, which is consistent with the literature.[96] The difference in the decomposition temperature is the consequence of the lower water content of Cop A LDH as compared to Cop W LDH, which corresponds to a weaker inter lamellar hydrogen bonding network.

The reconstruction products can be divided into two groups. Firstly, the Cop A250 DRC, Cop W250 DRC and Cop W350 DRC, products exhibit a decomposition behaviour similar to Cop W LDH, with T2 at around 380-380 °C. This is consistent with the XRD data since they show similar XRD patterns in term of peaks intensity and symmetry. The other reconstruction products have decomposition temperatures at or above 400 °C, which is significantly higher than their original LDHs. This may be a consequence of the strong interactions between the surface hydroxyl layer and the water molecules after reconstruction.

Table 5.5. Summary of the thermal properties of original LDHs and LDHs after reconstruction (DRC).

Sample	Cop A series			Cop W series		
	T1 (°C)	**T2 (°C)**	**T3 (°C)**	**T1 (°C)**	**T2 (°C)**	**T3 (°C)**
Original LDH	79	163	357	90	162	380
250 DRC	101	174	385	102	173	384
350 DRC	105	173	421	107	184	385
450 DRC	111	175	414	112	165	408
550 DRC	117	167	414	107	162	412, 429

The zeta potentials of the LDHs, before, and after reconstruction in water were shown in Figure 5.8. In general, the zeta potential is dependent on several factors such as pH, conductivity or ionic strength, and particle dispersion. Waizumi *et al.* suggested that zeta potential depend on a particle size but the explanation is unclear.[452] An increase in the zeta potentials for 2 to 5 times was observed in reconstructed products, which may be due to a reduction of particle size and formation of stable dispersion in water after reconstruction. This may be due to more exposed surface charge over the reconstructed products.[452] In addition, the reconstructed products give zeta potential values about 40 mV indicating a good stability

of the suspension in water, which has been reported in the literature (as discussed in Chapter Four, section 4.2.1).[452] It might also contribute to the replacement of carbonate anions by water molecules and nanoplatelets formation.[401, 402] There was no difference in the zeta potential values among the samples obtained from different calcination temperature from 350-550 °C or in Cop A and Cop W series. The zeta potential of both original LDHs is much lower than that of their reconstructed products indicating the poor long-term stability and agglomeration of LDHs in water,[453] which can be observed during measurement. Both original LDHs settle down to the bottom of the cuvette during the measurement.

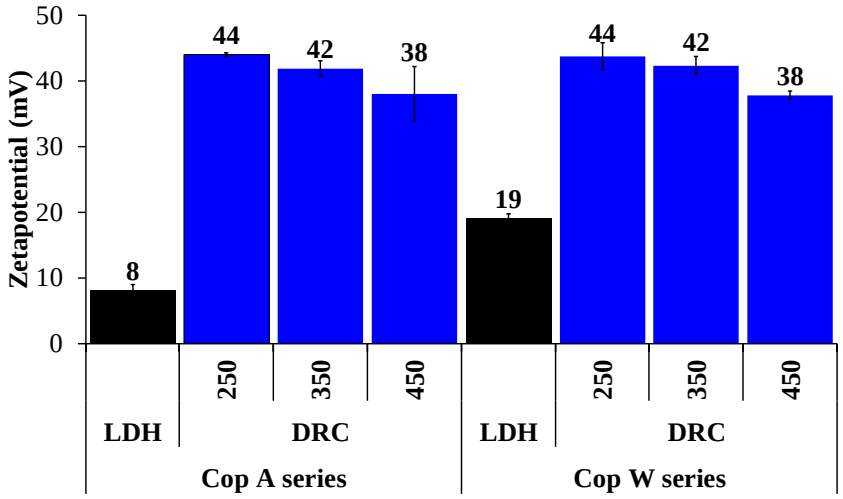


Figure 5.8. Zeta potential of LDHs (black) and DRC products (blue) of Cop A and Cop W series.

5.2.2. LDO reconstruction in non-aqueous solvents

The presence of water is vital for the LDH reconstruction and the dissolution-recrystallisation mechanism.[157, 451] In order to study the role of water in the reconstruction behaviour of LDHs, comparative studies in different solvents have been performed. The effects of six bulk solvents were used without purification as a reconstruction media instead of deionised water: ethanol, acetone, ethyl acetate, formamide, toluene and p-xylene, with their structures being shown in Figure 5.9. The LDO used in this study was Cop A450 LDO and reconstruction time was controlled at 24 hours.

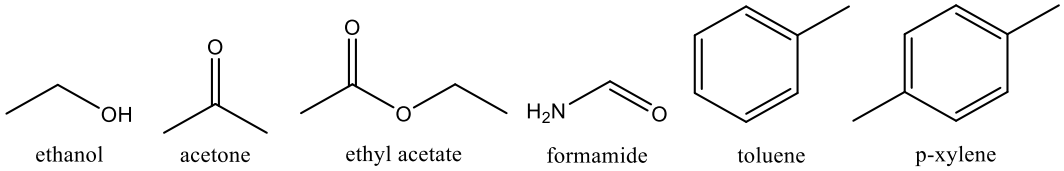


Figure 5.9. The structure of solvents used to study the role of water in the LDH reconstruction process.

Figure 5.10 shows the TEM images of products after reconstruction in different solvents for 24 hours. Apart from the product dispersed in formamide, all products are much aggregated in a manner similar to Cop W LDH. The formamide-dispersed sample gives nanosized product with a uniform size, resulting in intense and sharp peaks in the XRD pattern. The other solvents give products that show low intensity peaks indicating only partial reconstruction, which may be due to the rehydration resulting from the moisture present in the environment during the drying process and storage.

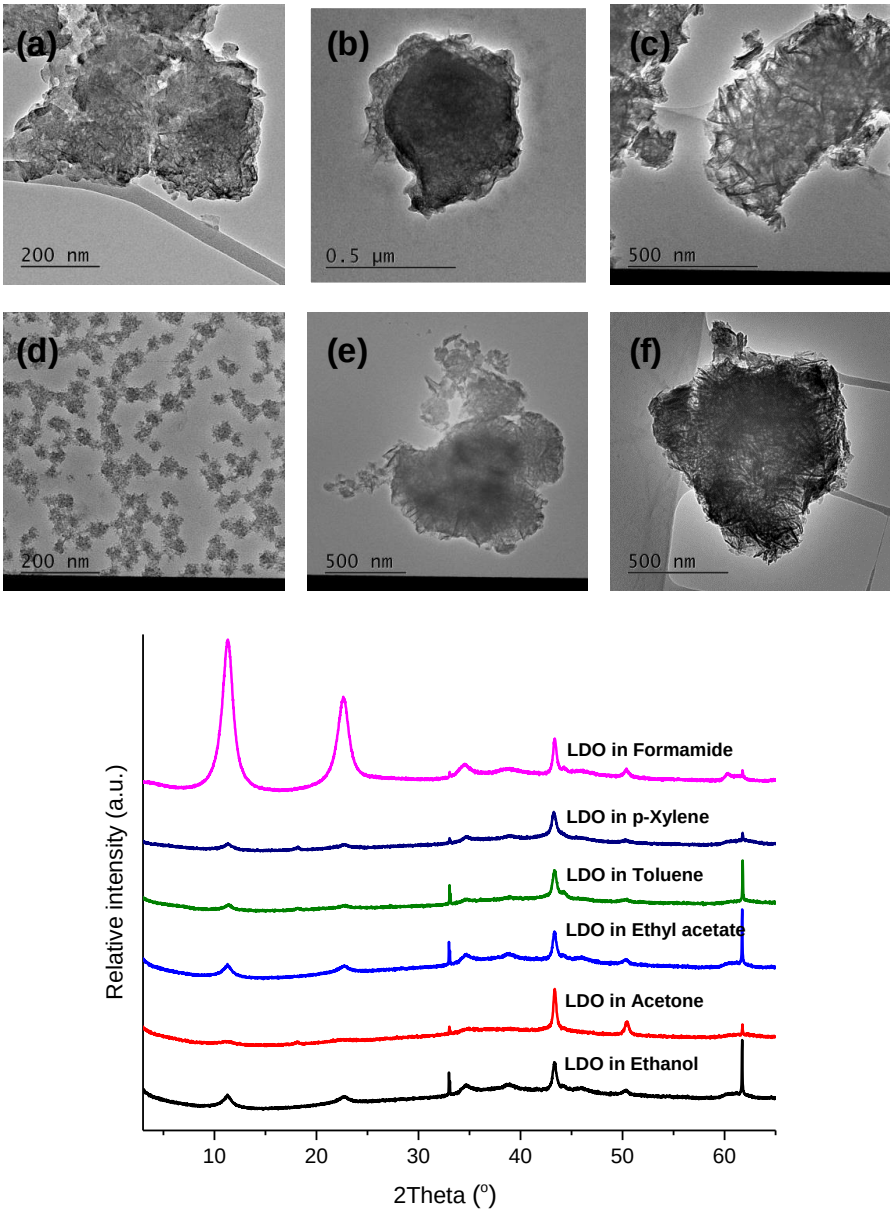
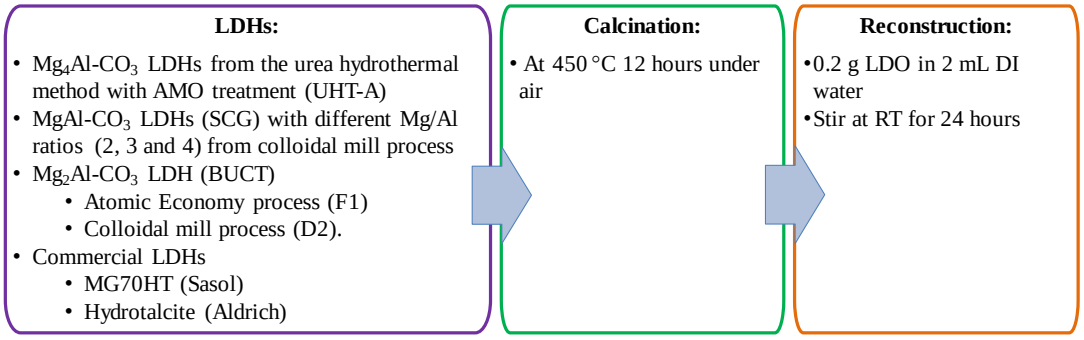


Figure 5.10. TEM images and XRD patterns of Cop A450LDO dispersed in different solvents at room temperature for 24 hours: (a) ethanol, (b) acetone, (c) ethyl acetate, (d) formamide, (e) toluene and (f) p-xylene (Bragg reflections due to the sample holder were observed at 2θ = 43-44° and 50° and reflections from the silicon wafer were located at 2θ = 33°, 62° and 69°.).

Formamide has been reported to exfoliate LDHs since it contains both a carbonyl group and an amino group which form strong interactions with the surface hydroxyl frameworks, structural water molecules and intercalated species.[310] During the reconstruction/rehydration process of LDHs, the metal oxide surface requires hydrogen bond donors to be transformed into the metal hydroxide, thus forming LDH. The amine group of formamide has the capacity to donate two hydrogen atoms (from the amine group) to the LDO surface as a hydrogen bond donor. In contrast, other solvents that have been considered in this study do not have such a strong hydrogen bond donor group as formamide, since most of them are hydrogen bond acceptors with lone pairs in their functional groups (ethanol, acetone, ethyl acetate) or with hydrogen atoms that can only participate in weak hydrogen bonding (toluene and p-xylene). Therefore, such solvents may not be useful during the rehydration of LDOs to form LDHs.

5.2.3. Effect of the LDHs morphology on the reconstruction behaviour in water

To explore the effect of LDHs morphology on the reconstruction behaviour, eight MgAl-CO_3 LDHs with different Mg/Al ratios and prepared by different synthesis methods were used, they were calcined at 450 °C for 12 hours, followed by stirring in deionised water for 24 hours under open atmosphere (without nitrogen flow), as shown in Scheme 5.4. These LDHs are Mg_4Al-CO_3 LDHs from the urea hydrothermal method with AMO washing (UHT-A), commercial LDHs [MG70HT (Sasol) and Hydrotalcite (Aldrich)], three MgAl-CO_3 LDHs with different Mg/Al ratios from a colloidal mill process provided by SCG Chemicals (Mg/Al = 2 (M2), 3 (M3), and 4 (M4)), and two Mg_2Al-CO_3 LDHs from Beijing University of Chemical Technology (BUCT) produced by Atomic Economy process[454] (F1) and colloidal mill process (D2).



Scheme 5.4. Overall process of reconstruction process in this study.

The XRD patterns of the original LDHs comparing with their DRC products are shown in the Appendix (Figure D7). The layered structure of all LDHs collapsed after calcination. The crystallinity is increased significantly after reconstruction. Only in some cases, such as Hydrotalcite Aldrich and BUCT F1 samples which are very highly crystalline LDHs, their DRC products show slightly lower crystallinity as compared to the original LDHs. The FTIR spectra in the Appendix (Figure D8) confirm that a success reconstruction of LDHs has taken place. All reconstruction products show the presence of carbonate anions with the characteristic peak at 1370 cm^{-1}. Similarly to the observation in Cop A and Cop W series, the layer charge of the reconstructed products should be balanced by both carbonate (CO_3^{2-}) and hydrogencarbonate (HCO_3^-) anions rather than the hydroxide anion, which was not detected by FTIR.[407] Table 5.6 shows the composition of LDHs and their reconstruction products in water (DRC) and no significant change in Mg/Al ratio (which were calculated from inductively coupled plasma mass spectrometer (ICP-MS) and elemental analysis (EA) results, Table D3 and D4).

Table 5.6. Formula of LDHs before and after reconstruction in deionised water, calculated by EA and ICP results.

Sample	Formula of LDHs
UHT AMO LDH	$[Mg_{0.69}Al_{0.31}(OH)_2](CO_3)_{0.15}\cdot 0.226H_2O\cdot 0.024$(Ethanol)
UHT DRC	$[Mg_{0.68}Al_{0.32}(OH)_2](HCO_3)_{0.22}(CO_3)_{0.05}\cdot 0.633H_2O$
M2 LDH	$[Mg_{0.67}Al_{0.33}(OH)_2](CO_3)_{0.16}\cdot 0.324H_2O$
M2 DRC	$[Mg_{0.67}Al_{0.33}(OH)_2](HCO_3)_{0.19}(CO_3)_{0.07}\cdot 0.659H_2O$
M3 LDH	$[Mg_{0.75}Al_{0.25}(OH)_2](CO_3)_{0.12}\cdot 0.739H_2O$
M3 DRC	$[Mg_{0.75}Al_{0.25}(OH)_2](HCO_3)_{0.17}(CO_3)_{0.04}\cdot 0.583H_2O$
M4 LDH	$[Mg_{0.79}Al_{0.21}(OH)_2](CO_3)_{0.10}\cdot 0.976H_2O$
M4 DRC	$[Mg_{0.79}Al_{0.21}(OH)_2](HCO_3)_{0.12}(CO_3)_{0.04}\cdot 0.904H_2O$

Table D2 in the Appendix shows the nitrogen BET surface area and the total pore volume of different LDHs used in this study, their LDOs and DRC products. In all cases, the surface area and pore volume increase drastically after calcination, suggesting the additional porous surface is created during calcination. This is in an agreement with the previous results as observed in Cop A and Cop W series (Table 5.2). The isotherms and pore size distribution curves in the Appendix (Figures D9 and D10) show an increased amount of mesopores and macropores in the LDOs as compared to the LDHs. However, after the DRC products have a

low surface area and have the characteristics of non-porous materials. For the DRC samples originated from Hydrotalcite, BUCT F1 and BUCT D2 LDHs still show the characteristics of mesoporous and macroporous materials.

In a manner similar to Cop A and Cop W 450LDOs, UHT LDO was selected to be dispersed in water and toluene for five minutes. Then, the dispersion was dropped onto the TEM grid and imaged, as shown in Figure 5.11. Although, the platelet shape of this LDH is preserved during calcination, a porous surface was observed in both samples dispersed in toluene and water. This suggests that the calcination process does not change the morphology of LDHs. In comparison to the Cop A and Cop W series (Figure 5.6), porous surface was not clearly seen in Cop A and Cop W products prepared in water but was still observed in UHT AMO product. This indicates that quick rehydration of LDHs originates from co-precipitation method since they have high surface area compared to UHT AMO LDH. In other words, the rehydration of UHT AMO LDH should be much slower than Cop LDHs.

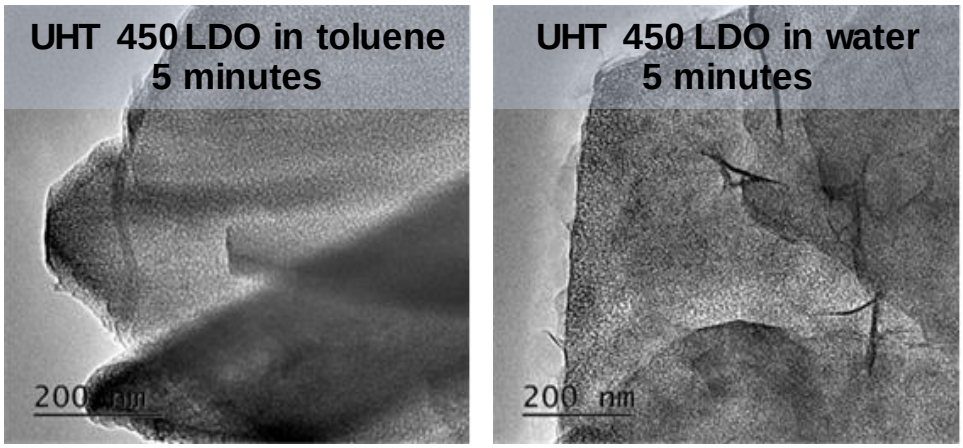


Figure 5.11. TEM images of UHT 450LDO after dispersed in toluene and deionised water for 5 minutes.

Table 5.7 and Figure 5.12 show the average particle size and the TEM images of different LDHs and their DRC products. Pristine LDHs used in this part of the investigation are platelet shaped with different particle sizes. In most cases, products after reconstruction are smaller than their pristine LDHs. This reduction of particle size is most evident in UHT LDH, where the particle size decreases from 3 microns to below 100 nm, although fragments of the broken particles from the original particle with a deposition of small particles on the surface were also observed. In some cases, donut-like morphology due to reforming of primary platelets into this secondary structure is observed in Hydrotalcite, BUCT F1 and BUCT D2 DRC products. This kind of morphology has been reported in the literature.[455-457]

Budhysuntanto *et al.*[456] prepared donut-shaped LDHs using microwave treatment and proposed the growth mechanism for this LDH by the nucleation of LDH crystal starts on the amorphous surface of magnesium oxide,[458] which provides re-entrant corners at two opposite sides,[459] which is the preferential sites for the addition of new growth units.[456] Upon the dissolution of magnesium oxide, the LDH crystal will grow laterally from both sides of the nucleation site surrounding the dissolving magnesium oxide, thus the secondary particles with donut-shaped LDHs are obtained.[456] This formation of a secondary structure during the reconstruction process may contribute to the high surface area of these products. This observation also supports the concept of dissolution-recrystallisation processes that have been proposed to occur during the reconstruction process.

Table 5.7. Average particle size of original LDHs and their products after reconstruction measured from TEM images. The TEM images were used to determine the mean values and standard deviation by measurement of 300 particles.

Original LDHs	Size of original LDHs	Size after reconstruction
UHT AMO LDH	3±1 μm	138±43 nm, 3±1 μm
M2	95±31 nm	72±32 nm
M3	89 ± 22 nm	76±40 nm
M4	51±17 nm	81±40 nm
MG70HT	217±82 nm	93±39 nm
Hydrotalcite	1.5±1 μm	126±43 nm, 672±204 nm
BUCT F1	1311±2269 nm	85±85 nm
BUCT D2	46±32 nm	41±15 nm

In order to compare the effect of morphology of the pristine LDHs, UHT AMO LDH and its LDOs, and DRC products were investigated in a TGA study, since the UHT AMO LDH was synthesised on the basis of Mg/Al ratio of 4 and same total metal concentration with the AMO treatment as in Cop A LDH. In addition, M2, M3 and M4 LDHs and their LDOs and DRC products were selected to explore the effect of Mg/Al ratios of 2, 3, and 4, respectively. Their TGA and DTG curves are shown in the Appendix (Figure D11) and summarised in Table 5.8. Most reconstruction products exhibit a slightly higher decomposition temperature than their pristine LDHs, which is in agreement with results for the LDHs from the co-precipitation method. This may refer to strong interaction between surface hydroxyl layer and water molecules after reconstruction, which can be indicated by a rigid product after drying and very low surface area.

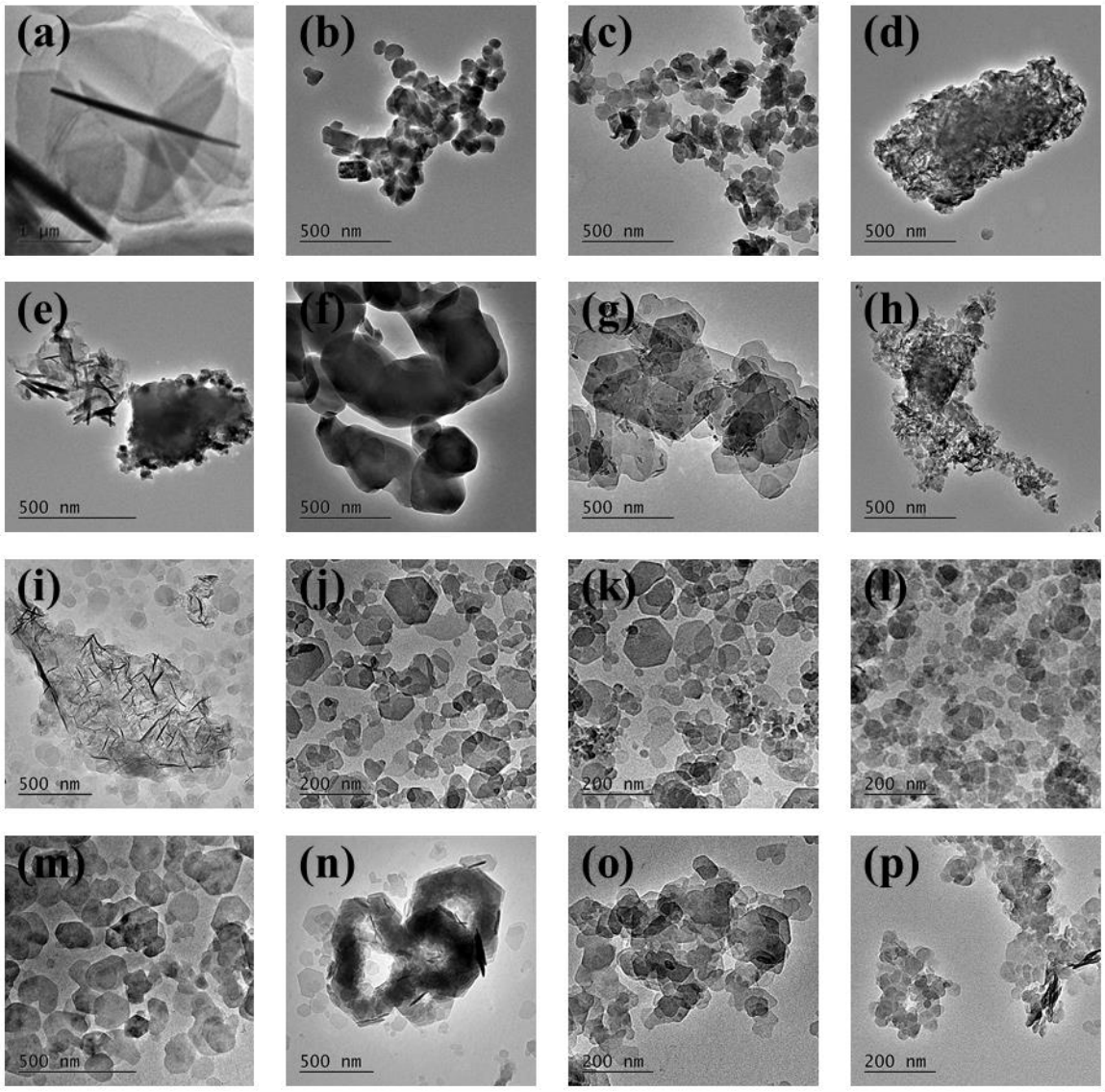


Figure 5.12. TEM images of original LDHs from different synthesis methods and sources: (a) UHT AMO LDH, LDHs from colloidal mill process (b) M2, (c) M3, (d) M4, commercial LDHs (e) MG70HT, (f) Hydrotalcite Aldrich, (g) BUCT F1 and (h) BUCT D2; and their DRC products after reconstruction in water at room temperature for 24 hours (i) UHT-DRC, (j) M2-DRC, (k) M3-DRC, (l) M4-DRC, (m) MG70HT-DRC, (n) Hydrotalcite Aldrich-DRC, (o) BUCT F1-DRC and (p) BUCT D2-DRC.

Table 5.8. Summary of the thermal properties of original LDHs and LDHs after reconstruction.

Sample	UHT AMO LDH	UHT AMO DRC	M2 LDH	M2 DRC	M3 LDH	M3 DRC	M4 LDH	M4 DRC
T1 (°C)	-	65	-	71	-	68	-	54
T2 (°C)	163, 216	203, 291	228	172, 214	207	133, 190	181	102
T3 (°C)	380	411, 434	322, 401	374	389	384, 407	383	404

All DRC products show zeta potential values > +40 mV, as present in the Appendix (Figure D12), which is much higher than for their pristine LDHs. Similarly to section 5.2.1, An increase in zeta potential of LDH after reconstruction is attributed to a reduction of particle size and formation of stable dispersion in water after reconstruction,[452] along with the replacement of carbonate anions by water molecules.[401, 402]

5.2.4. Effect of the reconstruction conditions on reconstruction behaviour in water

In order to observe changes in morphology, series of Cop A450 LDO, Cop W450 LDO and UHT 450LDO were stirred in deionised water for 5 minutes; 1, 6, 9, 18, 24, 72 hours and 1 week.

It was found that in both Cop A and Cop W samples, morphology changed from flower-like to platelets after 1 hour and particles become more uniform and larger with time, which was confirmed by TEM (Figure 5.13). Measurements of the particle size distribution have been performed by analysis TEM images (Figure 5.14) and by using dynamic light scattering method (DLS) (Figure D13 (a)). With prolonged reconstruction time for a week, particles grow larger in diameter (confirmed by TEM images, Figure 5.13) and tend to be agglomerated during the DLS measurement in both Cop A and Cop W DRC samples as can be observed in the particle size distribution curves from DLS measurement. However, the change in thickness value of particles should have been determined by Atomic force microscopy (AFM), which has not been performed in this study due to equipment-related difficulties and accessibility-related.

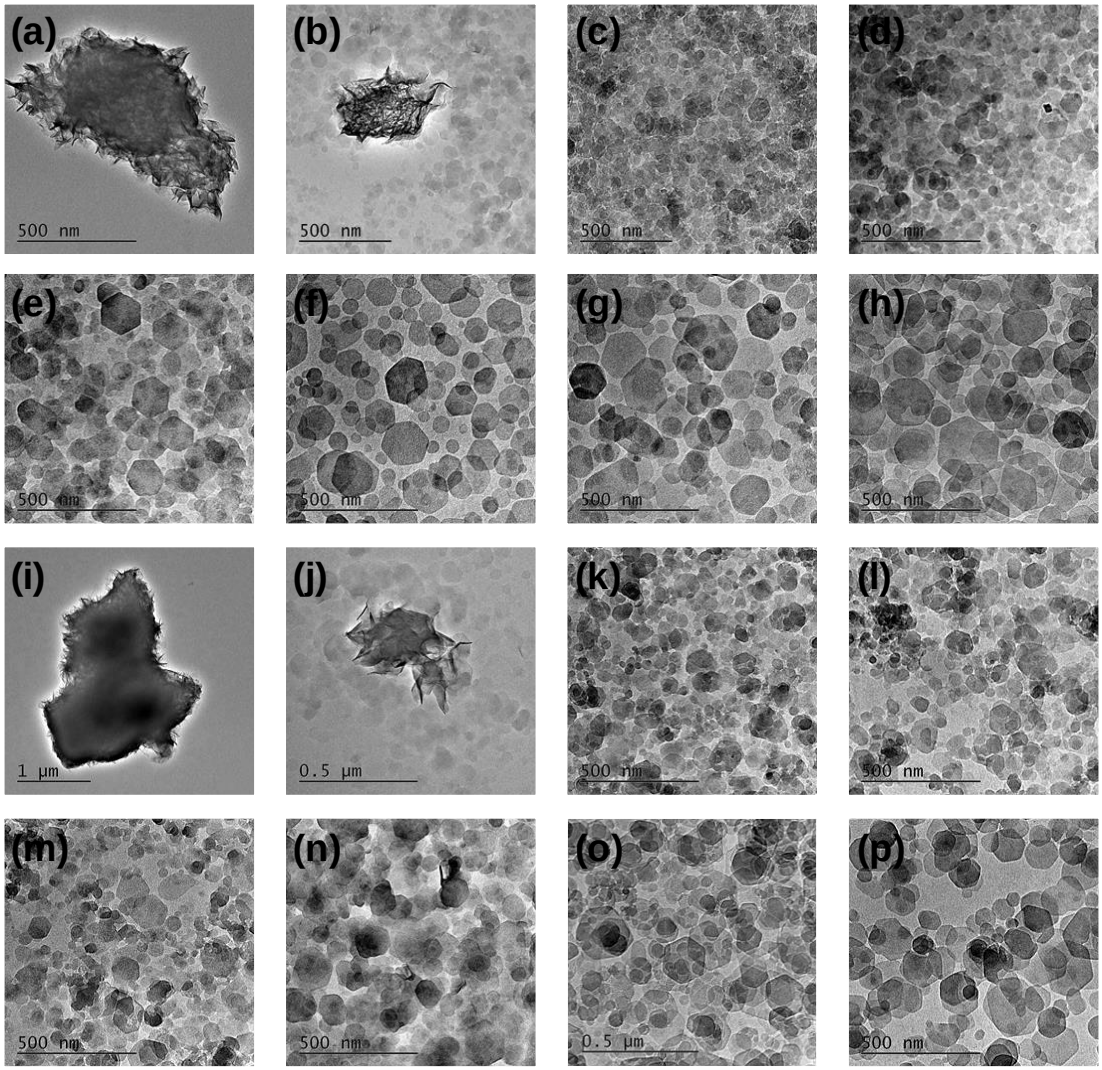


Figure 5.13. TEM images of Cop A450 DRC products at different reconstruction time in deionised water: (a) 5 minutes, (b) 1 hour, (c) 6 hours, (d) 9 hours, (e) 18 hours, (f) 24 hours, (g) 72 hours and (h) 1 week and Cop W450 DRC products at different reconstruction time in deionised water: (i) 5 minutes, (j) 1 hour, (k) 6 hours, (l) 9 hours, (m) 18 hours, (n) 24 hours, (o) 72 hours and (p) 1 week.

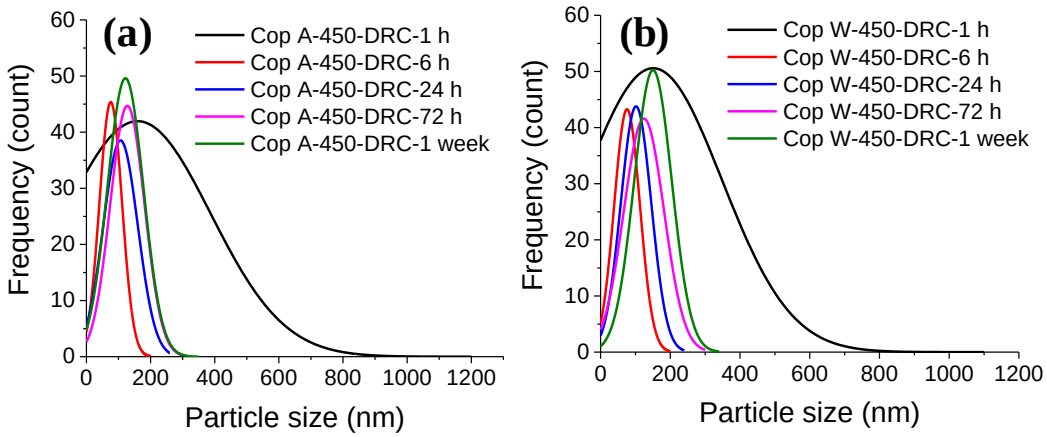


Figure 5.14. Particle size distributions (calculated from TEM images by measurement of 300 particles) of (a) Cop A450 and (b) Cop W450 DRC products at different reconstruction time in deionised water. Lines indicate the best fit of a Gaussian distribution, showing approximately a normal distribution.

The transformation of the particle morphology at different reconstruction times in deionised water can be seen from the TEM images of UHT 450 DRC in Figure 5.15. At an early stage of rehydration the surface of LDOs shows a large number of pores and small platelets that have been grown vertically on the surface of the big particles. During rehydration, the large particles start to break resulting in the formation of smaller particles. Eventually, most of the big particles disappear and at the same time the smaller particles become larger with increasing rehydration time. Ring-like or donut-like morphology was observed in sample that has been reconstructed in water for a week, which shows similar morphology as observed in the Hydrotalcite, BUCT F1 and BUCT D2 DRC products (Figure 5.12). These previous observations, together with this result may support the concept of a dissolution-recrystallisation process occurring during reconstruction of LDHs and suggest that the concept of memory effect of LDH is not true.[455-457]

It was also found that at a higher reconstruction temperature the obtained DRC product are larger platelets, which may be due to the high temperature induce the particle growth of the LDHs.[460] With high speed mixing, uniform platelets were formed within 1 hour, TEM images were shown in Appendix (Figure D14), which is time-saving and simple method for preparing nanoplatelets in water and may be useful on an industrial scale.

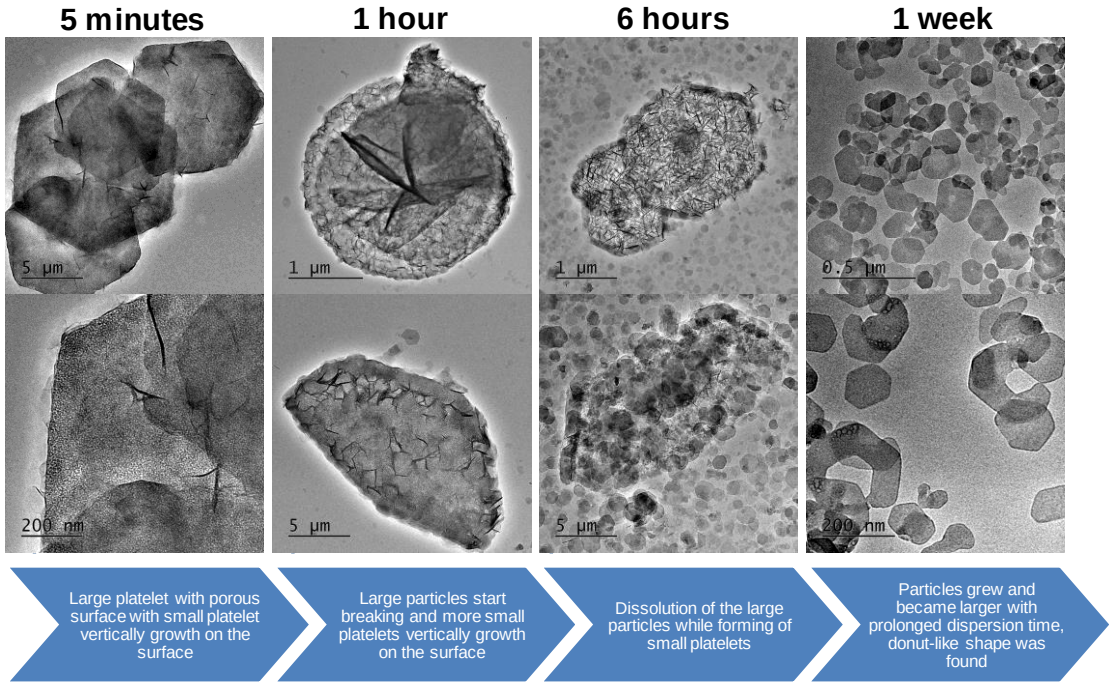


Figure 5.15. TEM images of rehydrated LDH in deionised water from UHT-AMO LDO (450 °C) at different reconstruction time.

Zeta potential studies in Figure 5.16 show a trend that is similar to what has previously been reported in the literature, where the charge of the particles increases with increasing reconstruction time, which may be due to redistribution of charge during dissolution-recrystallisation process of LDH and/or reorientation of some adsorbed carbonate species on the surface of the LDH particles.[458] This is also observed in other LDHs and these results are presented in the Appendix (Figure D15).

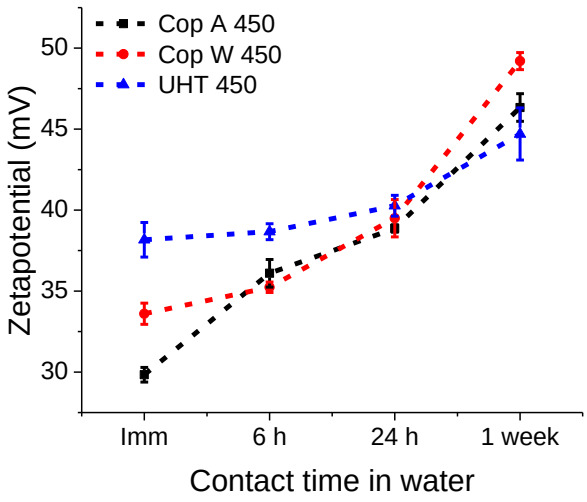


Figure 5.16. Zeta potential values of reconstruction products (Cop A450, Cop W450 and UHT 450 DRC products) in water at room temperature with varying dispersion times.

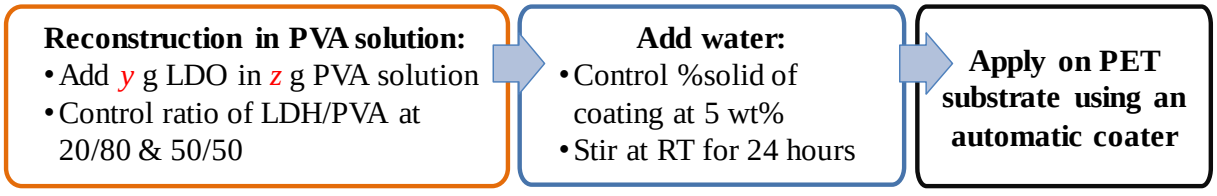
5.3. Reconstruction behaviour of LDHs in PVA

In section 5.2, it has been shown that LDHs can be reconstructed in water, forming uniform platelets after reconstruction. This section focuses on the application of this concept to a water-based or water soluble polymer.

Polyvinyl alcohol polymer (PVA) is strongly hydrophilic and water soluble. It is a biocompatible petroleum based polymer, fully biodegradable, and exhibits good film forming, high chemical resistance, as well as good adhesive and mechanical properties.[461, 462] PVA has been widely studied and applied in a wide range of industrial, commercial, medical and food applications.[463] It also has been approved for use in packaging products by the United States Department of Agriculture, USDA (i.e. packaging for meat and poultry products).[464, 465]

Recently, PVA/LDH nanocomposites have been reported to improve the properties of PVA by using several approaches such as layer-by layer (LbL) self-assembly[466, 467] and solution film-casting.[468, 469] Chen *et al.* prepared delaminated LDHs by exfoliation CoAl-NO_3 in formamide, the multilayer films were prepared by dipping the glass substrate into exfoliated dispersion of LDH, PVA solution and graphene oxide nanosheet dispersion using layer-by-layer-self-assembly process (LbLs).[466] Such approaches are time consuming and toxic (formamide is toxic) which deems them unsuitable for commercial applications especially in food packaging applications. No single step process using green chemicals has been reported to date.

In this study, a PVA solution was selected to be used as the reconstruction medium for LDOs, and the resulting coating mixture was directly applied on to the PET substrate using an automatic coater with a close wound bar. The procedure is defined as 'sequence#1' and shown in Scheme 5.5. The effect of calcination temperature was studied in Cop A and Cop W series at a calcination time of 12 hours. Furthermore, eight different LDHs were calcined at 450 °C for 12 hours before mixing with PVA aqueous solution. The ratio of LDH/PVA was either 20/80 or 50/50, and the total solid content was kept constant at 5%.



Scheme 5.5. Procedure for preparing the coating mixture- according to sequence#1.

5.3.1. Effect of calcination temperature on reconstruction behaviour in PVA

In this study, Cop A LDH and Cop W LDH were calcined over a range of temperature (250, 350, 450 and 550 °C) under air in a conventional furnace for 12 hours. After cooling down, calcined sample was added into PVA aqueous solution at certain amounts by controlling the weight ratio of LDH/PVA at 20/80 and 50/50. The total solid content of the mixture was adjusted to 5 wt% by adding deionised water. The mixtures were stirred at room temperature for 24 hours (under an open atmosphere) before further characterization and applying onto the PET substrate (Scheme 5.5 and section 6.8.4).

TEM images in Figure 5.17 show DRC products after reconstruction in PVA aqueous solution at the LDH/PVA ratio of 50/50. They exhibit behaviour similar to the DRC products reconstructed in water, which were discussed in section 5.2.1. The products show small platelet shape with high uniformity and crystallinity after calcination temperature at 350 °C as show in the XRD patterns in the Appendix (Figures D16 and D17).

The XRD patterns of PVA, LDHs and DRC products after reconstruction in PVA are shown in the Appendix (Figure D16 and D17) and the corresponding *d* spacing values are summarised in Table 5.9. Both pristine LDHs show a typical basal spacing value of MgAl-CO_3 LDHs.[470] For pure PVA, a broad feature around $2\theta = 20°$ corresponds to the (101) reflection plane of PVA in a monoclinic unit cell.[471-473]

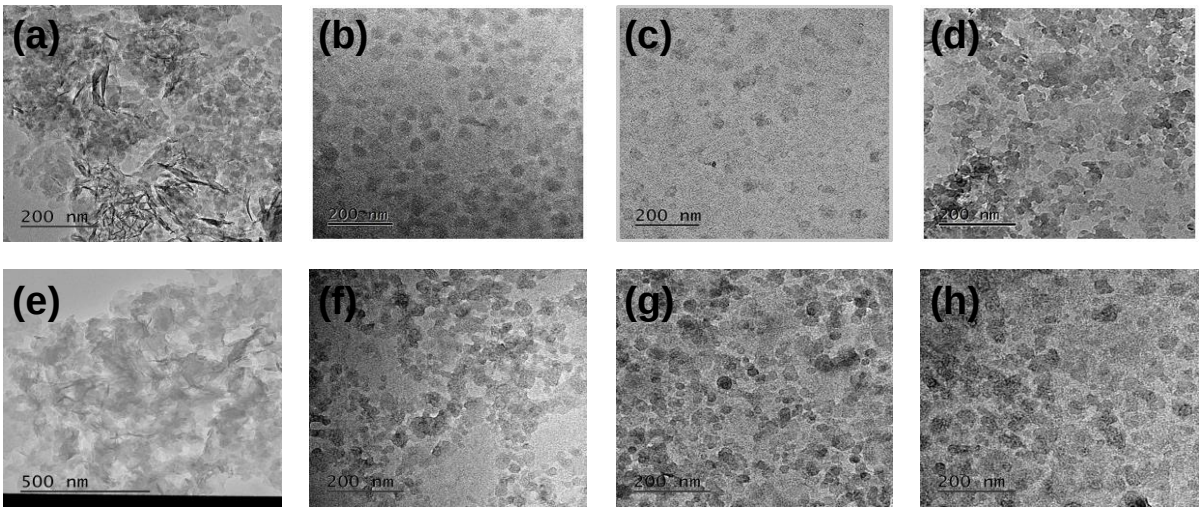


Figure 5.17. TEM of rehydrated LDH from DRC products after reconstruction in PVA Mowiol 4-88 aqueous solution (at ratio of 50/50); (a) Cop A250 DRC, (b) Cop A350 DRC, (c) Cop A450 DRC, and (d) Cop A550 DRC, (e) Cop W250 DRC, (f) Cop W350 DRC, (g) Cop W450 DRC, and (h) Cop W550 DRC.

Table 5.9. Summary of *d* spacing of LDHs and DRC products after reconstruction in PVA Mowiol 4-88.

Sample	*d* spacing (Å)	Sample	*d* spacing (Å)
Cop AMO LDH	7.91	Cop W LDH	7.84
Cop AMO LDH/PVA@5050	7.85	Cop W LDH/PVA@5050	7.84
Cop A250 DRC/PVA@2080	7.85	Cop W250 DRC/PVA@2080	7.94
Cop A350 DRC/PVA@2080	10.42, 7.76	Cop W350 DRC/PVA@2080	7.94
Cop A450 DRC/PVA@2080	11.13, 7.61	Cop W450 DRC/PVA@2080	7.66
Cop A550 DRC/PVA@2080	13.91, 7.32	Cop W550 DRC/PVA@2080	7.74
Cop A250 DRC/PVA@5050	7.96	Cop W250 DRC/PVA@5050	7.94
Cop A350 DRC/PVA@5050	7.91	Cop W350 DRC/PVA@5050	7.84
Cop A450 DRC/PVA@5050	7.91	Cop W450 DRC/PVA@5050	7.84
Cop A550 DRC/PVA@5050	7.85	Cop W550 DRC/PVA@5050	7.84

In the case of Cop A DRC series, after reconstruction of these LDOs in the PVA solution with the low amount of LDO, the position of the basal reflections shifts to a lower angle due to the expansion of the interlayer space. The basal spacing increases with increasing calcination temperature of the LDOs from 7.85 to 14 Å in Cop A250 DRC and Cop A550 DRC, respectively. This value agrees with PVA intercalated LDHs from the literature, suggesting the presence of PVA in the galleries of LDHs and a strong interaction between them.[474] However, this was not observed at higher amounts of LDO used and in all cases of Cop W DRC series, the basal space of typical MgAl-CO_3 LDHs was maintained at about 7.8-7.9 Å. This may be due to an insufficient amount of polymer being present to expand the interlayer region of LDHs when a high loading of LDO is used. Since Cop W LDHs contains larger amount of water in their structure (Table 5.1), more energy is required to remove water or even carbonate anions from the structure than for the Cop AMO LDHs. Hence, the attraction force between layers and water molecules is stronger, which hinders the exfoliation of LDHs even at low loading levels.

Comparison of the FTIR spectra of Cop A DRC products reconstructed in PVA, pristine Cop A LDH and PVA are shown in the Appendix (Figure D18). The Cop A LDH shows characteristic bands of carbonate containing LDHs. The broad bands around 3000-3600 cm^{-1} and bands at 1640 and 1370 cm^{-1} correspond to the O-H stretching vibration of the metal hydroxide layer and interlayer water, bending vibration of interlayer water and carbonate anion, respectively. The FTIR spectrum of PVA shows a broad band around 3000-3600 cm^{-1} in a similar region as in LDHs, which can be attributed to the hydroxyl groups and adsorbed water in PVA. In fact, PVA are synthetic polymers prepared from the hydrolysis, or partial

hydrolysis, of polyvinyl acetate.[465] The bands observed at 2942 and 1420 cm^{-1} are the stretching vibration of –CH and CH_2 groups and of the vibration of CH_2 bonds in PVA molecules. The carbonyl functional groups of residual acetate groups in PVA were detected at 1715 cm^{-1}.[474, 475] The spectrum for all direct reconstruction products shows characteristic bands of both LDHs and PVA, confirming the presence of both materials in the product.

5.3.2. Effect of the LDHs morphology on reconstruction behaviour in PVA

The reconstruction product from both Cop A and Cop W series in PVA solution exhibit nanoplatelets morphology. However, aggregated particles are still observed after reconstruction of other LDHs (such as in UHT, MG70HT, and Hydrotalcite Aldrich) in PVA solution as shown in Figure 5.18. This indicates that PVA molecules disturb the reconstruction behaviour and the growth of LDHs in this polymer. It has been previously discussed in Chapter 4 (section 4.4.1) that the aggregation of particles leads to an open structure of the coating layer and finally decreases the barrier performance of the coated film. Therefore, the non-uniform particles obtained after reconstruction in PVA from those LDHs are not suitable for barrier coating.

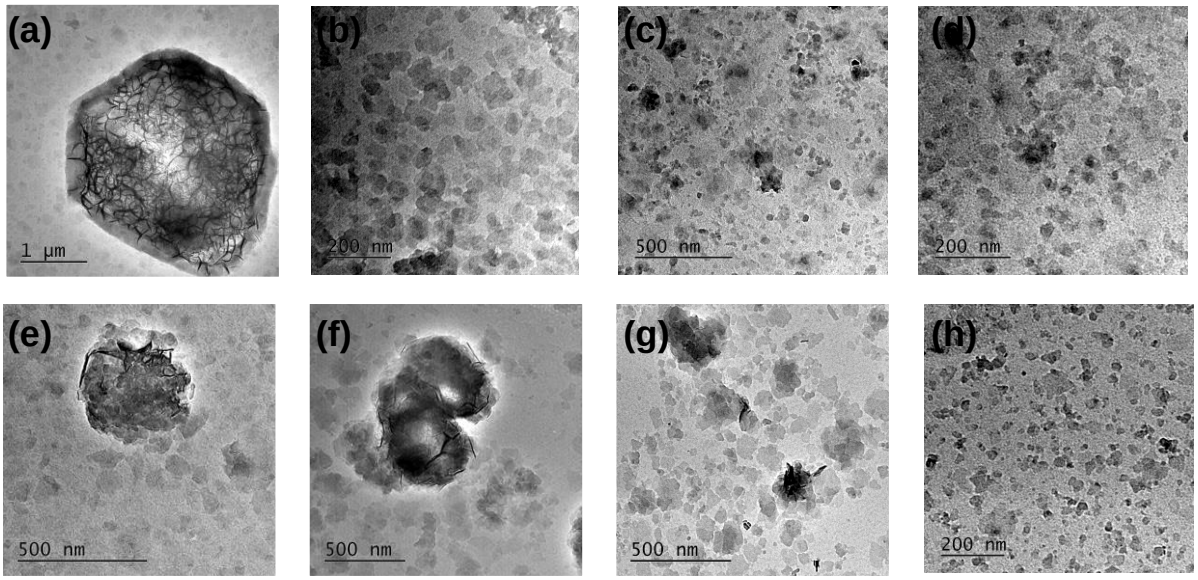
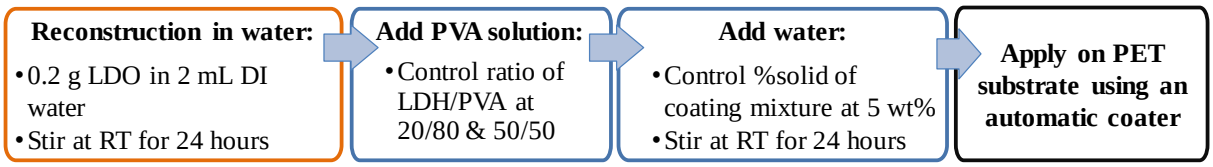


Figure 5.18. TEM images of DRC products after reconstruction in PVA Mowiol 4-88 aqueous solution (at LDH/PVA ratio of 50/50); (a) UHT DRC, (b) M2 DRC, (c) M3 DRC, (d) M4 DRC, (e) MG70HT DRC, (f) Hydrotalcite Aldrich DRC, (g) BUCT F1 DRC and (h) BUCT D2 DRC.

This problem can be avoided by using an alternative preparation sequence shown in Scheme 5.6, where LDOs are first dispersed in water, followed by the addition of PVA into the mixture at a controlled amount and defined as ‘sequence#2’.



Scheme 5.6. Procedure for preparing the coating mixture-according to sequence#2.

Figure 5.19 (a) and (b) show TEM images of Cop A350 and Cop A450 DRC after reconstruction using sequence#2, which exhibit uniform and larger particle product compared to the product from sequence#1 as presented in Figure 5.17 (b) and (c). Their XRD patterns are shown in Figure D19.

This approach was performed in other LDHs, as compared to their DRC products from sequence#1 (Figure 5.18). The TEM images of the DRC products obtained from sequence#2 as shown in the Appendix (Figure D20) and show uniform platelet particles with no observation of the original morphology of their pristine LDHs (as observed in sequence#1). As a result, XRD patterns of DRC products from sequence#2 show higher peak intensity than the sequence#1 (Figure D21).

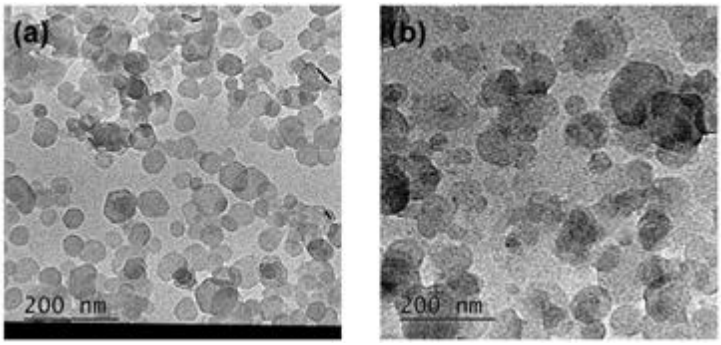


Figure 5.19. TEM images of DRC products prepared using sequece#2 (in PVA Mowiol 4-88 at LDH/PVA ratio of 50/50): (a) Cop A350 DRC and (b) Cop A450 DRC.

5.3.3. Effect of PVA properties on reconstruction behaviour

Since PVA polymers are prepared from the hydrolysis, or partial hydrolysis, of polyvinyl acetate,[465] they are generally classified into two groups, partially hydrolysed and fully hydrolysed. Different molecular weights of PVA (20,000−400,000) and degree of hydrolysis (% hydrolysis) can be obtained by varying the length of the initial vinyl acetate polymer and the hydrolysis condition (under basic or acidic conditions).[465] Results in section 5.3.2 indicate that PVA molecules disturb the reconstruction behaviour and the growth of LDHs. In order to confirm the effect of PVA molecules on the reconstruction behaviour of LDH, six PVAs with different molecular weights and % hydrolysis were compared in this section. PVA polymers used in this study were purchased from Sigma Aldrich and used without purification

(Mowiol 4-98, Mowiol 10-98, Mowiol 20-98, Mowiol 4-88, Mowiol 8-88, and Mowiol 18-88). Properties of the different PVA are shown in Table 5.10. They were used as a reconstruction medium for the Cop A450 LDO (Cop A LDH calcined at 450 °C for 12 hours) at room temperature for 24 hours. The LDH/PVA dry weight ratios were either controlled at 20/80 or 50/50 and the sequence#1 and #2 were also compared.

Table 5.10. PVA properties used in this study.

PVA	**4-98**	**10-98**	**20-98**	**4-88**	**8-88**	**18-88**
M_w (g/mol)	27,000	61,000	125,000	31,000	67,000	130,000
% Hydrolysis	98.0-98.8	98.0-98.8	98.0-98.8	86.7-88.7	86.7-88.7	86.7-88.7

It can clearly be seen from TEM images in Figure 5.20 that PVA molecules have a significant effect on the reconstruction behaviour of LDHs, especially in fully hydrolysed or high molecular weight PVA. Fully hydrolysed PVA have many OH groups on the PVA chain, which may disturb the re-arrangement/ orientation of LDH particles during the reconstruction process. The large PVA (either partial or fully hydrolysed) disturb the growth of LDH particles because the PVA chains are entangled, resulting in aggregated particles. Hence, the coating mixtures prepared by using the DRC products reconstructed directly in fully hydrolysed or large size PVAs may not suitable for using in the barrier coating application due to aggregation of LDH particles.

In similar manner to the effect of LDH morphology, the uniform particles without aggregation of LDHs were obtained once the sequence#2 was performed, TEM images in Figure 5.20. With the sequence#2, all DRC products show uniform platelets regardless of PVA properties. This observation can widen the application of this process in other water soluble or water-based polymers.

XRD patterns of the reconstructed Cop A450 DRC products in different PVA solutions and different adding sequences are shown in the Appendix (Figures D22 and D23). No peak shift was observed in most samples even at the DRC content in PVA solutions (at LDH/PVA ratio of 20/80). Basal spacing expansion of the reconstructed product was found only in the sample reconstructed in PVA Mowiol 4-88, which is a partially hydrolysed and low molecular weight PVA (the smallest PVA used in this study). In Mowiol 4-98, on the other hand, which has a similar molecular weight to the Mowiol 4-88, but is a fully hydrolysed, an increase of interlayer space was not observed. This may explain the effect of PVA on the interaction with

the LDHs during reconstruction process. The DRC products from adding sequence#2 show higher peak intensity than products from sequence#1 but no peak shift is observed in all cases.

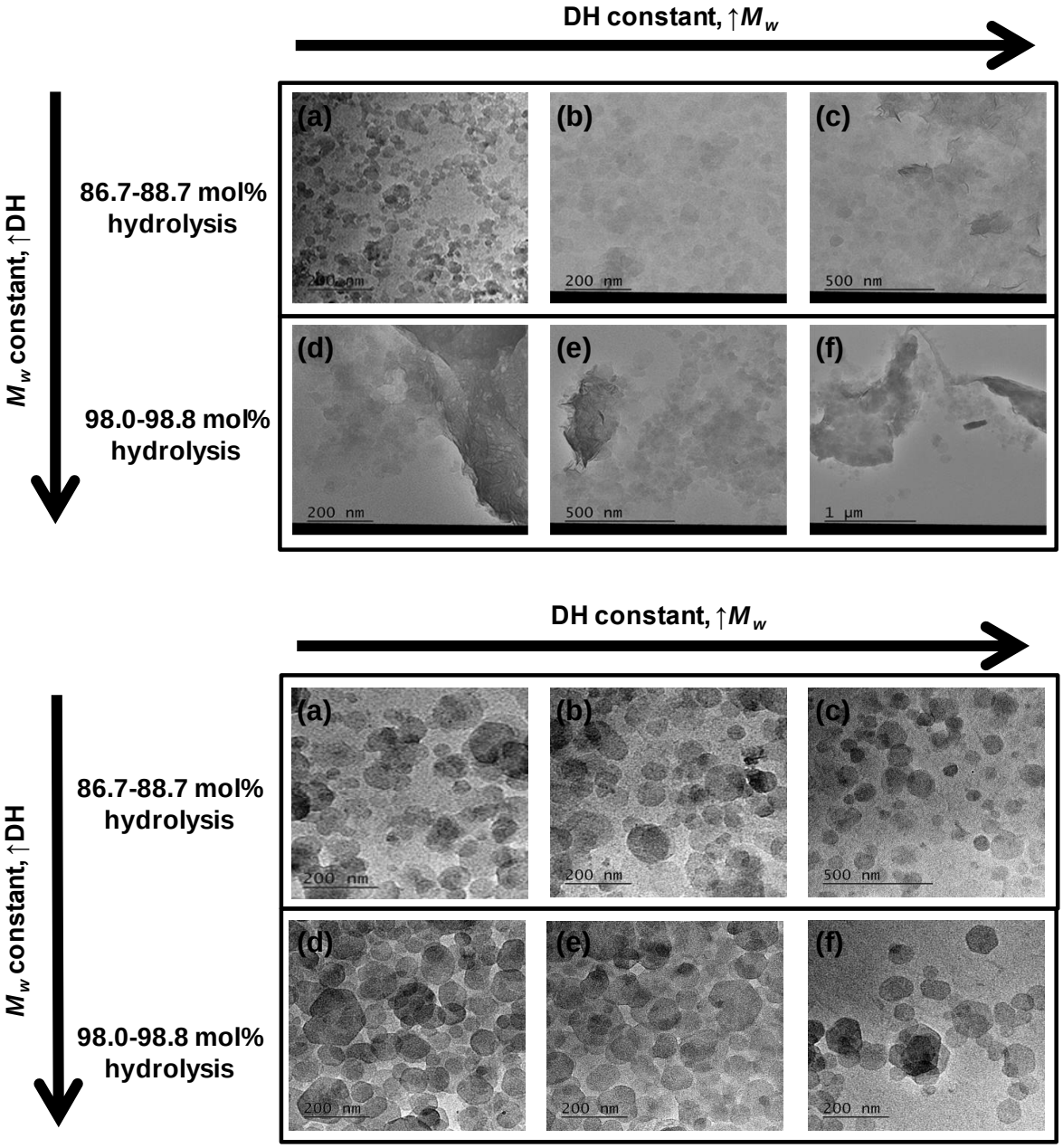


Figure 5.20. TEM images of Cop A450 DRC products in different PVA aqueous solutions (at LDH/PVA ratio of 50/50): (top) sequence#1 and (bottom) sequence#2: (a) Mowiol 4-88, (b) Mowiol 8-88, (c) Mowiol 18-88, (d) Mowiol 4-98, (e) Mowiol 10-98, and (f) Mowiol 20-98.

5.4. Barrier performance of coatings with direct reconstructed LDHs

To examine the performance of nanoplatelets produced from reconstructed product on barrier and optical properties of the coated films, coating mixture prepared from sequence#1 and sequence#2 in PVA Mowiol 4-88 were used for application on the PET substrate. Figure 5.21 shows FTIR spectra of the coated films, in which characteristic peaks of PET with additional peaks from PVA appeared and no LDH peaks were detected, which may be due to thin coating layer and low loading amount of LDHs used.

The oxygen transmission rate (OTR) values of coated films using reconstructed LDHs in PVA at room temperature and at 80 °C (following sequence#1) are shown in the Appendix (Figure D24). OTR values decrease significantly after coating with the Cop A450 DRC that has been directly reconstructed in PVA. No effect of the temperature during the coating mixture preparation on OTR values of coated films was observed.

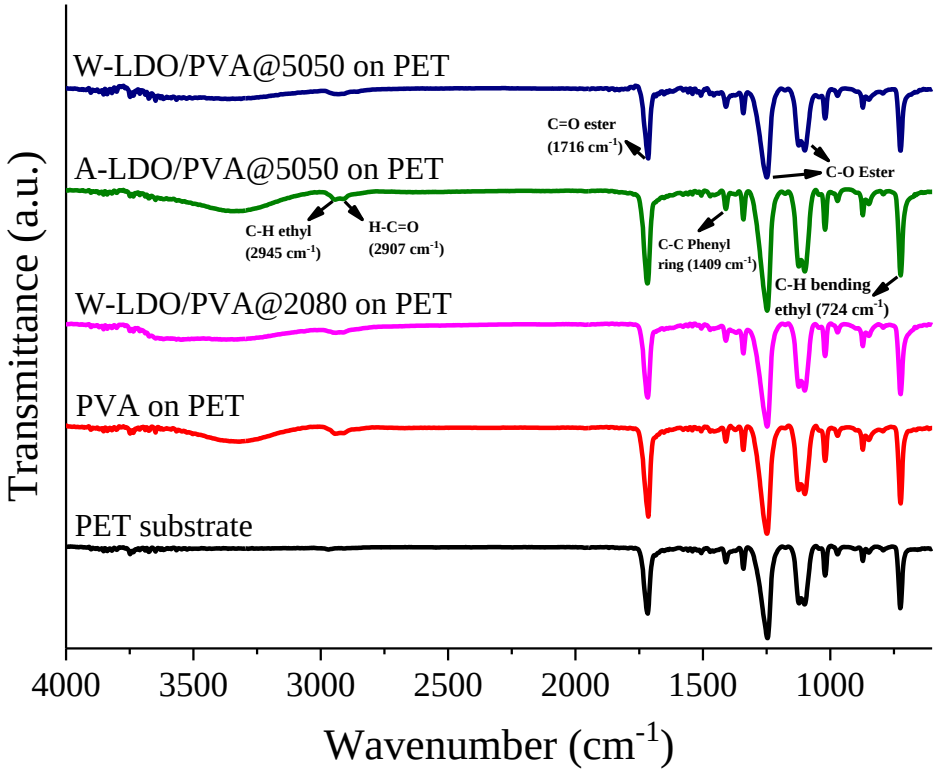


Figure 5.21. FTIR of the coated films.

5.4.1. Effect of LDH morphology

Cop A450 LDO and UHT 450 LDO were compared when preparing the coating mixture in order to study the effect of the original LDH morphology on their reconstruction behaviour in the PVA solution (following sequence#1). Coated films from these two LDHs with different loadings in PVA at 20/80 and 50/50 were compared. The coated film using the Cop A450 DRC reconstructed in PVA gives lower OTR values than the UHT 450 DRC (Figure 5.22). The loading effect was observed in coated films with the UHT 450 DRC, where the lower OTR value was obtained for the lower DRC content.

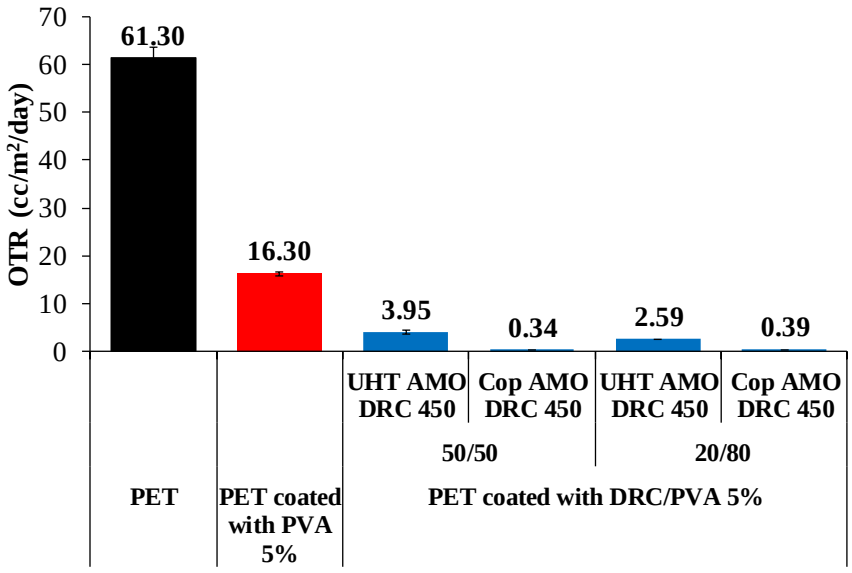


Figure 5.22. Oxygen transmission rate of coated film with DRC/PVA coating mixture: Cop-A450 DRC vs UHT-A450 DRC.

Overall, the transmittance of all coated films remains similar to that of the PET substrate. However, haze and clarity values of the coated films are affected by loading levels and LDH morphology. As previously discussed in Chapter 4 (section 4.4.1), haze values of coated film depend on the particle size of the inorganic material used; the larger particle size and high loading lead to high haze value of the coated film.[429] In addition, the broad particle size of particles leads to low clarity value of the coated film.[431] Therefore, higher haze and lower clarity values of the coated films are obtained using UHT 450 DRC or high DRC loadings in the coating mixture (Figure 5.23).

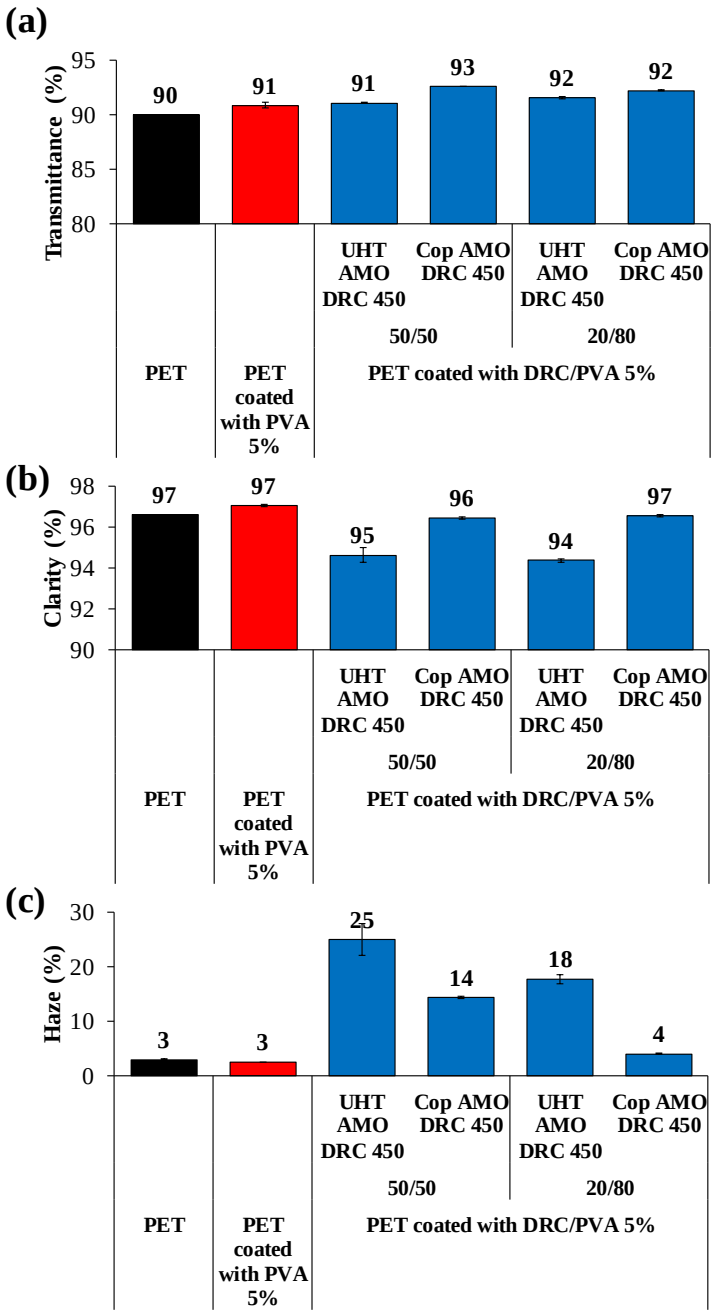


Figure 5.23. Optical properties of coated film with DRC/PVA coating mixture following sequence#1: Cop A450 DRC and UHT 450 DRC: (a) transmittance, (b) clarity and (c) haze.

5.4.2. Effect of calcination temperature on reconstruction behaviour in PVA

In section 5.2.1, it was found that calcination temperature has an impact on the reconstruction behaviour and morphology of LDHs. Hence, the effect of the calcination temperature on the LDH coating and barrier performance was explored.

Figure 5.24 shows that the calcination temperature required to produce low OTR value for Cop A series is 350 °C (0.12 $cc \cdot m^{-2} \cdot day^{-1}$) whereas Cop W series requires a higher calcination temperature of 450 °C to produce low OTR value of the coated film

(0.11 cc·m^{-2}·day^{-1}). No significant different in the OTR values was observed in coated films with the DRC from different calcination temperature. To be noted, the coated films with Cop W250 DRC exhibits bad coating coverage with very high OTR values >100 cc·m^{-2}·day^{-1} (not shown).

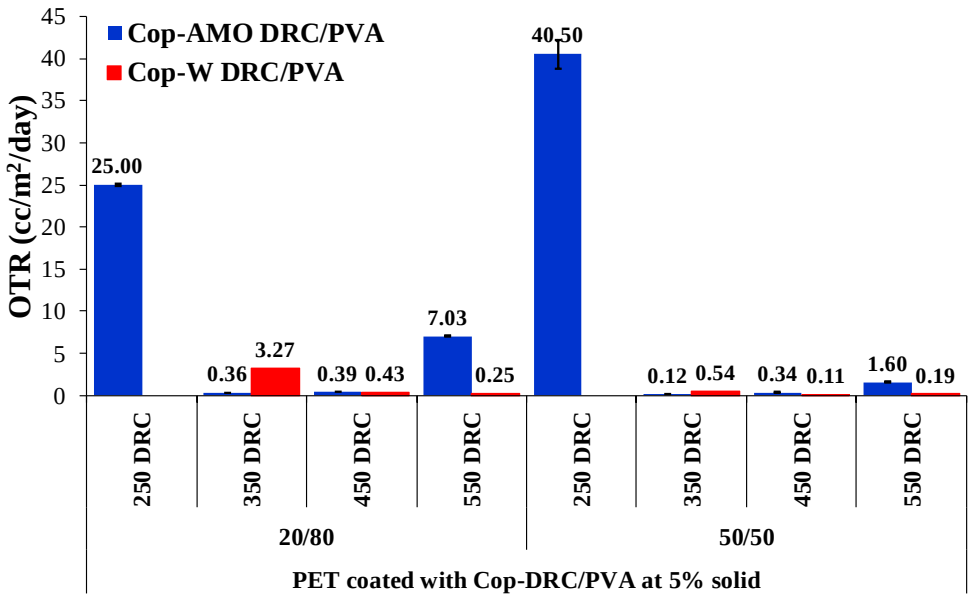


Figure 5.24. Oxygen transmission rate values of coated films.

Figure 5.25 shows cross-section SEM images of the coated films with Cop A450 and Cop W450 DRC with PVA (at the LDH/PVA ratio of 50/50). It is difficult to observe the coating layer in the SEM images. Therefore, the coating thickness for all coated films are assumed to be similar by controlling the solid content of the coating dispersion, rod/bar size and the coating speed used for all samples. Coating mixtures prepared from Cop A250 and Cop W250 give more opaque film with high haze and low clarity values compared to other samples (Figures D25 and D26).

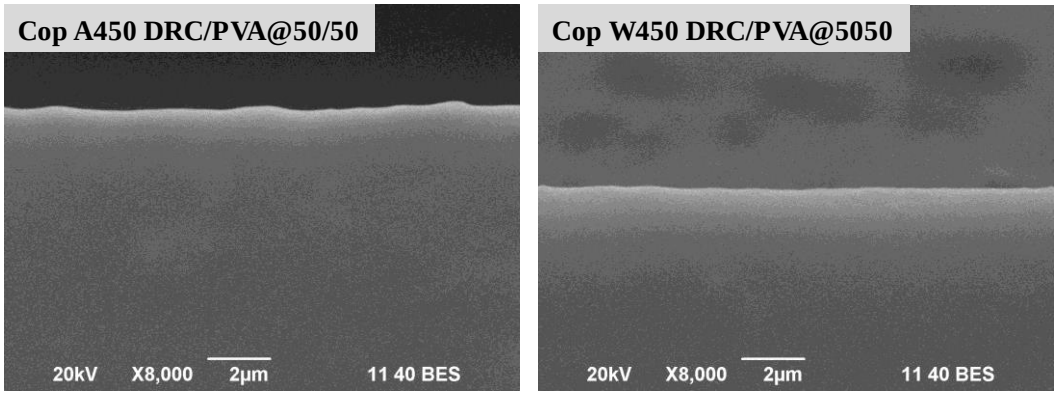
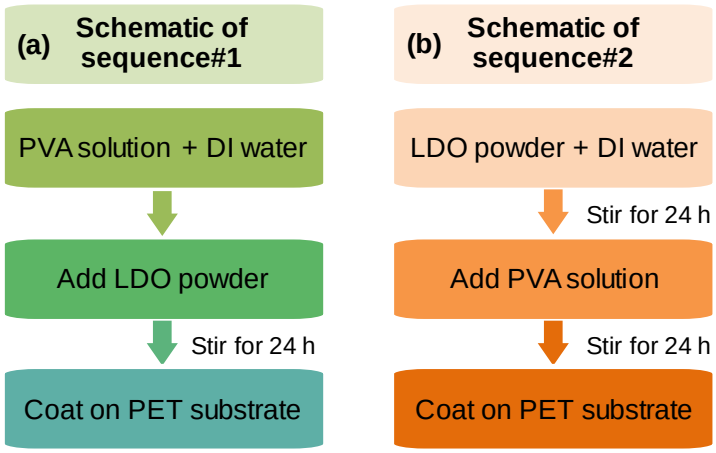


Figure 5.25. Cross sectional SEM of coated films with the coatings with Cop A450 and Cop W450 DRC in PVA at the ratio of 50/50 at 5% solid content.

5.4.3. Effect of adding sequence

The schematic of sequence#1 and #2 are compared in Scheme 5.7. The effect of the adding sequence for coating mixture preparation has been investigated by measuring the OTR values of the as produced coated film, as shown in Figure 5.26. The sequence#1, Scheme 5.7 (a), the OTR of coated films slightly increase with increasing calcination temperature of the Cop A LDOs used while the inverse results are observed with sequence#2. The possible explanation may be due to the reconstruction behaviour of those LDOs in different mediums (water or PVA solution).



Scheme 5.7. Summary the schematic of (a) sequence#1 and (b) sequence#2.

It is well-known that a higher calcination temperature, longer reconstruction time is required to recover the structure.[156] In sequence#1, the reconstruction process occurs directly in PVA solution (composes of PVA and water molecules). The Cop A350 LDO is quickly rehydrated, transformed into nanoplatelets which are stabilised by the PVA molecules, resulting in uniform particles and a low OTR value of the coated film of 0.12 $cc \cdot m^{-2} \cdot day^{-1}$. On the other hand, the reconstruction process of Cop A550 LDO takes longer time to recover the structure, along with the interference from the PVA molecules, which may somehow disturb the morphology transformation and reconstruction behaviour, finally resulting in higher in OTR value of 1.60 $cc \cdot m^{-2} \cdot day^{-1}$.

In sequence#2, Scheme 5.7 (b), all LDOs are firstly rehydrated in water forming uniformed platelets then mixed with the PVA solution; hence, the interference from PVA on the reconstruction process of the LDOs is avoided. As a result, a significant decrease in OTR values was observed in the Cop A550 DRC with the value of 0.12 $cc \cdot m^{-2} \cdot day^{-1}$. However, an increase of the OTR value in the Cop A350 DRC with the sequence#2 is still unclear.

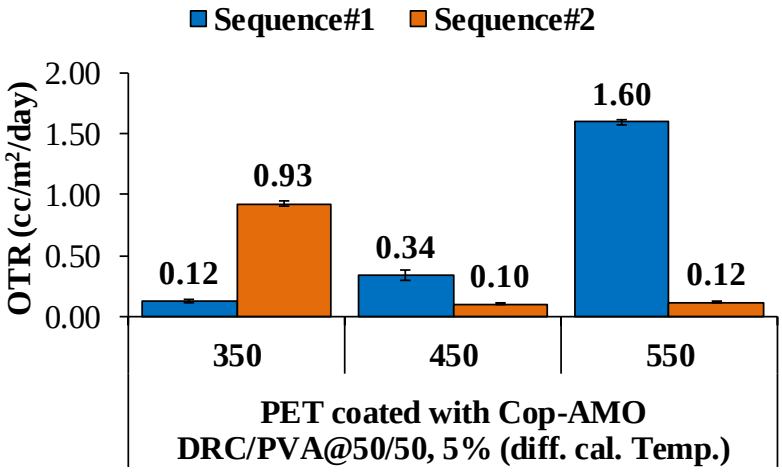
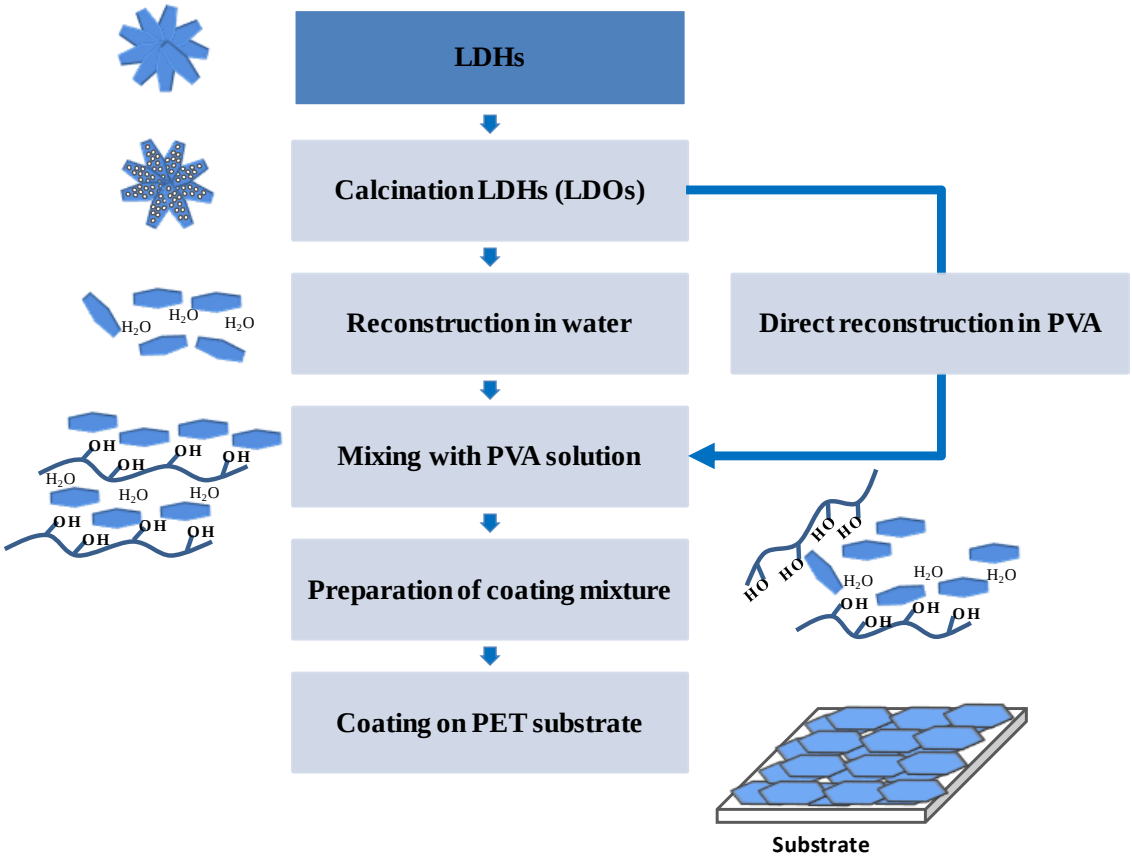


Figure 5.26. Oxygen transmission rate of coated film using two different adding sequences.

The overall process for preparing the barrier coating from the nanoplatelets prepared by the direct reconstruction approach is summarised in Scheme 5.8.



Scheme 5.8. Overall process of nanoplatelet LDHs preparation and their application in barrier coating.

The new adding sequence improves all optical properties of the coated films (Figure 5.27), as well as in the coating mixture with different PVA types (Figure D27). This is due to the coating mixtures prepared from the sequence#2 provide much better particle uniformity, as previously shown in the TEM images (Figure 5.19 and 5.20), resulting in low haze and high clarity of the coated films.

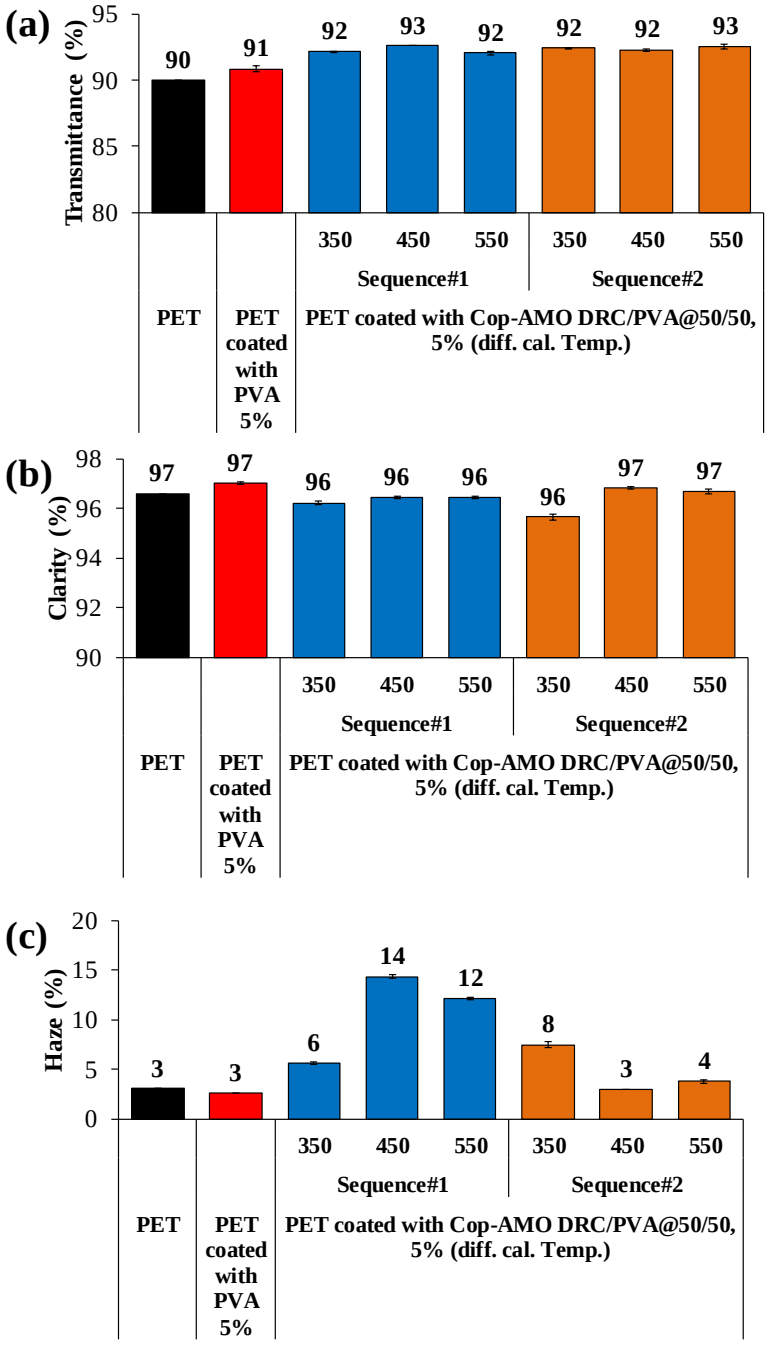


Figure 5.27. Optical properties of coated film with Cop A LDO/PVA at different calcination temperature and adding sequence: (a) transmittance, (b) clarity and (c) haze.

5.5. Conclusions

Nanoplatelet LDHs can be produced by the reconstruction of LDHs in water or in PVA solution (other water soluble or water based polymers can be used). Uniform nanoplatelets were obtained after the reconstruction process regardless of the original LDHs morphology. The LDHs need to be initially transformed into LDOs to diminish the hydrogen bonding interactions within the LDH structure, which increases the accessibility of water molecules through the LDO surface and results in the rapid formation of hydrogen bonding during reconstruction process. The fast regeneration of the layered structure can be related to the rapid change in the morphology of the reconstruction product. It occurs *via* the process of dissolution of the mixed-metal oxide as supported by previous studies.

Nanoplatelets can also be obtained by direct reconstruction in water soluble polymer, PVA; however, the molecular weight and the degree of hydrolysis of PVA can interrupt nanoplatelet formation. To obtain uniform particles, it has been shown that the LDO should be firstly dispersed in water before mixing with a water soluble polymer. Nanoplatelet dispersion in polymer solution using a reconstruction method is a facile and scalable process that should have significant commercial potential.

Highly efficient O_2 barrier coatings can be prepared by mixing the reconstructed LDH in PVA aqueous solution or directly adding LDO powders in PVA aqueous solution. The barrier coating mixtures are simultaneously applied onto the substrate in a single step (e.g. roller-and-bath apparatus) and could be potentially applied to the film in an industrial scale. Such coatings show similar OTR values as coatings containing LDHs reconstructed with amino acid. This process represents a significant improvement in the efficiency and cost of the method.

The present study provides a novel simple and efficient method for preparation of LDH nanoplatelets by simple calcination-recrystallisation of LDH in water or in solution of water soluble polymer. We proposed that the reconstruction occurs by dissolution of highly reactive LDO followed by recrystallisation of the LDH and formation of LDH nanosheets, regardless of the original morphology. This study provides better understanding in morphology change during reconstruction process, which suggests that the memory effect of the LDHs may not necessary be true. This new approach is much more practical, convenient, highly efficient, and eco-friendly since no solvent is used, which widens these materials for further modification and utilisation in many applications besides coating applications.

Chapter Six – Experimental details

6.1. Analytical techniques for LDH characterisation

6.1.1. X-ray powder diffraction (XRD)

X-ray powder diffraction (XRD) results were investigated by using a PANalytical X'Pert Pro diffractometer in reflection mode operating at a voltage of 40 kV and a current intensity of 40 mA with Cu-Kα radiation (λ = 1.5406 Å). LDHs and LDOs powder were placed into stainless steel sample holders.

For samples in Chapter Four and Five, 20 μL of reconstructed LDHs dispersion and coating mixture were cast on a silicon wafer, dried at room temperature before placing into the sample holder, data was collected from 3 to 70°.

A 1° slit was used in both cases. Bragg reflections due to sample holder were observed at 2θ = 43-44° and 50° and from silicon wafer were located at 2θ = 33°, 62° and 69°.

6.1.2. Fourier transform infrared spectroscopy (FTIR)

Fourier transform infrared (FTIR) spectra of samples were recorded on Thermo Scientific Nicolet iS5 FTIR spectrometer in attenuated total reflectance (ATR) mode. Spectra were obtained in the range of 600-4000 cm^{-1}; 50 scans with 4 cm^{-1} resolution.

6.1.3. Transmission electron microscopy (TEM)

Transmission electron microscopy (TEM) was conducted at the Research Complex at Harwell on Jeol JEM-2100 TEM equipped with LaB6 filament at an accelerating voltage of 200 kV. Prior to analysis, samples were diluted with deionised water and sonicated in deionised water for 15 minutes. A few droplets of the resulting suspension were left to dry on a copper grid covered with a carbon film (300 mesh, Agar scientific).

6.1.4. Scanning electron microscopy (SEM)

Scanning electron microscopy (SEM) was carried out at the Research Complex at Harwell on a JSM-6610LV low vacuum fitted with EDX spectrometer at an accelerating voltage of 20 kV. Samples were mounted on adhesive carbon tape attached to aluminium stubs then sputter-coated with a 10 nm layer of platinum using a Quorum Q150T ES Sputter Coater to facilitate image.

6.1.5. Zeta potential and Dynamic light scattering (DLS) measurements

Zeta potential measurements and DLS analysis were carried out at the Begbroke Science Park, Department of Materials, University of Oxford. LDH Samples were dispersed and sonicated in deionised water at 0.1 wt% for 15 minutes before measurement. The resulting suspension samples were filled in a folded capillary cell and directly measured by using a using a Malvern Zetasizer Nano ZS.

6.1.6. Water contact angle measurement

The water contact angle of the samples were prepared by following a reported procedure.[476] A glass slide sticked with a double sided tape was used a substrate. LDH powder samples were spread uniformly on the surface of the adhesive tape, gently pressed with a glass cover, and flushed with air to remove the free particles. This process was repeated several times until the adhesive tape was completely covered and homogeneously coated.

The water contact angle was evaluated with an IT Concept Tracker. 10 μL of deionised water was gently dropped onto the surface of adhesive tape coated with samples. The image of the water drop on the surface was captured. The contact angle values were determined by drawing a tangent close to the edge of the droplet using the snake-based approach (based on Laplace equation) using the DropeSnake plugin in the ImageJ software.[477] At lease three separate measurements carried out at the different locations on the surface and the average contact angle values were reported.[476]

6.1.7. Surface area and pore size analysis

Specific surface areas and pore size were analysed using the Brunauer–Emmett–Teller (BET) method. The samples were measured from the N_2 adsorption and desorption isotherms at 77 K collected from a Micromeritics TriStar II plus. Before each measurement, LDH samples were first degassed overnight at 110 °C. The BET equation is conventionally expressed in the linear form,[317] as shown in Equation 6.1.

$$\frac{p/p^{\circ}}{n(1-p/p^{\circ})} = \frac{1}{n_m C} + \frac{C-1}{n_m C}(p/p^{\circ}) \quad (1)$$

p/p° = the relative pressure

n = the specific amount adsorbed at a relative pressure

n_m = the specific monolayer capacity

C = BET constant (related to energy of adsorption of the 1st layer)

Pore size distribution was determined from the nitrogen adsorption using the Barrett, Joyner and Halenda (BJH) method, based on the application of the Kelvin equation (cylindrical pore shape is assumed), as shown in Equation 6.2, with a correction for the multilayer thickness on the pore walls.[317]

$$\ln\left(\frac{p}{p^{\circ}}\right) = -2\gamma V_m / RT(r_p - t_c) \quad (2)$$

γ = the surface tension of the bulk fluid

V_m = the molar liquid volume

r_p = the pore radius

t_c = the thickness of the adsorbed multilayer film

R = the universal gas constant

T = temperature

6.1.8. Thermogravimetric analysis

Thermogravimetric analyses were performed by using a Mettler Toledo TGA/DSC 1 system. In Chapter Two, 15 mg of sample (LDHs and cellulose fibre composites) was loaded into alumina crucible and heated from 30–700 °C at a rate of 5 °C/min under an air flow. Otherwise, sample was heated from 30–800 °C at a rate of 5 °C/min under a flow of dry N_2. Differential thermogravimetric analysis (DTG) is obtained from the 1st derivative of TGA data.

6.1.9. Surface hydroxyl titrations

Surface hydroxyl titrations of LDOs were performed by Dr. Christopher M. R. Wright (University of Oxford) using $Mg(CH_2Ph)_2(THF)_2$.[160] 5 mg LDH and ~10 mg $Mg(CH_2Ph)_2(THF)_2$ were mixed in 500 μL d_6-benzene containing $Si(SiMe_3)_4$ as an internal standard (c = 6.23 mmol dm^{-3}) in J. Young valve NMR spectroscopy tubes. Production of toluene resulting from protonation of the benzyl by the surface hydroxyls was monitored by ^{1}H NMR spectroscopy and the toluene methyl resonance integrated against that of $Si(SiMe_3)_4$.

6.1.10. Elemental analysis (EA)

Elemental C, H, N analysis was performed by a quantitative oxidative combustion technique by Mr Stephen Boyer at London Metropolitan University.

6.1.11. Inductively coupled plasma mass spectrometer (ICP-MS)

Mg and Al content were determined by ICP-MS analysis by Dr. Alaa Abdul-Sada at the University of Sussex on an Agilent 7500 Series ICP-MS in helium collision mode. Approximaely 20 mg of samples were digested in 10 mL of 10% nitric acid solution. These solutions were then diluted by a factor of 100 with dilute nitric acid prior to analysis. Each solution was analysed three times and the data averaged.

6.1.12. Density

Tap densities were determined by standard testing method (ASTM D7481-09) using a graduated cylinder.[96] The powder was filled into a volumetric cylinder and a precise weight of sample (m) was measured. The volume was measured before (V_0) and after 1000 taps (V_t). The loose bulk and tap densities were calculated by: Loose bulk density = m/V_0; Tap density = m/V_t.

6.1.13. Solid state NMR spectroscopy

The ^{1}H, ^{27}Al and ^{13}C solid state NMR spectroscopy were performed by Dr. Nicholas H. Rees (University of Oxford) on a Bruker Avance III HD spectrometer equipped with a 9.4 T magnet using 4.0 mm O.D zirconia rotors and a MAS rate of 10 kHz at 399.9, 104.2, and 100.6 MHz, respectively. For Chapter Three, the ^{1}H MAS NMR rate was 15 kHz.

The high resolution ^{1}H solid state NMR was performed by Dr. Nicholas H. Rees, Dr. Jean-Charles Buffet and Dr. Christopher M. R. Wright (University of Oxford) and Dr. Dinu Iuga (University of Warwick) at the UK 850 MHz Solid-State NMR Facility at the University of Warwick using the Bruker Avance III 850 MHz solid-state NMR spectrometer with 1.3 mm rotors and MAS rate of 60 kHz at 23°C. ^{1}H experiment with background suppression applied referenced to β-Aspagine-Alanine dipeptide.

6.2. Analytical techniques for papermaking and paper characterisation

Wet-end process parameters measurements and all paper properties were performed by Mr. Chaiyut Kaewkong, Miss Ratchaneewan Cherchalart, Mr. Udomsak Udomkitkul, Mr. Seksan Kaewvisit, Miss Chomcheun Junbang, Miss Tisanan Jampathet, Mr. Jeasada A-reruk, and Miss Suparat Noodammadan at Product Technology Development Center (PTDC), SCG Packaging PLC, Ratchaburi, Thailand. All measurements were test at least five times, the average and standard deviation values were reported

6.2.1. Wet-end process parameters measurement

Zeta potential measurement of fibre suspensions were performed using Mütek SZP-06 at SCG Packaging PLC, Thailand (Figure 6.1 (b)). A fibre suspension is placed under the plastic measuring cell equipped with a screen electrode and a ring electrode. Then the sample is vacuum-extracted into the cell where it forms a plug. An oscillating liquid flow is generated by varying the vacuum pressure, which induces a streaming potential. On the basis of the measured streaming potential, the conductivity and the pressure differential, finally, the zeta potential is calculated after several measurement cycles with the unit of mV.

Drainage time was performed following the TAPPI T221 by measuring the time required to form a standard sheet weighing 60 g/m^2.[478] All measurements were test at least five times, the average and standard deviation values were reported.

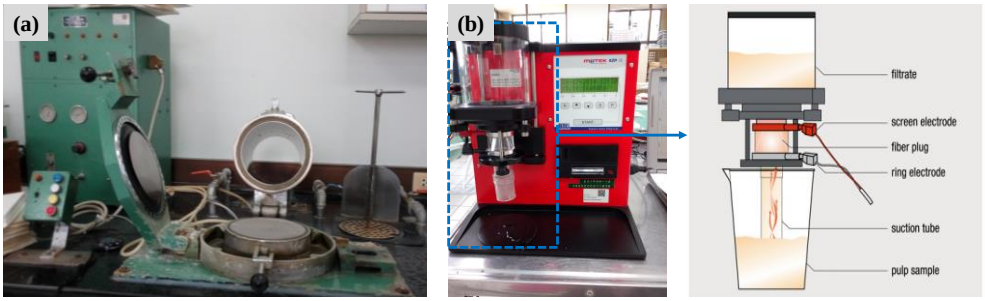


Figure 6.1. (a) Sheet former and (b) MütekTM SZP-06 System Zeta Potential.

6.2.2. SEM (surface and cross-section) for paper

Scanning electron microscopy (SEM) was carried out on a SEM JOEL JSM-6490LV fitted with EDX spectrometer at an accelerating voltage of 20 kV. Samples were mounted on adhesive carbon tape attached to aluminium stubs then sputter-coated with gold (at 18 mA for 90 seconds) using a SPI-Module Sputter Coater to facilitate image.

6.2.3. Contact angle measurement for coated paper

The water contact angle measurement of the coated paper samples were performed by using a Krüss Drop Shape Analyser DSA100. 10 µL of deionised water was gently dropped onto the surface of coated paper and the contact angle values were determined by sessile drop method. At lease five separate measurements carried out at the different locations on the surface and the average contact angle values were reported.

6.2.4. Water vapour transmission rate measurement

Coated paper samples were tested for water vapour transmission rate, according to the ASTM F 1249 standard method, using a water vapour permeation analyser (Systech Illinois Inc., Water Vapour Permeation Analyser 7000) at 38 °C and 90% RH. The water vapour transmission rate (WVTR) is recorded after a steady state permeation is reached and reported in units of $cc \cdot m^{-2} \cdot day^{-1}$.

6.2.5. Paper testing and characterisation

All paper properties testing were performed by Miss Ratchaneewan Cherchalart, Miss Chomcheun Junbang, Miss Tisanan Jampathet and Miss Suparat Noodammadan, at Product Technology Development Center (PTDC), SCG Packaging PLC, Ratchaburi, Thailand. The investigated paper properties in the studies are presented in Figure 6.2 and Table 6.1, which the method used, units and some general information about the properties are shown. All measurements were test at least five times, the average and standard deviation values were reported.

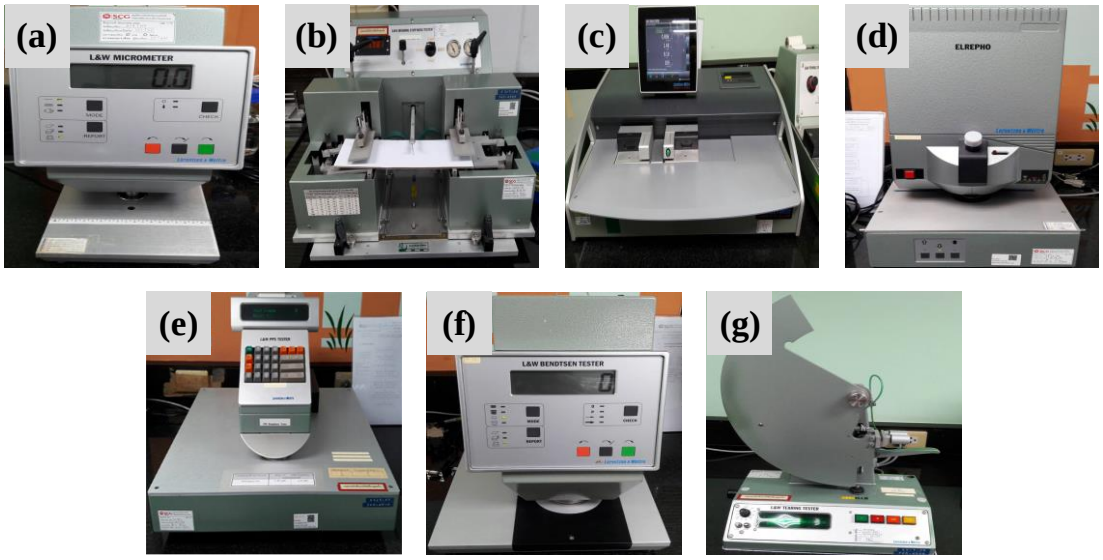


Figure 6.2. Equipments for paper testing: (a) L&W micrometer, (b) L&W bending stiffness tester, (c) L&W tensile tester, (d) L&W Elrepho, (e) L&W PPS tester, (f) L&W bendtsen tester, and (g) L&W tear tester.

Table 6.1. Paper properties investigated in this study.

Paper property	Method and Unit	Information and Instrument
Ash content	• ASTM D 586-97[479] • Percent Ash (%)	• Igniting a test specimen of paper in a furnace at 525 °C. • Percent ash content in sample is calculated by using the resulting weight of ash in the sample on a moisture-free sample basis.
Grammage	• TAPPI T 410[478] • g/m^2	• Weight per unit area of paper, so-called basis weight.
Thickness	• TAPPI T 411 om-97[480] • µm	• L&W micrometer. • Thickness measurements of paper.
Paper density	• TAPPI T 410[478] • g/cm^3	• Grammage devided by thickness.
Stiffness index (so-called bending stiffness index)	• ISO 5628[481, 482] • Nm^7/kg^3	• L&W Bending Stiffness tester. • The stiffness index is defined by a proportional of the bending stiffness to grammage raised to the power 3.
Bendtsen porosity	• ISO 5636-3[483] • ml/min	• L&W Bendtsen Tester. • Determination of the air permeance of a porous substrate by measuring resistance to airflow through a material.
Parker-Print-Surf (PPS) roughness	• TAPPI T 555[484] • µm	• L&W PPS tester. • The air leakage between the paper surface and a thin metal band under conditions that simulates the printing process, which is expressed as the mean distance in µm after conversion.
Tensile index	• TAPPI T 494[481, 485] • Nm/g	• L&W Tensile tester. • It is the tensile strength in N/m divided by grammage. • A paper strip (with specified width and length) is clamped at each end and strained the material until it breaks, the tensile force per unit width is reported.
Tear index	• TAPPI T 414[486] • $mN \cdot m^2/g$	• L&W Tearing Tester. • The mean force required to continue the tearing of an initial cut in a single sheet of paper is expressed as the internal tearing resistance.
Optical properties	• TAPPI T 1214[487] • Opacity • Scattering coefficeient or s (m^2/kg) • Absorption coefficeient or k (m^2/kg) • colour (CIE L a b) • Brightness (%) • Whiteness (%)	• L&W Elreph spectrophotometer. • The opacity is the ratio between the reflectance factor for a specific sheet of paper, measured over a black surface and the reflectance factor for an opaque pad of the same test piece. • s is a measure of the test piece's ability to disperse light. • k indicates the test piece's ability to absorb light. • Colour is the test pieces L*, a* and b* values determined according to the CIE 1976 system. • Brightness (diffuse blue reflectance factor) is the intrinsic factor calculated with a weighting function with an effective wavelength of 457 nm and a width at half height of 44 nm. • Whiteness is a measure of the white appearance of a paper sample. By calculation the observer's visual perception of this whiteness is simulated. The whiteness is calculated according to the CIE or Ganz-Griesser method. • The measurement is performed at D65/10° illuminant/observer.

6.3. Analytical techniques for coated films characterisation

6.3.1. Oxygen transmission rate measurement

Films and coated substrates are tested for oxygen transmission rate using an oxygen permeation analyser (Systech Illinois Inc., Oxygen Permeation Analyser 8001) at 23 °C and 0% RH. The oxygen transmission rate (OTR) is recorded after a steady state permeation is reached and reported in units of $cc \cdot m^{-2} \cdot day^{-1}$.

6.3.2. Optical properties of coated films

All film properties were tested at Product Technology Development Center (PTDC), SCG Packaging PLC, Ratchaburi, Thailand. All measurements were tested at least five times, average and standard deviation values were reported.

All thickness measurements are tested by using a thickness tester (Thwing-Albert Instrument Company, ProGage Thickness Tester). Average of ten measurements is reported in units of micron.

The transmittance of the coated and uncoated substrates was assessed by a haze meter (The haze-gard I, BYK-Gardner GmbH Inc) according to ASTM D 1003. It is the ratio of transmitted light to the incident light, which is influenced by the absorption and reflection properties of the materials. The specimen is placed at the film holder at the entrance port of the haze meter in order to measure the transmittance. Average of ten measurements is reported in units of percent.

The transmittance of the coated and uncoated substrates was assessed by a haze meter (the haze-gard I, BYK-Gardner GmbH Inc) according to ASTM D 1003. It is the ratio of transmitted light to the incident light, which is influenced by the absorption and reflection properties of the materials. The specimen is placed at the film holder at the entrance port of the haze meter in order to measure the transmittance. Average of ten measurements is reported in units of percent.

The clarity of the coated and uncoated substrates was assessed by a haze meter (the haze-gard I, BYK-Gardner GmbH Inc). This measurement describes how ell very fine details can be seen through the specimen. It needs to be determined in an angle range smaller than 2.5 degrees. The specimen is placed at the film holder at the entrance port of the haze meter in order to measure the clarity. An average of ten measurements is reported in units of percent.

6.4. Starting materials and chemicals

$Mg(NO_3)_2 \cdot 6H_2O$ (AR), $Al(NO_3)_3 \cdot 9H_2O$ (AR), NaOH (AR), Na_2CO_3 (AR), urea, sodium docecylsulfate, lauric acid, stearic acid, amino acids (glycine, β-alanine, β-aminobutyric acid, β-leucine, β-phenylalanine, γ-aminobutyric acid, serine, asparagine, aspartic acid, and glutamic acid), sodium lactate, ethylene diamine, oxalic acid, glucose, PVA polymers (Mowiol 4-98, Mowiol 10-98, Mowiol 20-98, Mowiol 4-88, Mowiol 8-88 and Mowiol 18-88), and all solvents were purchased from Sigma-Aldrich Co. LLC., and used without further purification. Deionised water was used throughout the experimental processes.

6.5. Experimental details for Chapter Two

6.5.1. $Mg_3Al\text{-}CO_3$ LDHs synthesis

$Mg_3Al\text{-}CO_3$ LDH by co-precipitation method

$Mg_3Al\text{-}CO_3$ LDHs were synthesised using a method adapted from Chen *et al.*.[96, 195, 197]

The mixed metal solution was prepared from 37.5 mmol of $Mg(NO_3)_2 \cdot 6H_2O$, 12.5 mmol of $Al(NO_3)_3 \cdot 9H_2O$ in 50 mL deionised water and added drop-wise into 50 mL of 25 mmol Na_2CO_3 solution while stirring with adding time of 1 hour. A constant pH of 10 was maintained by addition of 4 M NaOH to the reaction mixture using an auto-titrator (Syrris, Atlas Syringe Pump) at feeding rate of 5 mL/min. After stirring at room temperature for 18 hours, the product was filtered, washed with deionised water until pH 7 and dried in an oven at 65 °C for 24 hours.

$Mg_3Al\text{-}CO_3$ LDH by urea method

$Mg_3Al\text{-}CO_3$ LDH by urea method was synthsised and adapted from Okamoto *et al.*.[134]

$Mg_3Al\text{-}CO_3$-LDH was prepared using urea from the mixture of $Mg(NO_3)_2 \cdot 6H_2O$, 4.7 g of $Al(NO_3)_3 \cdot 9H_2O$, and 6.0 g of urea in 100 mL deionised water. The solution was maintained at 100 °C for 18 hours under stirring. Then, the obtained solid was washed with deionised water, collected by filtration, subsequently dried in an oven at 65 °C for 24 hours.

$Mg_3Al\text{-}CO_3$ LDH by post hydrothermal method

Hydrothermal method is a post treatment of the LDH synthesis method. It was performed before starting to age the prepared mixture, in both co-precipitation and urea methods. The solution was transferred into a 40 mL Teflon lined stainless autoclave at 100 °C for 18 hours. The products were washed with deionised water and dried in an oven at 65 °C for 24 hours.

6.5.2. Fibre pretreatment

Whatman filter paper number 3 was employed to study the effect of fibre pretreatment. The consistency of the fibre slurry was kept at 1% in all fibre preparation experiments. Effect of the dispersing medium and time were studied. 25 mmol of Na_2CO_3 in 50 mL of deionised water was used as a fibre pretreatment solutions with the dispersion time of 3 days to make full-dispersed fibre slurry. In case of dispersion time, fibre slurry was stirred in sodium carbonate solution with various dispersion time from 2 hours to 3 days.

Bleached Softwood fibre was received from SCG Packaging PLC, Thailand to study the effect of the wood fibre on the composites characteristics and the effect of the synthesis routes of the obtained composites were also explored on this fibre.

6.5.3. Preparation of Mg_3Al-CO_3 LDH /Cellulose Fibre composites

Four synthetic routes were carried out to study the synthesis Mg_3Al-CO_3 LDH/cellulose fibre composites. The selected fibre was dispersed in chosen alkaline anion solution (carbonate anion solution) for one day. Then it was mixed with the metal solution to precipitate the LDHs.

Co-precipitation method

0.5 g of chosen fibre was dispersed in sodium carbonate solution (25 mmol of Na_2CO_3 in 50 mL of deionised water) with stirring at room temperature for 1 day. This way followed by addition of the mixed metal salt solution (as mention in 6.5.1) dropwise while stirring with adding time of 1 hour. The system was controlled at a constant pH of 10 by adding dropwise of 4 M NaOH using an auto-titrator (Syrris, Atlas Syringe Pump) at feeding rate of 5 mL/min. All reaction systems were aged for 18 hours at room temperature. Finally, the products were washed by deionised water until neutral pH by using 200 micron mesh sieve stainless steel wire mesh to remove loosen LDH particles from fibre surface and subsequently dried in a vacuum oven overnight.

Urea method

The mixed metal salt solution was prepared as in the co-precipitation method. However, the mixed salt solution was rapidly added to the fibre slurry comprising 0.5 g of chosen fibre, 100 mmol of urea in 50 mL of deionised water. The reaction mixture was stirred at 100 °C for 18 hours. Then using the same procedure for washing and drying as in above mentioned for co-precipitation method.

Hydrothermal method

In this study, hydrothermal treatment was performed in all synthesis methods mentioned above, co-precipitation and urea methods. After mixing the fibre slurry with the metal salt solution, the mixture was transferred into a 40 ml Teflon lined stainless autoclave at 100 °C for 18 hours. Then using the same procedure for washing and drying as in above mentioned.

6.5.4. Preparation of paper sheets and wet-end process parameters measurement

Paper sheet forming and wet-end process parameters measurements were performed by Mr. Udomsak Udomkitkul, at Product Technology Development Center (PTDC), SCG Packaging PLC, Ratchaburi, Thailand.

Paper handsheets having a basis weight of 60 g/m^2 were prepared for all of the experiment. Phoenix fibres was used as a based fibres and blank sample. The Phoenix fibre was dispersed in water and subsequently refined using the standard PFI mill following T248cm-00 TAPPI standard method (KRK Kumagai) to reach the freeness value at 380 CFS (Cannadian Standard Freeness). The LDH/fibre composites from each synthesis methods were added from 0, 10, and 20% by mass to the based fibre. Then the mixed fibres slurred were diluted to 0.5% consistency and formed a sheet of paper using the TAPPI standard sheet former machine following TAPPI T-205om-88, T-221om-88 (KRK Kumagai) at a basis weight of 60 g/m^2 (Figure 6.1 (a)), pressed to dewater by the machine press following TAPPI T-205om-88 (KRK Kumagai) and dried at 100 °C by a drum dryer.

6.5.5. Mg_3Al-NO_3-LDH by co-precipitation method

The mixed metal solution was prepared from 37.5 mmol of $Mg(NO_3)_2 \cdot 6H_2O$, 12.5 mmol of $Al(NO_3)_3 \cdot 9H_2O$ in 50 mL degassed water. 24.7 mmol of $NaNO_3$ and 100 mmol of NaOH were dissolved in 50 mL of degassed water as a nitrate anion solution. The mixed metal solution was added dropwise while stirring with adding time of 1 hour to the anion solution under a constant flow of N_2 gas. The pH of mixture was controlled at 10 by using 4 M of NaOH using an auto-titrator (Syrris, Atlas Syringe Pump) at feeding rate of 5 mL/min. After ageing time of 18 hours under N_2 flow with stirring at room temperature, the slurry was washed by degassed water until the pH was close to 7. Then, the obtained LDH solid was filtered and dried in an oven at 65 °C for 24 hours.

6.5.6. Synthesis of organo-LDHs by co-precipitation method

Two organic molecules were used; dodecylsulfate (DS) and laurate (LR). The mixed metal salts solution was firstly prepared by dissolving $Mg(NO_3)_2 \cdot 6H_2O$ (37.5 mmol) and $Al(NO_3)_3 \cdot 9H_2O$ (12.5 mmol) in 50 mL of a degassed 1:1 mixture of deionised water/ethanol (Solution A). The solution of organic molecule was prepared separately (Solution B) by adding a certain amount of selected organic molecule and sodium hydroxide (50 mmol) were dissolved in 50 mL of a degassed 1:1 mixture of deionised water/ethanol at 80 °C.

Solution A was added to Solution B dropwise over the period of 1 hour with vigorous stirring and the pH of the precipitation was maintained at ~10 using 2 M NaOH solution in a degassed 1:1 mixture of deionised water/ethanol using an auto-titrator (Syrris, Atlas Syringe Pump) at feeding rate of 5 mL/min. The resulting reaction mixture was aged under N_2 in an oil bath heated at 80 °C for 18 hours while stirring at 700 rpm. After ageing, the LDH product was washed with 1 L of 1:1 mixture of ethanol and deionised water at 80 °C, followed by drying in an oven at 65 °C for 24 hours.

For Mg_3Al-DS LDH, sodium dodecylsulfate was varied from 3, 6, 12, and 24 mmol while in Mg_3Al-LR LDH, lauric acid was varied from 3, 6, 12, 24, and 48 mmol.

6.5.7. Synthesis of organo-LDHs by urea method

Three organic molecules were used; dodecylsulfate (DS), laurate (LR), and stearate (SR). The mixed metal salts solution and urea was firstly prepared by dissolving $Mg(NO_3)_2 \cdot 6H_2O$ (37.5 mmol), $Al(NO_3)_3 \cdot 9H_2O$ (12.5 mmol), and urea (100 mmol) in 200 mL of deionised water (Solution C). 12 mmol of selected organic molecule was dissolved in 50 mL deionised water at 80 °C and the pH was adjusted to 10 by dropwise addition of 4 M NaOH (Solution D). Solution C was quickly added to Solution D during vigorous stirring and heated at 100 °C for 18 hours with stirring at 700 rpm. After ageing, the LDH product was washed with 1 L of 1:1 mixture of ethanol and deionised water at 80 °C, followed by drying in an oven at 65 °C for 24 hours.

6.5.8. Water resistant coating for paper

The strearated intercalated organo-LDH powder prepared using urea method (U-SR LDH) was dispersed in ethanol to get a well-dispersed slurry then directly added to the styrene butadiene latex (SB latex) with pigment/latex ratio of 10/3 and contolled at 20% solid content. Alternatively, the commercial kaolin clay was used to prepare the coating mixture. A commercial kraft linerboard of 125 g/m^2, kindly provided by SCG Packaging, PLC, was

used as the coating substrate and applied coating with a coat weight of 5 g/m^2 by hand coating performed by Mr. Seksan Kaewvisit at Product Technology Development Center (PTDC), SCG Packaging PLC, Ratchaburi, Thailand.

6.5.9. Barrier coating for paper

Different pigments were employed including kaolin as a main pigment, U-CO_3 LDH and U-SR LDH as co-pigments and conventional high barrier performance nanoclay was also compared and set as a target in this study. The detail of formulation are shown in Table 6.2. The U-SR LDH was dispersed in ethanol to afford a well-dispersed slurry then directly added to the SB latex with pigment/latex ratio of 4/5 and finally mixed with kaolin slurry. Total solid contents were controlled at 50% and applied on commercial machine glaze paper of 35 g/m^2 grammage with a coat weight of 10 g/m^2 by hand coating performed by Mr. Seksan Kaewvisit at Product Technology Development Center (PTDC), SCG Packaging PLC, Ratchaburi, Thailand.

Table 6.2. Coating compositions for paper coating experiment.

Sample	Part (%)			
	Kaolin clay	**U-SR LDH**	**U-CO_3 LDH**	**Nanoclay**
Kaolin 100%	100	-	-	-
Kaolin/U-SR LDH (90/10)	90	10	-	-
Kaolin/U-CO_3 LDH (90/10)	90	-	10	-
Nanoclay 100%	-	-	-	100

6.6. Experimental details for Chapter Three

6.6.1. Synthesis of Conventional, AMO and AIM LDHs

Synthesis of flower shape like Mg_4Al-CO_3 LDHs *via* co-precipitation method

Mg_4Al-CO_3 LDHs flower like shape were synthesised and treated with solvent using a method adapted from Wang *et al.* and Chen *et al.*.[96, 195, 197]

The mixed metal salts solution of $Mg(NO_3)_2{\cdot}6H_2O$ (80 mmol) and $Al(NO_3)_3{\cdot}9H_2O$ (20 mmol) in 50 mL deionised water was added dropwise into 50 mL of 25 mmol Na_2CO_3 solution while stirring for 1 hour. Constant pH of 10 was maintained by addition of 4 M NaOH to the reaction mixture using an auto-titrator (Syrris, Atlas Syringe Pump) at feeding rate of 5 mL/min. After stirring at room temperature for 24 hours, the product was filtered and washed with deionised water until pH 7. Then the wet cake was re-dispersed in 100 mL of deionised water and divided into four portions. Each portion was filtered and rinsed with 500

mL of a washing solvent then re-dispersed and stirred in 300 mL of this solvent at room temperature for 4 hours. The solvent was removed by filtration and the obtained LDH was further rinsed with 200 mL of this solvent. The product was dried at room temperature in a vacuum oven overnight.

Mg_2Al-CO_3 LDH and Mg_3Al-CO_3 LDH were prepared using similar procedure as mentioned above. The mixed metal solution was prepared using 50 mL aqueous solution of 33.3 and 37.5 mmol of $Mg(NO_3)_2{\cdot}6H_2O$ and 16.7 and 12.5 mmol of $Al(NO_3)_3{\cdot}9H_2O$, for Mg_2Al-CO_3 LDH and Mg_3Al-CO_3 LDH, respectively. Then the same procedure as mentioned above was used.

Synthesis of platelet shape Mg_4Al-CO_3 LDHs *via* urea hydrothermal method

Synthesis method for platelet shape Mg_4Al-CO_3 LDHs was modified from Okamoto *et al.*.[134] An aqueous solution of $Mg(NO_3)_2{\cdot}6H_2O$ (40 mmol), $Al(NO_3)_3{\cdot}9H_2O$ (10 mmol) and urea (160 mmol) in 100 mL deionised water was prepared. The solution was transferred to a Teflon-lined autoclave and heated in an oven at 100 °C for 24 hours. After cooling to room temperature, the precipitate products were washed several times with deionised water by filtration until pH 7. Then the wet cake was re-dispersed in 100 mL of deionised water and separated into four portions. A portion of dispersion was filtered and followed steps as mentioned above. Solvents used were acetone, ethanol, 1-hexanol, and ethyl acetate.

Effect of solvent types: AMO vs. AIM solvents

Both AMO and AIM solvents were compared in this study. The AMO solvents were acetone, ethanol, isopropyl alcohol, and 1-methyl-2-pyrrolidinone. Several AIM solvents with different functional groups and structures were employed; alcohol (1-butanol and 1-hexanol), ester (ethyl acetate), ether (diethyl ether and tert-butyl methyl ether (MTBE)), amine (triethylamine), nitro (nitromethane), ketone (2-butanone or methyl ethyl ketone (MEK)), hydrocarbon (hexane, toluene), and halogenated (chloroform).

Effect of solvent structures: ketone, ether, hydrocarbon and halogenated solvents

Series of ether, ketone, hydrocarbon, and halogenated solvents were introduced. Ether were diethyl ether, tert-butyl methyl ether (MTBE), diisopropyl ether, di-n-butyl ether, cyclopentyl methyl ether (CPME), tert-amyl methyl ether (TAME), and anisole. Ketone were 2-butanone (MEK), 2-pentanone, 3-pentanone, 4-heptanone, 5-nonanone, 3-methyl-2-butanone, 4-methyl-2-pentanone or methyl isobutyl ketone (MIBK), and

diisopropylketone. Hydrocarbon were n-hexane and cyclohexane and halogenated were chloroform and dichloromethane.

Effect of process parameters

In some sets of study, the rising volume of diethyl ether and ethyl acetate was varied from 100, 300, 500 and 1000 mL.

In this study, we compared mixing speed at 750 and 10,000 rpm using stirrer plate and homogeniser, respectively. The dispersion was mixed for 30 minutes. Hexane was used as a solvent for comparison to water.

Effect of solvent recycling

To confirm the benefit of using AIM solvent rather than AMO solvent, effect of recycled both AMO and AIM solvents needs to be compared. In this study, ethanol and 1-hexanol is representative of AMO and AIM solvents, respectively. Considering the amount of solvent use in each step during solvent treatment, the rinsing step consumes largest volume than others. Therefore, we recycled solvent collecting from this step to rinse LDHs in the new batch. The solvent was recycled four times.

6.7. Experimental details for Chapter Four

6.7.1. Synthesis of LDHs

Synthesis of flower shape like $Mg_4Al\text{-}CO_3$ LDHs *via* co-precipitation method

$Mg_4Al\text{-}CO_3$ LDH flower like shape was synthesised following the procedure in 6.6.1.

After stirring at room temperature for 24 hours, the product was filtered and washed with deionised water until the pH was close to 7. Then, the wet cake was re-dispersed in 100 mL of deionised water. The wet cake was rinsed with 500 mL of ethanol then re-dispersed and stirred in 300 mL of this solvent at room temperature for 4 hours. The solvent was removed by filtration and the obtained LDH was further rinsed by 200 mL of this solvent. The product was dried in the vacuum oven overnight. The product washed with water was noted as Cop-W LDH while the one treated with ethanol noted as Cop-AMO LDH.

Synthesis of platelet shape $Mg_4Al\text{-}CO_3$ LDHs *via* urea hydrothermal method

$Mg_4Al\text{-}CO_3$ LDH platelet shape was synthesised following the procedure in 6.6.1.

After the reactions were cooled to room temperature, the precipitated products were washed several times with deionised water by filtration and treated with ethanol using the same procedure mentioned above and the product was noted as UHT-AMO LDH.

6.7.2. Calcination and reconstruction of LDHs

LDHs powder was transferred to the crucible and calcined in a furnace at 450 °C for 12 hours. After cooling, the calcined product, LDOs, was kept in a seal vial and used within few days.

0.2 of LDO powder was added to 2.66 mmol of selected organic solution in 2 mL of deionised water. The mixture was heated at 80 °C in a round bottom flask for 24 hours. Alternatively, the reaction was performed in an autoclave reactor. Then the reaction was cooled down to room temperature naturally. The obtain product was washed with deionised water by centrifugation three times and used without drying. Unwashed product was also compared. The final solid content of product was determined before use in the next step.

The organic molecules used in this study are amino acids (glycine, β-alanine, β-aminobutyric acid, β-leucine, β-phenylalanine, γ-aminobutyric acid, serine, asparagine, aspartic acid, and glutamic acid), sodium lactate, ethylene diamine, oxalic acid and glucose.

6.7.3. Barrier coating performance of LDHs with different size and commercial clays

Three LDHs (0.5, 4 and 7 μm size) and two commercial clays were used as filler to prepare coating mixture. LDH (4 μm) was synthesised using the urea hydrothemal method (section 6.6.1) whereas the 0.5 and 7 μm LDHs were provided from Beijing University of Chemical Technology (BUCT), China. Two commercial kaolin clays coated grade, Barrisurf (Imerys Minerals Ltd.,) and Nuclay (Engelhard Corporation), were kindly supplied from SCG Packaging, PLC, Thailand.

An aqueous barrier coating solution is prepared as follows. An aqueous polyviny alcohol (PVA, Mowiol 4-88, M_w 31,000, 88% hydrolysis, Sigma-Aldrich) solution of defined solid content is freshly prepared; the required amount of polymer is weight, added to required amount of pre-heat deionised water under vigorous stirring. The mixture is stirred and heated at 90 °C. After complete dissolution of polymer, the PVA solution is cooled down and kept at the room temperature. Suspension of each LDHs and clays was prepared at 10 wt% in water and sonicated for 20-30 minutes before used. The LDH and PVA solutions of different proportions are vigorous mixed to obtain the coatings with weight ratios of LDH/PVA or clay/PVA at 20/80 and 50/50. The solid of coating formulations are controlled at 10%.

6.7.4. Barrier coating performance of LDHs with nanoplatelets from amino acid reconstruction

The amino acid-modified LDHs prepared in 6.7.2 were mixed with an aqueous solution of PVA to yield a coated mixing of 5 wt% solids. The ratio of amino acid-modified LDH to PVA (LDH/PVA ratio) within the coating mixture was 70/30, 50/50 or 40/60.

6.7.5. Coated films preparation

The coating solution is applied to 23 μm thick corona-treated polyethylene terephthalate substrate (SARAFIL Transparent TF101, Polyplex Thailand), which is supplied by SCG Packaging PLC, by a Mayer rod coater and an automatic coater (K101, RK Print Coat Instruments Ltd.) equipped with a close wound rod having wire diameter of 0.08 mm, called yellow rod. The substrate film is secured in the middle of the coating area and the rod is placed on the upper top of the film. Approximately 1-2 mL of the prepared coating solution is applied in the gap between the rod and the substrate along the width of the substrate. A Mayer rod moves down the substrate with a controlled speed and the coated film is obtained. All coated samples are dried naturally at room temperature. Coating thickness is controlled by using a yellow rod and fixing speed of the coater at #7 for all coatings.

6.8. Experimental details for Chapter Five

6.8.1. LDHs used in this study

LDHs used in this study were $Mg_4Al\text{-}CO_3$ LDHs from co-precipitation method with water (Cop-W) and AMO washing (Cop-A), from urea hydrothermal method with AMO washing (UHT-A) as described in 6.7.1. In addition, seven LDHs including commercial LDHs (MG70HT and Hydrotalcite Aldrich), three $MgAl\text{-}CO_3$ LDHs with different Mg/Al ratios from colloidal mill process provided by SCG Chemicals (Mg/Al = 2 (M2), 3 (M3), and 4 (M4)), and two $Mg_2Al\text{-}CO_3$ LDHs from BUCT produced by Atomic Economy process (F1) and colloidal mill process (D2), were studied.

6.8.2. Calcination/reconstruction in water

LDHs powder was transferred to the crucible and calcined in the furnace at 450 °C for 12 hours. After cooling, the calcined products, LDOs, were kept in the seal vial and used within a few days. 0.2 g of calcined powder was added to 2 mL of deionised water and stirred at room temperature for 24 hours under an open atmosphere in a closed container.

The effect of calcination temperature was explored in co-precipitation LDHs at different calcination temperature (250, 350, 450 and 550 ℃) for 12 hours.

The effect of reconstruction time was fully explored in co-precipitation LDHs using LDO calcined at 450 °C at different reconstruction time in water (1, 6, 9, 18, 24, 72 hours and 1 week).

6.8.3. Calcination/reconstruction in non-aqueous solvents

LDHs powder prepared by co-precipitation method with AMO treatment was transferred to the crucible and calcined in the furnace at 450 °C for 12 hours. After cooling, 0.2 g of calcined powder was added to 2 mL of selected solvent and stirred at room temperature for 24 hours under an open atmosphere in a closed container. Solvents used are ethanol, acetone, ethyl acetate, formamide, toluene, and p-xylene. They are bulk solvents and used without purification.

6.8.4. Calcination/reconstruction in PVA aqueous solution

LDHs powder prepared by co-precipitation method was transferred to the crucible and calcined in the furnace at 450 °C for 12 hours. After cooling, 0.2 g of calcined powder was added into a certain amount of a selected PVA aqueous solution and stirred at room temperature for 24 hours under an open atmosphere in a sealed container. The ratio of LDH/PVA was control either at 50/50 or 20/80 and the total solid content was kept constant at 5%. This approach is named as sequence#1.

Alternatively, LDO was firstly added into water then stirred for 24 hours before being added to a PVA solution and stirred for a further 24 hours. The ratio of LDH/PVA was controlled either at 50/50 or 20/80 and the total solid content was kept constant at 5%. This approach is named as sequence#2.

PVA polymers used in this study are selected from (Mowiol 4-98, Mowiol 10-98, Mowiol 20-98, Mowiol 4-88, Mowiol 8-88 and Mowiol 18-88).

6.8.5. Coated films preparation

The various coating mixtures prepared in section 6.8.4 were coated onto a 23 μm thick PET substrate following the same procedure as described in section 6.7.5.

References

1. B. A. Morris, *The Science and Technology of Flexible Packaging: Multilayer Films from Resin and Process to End Use*, Matthew Deans, Elsevier, Oxford, United Kingdom, 2016.
2. D. Raheem, *Emir. J. Food Agric.*, 2013, **25**, 177-188.
3. *Packaging: Market and challenges in 2016*, All4Pack, Paris, France, 2016.
4. U. Reiners, *Journal*, 2017, 1-23.
5. G. Moore, *The Future of Paper and Board in Central and Eastern Europe*, Report Market report, Smithers Pira, Surrey, United Kingdom, 2015.
6. *Global Paper and Paperboard Container and Packaging Market 2016-2020*, Technavio, Toronto, United States of America, 2016.
7. N. Farmer, in *Trends in Packaging of Food, Beverages and Other Fast-Moving Consumer Goods (FMCG)*, Woodhead Publishing, 2013, pp. 1-21.
8. G. A. Smook and M. J. Kocurek, *Handbook for Pulp & Paper Technologists*, Peachtree Corners, Tappi Press, Georgia, United States, 4th edn., 2016.
9. J. Shen, Z. Song, X. Qian and W. Liu, *BioRes.*, 2009, **4**, 1190-1209.
10. M. A. Hubbe and R. A. Gill, *BioRes.*, 2016, **11**, 2886-2963.
11. M. A. Hubbe, presented in part at the TAPPI 2004 Paper Summit, Spring Technical & International Environmental Conference, Atlanta, United States of America 2004.
12. M. Laufmann and S. Hubschmid, in *Handbook of Paper and Board*, Wiley-VCH Verlag GmbH & Co. KGaA, 2013, pp. 109-143.
13. H. Holik, *Handbook of Paper and Board*, John Wiley & Sons, Weinheim, Germany, 2nd edn., 2013.
14. N. Keegan, *Raw Materials for Pigments, Fillers and Extenders*, Industrial minerals information limited, 1999.
15. J. Grönfors, *Use of fillers in paper and paperboard grades*, Final Thesis, Tampere University of Applied Sciences 2010.
16. H. E. Bergna and W. O. Roberts, *Colloidal Silica: Fundamentals and Applications*, CRC Press, New York, United States, 2005.
17. D. Seo, W. H. Im, H. J. Youn and H. L. Lee, *Nord. Pulp Pap. Res. J.*, 2012, **27**, 382-387.
18. *Mondi taps Minerals Technologies for high-filler loading plant at Slovakia paper mill*, RISI Technology Channels, New York, United States of America, 2012.
19. *Omya Multifill: The roadmap to higher mineral contents*, Omya International AG, Oftringen, Switzerland, 2015.
20. J. Paltakari, *Pigment Coating and Surface Sizing of Paper*, Tappi, Paperi ja Puu, Helsinki, Findland, 2 edn., 2009.
21. J. M. Gess and J. M. Rodriguez, *The sizing of paper*, Tappi Press, Atlanta, United States, 3 edn., 2005.
22. M. S. Saraiva, J. A. F. Gamelas, A. P. Mendes de Sousa, B. M. Reis, J. L. Amaral and P. J. Ferreira, *Materials*, 2010, **3**, 201-215.
23. C. Andersson, *Packag. Technol. Sci.*, 2008, **21**, 339-373.
24. R. E. Popil, unpublished work.
25. A. Emblem, *Packaging Technology: Fundamentals, Materials and Processes*, Woodhead Publishing Linited, Cambridge, United Kingdom, 2012.
26. R. Coles, D. McDowell and M. J. Kirwan, *Food Packaging Technology*, CRC Press, United States, 2003.

27. T. Dunn, *Manufacturing Flexible Packaging: Materials, Machinery, and Techniques*, William Andrew, Elsevier, 2014.
28. M. Xanthos, in *Functional Fillers for Plastics*, Wiley-VCH Verlag GmbH & Co. KGaA, 2005, pp. 1-16.
29. G. Pritchard, *Novel and Traditional Fillers for Plastics: Technology and Market Developments: a Rapra Industry Analysis Report*, iSmithers Rapra Publishing, 1999.
30. G. Pritchard, *Plastics Additives: A Rapra Market Report*, Rapra Technology Limited, Shropshire, United Kingdom, 2005.
31. J. Jancar, E. Fekete, P. R. Hornsby, J. Jancar, B. Pukanszky and R. N. Rothon, *Mineral Fillers in Thermoplastics I: Raw Materials and Processing*, Springer Berlin Heidelberg, Heidelberg, Germany, 1998.
32. J. J. Kellar, *Functional Fillers and Nanoscale Minerals: New Markets/New Horizons*, Society for Mining, Metallurgy, and Exploration, Inc. (SME), Colorado, United States, 2006.
33. *United States Pat.*, US3442686 A, 1969.
34. *United States Pat.*, US9221956 B2, 2011.
35. H. Chatham, *Surf. Coat. Technol.*, 1996, **78**, 1-9.
36. K. M. Holder, B. R. Spears, M. E. Huff, M. A. Priolo, E. Harth and J. C. Grunlan, *Macromol. Rapid Commun.*, 2014, **35**, 960-964.
37. P. E. Burrows, G. L. Graff, M. E. Gross, P. M. Martin, M. K. Shi, M. Hall, E. Mast, C. Bonham, W. Bennett and M. B. Sullivan, *Displays*, 2001, **22**, 65-69.
38. R. S. Kumar, M. Auch, E. Ou, G. Ewald and C. S. Jin, *Thin Solid Films*, 2002, **417**, 120-126.
39. Y. Dou, S. Xu, X. Liu, J. Han, H. Yan, M. Wei, D. G. Evans and X. Duan, *Adv. Funct. Mater.*, 2014, **24**, 514-521.
40. S. Solovyov and A. Goldman, *Mass Transport & Reactive Barriers in Packaging: Theory, Applications, & Design*, DEStech Pub., 2008.
41. Y. Cui, S. I. Kundalwal and S. Kumar, *Carbon*, 2016, **98**, 313-333.
42. A. Arora and G. W. Padua, *J. Food Sci.*, 2010, **75**, R43-R49.
43. N. Inagaki, S. Tasaka and H. Hiramatsu, *J. Appl. Polym. Sci.*, 1999, **71**, 2091-2100.
44. K. S. Triantafyllidis, P. C. LeBaron, I. Park and T. J. Pinnavaia, *Chem. Mater.*, 2006, **18**, 4393-4398.
45. M. A. Priolo, D. Gamboa, K. M. Holder and J. C. Grunlan, *Nano Lett.*, 2010, **10**, 4970-4974.
46. M. W. Möller, D. A. Kunz, T. Lunkenbein, S. Sommer, A. Nennemann and J. Breu, *Adv. Mater.*, 2012, **24**, 2142-2147.
47. C. N. Wu, T. Saito, S. Fujisawa, H. Fukuzumi and A. Isogai, *Biomacromolecules*, 2012, **13**, 1927-1932.
48. S. Ming, G. Chen, J. He, Y. Kuang, Y. Liu, R. Tao, H. Ning, P. Zhu, Y. Liu and Z. Fang, *Langmuir*, 2017, **33**, 8455-8462.
49. M. Schmid, S. Sängerlaub, O. Miesbauer, V. Jost, J. Werthan, C. Stinga, D. Samain, C. Stramm, K. Noller and K. Müller, *Polym.*, 2014, **6**.
50. F. Hannay, *Rigid Plastics Packaging: Materials, Processes and Applications*, iSmithers Rapra Publishing, 2002.
51. L. Tammaro, V. Vittoria and V. Bugatti, *Eur. Polym. J.*, 2014, **52**, 172-180.
52. T. D. Fornes, P. J. Yoon, H. Keskkula and D. R. Paul, *Polym.*, 2001, **42**, 09929-09940.
53. H. S. Lee, P. D. Fasulo, W. R. Rodgers and D. R. Paul, *Polym.*, 2005, **46**, 11673-11689.
54. W. J. Choi, H. J. Kim, K. H. Yoon, O. H. Kwon and I. C. Hwang, *J. Appl. Polym. Sci.*, 2006, **100**, 4875-4879.

55. T. Pan, S. Xu, Y. Dou, X. Liu, Z. Li, J. Han, H. Yan and M. Wei, *J. Mater. Chem. A*, 2015, **3**, 12350-12356.
56. Y. Dou, A. Zhou, T. Pan, J. Han, M. Wei, D. G. Evans and X. Duan, *Chem. Commun.*, 2014, **50**, 7136-7138.
57. Y. Dou, T. Pan, S. Xu, H. Yan, J. Han, M. Wei, D. G. Evans and X. Duan, *Angew. Chem. Int. Ed.*, 2015, **54**, 9673-9678.
58. L. E. Nielsen, *J. Macromol. Sci., Chem.*, 1967, **1**, 929-942.
59. M. A. Osman, V. Mittal and H. R. Lusti, *Macromol. Rapid Commun.*, 2004, **25**, 1145-1149.
60. T. Ebina and F. Mizukami, *Adv. Mater.*, 2007, **19**, 2450-2453.
61. R. K. Bharadwaj, *Macromolecules*, 2001, **34**, 9189-9192.
62. C. Yang, W. H. Smyrl and E. L. Cussler, *J. Membrane Sci.*, 2004, **231**, 1-12.
63. S. Takahashi, H. A. Goldberg, C. A. Feeney, D. P. Karim, M. Farrell, K. O'Leary and D. R. Paul, *Polym.*, 2006, **47**, 3083-3093.
64. H. E. Miltner, G. V. Assche, A. Pozsgay, B. Pukánszky and B. V. Mele, *Polym.*, 2006, **47**, 826-835.
65. T. V. Duncan, *J. Colloid Interface Sci.*, 2011, **363**, 1-24.
66. M. W. Möller, T. Lunkenbein, H. Kalo, M. Schieder, D. A. Kunz and J. Breu, *Adv. Mater.*, 2010, **22**, 5245-5249.
67. M. Tolinski, *Additives for Polyolefins: Getting the Most out of Polypropylene, Polyethylene and TPO*, Elsevier Science, 2015.
68. T. G. Gopakumar, N. S. Patel and M. Xanthos, *Polym. Compos.*, 2006, **27**, 368-380.
69. L. Zhai, G. Li, Y. Xu, M. Xiao, S. Wang and Y. Meng, *J. Appl. Polym. Sci.*, 2015, **132**, 1-6.
70. S. Sinha Ray and M. Okamoto, *Prog. Polym. Sci.*, 2003, **28**, 1539-1641.
71. C. P. McAdam, N. E. Hudson, J. J. Liggat and R. A. Pethrick, *J. Appl. Polym. Sci.*, 2008, **108**, 2242-2251.
72. M. Leonard, presented in part at the AIMCAL Europe Web Coating Conference, Prague, Czech Republic, 2012.
73. M. Nakaya, A. Uedono and A. Hotta, *Coatings*, 2015, **5**, 987-1001.
74. D. Nwabunma and T. Kyu, *Polyolefin Composites*, Wiley, 2008.
75. S. C. Tjong and Y. W. Mai, *Physical Properties and Applications of Polymer Nanocomposites*, Elsevier Science, 2010.
76. V. Nicolosi, M. Chhowalla, M. G. Kanatzidis, M. S. Strano and J. N. Coleman, *Science*, 2013, **340**.
77. J. T. Chen, Y. J. Fu, Q. F. An, S. C. Lo, S. H. Huang, W. S. Hung, C. C. Hu, K. R. Lee and J. Y. Lai, *Nanoscale*, 2013, **5**, 9081-9088.
78. M. A. Priolo, D. Gamboa and J. C. Grunlan, *Appl. Mater. Interfaces*, 2010, **2**, 312-320.
79. Y. Shu, P. Yin, B. Liang, H. Wang and L. Guo, *Appl. Mater. Interfaces*, 2014, **6**, 15154-15161.
80. Y. Shu, P. Yin, B. Liang, H. Wang and L. Guo, *Ind. Eng. Chem. Res.*, 2015, **54**, 8940-8946.
81. Y. Song, D. A. Hagen, S. Qin, K. M. Holder, K. Falke and J. C. Grunlan, *Appl. Mater. Interfaces*, 2016, **8**, 34784-34790.
82. X. Duan and D. G. Evans, *Layered Double Hydroxides*, Springer, 2006.
83. V. Rives, *Layered Double Hydroxides: Present and Future*, Nova Science Publishers, 2001.
84. R. Salomão, L. M. Milena, M. H. Wakamatsu and V. C. Pandolfelli, *Ceram. Int.*, 2011, **37**, 3063-3070.

85. H. H. Murray, *Applied Clay Mineralogy: Occurrences, Processing and Applications of Kaolins, Bentonites, Palygorskitesepiolite, and Common Clays*, Elsevier Science, 2006.
86. J. H. Choy, S. J. Choi, J. M. Oh and T. Park, *Appl. Clay Sci.*, 2007, **36**, 122-132.
87. F. Bergaya, B. K. G. Theng and G. Lagaly, *Handbook of Clay Science*, Elsevier, Amsterdam, Netherlands, 2011.
88. S. Mohanty, S. K. Nayak, B. S. Kaith and S. Kalia, *Polymer Nanocomposites based on Inorganic and Organic Nanomaterials*, Wiley, 2015.
89. G. Heinrich, *Advanced Rubber Composites*, Springer Science & Business Media, 2011.
90. E. Manasse, *Atti Soc. Toscana Sc. Nat.*, 1915, **24**, 92.
91. W. Feitknecht, *Helv. Chim. Acta.*, 1942, **25**, 555-569.
92. W. Feitknecht and M. Gerber, *Helv. Chim. Acta.*, 1942, **25**, 106-137.
93. R. Allmann, *Acta Crystallographica Section B: Structural Crystallography and Crystal Chemistry*, 1968, **24**, 972-977.
94. H. F. W. Taylor, *Mineral Mag.*, 1969, **37**, 338-342.
95. T. S. Duffy, J. Shu, H. K. Mao and R. J. Hemley, *Phys. Chem. Miner.*, 1995, **22**, 277-281.
96. C. Chen, M. Yang, Q. Wang, J. C. Buffet and D. O'Hare, *J. Mater. Chem. A*, 2014, **2**, 15102-15110.
97. G. Hu, *Synthesis and characterisation of novel layered double hydroxide structures and the development of LDH/polymer nanocomposites*, Doctoral Dissertation, University of Oxford, 2007.
98. G. Marcelin, N. J. Stockhausen, J. F. M. Post and A. Schutz, *J. Phys. Chem.*, 1989, **93**, 4646-4650.
99. M. Chen, W. Shen, X. Lu, R. Zhu, H. He and J. Zhu, *J. Phys. Chem. C.*, 2016, **120**, 12924-12931.
100. A. I. Khan and D. O'Hare, *J. Mater. Chem.*, 2002, **12**, 3191-3198.
101. K. R. Poeppelmeier and S. J. Hwu, *Inorg. Chem.*, 1987, **26**, 3297-3302.
102. C. Forano, T. Hibino, F. Leroux and C. Taviot-Guého, in *Developments in Clay Science*, eds. F. Bergaya, B. K. G. Theng and G. Lagaly, Elsevier, 2006, vol. 1, pp. 1021-1095.
103. S. Velu, K. Suzuki, M. P. Kapoor, S. Tomura, F. Ohashi and T. Osaki, *Chem. Mater.*, 2000, **12**, 719-730.
104. C. I. Markland, *Novel aspects of layered double hydroxide chemistry*, Doctoral Dissertation, University of Oxford, 2013.
105. M. Darder, M. López-Blanco, P. Aranda, F. Leroux and E. Ruiz-Hitzky, *Chem. Mater.*, 2005, **17**, 1969-1977.
106. H. Nakayama, N. Wada and M. Tsuhako, *Int. J. Pharm.*, 2004, **269**, 469-478.
107. J. H. Choy, S. Y. Kwak, J. S. Park, Y. J. Jeong and J. Portier, *J. Am. Ceram. Soc.*, 1999, **121**, 1399-1400.
108. L. Desigaux, M. B. Belkacem, P. Richard, J. Cellier, P. Léone, L. Cario, F. Leroux, C. Taviot-Guého and B. Pitard, *Nano Lett.*, 2006, **6**, 199-204.
109. R. Allmann and H. P. Jepsen, *Neues Jahrbuch für Mineralogie Monatshefte*, 1969, **1969**, 544-551.
110. A. V. Arakcheeva, D. Y. Pushcharovskii, R. K. Rastsvetaeva, D. Atencio and G. U. Lubman, *Crystallography Reports*, 1996, **41**, 972-981.
111. F. Bergaya and G. Lagaly, in *Handbook of Clay Science*, Elsevier, Amsterdam, Netherlands, 2006, vol. 1, ch. 1, pp. 1-18.
112. A. De Roy, C. Forano, K. El Malki and J.-P. Besse, in *Expanded Clays and other microporous solids*, Springer, 1992, pp. 108-169.
113. K. Yan, G. Wu and W. Jin, *Energy Technology*, 2016, **4**, 354-368.

114. M. Richetta, P. Medaglia , A. Mattoccia, A. Varone and R. Pizzoferrato, *J. Mater. Sci. Eng.*, 2017, **6**, 360.
115. W. H. Zhang, X. D. Guo, J. He and Z. Y. Qian, *J. Eur. Ceram. Soc.*, 2008, **28**, 1623-1629.
116. D. E. Sparks, T. Morgan, P. M. Patterson, S. A. Tackett, E. Morris and M. Crocker, *Appl. Catal., B*, 2008, **82**, 190-198.
117. F. Cavani, F. Trifirò and A. Vaccari, *Catal. Today*, 1991, **11**, 173-301.
118. S. K. Yun and T. J. Pinnavaia, *Chem. Mater.*, 1995, **7**, 348-354.
119. Z. Chang, D. G. Evans, X. Duan, C. Vial, J. Ghanbaja, V. Prevot, M. de Roy and C. Forano, *J. Solid State Chem.*, 2005, **178**, 2766-2777.
120. Z. P. Xu, G. Stevenson, C.-Q. Lu and G. Q. Lu, *J. Phys. Chem. B*, 2006, **110**, 16923-16929.
121. Z. P. Xu, G. S. Stevenson, C.-Q. Lu, G. Q. Lu, P. F. Bartlett and P. P. Gray, *J. Am. Ceram. Soc.*, 2006, **128**, 36-37.
122. M. J. Climent, A. Corma, S. Iborra, K. Epping and A. Velty, *J. Catal.*, 2004, **225**, 316-326.
123. F. Prinetto, G. Ghiotti, P. Graffin and D. Tichit, *Microporous Mesoporous Mater.*, 2000, **39**, 229-247.
124. A. I. Vogel and G. Svehla, *Vogel's Qualitative Inorganic Analysis*, Longman, Eastbourne, United Kingdom, 7th edn., 1996.
125. J. M. Oh, S. H. Hwang and J. H. Choy, *Solid State Ionics*, 2002, **151**, 285-291.
126. T. Hibino and H. Ohya, *Appl. Clay Sci.*, 2009, **45**, 123-132.
127. M. Ogawa and H. Kaiho, *Langmuir*, 2002, **18**, 4240-4242.
128. M. Adachi-Pagano, C. Forano and J.-P. Besse, *J. Mater. Chem.*, 2003, **13**, 1988-1993.
129. U. Costantino, F. Marmottini, M. Nocchetti and R. Vivani, *Eur. J. Inorg. Chem.*, 1998, 1439-1446.
130. J. Nývlt, *The Kinetics of Industrial Crystallization*, Elsevier, 1985.
131. J. J. Gilman, *The Art and Science of Growing Crystals*, John Wiley & Sons, 1963.
132. A. Ranodolph, *Theory of Particulate Processes: Analysis and Techniques of Continuous Crystallization*, Academic Press, New York, United States, 2012.
133. P. G. Vekilov, *J. Cryst. Growth*, 2005, **275**, 65-76.
134. K. Okamoto, N. Iyi and T. Sasaki, *Appl. Clay Sci.*, 2007, **37**, 23-31.
135. J. J. Bravo-Suárez, E. A. Páez-Mozo and S. T. Oyama, *Quim. Nova*, 2004, **27**, 601-614.
136. N. Iyi, T. Matsumoto, Y. Kaneko and K. Kitamura, *Chem. Lett.*, 2004, **33**, 1122-1123.
137. N. Iyi, K. Okamoto, Y. Kaneko and T. Matsumoto, *Chem. Lett.*, 2005, **34**, 932-933.
138. N. Iyi and T. Sasaki, *J. Colloid Interface Sci.*, 2008, **322**, 237-245.
139. S. Kannan and R. Vir Jasra, *J. Mater. Chem.*, 2000, **10**, 2311-2314.
140. S. Möhmel, I. Kurzawski, D. Uecker, D. Müller and W. Gessner, *Cryst. Res. Technol.*, 2002, **37**, 359-369.
141. G. Fetter, A. Botello, V. H. Lara and P. Bosch, *J. Porous Mater.*, 2001, **8**, 227-232.
142. Y. Seida, Y. Nakano and Y. Nakamura, *Clays Clay Miner.*, 2002, **50**, 525-532.
143. F. Kovanda, D. Koloušek, Z. Cílová and V. Hulínský, *Appl. Clay Sci.*, 2005, **28**, 101-109.
144. L. Hickey, J. T. Kloprogge and R. L. Frost, *J. Mater. Sci.*, 2000, **35**, 4347-4355.
145. S. Miyata, *Clays Clay Miner*, 1980, **28**, 50-56.
146. A. Faour, V. Prévot and C. Taviot-Gueho, *J. Phys. Chem. Solids*, 2010, **71**, 487-490.
147. F. M. Labajos, V. Rives and M. A. Ulibarri, *J. Mater. Sci.*, 1992, **27**, 1546-1552.
148. P. J. Sideris, U. G. Nielsen, Z. Gan and C. P. Grey, *Science*, 2008, **321**, 113.

149. T. J. Pinnavaia, M. Chibwe, V. R. L. Constantino and S. K. Yun, *Appl. Clay Sci.*, 1995, **10**, 117-129.
150. N. Morel-Desrosiers, J. Pisson, Y. Israeli, C. Taviot-Gueho, J.-P. Besse and J.-P. Morel, *J. Mater. Chem.*, 2003, **13**, 2582-2585.
151. Y. Israeli, C. Taviot-Gueho, J. P. Besse, J. P. Morel and N. Morel-Desrosiers, *J. Chem. Soc., Dalton Trans.*, 2000, 791-796.
152. R. Celis, M. Á. Adelino, B. Gámiz, M. C. Hermosín, W. C. Koskinen and J. Cornejo, *Appl. Clay Sci.*, 2014, **96**, 81-90.
153. K. L. Erickson, T. E. Bostrom and R. L. Frost, *Mater. Lett.*, 2005, **59**, 226-229.
154. F. Millange, R. I. Walton and D. O'Hare, *J. Mater. Chem.*, 2000, **10**, 1713-1720.
155. T. Stanimirova, I. Vergilov, G. Kirov and N. Petrova, *J. Mater. Sci.*, 1999, **34**, 4153-4161.
156. J. Rocha, M. Del Arco, V. Rives and M. A. Ulibarri, *J. Mater. Chem.*, 1999, **9**, 2499-2503.
157. A. J. Marchi and C. R. Apesteguía, *Appl. Clay Sci.*, 1998, **13**, 35-48.
158. H. Pfeiffer, E. Lima, V. Lara and J. S. Valente, *Langmuir*, 2010, **26**, 4074-4079.
159. H. Pfeiffer, L. Martínez, E. Lima, J. Flores, M. A. Vera and J. S. Valente, *J. Phys. Chem. C.*, 2010, **114**, 8485-8492.
160. C. M. R. Wright, K. Ruengkajorn, A. F. R. Kilpatrick, J.-C. Buffet and D. O'Hare, *Inorg. Chem.*, 2017, **56**, 7842-7850.
161. W. T. Reichle, *Solid State Ionics*, 1986, **22**, 135-141.
162. L. T. Zhuravlev, *Colloids Surf., A Physicochem. Eng. Asp.*, 2000, **173**, 1-38.
163. V. Y. Davydov, A. V. Kiselev and L. T. Zhuravlev, *T. Faraday. Soc.*, 1964, **60**, 2254-2264.
164. R. Mueller, H. K. Kammler, K. Wegner and S. E. Pratsinis, *Langmuir*, 2003, **19**, 160-165.
165. M. Lelli, D. Gajan, A. Lesage, M. A. Caporini, V. Vitzthum, P. Miéville, F. Héroguel, F. Rascón, A. Roussey, C. Thieuleux, M. Boualleg, L. Veyre, G. Bodenhausen, C. Coperet and L. Emsley, *J. Am. Ceram. Soc.*, 2011, **133**, 2104-2107.
166. P. J. Bailey, R. A. Coxall, C. M. Dick, S. Fabre, L. C. Henderson, C. Herber, S. T. Liddle, D. Loroño-González, A. Parkin and S. Parsons, *Chem. Eur. J.*, 2003, **9**, 4820-4828.
167. M. Bellotto, B. Rebours, O. Clause, J. Lynch, D. Bazin and E. Elkaïm, *J. Phys. Chem.*, 1996, **100**, 8535-8542.
168. K. K. Rao, M. Gravelle, J. S. Valente and F. Figueras, *J. Catal.*, 1998, **173**, 115-121.
169. Y. You, H. Zhao and G. F. Vance, *Colloids Surf., A Physicochem. Eng. Asp.*, 2002, **205**, 161-172.
170. A. Corma, V. Fornes, F. Rey, A. Cervilla, E. Llopis and A. Ribera, *J. Catal.*, 1995, **152**, 237-242.
171. S. I. Katahira, K. Yasue and M. Inagaki, *J. Mater. Res.*, 2011, **14**, 1178-1180.
172. H. Tagaya, A. Ogata, T. Kuwahara, S. Ogata, M. Karasu, J. I. Kadokawa and K. Chiba, *Microporous Mater.*, 1996, **7**, 151-158.
173. S. Aisawa, H. Hirahara, K. Ishiyama, W. Ogasawara, Y. Umetsu and E. Narita, *J. Solid State Chem.*, 2003, **174**, 342-348.
174. S. Aisawa, H. Hirahara, S. Takahashi, Y. Umetsu and E. Narita, *Chem. Lett.*, 2004, **33**, 306-307.
175. K. Chibwe and W. Jones, *J. Chem. Soc., Chem. Commun.*, 1989, 926-927.
176. F. Kooli, C. Depege, A. Ennaqadi, A. de Roy and J. P. Besse, *Clays Clay Miner.*, 1997, **45**, 92.

177. J. H. Yang, W. Zhang, H. Ryu, J. H. Lee, D. H. Park, J. Y. Choi, A. Vinu, A. A. Elzatahry and J. H. Choy, *J. Mater. Chem. A*, 2015, **3**, 22730-22738.
178. D. Chaara, F. Bruna, M. A. Ulibarri, K. Draoui, C. Barriga and I. Pavlovic, *J. Hazard. Mater.*, 2011, **196**, 350-359.
179. B. Wang, H. Zhang, D. G. Evans and X. Duan, *Mater. Chem. Phys.*, 2005, **92**, 190-196.
180. K. Inomata and M. Ogawa, *Bull. Chem. Soc. Jpn.*, 2006, **79**, 336-342.
181. M. Meyn, K. Beneke and G. Lagaly, *Inorg. Chem.*, 1990, **29**, 5201-5207.
182. H. Kopka, K. Beneke and G. Lagaly, *J. Colloid Interface Sci.*, 1988, **123**, 427-436.
183. R. Trujillano, M. J. Holgado and V. Rives, *Stud. Surf. Sci. Catal.*, 2002, **142**, 1387-1394.
184. R. Rosa, C. Leonelli, C. Villa and G. Priarone, *Journal of Microwave Power and Electromagnetic Energy*, 2013, **47**, 12-23.
185. S. Carlino, *Solid State Ionics*, 1997, **98**, 73-84.
186. N. Iyi, K. Tamura and H. Yamada, *J. Colloid Interface Sci.*, 2009, **340**, 67-73.
187. M. Borja and P. K. Dutta, *J. Phys. Chem.*, 1992, **96**, 5434-5444.
188. S. Miyata and T. Kumura, *Chem. Lett.*, 1973, **2**, 843-848.
189. K. Esumi and S. Yamamoto, *Colloids Surf., A Physicochem. Eng. Asp.*, 1998, **137**, 385-388.
190. N. Nhlapo, T. Motumi, E. Landman, S. M. C. Verryn and W. W. Focke, *J. Mater. Sci.*, 2008, **43**, 1033-1043.
191. M. Adachi Pagano, C. Forano and J. P. Besse, *Chem. Commun.*, 2000, 91-92.
192. J. Zhang, X. Xie, C. Li, H. Wang and L. Wang, *RSC Adv.*, 2015, **5**, 29757-29765.
193. P. Li, F. Lv, Z. Xu, G. Qi and Y. Zhang, *J. Mater. Sci.*, 2013, **48**, 5437-5446.
194. K. Cermelj, *Synthesis and characterisation of layered double hydroxide nanosheets*, Master's Thesis, University of Oxford, 2016.
195. Q. Wang and D. O'Hare, *Chem. Commun.*, 2013, **49**, 6301-6303.
196. C. Chen, A. Wangriya, J. C. Buffet and D. O'Hare, *Dalton Trans.*, 2015, **44**, 16392-16398.
197. Q. Wang, X. Zhang, J. Zhu, Z. Guo and D. O'Hare, *Chem. Commun.*, 2012, **48**, 7450-7452.
198. Q. Wang and D. O'Hare, *Chem. Rev.*, 2012, **112**, 4124-4155.
199. V. V. Naik, T. N. Ramesh and S. Vasudevan, *The Journal of Physical Chemistry Letters*, 2011, **2**, 1193-1198.
200. T. Hibino and W. Jones, *J. Mater. Chem.*, 2001, **11**, 1321-1323.
201. M. Yang, O. McDermott, J. C. Buffet and D. O'Hare, *RSC Adv.*, 2014, **4**, 51676-51682.
202. C. Li, M. Wei, D. G. Evans and X. Duan, *Small*, 2014, **10**, 4469-4486.
203. S. Omwoma, W. Chen, R. Tsunashima and Y. F. Song, *Coord. Chem. Rev.*, 2014, **258–259**, 58-71.
204. S. P. Newman and W. Jones, *New J. Chem.*, 1998, **22**, 105-115.
205. K. H. Goh, T. T. Lim and Z. Dong, *Water Res.*, 2008, **42**, 1343-1368.
206. C. Del Hoyo, *Appl. Clay Sci.*, 2007, **36**, 103-121.
207. L. Du, B. Qu and M. Zhang, *Polym. Degrad. Stab.*, 2007, **92**, 497-502.
208. K. Itaya, H. C. Chang and I. Uchida, *Inorg. Chem.*, 1987, **26**, 624-626.
209. S. Therias, C. Mousty, C. Forano and J. P. Besse, *Langmuir*, 1996, **12**, 4914-4920.
210. K. Yao, M. Taniguchi, M. Nakata, K. Shimazu, M. Takahashi and A. Yamagishi, *J. Electroanal. Chem.*, 1998, **457**, 119-128.
211. M. Morigi, E. Scavetta, M. Berrettoni, M. Giorgetti and D. Tonelli, *Anal. Chim. Acta*, 2001, **439**, 265-272.
212. S. Guo, D. G. Evans and D. Li, *J. Phys. Chem. Solids*, 2006, **67**, 1002-1006.

213. D. G. Evans and X. Duan, *Chem. Commun.*, 2006, 485-496.
214. G. Li and W. Liu, *BioRes.*, 2011, **6**, 1972-1987.
215. S. von Haartman, E. Heikkilä, C. Lange and P. Fardim, *BioRes.*, 2014, **9**, 2274-2288.
216. S. Wang, J. Huang and F. Chen, *BioRes.*, 2012, **7**, 997-1007.
217. *United States Pat.*, US 6682788 B2, 2004.
218. *United States Pat.*, US 6432550 B1, 2002.
219. V. M. Dias, A. Kuznetsova, J. Tedim, A. A. Yaremchenko, M. L. Zheludkevich, I. Portugal and D. V. Evtuguin, *World J. Nano Sci. Eng.*, 2015, **5**, 126-139.
220. V. Marchante and M. Beltrán, in *Polyethylene-Based Blends, Composites and Nanocomposites*, John Wiley & Sons, Inc., 2015, pp. 257-280.
221. V. Rives, F. M. Labajos and M. Herrero, in *Polyethylene-Based Blends, Composites and Nanocomposites*, John Wiley & Sons, Inc., 2015, pp. 163-199.
222. A. Abdellatief and B. A. Welt, *Packag. Technol. Sci.*, 2013, **26**, 281-288.
223. J. Grönfors, *Use of fillers in paper and paperboard grades*, Final Thesis, Tampere University of Applied Sciences, 2010.
224. V. S. Chauhan, S. P. Singh and P. K. Bajpai, *BioRes.*, 2007, **2**, 560-571.
225. I. Ali, *Study of the mechanical behavior of recycled fibers. Applications to papers and paperboards*, Doctoral dissertation, University of Grenoble, 2012.
226. P. Kumar, S. K. Guatam, V. Kumar and S. P. Singh, *BioRes.*, 2009, **4**, 1635-1646.
227. Y. Sang, M. McQuaid and P. Englezos, *BioRes.*, 2011, **6**, 656-671.
228. S. R. Middleton and A. M. Scallan, *J. Pulp Pap. Sci.*, 1989, **15**, J229-J235.
229. *United States Pat.*, US6235150 B1, 2001.
230. M. L. Miller and D. C. Paliwal, *J. Pulp Pap. Sci.*, 1985, **11**, 84-88.
231. S. Mandal and S. Mayadevi, *Chemosphere*, 2008, **72**, 995-998.
232. C. E. Lange, M. Lastusaari, M. Reza, K. S. Latifi, P. Kallio and P. Fardim, *Fibers*, 2015, **3**, 103-133.
233. C. Lange, T. Lundin and P. Fardim, *Holzforschung*, 2012, **66**, 433-441.
234. C. Lange, *Hybridization of pulp fibres with LDH for applications in composites and lightweight fibrous foam*, Doctoral Dissertation, Åbo Akademi University, 2017.
235. T. Hirvikorpi, Doctoral Dissertation, Aalto University, 2011.
236. K. V. Rastogi and P. Samyn, *Coatings*, 2015, **5**, 887-930.
237. R. E. Popil, unpublished work.
238. E. Bohlin, *Surface and porous structure of pigment coatings : Interactions with flexographic ink and effects on print quality*, Doctoral Dissertation, Karlstad University, 2013.
239. E. Lehtinen, *Pigment coating and surface sizing of paper*, Tappi, 2000.
240. V. Mannari and C. J. Patel, *Understanding Coatings Raw Materials*, Vincentz Network, 2015.
241. L. Y. Mwaikambo and M. P. Ansell, *J. Appl. Polym. Sci.*, 2002, **84**, 2222-2234.
242. T. P. Nevell and S. H. Zeronian, *Cellulose Chemistry and its Applications*, Halsted Press, John Wiley, New York, United States, 1985.
243. A. Oushabi, S. Sair, F. Oudrhiri Hassani, Y. Abboud, O. Tanane and A. El Bouari, *S. Afr. J. Chem. Eng.*, 2017, **23**, 116-123.
244. N. Le Moigne, *Swelling and dissolution mechanisms of cellulose fibres*, Doctoral Dissertation, École Nationale Supérieure des Mines de Paris, 2008.
245. T. M. Lacerda, M. P. de Paula, M. D. Zambon and E. Frollini, *Cellulose*, 2012, **19**, 351-362.
246. K. H. Choi, A. R. Kim and B. U. Cho, *BioRes.*, 2016, **11**, 3769-3782.
247. N. Le Moigne and P. Navard, *Cellulose*, 2010, **17**, 31-45.

248. S. Zhang, W. C. Wang, F. X. Li and J. Y. Yu, *Cellul. Chem. Technol.*, 2013, **47**, 671-679.
249. L. Yang, J. Cao, Y. Jin, H. M. Chang, H. Jameel, R. Phillips and Z. Li, *Bioresour. Technol.*, 2012, **124**, 283-291.
250. D. Ray, M. Das and D. Mitra, *BioRes.*, 2009, **4**, 730-739.
251. M. P. Ho, H. Wang, K. T. Lau, J. H. Lee and D. Hui, *Compos. Part B-Eng.*, 2012, **43**, 2801-2812.
252. A. Valadez-Gonzalez, J. M. Cervantes, R. Olayo and P. J. Herrera-Franco, *Compos. Part B-Eng.*, 1999, **30**, 309-320.
253. M. N. Costa, B. Veigas, J. M. Jacob, D. S. Santos, J. Gomes, P. V. Baptista, R. Martins, J. Inácio and E. Fortunato, *Nanotechnology*, 2014, **25**, 1-12.
254. M. S. Ilvessalo-Pfäffli, *Fiber Atlas: Identification of Papermaking Fibers*, Springer Science & Business Media, 1995.
255. *United States Pat.*, US5580354 A, 1996.
256. *United States Pat.*, US3954553 A, 1976.
257. L. Jiao, J. Ma and H. Dai, *PLoS One*, 2015, **10**, 1-16.
258. J. Perel, *J. Text. Inst.*, 1990, **81**, 241-244.
259. L. Segal, J. J. Creely, A. E. Martin and C. M. Conrad, *Text. Res. J.*, 1959, **29**, 786-794.
260. S. Awadel-Karim, M. M. Nazhad and L. Paszner, *Holzforschung*, 1999, **53**, 1.
261. B. Balcomb, M. Singh and S. Singh, *ChemistryOpen*, 2015, **4**, 137-145.
262. S. Britto, S. Joseph and P. Vishnu Kamath, *Journal of Chemical Sciences*, 2010, **122**, 751-756.
263. W. Yang, Y. Kim, P. K. T. Liu, M. Sahimi and T. T. Tsotsis, *Chem. Eng. Sci.*, 2002, **57**, 2945-2953.
264. M. Benítez-Guerrero, J. López-Beceiro, P. E. Sánchez-Jiménez and J. Pascual-Cosp, *Thermochim. Acta*, 2014, **581**, 70-86.
265. H. Yang, R. Yan, H. Chen, D. H. Lee and C. Zheng, *Fuel*, 2007, **86**, 1781-1788.
266. M. Benítez-Guerrero, J. López-Beceiro, P. E. Sánchez-Jiménez and J. Pascual-Cosp, *Thermochim. Acta*, 2014, **581**, 70-86.
267. S. K. Sundaram, S. Jayabal and K. Nijandhan, *Cellul. Chem. Technol.*, 2015, **49**, 61-64.
268. E. Evans, E. F. M. Gabriel, W. K. T. Coltro and C. D. Garcia, *The Analyst*, 2014, **139**, 2127-2132.
269. R. W. Hurter and P. Eng, *Proceedings of the World Wood Summit: 31 August-2 Sept 1998*, 1998.
270. L. D. Shackford, presented in part at the 36th international pulp and paper congress and exhibition, São Paulo, Brazil, 2003.
271. M. F. Rosa, E. S. Medeiros, J. A. Malmonge, K. S. Gregorski, D. F. Wood, L. H. C. Mattoso, G. Glenn, W. J. Orts and S. H. Imam, *Carbohydr. Polym.*, 2010, **81**, 83-92.
272. T. E. Motaung and A. Mtibe, *Mater. Sci. Appl.*, 2015, **6**, 1022-1032.
273. K. Klemkaite, I. Prosycevas, R. Taraskevicius, A. Khinsky and A. Kareiva, *Cent. Eur. J. Chem.*, 2011, **9**, 275-282.
274. C. Plomion, G. Leprovost and A. Stokes, *Plant Physiol.*, 2001, **127**, 1513.
275. N. Gierlinger and M. Schwanninger, *Plant Physiol.*, 2006, **140**, 1246-1254.
276. C. Uma Maheswari, K. Obi Reddy, E. Muzenda, B. R. Guduri and A. Varada Rajulu, *Biomass Bioenergy*, 2012, **46**, 555-563.
277. M. Sain and S. Panthapulakkal, *Ind. Crops Prod.*, 2006, **23**, 1-8.
278. B. Xiao, X. F. Sun and R. Sun, *Polym. Degrad. Stab.*, 2001, **74**, 307-319.
279. C. Pappas, P. A. Tarantilis, I. Daliani, T. Mavromoustakos and M. Polissiou, *Ultrason. Sonochem.*, 2002, **9**, 19-23.

280. M. Aramendia, V. Borau, C. Jiménez, J. M. Marinas, J. R. Ruiz and F. J. Urbano, *J. Solid State Chem.*, 2002, **168**, 156-161.
281. C. O. Oriakhi, I. V. Farr and M. M. Lerner, *J. Mater. Chem.*, 1996, **6**, 103-107.
282. I. Thorn and C. O. Au, *Applications of Wet-End Paper Chemistry*, Springer, 2009.
283. C. Dong, D. Song, T. Patterson, A. Ragauskas and Y. Deng, *Ind. Eng. Chem. Res.*, 2008, **47**, 8430-8435.
284. Y. V. Sood, R. Tyagi, S. Tyagi, P. C. Pande and R. Tondon, *J. Sci. Ind. Res.*, 2010, **69**, 300-304.
285. R. Schmut, *Ind. Eng. Chem. Res.*, 1964, **56**, 28-33.
286. M. A. Hubbe, *BioRes.*, 2014, **9**, 1-130.
287. A. Johansson, *Correlations between fibre properties and paper properties*, Master's Thesis, KTH Royal Institute of Technology, 2011.
288. R. S. Abdullah and H. J. Mustaffa, *Sains Malaysiana*, 2010, **39**, 239-242.
289. K. Khwaldia, E. Arab-Tehrany and S. Desobry, *Compr. Rev. Food Sci. Food Saf.*, 2010, **9**, 82-91.
290. P. Bajpai, *Pulp and Paper Industry: Chemicals*, Elsevier Science, 2015.
291. Q. Tao, J. Yuan, R. L. Frost, H. He, P. Yuan and J. Zhu, *Appl. Clay Sci.*, 2009, **45**, 262-269.
292. N. Iyi, K. Tamura and H. Yamada, *J. Colloid Interface Sci.*, 2009, **340**, 67-73.
293. A. Racaud, R. Antoine, P. Dugourd and J. Lemoine, *J. Am. Soc. Mass. Spectrom.*, 2010, **21**, 2077-2084.
294. M. Watanabe and S. Fujihara, *J. Solid State Chem.*, 2014, **210**, 130-137.
295. H. Chen, F. Zhang, S. Fu and X. Duan, *Adv. Mater.*, 2006, **18**, 3089-3093.
296. Z. P. Xu, Y. Jin, S. Liu, Z. P. Hao and G. Q. Lu, *J. Colloid Interface Sci.*, 2008, **326**, 522-529.
297. Q. Zheng and C. Lü, *Procedia IUTAM*, 2014, **10**, 462-475.
298. Z. Yoshimitsu, A. Nakajima, T. Watanabe and K. Hashimoto, *Langmuir*, 2002, **18**, 5818-5822.
299. I. Dékány, F. Berger, K. Imrik and G. Lagaly, *Colloid. Polym. Sci.*, 1997, **275**, 681-688.
300. S. Wiesen, N. Tippkötter, K. Muffler, K. Suck, U. Sohling, F. Ruf and R. Ulber, *Adsorption*, 2015, **21**, 459-466.
301. T. Zhang, Y. Zhou, Y. Wang, X. Bu, H. Wang and M. Zhang, *Appl. Clay Sci.*, 2015, **103**, 67-70.
302. P. Mukerjee and K. J. Mysels, *Critical micelle concentrations of aqueous surfactant systems*, National Bureau of Standards, National Bureau of Standards, Washington D.C., United States, 1971.
303. N. Iyi, K. Tamura and H. Yamada, *J. Colloid Interface Sci.*, 2009, **340**, 67-73.
304. F. R. Costa, A. Leuteritz, U. Wagenknecht, D. Jehnichen, L. Häußler and G. Heinrich, *Appl. Clay Sci.*, 2008, **38**, 153-164.
305. C. Nyambo, P. Songtipya, E. Manias, M. M. Jimenez-Gasco and C. A. Wilkie, *J. Mater. Chem.*, 2008, **18**, 4827-4838.
306. S. Kubik, *Chem. Soc. Rev.*, 2009, **38**, 585-605.
307. O. Pedersen, T. D. Colmer and K. Sand-Jensen, *Frontiers in Plant Science*, 2013, **4**, 140.
308. P. Roach, N. J. Shirtcliffe and M. I. Newton, *Soft Matter*, 2008, **4**, 224-240.
309. Q. Sun, F. J. Schork and Y. Deng, *Compos. Sci. Technol.*, 2007, **67**, 1823-1829.
310. R. Ma, Z. Liu, L. Li, N. Iyi and T. Sasaki, *J. Mater. Chem.*, 2006, **16**, 3809-3813.
311. Q. Wang, H. H. Tay, Z. Guo, L. Chen, Y. Liu, J. Chang, Z. Zhong, J. Luo and A. Borgna, *Appl. Clay Sci.*, 2012, **55**, 18-26.

312. S. O'Leary, D. O'Hare and G. Seeley, *Chem. Commun.*, 2002, 1506-1507.
313. Q. Wu, A. Olafsen, Ø. B. Vistad, J. Roots and P. Norby, *J. Mater. Chem.*, 2005, **15**, 4695-4700.
314. I. Smallwood, *Handbook of Organic Solvent Properties*, Butterworth-Heinemann, 2012.
315. V. Drits, J. Srodon and D. D. Eberl, *Clays Clay Miner.*, 1997, **45**, 461-475.
316. M. Schmal, *Heterogeneous Catalysis and its Industrial Applications*, Springer International Publishing, 2016.
317. M. Thommes, K. Kaneko, A. V. Neimark, J. P. Olivier, F. Rodriguez-Reinoso, J. Rouquerol and K. S. W. Sing, *Pure Appl. Chem.*, 2015, **87**, 1051-1069.
318. G. Carja, R. Nakamura, T. Aida and H. Niiyama, *Microporous Mesoporous Mater.*, 2001, **47**, 275-284.
319. P. Gonzalez Rodriguez, M. de Ruiter, T. Wijnands and J. E. ten Elshof, *Sci. Rep.*, 2017, **7**, 481.
320. K. S. W. Sing, *Pure Appl. Chem.*, 1985, **57**, 603-619.
321. B. D. Zdravkov, J. J. Čermák, M. Šefara and J. Janků, *Cent. Eur. J. Chem.*, 2007, **5**, 385-395.
322. J. Rouquerol, D. Avnir, C. W. Fairbridge, D. H. Everett, J. M. Haynes, N. Pernicone, J. D. F. Ramsay, K. S. W. Sing and K. K. Unger, *Pure Appl. Chem.*, 1994, **66**, 1739-1758.
323. J. Haber, *Pure Appl. Chem.*, 1991, **63**, 1227-1246.
324. L. Pauling, *The Nature of the Chemical Bond and the Structure of Molecules and Crystals: An Introduction to Modern Structural Chemistry*, Cornell University Press, 1960.
325. A. D. McNaught and A. Wilkinson, *IUPAC. Compendium of Chemical Terminology, 2nd ed. (the "Gold Book")*, WileyBlackwell; 2nd Revised edition edition.
326. S. B. Hendricks, O. R. Wulf, G. E. Hilbert and U. Liddel, *J. Am. Ceram. Soc.*, 1936, **58**, 1991-1996.
327. G. R. Desiraju and T. Steiner, *The weak hydrogen bond: in structural chemistry and biology*, Oxford University Press, 2001.
328. L. C. Allen and P. A. Kollman, *Chem. Rev*, 1972, **72**, 283.
329. E. S. Kryachko, A. Karpfen and F. Remacle, *J. Phys. Chem. A*, 2005, **109**, 7309-7318.
330. G. Marie-Pierre, S. Michiel and S. Marialore, *J. Phys.: Condens. Matter*, 2012, **24**, 124106.
331. V. Erastova, M. T. Degiacomi, D. O'Hare and H. C. Greenwell, *RSC Adv.*, 2017, **7**, 5076-5083.
332. K. Kulińska and M. Wiewiórowski, *Can. J. Chem.*, 1988, **66**, 2166-2171.
333. T. M. Letcher, *Thermodynamics, Solubility and Environmental Issues*, Elsevier, 2007.
334. B. Bozbiyik, T. Duerinck, J. Lannoeye, D. E. De Vos, G. V. Baron and J. F. M. Denayer, *Microporous Mesoporous Mater.*, 2014, **183**, 143-149.
335. C. F. Poole, in *The Essence of Chromatography*, Elsevier Science, Amsterdam, 2003, ch. Chapter 4, p. 267.
336. A. van der Pol, B. L. Mojet, E. van de Ven and E. de Boer, *J. Phys. Chem.*, 1994, **98**, 4050-4054.
337. P. J. Sideris, F. Blanc, Z. Gan and C. P. Grey, *Chem. Mater.*, 2012, **24**, 2449-2461.
338. J. P. Yesinowski, H. Eckert and G. R. Rossman, *J. Am. Ceram. Soc.*, 1988, **110**, 1367-1375.
339. S. Cadars, G. Layrac, C. Gérardin, M. Deschamps, J. R. Yates, D. Tichit and D. Massiot, *Chem. Mater.*, 2011, **23**, 2821-2831.
340. U. Sternberg and E. Brunner, *J. Magn. Reson., Ser A.*, 1994, **108**, 142-150.

341. N. D. Jensen, M. Bjerring and U. G. Nielsen, *Solid State Nucl. Magn. Reson.*, 2016, **78**, 9-15.
342. M. A. Aramendia, V. Borau, C. Jiménez, J. M. Marinas, F. J. Romero and J. R. Ruiz, *J. Solid State Chem.*, 1997, **131**, 78-83.
343. F. Rey, V. Fornes and J. M. Rojo, *J. Chem. Soc., Faraday Trans.*, 1992, **88**, 2233-2238.
344. L. E. Nielsen, *J. Macromol. Sci. A*, 1967, **1**, 929-942.
345. M. W. Möller, T. Lunkenbein, H. Kalo, M. Schieder, D. A. Kunz and J. Breu, *Adv. Mater.*, 2010, **22**, 5245-5249.
346. Z. Tang, N. A. Kotov, S. Magonov and B. Ozturk, *Nat. Mater.*, 2003, **2**, 413-418.
347. I. A. Aksay, M. Trau, S. Manne, I. Honma, N. Yao, L. Zhou, P. Fenter, P. M. Eisenberger and S. M. Gruner, *Science*, 1996, **273**, 892.
348. K. S. Aneja, H. L. M. Böhm, A. S. Khanna and S. Böhm, *FlatChem*, 2017, **1**, 11-19.
349. Y. Hernandez, V. Nicolosi, M. Lotya, F. M. Blighe, Z. Sun, S. De, I. T. McGovern, B. Holland, M. Byrne, Y. K. Gun'Ko, J. J. Boland, P. Niraj, G. Duesberg, S. Krishnamurthy, R. Goodhue, J. Hutchison, V. Scardaci, A. C. Ferrari and J. N. Coleman, *Nat. Nanotechnol.*, 2008, **3**, 563-568.
350. M. Lotya, Y. Hernandez, P. J. King, R. J. Smith, V. Nicolosi, L. S. Karlsson, F. M. Blighe, S. De, Z. Wang, I. T. McGovern, G. S. Duesberg and J. N. Coleman, *J. Am. Ceram. Soc.*, 2009, **131**, 3611-3620.
351. U. Khan, A. O'Neill, M. Lotya, S. De and J. N. Coleman, *Small*, 2010, **6**, 864-871.
352. S. Vadukumpully, J. Paul and S. Valiyaveettil, *Carbon*, 2009, **47**, 3288-3294.
353. Y. Chen, G. Yang, Z. Zhang, X. Yang, W. Hou and J.-J. Zhu, *Nanoscale*, 2010, **2**, 2131-2138.
354. A. V. Murugan, A. K. Viswanath, C. S. Gopinath and K. Vijayamohanan, *J. Appl. Phys.*, 2006, **100**, 074319.
355. G. Alberti, C. Dionigi, E. Giontella, S. Murcia-Mascarós and R. Vivani, *J. Colloid Interface Sci.*, 1997, **188**, 27-31.
356. L. Sun, W. J. Boo, D. Sun, A. Clearfield and H.-J. Sue, *Chem. Mater.*, 2007, **19**, 1749-1754.
357. P. F. Luckham and S. Rossi, *Adv. Colloid Interface Sci.*, 1999, **82**, 43-92.
358. Y. Cui, S. Kumar, B. Rao Kona and D. van Houcke, *RSC Adv.*, 2015, **5**, 63669-63690.
359. W. Hou, L. Kang, R. Sun and Z.-H. Liu, *Colloids Surf., A Physicochem. Eng. Asp.*, 2008, **312**, 92-98.
360. Z. Liu, R. Ma, M. Osada, N. Iyi, Y. Ebina, K. Takada and T. Sasaki, *J. Am. Ceram. Soc.*, 2006, **128**, 4872-4880.
361. F. Leroux and J. P. Besse, *Chem. Mater.*, 2001, **13**, 3507-3515.
362. Z. h. Liu, X. Yang, Y. Makita and K. Ooi, *Chem. Mater.*, 2002, **14**, 4800-4806.
363. J. Miao, M. Xue, H. Itoh and Q. Feng, *J. Mater. Chem.*, 2006, **16**, 474-480.
364. M. Yoonessi, H. Toghiani, T. L. Daulton, J.-S. Lin and C. U. Pittman, *Macromolecules*, 2005, **38**, 818-831.
365. J. Yu, Q. Wang, D. O'Hare and L. Sun, *Chem. Soc. Rev.*, 2017.
366. M. Jobbágy and N. Iyi, *J. Phys. Chem. C.*, 2010, **114**, 18153-18158.
367. R. Ma and T. Sasaki, *Adv. Mater.*, 2010, **22**, 5082-5104.
368. N. Mao, C. H. Zhou, D. S. Tong, W. H. Yu and C. X. Cynthia Lin, *Appl. Clay Sci.*, 2017, **144**, 60-78.
369. J. Yu, B. R. Martin, A. Clearfield, Z. Luo and L. Sun, *Nanoscale*, 2015, **7**, 9448-9451.
370. J. Yu, J. Liu, A. Clearfield, J. E. Sims, M. T. Speiegle, S. L. Suib and L. Sun, *Inorg. Chem.*, 2016, **55**, 12036-12041.
371. T. B. Hur, T. X. Phuoc and M. K. Chyu, *J. Appl. Phys.*, 2010, **108**, 114312.

372. G. Hu, N. Wang, D. O'Hare and J. Davis, *Chem. Commun.*, 2006, 287-289.
373. Y. Wei, F. Li and L. Liu, *RSC Adv.*, 2014, **4**, 18044-18051.
374. C. Forano, T. Hibino, F. Leroux and C. Taviot-Guého, *Developments in Clay Science*, 2006, **1**, 1021-1095.
375. T. Hibino, *Chem. Mater.*, 2004, **16**, 5482-5488.
376. L. Li, R. Ma, Y. Ebina, N. Iyi and T. Sasaki, *Chem. Mater.*, 2005, **17**, 4386-4391.
377. S. Aisawa, H. Kudo, T. Hoshi, S. Takahashi, H. Hirahara, Y. Umetsu and E. Narita, *J. Solid State Chem.*, 2004, **177**, 3987-3994.
378. D. G. Crivoi, *Hybrid materials: discovering properties and mechanisms*, Doctoral Dissertation, Universitat Rovira i Virgili, 2016.
379. J. Yu and D. O'Hare, *Preparation of LDH for gas barrier coatings*, Chemistry, University of Oxford, Centre of excellence, 2017.
380. T. Hibino and M. Kobayashi, *J. Mater. Chem.*, 2005, **15**, 653-656.
381. Q. Wu, A. O. Sjastad, O. B. Vistad, K. D. Knudsen, J. Roots, J. S. Pedersen and P. Norby, *J. Mater. Chem.*, 2007, **17**, 965-971.
382. Q. Wu, A. Olafsen, O. B. Vistad, J. Roots and P. Norby, *J. Mater. Chem.*, 2005, **15**, 4695-4700.
383. P. Mongondry, J. F. Tassin and T. Nicolai, *J. Colloid Interface Sci.*, 2005, **283**, 397-405.
384. A. Mourchid, A. Delville, J. Lambard, E. LeColier and P. Levitz, *Langmuir*, 1995, **11**, 1942-1950.
385. N. Iyi, S. Ishihara, Y. Kaneko and H. Yamada, *Langmuir*, 2013, **29**, 2562-2571.
386. S. Aisawa, S. Takahashi, W. Ogasawara, Y. Umetsu and E. Narita, *J. Solid State Chem.*, 2001, **162**, 52-62.
387. N. Iyi, Y. Ebina and T. Sasaki, *J. Mater. Chem.*, 2011, **21**, 8085-8095.
388. N. Iyi, Y. Ebina and T. Sasaki, *Langmuir*, 2008, **24**, 5591-5598.
389. S. Aisawa, S. Sasaki, S. Takahashi, H. Hirahara, H. Nakayama and E. Narita, *J. Phys. Chem. Solids*, 2006, **67**, 920-925.
390. R. Pethig, *IEEE Transactions on Electrical Insulation*, 1984, **EI-19**, 453-474.
391. W. M. Arnold and U. Zimmermann, *Biochem. Soc. Trans.*, 1993, **21**, 475S.
392. V. Erastova, M. T. Degiacomi, D. G. Fraser and H. C. Greenwell, *Nat. Commun.*, 2017, **8**, 2033.
393. M. Onikata, M. Kondo and S. Yamanaka, *Clays Clay Miner.*, 1999, **47**, 678.
394. C. B. Ching, K. Hidajat and M. S. Uddin, *Sep. Sci. Technol.*, 1989, **24**, 581-597.
395. S. P. Newman, T. Di Cristina, P. V. Coveney and W. Jones, *Langmuir*, 2002, **18**, 2933-2939.
396. M. S. San Román and M. J. Holgado, *Open J. Inorg. Chem.*, 2015, **5**, 52.
397. M. J. Hernandez-Moreno, M. A. Ulibarri, J. L. Rendon and C. J. Serna, *Phys. Chem. Miner.*, 1985, **12**, 34-38.
398. B. Salopek, D. Krasic and S. Filipovic, *Rudarsko-geolosko-naftni zbornik*, 1992, **4**, 147.
399. J. Y. Lee, G. H. Gwak, H. M. Kim, T. i. Kim, G. J. Lee and J. M. Oh, *Appl. Clay Sci.*, 2016, **134**, 44-49.
400. Z. P. Xu, G. S. Stevenson, C. Q. Lu, G. Q. Lu, P. F. Bartlett and P. P. Gray, *J. Am. Chem. Soc.*, 2006, **128**, 36.
401. R. Rojas Delgado, M. Arandigoyen Vidaurre, C. P. De Pauli, M. A. Ulibarri and M. J. Avena, *J. Colloid Interface Sci.*, 2004, **280**, 431-441.
402. B. Vincent, *Adv. Colloid Interface Sci.*, 1974, **4**, 193-277.
403. I. Ostolska and M. Wiśniewska, *Colloid. Polym. Sci.*, 2014, **292**, 2453-2464.
404. A. A. Tsukanov and S. G. Psakhie, *Sci. Rep.*, 2016, **6**, 19986.

405. L. Jie, L. Yuwen, S. Jingyan, W. Zhiyong, H. Ling, Y. Xi and W. Cunxin, *Thermochim. Acta*, 2008, **467**, 20-29.
406. G. Choi, J. H. Yang, G. Y. Park, A. Vinu, A. Elzatahry, C. H. Yo and J. H. Choy, *Eur. J. Inorg. Chem.*, 2015, **2015**, 925-930.
407. A. Di Bitetto, G. Kervern, E. André, P. Durand and C. Carteret, *J. Phys. Chem. C.*, 2017, **121**, 6104-6112.
408. T. Stanimirova, G. Kirov and E. Dinolova, *J. Mater. Sci. Lett.*, 2001, **20**, 453-455.
409. T. Stanimirova and G. Kirov, *Appl. Clay Sci.*, 2003, **22**, 295-301.
410. T. Stanimirova and V. Balek, *J. Therm. Anal. Calorim.*, 2008, **94**, 477-481.
411. E. H. Ajandouz and A. Puigserver, *J. Agric. Food. Chem.*, 1999, **47**, 1786-1793.
412. D. Giscard, T. Kamgaing, R. C. T. Temgoua, E. Ymele, F. M. M. Tchieno and I. K. Tonlé, *Int. J. Sci. Basic Appl. Res.*, 2016, **5**.
413. O. Onija, G. Borodi, I. Kacso, M. N. Pop, D. Dadarlat, I. Bratu and N. Jumate, *AIP Conf. Proc.*, 2012, **1425**, 35-38.
414. K. Okudaira, Y. Kameshima, T. Isobe, A. Nakajima and K. Okada, *J. Jpn. Soc. Colour Mater.*, 2010, **84**, 2-6.
415. N. Farmer, in *Trends in Packaging of Food, Beverages and Other Fast-Moving Consumer Goods (FMCG)*, Woodhead Publishing, Cambrigde, United Kingdom, 2013, p. 344.
416. M. W. Möller, D. A. Kunz, T. Lunkenbein, S. Sommer, A. Nennemann and J. Breu, *Adv. Mater.*, 2012, **24**, 2142-2147.
417. H. Bai, C. Huang, H. Xiu, Q. Zhang, H. Deng, K. Wang, F. Chen and Q. Fu, *Biomacromolecules*, 2014, **15**, 1507-1514.
418. M. A. Osman, V. Mittal, M. Morbidelli and U. W. Suter, *Macromolecules*, 2003, **36**, 9851-9858.
419. D. A. Hagen, L. Saucier and J. C. Grunlan, *ACS Appl. Mater. Interfaces*, 2014, **6**, 22914-22919.
420. J. J. Kochumalayil and L. A. Berglund, in *Encyclopedia of Polymeric Nanomaterials*, eds. S. Kobayashi and K. Müllen, Springer Berlin Heidelberg, Berlin, Heidelberg, 2014, pp. 1-8.
421. L. Sun, W. J. Boo, A. Clearfield, H. J. Sue and H. Q. Pham, *J. Membrane Sci.*, 2008, **318**, 129-136.
422. L. W. Beatty and I. Penboss, in *Surface Coatings: Volume 1 Raw Materials and Their Usage*, Springer Netherlands, Dordrecht, 1993, pp. 325-331.
423. H. C. Langowski, in *Plastic Packaging*, Wiley-VCH Verlag GmbH & Co. KGaA, 2008, pp. 297-347.
424. H. D. Huang, P. G. Ren, J. Chen, W. Q. Zhang, X. Ji and Z. M. Li, *J. Membrane Sci.*, 2012, **409**, 156-163.
425. C. Andersson, *Packag. Technol. Sci.*, 2008, **21**, 339-373.
426. D. R. Paul and L. M. Robeson, *Polym.*, 2008, **49**, 3187-3204.
427. Å. Nyflött, *Structural studies and modelling of oxygen transport in barrier materials for food packaging*, Doctoral Dissertation, Karlstad University, 2014.
428. H. I. Elim, B. Cai, Y. Kurata, O. Sugihara, T. Kaino, T. Adschiri, A.-L. Chu and N. Kambe, *J. Phys. Chem. B*, 2009, **113**, 10143-10148.
429. T. Itoh, T. Uchida, N. Izu, I. Matsubara and W. Shin, *Materials*, 2013, **6**, 2119-2129.
430. F. Bertrand, S. A. German, A. Anwar, V. Irune, B. Gemma, R. D. M. Yolanda and B. Lennart, *Sci. Technol. Adv. Mat.*, 2013, **14**, 023001.
431. Z. W. Wicks, F. N. Jones, S. P. Pappas and D. A. Wicks, *Organic Coatings: Science and Technology*, Wiley, New Jersey, United States, 2007.

432. S. Miyata, *Clays Clay Miner.*, 1980, **28**, 50-56.
433. G. Abellan, E. Coronado, C. Marti-Gastaldo, E. Pinilla-Cienfuegos and A. Ribera, *J. Mater. Chem.*, 2010, **20**, 7451-7455.
434. J. Liang, R. Ma, N. Iyi, Y. Ebina, K. Takada and T. Sasaki, *Chem. Mater.*, 2010, **22**, 371-378.
435. W. Bao, J. Wang, Q. Wang, D. O'Hare and Y. Wan, 2016, **6**, 1-6.
436. F. Song and X. Hu, 2014, **5**, 1-9.
437. E. Kanezaki, *Inorg. Chem.*, 1998, **37**, 2588-2590.
438. S. Mallakpour and M. Dinari, *Prog. Org. Coat.*, 2014, **77**, 583-589.
439. E. Angelescu, O. D. Pavel, R. Bîrjega, M. Florea and R. Zăvoianu, *Appl. Catal., A*, 2008, **341**, 50-57.
440. A. R. Auxilio, P. C. Andrews, P. C. Junk and L. Spiccia, *Dyes and Pigments*, 2009, **81**, 103-112.
441. M. A. Ulibarri, I. Pavlovic, C. Barriga, M. C. Hermosín and J. Cornejo, *Appl. Clay Sci.*, 2001, **18**, 17-27.
442. O. D. Pavel, R. Bîrjega, M. Che, G. Costentin, E. Angelescu and S. Şerban, *Catal. Commun.*, 2008, **9**, 1974-1978.
443. J. Palomeque, J. Lopez and F. Figueras, *J. Catal.*, 2002, **211**, 150-156.
444. A. E. Palomares, J. G. Prato, F. Rey and A. Corma, *J. Catal.*, 2004, **221**, 62-66.
445. K. Takehira, T. Kawabata, T. Shishido, K. Murakami, T. Ohi, D. Shoro, M. Honda and K. Takaki, *J. Catal.*, 2005, **231**, 92-104.
446. S. Lowell and J. E. Shields, *Powder surface area and porosity*, Springer Science & Business Media, 2013.
447. O. P. Ferreira, O. L. Alves, D. X. Gouveia, A. G. Souza Filho, J. A. C. de Paiva and J. M. Filho, *J. Solid State Chem.*, 2004, **177**, 3058-3069.
448. V. R. L. Constantino and T. J. Pinnavaia, *Inorg. Chem.*, 1995, **34**, 883-892.
449. Y. Zhao, J. G. Li, F. Fang, N. Chu, H. Ma and X. Yang, *Dalton Trans.*, 2012, **41**, 12175-12184.
450. F. Winter, X. Xia, B. P. C. Hereijgers, J. H. Bitter, A. J. van Dillen, M. Muhler and K. P. de Jong, *J. Phys. Chem. B*, 2006, **110**, 9211-9218.
451. G. Mascolo and M. C. Mascolo, *Microporous Mesoporous Mater.*, 2015, **214**, 246-248.
452. K. Waizumi, S. Nawata and A. Kimura, *J. Jpn. Soc. Microgravity Appl.*, 2008, **25**.
453. X. Sun, E. Neuperger and S. K. Dey, *J. Colloid Interface Sci.*, 2015, **459**, 264-272.
454. X. Xu, D. Li, J. Song, Y. Lin, Z. Lv, M. Wei and X. Duan, *Particuology*, 2010, **8**, 198-201.
455. K. Okamoto, N. Iyi and T. Sasaki, *Appl. Clay Sci.*, 2007, **37**, 23-31.
456. W. N. Budhysutanto, F. J. Van Den Bruele, B. D. Rossenaar, D. Van Agterveld, W. J. P. Van Enckevort and H. J. M. Kramer, *J. Cryst. Growth*, 2011, **318**, 110-116.
457. C. X. Liu and W. G. Hou, *J. Dispersion Sci. Technol.*, 2009, **30**, 174-177.
458. Z. P. Xu and G. Q. Lu, *Chem. Mater.*, 2005, **17**, 1055-1062.
459. W. J. P. van Enckevort, *J. Cryst. Growth*, 2003, **259**, 190-207.
460. T. Zhang, H. Yu, Y. Zhou, J. Rong, F. Qiu and Y. Zhang, *RSC Adv.*, 2015, **5**, 82415-82420.
461. C. B. Frech, *J. Chem. Educ.*, 2002, **79**, 1072.
462. K. Qiu and A. N. Netravali, *Compos. Sci. Technol.*, 2012, **72**, 1588-1594.
463. V. Goodship and D. K. Jacobs, *Polyvinyl alcohol: materials, processing and applications*, Smithers Rapra Technology, 2009.
464. S. R. Kanatt, M. S. Rao, S. P. Chawla and A. Sharma, *Food Hydrocolloids*, 2012, **29**, 290-297.

465. C. C. DeMerlis and D. R. Schoneker, *Food Chem. Toxicol.*, 2003, **41**, 319-326.
466. D. Chen, X. Wang, T. Liu, X. Wang and J. Li, *ACS Appl. Mater. Interfaces*, 2010, **2**, 2005-2011.
467. S. Huang, X. Cen, H. Peng, S. Guo, W. Wang and T. Liu, *J. Phys. Chem. B*, 2009, **113**, 15225-15230.
468. B. Ramaraj, S. K. Nayak and K. R. Yoon, *J. Appl. Polym. Sci.*, 2010, **116**, 1671-1677.
469. C. X. Zhao, Y. Liu, D. Y. Wang, D. L. Wang and Y. Z. Wang, *Polym. Degrad. Stab.*, 2008, **93**, 1323-1331.
470. N. H. Huang and J. Q. Wang, *Express Polym. Lett.*, 2009, **3**, 595-604.
471. C. W. Bunn, *Nature*, 1948, **161**, 929-930.
472. R. C. L. Mooney, *J. Am. Ceram. Soc.*, 1941, **63**, 2828-2832.
473. R. Ricciardi, F. Auriemma, C. De Rosa and F. Lauprêtre, *Macromolecules*, 2004, **37**, 1921-1927.
474. S. Mallakpour, M. Dinari and M. Hatami, *J. Therm. Anal. Calorim.*, 2015, **120**, 1293-1302.
475. V. A. Pereira, I. N. Q. de Arruda and R. Stefani, *Food Hydrocolloids*, 2015, **43**, 180-188.
476. A. Sarkar, A. K. Ghosh and S. Mahapatra, *J. Mater. Chem.*, 2012, **22**, 11113-11120.
477. A. F. Stalder, G. Kulik, D. Sage, L. Barbieri and P. Hoffmann, *Colloids Surf., A Physicochem. Eng. Asp.*, 2006, **286**, 92-103.
478. *T 221 cm-99 Drainage time of pulp*, TAPPI Press, Atlanta, Georgia, United States, 1999.
479. *ASTM D 586-97 Standard Test Method for Ash in Pulp, Paper and Products*, ASTM International, West Conshohocken, Pennsylvania, United States, 2002.
480. *T 411 om-97 Thickness (caliper) of paper, paperboard, and combined board*, TAPPI Press, Atlanta, Georgia, United States, 1997.
481. D. Gruyter, *Paper Products Physics and Technology*, De Gruyter, 2009.
482. *ISO 5628 Determination of bending stiffness-General principles for two-point, three-point and four-point methods*, International Organization for Standardization, Geneva, Switzerland, 2012.
483. *ISO 5636-3:2013 Determination of air permeance (medium range) Part 3: Bendtsen method*, International Organization for Standardization, Geneva, Switzerland, 3 edn., 2013.
484. TAPPI, *T 555 Roughness of paper and paperboard (Print-surf method)*, TAPPI Press, Atlanta, Georgia, United States, 1997.
485. *T494 om-01 Tensile properties of paper and paperboard*, TAPPI Press, Atlanta, Georgia, United States, 2006.
486. *T 414 Internal tearing resistance of Paper (Elmendorf-type method)*, TAPPI Press, Atlanta, Georgia, United States, 1998.
487. *T 1214 Interrelation of reflectance, R0; reflectivity, R∞; TAPPI opacity, C0.89; scattering, s; and absorption, k*, TAPPI Press, Atlanta, Georgia, United States, 1998.

Appendix A – Appendices to Chapter Two

A.1 Powder X-ray diffraction data and Crystallinity index of cellulose fibre

Table A.1. Crystallinity index of cellulose fibre before and after dispersed in sodium carbonate solution at different period of time.

Sample	Crystallnity Index of cellulose (%)	d_{002} of cellulose (Å)	d_{003} of LDHs (Å)
W-cellulose fibre	88	3.88	-
W-cellulose fibre 2 hours	88	3.88	-
W-cellulose fibre 4 hours	88	3.89	-
W-cellulose fibre 1 day	89	3.87	-
W-cellulose fibre 2 days	89	3.87	-
W-cellulose fibre 3 days	86	3.89	-
LDH/W-cellulose fibre 2 hours	-	-	7.77
LDH/W-cellulose fibre 4 hours	-	-	7.78
LDH/W-cellulose fibre 1 day	-	-	7.72
LDH/W-cellulose fibre 2 days	-	-	7.69
LDH/W-cellulose fibre 3 days	-	-	7.83

A.2 Transmission electron microscopy and scanning electron microscopy

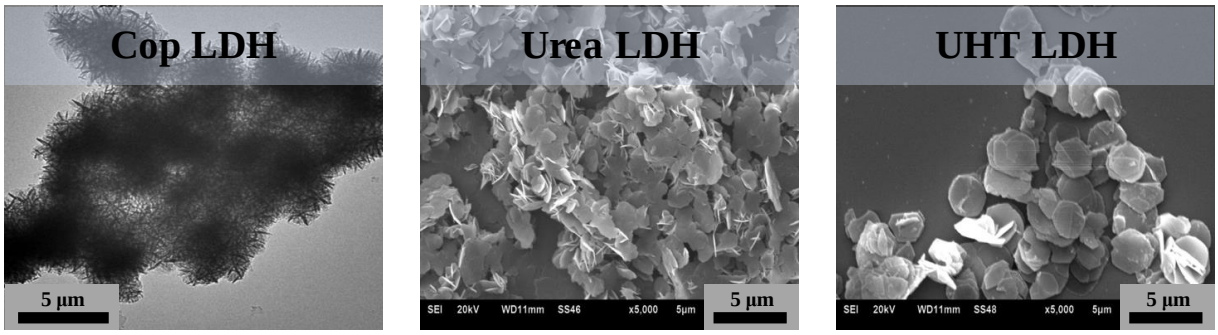


Figure A1. TEM and SEM images of MgAl-CO_3 LDHs from different synthetic methods.

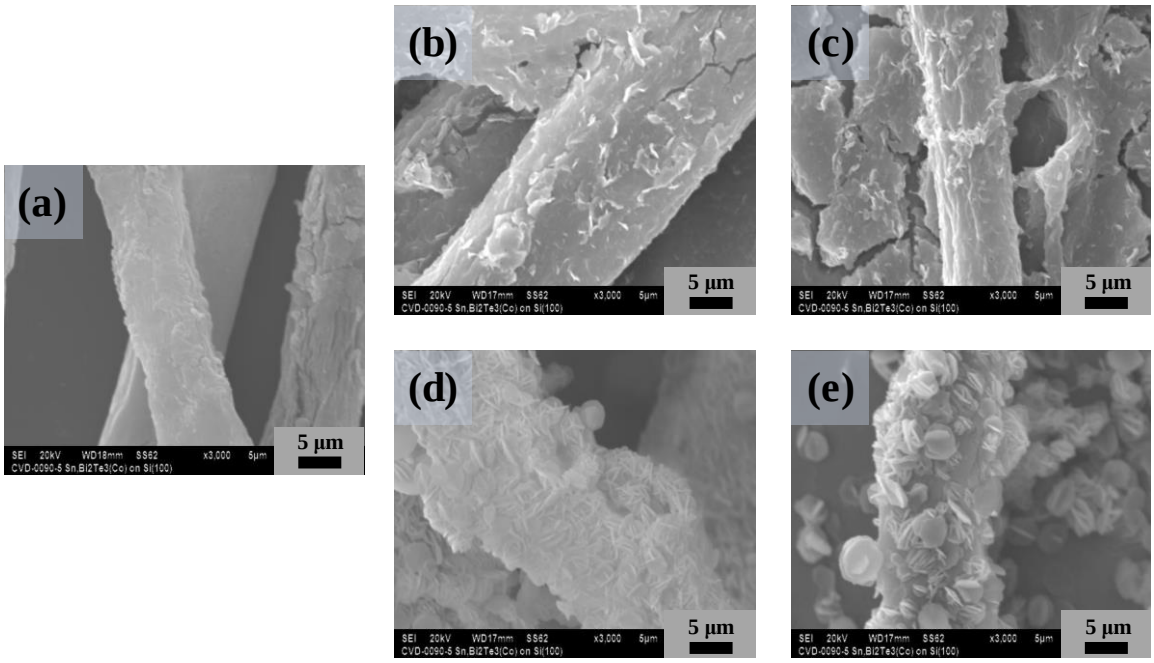


Figure A2. SEM images of obtained LDH/SW fibre composites from different methods: (a) Cop LDH/SW-fibre, (b) Urea#1 LDH/SW-fibre, (c) Urea#2 LDH/SW-fibre, (d) UHT#1 LDH/SW-fibre, and (e) UHT#2 LDH/SW-fibre.

A.3 Paper properties

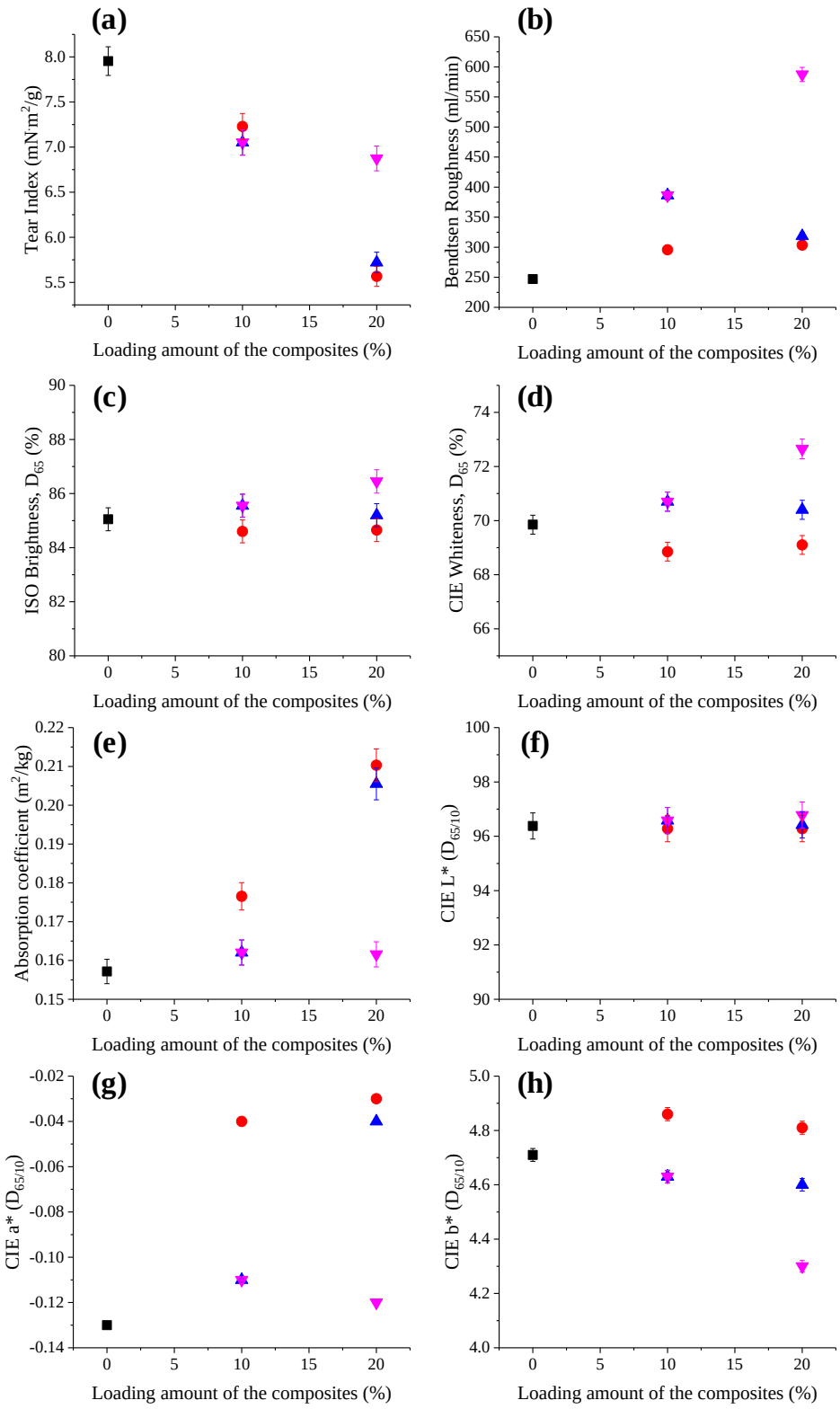


Figure A3. Physical properties of paper samples: (a) Tear index, (b) Bendtsen roughness, (c) ISO Brightness, (d) CIE Whiteness (e) Absorption coefficient, (f) CIE L*, (g) CIE a*, and (h) CIE b*. ■ Blank, ● Cop LDH/SW fibre, ▲ Urea#1 LDH/SW fibre and ▼ UHT#1 LDH/SW fibre.

A.4 Elemental analysis data

Table A.2. Elemental analysis data for percentage of carbon (% C), hydrogen (% H) and nitrogen (% N) in samples.

Sample	% C			% H			% N		
	#1	**#2**	**Average**	**#1**	**#2**	**Average**	**#1**	**#2**	**Average**
Cop-MgAl-NO_3 LDH	0.65	0.75	0.70	3.74	3.51	3.63	2.91	2.89	2.90
Cop-MgAl-DS 3 mmol	9.92	9.75	9.84	4.80	4.80	4.80	1.91	1.83	1.87
Cop-MgAl-DS 6 mmol	16.00	15.98	15.99	5.68	5.65	5.67	1.35	1.40	1.38
Cop-MgAl-DS 12 mmol	24.09	24.10	24.10	6.74	6.69	6.72	0.82	0.00	0.41
Cop-MgAl-DS 24 mmol	28.81	28.89	28.85	7.07	7.15	7.11	0.00	0.00	0.00
Cop-MgAl-LR 3 mmol	5.80	5.87	5.84	4.14	4.19	4.17	3.08	3.08	3.08
Cop-MgAl-LR 6 mmol	12.15	12.09	12.12	5.03	5.02	5.03	2.29	2.36	2.33
Cop-MgAl-LR 12 mmol	19.07	21.52	20.30	5.62	6.31	5.97	1.57	1.71	1.64
Cop-MgAl-LR 24 mmol	26.63	25.11	25.87	6.84	6.33	6.59	1.00	0.97	0.99
Cop-MgAl-LR 48 mmol	26.64	28.79	27.72	6.29	7.28	6.79	0.69	0.58	0.64
U-CO_3 LDH	1.72	1.67	1.70	3.94	4.14	4.04	1.13	0.94	1.04
U-DS LDH	32.15	32.24	32.20	7.26	7.33	7.30	<0.1	<0.1	<0.1
U-LR LDH	40.54	40.59	40.57	7.26	7.18	7.22	<0.1	<0.1	<0.1
U-SR LDH	43.43	43.43	43.43	8.54	8.58	8.56	<0.1	<0.1	<0.1

Appendix B – Appendices to Chapter Three

B.1. Characterising data for different solvent-treated LDHs

B.1.1. Powder X-ray diffraction

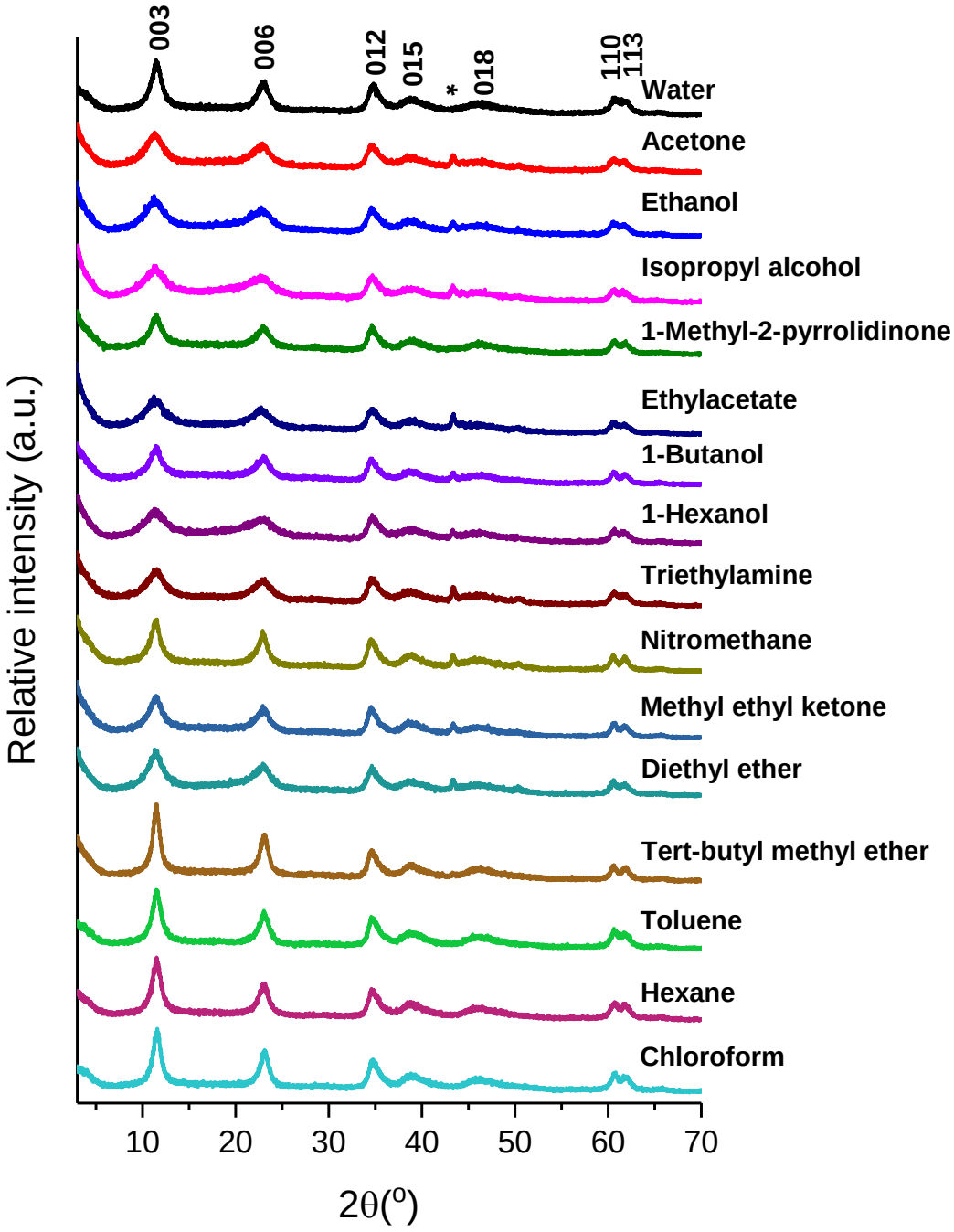


Figure B1. Powder X-ray diffraction patterns of some solvent-treated $Mg_4Al–CO_3$ LDHs. * is a Bragg reflection from the Al sample holder.

B.1.2. N_2 adsorption desorption isotherms

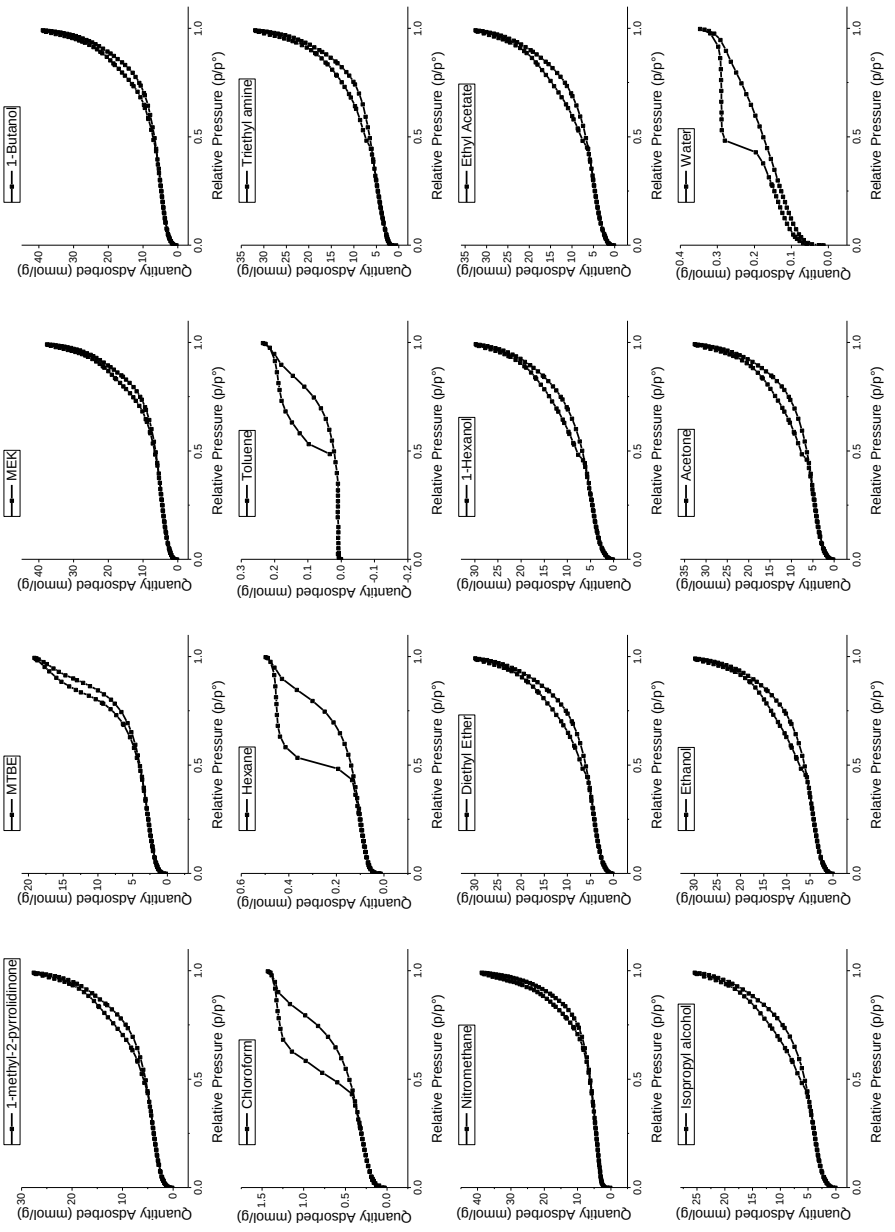


Figure B2. The N_2 adsorption-desorption isotherms of different ether solvent-treated $Mg_4Al–CO_3$ LDHs.

B.1.3. BJH desorption pore size distributions

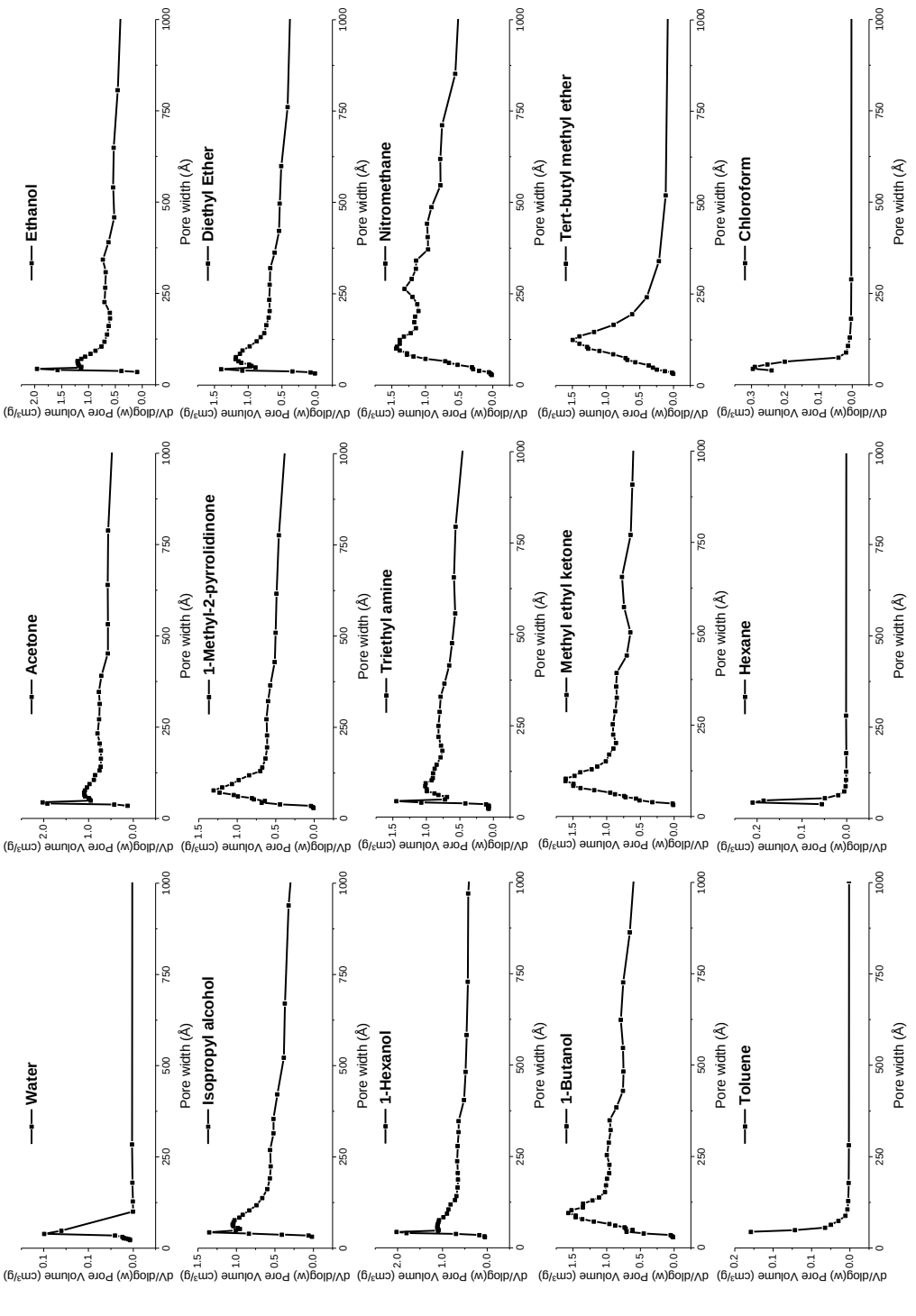


Figure B3. The Barrett-Joyner-Halenda (BJH) desorption pore size distributions of different solvent-treated $Mg_4Al–CO_3$ LDHs.

B.1.4. Surface properties data

Table B.1. Summary of the surface properties of different solvent-treated $Mg_4Al–CO_3$ LDHs.

Sample		BET surface area (m^2/g)	Pore Volume (cm^3/g)*	Adsorption average pore diameter (Å)	Loose bulk density (g/ml)	Tap density (g/ml)
Water		9	0.011	46	1.07	1.21
Aqueous miscible solvent	Acetone	354	1.12	126	0.15	0.24
	Ethanol	332	1.03	124	0.16	0.27
	Isopropyl alcohol	302	0.87	116	0.12	0.22
	1-Methyl-2-pyrrolidinone	297	1.02	120	0.24	0.30
Aqueous immiscible solvent	Ethyl acetate	377	1.12	121	0.14	0.20
	1-Butanol	369	1.42	135	0.16	0.24
	1-Hexanol	364	1.02	112	0.15	0.23
	Triethylamine	363	1.10	121	0.16	0.22
	Nitromethane	331	1.33	160	0.15	0.27
	Methyl ethyl ketone	353	1.29	146	0.15	0.23
	Diethyl ether	327	1.02	125	0.12	0.20
	Tert-butyl methyl ether	213	0.65	122	0.33	0.47
	Toluene	1	0.008	456	1.33	1.33
	Hexane	7	0.017	90	1.15	1.15
	Chloroform	24	0.048	82	1.04	1.22

*Single point adsorption total pore volume of pores less than 2,283.340 Å width at p/p° = 0.991694568.

B.1.5. Thermogravimetric analysis

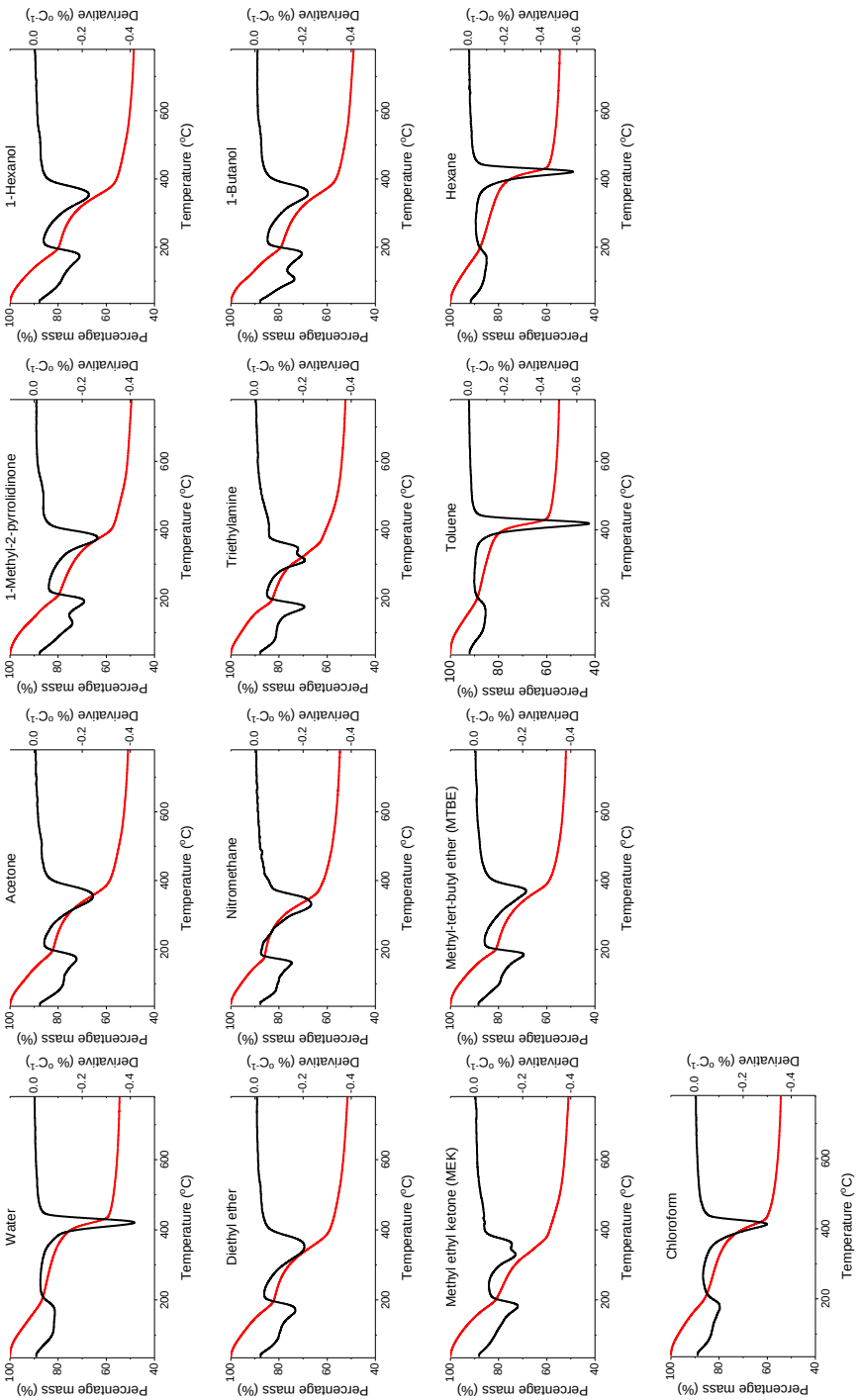


Figure B4. TGA (red line) and DTG (black line) curves of different solvent-treated $Mg_4Al–CO_3$ LDHs.

B.2. Characterising data for different ether and ketone solvents treated LDHs

B.2.1. Surface properties data

Table B.2. Summary of the surface properties of different ether and ketone solvents treated $Mg_4Al–CO_3$ LDHs.

Solvent			BET surface area (m^2/g)	Pore Volume (cm^3/g)*	Adsorption average pore diameter (Å)	Loose bulk density (g/ml)	Tap density (g/ml)
Ether solvents	$R_1 = R_2$	Diethyl ether	327	1.02	125	0.12	0.20
		Diisopropyl ether	196	0.53	102	0.40	0.46
		Di-n-butyl ether	200	0.53	94	0.36	0.46
	$R_1 = CH_3$	Tert-butyl methyl ether	213	0.33	122	0.33	0.47
		Tert-amyl methyl ether	275	0.78	104	0.36	0.49
		Cyclopentyl methyl ether	244	0.89	113	0.29	0.41
		Anisole	125	0.20	71	1.08	1.35
Ketone solvents	$R_1 = R_2$	3-Pentanone	224	0.82	146	0.24	0.38
		Diisopropylketone	332	0.81	121	0.38	0.43
		4-Heptanone	347	0.88	102	0.42	0.53
		5-Nonanone	224	0.45	95	0.47	0.56
	$R_1 = CH_3$	Methyl ethyl ketone	353	1.29	146	0.15	0.23
		2-Pentanone	250	0.97	155	0.19	0.32
		3-Methyl-2-butanone	232	0.41	70	0.23	0.30
		4-Methyl-2-pentanone	232	0.94	137	0.22	0.28

*Single point adsorption total pore volume of pores less than 2,283.340 Å width at p/p° = 0.991694568.

B.2.2. N_2 adsorption desorption isotherms

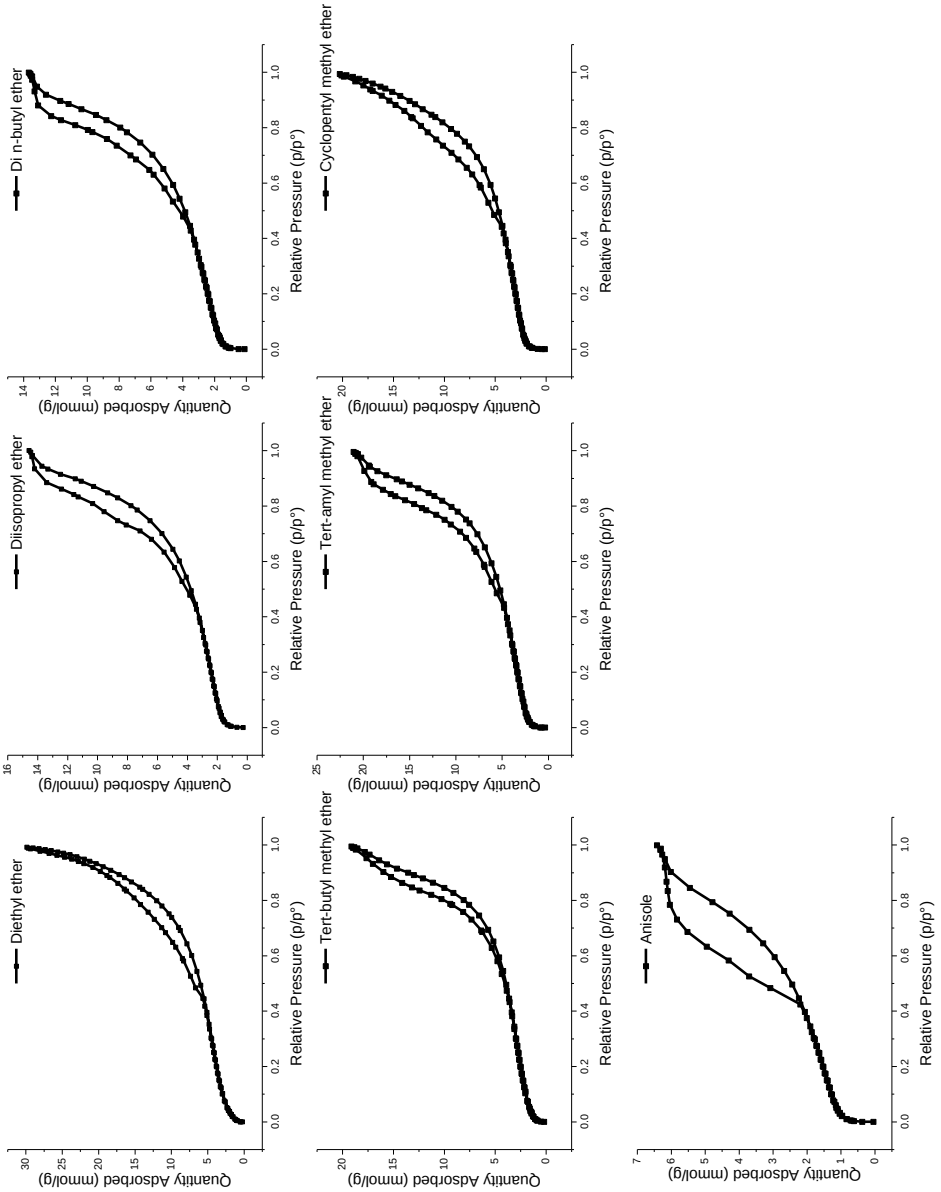


Figure B5. The N_2 adsorption-desorption isotherms of different ether solvent-treated $Mg_4Al\text{-}CO_3$ LDHs.

B.2.3. BJH desorption pore size distributions

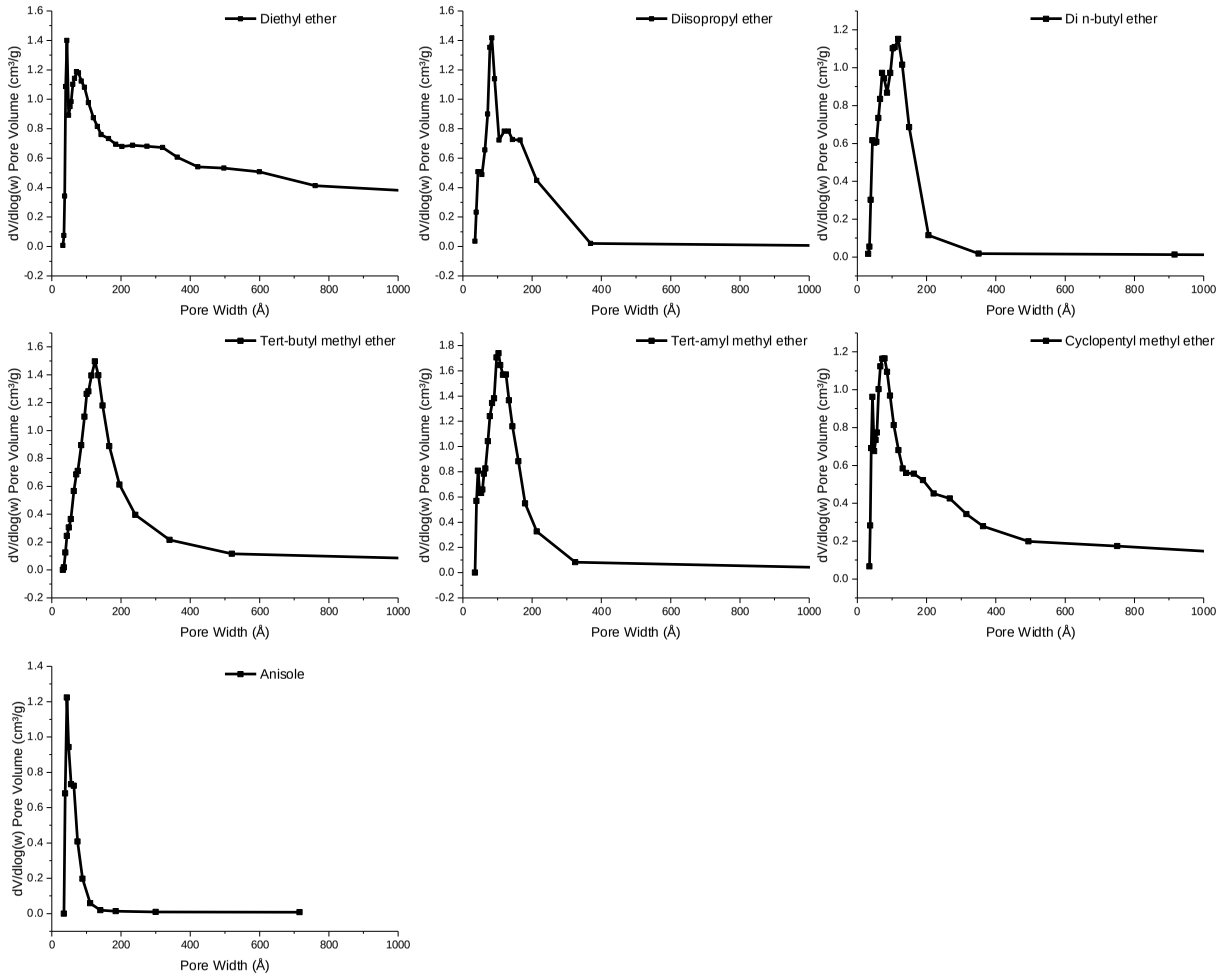


Figure B6. The Barrett-Joyner-Halenda (BJH) desorption pore size distributions of different ether solvent-treated Mg_4Al-CO_3 LDHs.

B.2.4. N_2 adsorption desorption isotherms

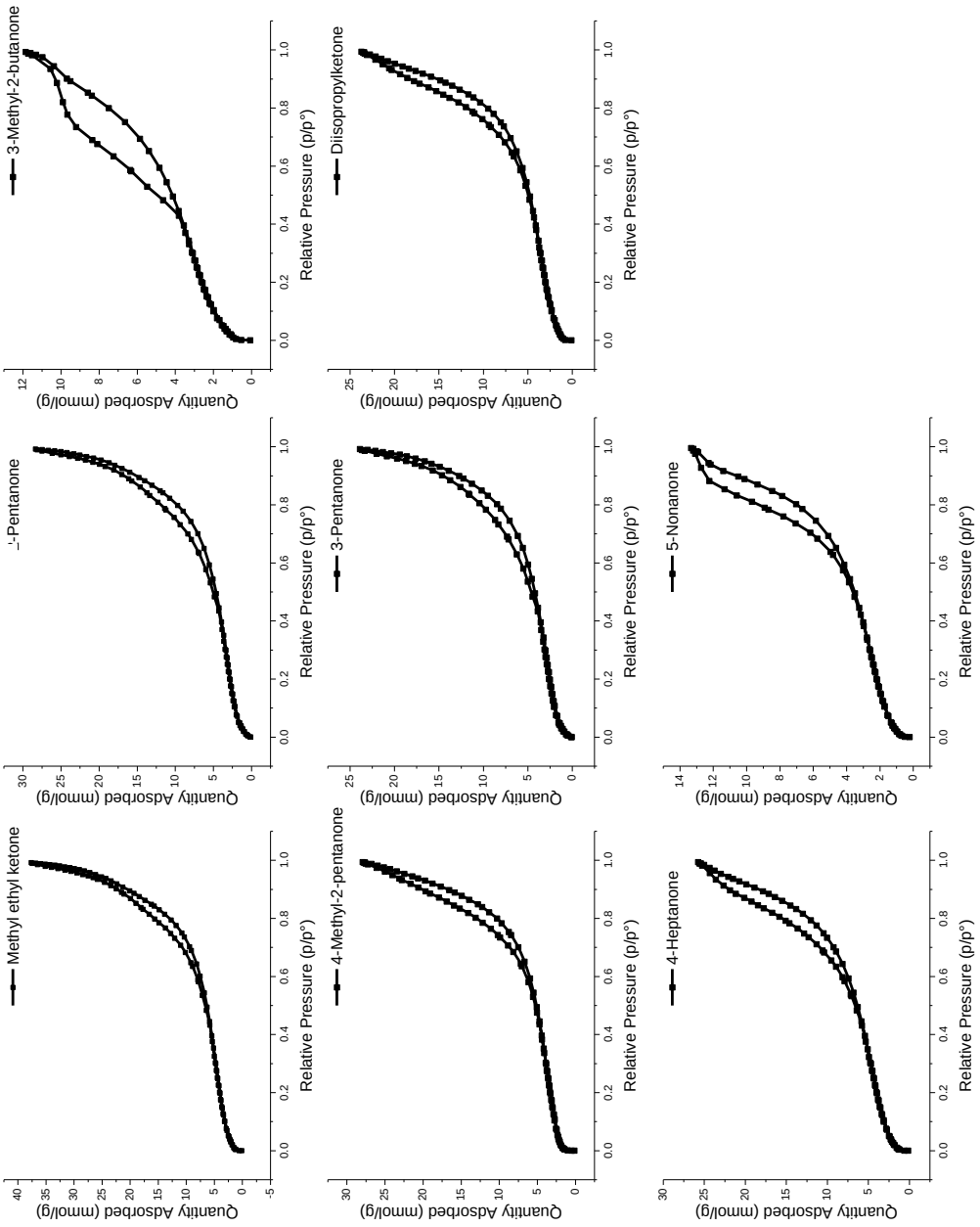


Figure B7. The N_2 adsorption-desorption isotherms of different ketone solvent-treated Mg_4Al-CO_3 LDHs.

B.2.5. BJH desorption pore size distributions

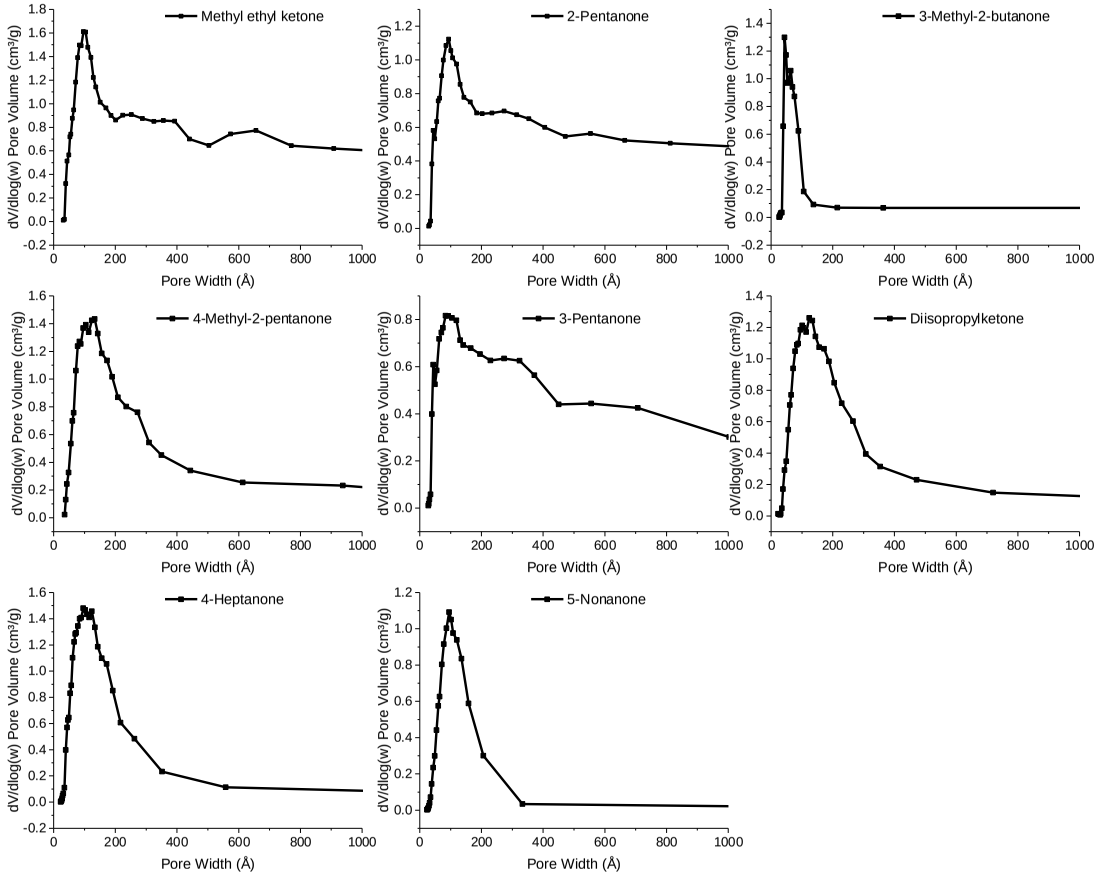


Figure B8. The Barrett-Joyner-Halenda (BJH) desorption pore size distributions of different ketone solvent-treated Mg_4Al-CO_3 LDHs.

B.2.6. LDHs Formula

Table B.3. Summary of water (*b*) and solvent (*c*) content in the AIM-LDHs from different ether solvents determined by elemental analysis

Ether solvents		*b*	*c*	Formula of LDHs*
$R_1 = R_2$	Diethyl ether	0.370	0.021	$[Mg_{0.80}Al_{0.20}(OH)_2(CO_3)_{0.10}]\cdot 0.370H_2O\cdot 0.021$(Diethyl ether)
	Diisopropyl ether	0.525	0.012	$[Mg_{0.80}Al_{0.20}(OH)_2(CO_3)_{0.10}]\cdot 0.525H_2O\cdot 0.012$(Diisopropyl ether)
	Di-n-butyl ether	0.630	0.013	$[Mg_{0.80}Al_{0.20}(OH)_2(CO_3)_{0.10}]\cdot 0.630H_2O\cdot 0.013$(Di-n-butyl ether)
$R_1 = CH_3$ group	Methyl tert-butyl ether	0.247	0.040	$[Mg_{0.80}Al_{0.20}(OH)_2(CO_3)_{0.10}]\cdot 0.247H_2O\cdot 0.040$(Methyl tert-butyl ether)
	Tert-amyl methyl ether	0.503	0.016	$[Mg_{0.80}Al_{0.20}(OH)_2(CO_3)_{0.10}]\cdot 0.503H_2O\cdot 0.016$(Tert-amyl methyl ether)
	Cyclopentyl methyl ether	0.490	0.011	$[Mg_{0.80}Al_{0.20}(OH)_2(CO_3)_{0.10}]\cdot 0.490H_2O\cdot 0.011$(Cyclopentyl methyl ether)
	Anisole	0.506	0.007	$[Mg_{0.80}Al_{0.20}(OH)_2(CO_3)_{0.10}]\cdot 0.506H_2O\cdot 0.007$(Anisole)

* The solvent treated LDHs is defined as $[M^{z+}_{1-x}M'^{y+}_{x}(OH)_2]^{a+}(X^{n-})_{a/n}\cdot bH_2O\cdot c$(solvent), wherein M and M′ are metal cations, z = 1 or 2; y = 3 or 4, $0 < x < 1$, b = 0–10, c = 0–10, X is an anion, n is 1 to 3 and $a = z(1 - x) + xy - 2$.

Table B.4. Summary of water (*b*) and solvent (*c*) content in the AIM-LDHs from different ketone solvents determined by elemental analysis

Ketone solvents		*b*	*c*	Formula of LDHs*
$R_1 = R_2$	3-Pentanone	0.062	0.181	$[Mg_{0.80}Al_{0.20}(OH)_2(CO_3)_{0.10}]\cdot 0.062H_2O\cdot 0.181$(3-Pentanone)
	Diisopropyl ketone	0.310	0.053	$[Mg_{0.80}Al_{0.20}(OH)_2(CO_3)_{0.10}]\cdot 0.310H_2O\cdot 0.053$(Diisopropylketone)
	4-Heptanone	0.309	0.059	$[Mg_{0.80}Al_{0.20}(OH)_2(CO_3)_{0.10}]\cdot 0.309H_2O\cdot 0.059$(4-Heptanone)
$R_1 = CH_3$ group	2-Butanone	0.051	0.082	$[Mg_{0.80}Al_{0.20}(OH)_2(CO_3)_{0.10}]\cdot 0.051H_2O\cdot 0.082$(2-Butanone)
	2-Pentanone	0.130	0.302	$[Mg_{0.80}Al_{0.20}(OH)_2(CO_3)_{0.10}]\cdot 0.130H_2O\cdot 0.302$(2-Pentanone)
	3-Methyl-2-butanone	0.431	0.136	$[Mg_{0.80}Al_{0.20}(OH)_2(CO_3)_{0.10}]\cdot 0.431H_2O\cdot 0.136$(3-Methyl-2-butanone)
	4-Methyl-2-pentaone	0.564	0.049	$[Mg_{0.80}Al_{0.20}(OH)_2(CO_3)_{0.10}]\cdot 0.564H_2O\cdot 0.049$(4-Methyl-2-pentanone)

* The solvent treated LDHs is defined as $[M^{z+}_{1-x}M'^{y+}_{x}(OH)_2]^{a+}(X^{n-})_{a/n}\cdot bH_2O\cdot c$(solvent), wherein M and M′ are metal cations, z = 1 or 2; y = 3 or 4, $0 < x < 1$, b = 0–10, c = 0–10, X is an anion, n is 1 to 3 and $a = z(1 - x) + xy - 2$.

B.2.7. Transmission electron microscopy

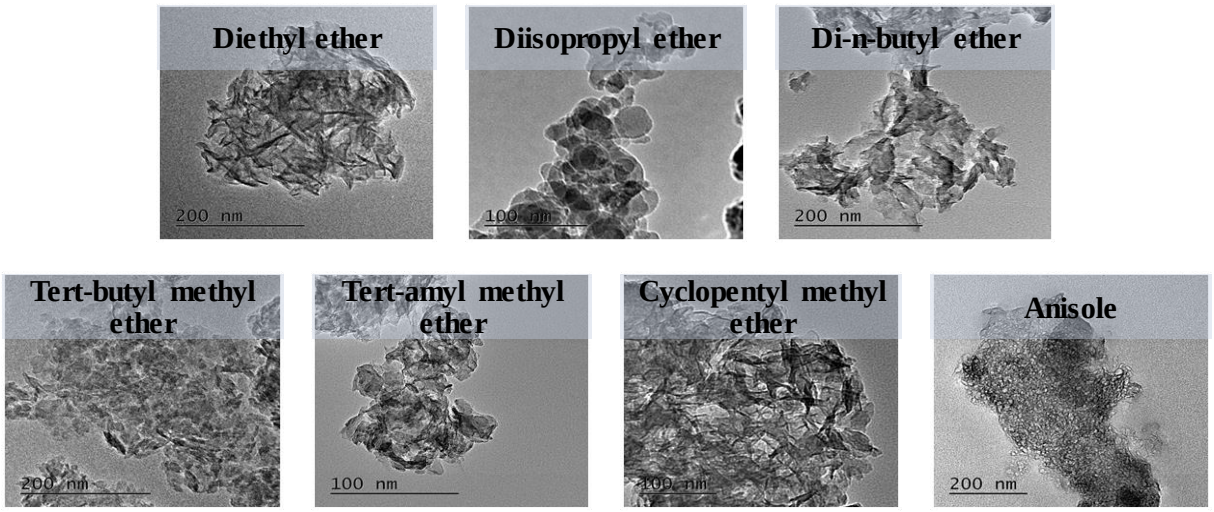


Figure B9. TEM of Mg_4Al-CO_3 LDH treated with different ether solvents.

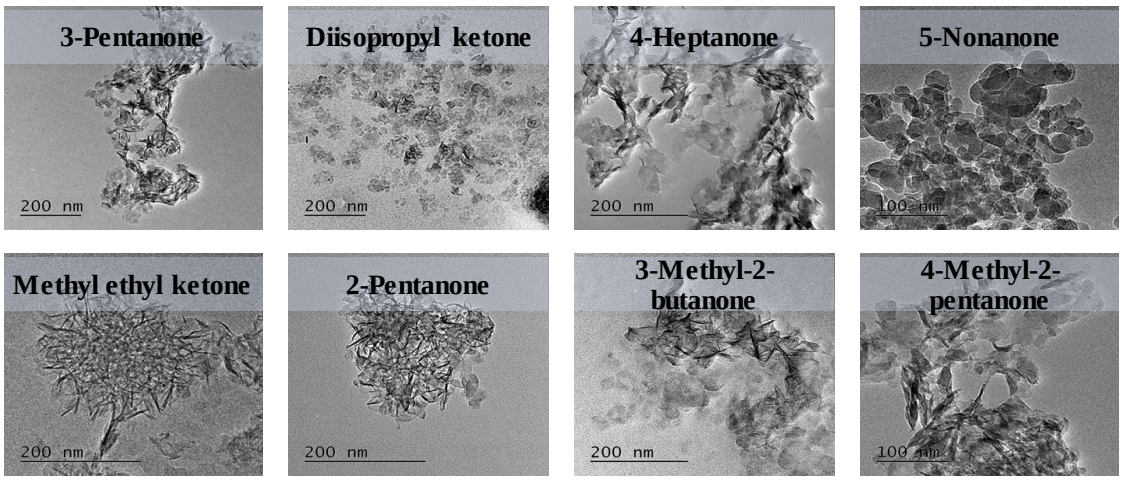


Figure B10. TEM of Mg_4Al-CO_3 LDH treated with different ketone solvents.

B.3. Characterising data for ether solvents treated at different dispersion times

B.3.1. Surface properties data

Table B.5. Summary of the surface properties of ether solvents treated Mg_4AlCO_3–LDHs at different dispersion time.

Effect of dispersion time: Ether solvents		BET surface area (m^2/g)	Pore Volume (cm^3/g)*	Adsorption average pore diameter (Å)	Loose bulk density (g/ml)	Tap density (g/ml)
Diisopropyl ether	4 h	196	0.53	102	0.40	0.46
	8 h	214	0.74	108	0.31	0.41
Di-n-butyl ether	4 h	200	0.53	94	0.36	0.46
	8 h	232	0.76	121	0.27	0.38
Anisole	4 h	125	0.20	71	1.08	1.35
	24 h	236	0.74	119	0.31	0.42

*Single point adsorption total pore volume of pores less than 2,283.340 Å width at p/p° = 0.991694568.

B.3.2. LDHs Formula

Table B.6. Summary of water (*b*) and solvent (*c*) content in the AIM-LDHs from different ether solvents with varied dispersion time determined by elemental analysis.

Ether solvents	Dispersion time	*b*	*c*	Formula of LDHs*
Diisopropyl ether	4 h	0.525	0.012	$[Mg_{0.80}Al_{0.20}(OH)_2(CO_3)_{0.10}]\cdot 0.525H_2O\cdot 0.012$(Diisopropyl ether)
	8 h	0.260	0.013	$[Mg_{0.80}Al_{0.20}(OH)_2(CO_3)_{0.10}]\cdot 0.260H_2O\cdot 0.013$(Diisopropyl ether)
Di-n-butyl ether	4 h	0.630	0.013	$[Mg_{0.80}Al_{0.20}(OH)_2(CO_3)_{0.10}]\cdot 0.630H_2O\cdot 0.013$(Di-n-butyl ether)
	8 h	0.387	0.009	$[Mg_{0.80}Al_{0.20}(OH)_2(CO_3)_{0.10}]\cdot 0.387H_2O\cdot 0.009$(Di-n-butyl ether)
Cyclopentyl methyl ether	4 h	0.490	0.011	$[Mg_{0.80}Al_{0.20}(OH)_2(CO_3)_{0.10}]\cdot 0.490H_2O\cdot 0.011$(Cyclopentyl methyl ether)
	24 h	0.328	0.056	$[Mg_{0.80}Al_{0.20}(OH)_2(CO_3)_{0.10}]\cdot 0.328H_2O\cdot 0.056$(Cyclopentyl methyl ether)
Anisole	4 h	0.506	0.007	$[Mg_{0.80}Al_{0.20}(OH)_2(CO_3)_{0.10}]\cdot 0.506H_2O\cdot 0.007$(Anisole)
	24 h	0.022	0.009	$[Mg_{0.80}Al_{0.20}(OH)_2(CO_3)_{0.10}]\cdot 0.022H_2O\cdot 0.009$(Anisole)

* The solvent treated LDHs is defined as $[M^{z+}{}_{1-x}M'^{y+}{}_x(OH)_2]^{a+}(X^{n-})_{a/n}\cdot bH_2O\cdot c$(solvent), wherein M and M′ are metal cations, z = 1 or 2; y = 3 or 4, $0 < x < 1$, b = 0–10, c = 0–10, X is an anion, n is 1 to 3 and $a = z(1 - x) + xy - 2$.

B.3.3. N_2 adsorption desorption isotherms and BJH desorption pore size distributions

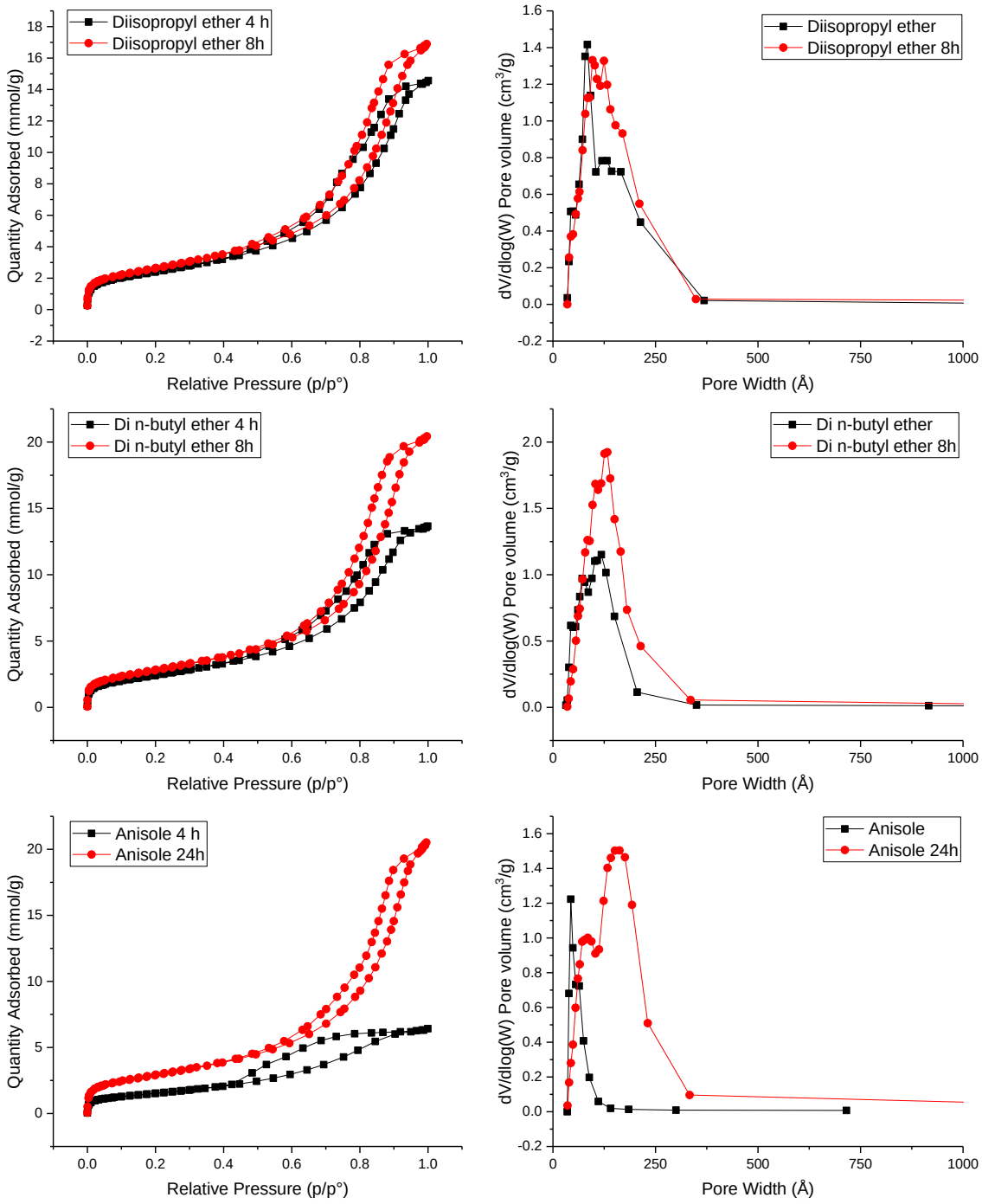


Figure B11. The N_2 adsorption-desorption isotherms and the Barrett-Joyner-Halenda (BJH) desorption pore size distributions of different ether solvent-treated Mg_4Al-CO_3 LDHs with varied dispersion time.

B.3.4. Transmission electron microscopy

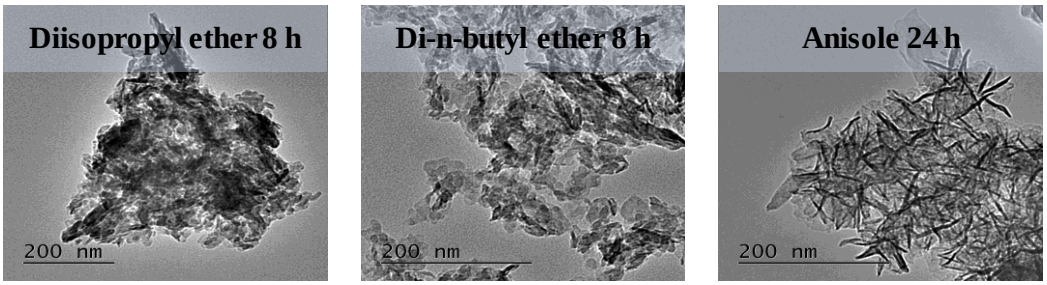


Figure B12. TEM of ether washed LDHs with varied dispersion time.

B.4. Characterising data for weak hydrogen bonding solvents treated LDHs

B.4.1. Surface properties data

Table B.7. Summary of the surface properties of different weak hydrogen bonding solvents treated $Mg_4Al–CO_3$ LDHs at different dispersion times.

Effect of dispersion time: Weak H-bond solvents			**BET surface area (m^2/g)**	**Pore Volume (cm^3/g)***	**Adsorption average pore diameter (Å)**	**Loose bulk density (g/ml)**	**Tap density (g/ml)**
Halogenated solvents	Chloroform	4 h	24	0.048	82	1.04	1.22
		24 h	149	0.43	121	0.55	0.73
		48 h	178	0.50	144	0.39	0.58
		72 h	247	0.82	133	0.25	0.33
	Dichloromethane	4 h	95	0.16	69	0.73	1.09
		24 h	165	0.52	139	0.43	0.47
		48 h	179	0.62	139	0.37	0.47
		72 h	141	0.44	129	0.30	0.38
Alkyl hydrocarbon	Hexane	4 h	7	0.017	90	1.15	1.15
		24 h	94	0.22	95	0.66	0.92
		48 h	133	0.39	116	0.36	0.58
		72 h	76	0.22	114	0.26	0.43
		96 h	104	0.30	116	0.27	0.38
		120 h	99	0.28	94	0.66	0.92
	Cyclohexane	4 h	81	0.15	68	0.92	1.38
		24 h	87	0.18	72	0.72	1.20
		48 h	86	0.17	71	0.56	0.97
		72 h	130	0.25	81	0.48	0.73
		96 h	147	0.49	113	0.34	0.50
		120 h	138	0.56	150	0.36	0.51
Aryl hydrocarbon	Toluene	4 h	1	0.008	456	1.33	1.33
		24 h	151	0.38	89	0.54	0.87
		48 h	160	0.52	109	0.38	0.63
		72 h	206	0.50	98	0.28	0.37

*Single point adsorption total pore volume of pores less than 2,283.340 Å width at p/p° = 0.991694568.

B.4.2. N_2 adsorption desorption isotherms

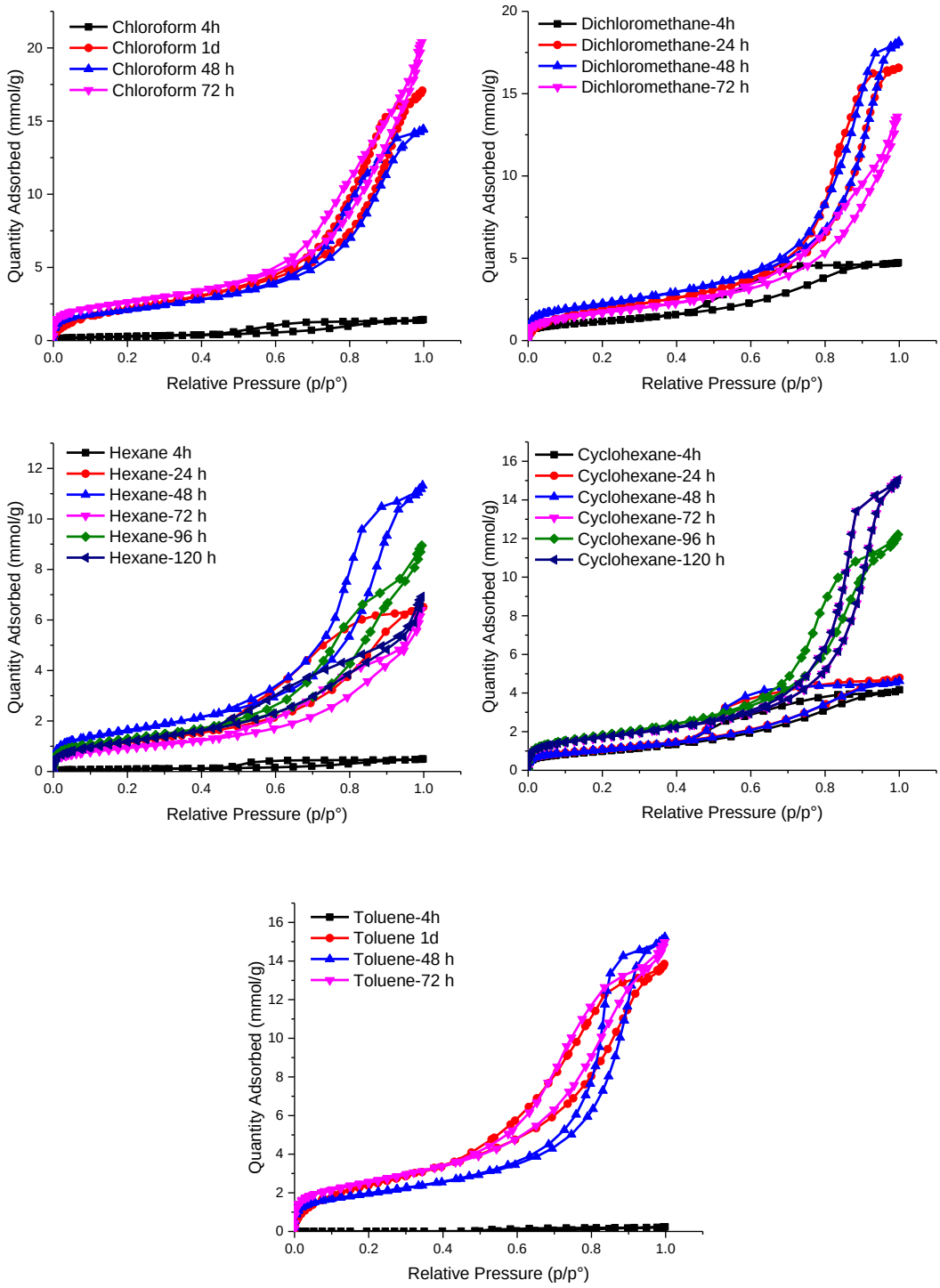


Figure B13. The N_2 adsorption-desorption isotherms of weak hydrogen bonding solvents treated Mg_4Al-CO_3 LDHs with varied dispersion time.

B.4.3. BJH desorption pore size distributions

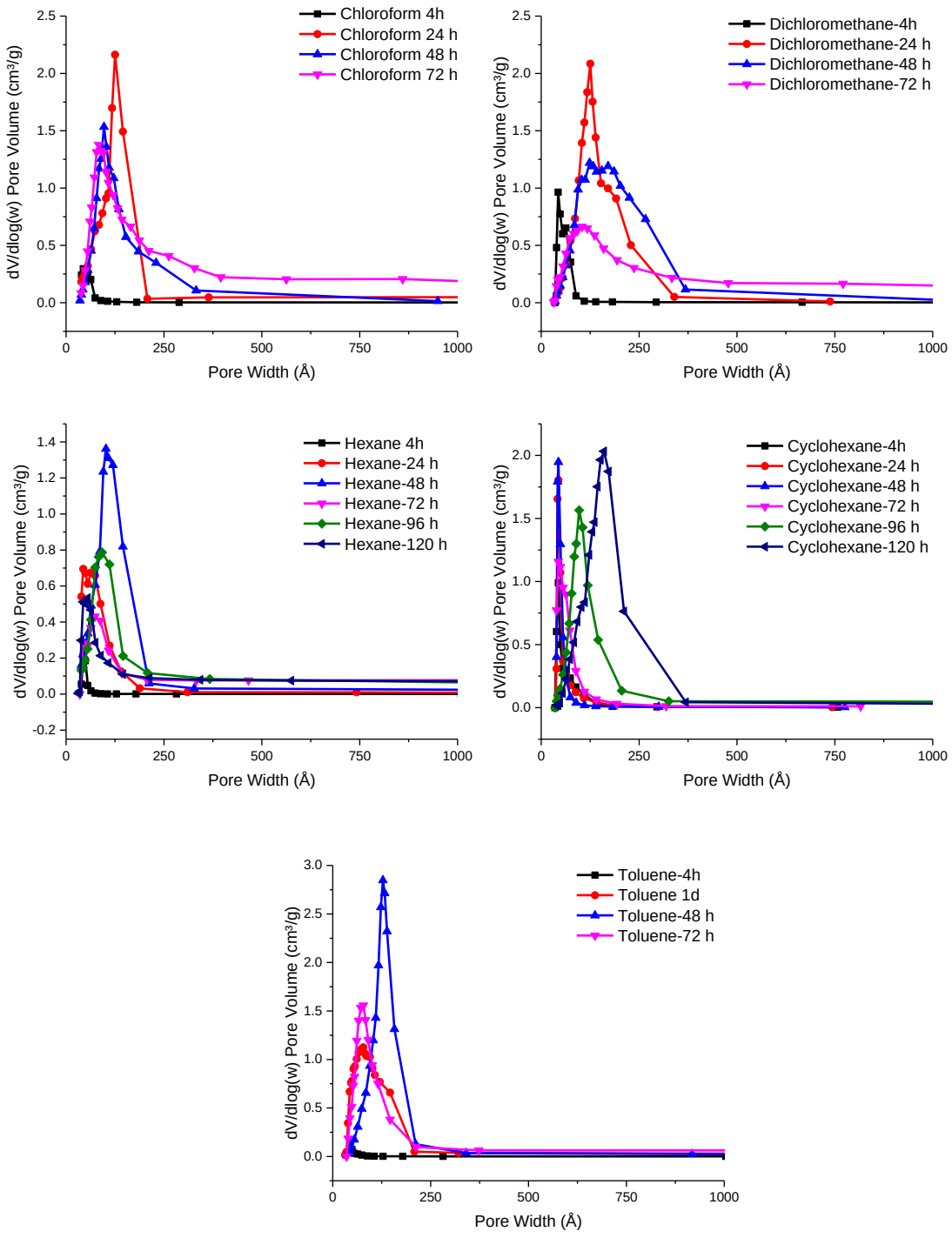


Figure B14. The Barrett-Joyner-Halenda (BJH) desorption pore size distributions of weak hydrogen bonding solvents treated Mg_4Al-CO_3 LDHs with varied dispersion time.

B.4.4. LDHs Formula

Table B.8. Summary of water (*b*) and solvent (*c*) content in the AIM-LDHs from different weak H-bond solvents with varied dispersion time determined by elemental analysis

Weak H-bond solvents	Dispersion time	*b*	*c*	Formula of LDHs*
Toluene	4 h	0.402	0.001	$[Mg_{0.80}Al_{0.20}(OH)_2(CO_3)_{0.10}]\cdot 0.402H_2O\cdot 0.001$(Toluene)
	24 h	0.532	0.004	$[Mg_{0.80}Al_{0.20}(OH)_2(CO_3)_{0.10}]\cdot 0.532H_2O\cdot 0.004$(Toluene)
	48 h	0.630	0.001	$[Mg_{0.80}Al_{0.20}(OH)_2(CO_3)_{0.10}]\cdot 0.630H_2O\cdot 0.001$(Toluene)
	72 h	0.486	0.005	$[Mg_{0.80}Al_{0.20}(OH)_2(CO_3)_{0.10}]\cdot 0.486H_2O\cdot 0.005$(Toluene)
Hexane	4 h	0.548	0.002	$[Mg_{0.80}Al_{0.20}(OH)_2(CO_3)_{0.10}]\cdot 0.548H_2O\cdot 0.002$(Hexane)
	24 h	0.596	0.006	$[Mg_{0.80}Al_{0.20}(OH)_2(CO_3)_{0.10}]\cdot 0.596H_2O\cdot 0.006$(Hexane)
	48 h	0.518	0.003	$[Mg_{0.80}Al_{0.20}(OH)_2(CO_3)_{0.10}]\cdot 0.518H_2O\cdot 0.003$(Hexane)
	72 h	0.550	0.004	$[Mg_{0.80}Al_{0.20}(OH)_2(CO_3)_{0.10}]\cdot 0.550H_2O\cdot 0.004$(Hexane)
	96 h	0.356	0.017	$[Mg_{0.80}Al_{0.20}(OH)_2(CO_3)_{0.10}]\cdot 0.356H_2O\cdot 0.017$(Hexane)
	120 h	0.211	0.020	$[Mg_{0.80}Al_{0.20}(OH)_2(CO_3)_{0.10}]\cdot 0.211H_2O\cdot 0.020$(Hexane)
Chloroform	4 h	0.593	0.042	$[Mg_{0.80}Al_{0.20}(OH)_2(CO_3)_{0.10}]\cdot 0.593H_2O\cdot 0.042$(Chloroform)
	24 h	0.683	0.020	$[Mg_{0.80}Al_{0.20}(OH)_2(CO_3)_{0.10}]\cdot 0.683H_2O\cdot 0.020$(Chloroform)
	48 h	0.649	0.022	$[Mg_{0.80}Al_{0.20}(OH)_2(CO_3)_{0.10}]\cdot 0.649H_2O\cdot 0.022$(Chloroform)
	72 h	0.430	0.045	$[Mg_{0.80}Al_{0.20}(OH)_2(CO_3)_{0.10}]\cdot 0.430H_2O\cdot 0.045$(Chloroform)
Cyclohexane	4 h	0.467	0.004	$[Mg_{0.80}Al_{0.20}(OH)_2(CO_3)_{0.10}]\cdot 0.467H_2O\cdot 0.004$(Cyclohexane)
	24 h	0.473	0.004	$[Mg_{0.80}Al_{0.20}(OH)_2(CO_3)_{0.10}]\cdot 0.473H_2O\cdot 0.004$(Cyclohexane)
	48 h	0.455	0.006	$[Mg_{0.80}Al_{0.20}(OH)_2(CO_3)_{0.10}]\cdot 0.455H_2O\cdot 0.006$(Cyclohexane)
	72 h	0.632	0.007	$[Mg_{0.80}Al_{0.20}(OH)_2(CO_3)_{0.10}]\cdot 0.632H_2O\cdot 0.007$(Cyclohexane)
	96 h	0.483	0.006	$[Mg_{0.80}Al_{0.20}(OH)_2(CO_3)_{0.10}]\cdot 0.483H_2O\cdot 0.006$(Cyclohexane)
	120 h	0.498	0.004	$[Mg_{0.80}Al_{0.20}(OH)_2(CO_3)_{0.10}]\cdot 0.498H_2O\cdot 0.004$(Cyclohexane)
Dichloromethane	4 h	0.616	0.014	$[Mg_{0.80}Al_{0.20}(OH)_2(CO_3)_{0.10}]\cdot 0.616H_2O\cdot 0.014$(Dichloromethane)
	24 h	0.896	0.230	$[Mg_{0.80}Al_{0.20}(OH)_2(CO_3)_{0.10}]\cdot 0.896H_2O\cdot 0.230$(Dichloromethane)
	48 h	0.732	0.015	$[Mg_{0.80}Al_{0.20}(OH)_2(CO_3)_{0.10}]\cdot 0.732H_2O\cdot 0.015$(Dichloromethane)
	72 h	0.771	0.196	$[Mg_{0.80}Al_{0.20}(OH)_2(CO_3)_{0.10}]\cdot 0.771H_2O\cdot 0.196$(Dichloromethane)

* The solvent treated LDHs is defined as $[M^{z+}_{1-x}M'^{y+}_{x}(OH)_2]^{a+}(X^{n-})_{a/n}\cdot bH_2O\cdot c$(solvent), wherein M and M′ are metal cations, z = 1 or 2; y = 3 or 4, $0 < x < 1$, b = 0–10, c = 0–10, X is an anion, n is 1 to 3 and $a = z(1 - x) + xy - 2$.

B.4.5. Transmission electron microscopy

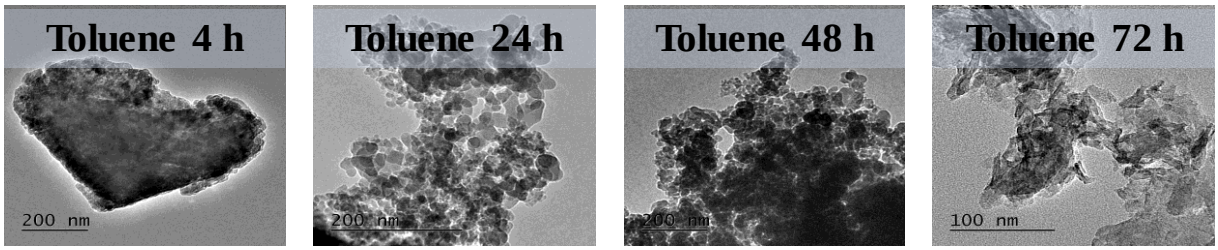


Figure B15. TEM of toluene washed LDHs with varied dispersion times.

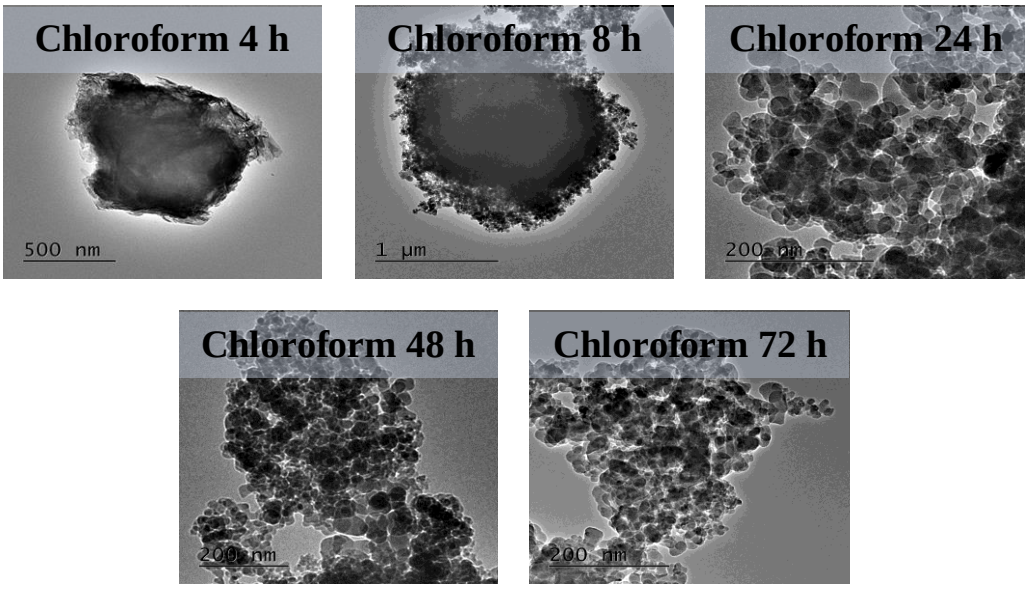


Figure B16. TEM of chloroform washed LDHs with varied dispersion times.

B.4.6. Solvation parameters

Table B.9. Solvation parameters and dielectric constant of solvents

Solvent	*r*	*s*	*a*	*b*
Toluene	-0.22	0.94	0.47	0.10
Chloroform	-0.60	1.26	0.28	1.37
Hexane	-0.17	0	0	0
Cyclohexane	0	-0.18	0	0
Ethanol	-0.21	0.79	3.63	1.31
Water	0.82	2.74	3.90	4.80

r = electron lone pair interaction
s = diploe-type interactions
a = hydrogen-bond basicity
b = hydrogen-bond acidity

B.5. Characterising data for solvent-treated LDHs with different process parameters

B.5.1. Powder X-ray diffraction

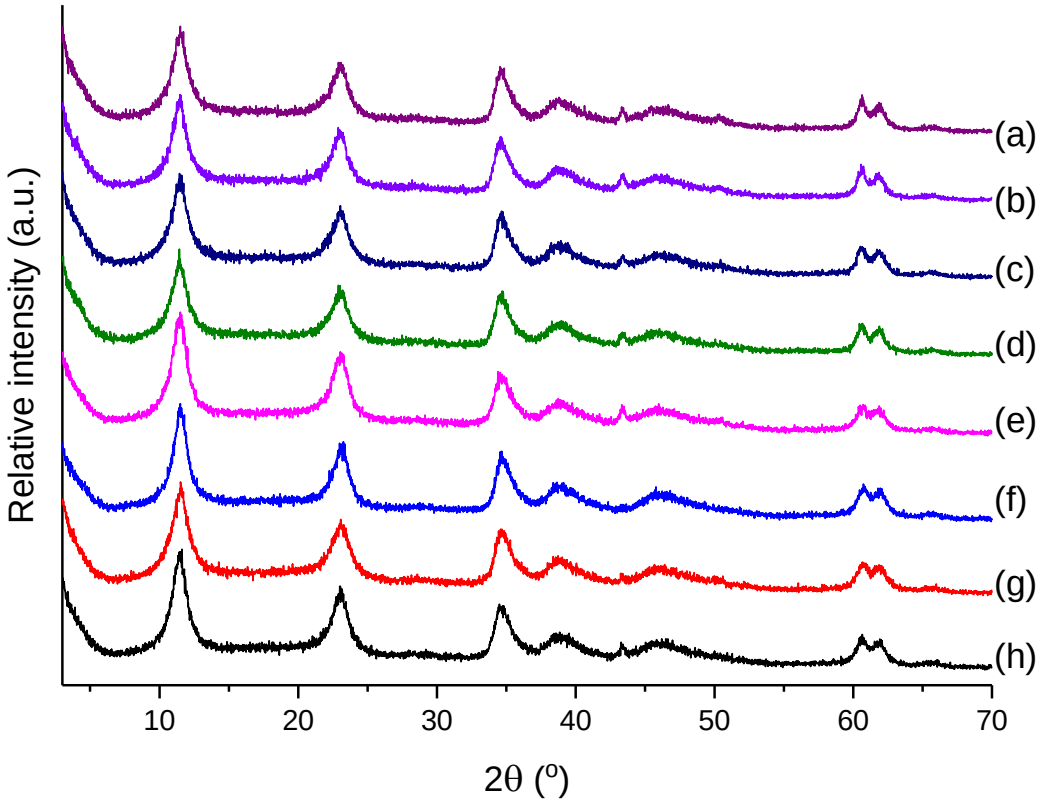


Figure B17. XRD patterns of Mg_4Al-CO_3 AIM-LDH treated with different volumes of ethyl acetate (a) 100, (b) 300, (c) 500, (d) 1000 mL and diethyl ether (e) 100, (f) 300, (g) 500, and (h) 1000 mL.

Table B.10. Mean crystallite domain lengths and unit cell parameters of AIM-LDHs with different rinsing volume of diethyl ether and ethyl acetate

Solvent	Rinsing volume (mL)	*d*-spacing		CDL_{003} (Å)*	Unit cell parameter		No. of layers
		d_{003} (Å)	d_{110} (Å)		*a*	*c*	
Diethyl ether	100 mL	7.73	1.52	59.5	3.05	23.18	8
	300 mL	7.68	1.52	64.7	3.05	23.05	8
	500 mL	7.69	1.52	54.0	3.05	23.08	7
	1000 mL	7.73	1.52	60.4	3.05	23.19	8
Ethyl acetate	100 mL	7.71	1.52	55.4	3.05	23.12	7
	300 mL	7.73	1.53	60.6	3.05	23.20	8
	500 mL	7.71	1.53	57.4	3.05	23.13	7
	1000 mL	7.73	1.53	56.6	3.05	23.19	7

* Mean crystallite domain lengths along *c*-axis (CDL_{003}) obtained from the Scherrer equation. $CDL = K\lambda(\beta\cos\theta)^{-1}$, K = 0.89, λ = 1.5406 Å, $\beta = FWHM_{003}$.

B.5.2. LDHs Formula

Table B.11. Summary of water (*b*) and solvent (*c*) content in the AMO-LDHs and AIM-LDHs with different rinsing volume compared to conventional C-LDHs as determined by elemental analysis.

Solvent	Rinsing volume (mL)	*b*	*c*	Formula of LDHs*
Acetone	100 mL	0.278	0.088	$[Mg_{0.80}Al_{0.20}(OH)_2(CO_3)_{0.10}]\cdot 0.278H_2O\cdot 0.088$(Acetone)
	500 mL	0.225	0.113	$[Mg_{0.80}Al_{0.20}(OH)_2(CO_3)_{0.10}]\cdot 0.225H_2O\cdot 0.133$(Acetone)
Ethanol	100 mL	0.236	0.208	$[Mg_{0.80}Al_{0.20}(OH)_2(CO_3)_{0.10}]\cdot 0.236H_2O\cdot 0.208$(Ethanol)
	500 mL	0.245	0.215	$[Mg_{0.80}Al_{0.20}(OH)_2(CO_3)_{0.10}]\cdot 0.245H_2O\cdot 0.215$(Ethanol)
1-Butanol	100 mL	0.220	0.118	$[Mg_{0.80}Al_{0.20}(OH)_2(CO_3)_{0.10}]\cdot 0.220H_2O\cdot 0.118$(1-Butanol)
	500 mL	0.041	0.099	$[Mg_{0.80}Al_{0.20}(OH)_2(CO_3)_{0.10}]\cdot 0.041H_2O\cdot 0.099$(1-Butanol)
1-Hexanol	100 mL	0.176	0.075	$[Mg_{0.80}Al_{0.20}(OH)_2(CO_3)_{0.10}]\cdot 0.176H_2O\cdot 0.075$(1-Hexanol)
	500 mL	0.110	0.087	$[Mg_{0.80}Al_{0.20}(OH)_2(CO_3)_{0.10}]\cdot 0.110H_2O\cdot 0.087$(1-Hexanol)
Diethyl ether	100 mL	0.537	0.089	$[Mg_{0.80}Al_{0.20}(OH)_2(CO_3)_{0.10}]\cdot 0.537H_2O\cdot 0.089$(Diethyl ether)
	500 mL	0.370	0.021	$[Mg_{0.80}Al_{0.20}(OH)_2(CO_3)_{0.10}]\cdot 0.370H_2O\cdot 0.021$(Diethyl ether)

* The solvent treated LDHs is defined as $[M^{z+}_{1-x}M'^{y+}_{x}(OH)_2]^{a+}(X^{n-})_{a/n}\cdot bH_2O\cdot c$(solvent), wherein M and M′ are metal cations, $z = 1$ or 2; $y = 3$ or 4, $0 < x < 1$, $b = 0$–10, $c = 0$–10, X is an anion, n is 1 to 3 and $a = z(1 - x) + xy - 2$.

B.5.3. Transmission electron microscopy

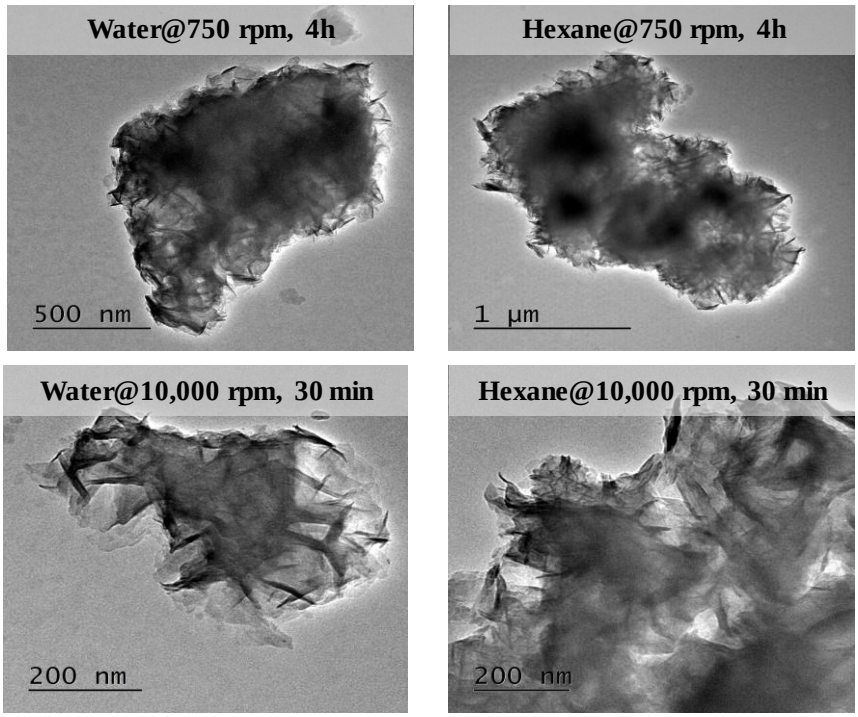


Figure B18. TEM of densities of $Mg_4Al–CO_3$ LDHs treated with water and hexane washed at mixing speed of 750 rpm (4hours) and 10,000 rpm (30 minutes).

B.6. Characterising data for solvents treated LDHs at after solvent recycling

B.6.1. Surface properties data

Table B.12. Summary of the surface properties of solvents treated $Mg_4Al\text{-}CO_3$ LDHs at after solvent recycling.

Effect of solvent recycling		BET surface area (m^2/g)	Pore Volume (cm^3/g)*	Adsorption average pore diameter (Å)	Loose bulk density (g/ml)	Tap density (g/ml)
Ethanol	Fresh	321	0.85	206	0.40	0.55
	1st	274	0.95	138	0.30	0.50
	2nd	231	0.87	150	0.30	0.51
	3rd	222	0.56	101	0.40	0.69
	4th	234	0.55	94	0.44	0.77
1-Hexanol	Fresh	361	1.34	148	0.23	0.33
	1st	359	1.29	144	0.21	0.32
	2nd	364	1.29	142	0.22	0.33
	3rd	360	1.30	144	0.26	0.33
	4th	361	1.41	157	0.25	0.31

* Single point adsorption total pore volume of pores less than 2,283.340 Å width at p/p° = 0.991694568.

B.6.2. LDHs Formula

Table B.13. Summary of water (*b*) and solvent (*c*) content in the AMO-LDHs and AIM-LDHs from different solvent recycling times determined by elemental analysis.

Washing solvent	Solvent recycle time(s)	*b*	*c*	Formula of LDHs*
Ethanol: Solvent recycle time(s)	0	0.245	0.215	$[Mg_{0.80}Al_{0.20}(OH)_2(CO_3)_{0.10}]\cdot 0.245H_2O\cdot 0.215$(Ethanol)
	1	0.018	0.268	$[Mg_{0.80}Al_{0.20}(OH)_2(CO_3)_{0.10}]\cdot 0.018H_2O\cdot 0.268$(Ethanol)
	2	0.019	0.247	$[Mg_{0.80}Al_{0.20}(OH)_2(CO_3)_{0.10}]\cdot 0.019H_2O\cdot 0.247$(Ethanol)
	3	0.045	0.215	$[Mg_{0.80}Al_{0.20}(OH)_2(CO_3)_{0.10}]\cdot 0.045H_2O\cdot 0.215$(Ethanol)
	4	0.048	0.219	$[Mg_{0.80}Al_{0.20}(OH)_2(CO_3)_{0.10}]\cdot 0.048H_2O\cdot 0.219$(Ethanol)
Hexanol: Solvent recycle time(s)	0	0.232	0.113	$[Mg_{0.80}Al_{0.20}(OH)_2(CO_3)_{0.10}]\cdot 0.232H_2O\cdot 0.113$(1-Hexanol)
	1	0.257	0.091	$[Mg_{0.80}Al_{0.20}(OH)_2(CO_3)_{0.10}]\cdot 0.257H_2O\cdot 0.091$(1-Hexanol)
	2	0.260	0.146	$[Mg_{0.80}Al_{0.20}(OH)_2(CO_3)_{0.10}]\cdot 0.260H_2O\cdot 0.146$(1-Hexanol)
	3	0.240	0.188	$[Mg_{0.80}Al_{0.20}(OH)_2(CO_3)_{0.10}]\cdot 0.240H_2O\cdot 0.188$(1-Hexanol)
	4	0.172	0.225	$[Mg_{0.80}Al_{0.20}(OH)_2(CO_3)_{0.10}]\cdot 0.172H_2O\cdot 0.225$(1-Hexanol)

* The solvent treated LDHs is defined as $[M^{z+}_{1-x}M'^{y+}_{x}(OH)_2]^{a+}(X^{n-})_{a/n}\cdot bH_2O\cdot c$(solvent), wherein M and M′ are metal cations, $z = 1$ or 2; $y = 3$ or 4, $0 < x < 1$, $b = 0$–10, $c = 0$–10, X is an anion, n is 1 to 3 and $a = z(1 - x) + xy - 2$.

B.7. Characterising data for solvent-treated on different Mg/Al ratios LDHs

B.7.1. LDHs Formula

Table B.14. Summary of water (*b*) and solvent (*c*) content in the AMO-LDHs and AIM-LDHs compared to conventional C-LDHs with different Mg/Al ratios LDHs as determined by elemental analysis.

Washing solvent		*b*	*c*	Formula of LDHs*
Mg/Al = 2	Water	0.415	0.000	$[Mg_{0.67}Al_{0.33}(OH)_2(CO_3)_{0.165}]\cdot 0.532H_2O$
	Acetone	0.081	0.074	$[Mg_{0.67}Al_{0.33}(OH)_2(CO_3)_{0.165}]\cdot 0.170H_2O\cdot 0.080$(Acetone)
	Diethyl ether	0.246	0.044	$[Mg_{0.67}Al_{0.33}(OH)_2(CO_3)_{0.165}]\cdot 0.349H_2O\cdot 0.047$(Diethyl ether)
Mg/Al = 3	Water	0.461	0.000	$[Mg_{0.75}Al_{0.25}(OH)_2(CO_3)_{0.125}]\cdot 0.508H_2O$
	Acetone	0.248	0.067	$[Mg_{0.75}Al_{0.25}(OH)_2(CO_3)_{0.125}]\cdot 0.288H_2O\cdot 0.069$(Acetone)
	Ethanol	0.396	0.176	$[Mg_{0.75}Al_{0.25}(OH)_2(CO_3)_{0.125}]\cdot 0.441H_2O\cdot 0.181$(Ethanol)
	Diethyl ether	0.182	0.086	$[Mg_{0.75}Al_{0.25}(OH)_2(CO_3)_{0.125}]\cdot 0.220H_2O\cdot 0.088$(Diethyl ether)
Mg/Al = 4	Water	0.634	0.000	$[Mg_{0.80}Al_{0.20}(OH)_2(CO_3)_{0.10}]\cdot 0.634H_2O$
	Acetone	0.225	0.113	$[Mg_{0.80}Al_{0.20}(OH)_2(CO_3)_{0.10}]\cdot 0.225H_2O\cdot 0.113$(Acetone)
	Ethanol	0.245	0.215	$[Mg_{0.80}Al_{0.20}(OH)_2(CO_3)_{0.10}]\cdot 0.245H_2O\cdot 0.215$(Ethanol)
	Diethyl ether	0.370	0.021	$[Mg_{0.80}Al_{0.20}(OH)_2(CO_3)_{0.10}]\cdot 0.370H_2O\cdot 0.021$(Diethyl ether)

* The solvent treated LDHs is defined as $[M^{z+}_{1-x}M'^{y+}_x(OH)_2]^{a+}(X^{n-})_{a/n}\cdot bH_2O\cdot c$(solvent), wherein M and M′ are metal cations, z = 1 or 2; y = 3 or 4, $0 < x < 1$, b = 0–10, c = 0–10, X is an anion, n is 1 to 3 and $a = z(1 - x) + xy - 2$.

B.7.2. Transmission electron microscopy

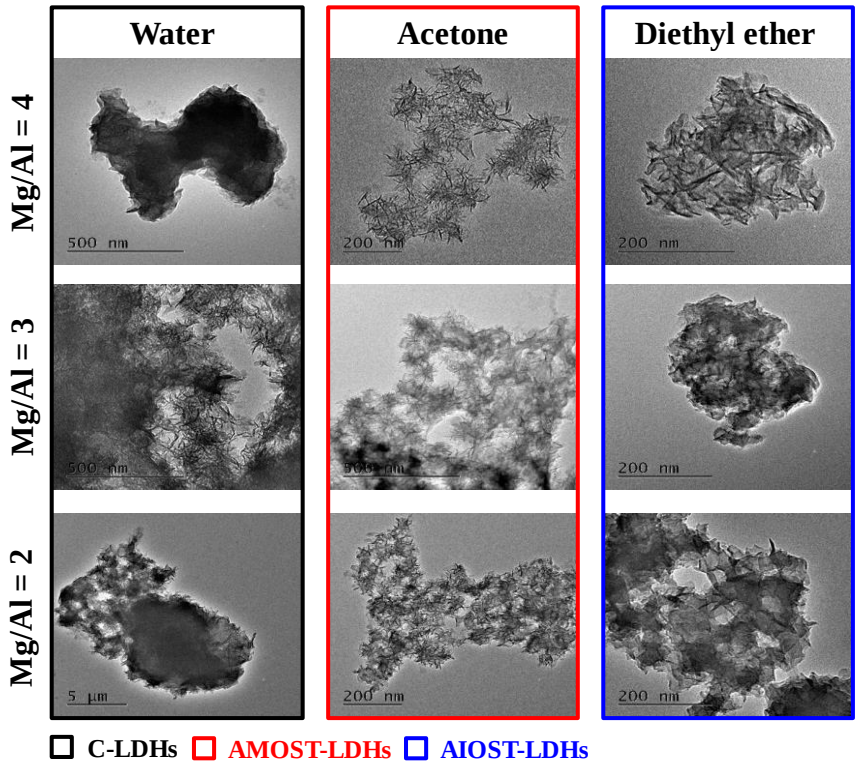


Figure B19. TEM of water washed, AMO- and AIM-LDHs with different ratios of Mg/Al.

B.8. Characterising data for solvent-treated platelet like LDHs

B.8.1. N_2 adsorption desorption isotherms

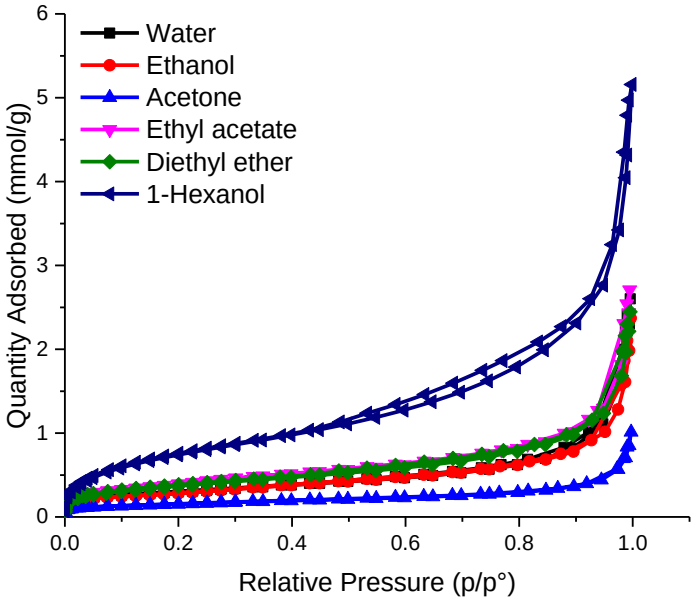


Figure B20. The N_2 adsorption-desorption isotherms of different solvent-treated platelet Mg_4Al-CO_3 LDHs.

B.8.2. BJH desorption pore size distributions

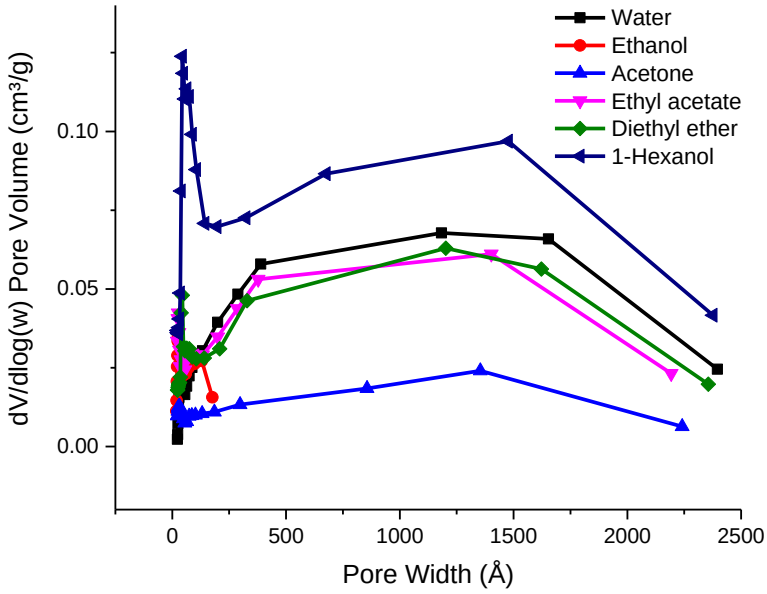


Figure B21. The Barrett-Joyner-Halenda (BJH) desorption pore size distributions of different solvent-treated platelet Mg_4Al-CO_3 LDHs.

B.8.3. Surface properties data

Table B.15. Summary of the surface properties of different solvents treated platelet $Mg_4Al{-}CO_3$ LDHs.

Solvent		BET surface area (m^2/g)	Pore Volume (cm^3/g)*	Adsorption average pore diameter (Å)	Loose bulk density (g/ml)	Tap density (g/ml)
Water		24	0.071	122	0.15	0.25
Aqueous miscible solvent	Acetone	12	0.027	88	0.14	0.18
	Ethanol	22	0.062	109	0.11	0.16
Aqueous immiscible solvent	Ethyl acetate	31	0.078	101	0.06	0.10
	Diethyl ether	31	0.073	95	0.17	0.19
	1-Hexanol	64	0.153	95	0.18	0.22

* Single point adsorption total pore volume of pores less than 2,283.340 Å width at p/p° = 0.991694568.

B.8.4. Powder X-ray diffraction

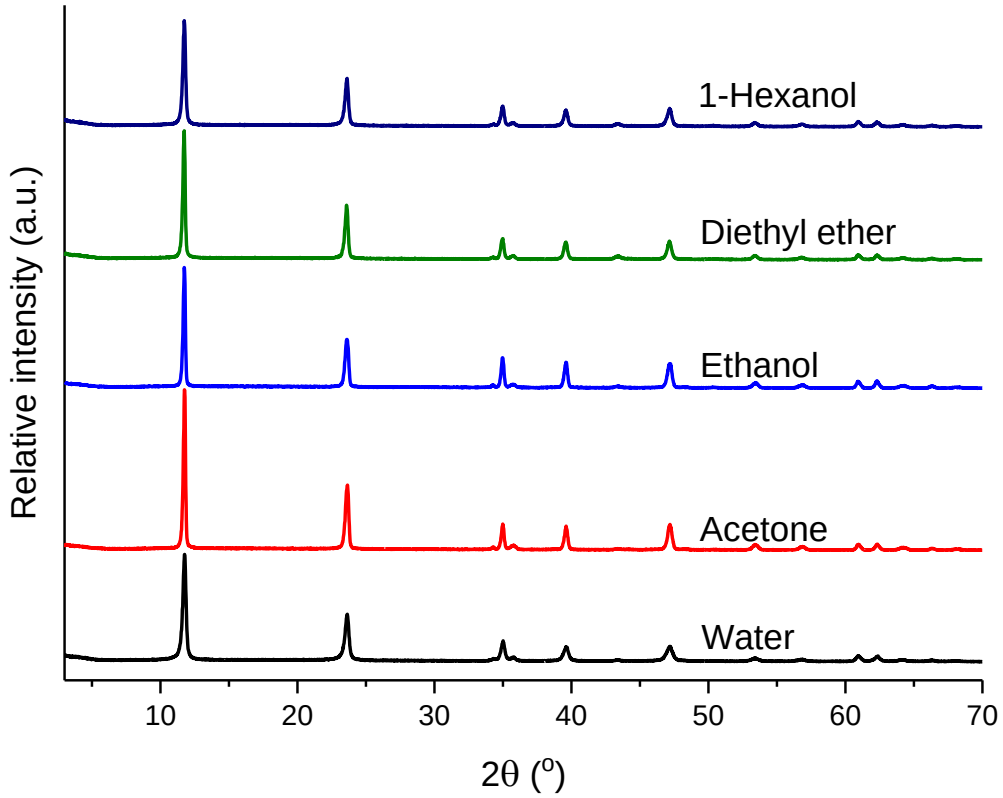


Figure B22. XRD pattern of platelet $Mg_4Al{-}CO_3$ LDHs treated with different solvents.

B.9. Solid state NMR spectroscopy studies

B.9.1. ^{1}H MAS solid state NMR spectroscopy

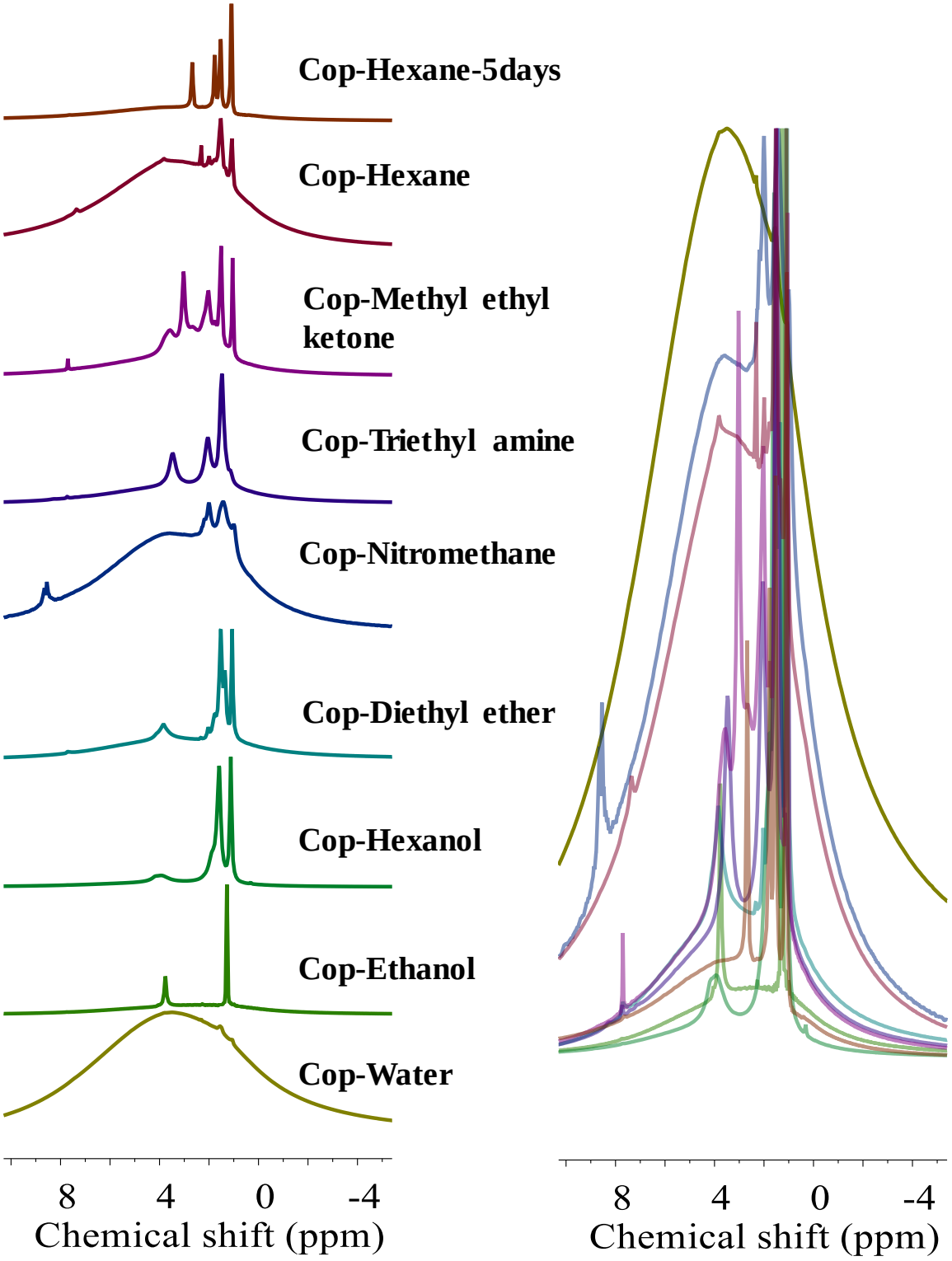


Figure B23. ^{1}H MAS solid state NMR spectrum of LDHs at with 9.4T and a MAS rate of 15 kHz at 23 °C.

B.9.2. ^{13}C CP MAS solid state NMR spectroscopy

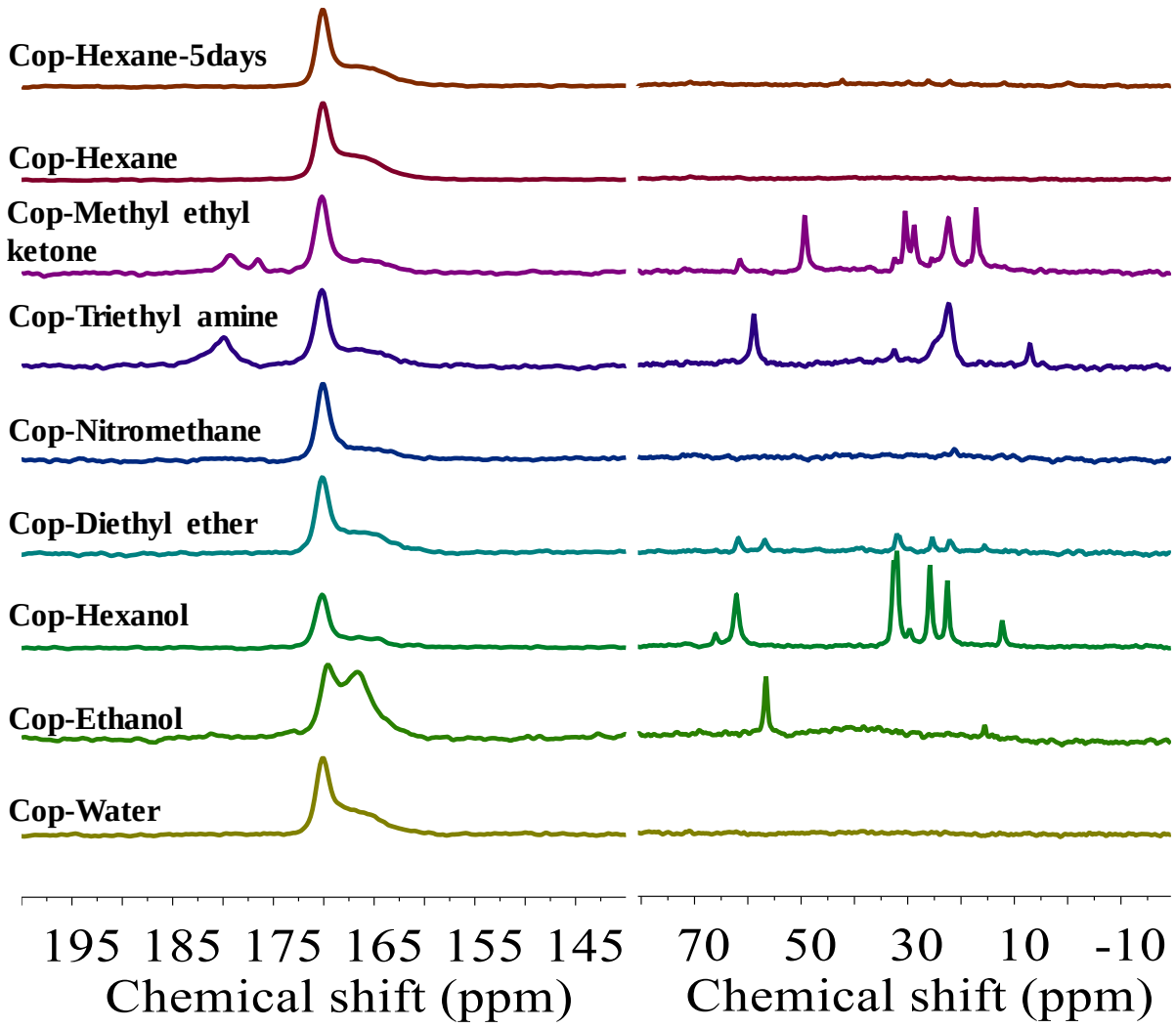


Figure B24. ^{13}C CP MAS solid state NMR spectrum of LDHs with 9.4T and a MAS rate of 10 kHz at 23 °C.

B.9.3. ^{27}Al MAS solid state NMR spectroscopy

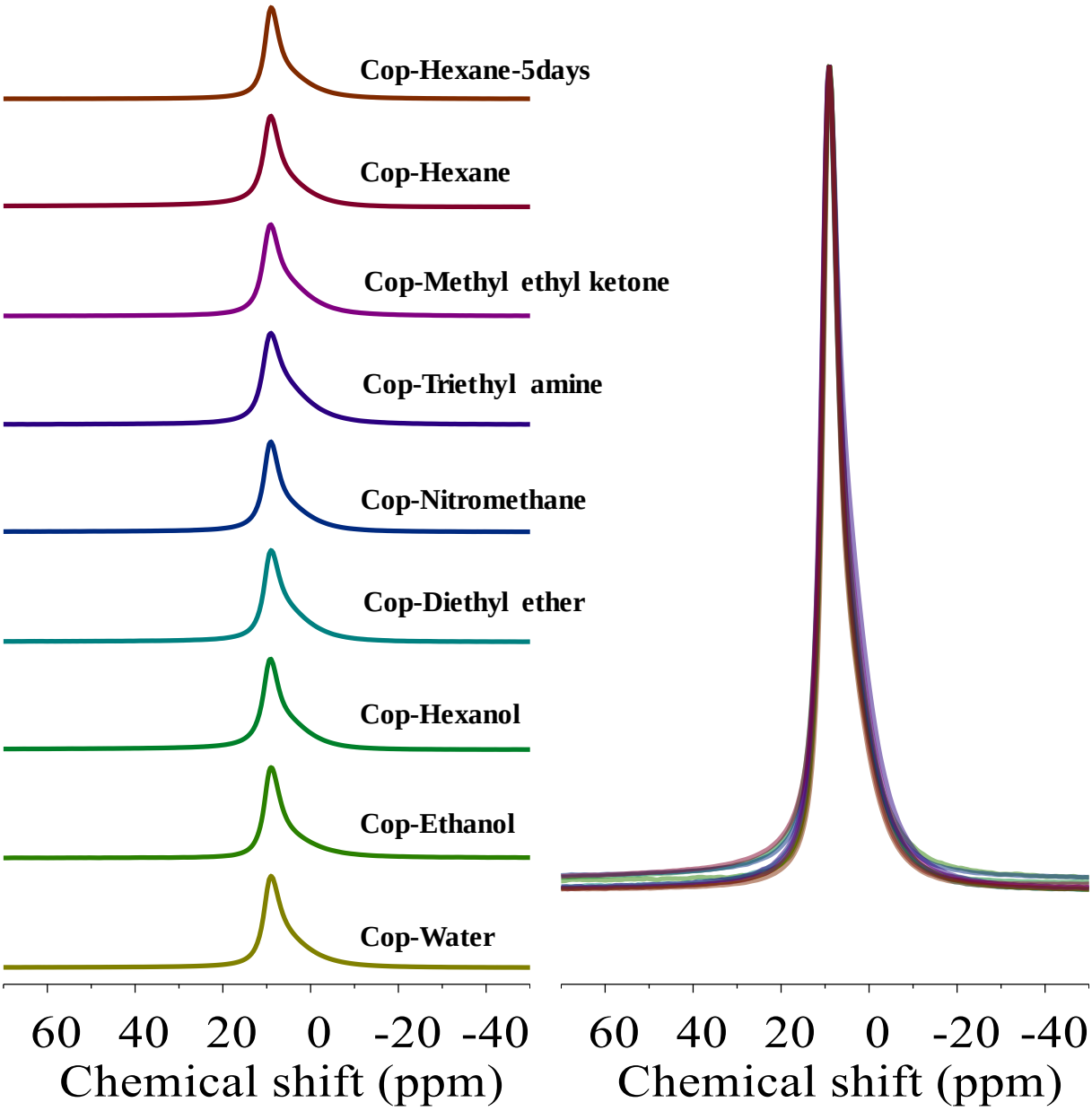


Figure B25. ^{27}Al MAS solid state NMR spectrum of LDHs with 9.4T and a MAS rate of 10 kHz at 23 °C.

Appendix C – Appendices to Chapter Four

C.1. Solubility data of compounds

Table C.1. Compounds in this study.

Compound type	Compound name	Solubility in water (g/L)
Amino acid with nonpolar side chain	Glycine	250
	β-Alanine	545
	β-Leucine	24.26
	β-Phenylalainine	27
	β-Aminobutyric acid (BABA)	1000
	γ-Aminobutyric acid (BABA)	1300
Amino acid with polar side chain	Serine	425
	Asparagine	29.4
Amino acid with acidic side chain	Aspartic acid	4.5
	Glutamic acid	7.5
Alpha-hydroxy acid salt	Sodium lactate	1500
Diamino	Ethylene diamine (liquid)	Miscible
Dicarboxylic	Oxalic acid	143
Polyhydroxy (sugar)	Glucose	909

C.2. Appearance of reconstructed products using nonpolar amino acids

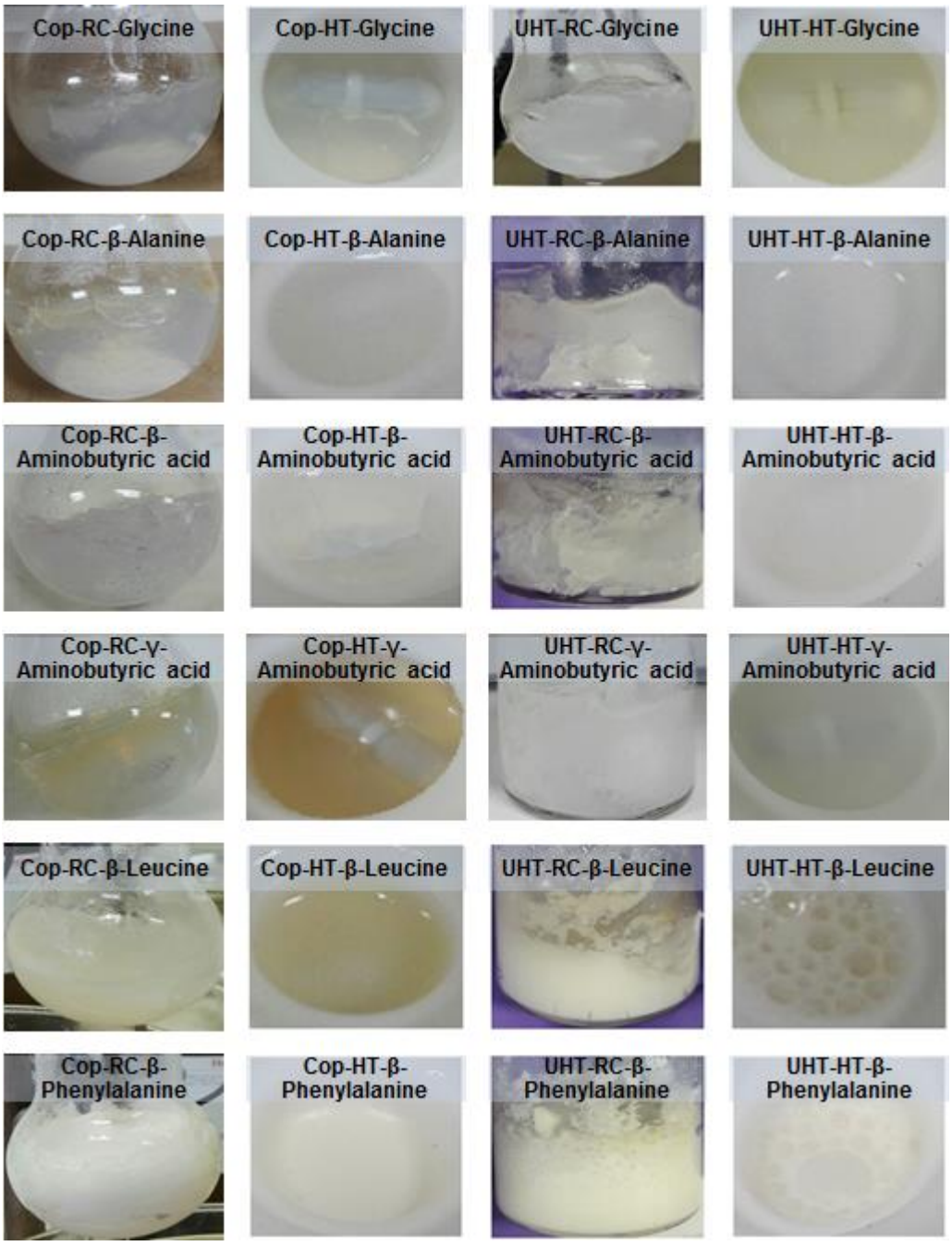


Figure C1. Appearance of products obtained after reconstruction of LDHs in different nonpolar amino acids. Products were defined as Cop-RC-amino acid and Cop-HT-amino acid for the ones originated from Cop-AMO LDHs and as UHT-RC-amino acid and UHT-HT-amino acid for the ones initiated from UHT-AMO LDHs. RC and HT indicate reaction condition in round bottom flask and autoclave hydrothermal reactor, respectively.

C.3. Characteristic data for reconstructed LDHs originated from Cop-AMO LDHs

C.3.1. Fourier transform infrared spectroscopy

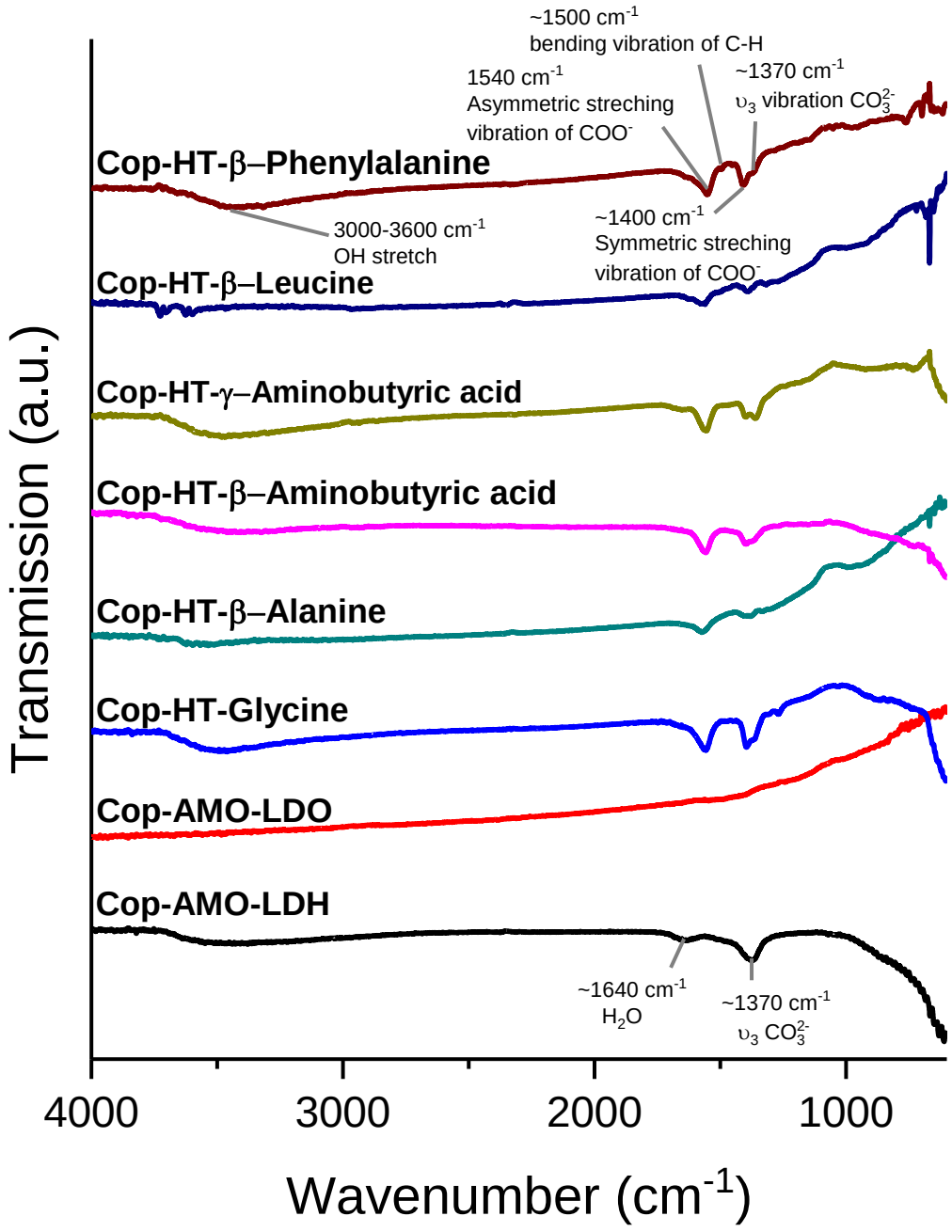


Figure C2. FTIR spectra of reconstructed of reconstructed Cop-HT LDHs by nonpolar amino acids.

C.3.2. Thermogravimetric analysis

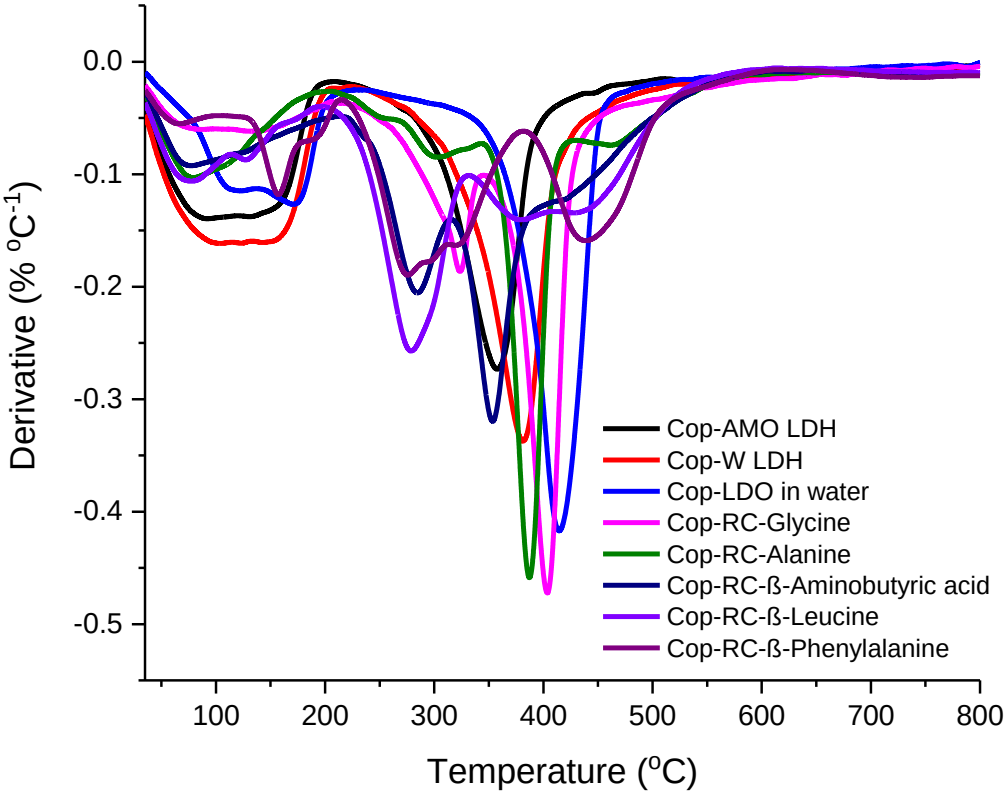


Figure C3. Differential thermogravimetric curves (DTG) of Cop-RC-amino acid LDHs.

C.3.3. LDHs Composition Data

Table C.2. Elemental analysis results of LDHs before and after reconstruction.

Sample	%C (wt%)			%H (wt%)			%N (wt%)		
	#1	#2	AVG	#1	#2	AVG	#1	#2	AVG
Cop-AMO LDH	3.91	3.09	3.50	4.87	3.82	4.35	0.00	0.00	0.00
Cop-W LDH	1.83	2.18	2.01	3.48	3.60	3.54	0.00	0.00	0.00
Cop-LDO in water	1.45	1.47	1.46	4.27	4.30	4.29	0.00	0.00	0.00
Cop-RC-Glycine	5.13	5.64	5.39	3.30	3.59	3.45	3.20	3.02	3.11
Cop-RC-β-Alanine	11.18	12.15	11.67	6.22	6.96	6.59	4.05	4.60	4.33
Cop-RC-β-Aminobutyric acid	11.73	9.00	10.37	5.45	4.07	4.76	3.40	2.70	3.05
Cop-RC-β-Leucine	19.22	16.40	17.81	6.10	6.31	6.21	3.74	3.18	3.46
Cop-RC-β-Phenylalanine	29.40	27.76	28.58	5.61	4.14	4.88	3.73	2.85	3.29

Table C.3. ICP results of LDHs before and after reconstruction.

Sample	%Weight from ICP results				%Mole		Total mole fraction	%Mole fraction in total		Mg/Al ratio
	Mg (avg.)	sd	Al (avg.)	sd	Mg %	Al %	Mg + Al	Mg	Al	
Cop-AMO LDH	20.95	0.21	5.73	0.10	0.86	0.21	1.07	0.80	0.20	4.06
Cop-LDO in water	27.50	0.25	8.01	0.16	1.13	0.30	1.43	0.79	0.21	3.81
Cop-RC-Glycine	22.22	0.24	7.29	0.13	0.91	0.27	1.18	0.77	0.23	3.38
Cop-RC-β-Alanine	23.16	0.19	7.13	0.10	0.95	0.26	1.22	0.78	0.22	3.60
Cop-RC-β-Aminobutyric acid	22.86	0.06	7.03	0.04	0.94	0.26	1.20	0.78	0.22	3.61
Cop-RC-β-Leucine	19.81	0.06	6.39	0.07	0.82	0.24	1.05	0.77	0.23	3.44
Cop-RC-β-Phenylalanine	17.56	0.10	6.87	0.07	0.72	0.25	0.98	0.74	0.26	2.84

Table C.4. Formula of LDHs before and after reconstruction.

Sample	Formula of LDHs
Cop-AMO LDH	$[Mg_{0.80}Al_{0.20}(OH)_2(CO_3)_{0.10}]\cdot 0.245H_2O\cdot 0.215$(Ethanol)
Cop-W LDH	$[Mg_{0.80}Al_{0.20}(OH)_2(CO_3)_{0.10}]\cdot 0.634H_2O$
Cop-LDO in water	$[Mg_{0.79}Al_{0.21}(OH)_2(HCO_3)_{0.031}(CO_3)_{0.095}]\cdot 1.194H_2O$
Cop-RC-Glycine	$[Mg_{0.77}Al_{0.23}(OH)_2(HCO_3)_{0.031}(CO_3)_{0.100}]\cdot 0.053H_2O\cdot 0.111$(Glycine)
Cop-RC-β-Alanine	$[Mg_{0.78}Al_{0.22}(OH)_2(HCO_3)_{0.031}(CO_3)_{0.095}]\cdot 2.212H_2O\cdot 0.420$(β-Alanine)
Cop-RC-β-Aminobutyric acid	$[Mg_{0.78}Al_{0.22}(OH)_2(HCO_3)_{0.031}(CO_3)_{0.095}]\cdot 2.465H_2O\cdot 0.206$(β-Aminobutyric acid)
Cop-RC-β-Leucine	$[Mg_{0.77}Al_{0.23}(OH)_2(HCO_3)_{0.031}(CO_3)_{0.100}]\cdot 0.033H_2O\cdot 0.195$(β-Leucine)
Cop-RC-β-Phenylalanine	$[Mg_{0.74}Al_{0.26}(OH)_2(HCO_3)_{0.031}(CO_3)_{0.115}]\cdot 0.281H_2O\cdot 0.308$(β-Phenylalanine)

C.4. Characteristic data for reconstructed LDHs originated from UHT-AMO LDHs

C.4.1. Powder X-ray diffraction

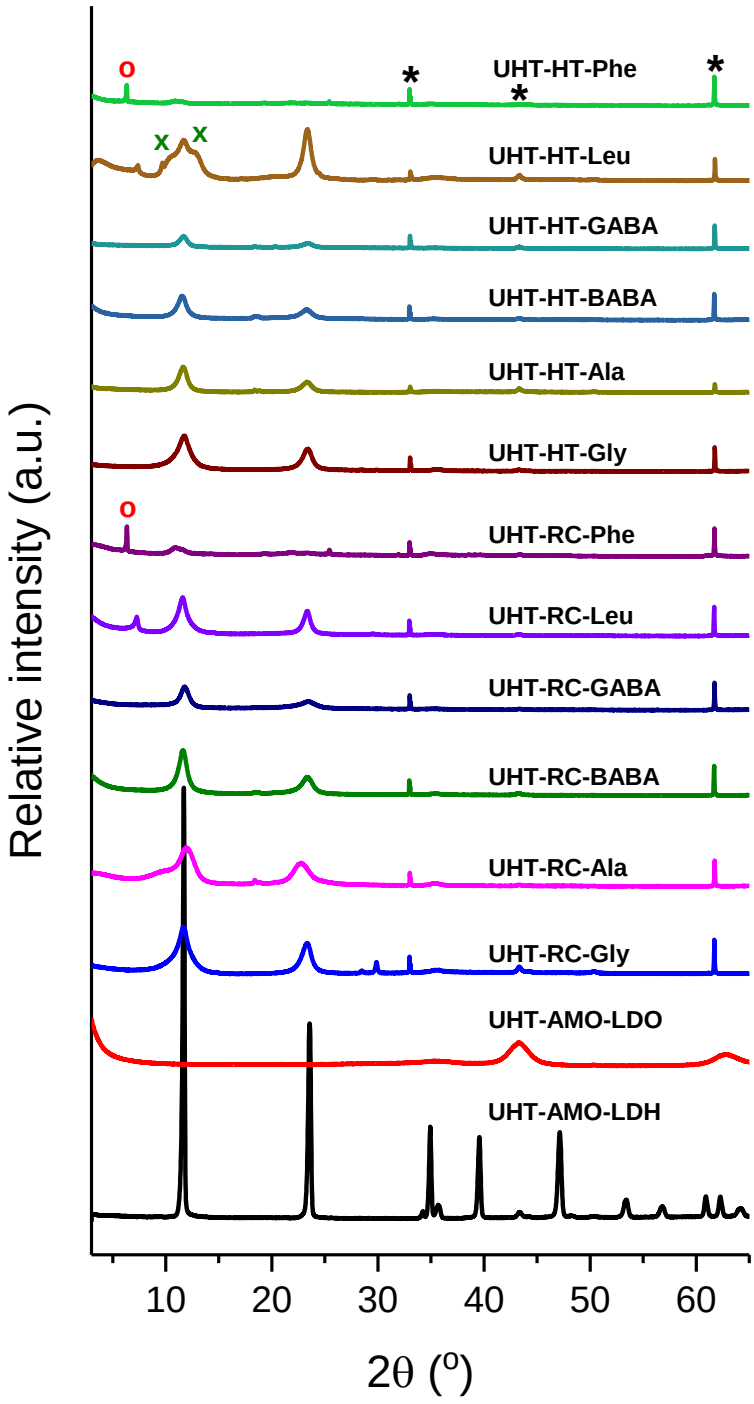


Figure C4. XRD pattern of reconstructed LDHs (originated from UHT-AMO LDHs) by nonpolar amino acids. **o** and **x** denote the Bragg reflections of impurities from phenylalanine (**o**) and leucine (**x**). (*Bragg reflections due to the sample holder were observed at 2θ = 43-44° and 50° and reflections from the silicon wafer were located at 2θ = 33° and 62°.)

C.4.2. Fourier transform infrared spectroscopy

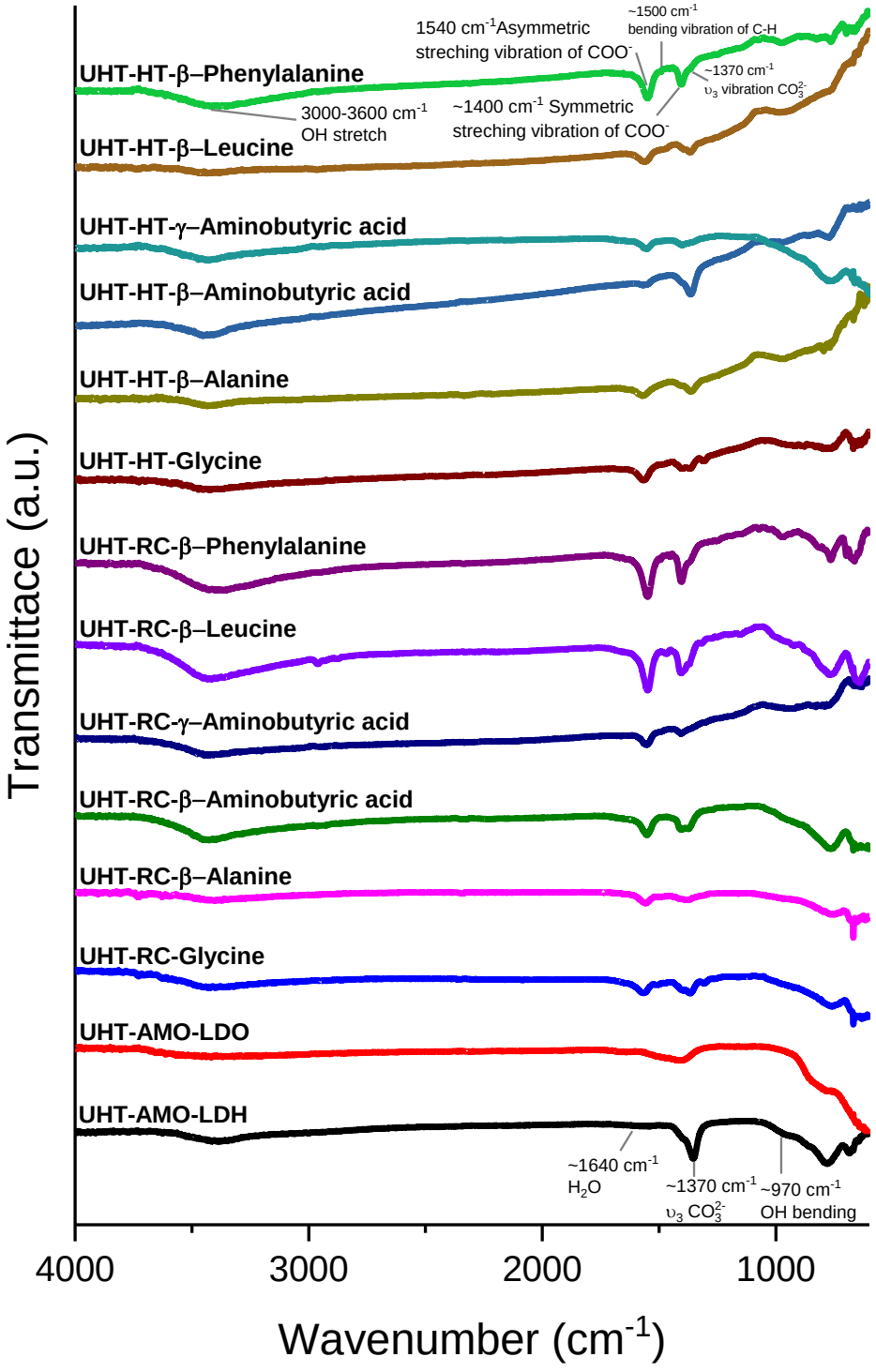


Figure C5. FTIR spectra of reconstructed LDHs (originated from UHT-AMO LDHs) by nonpolar amino acids.

C.5. Appearance of reconstructed products using other compounds



Figure C6. Reconstructed products (originated from Cop-AMO LDHs) with polar amino acids

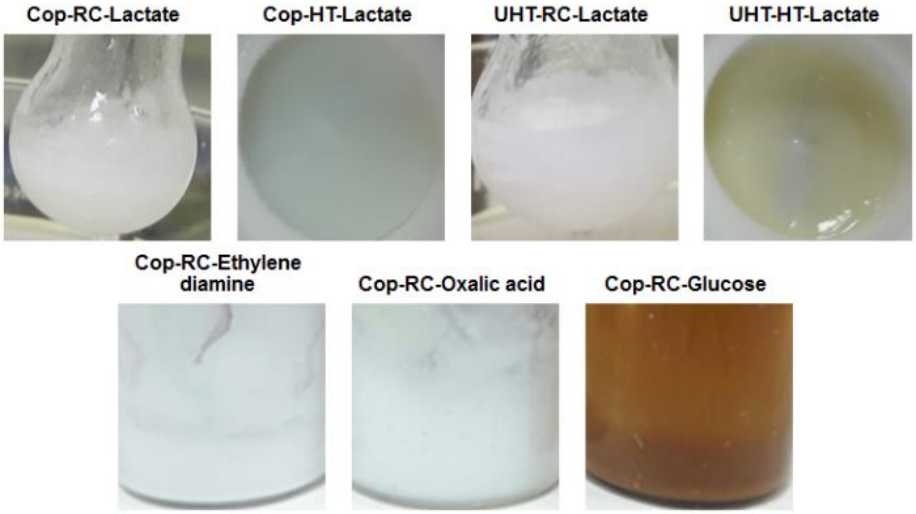


Figure C7. Reconstructed products (originated from Cop-AMO LDHs) with other compounds.

C.6. Barrier performance of amino acid reconstructed LDHs

C.6.1. Oxygen transmission rate data

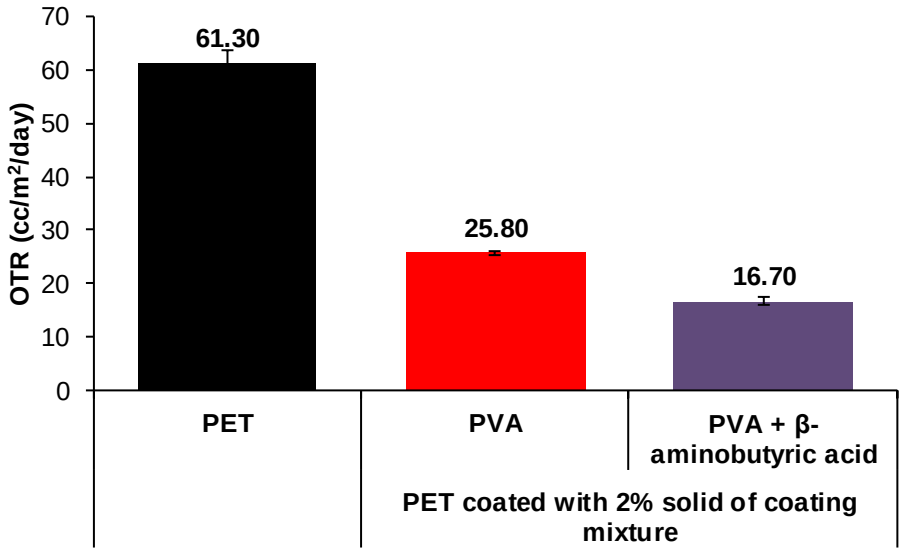


Figure C8. Oxygen transmission rate results of the coated film: Effect of amino acid on barrier property (without LDH).

C.6.2. Scanning electron microscopy

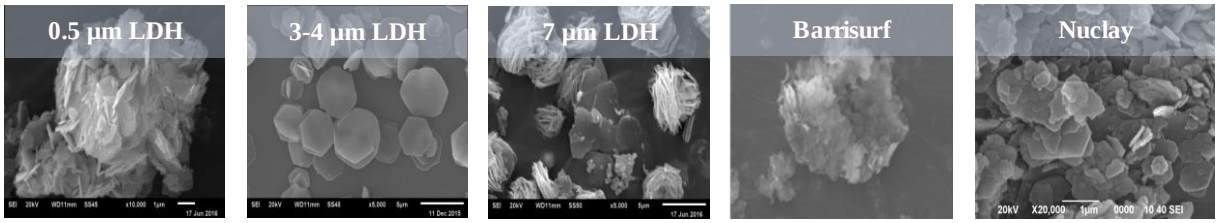


Figure C9. SEM of different LDHs and commercial clays used in this study.

C.6.3. Coated film properties

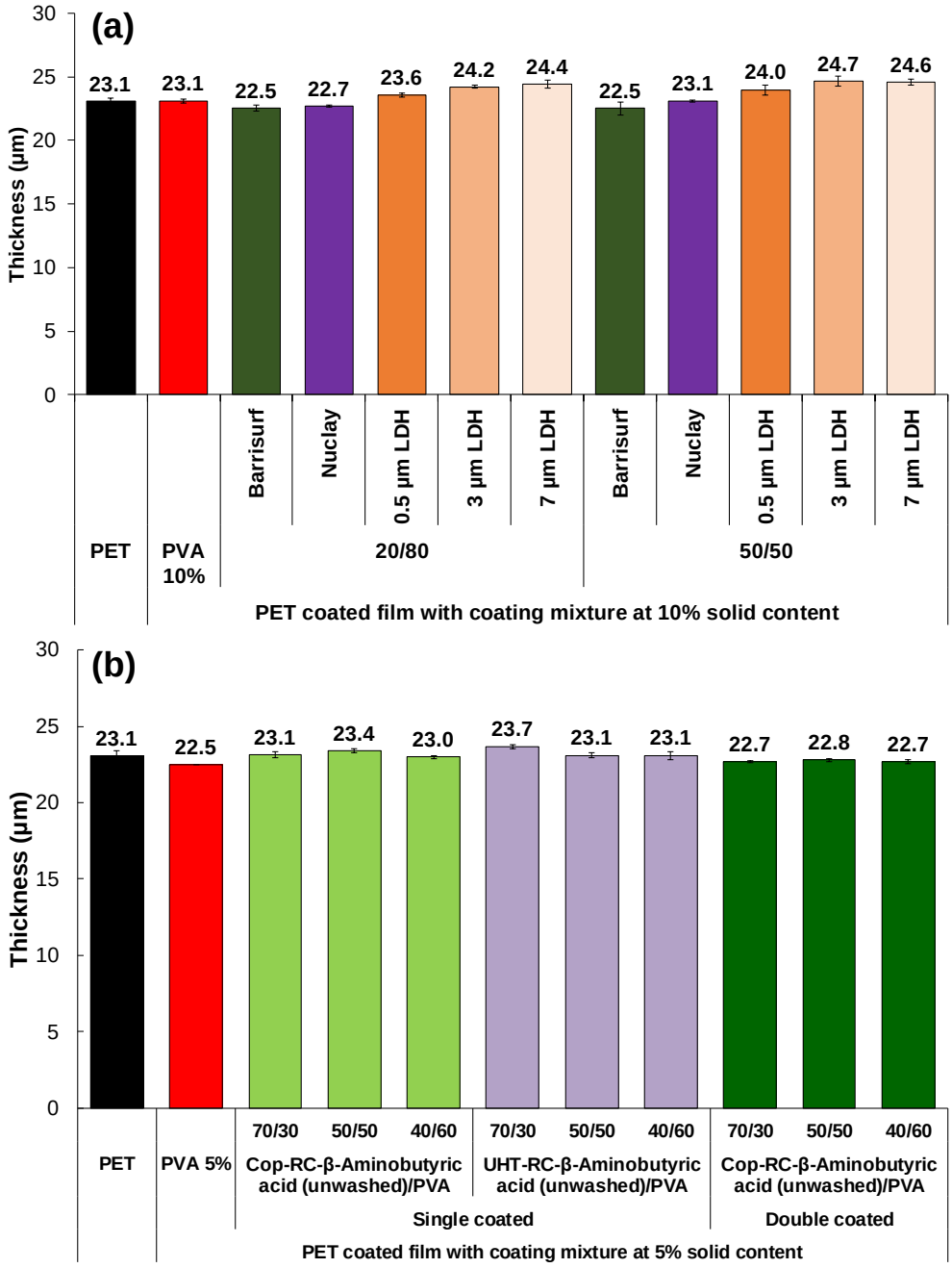


Figure C10. Thickness of films (a) coated films with different LDHs and clays and (b) coated films with amino acid reconstructed LDHs at different LDH/PVA or clay/PVA ratios.

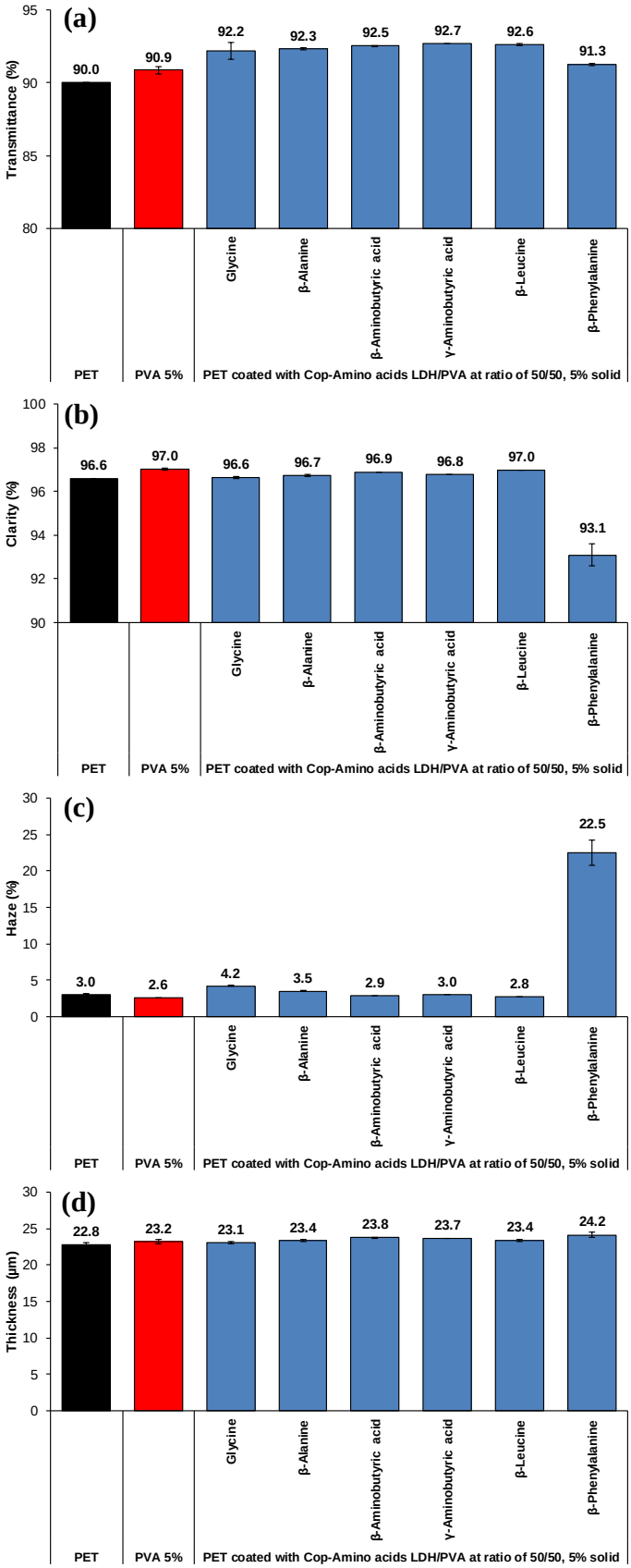


Figure C11. Optical properties of coated films: (a) % transmission, (b) % clarity, (c) % haze and (d) film thickness.

Appendix D – Appendices to Chapter Five

D.1. Appearance of reconstructed products in water

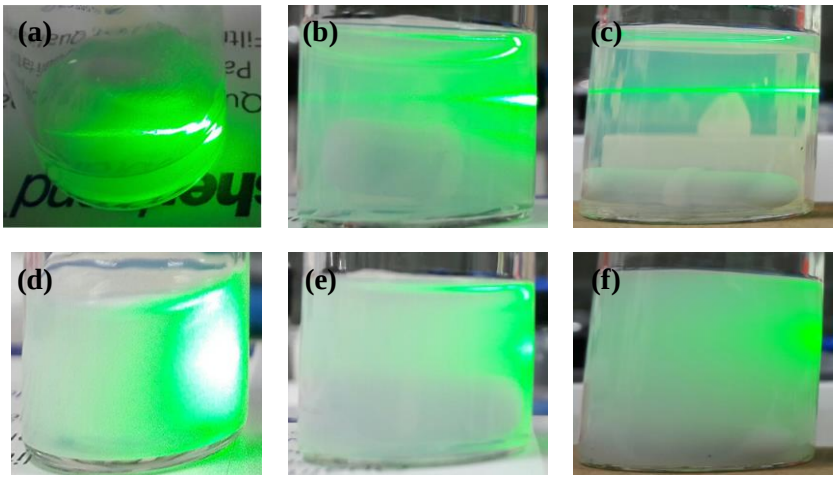


Figure D1. Green laser beam shows Tyndall effect for (a)-(c) Cop A450 DRC and (d)-(f) Cop W450 DRC samples at different concentrations: (a) and (d) 100 g/L, (b) and (e) 50 g/L and (c) and (f) 20 g/L.

D.2. Characteristic data for reconstructed LDHs in water: Effect of calcination temperature

D.2.1. Powder X-ray diffraction data

Table D1. Summary of the XRD data of original LDHs and products after reconstruction.

Sample	Bragg reflection												Unit cell parameter*	
	003			006			009			110			*a* (=b) parameter (Å)	*c* parameter (Å)
	2θ (°)	FWHM (°)	*d* spacing (Å)	2θ (°)	FWHM (°)	*d* spacing (Å)	2θ (°)	FWHM (°)	*d* spacing (Å)	2θ (°)	FWHM (°)	*d* spacing (Å)		
Cop A LDH	11.15	1.220	7.93	22.45	1.267	3.96	34.45	0.796	2.60	60.19	0.940	1.54	3.072	23.796
Cop A250-DRC	11.10	0.888	7.96	22.33	1.067	3.98	34.36	1.037	2.61	60.10	0.772	1.54	3.077	23.884
Cop A350-DRC	11.19	0.451	7.90	22.51	0.492	3.95	34.17	0.679	2.62	60.19	0.505	1.54	3.072	23.707
Cop A450-DRC	11.18	0.456	7.91	22.48	0.497	3.95	34.09	0.645	2.63	60.18	0.572	1.54	3.073	23.722
Cop A550-DRC	11.18	0.408	7.91	22.48	0.475	3.95	34.07	0.666	2.63	60.17	0.487	1.54	3.073	23.730
Cop W LDH	11.20	1.262	7.90	22.53	1.318	3.94	34.47	1.261	2.60	60.30	1.059	1.53	3.067	23.687
Cop W250-DRC	11.09	0.930	7.97	22.29	1.095	3.98	34.33	1.039	2.61	60.05	0.826	1.54	3.079	23.916
Cop W350-DRC	11.16	0.728	7.92	22.49	0.762	3.95	34.38	1.032	2.61	60.22	0.821	1.54	3.071	23.758
Cop W450-DRC	11.22	0.429	7.88	22.53	0.503	3.94	34.11	0.700	2.63	60.20	0.625	1.54	3.072	23.649
Cop W550-DRC	11.18	0.443	7.91	22.51	0.564	3.95	34.08	0.875	2.63	60.18	0.819	1.54	3.073	23.717

*Unit cell parameters indexed to a hexagonal unit cell (space group $R\bar{3}m$). FWHM is full-width at half-maximum height values of a reflection located at 2θ.

Table D1. (continue) Summary of the XRD data of original LDHs and products after reconstruction.

Sample	Bragg reflection					
	015		018		113	
	2θ (°)	***d* spacing (Å)**	**2θ (°)**	***d* spacing (Å)**	**2θ (°)**	***d* spacing (Å)**
Cop A LDH	38.65	2.33	45.67	1.98	61.35	1.51
Cop A250-DRC	38.53	2.33	45.49	1.99	61.27	1.51
Cop A350-DRC	38.34	2.35	46.04	1.97	61.53	1.51
Cop A450-DRC	38.40	2.34	45.96	1.97	61.39	1.51
Cop A550-DRC	38.51	2.34	45.91	1.98	61.42	1.51
Cop W LDH	38.63	2.33	45.76	1.98	61.42	1.51
Cop W250-DRC	38.45	2.34	45.40	2.00	61.25	1.51
Cop W350-DRC	38.41	2.34	45.52	1.99	61.45	1.51
Cop W450-DRC	38.49	2.34	46.00	1.97	61.44	1.51
Cop W550-DRC	38.60	2.33	45.88	1.98	61.42	1.51

D.2.2. Fourier transform infrared spectroscopy

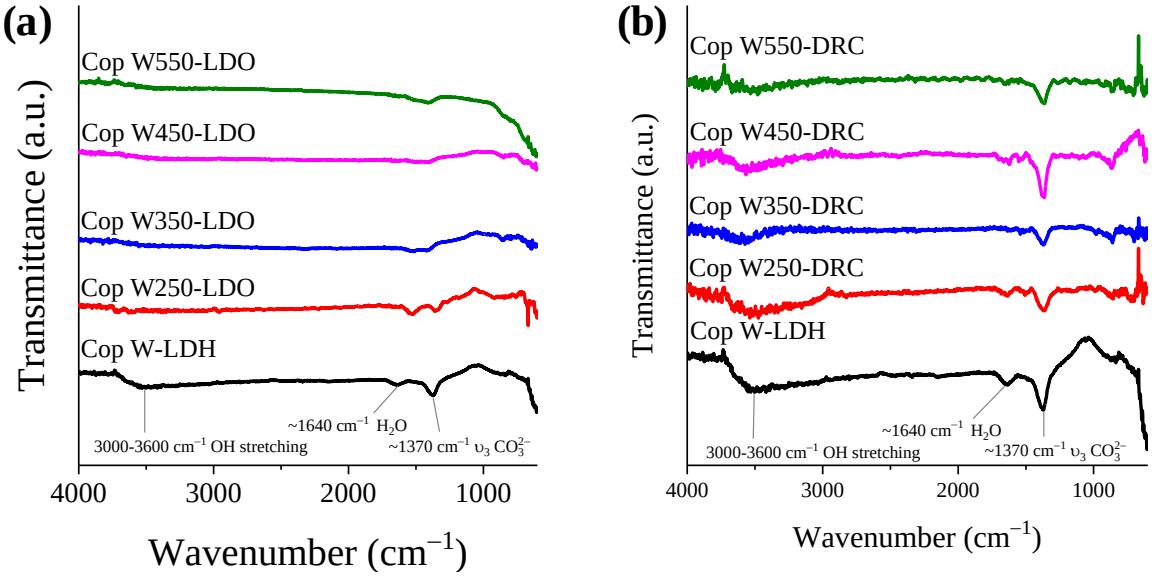


Figure D2. FTIR spectra of Cop W LDHs compared to (a) their LDOs at different calcination temperatures and (b) their reconstruction products in water at room temperature for 24 hours (DRC).

D.2.3. N_2 adsorption desorption isotherms

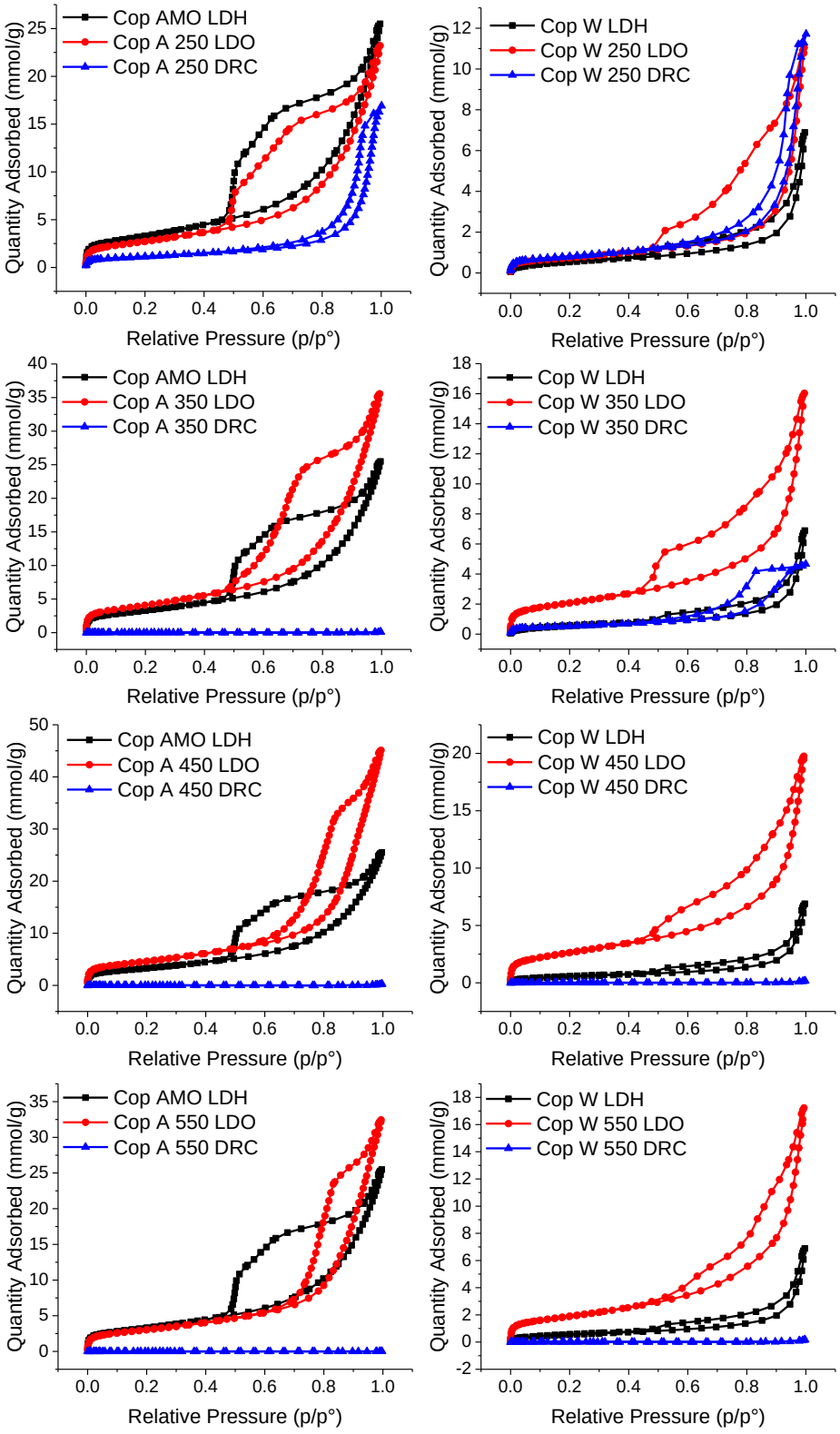


Figure D3. The N_2 adsorption-desorption isotherms of Cop AMO and Cop Water LDHs (black), their LDOs at different calcination temperature (red) and their reconstruction products in water at room temperature for 24 hours or DRC (blue).

D.2.4. BJH desorption pore size distributions

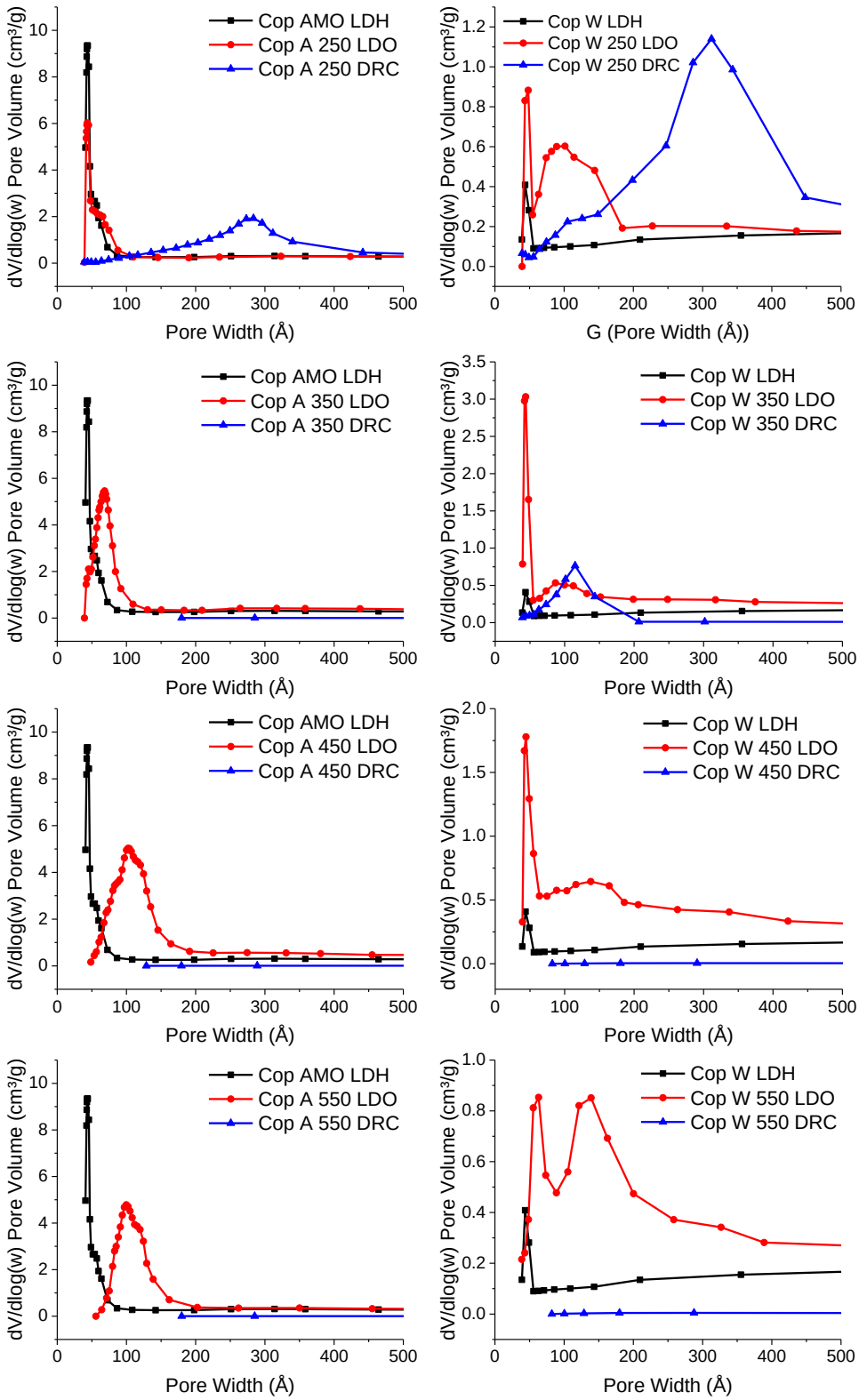


Figure D4. The Barrett-Joyner-Halenda (BJH) desorption pore size distributions of Cop AMO and Cop Water LDHs (black), their LDOs at different calcination temperature (red) and their reconstruction products in water at room temperature for 24 hours or DRC (blue).

D.2.5. Dynamic light scattering measurement

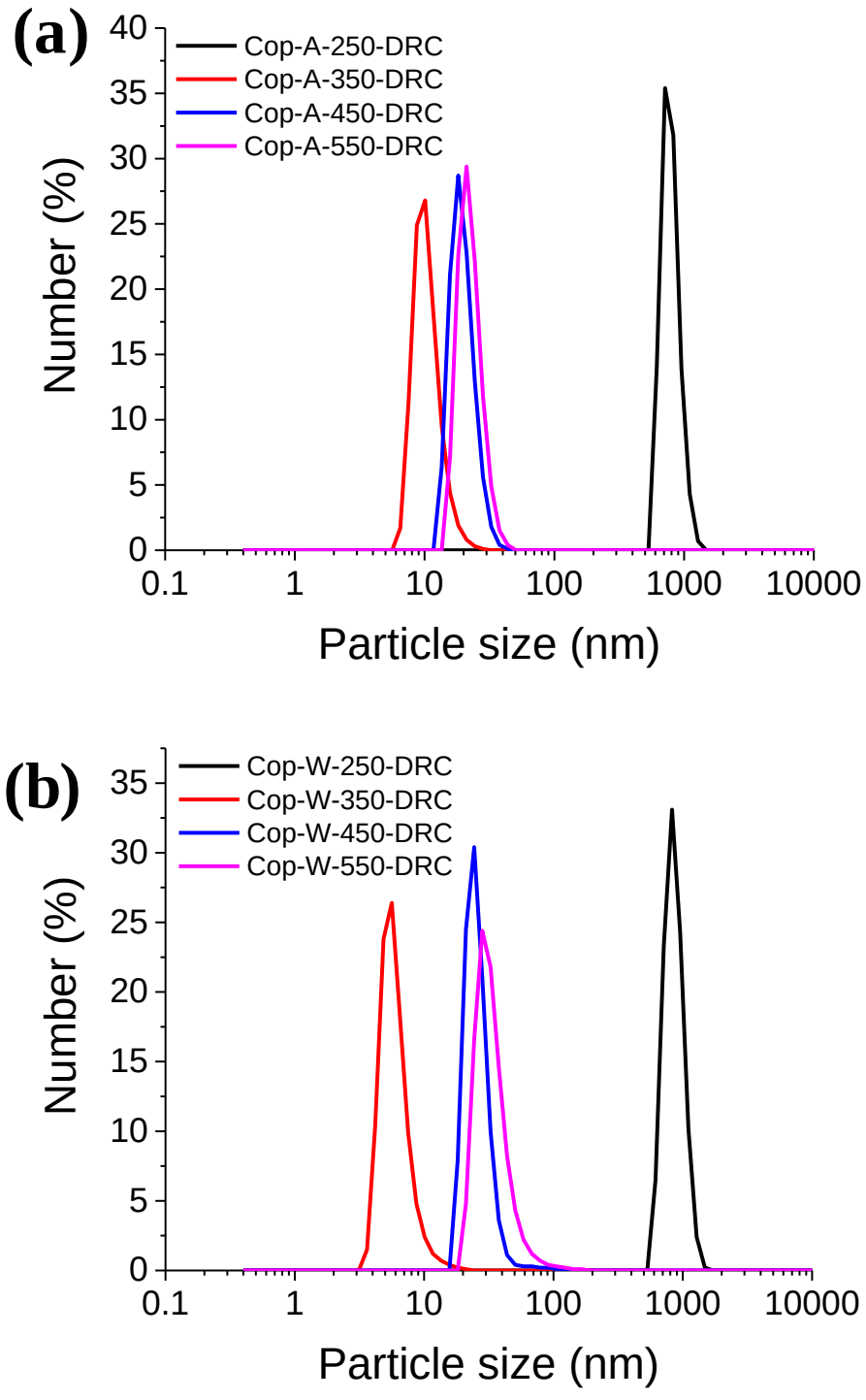


Figure D5. Particle size distribution curves from dynamic light scattering measurement (DLS) of reconstruction products in water at room temperature for 24 hours or DRC for (a) Cop A DRC products and (b) Cop W DRC products.

D.2.6. Thermogravimetric analysis

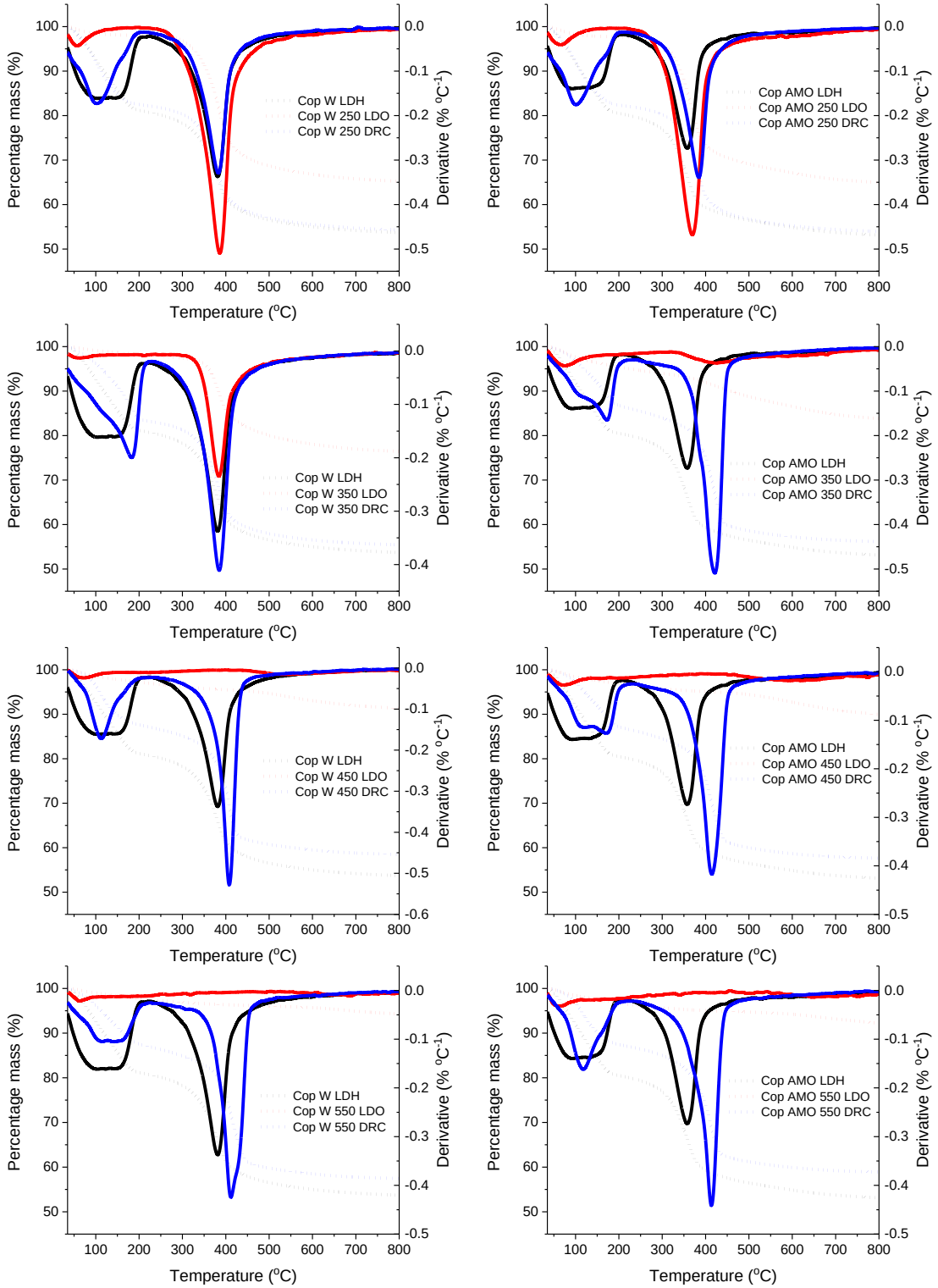


Figure D6. TGA (dashed line) and DTG (full line) curves of Cop AMO and Cop Water LDHs (black), their LDOs at different calcination temperatures (red) and their direct reconstruction products in water at room temperature for 24 hours or DRC (blue).

D.3. Characteristic data for reconstructed LDHs in water: Effect of the LDHs morphology

D.3.1. Powder X-ray diffraction

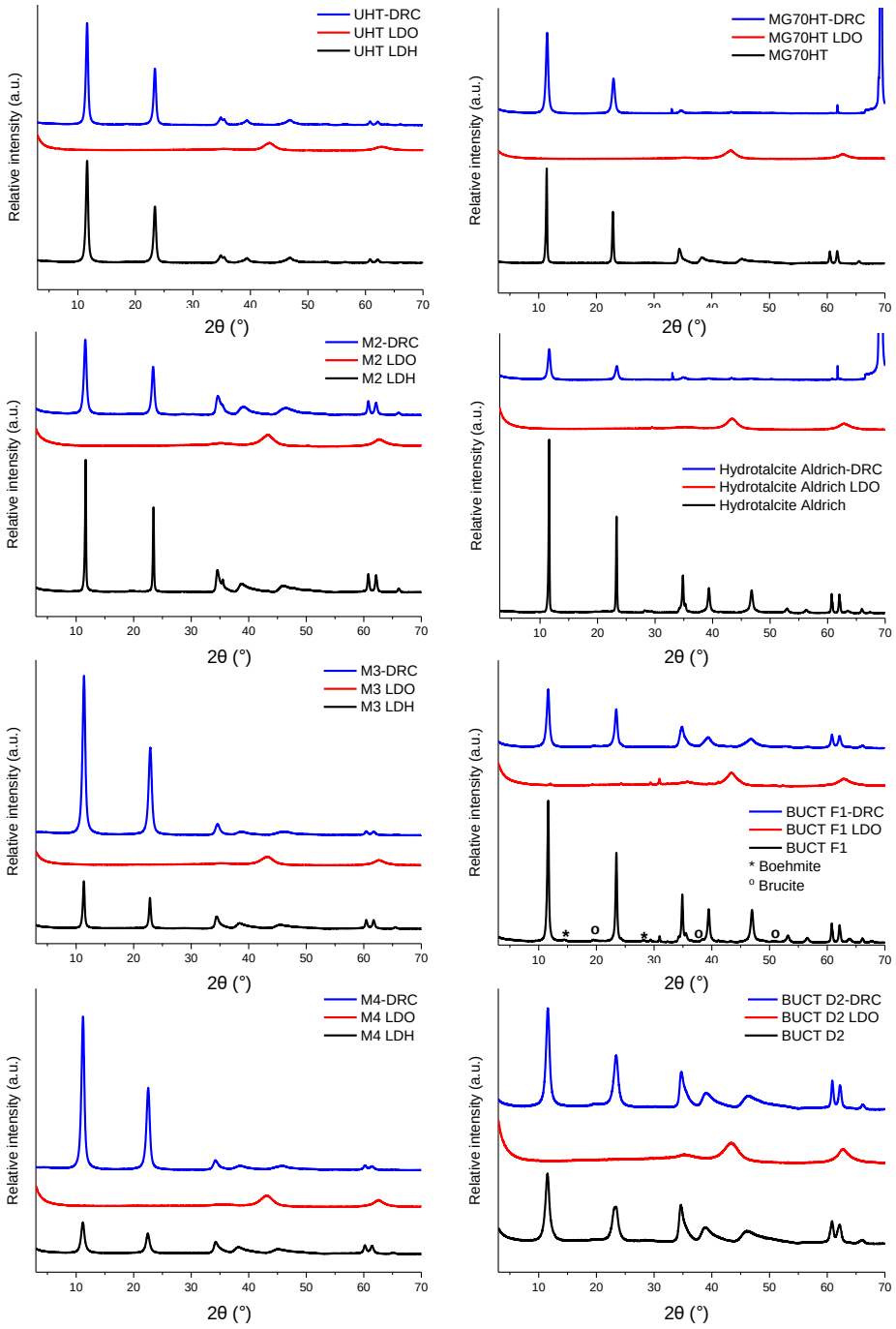


Figure D7. XRD patterns of different LDHs (black), their LDOs at calcination temperature of 450 °C (red) and their reconstruction products in water at room temperature for 24 hours or DRC (blue). (Bragg reflections due to sample holder were observed at 2θ = 43-44º and 50º and from silicon wafer were located at 2θ = 33º, 62º and 69º.)

D.3.2. Fourier transform infrared spectroscopy

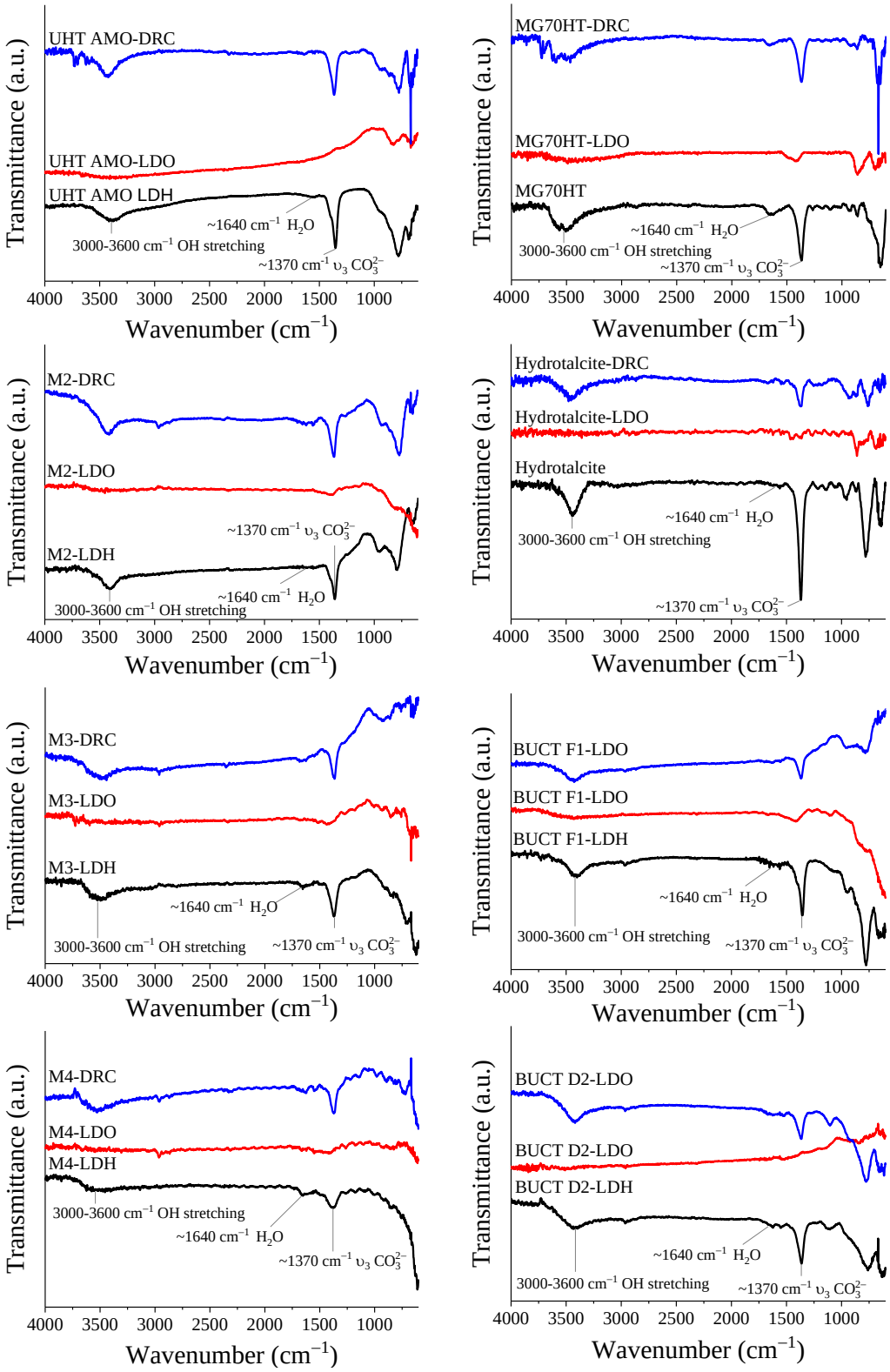


Figure D8. FTIR spectra of different LDHs (black), their LDOs at calcination temperature of 450 °C (red) and their reconstruction products in water at room temperature for 24 hours or DRC (blue).

D.3.3. Surface properties data

Table D2. N_2 BET surface area and total pore volume of different LDHs, their LDOs at calcination temperature of 450 °C and direct reconstruction products (DRC).

Sample		BET surface area (m^2/g)	Total pore volume (cm^3/g)
UHT AMO	LDH	23±0	0.06±0.00
	LDO	137±3	0.11±0.00
	DRC	10±0	0.10±0.00
M2	LDH	33±1	0.17±0.00
	LDO	185±4	0.31±0.01
	DRC	33±1	0.22±0.00
M3	LDH	50±1	0.34±0.01
	LDO	142±3	0.55±0.01
	DRC	0.5±0.0	0.00±0.00
M4	LDH	74±1	0.22±0.00
	LDO	183±4	0.45±0.01
	DRC	0.00±0.00	0.00±0.00
MG70HT	LDH	19±0	0.08±0.00
	LDO	186±4	0.19±0.00
	DRC	0.1±0	0.00±0.00
Hydrotalcite	LDH	6.6±0	0.02±0.00
	LDO	272±5	0.21±0.00
	DRC	12±0	0.12±0.00
BUCT F1	LDH	26±1	0.13±0.00
	LDO	148±3	0.23±0.00
	DRC	46±1	0.42±0.01
BUCT D2	LDH	100±2	0.38±0.01
	LDO	241±5	0.66±0.01
	DRC	66±1	0.38±0.01

D.3.4. LDHs composition data

Table D3. ICP results of LDHs before and after reconstruction in water.

Sample	% Weight from ICP results				% Mole		Total mole fraction	% Mole fraction in total		Mg/Al ratio
	Mg (avg)	sd.	Al (avg)]	sd.	Mg %	Al %	Mg+Al	Mg	Al	
Original Cop A LDH	20.95	0.21	5.73	0.10	0.86	0.21	1.07	0.80	0.20	4.06
Cop A350 DRC	25.73	0.13	7.42	0.12	1.06	0.27	1.33	0.79	0.21	3.85
Cop A450 DRC	27.50	0.25	8.01	0.16	1.13	0.30	1.43	0.79	0.21	3.81
Cop A550 DRC	28.14	0.27	8.24	0.14	1.16	0.31	1.46	0.79	0.21	3.79
Cop W450 DRC	28.04	0.41	8.35	0.19	1.15	0.31	1.46	0.79	0.21	3.73
UHT AMO LDH	20.83	0.34	10.35	0.23	0.86	0.38	1.24	0.69	0.31	2.23
UHT DRC	24.68	0.14	13.08	0.19	1.02	0.48	1.50	0.68	0.32	2.09
M2 LDH	23.01	0.10	12.57	0.05	0.95	0.47	1.41	0.67	0.33	2.03
M2 DRC	21.20	0.19	11.57	0.12	0.87	0.43	1.30	0.67	0.33	2.03
M3 LDH	25.61	0.12	9.43	0.12	1.05	0.35	1.40	0.75	0.25	3.01
M3 DRC	24.30	0.27	9.05	0.06	1.00	0.34	1.34	0.75	0.25	2.98
M4 LDH	27.02	0.21	7.83	0.10	1.11	0.29	1.40	0.79	0.21	3.83
M4 DRC	26.09	0.21	7.61	0.09	1.07	0.28	1.36	0.79	0.21	3.81

Table D4. Elemental analysis results of LDHs before and after reconstruction in water.

Sample	%C (wt%)			%H (wt%)			%N (wt%)		
	#1	#2	AVG	#1	#2	AVG	#1	#2	AVG
Original Cop A LDH	3.91	3.09	3.50	4.87	3.82	4.35	0.00	0.00	0.00
Cop A350 DRC	1.79	1.78	1.79	4.22	4.25	4.24	0.00	0.00	0.00
Cop A450 DRC	1.45	1.47	1.46	4.27	4.30	4.29	0.00	0.00	0.00
Cop A550 DRC	0.94	1.00	0.97	4.42	4.43	4.43	0.00	0.00	0.00
Original Cop W LDH	1.83	2.18	2.01	3.48	3.60	3.54	0.00	0.00	0.00
Cop W350 DRC	2.30	2.32	2.31	4.23	4.19	4.20	0.00	0.00	0.00
Cop W450 DRC	0.91	0.94	0.93	4.43	4.45	4.44	0.00	0.00	0.00
Cop W550 DRC	1.21	1.38	1.30	4.34	4.37	4.36	0.00	0.00	0.00
UHT AMO LDH	3.86	3.85	3.86	3.48	3.60	3.55	0.00	0.00	0.00
UHT DRC	1.17	1.38	1.11	4.37	3.64	4.01	0.00	0.00	0.00
M2 LDH	2.79	2.07	2.43	4.05	3.01	3.53	0.00	0.00	0.00
M2 DRC	1.28	1.06	1.17	4.44	3.64	4.04	0.00	0.00	0.00
M3 LDH	2.35	2.75	2.55	3.95	4.49	4.22	0.00	0.00	0.00
M3 DRC	0.79	0.71	0.75	4.26	3.85	4.06	0.00	0.00	0.00
M4 LDH	3.34	2.48	2.91	5.34	3.78	4.56	0.00	0.00	0.00
M4 DRC	1.11	1.56	1.34	5.60	6.59	6.10	0.00	0.00	0.00
MG70HT	1.72	2.08	1.90	2.70	3.39	3.05	0.00	0.00	0.00
MG70HT DRC	0.48	0.50	0.49	4.70	4.62	4.66	0.00	0.00	0.00
Hydrotalcite	5.14	5.19	5.17	4.17	4.18	4.18	0.00	0.00	0.00
Hydrotalcite DRC	0.68	0.79	0.74	4.50	4.54	4.52	0.00	0.00	0.00
BUCT F1 LDH	2.13	2.18	2.16	3.03	3.00	3.02	0.00	0.00	0.00
BUCT F1 DRC	1.49	1.08	1.29	3.27	4.28	3.78	0.00	0.00	0.00
BUCT D2 LDH	2.65	2.27	2.46	4.67	3.99	4.33	0.00	0.00	0.00
BUCT D2 DRC	0.72	1.55	1.14	3.87	5.75	4.81	0.00	0.00	0.00

D.3.5. N_2 adsorption desorption isotherms

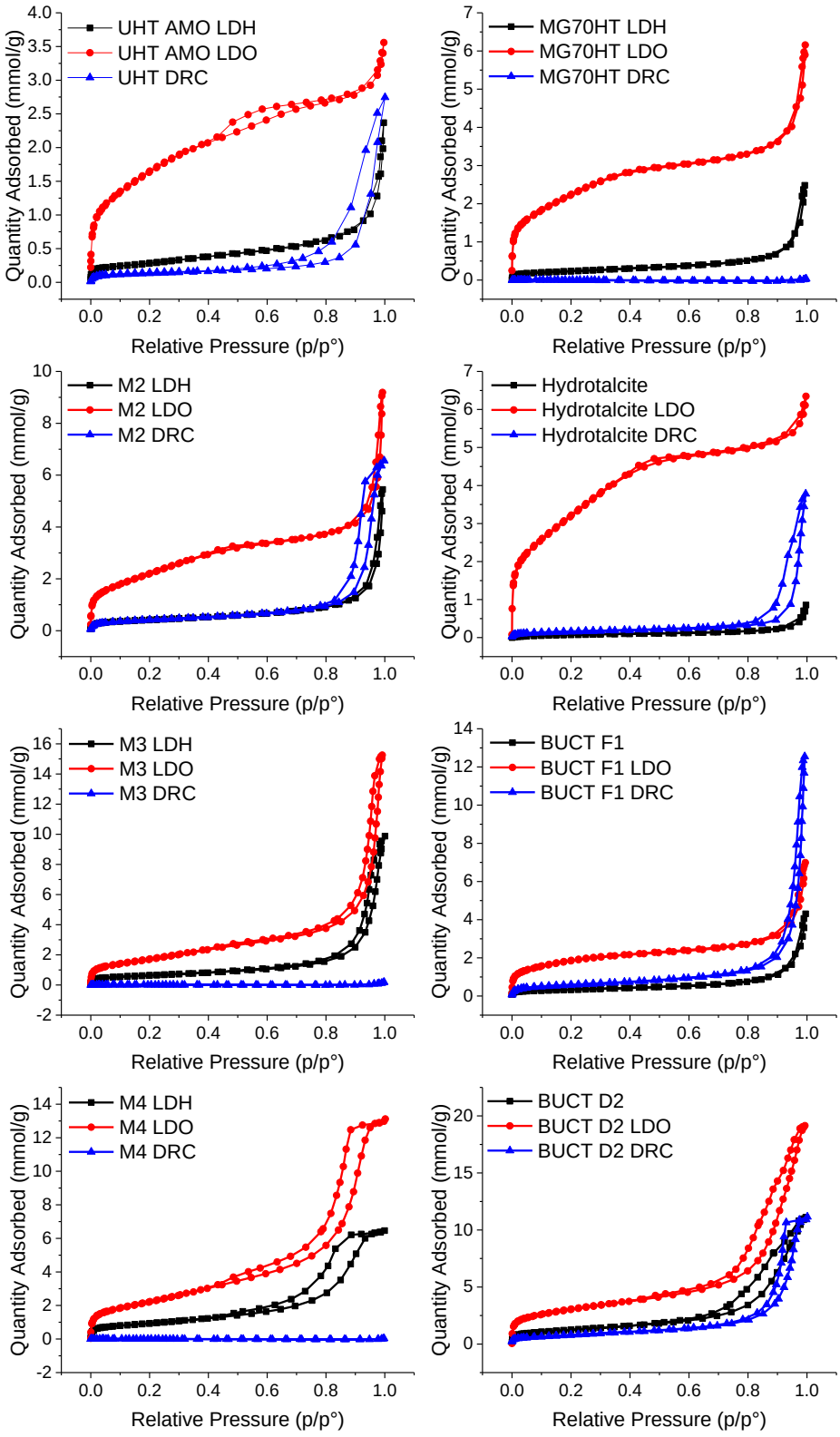


Figure D9. The N_2 adsorption-desorption isotherms of different LDHs (black), their LDOs at calcination temperature of 450 °C (red) and their reconstruction products in water at room temperature for 24 hours or DRC (blue).

D.3.6. BJH desorption pore size distributions

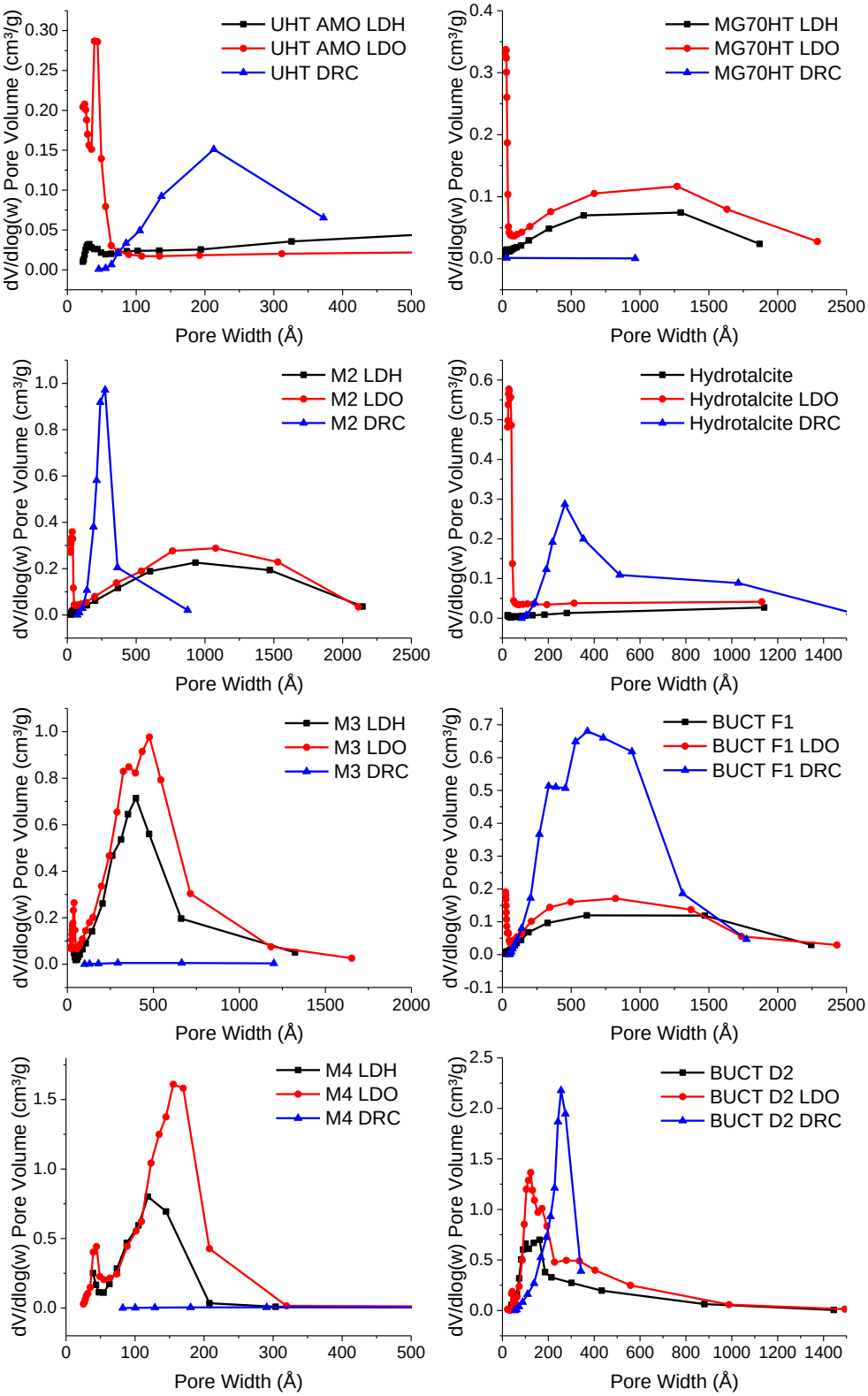


Figure D10. The Barrett-Joyner-Halenda (BJH) desorption pore size distributions of different LDHs (black), their LDOs at calcination temperature of 450 °C (red) and their reconstruction products in water at room temperature for 24 hours or DRC (blue).

D.3.7. Thermogravimetric analysis

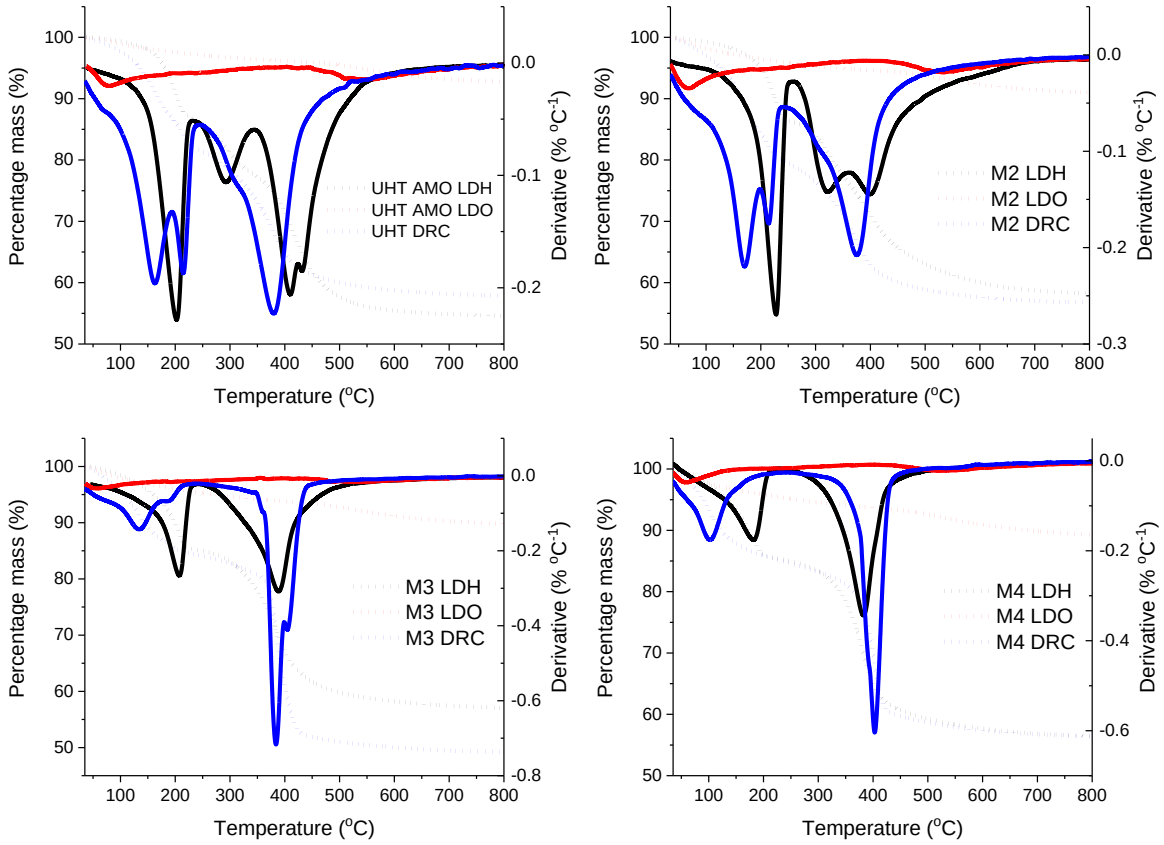


Figure D11. TGA (dashed line) and DTG (full line) curves of different LDHs (black), their LDOs at calcination temperature of 450 °C (red) and their reconstruction products in water at room temperature for 24 hours or DRC (blue).

D.3.8. Zeta potential measurement

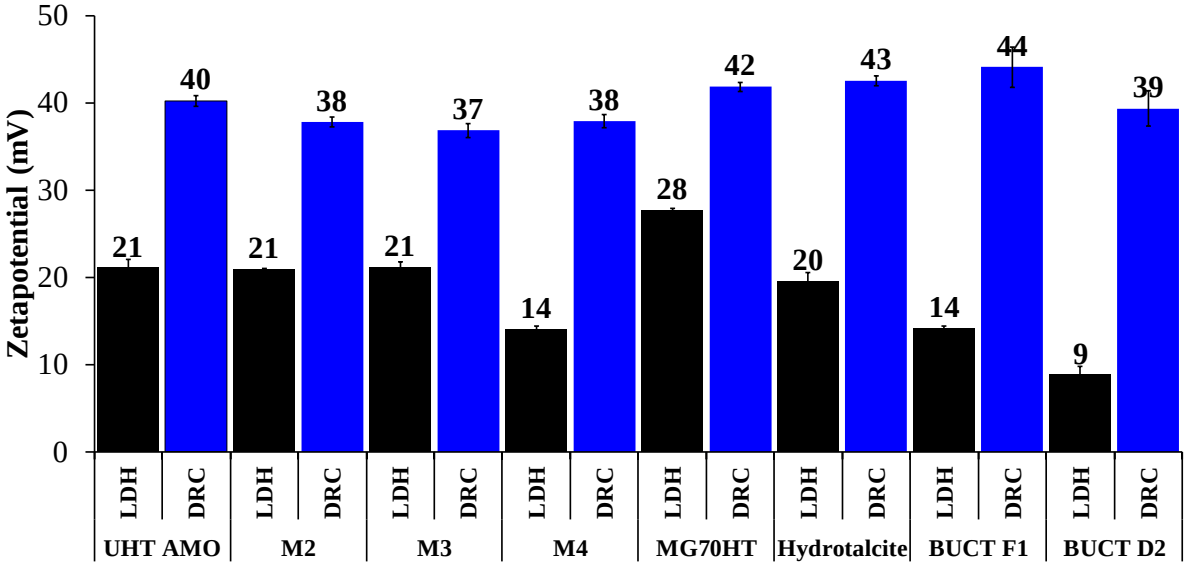


Figure D12. Zeta potential of different LDHs (black) and their reconstruction products in water at room temperature for 24 hours or DRC (blue).

D.4. Characteristic data for reconstructed LDHs in water: Effect of reconstruction conditions

D.4.1. Dynamic light scattering measurement

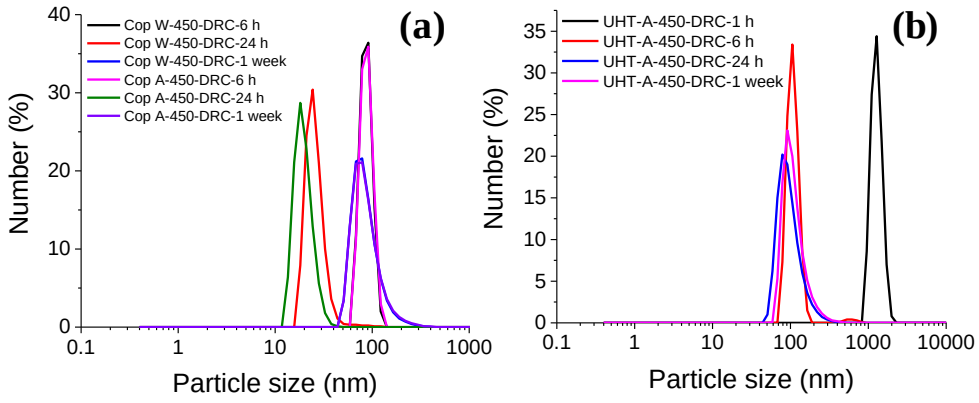


Figure D13. Particle size distribution curves from dynamic light scattering measurement (DLS) of reconstruction products (DRC) in water at room temperature with varying dispersion times: (a) Cop A450 and Cop W450 DRC products and (b) UHT A450 DRC products.

D.4.2. Transmission electron microscopy

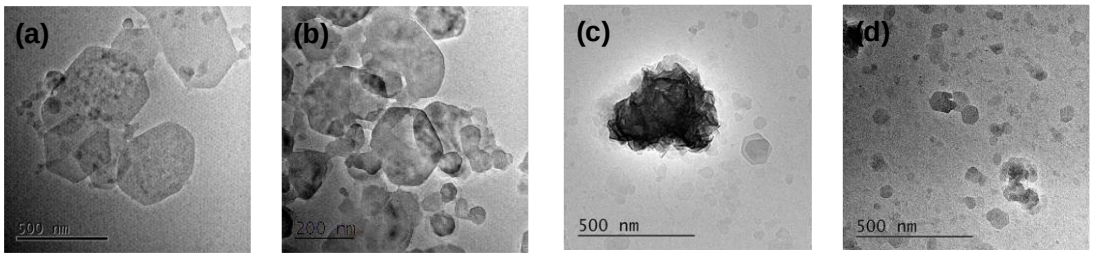


Figure D14. TEM images of DRC products after reconstruction in water at 80 °C: (a) Cop A450 DRC and (b) UHT 450 DRC, and Cop A450 DRC products after reconstruction at room temperature with different stirring speed for 1 hour: (c) 750 rpm and (d) 8,000 rpm.

D.4.3. Zeta potential measurement

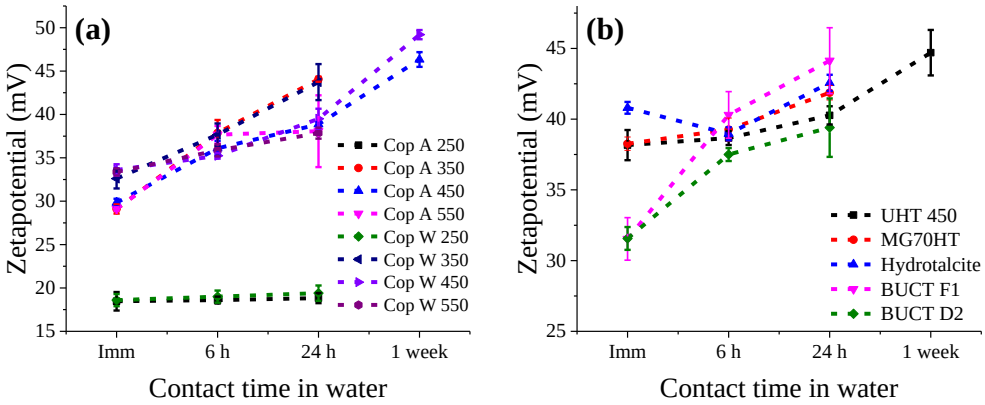


Figure D15. Zeta potential values of reconstruction products (DRC) in water at room temperature with varying dispersion times: (a) Cop A and Cop W DRC products and (b) DRC products from different LDHs.

D.5. Characteristic data for reconstructed LDHs in PVA: Effect of calcination temperature

D.5.1. Powder X-ray diffraction

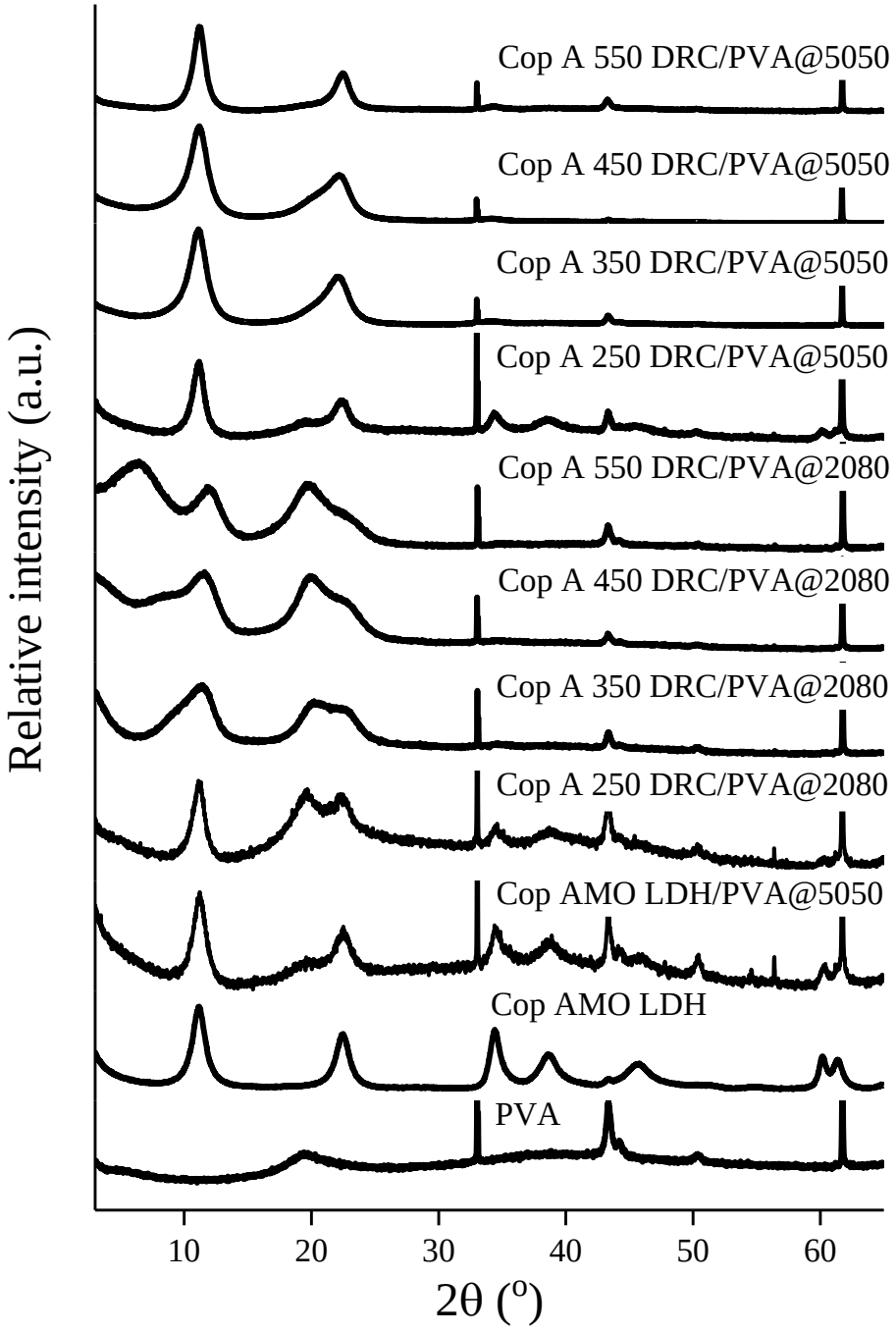


Figure D16. XRD patterns of Cop AMO LDHs after reconstruction directly in PVA Mowiol4-88 aqueous solution. (Bragg reflections due to sample holder were observed at 2θ = 43-44° and 50° and from silicon wafer were located at 2θ = 33°, 62° and 69°.)

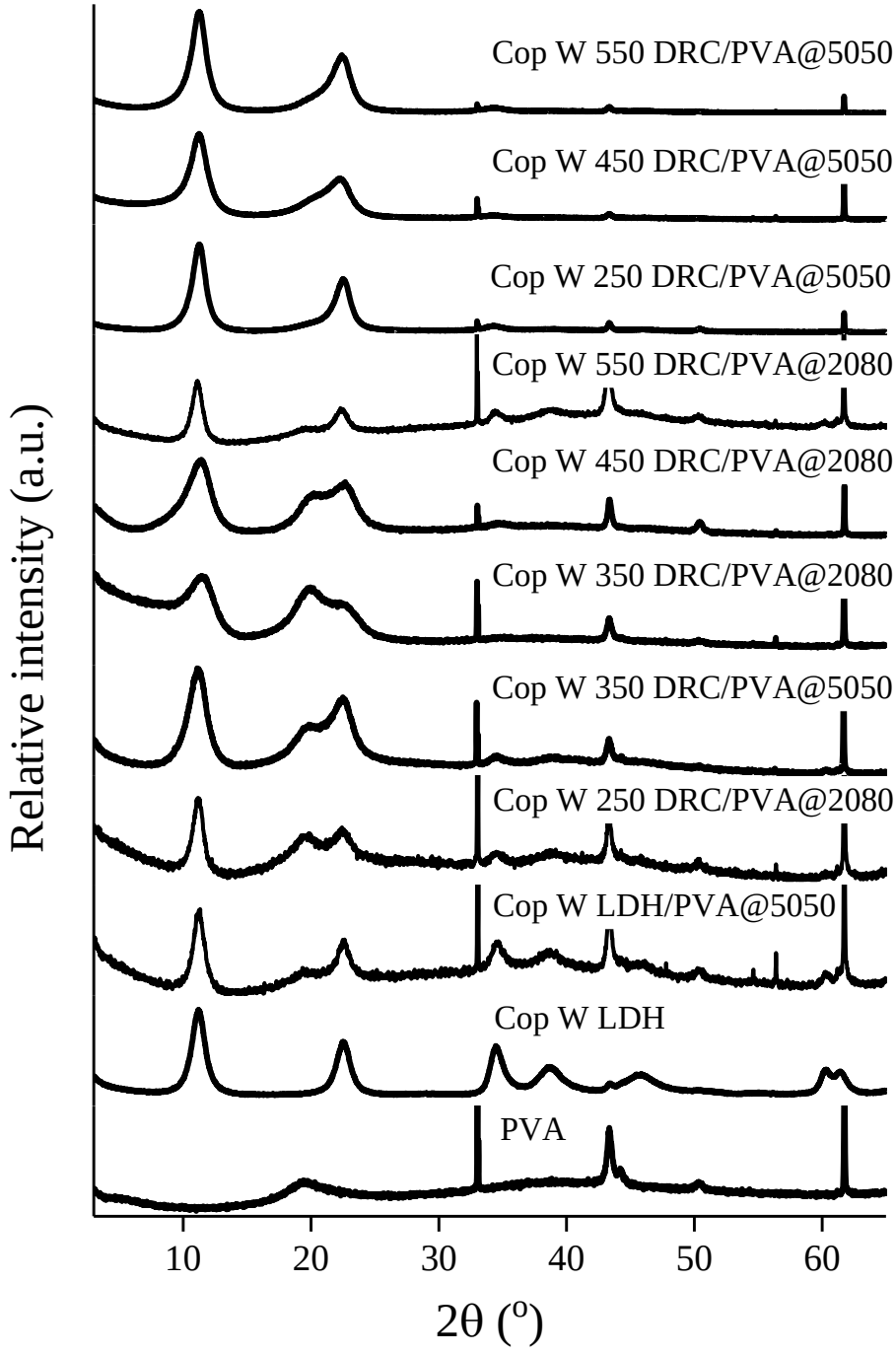


Figure D17. XRD patterns of Cop W LDHs after reconstruction directly in PVA Mowiol4-88 aqueous solution. (Bragg reflections due to sample holder were observed at 2θ = 43-44° and 50° and from silicon wafer were located at 2θ = 33°, 62° and 69°.)

D.5.2. Fourier transform infrared spectroscopy

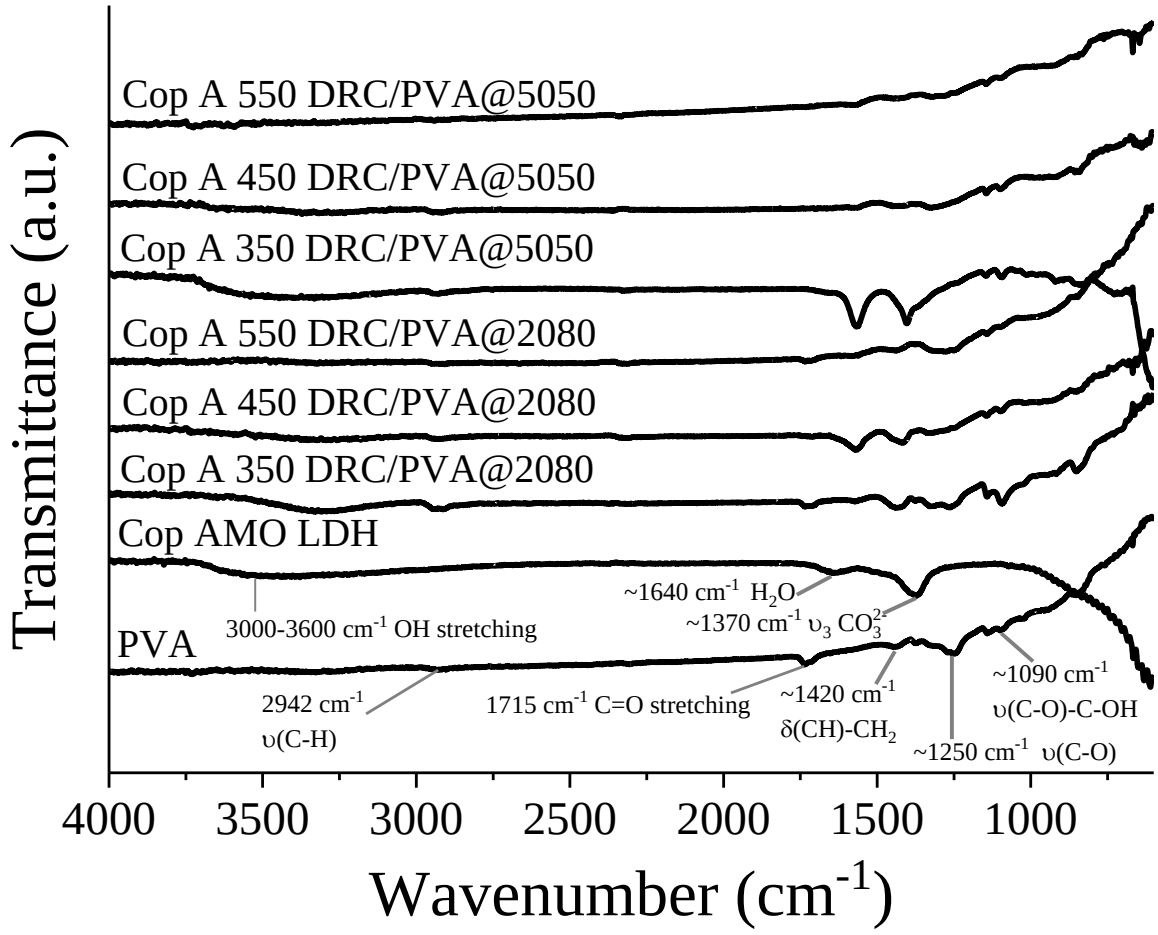


Figure D18. FTIR spectra of direct reconstruction products in PVA solution.

D.6. Characteristic data for reconstructed LDHs in PVA: Effect of the LDHs morphology

D.6.1. Powder X-ray diffraction

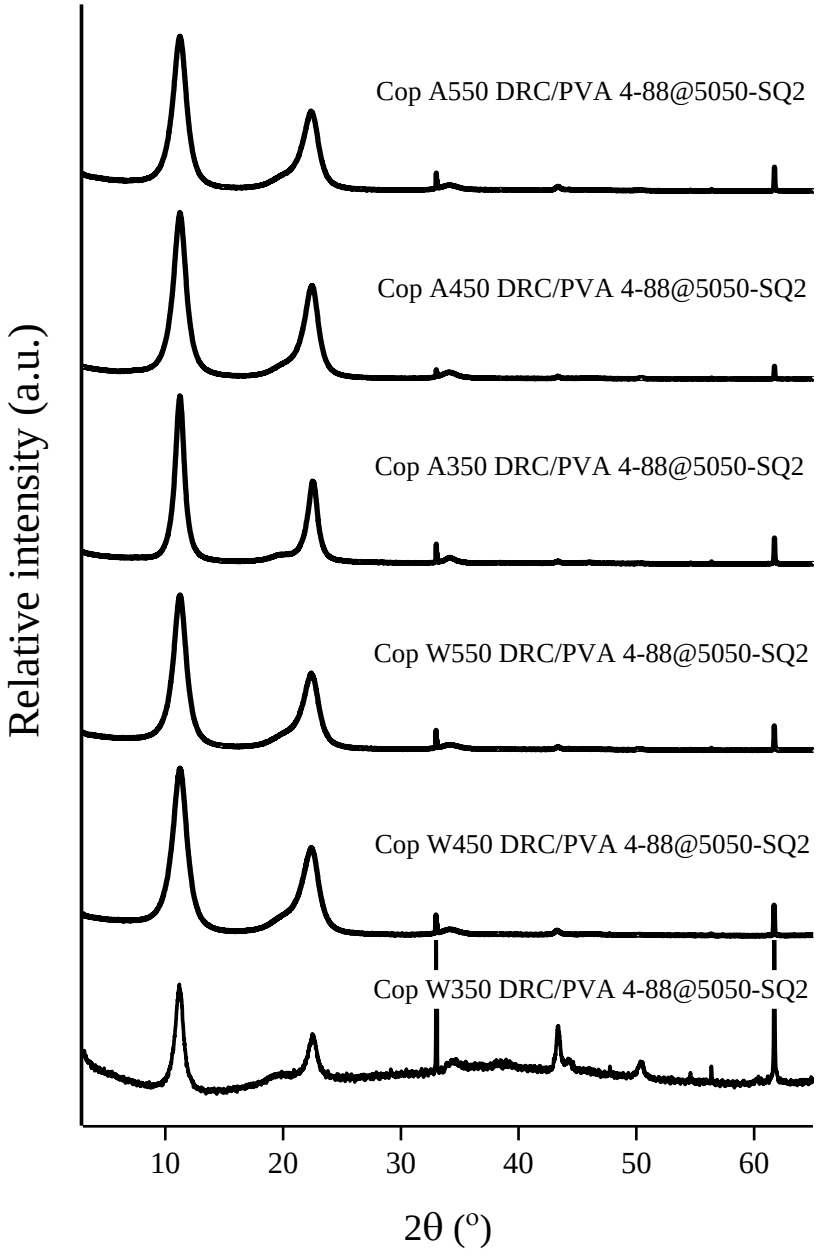


Figure D19. XRD patterns of reconstructed Cop A and Cop W DRC in PVA Mowiol 4-88 at ratio of 50/50 with sequence#2. (Bragg reflections due to sample holder were observed at 2θ = 43-44° and 50° and from silicon wafer were located at 2θ = 33°, 62° and 69°.)

D.6.2. Transmission electron microscopy

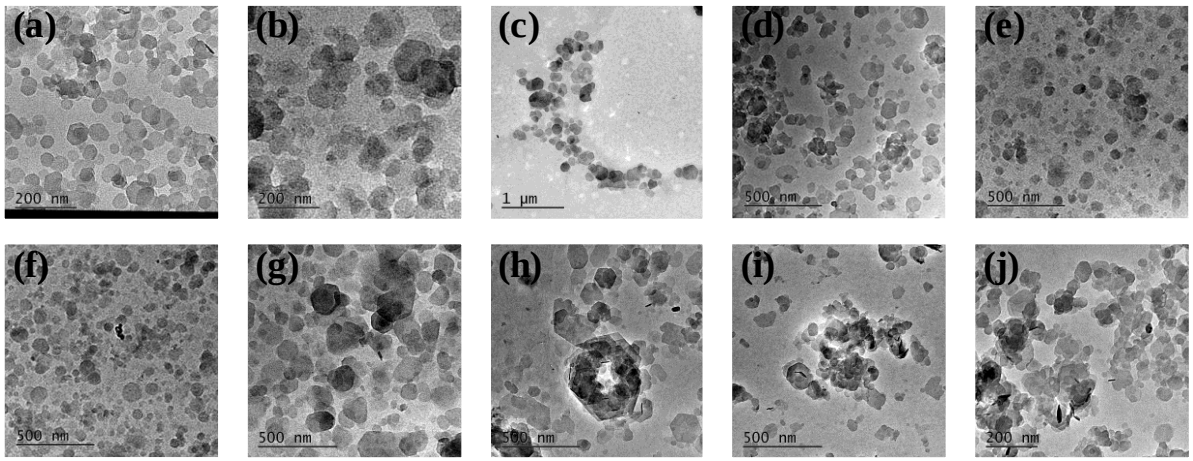


Figure D20. TEM images of DRC products after reconstruction with sequence#2 (in PVA Mowiol 4-88 aqueous solution at LDH/PVA ratio of 50/50); (a) Cop A350 DRC, (b) Cop A450 DRC, (c) UHT DRC, (d) M2 DRC, (e) M3 DRC, (f) M4 DRC, (g) MG70HT DRC, (h) Hydrotalcite Aldrich DRC, (i) BUCT F1 DRC and (j) BUCT D2 DRC.

D.6.3. Powder X-ray diffraction

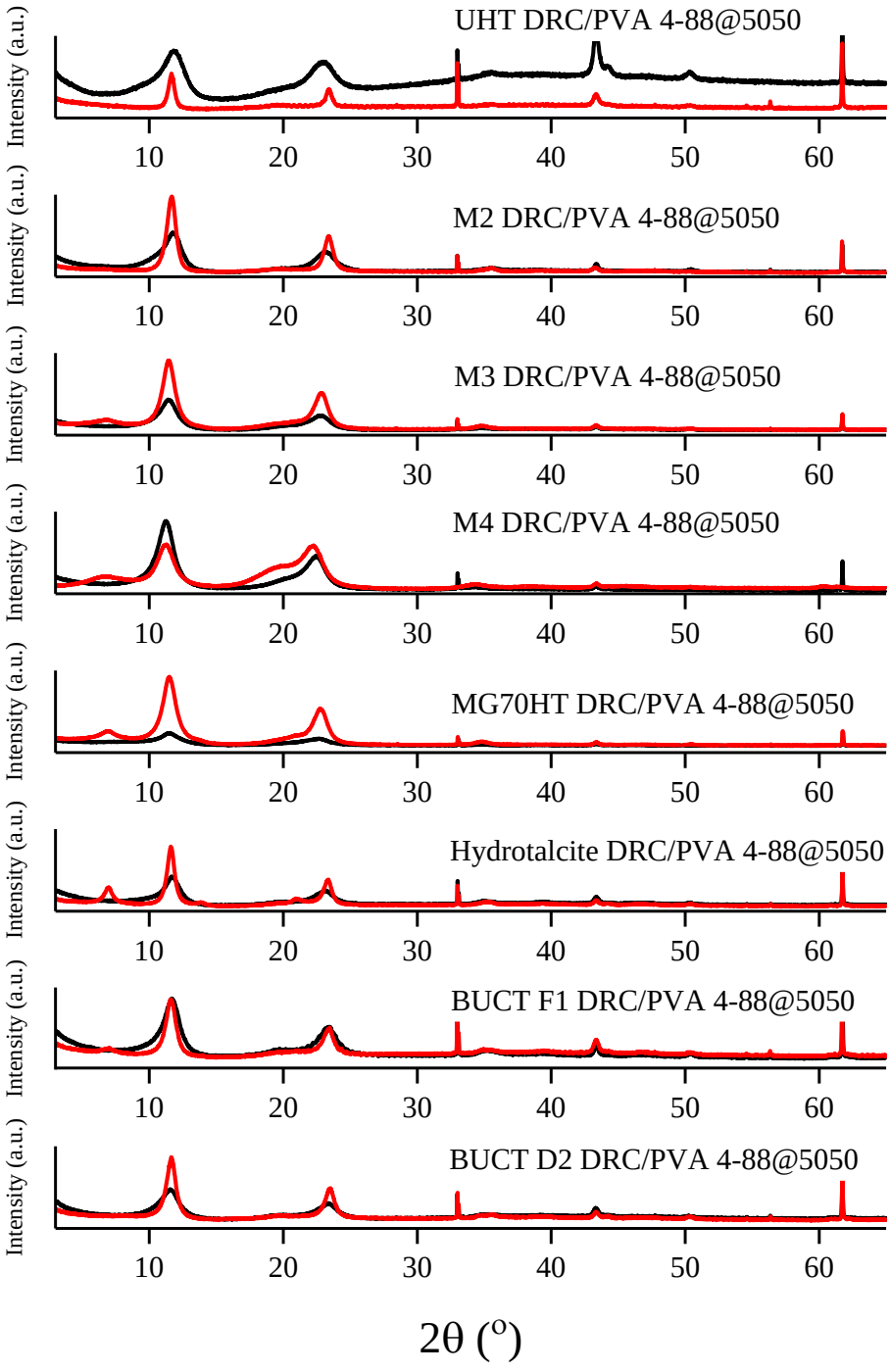


Figure D21. XRD patterns of different LDHs reconstructed in PVA Mowiol 4-88 at ratio of 50/50 with sequence#1(black) and #2 (red). (Bragg reflections due to sample holder were observed at 2θ = 43-44° and 50° and from silicon wafer were located at 2θ = 33°, 62° and 69°.)

D.7. Characteristic data for reconstructed LDHs in PVA: Effect of PVA properties

D.7.1. Powder X-ray diffraction

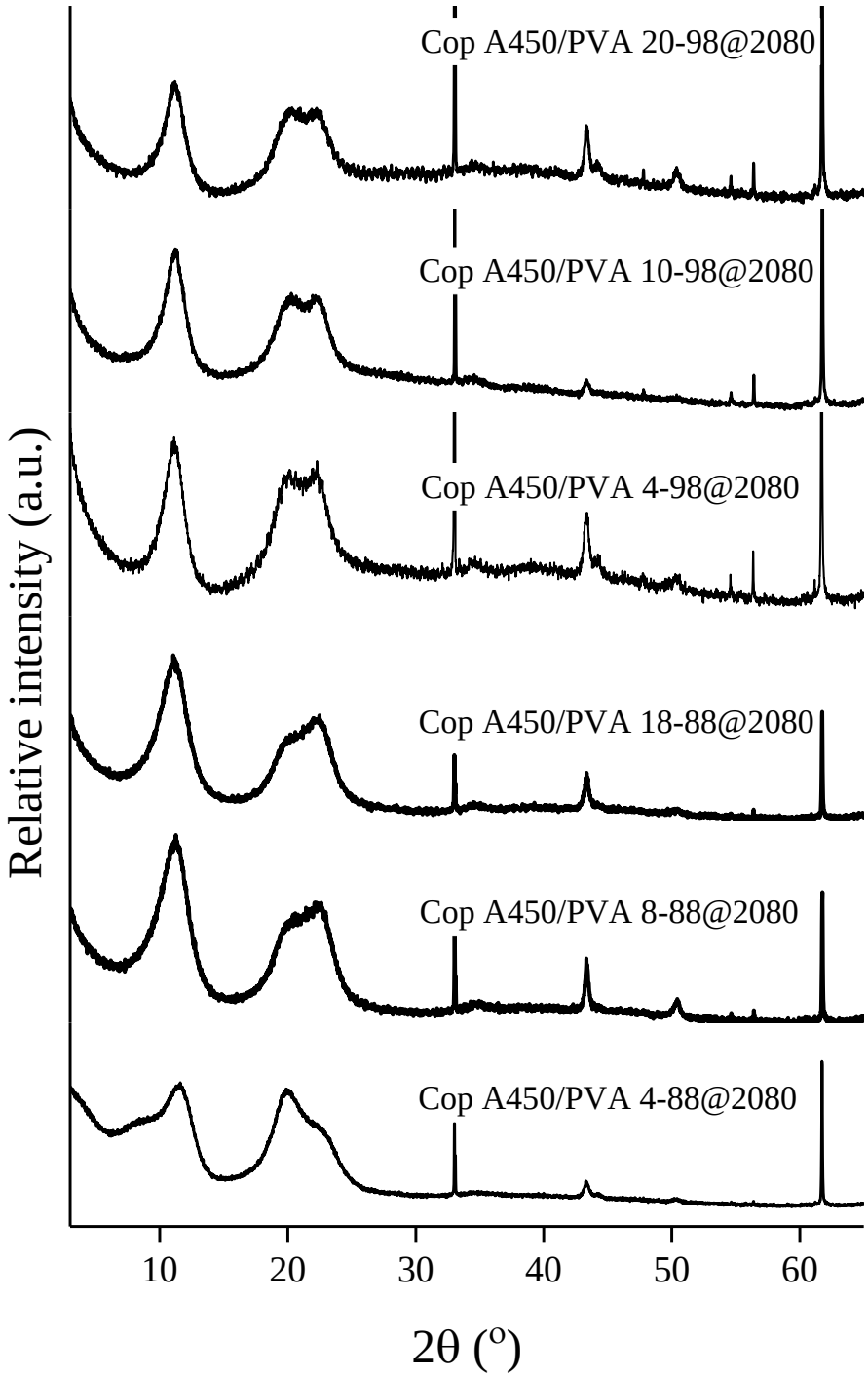


Figure D22. XRD patterns of reconstructed Cop A450 DRC in different PVA at ratio of 20/80 with sequence#1. (Bragg reflections due to sample holder were observed at 2θ = 43-44° and 50° and from silicon wafer were located at 2θ = 33°, 62° and 69°.)

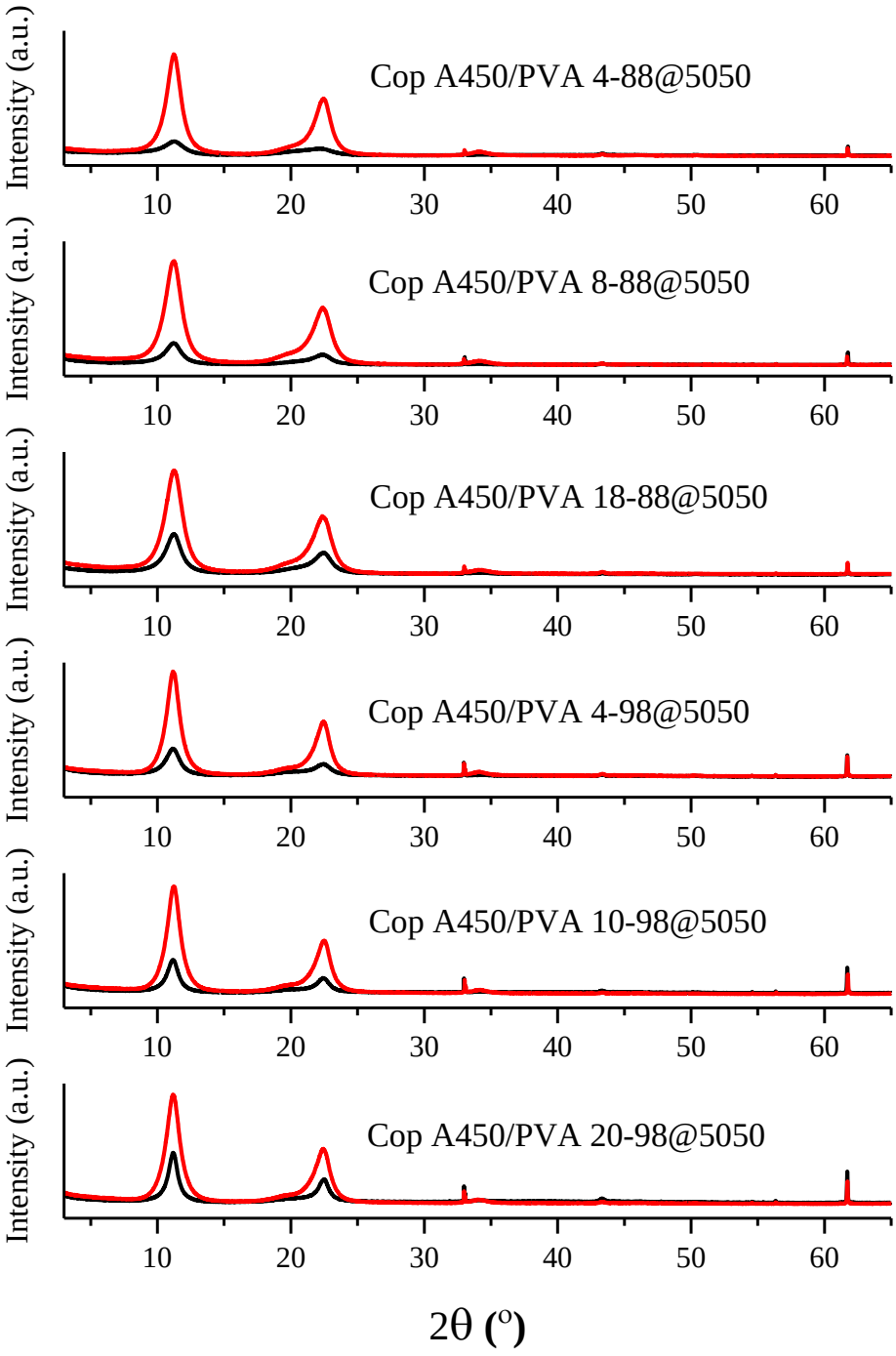


Figure D23. XRD patterns of reconstructed Cop A450 DRC in different PVA at ratio of 50/50 with sequence#1(black) and #2 (red). (Bragg reflections due to sample holder were observed at 2θ = 43-44° and 50° and from silicon wafer were located at 2θ = 33°, 62° and 69°.)

D.8. Coated film properties

D.8.1. Oxygen transmission rate data

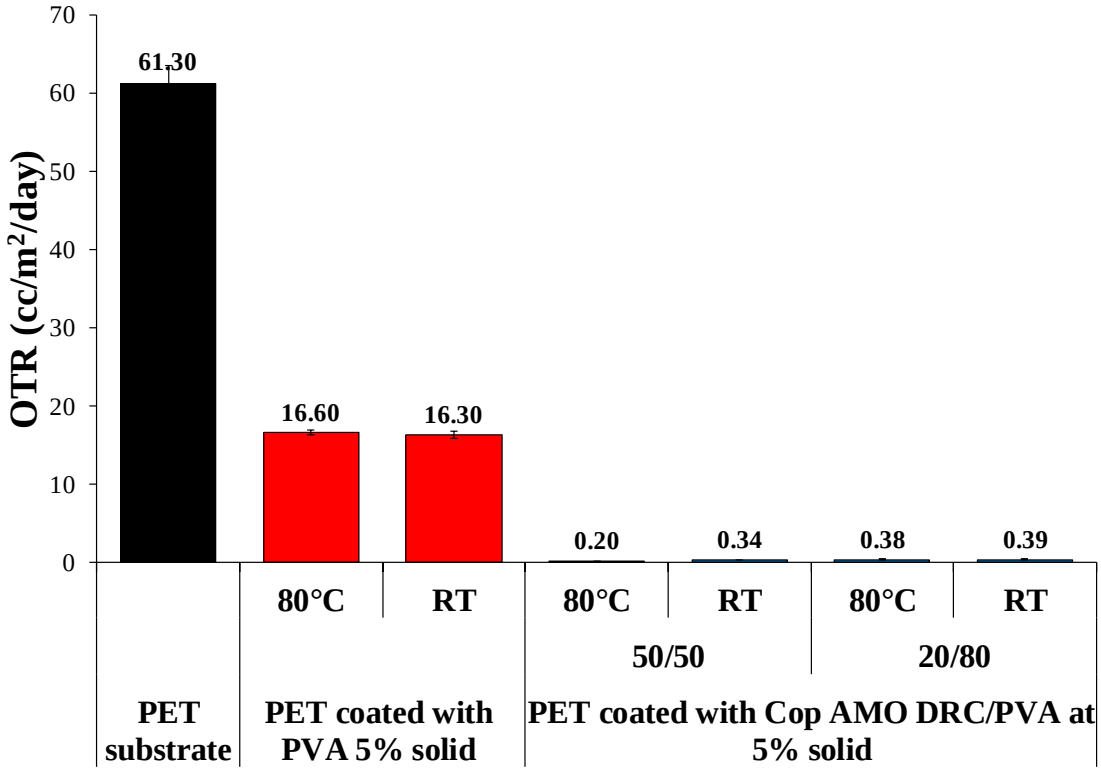


Figure D24. Oxygen transmission rate of coated film with Cop A DRC/PVA coating mixture prepared at room temperature vs. 80 °C (with sequence#1).

D.8.2. Coated film optical properties

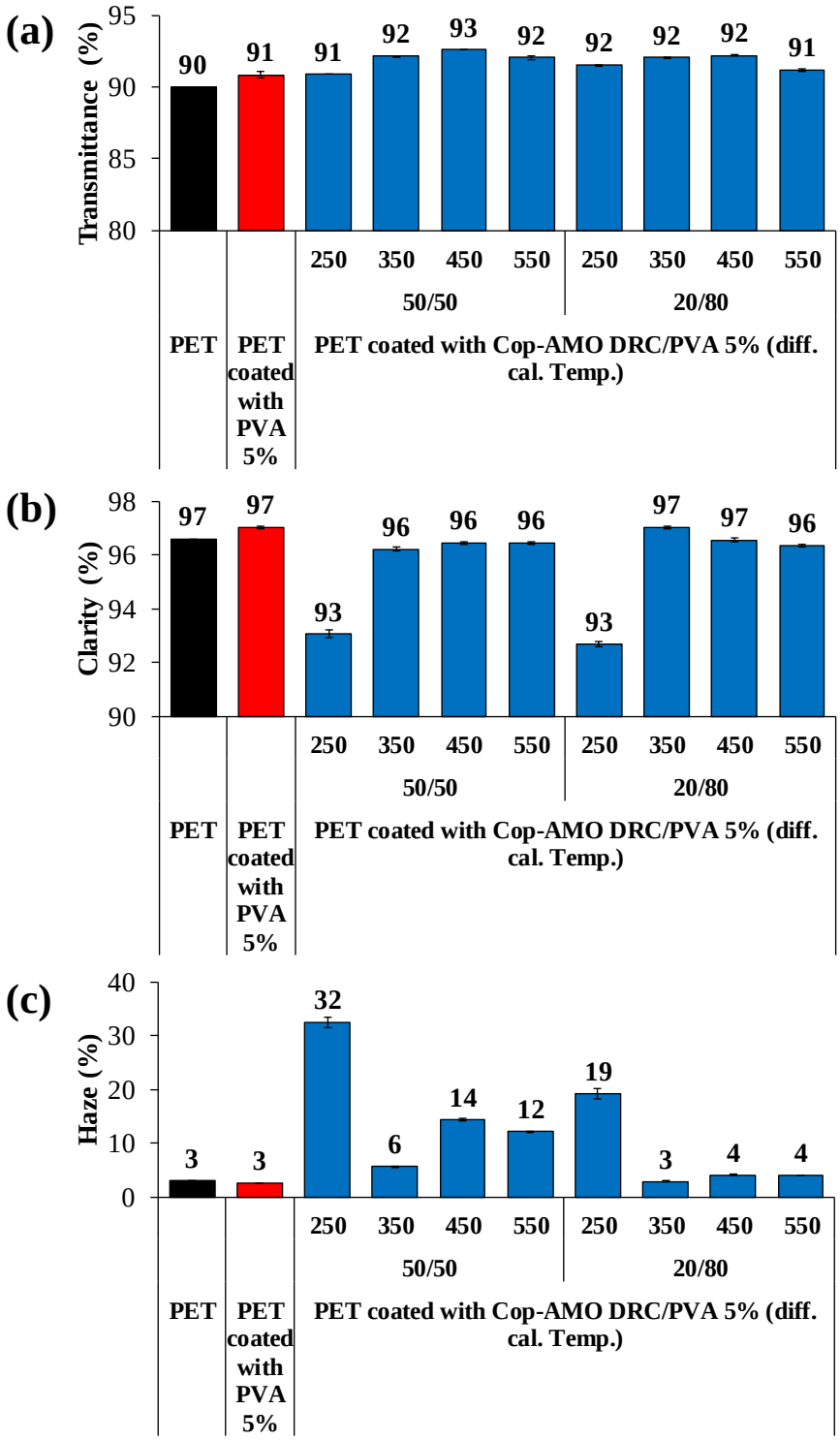


Figure D25. Optical properties of coated films with Cop A DRC/PVA at different calcination temperature: (a) transmittance, (b) clarity and (c) haze.

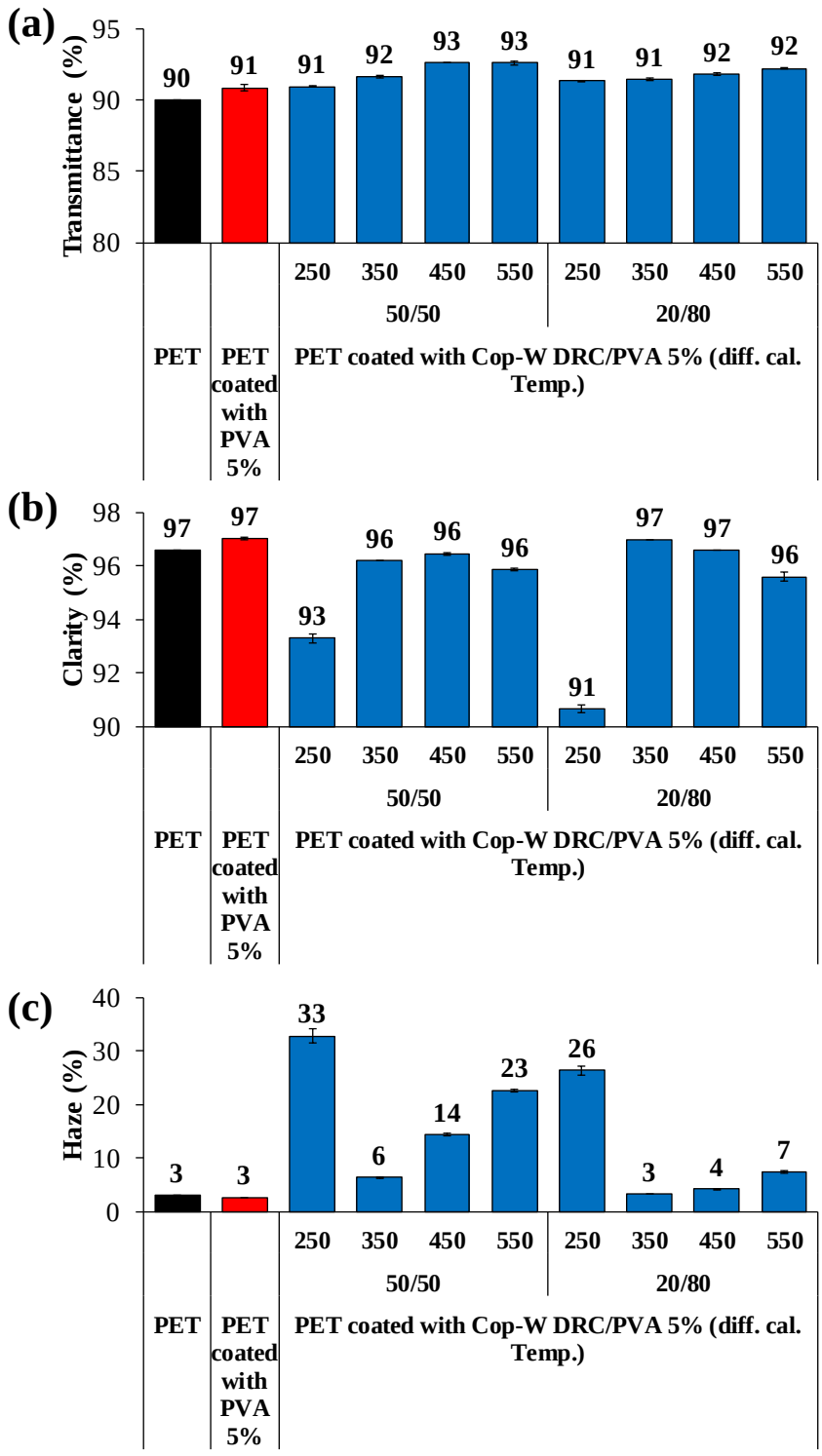


Figure D26. Optical properties of coated films with Cop W DRC/PVA at different calcination temperature: (a) transmittance, (b) clarity and (c) haze.

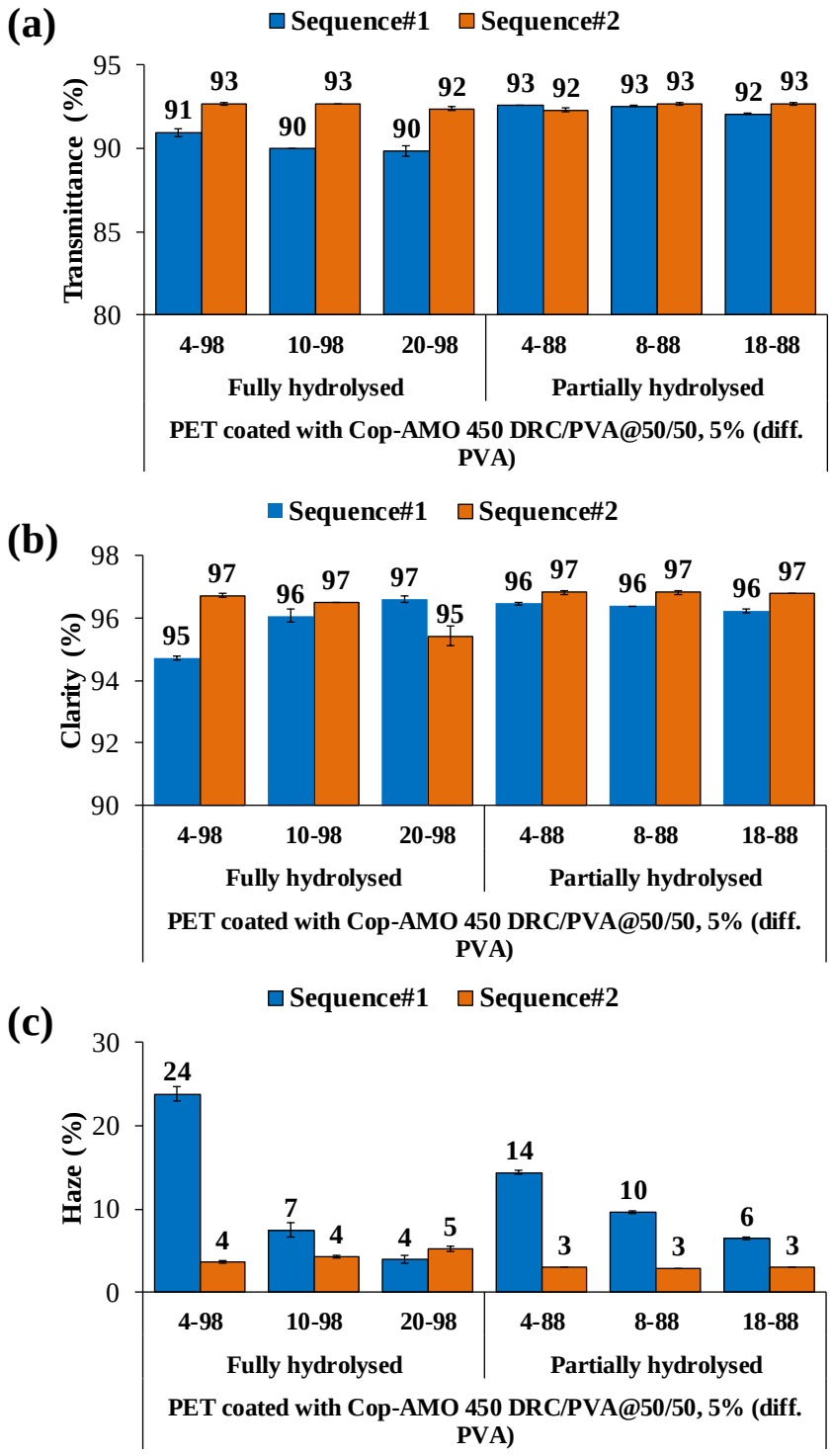


Figure D27. Optical properties of coated film with Cop A LDO/PVA with different PVA and adding sequence: (a) transmittance, (b) clarity and (c) haze.